### **Oxygen Transport Ceramic Membranes**

## **Final Report**

July 1999 – August 2008

Principal Author:
Prof. S. Bandopadhyay

Issued: August 2008

**DOE Award # DE-FC26-99FT40054** 

Petroleum Development Laboratory University of Alaska Fairbanks Fairbanks, AK 99775

### **Contributing Authors**:

- 1. Prof. Thomas W. Eagar, Dr. Harold R Larson, Mr. Raymundo Arroyave and Ms. Jocelyn L. Wiese Massachusetts Institute of Technology, Dept. of Material Science and Engineering
- 2. Prof. S. Bandopadhyay, Prof. Robert H. Trent, Dr. Nagendra Nagabhushana, Dr. Thangamani Nithyanantham and Dr. Somnath Biswas, University of Alaska Fairbanks
- 3. Dr. Y-W. Sin and Prof. H. U. Anderson, Materials Research Center, University of Missouri-Rolla
- 4. Prof. Alan Jacobson and Prof. C.A. Mims; University of Houston/University of
- 4. Prof. Niegel Brown, University of Illinois Chicago

### **DISCLAIMER**

This report was prepared as an account of work sponsored by an agency of the United States Government. Neither the United States Government nor any agency thereof, nor any of their employees, makes any warranty, express or implied, or assumes any legal liability or responsibility for the accuracy, completeness, or usefulness of any information, apparatus, product, or process disclosed, or represents that its use would not infringe privately owned rights. Reference herein to any specific commercial product, process, or service by trade name, trademark, manufacturer, or otherwise does not necessarily constitute or imply its endorsement, recommendation, or favoring by the United States Government or any agency thereof. The views and opinions of authors expressed herein do not necessarily state or reflect those of the United States Government or any agency thereof.

### **ABSTRACT**

The focus of this research was to develop new membrane materials by synthesizing different compounds and determining their defect structures, crystallographic structures and electrical properties. In addition to measuring electrical conductivity, oxygen vacancy concentration was also evaluated using thermogravimetry, Neutron diffraction and Mössbauer Spectroscopy. The reducing conditions (CO<sub>2</sub>/CO/H<sub>2</sub> gas mixtures with steam) as encountered in a reactor environment can be expected to have significant influence on the mechanical properties of the oxides membranes. Various La based materials with and without Ti were selected as candidate membrane materials for OTM. The maximum electrical conductivity of LSF in air as a function of temperature was achieved at < 600°C and depends on the concentration of Sr (acceptor dopant). Oxygen occupancy in LSF was estimated using Neutron diffractometry and Mössbauer Spectroscopy by measuring magnetic moment changes depending on the Fe<sup>3+</sup> and Fe<sup>4+</sup> ratio. After extensive studies of candidate materials, lanthanum ferrites (LSF and LSFT) were selected as the favored materials for the oxygen transport membrane (OTM). LSF is a very good material for an OTM because of its high electronic and oxygen ionic conductivity if long term stability and mechanical strength are improved. LSFT not only exhibits p-type behavior in the high oxygen activity regime, but also has n-type conduction in reducing atmospheres. Higher concentrations of oxygen vacancies in the low oxygen activity regime may improve the performance of LSFT as an OTM. The hole concentration is related to the difference in the acceptor and donor concentration by the relation p = $[Sr'_{La}] - [Ti^{\bullet}_{Fe}].$  The chemical formulation predicts that the hole concentration is, p = 0.8-0.45 or 0.35. Experimental measurements indicated that p is about  $\sim 0.35$ . The activation energy of conduction is 0.2 eV which implies that LSCF conducts via the small polaron conduction mechanism.

Scanning transmission electron microscopy (STEM) and electron energy loss spectroscopy (EELS) were used to develop strategies to detect and characterize vacancy creation, dopant segregations and defect association in the oxygen conducting membrane material. The  $pO_2$  and temperature dependence of the conductivity, non-stoichiometry and thermal-expansion behavior of compositions with increasing complexity of substitution on the perovskite A and B sites were studied. Studies with the perovskite structure show anomalous behavior at low oxygen partial pressures ( $<10^{-5}$  atm). The anomalies are due to non-equilibrium effects and can be avoided by using very strict criteria for the attainment of equilibrium. The slowness of the oxygen equilibration kinetics arises from two different mechanisms. In the first, a two phase region occurs between an oxygen vacancy ordered phase such as brownmillerite SrFeO<sub>2.5</sub> and perovskite SrFeO<sub>3-x</sub>. The slow kinetics is associated with crossing the two phase region. The width of the miscibility gap decreases with increasing temperature and consequently the effect is less

pronounced at higher temperature. The preferred kinetic pathway to reduction of perovskite ferrites when the vacancy concentration corresponds to the formation of significant concentrations of  $Fe^{2+}$  is via the formation of a Ruddlesden –Popper (RP) phases as clearly observed in the case of  $La_{0.5}Sr_{0.5}FeO_{3-x}$  where  $LaSrFeO_4$  is found together with Fe. In more complex compositions, such as LSFTO, iron or iron rich phases are observed locally with no evidence for the presence of discrete RP phase.

Fracture strength of tubular perovskite membranes was determined in air and in reducing atmospheric conditions. The strength of the membrane decreased with temperature and severity of reducing conditions although the strength distribution (Weibull parameter, m) was relatively unaltered. Surface and volume dominated the fracture origins and the overall fracture was purely transgranular. The dual phase membranes have been evaluated for structural properties. An increasing crack growth resistance was observed for the membranes heat-treated at 1000°C in air and N<sub>2</sub> with increasing crack length. The combined effect of thermal and elastic mismatch stresses on the crack path was studied and the fracture behavior of the dual phase composite at the test conditions was analyzed.

Ceramic/metal (C/M) seals are needed to form a leak-tight interface between the OTM and a nickel-base super alloy. It was concluded that Ni-based brazing alloys provided the best option in terms of brazing temperature and final operating conditions after analyzing several possible brazing systems. A mechanical testing procedure has been developed. This model was tested with model ceramic/metal systems but it is expected to be useful for testing concentric perovskite/metal seals.

# TABLE OF CONTENTS

	EXECUTIVE SUMMARY	1
Chapter 1	Development of Ceramic Membrane/Metal Joints	10
1.1	Introduction	10
1.2	Experiments using Zirconia-based ceramics	11
1.2.1	Other Metallization Approaches	13
1.2.2	Mechanical Properties of the Joints	14
1.2.3	Measurement of Shear Strength	15
1.2.4	Finite Element Modeling	17
1.2.5	Correlation between Strain Energy and Joint Shear Strength	18
1.2.6	Perovskite-Metal Interactions	19
1.2.7	Reaction Bonding Experiments with La-Sr-Fe-O Perovskites	20
1.2.8	Reaction Bonding Experiments with La-Sr-Cr-Fe-O Perovskites	24
1.2.9	Zirconia Ceramics as Diffusion Barriers	29
1.2.10	Modeling of Zirconia/Ti Interactions	30
1.3	Conclusion	33
Chapter 2	Determine material mechanical properties under conditions of	34
2.1	high temperature and reactive atmosphere Introduction	2.4
2.2	<b>Experimental Methods and Materials Characterized</b>	34 35
2.2.1	X-Ray Diffraction	35
2.2.2	Scanning Electron Microscopy	35
2.2.3	Thermal Analyses	35
2.2.4	Thermal Expansion Studies	35
2.2.5	Elastic Modulii Studies	35
2.2.6	Hardness and Fracture Toughness	36
2.2.7	Strength of Materials	37
2.2.7.1	Strength Determination at Elevated Tempertaure and reducing Atmosphere	37
2.2.7.2	C-Ring Method	40
2.2.7.3	4- point bend Method	12

2.2.8	Weibull Analysis	42
2.3	Materials Characterized	44
2.4	Results and Discussion	44
2.41	OTM (LSCFO) Tubes 20572-25PX and 20572-25T	44
2.4.1.1	Specimen Preparation	44
2.4.1.2	Results	45
2.4.1.2.1	Effect of Temperature, Pressure and Environment	45
2.4.1.2.2	Weibull modulus as a function of environment	51
2.4.1.2.3	Fracture and Fracture Mechanisms	53
2.4.1.3	Conclusion	56
2.4.2	OTM Tubes 20573 (a-f) $La_{0.2}Sr_{0.8}Fe_{0.8}Cr_{0.2}O_{3-\delta}$	57
2.4.2.1	Experimental procedure	57
2.4.2.2	Effect of Temperature, Pressure and Environment	58
2.4.2.3	Hardness and Indentation Fracture toughness of membranes	61
2.4.2.4	Fracture of membranes in oxygen chemical gradients	63
2.4.2.5	Results	64
2.4.2.6	Discussions	65
2.4.2.6.1	Stresses arising due to Specimen geometry and Oxygen transport	66
2.4.2.6.2	Stresses due to decomposition of the parent perovskite	67
2.4.3	Evaluation of OTM bars	70
2.4.3.1	Experimental Procedure	71
2.4.3.2.	Results and Discussions	72
2.4.3.2.1	Hardness and Fracture Toughness	73
2.4.3.2.2	Development Of Reliability Model for OTM's	76
2.4.3.2.3	Indentation flaw characterization in $La_{0.2}Sr_{0.8}Fe_{0.8}Cr_{0.2}O$	76
2.4.3.2.4	Indentation flaw characterization in a model $La_{06}Sr_{0.4}F$	77
2.4.3.2.5	Residual stresses effects in La <sub>0.2</sub> Sr <sub>0.8</sub> Fe <sub>0.8</sub> Cr <sub>0.2</sub> O <sub>3-x</sub>	81
2.4.3.2.6	Strength Degradation and slow crack growth (SCG) studies.	83
2.4.3.2.7	XRD Analysis	08

2.4.3.2.8	TGA/DTA analysis	111
2.4.4	Evaluation of OTM bars - LSFT & LSFT-CGO	113
2.4.4.1	Introduction	113
2.4.4.2	Experimental	113
2.4.4.3	Microstructure	114
2.4.4.3.1	Microstructural analysis of dual phase membranes (40-60vol%)	116
2.4.4.4	Density Measurements	120
2.4.4.5	Xray Diffraction Analyses	120
2.4.4.5.1	Energy Dispersive X-ray analysis (EDXA)	120
2.4.4.5.2	X-ray diffraction analysis of the membranes	122
2.4.4.6	Hardness and Fracture Toughness	124
2.4.4.6.1	Hardness of the LSFT and dual phase membranes	124
2.4.4.6.2	Crack Propagation behavior	134
2.4.4.6.3	Fracture Toughness of LSFT and dual phase membranes	135
2.4.4.7	Flexural strength and Fractography	141
2.4.4.8	Thermal Analyses	157
2.4.4.9	Thermal Expansion Studies	164
2.4.4.9.1	Chemical Expansion	164
2.4.5	Evaluation of OTM Supports – YSZ	168
2.4.5.1	Experimental	168
2.4.5.2	Flexural strength and Fractography	169
2.4.5.3	Slow crack growth studies	177
2.5	Conclusion	184
2.6	List of Acronyms and Abbreviations	185
2.7	References	185
2.8	Publications	185
Chapter 3	Preparation and Characterization of Dense Ceramic oxygen Permeable Membranes	187
3.1	Introduction	187
3.2	Experimental	187

3.2.1	Electrical Conductivity	187
3.2.2	Thermogravimetric analysis (TGA)	187
3.2.3	Neutron Diffraction	188
3.2.4	Mössbauer Spectroscopy	189
3.2.5	XRD	190
3.2.6	Impedence Spectroscopy	190
3.3	Results and Discussion	190
3.3.1	Studies of Ferrites for OTM using Electrical Conductivity, Neutron Diffractometry and Mössbauer Spectroscopy	190
3.3.1.1	Electrical Conductivity of La <sub>1-x</sub> Sr <sub>x</sub> FeO <sub>3-δ</sub>	190
3.3.1.2	Neutron Diffraction and Mössbauer Spectroscopy Study for LSF	193
3.3.2	Study of La <sub>0.2</sub> Sr <sub>0.8</sub> Fe <sub>0.55</sub> Ti <sub>0.45</sub> O <sub>3-8</sub> (LSFT) for OTM using Electrical conductivity, Seebeck coefficient and Mössbauer Spectroscopy	198
3.3.2.1	Ti doped LSF	198
3.3.2.2	LSFT Powder Preparation	199
3.3.2.3	Oxygen Occupancy Study	201
3.3.2.4	Electrical Conductivity and Seebeck Coefficient of LSFT in Air	204
3.3.2.5 3.3.2.6	Electrical Conductivity and Seebeck Coefficient as a function of oxygen activity Mössbauer Spectroscopy	207
3.4	Conclusions	210
3.5	References	214
3.6		215
	Publication from Program	215
Chapter 4	Assessment of Microstructure of the Membrane Materials to Evaluate the Effects of vacancy-Impurity Association, defect Clusters, and Vacancy Dopant Association on the Membrane Performance and Stability	218
4.1	Introduction	219
4.2	Experimental Techniques	224
4.3	Results	224
4.4	Discussion	233
4.5	Conclusions	237
4.6	References	239
4.7	Publication resulted from this research	241

Chapter 5	Measurement of Surface Activation/Reaction Rates in Ion Transport Membranes using Isotope Tracer and Transient Kinetic Techniques.	244
5.1	Introduction	244
5.2	Experimental	245
5.3	Sample Preparation	245
5.3.1	$SrFeO_{3-x}$	245
5.3.2	$La_{0.5}Sr_{0.5}FeO_3$	246
5.3.3	$La_{0.6}Sr_{0.4}Fe_{0.8}Co_{0.2}O_{3-x}$	247
5.3.4	$La_{0.2}Sr_{0.8}Fe_{0.8}Cr_{0.2}O_{3-x}$	247
5.3.5	$La_{0.5}Sr_{0.5}Fe_{0.8}Ga_{0.2}O_{3-x}$	248
5.3.6	$La_{0.2}Sr_{0.8}Fe_{0.55}Ti_{0.45}O_{3-x}$	249
5.4	Experimental Methods	252
5.4.1.	Electrical Conductivity Measurements using an Electrochemical Cell	252
5.4.2	Solid-state coulometric titrations	253
5.4.3	Polarization Measurents	255
5.4.4	Seebeck Measurements	256
5.4.5	Thermal Expansion	257
5.4.6	Conductivity Relaxation Studies	258
5.5	Results and Discussion	259
5.5.1	SrFeO <sub>3-x</sub>	259
5.5.1.1	Introduction	259
5.5.1.2	Coulometric titration measurements of the oxygen non-stoichiometry	260
5.5.1.3	Point defect model	262
5.5.1.4	Conductivity Measurements	263
5.5.2	$La_{0.5}Sr_{0.5}FeO_{3-x}$ and $La_{0.2}Sr_{0.8}FeO_3$	266
5.5.3.	$La_{0.2}Sr_{0.8}Fe_{0.8}Cr_{0.2}O_{3-x}$ .	267
5.5.3.1	Electrical Conductivity	267
5.5.3.2	Stoichiometry	270
5.5.3.3	Phase Transition	270
5.5.3.4	Thermodynamics	272
5.5.3.5	Electrical conductivity relaxation	273

5.54	$La_{0.5}Sr_{0.5}Fe_{0.8}Ga_{0.2}O_{3-x}$	275
5.5.4.1	Electrical Conductivity	275
5.5.5	$La_{0.2}Sr_{0.8}Fe_{0.55}Ti_{0.45}O_{3-x}$	277
5.5.5.1	Stoichiometry	277
5.5.5.2	Conductivity	280
5.5.5.3	Polarization Measurements	282
5.5.5.4	Thermopower measurements	285
5.5.5.5	Thermal Expansion Data	285
5.5.5.6	Neutron Diffraction	290
5.5.5.7	Non-equilibrium behavior	292
5.6	Conclusions	297
5.8	List of Acronyms and Abbreviations	298
5.9	Publications	298
5.10	Presentations	300
5.11	References	301

# **LIST OF FIGURES**

Zirconia/Metal Joint using Cu-10Ti Braze Alloy

Figure 1

Figure 2	Zirconia - Cu-Zr Interactions
Figure 3	Use of alternative metallization techniques: Reactive coating with Ni- based brazing alloys
Figure 4	Mechanical tests specimens
Figure 5	Relationship between joint overlap length and joint shear strength. (L) 0.0035" braze thickness. (R) 0.005" braze thickness
Figure 6	Relationship between joint overlap and total joint strain energy
Figure 7	Correlations between measured joint shear strength and calculated elastic, plastic, and total strain energy in the filler metal.
Figure 8	a) Ceramic Membrane/Braze/Metal Interface b) Perovskite/Metal Joints Using Ni-
	based Brazing Alloys
Figure 9	Ceramic/braze interface. Compositions obtained using EDS.
Figure 10	EDS spectra of different zones shown in Figure 9
Figure 11	Perovskite/Cr/Ni/Inconel Joint. Secondary and Backscattered Image
Figure 12	Perovskite/Ni-B/Inconel Joint SEM 807x
Figure 13	Interface between Perovskite and Ni-based Brazing Alloys. Ti-based diffusion barrier was used.
Figure 14	Interfacial modification of perovskite substrates.
Figure 15	Zirconia/Ni-TLPB Alloy/Ni-based Super Alloy Interface.
Figure 16	Ti-O Phase Diagram
Figure 17	Concentration profile of a Ti layer in contact with a zirconia substrate, according to the solution of the Cahn-Hilliard equation.
Figure 18	Autoclaves and fixtures used for strength test
Figure 19	Laboratory set up for testing strength of ceramic membranes for tubes
Figure 20	Laboratory set up for testing strength of ceramic membranes for bars
Figure 21	Stress distribution in a C-ring specimen subjected to uniaxial compressive load. The stress is tensile on the outer skin of the tube $(r_o)$ and compressive at the inner surface $(r_1)$

Figure 22	Schematic of the C-ring test adapted for the tubular OTM materials.
Figure 23	Sampling Procedures for random sampling of specimens for strength evaluation
Figure 24	Weibull studies on reference material: 99.8% Alumina
Figure 25	Dimensional variation observed in C-ring specimens for Weibull Modulus study
Figure 26	Macro-fracture observed in 20572 tubes: a) Smooth fracture in 20572-25Px and b) Jagged fracture in 20572-25T
Figure 27	Transgranular fracture in: a) 20572-PX and b) 20572-PT. Instances of microcleavage are evident in 20572-25T
Figure 28	Transgranular fracture in: a) 20572-PX and b) 20572-PT. Instances of microcleavage are evident in 20572-25T
Figure 29	Weibull graphs on 20572 tubes. a) 20572-25Px and b) 20572-25T
Figure 30	Influence of temperature, pressure and environment on the fracture strength of perovskite tubes
Figure 31	Dimensional variation recorded in the `as-processed' tubes for evaluation of fracture strength for Weibull Analysis. a) for N <sub>2</sub> and b) for CO <sub>2</sub> /CO environment
Figure 32	Weibull plots of `as-processed' in: a) $N_2$ and b) $CO_2/CO$ environment
Figure 33	Transgranular fracture observed in samples tested in $N_2$ at 1000°C illustrating: a) grains with accentuated grain boundary relief and b) Grain boundary cavitations.
Figure 34	Transgranular fracture in a single grain indicating : a) Precipitation and pull out in the grains and b) banded structure in the grain
Figure 35	Fracture observed in samples tested in 90%CO <sub>2</sub> /10%CO.
Figure 36	Influence of temperature, and pressure on the fracture strength of perovskite
Figure 37	Effect of oxygen partial pressure on the strength of Perovskite tubes
Figure 38	X-ray plot of the Perovskites after exposure to the environment. The phases formed are: (X) SrCrO <sub>3</sub> ; (O) SrFe <sub>12</sub> O <sub>12</sub> ; (C) SrO and (D) CrFeSr <sub>2</sub> O <sub>5.6</sub>
Figure 39	Vickers indent in the material for fracture toughness studies. The arrows mark the crack extending from the indent tip and used for computing fracture toughness

Figure 40 A schematic diagram of a membrane reactor. Figure 41a Gradient Fracture in N<sub>2</sub> at 1000°C Figure 41b Fracture gradient in CO<sub>2</sub>/CO at 1000°C Figure 42 Higher magnification viewgraphs of gradient fracture in reducing conditions. (a), (c) and (e) are in Nitrogen and (b), (d) and (f) are in 90%CO<sub>2</sub>/CO atmosphere. Figure 43 Intergranular fracture observed in a) Nitrogen and (b) 90%CO<sub>2</sub>/CO environment. In Nitrogen, the grains are broken down while in CO<sub>2</sub>/CO fine precipitates of SrO are formed on the surfaces of the grain. Figure 44 a) ASTM standard type A samples of LSF, LSC and LSCF composition to study strength degradation with environment and b) ASTM standard type B samples of LSFCO provided by Praxair. Figure 45 ASTM fixtures designed for 4-Point flexure testing of membrane bars. A) ASTM D and b) ASTM A Figure 46 XRD analysis of LSCF- 8282 prior to and after sintering indicating retention of parent perovskite structure. Figure 47 Vickers indents on LSCF – 8282 for fracture toughness and crack growth studies Figure 48 Hardness and toughness variation in La<sub>0.2</sub>Sr<sub>0.8</sub>Co<sub>0.8</sub>Fe<sub>0.2</sub>O<sub>3-8</sub> Figure 49 An indented and cation distribution along a growing crack in the La<sub>0.2</sub>Sr<sub>0.8</sub>Fe<sub>0.8</sub>Cr<sub>0.2</sub>O<sub>3-x</sub> system: b) close to the indent; c) at half distance from the indent and d) at the crack tip Figure 50 An indented flaw exposed to air at 1000°C in the A) LSCF and B) La<sub>06</sub>Sr<sub>0.4</sub>FeO<sub>3-x</sub> system. The crack tip shows healing (in red) upon exposure as also contributing to more damage (in blue) Figure 51 Cross-section of an indent flaw formed at load P = 9.8 N in a) LSCF -8282 and b) LSFCO-2. Fracture in LSCF-8282 is intergranular as compared to transgranular mode in LSCFO-2 Figure 52 Stress fields around an indent flaw formed at load P = 9.8 N in LSFCO-2. The median crack was ~ 50μm as compared to ~100μm in LSCF-8282 Figure 53 Crack opening displacement as a function of distance behind the crack tip for

LSFCO-2. The profile provided a value of  $K_{tip} = 0.9 \text{ MPa.m}^{0.5}$ 

An indented crack exposed to environment and elevated temperature shows reduction of radial crack lengths. a) In air at  $1000^{\circ}$ C ( $P_{O2} = -0.7$  atm.) and b) in  $N_2$ /Air at  $1000^{\circ}$ C ( $P_{O2} = -0.7$ ) atm.)

Figure 54

= -4/-0.7 atm.)

Figure 55	Thermally etched microstructure of a) LSFCO-2 and b) LSFCO-3	
Figure 56	Load-displacement trace of OTM bars test in flexure at varying strain rates.	
Figure 57	OTM flexural strength tested in varying stress rates at RT in air	
Figure 58	OTM flexural strength at varying stress rates in N <sub>2</sub> /Air at 1000°C.	
Figure 59	Flexure strength as a function of stress rate (log/log plot).	
Figure 60	Testing configuration for crack growth studies	
Figure 61	Load-displacement plots for fracture toughness studies in environment	
Figure 62	Load-displacement plots for fatigue pre-cracking in environment conditions.	
Figure 63	Pre-cracking fixture and stable crack growth in indented dense OTM samples. a) Vickers indent along the center line; b) Bridge Cracking fixture; c) 4-Point failure at the pre-cracked point; d) Stereo micrograph indicating stable crack growth and fast fracture.	
Figure 64	OTM bar loaded to fracture after pre-cracking by Bridge-Compression technique	
Figure 65	Surface flaw as fracture origin	
Figure 66	Intergranular fracture in OTM bars	
Figure 67	(a) Intergranular fracture of grains along OTM with presence of fine precipitates(b)Trans/Intergranular fracture and formation of fine precipitates	
Figure 68	Interaction of microstructure with secondary cracks. Increased formation of precipitates in observed	
Figure 69	Transgranular fracture and presence of two types of precipitates	
Figure 70	Slow transgranular crack growth with increased formation of two types of precipitates	
Figure 71	Fast Transgranular fracture at the edge. The so called compressive curl consistently leads to transgranular Fracture	
Figure 72	XRD plots of the OTM samples in a) as received, b) exposed to Air at $1000^{\circ}$ C; c) exposed to $N_2/Air$ at $1000^{\circ}$ C and fractured at varying stress rates in $N_2/Air$ at $1000^{\circ}$ C	
Figure 73	XRD of the major peaks (2Theta = 32 and 77) plots of the OTM samples indicating a perceptible shift and decomposition of the single peaks	

Figure 74	Flow chart of decomposition route for LSFCO	
Figure 75	Refinement of OTM material in as received and as exposed to air and $N_2$ /air a 1000°C. Insets b and c, indicate the observed shift in $2\theta$ values	
Figure 76	Refinement of OTM material in as received and fractured in air (RT) and $N_2$ /air a 1000°C. Insets b and c, indicate the observed shift in $2\theta$ values	
Figure 77	Refinement of OTM material fractured in $N_2$ /air at 1000°C at different stressing rates. Insets b and c, indicate the observed decomposition of the major peak and shift in $2\theta$ values	
Figure 78	Weight change, DTA and temperature data as a function of time.	
Figure 79	Post-fracture thermal analysis of LSFCO-3 OTM material	
Figure 80	Post-fracture thermal analysis of LSFCO-3 OTM material.	
Figure 81	Stoichiometry (3- $\delta$ ) of the fractured samples calculated from weight change measurements in a TGA	
Figure 82	TGA/DTA run on samples with prior thermal/stress history negated by initial heating in N <sub>2</sub> .  1: As received, 2: 600μm/min, 3:60μm/min, 4: 6μm/min and 5: 3μm/min	
Figure 83	a) Combined Temperature/Pressure test run to evaluate crack growth in OTM membranes. b) Increase in hydrostatic pressure leads to increased stress for crack growth and final fracture.	
Figure 84	Fracture in OTM membranes under combined elevated temperature and pressure loading. The fracture origins are at the multiple indents placed on the tensile surface.	
Figure 85	X-ray analysis of fractured OTM membranes under combined elevated temperature and pressure loading. 1) 25 PSI and 2)50 PSI.	
Figure 86	TGA/DTA analysis of fractured OTM membranes under combined elevated temperature and pressure loading. 1) 25 PSI and 2)50 PSI.	
Figure 87	Fully sintered and dense dual phase membranes.	
Figure 88	SEM microstructure of LSFT sintered at 1400°C. Microstructure (a) shows a densely packed grain structure and the closer observation (b) reveals the presence of two types of grains, platy hexagonal grains and closely packed fine grains.	

- Figure 89 Grain size and distribution in sintered LSFT; (a) shows the average grain size and (b) exhibits the grain size distribution. The bimodal distribution of grains is clearly seen in the plot as well as in the microstructure. Figure 90 SEM micrographs of dual phase membrane. The dense spherical regions (which are dark in color in Figure 35a) are enclosed by the less dense, continuous phase which accommodates the pores. The closer observation (Figure 35b) shows that the dense regions have a clear circular boundary or crack. The white arrow marks are used to point the circular cleavage. Figure 91 Size distribution of the discontinuous phase in the dual phase membrane microstructure. Figure 92 (a) The circular crack or cleavage at higher magnification. The crack is transgranular and encompasses a dense region; (b) Micrograph of the dense region. Figure 93 Microstructures of the dual phase membrane. The Figure (a) shows the presence of pores which are clustered together. The closer observation of the microstructure shown in Figure (b) reveals that the grain growth is controlled in the porous region. Figure 94 A crater is shown in the micrograph which might have formed during removal of organic additives during the sintering. Figure 95 Grain size distribution in the dual phase microstructure. Figure 96 EDX analysis spectrum of LSFT membrane. Figure 97 EDX analysis spectrum of dual phase membrane. Figure 98 XRD plots of the LSFT membranes. Figure 99 XRD plots of the dual phase membranes. Hardness of the LSFT membrane Figure 100 Figure 101 Hardness of the dual phase membrane. Figure 102 (a) Median and (b) Palmqvist crack systems induced by Vicker indentation.
- Figure 103 Vicker's indentations in (a-b) LSFT membrane and (c-d) in dual phase membrane. Note in the LSFT-CGO the crack patterns are mainly median cracks and in dual phase the Palmqvist cracks are also seen (in Figure 46-a). In Figure 46-c the

Figure 104	Influence of microstructural heterogeneities on initiation and propagation of cracks. The indentation is made on the dense region in the dual phase microstructure. While the crack has not formed in the dense region, a crack has emanated from the diagonal that is closer to the porous region.
Figure 105	Crack propagation in the LSFT membrane (a) grain bridging (b) crack deflection by boundaries and pores
Figure 106	Discontinuous crack and rupture of bridging grain. Note the extensive grain bridging all along the crack length (a). A closer observation of the other crack reveals the effect of bridging ligaments on closing the crack propagation (b). Fina rupture of the grain (c)
Figure 107	Surface traction in an advancing crack caused by frictional interlocking of grains
Figure 108	Crack bridging by dense region in the dual phase membrane.
Figure 109	Crack propagation behavior in the dual phase membrane. Crack deflection by the dense regions.
Figure 110	Crack branching and frictional interlocking of grains
Figure 111	Dependence of L/a of LSFT on indentation load
Figure 112	Dependence of L/a of dual phase membrane on indentation load.
Figure 113	Fracture toughness of the LSFT and dual phase membranes
Figure 114	Hardness of the LSFT and dual phase membranes
Figure 115	SEM micrographs of the as received LSFT. The fracture surface shows a transgranular fracture behavior.
Figure 116	Photographs of as-sintered and test specimens.
Figure 117	LSFT-CGO specimen on the 4-point fixture (a) before (b) after strength test a room temperature.
Figure 118	Effect of strain rate on the fracture load.
Figure 119	Effect of temperature and environment on flexural strength of the LSFT-CGC membranes.

indentation is in the dense region where as in Figure 46-d the indentation is on

porous region.

- Figure 120 SEM micrographs of the 'as-received' LSFT-CGO membranes. The dark phase is LSFT and the bright phase is CGO. Percolation of the two-phases is clearly observed in (a) and no micro cracks and any other flaws caused by the thermal expansion mismatch are visible at the grain boundaries (b).
- Figure 121 Effect of temperature and environment on the flexural strength of the dual phase membrane
- Figure 122 Stereo micrographs of fracture surfaces: (a) room temperature, (b) at 1000°C in air, (c) at 1000°C in N2. The volume flaw (in a) and the surface flaw (in c) are marked by arrows.
- Figure 123 SEM micrographs of fracture surfaces at room temperature (a) at  $1000^{\circ}$ C in air (b) and at  $1000^{\circ}$ C in  $N_2$  (c). Fracture was mainly transgranular at the room temperature and intergranular at  $1000^{\circ}$ C in  $N_2$  atmosphere.
- Figure 124 SEM micrographs of the 'as-received' LSFT-CGO (50/50 vol%) membranes. The dark phase is LSFT and the bright phase is CGO. Percolation of the two-phases is clearly observed in (a) and no micro cracks and any other flaws caused by the thermal expansion mismatch are visible at the grain boundaries (b).
- Figure 125 Effect of temperature and environment on flexural strength of the LSFT-CGO (50/50 vol%)
- Figure 126 Secondary electron and back scattered electron images of the fracture surfaces: LSFT-CGO (50/50) fractured at room temperature (a-b); LSFT-CGO (50/50) fractured at 1000°C in air (c-d) and LSFT-CGO (50/50) fractured at 1000°C in N<sub>2</sub> (e-f).
- Figure 127 The room temperature failure of the LSFT-CGO (50/50). Note the torturous failure of CGO grains
- Figure 128 LSFT-CGO (50/50) fractured at  $1000^{\circ}$ C in air (a-b) and  $N_2$  (c-d).
- Figure 129 The EDS spectrum of the precipitates formed on the LSFT grains in the LSFT-CGO (50/50) fractured at 1000°C in  $N_2$
- Figure 130 XRD plots of the (a) LSFT (b) dual phase membranes.
- Figure 131 (a). Change in weight (b) DTA and temperature data as function of time for LSFT in air and N<sub>2</sub> environment
- Figure 132 The weight change during annealing of LSFT-CGO measured by TGA
- Figure 133 The weight change during annealing of LSFT-CGO calcined at 1000°C and 1250°C measured by TGA at 1000°C.

Figure 134 Effect of flexural test atmosphere on the weight change of the LSFT-CGO. The dilatometer installed at the ceramic membrane lab and the sample holder with Figure 135 a LSFT-CGO membrane is shown in the inset. Figure 136 The variation of the total expansion coefficients of LSFT and LSFT-CGO on heating in air and at  $N_2$  at 5k min<sup>-1</sup>. A typical indentation crack produced on the membrane at room temperature. Figure 137 Arrow mark indicates the direction of crack path. Figure 138 The X-ray diffractograms of the pulverized YSZ supports: (a) Composition A, (b) Composition B and (c) Composition C. Figure 139 Effect of temperature on strength of YSZ-C supports; typical strengthdisplacement curves (a) and strength of YSZ-C as a function of test temperature. Figure 140 Strength- displacement curves of YSZ- A (a) and YSZ- B (b) at room temperature and at 900°C in air. Figure 141 Thermal expansion behaviors of the all three YSZ supports in air. Figure 142 Effect of loading rate on the flexural strength of the YSZ- A supports Figure 143 Effect of loading rate on the flexural strength of the YSZ-B supports Figure 144 Effect of loading rate on the flexural strength of the YSZ-C supports Figure 145 Microstructure of the YSZ supports; Composition A (a and b), Composition B (c and d) and Composition C (e and f). Figure 146 Fracture surfaces of YSZ-A at room temperature (a) and at 900°C (b) in air Figure 147 Fracture surfaces of YSZ-B at room temperature (a) and at 900°C (b) in air Figure 148 Fracture surfaces of YSZ-C at room temperature (a), at 500°C (b) and at 900°C (c) in air Figure 149 Fracture behavior of YSZ- A in room temperature (a) and at 900°C (b); YSZ-B in room temperature (c) and at 900°C (d). The fracture origin is marked in Fig. (a). Fracture behavior of agglomerates at YSZ-C at 900°C in air Figure 150 Figure 151 A plot of conductivity ( $\sigma$ ) vs. temperature (°C) for La<sub>0.80</sub>Sr<sub>0.20</sub>FeO<sub>3</sub>, La<sub>0.60</sub>Sr<sub>0.40</sub>FeO<sub>3</sub> and La<sub>0.55</sub>Sr<sub>0.45</sub>FeO<sub>3</sub> measured in air.

Figure 152	A plot of conductivity $ln(\sigma T)$ vs. 1/T for $La_{0.80}Sr_{0.20}FeO_3$ , $La_{0.60}Sr_{0.40}FeO_3$ and $La_{0.55}Sr_{0.45}FeO_3$ measured in air. Activation energy can be calculated from the slope over relative low temperature regime (200 – 500°C)
Figure 153	Neutron diffraction of $La_{0.60}Sr_{0.40}FeO_{3-\delta}$ quenched from 1500°C. The inserted figure is the low angle part of the sample without quenching.
Figure 154	Lattice parameter of $La_{0.60}Sr_{0.40}FeO_{3-\delta}$ quenched from various temperatures.
Figure 155	Comparison of Mossbauer spectra of LSF samples between unquenched and quenched from $1500^{\rm o}{\rm C}$
Figure 156	Correlation between oxygen vacancy and magnetic moment of $La_{0.60}Sr_{0.40}FeO_{3-\delta}$ using neutron diffractometery
Figure 157	Plot of Fe average valence state and fraction of $Fe^{3+}$ and $Fe^{4+}$ in $La_{0.60}Sr_{0.40}FeO_{3-\delta}$ quenched from various temperatures.
Figure 158	$\sigma$ vs. $pO_2$ of $La_{0.2}Sr_{0.8}TiO_3$ at $800^{o}C$ (annealing temperature was $1200^{o}C)$
Figure 159	Conductivity of LSF as a function of temperature in air
Figure 160	XRD profiles of LSFT annealed in forming gas (10% $H_2$ / 90% $N_2$ ) at 1000°C [5]
Figure 161	XRD profiles of LSFT annealed at 600, 1200, 1300, and 1400°C
Figure 162	Oxygen occupancy (3-δ) of LSFT as function of oxygen activity at 1200°C
Figure 163	Stoichiometry of La <sub>0.2</sub> Sr <sub>0.8</sub> Fe <sub>0.55</sub> Ti <sub>0.45</sub> O <sub>3-δ</sub> (LSFT)
Figure 164	Weight changes of LSFT as a function of oxygen activity at 1200°C
Figure 165	Total conductivity and Seebeck coefficient of LSFT as a function of temperature.
Figure 166	Charge carrier concentration and Seebeck coefficient of LSFT as a function of temperature
Figure 167	Net acceptor dopant concentration and Seebeck coefficient of LSFT as a function of temperature
Figure 168	$\boldsymbol{\sigma}$ vs. 1/T of LSFT and corresponding mobility measured in air as a function of temperature
Figure 169	Electrical conductivity as a function of oxygen activity of LSFT at 1000 and 1200°C.
Figure 170	Log $\sigma$ vs. Po <sub>2</sub> of dense Sr <sub>0.9</sub> Ti <sub>0.6</sub> Fe <sub>0.4</sub> O <sub>3-<math>\delta</math></sub> (sintered at 1600°C) at 800°C

- Figure 171 Seebeck coefficient vs. Log Po<sub>2</sub> of  $\sim 50\%$  dense La<sub>0.2</sub>Sr<sub>0.8</sub>Fe<sub>0.55</sub>Ti<sub>0.45</sub>O<sub>3- $\delta$ </sub> (LSFT) at 900°C
- Figure 172 (a) Mössbauer spectra of LSFT samples quenched from 1100°C and 1200°C to room temperature.
- Figure 173 Isomer shift of two types of Fe ions in LSFT quenched to room temperature from the temperatures ranging between 1100 and 1500°C. Included is the isomer shift of the specimen, which was annealed at 1400°C and then cooled to room temperature at 3°C/min.
- Figure 174 The fraction of the two types of Fe ions in LSFT quenched to room temperature from the temperatures ranging between 1100 and 1500°C. Included is the Fe ion fraction in the specimen which was annealed at 1400°C and then cooled to room temperature at 3°C/min.
- Figure 175 (a) Schematic of the STEM. (b) The Z-contrast image and energy loss spectrum can be interpreted as a simple convolution of the experimental probe and the object function. With lower spatial resolution, the EDS spectrum can also be interpreted in this manner.
- a) Z-contrast micrograph of sintered (La, Sr)FeO<sub>3</sub> [001] showing the cubic perovskite structure, with the brighter (La, Sr) columns, and the less bright Fe-O columns. b) EEL-spectra nano-meter scale probe-diameter. The spectra are a sum of 14 individual spectra with an acquisition time of 2 sec and show the O K-, the Fe L- and the La M-edges
- a) Low magnification dark field image of the bulk of a sintered LSFO grain exhibiting dark features. b) Atomic resolution of one dark line, showing the internal structure of this feature and the shift between the adjacent bulk crystal structures.
- a) Atomic resolution EELS of one dark line, showing the internal structure of this feature and the shift between the adjacent bulk crystal structures. b) O K-edge from the stacking fault and from the bulk, showing the differences in the fine-structure and the higher intensity in the stacking fault. e) Fe L- and La M-edges from the same positions
- Figure 179 Z-Contrast image with marked change in contrast in every second FeO<sub>2</sub> column.
- a) Z-Contrast image of LSFO [001] at 724 K with clearly visible ordered domain, inlet shows diffraction pattern with additional spot. EELS of bright and dark columns in (La.Sr)FeO<sub>3</sub> at 724 K b) O K-edge c) Fe L-edges with arrows marking the differences

- Figure 181 Z-Contrast image of LSFO at 724 K after heating at 1073 K, showing the change in contrast very clearly. The white spots in the image are caused by contamination built up on the surface during the heating process
- Figure 182 Z-Contrast image of (La,Sr)FeO<sub>3</sub>, previously treated at 1024 K in 10<sup>-10</sup> Pa showing stacking faults and ordered structure parallel to them
- Figure 183 EELS of (La, Sr) FeO3 from the bulk, the stacking fault and the brighter middle column, normalized to the iron core loss edge intensities. a) Oxygen K-edge b) Fe L- and La Ma-edges
- Figure 184 Secondary electron (bright field) images indicating presence of precipitates in the matrix
- Figure 185 Elemental profiles of the area shown in figure 184
- a) Schematic drawing of the proposed secondary Ruddelsden-Popper phase in a perovskite oxide material, which compensates for the local anion non-stoichiometry. The rock-salt layer consists of two atomic layers of Fe-O. b) Schematic drawing of the Aurivillius phase, which consists of a perovskite layer sandwiched between two layers of Fe-O
- Figure 187 X-ray powder diffraction pattern (left) and a back scattered electron micrograph (right) of SrFeO<sub>3-x</sub> prepared by the SHS method.
- Figure 188 Back Scattered Electron Image (BEI) of LSF prepared by SHS.
- Figure 189 Sintered tubes of a) La<sub>0.6</sub>Sr<sub>0.4</sub>Fe<sub>0.8</sub>Co<sub>0.2</sub>O<sub>3-x</sub> and b) La<sub>0.2</sub>Sr<sub>0.8</sub>Cr<sub>0.2</sub>Fe<sub>0.8</sub>O<sub>3-x</sub> for use in isotopic transient measurements.
- Figure 190 X- ray diffraction data for La<sub>0.2</sub>Sr<sub>0.8</sub>Fe<sub>0.55</sub>Ti<sub>0.45</sub>O<sub>3-x</sub> samples annealed at different temperatures.
- Figure 191 Back-scattered electron images of La<sub>0.2</sub>Sr<sub>0.8</sub>Fe<sub>0.55</sub>Ti<sub>0.45</sub>O<sub>3-x</sub>.
- Figure 192 X- ray diffraction data for  $La_{0.2}Sr_{0.8}Fe_{0.55}Ti_{0.45}O_{3-x}$  samples annealed at different temperatures batch #2.
- Figure 193 A cell for conductivity measurements. 1: thermocouple, 2: YSZ sensor, 3: YSZ pump, 4: sample, 5: alumina tube, 6: alumina ring, 7: glass ring, 8. Pt wires.
- a) Coulometric titration cell: 1. thermocouple, 2.YSZ, 3. pyrex sealant, 4. sample powder, 5. Pt electrodes and wires, 6. alumina; b). Coulometric titration system: 1. Furnace, 2. electrochemical cell, 3. thermocouple, 4. quartz tube, 5. metal frame, 6. Pt wires, 7. spring, 8. gas in, 9. gas out.
- Figure 195 a) The symmetric electrochemical cell for polarization measurement and (b) scanning electron micrograph of YSZ covered with Pt after annealed at 1300 °C for 30 min.
- Figure 196 Electrochemical cell used for thermo-power measurements.
- Figure 197 Phase Diagram of SrFeO<sub>3-x</sub> after Takeda *et al.* (9).

- Figure 198 Coulometric titration data for the pO<sub>2</sub> dependence of the oxygen non-stoichiometry of SrFeO<sub>3-x</sub> at 1000 °C, (a) raw data and (b) after leakage correction. After correction the data measured on increasing and decreasing pO<sub>2</sub> agree over the entire pO<sub>2</sub> range, as shown in Figure 12 (b). Similar results were observed at the other temperatures.
- a) The dependence of the equilibrium non-stoichiometry x in SrFeO<sub>3-x</sub> on pO<sub>2</sub> at different temperatures. Lines are to guide the eye only; b) The temperature and pO<sub>2</sub> dependence of the non-stoichiometry x, in SrFeO<sub>3-x</sub>, shown as lines of constant composition.
- Figure 200 Experimental and calculated non- stoichiometry and defect concentrations.
- Figure 201 Conductivity isotherms for  $SrFeO_{3-x}$  as a function of  $log(pO_2)$  taken from reference (10).
- Figure 202 a) Conductivity of  $SrFeO_{3-x}$  at 1000 °C, filled and open circles represent measurements made on decreasing and increasing  $pO_2$ , respectively; b) Conductivity of  $SrFeO_{3-x}$  at 750 °C, the filled circles correspond to measurements from high to low  $pO_2$ , data with the other symbols were obtained from low to high  $pO_2$ .
- Figure 203 The low pressure conductivity of SrFeO<sub>3-x</sub> at 750 and 850 °C.
- Figure 204 Comparison of D<sub>chem</sub> values measured by electrical conductivity relaxation.
- Figure 205 Comparison of k<sub>chem</sub> values measured by electrical conductivity relaxation.
- Figure 206 pO<sub>2</sub> dependence of electrical conductivities and oxygen non-stoichiometry at 752, 802, 854, 902, 942, 985, 1024, and 1055°C.
- Figure 207 a) pO<sub>2</sub> dependence of electrical conductivities in the pO<sub>2</sub> =  $10^{-5} \sim 10^{-1}$  atm b) The temperature dependence of p-n transition behavior.
- Figure 208 Comparison of conductivity isotherms according to the direction: "high to low pO<sub>2</sub>" run and "low to high pO<sub>2</sub>" run. For clarity, "high to low pO<sub>2</sub>" runs are offset.
- Figure 209 The phase diagram of  $La_{0.2}Sr_{0.8}Fe_{0.8}Cr_{0.2}O_{3-x}$ .
- Figure 210 The partial molar free energy and the partial molar enthalpy and entropy.
- Figure 211 Evolution of the time constant and the effect of CO<sub>2</sub>.
- Figure 212 t<sup>1/2</sup> dependence of the time constant at 821°C for La<sub>0.2</sub>Sr<sub>0.8</sub>Cr<sub>0.2</sub>Fe<sub>0.8</sub>O<sub>3</sub>.
- Figure 213 Partial pressure dependence of the electrical conductivity of La<sub>0.5</sub>Sr<sub>0.5</sub>Fe<sub>0.8</sub>Ga<sub>0.2</sub>O<sub>3-x</sub>.
- Figure 214 Conductivity data for La<sub>0.5</sub>Sr<sub>0.5</sub>Fe<sub>0.8</sub>Ga<sub>0.2</sub>O<sub>3-x</sub>; b) a comparison of Cr (red) and Ga (blue) at 800 °C.
- Figure 215 Determination of stoichiometric composition by using the minimum value of  $\partial \delta \partial pO_2$  for La<sub>0.2</sub>Sr<sub>0.8</sub>Fe<sub>0.55</sub>Ti<sub>0.45</sub>O<sub>3-8</sub> at 950 °C.

Figure 216	Average stoicniometry data.	
Figure 217	The $\delta$ dependence on temperature at constant pO <sub>2</sub> (left) and the pO <sub>2</sub> dependence on temperature at constant $\delta$ (right).	
Figure 218	DC conductivity data for $La_{0.2}Sr_{0.8}Fe_{0.55}Ti_{0.45}O_{3-x}$ in different gas atmospheres as a function of reciprocal temperature.	
Figure 219	Conductivity measurements for $La_{0.2}Sr_{0.8}Fe_{0.55}Ti_{0.45}O_{3-x}$ as a function of $pO_2$ at different temperatures. Open and closed symbols represent data taken on increasing and decreasing $pO_2$ .	
Figure 220	A depolarization curve of $La_{0.2}Sr_{0.8}Fe_{0.55}Fe_{0.45}O_{3-\delta}$ at 850 °C in air (a) Voltage response of cell during the depolarization process (b) logarithmic plot of (a).	
Figure 221	Thermopower results for LSFTO	
Figure 222	Dilatometry data for $La_{0.2}Sr_{0.8}Fe_{0.55}Ti_{0.45}O_{3-\delta}$ (a) dL vs. time and (b) dL vs. temperature. The dotted line in a indicates the temperature profile.	
Figure 223	The variation of the total expansion coefficients of $La_{0.2}Sr_{0.8}Fe_{0.55}Ti_{0.45}O_{3-\delta}$ on heating and cooling in air at 3 °C min <sup>-1</sup> .	
Figure 224	Expansion of La <sub>0.2</sub> Sr <sub>0.8</sub> Fe <sub>0.55</sub> Ti <sub>0.45</sub> O <sub>3-<math>\delta</math></sub> in air and argon, the difference between th two lines is the chemical expansion on changing from pO <sub>2</sub> = 0.21 atm to 2×10 atm; (b) the change in chemical expansion with temperature.	
Figure 225	The chemical expansion and corresponding stoichiometry variations for $La_{0.2}Sr_{0.8}Fe_{0.55}Ti_{0.45}O_{3-\delta}$ as a function of $pO_2$ at four different temperatures. The data are normalized to the total change in each case.	
Figure 226	In situ Neutron Diffraction Data for $La_{0.2}Sr_{0.8}Fe_{0.55}Ti_{0.45}O_{3-\delta}$ at 1040 °C.	
Figure 227	Comparison of the oxygen stoichiometry measure by neutron diffraction and coulometric titration.	
Figure 228	Comparison of two different sets of conductivity data measured for $La_{0.2}Sr_{0.8}Fe_{0.55}Ti_{0.45}O_{3-x}$ at 850 °C with different criteria for attainment of equilibrium.	
Figure 229	The dependence of the chemical expansion on non - stoichiometry in $La_{0.2}Sr_{0.8}Fe_{0.55}Ti_{0.45}O_{3-x}$ .	
Figure 230	(a) a high resolution image of a defect free LSFTO grain, (b-d) three different magnifications a grain showing the presence of Fe nanoparticles and amorphous iron rich regions.LaSrFeTiO Bulk Sample 0285545#2.	

# **LIST OF TABLES**

Table 1	Selected Thermo-Physical Properties of Materials Used in Experiments
Table 2	Strength of 20572 tubes determined by C-ring tests
Table 3	Hardness and Fracture toughness as a function of reducing conditions
Table 4	Fabrication of perovskite bars for flexure tests.
Table 5	Room temperature Indentation hardness and toughness values for the composition being evaluated
Table 6	Indentation hardness and toughness of the composition in different environment
Table 7	Slow Crack Growth tests in air at Room Temperature
Table 8	Slow Crack Growth tests in N <sub>2</sub> /Air at 1000°C
Table 9	Fracture toughness (K <sub>c</sub> ) of OTM (LSFCO-3) in N <sub>2</sub> /Air at 1000°C
Table 10	Crystal Symmetry and lattice parameters obtained from refinement of XRD data
Table 11	Thermal analysis of LSFCO-2 samples.
Table 12	Weight loss and DTA peaks in sample fracture in $N_2$ at elevated temperature and pressure
Table 13	Density of the membranes
Table 14	Lattice parameters obtained from refinement of XRD data
Table 15	Fracture toughness of the LSFT membrane
Table 16	Fracture toughness of the LSFT-CGO membrane
Table 17.	LSFT-CGO Flexural strength tests at RT and at 1000°C in N <sub>2</sub> atmosphere.
Table 18.	Change in weight and corresponding temperatures of OTM membranes in air and $N_2$ environment
Table 19.	The average internal stresses in the dual phase membranes at all test conditions
Table 20.	The flexural strength and Young's modulus values of the YSZ supports
Table 21.	Lattice parameters and lattice volume of YSZ supports

Table 22.	Hardness values of the YSZ porous supports
Table 23.	The oxygen partial pressure used in this experiment at 1000°C
Table 24	Activation for mobility of LSF and LSCF
Table 25.	The composition of La <sub>0.2</sub> Sr <sub>0.8</sub> Fe <sub>0.55</sub> Ti <sub>0.45</sub> O <sub>3-x</sub> batch #2
Table 26.	Results from the model fit to the $pO_2$ dependence of the total conductivity data

#### **EXECUTIVE SUMMARY**

Conversion of natural gas to liquid fuels and chemicals is a major goal for the Nation as it enters the 21<sup>st</sup>Century. Technically robust and economically viable processes are needed to capture the value of the vast reserves of natural gas on Alaska's North Slope, and wean the Nation from dependence on foreign petroleum sources. Technologies that are emerging to fulfill this need are all based syngas as an intermediate. Syngas (a mixture of hydrogen and carbon monoxide) is a fundamental building block from which chemicals and fuels can be derived. Lower cost syngas translates directly into more cost-competitive fuels and chemicals.

The currently practiced commercial technology for making syngas is either steam methane reforming (SMR) or a two-step process involving cryogenic oxygen separation followed by natural gas partial oxidation (POX). These high-energy, capital-intensive processes do not always produce syngas at a cost that makes its derivatives competitive with current petroleum-based fuels and chemicals.

In the mid 80's BP invented a radically new technology concept that will have a major economic and energy efficiency impact on the conversion of natural gas to liquid fuels, hydrogen, and chemicals. This technology, called Electropox, integrates oxygen separation with the oxidation and steam reforming of natural gas into a single process to produce syngas with an economic advantage of 30 to 50 percent over conventional technologies.

The Electropox process uses novel and proprietary solid metal oxide ceramic oxygen transport membranes [OTMs], which selectively conduct both oxide ions and electrons through their lattice structure at elevated temperatures. Under the influence of an oxygen partial pressure gradient, oxygen ions move through the dense, nonporous membrane lattice at high rates with 100 percent selectivity. Transported oxygen reacts with natural gas on the fuel side of the ceramic membrane in the presence of a catalyst to produce syngas.

In 1997 BP entered into an OTM Alliance with Praxair, Amoco, Statoil and Sasol to advance the Electropox technology in an industrially sponsored development program. These five companies have been joined by Phillips Petroleum and now are carrying out a multi-year \$40+ million

program to develop and commercialize the technology. The program targets materials, manufacturing and engineering development issues and culminates in the operation of semi-works and demonstration scale prototype units.

The Electropox process represents a truly revolutionary technology for conversion of natural gas to synthesis gas not only because it combines the three separate unit operations of oxygen separation, methane oxidation and methane steam reforming into a single step, but also because it employs a chemically active ceramic material in a fundamentally new way. On numerous fronts the commercialization of Electropox demands solutions to problems that have never before been accomplished. Basic problems in materials and catalysts, membrane fabrication, model development, and reactor engineering all need solutions to achieve commercial success.

Some important issues have been selected as needing understanding on a fundamental level at which the applied Alliance program cannot achieve the breadth and depth of understanding needed for rapid advancement.

### These issues include

- 1. oxygen diffusion kinetics (University of Houston)
- 2. grain structure and atomic segregation (University of Illinois Chicago)
- 3. phase stability and stress development (University of missouri Rolla)
- 4. mechanical property evaluation in thermal and chemical stress fields (University of Alaska Fairbanks)
- 5. graded ceramic/metal seals (Massachusetts Institute of Technology)

Some of the results related to important issues are briefly described in the following paragraphs.

The development of reliable ceramic/metal (C/M) seals is fundamental to the development of gas-to-liquid Electropox® technologies. These seals are needed to form a leak-tight interface between the oxygen-conductive ceramic membrane (OCCM) (Perovskites) and a nickel-base super alloy. Several possible brazing systems to be used in perovskite/metal seals were investigated. It was concluded that Ni-based brazing alloys provided the best option in terms of brazing temperature and final operating conditions. Although it was possible to create flat perovskite/metal seals, it was observed that there was an excessive reaction at the ceramic/braze interface. Observed cracks parallel to the perovskite/metal interface were attributed to this interfacial decomposition of the perovskite. In order to limit the extent of interfacial reactions, diffusion barriers were tested.

A mechanical testing procedure has been developed. This model was tested with model ceramic/metal systems but it is expected to be useful for testing concentric perovskite/metal seals. A finite element model of the concentric joint has been developed. Although it has been actually tested with data corresponding to alumina-based ceramics, the model was used in conjunction with the experiments to establish a reliable relationship between the strength of dissimilar material joints and the total strain energy stored in the system. The model developed in this work may eventually be applied to describe the detrimental liquid metal/perovskite interactions that prevent the creation of reliable perovskite/metal interfaces without the use of protective diffusion barriers.

An important issue in the development of perovskite-type oxygen conducting membranes has been the structural, chemical and mechanical stability of the materials at high temperatures and in reducing environments. The reducing conditions (CO<sub>2</sub>/CO/H<sub>2</sub> gas mixtures with steam) as encountered in a reactor environment can be expected to have significant influence on the mechanical properties of the oxides membranes.

Fracture strength of tubular perovskite membranes was determined in air and in reducing atmospheric conditions. The strength of the membrane decreased with temperature and severity of reducing conditions although the strength distribution (Weibull parameter,m) was relatively unaltered. Surface and volume dominated the fracture origins and the overall

fracture was purely transgranular. Crack growth studies with Vickers indents as pre-starter flaws however, indicated a mixture of intergranular and transgranular fracture. The change in fracture mode provides useful insight on the microscopic-events controlling the strength and fracture in perovskite exposed to reducing environments.

The interactions between the dopant ions, oxygen vacancies, structure and/or phase transitions significantly influence the strain in the lattice. The interaction influences the fracture morphology and probably manifests in the formation of bands in the fractured grains. The concentration of the oxygen vacancies in the membranes could significantly alter the stress distribution in the tubular membrane.

Dense single phase La<sub>0.2</sub>Sr<sub>0.8</sub>Fe<sub>0.6</sub>Ti<sub>0.4</sub>O<sub>3-δ</sub> and dual phase La<sub>0.2</sub>Sr<sub>0.8</sub>Fe<sub>0.6</sub>Ti<sub>0.4</sub>O<sub>3-δ</sub>/CGO OTM bars were analyzed for microstructure. The hardness was measured and a maximum hardness of 6.0 GPa for LSFT and 6.2 GPa for dual phase membrane was observed. In LSFT, the scatter in hardness values decreased with increasing load which confirms the uniform distribution of pores in the membrane. In the dual phase membrane this behavior, however, was not observed. Bulk densities of the LSFT and dual phase membranes were determined using Archimedes method. The bulk density was 5.029 and 5.57 g/cc for LSFT and dual phase membranes, respectively.

Fracture toughness of the LSFT and dual phase membranes were calculated using the Vicker's indentation method. An extensive analysis of the crack propagation behavior confirms the toughening mechanisms involved in determining the fracture toughness are the grain bridging, crack branching and the crack deflection. In the LSFT membrane the grain bridging was found to be the most prominent toughening mechanism. This may be due to the intergranular fracture behavior of the membrane. In the case of LSFT-CGO membrane, however, the prominent toughening mechanism was crack deflection due to the dense aggregation. The LSFT and dual phase membranes were heat treated at 1000°C for 60min and also in different atmospheres such as air and N2. The Fracture toughness and hardness of the heat treated membranes were calculated using Vicker's indentation method and the effect of indentation load and atmosphere on the mechanical properties were studied. The crack propagation behavior and the fracture toughness values suggested that the inert atmosphere

significantly affects the fracture behavior. The effect of loading time on the fracture toughness values is not so significant.

LSFT and LSFT-CGO membranes exhibit a reversible weight loss along with the irreversible weight loss when they are heated in air. The reversible weight loss is mainly due to the loss of oxygen at high temperature. The total weight loss in the  $N_2$  atmosphere is significantly higher than the weight loss occured in air and is completely irreversible. Overall, in  $N_2$  atmosphere, the decomposition of membranes starts earlier than it was observed in air.

Thermal analysis of the fractured dual phase membranes at 1000°C in air and N<sub>2</sub> atmosphere has been carried out and the results were compared with that of the as received dual phase membranes carried out in air and N<sub>2</sub>. The weight gain was observed at the fractured samples are reversible caused by non-stoichiometry by the membrane. The dual phase samples were calcined at 1000 and 1250°C in air and annealed at 1000°C in air and N<sub>2</sub> for TGA. The results showed the temperatures at which the weight gain stabilizes during annealing for TGA and confirmed the non-stoichiometry at the elevated temperatures. Fractured dual phase membranes at 1000°C in N<sub>2</sub> and CO/CO<sub>2</sub> environment were annealed at 1000°C in air and N<sub>2</sub> and their weight gain was estimated. The dual phase membranes have been evaluated for structural properties. An increasing crack growth resistance was observed for the membranes heat-treated at 1000°C in air and N<sub>2</sub> with increasing crack length.

The TEC of LSFT was studied in air and  $N_2$  to understand the internal residual stresses resulted by the thermal expansion mismatch. At room temperature, a medium-high energy failure was observed for the dual phase membrane which is reflected by the fracture surface. The membranes fractured at room temperature and at  $1000^{\circ}$ C showed mostly transgranular torturous fractures. The combined effect of thermal and elastic mismatch stresses on the crack path was studied and the fracture behavior of the dual phase composite at the test conditions was analyzed.

The SEM and EDS analysis of the fracture surfaces also clearly showed the presence of strontium or Fe rich precipitates along the LSFT grains.

The flexural strengths of the porous YSZ supports were evaluated at room temperature and at elevated temperatures. At elevated temperatures the strength of the supports decreases drastically. The composition C exhibits a very inferior strength value at 900°C in air among all the three supports. For all three compositions the porosity significantly affects the flexural strength of the supports at elevated temperatures.

At elevated temperature dense ceramic membranes have excellent selectivity for oxygen separation from air because the selectivity process is performed by oxygen diffusion processes. The membrane material must have high electronic conductivity, oxygen ionic conductivity and sufficient mechanical strength to withstand operating stresses. Mixed-conducting perovskites such as Sr doped lanthanum ferrites were selected for this purpose because of their high electronic and ionic conductivities. However, highly efficient and long term stable perovskite materials need to be developed. The focus of this research was to develop new membrane materials by synthesizing different compounds and determining their defect structures, crystallographic structures and electrical properties. In addition to measuring electrical conductivity, oxygen vacancy concentration was also evaluated using thermogravimetry, Neutron diffraction and Mössbauer Spectroscopy. The collected data were then analyzed to evaluate the most suitable materials for the goal.

After years of research on various compositions of perovskite materials, La<sub>1-x</sub>Sr<sub>x</sub>FeO<sub>3</sub> (LSF) and La<sub>0.2</sub>Sr<sub>0.8</sub>Fe<sub>1-y</sub>Ti<sub>y</sub>O<sub>3</sub> (LSFT) were selected as candidate membrane materials for OTM. The maximum electrical conductivity of LSF in air as a function of temperature was achieved at  $< 600^{\circ}$ C and depends on the concentration of Sr (acceptor dopant). The estimated maximum conductivities are as follows:  $\sigma_{L55SF}$  (240 S/cm, La<sub>0.55</sub>Sr<sub>0.45</sub>FeO<sub>3</sub>)  $> \sigma_{L6SF}$  (170 S/cm, La<sub>0.60</sub>Sr<sub>0.40</sub>FeO<sub>3</sub>)  $> \sigma_{L8SF}$  (100 S/cm, La<sub>0.80</sub>Sr<sub>0.20</sub>FeO<sub>3</sub>). Small polaron conduction was proposed in these p-type conductors because conductivity behavior and mobilities were similar to those in chromites, manganate and cobaltites. The activation energy for mobility of LSF is 0.23  $\sim$  0.28 eV which also suggests small polaron conduction. Neutron diffraction and Mössbauer Spectroscopy studies on LSF showed a strong relation between magnetic moment and crystal structure. For example, the LSF quenched from 600-1200°C to room temperature shows rhombohedral structure, while quenched from >1200°C is subjected to the

lattice distortion and becomes cubic. This distortion involves about 1.1% of unit cell volume increase which gives rise to the increase of the oxygen vacancy concentration and ionic radius of Fe. Oxygen occupancy in LSF was estimated using Neutron diffractometry and Mössbauer Spectroscopy by measuring magnetic moment changes depending on the Fe<sup>3+</sup> and Fe<sup>4+</sup> ratio. The estimated oxygen content ( $\delta$ ) using unquenched and quenched samples (quenching from 700 – 1500°C to room temperature) is from 0.02 (unquenched sample) to 0.18 (quenched from 1500°C) in La<sub>0.60</sub>Sr<sub>0.40</sub>FeO<sub>3- $\delta$ </sub>.

Ti was added to LSF (LSFT) to improve long term stability and chemical/mechanical strength at reducing atmospheres. For example, after total dissociation in 1x10<sup>-13</sup> atm of oxygen activity at 1200°C, LSFT re-gained its weight and conductivity upon re-oxidation. However, Ti doping decreases the total conductivity because the carrier concentration (ptype) decreases due to  $p = [Sr'_{1a}] - [Ti^{\bullet}_{Fe}]$ . The maximum electrical conductivity of La<sub>0.2</sub>Sr<sub>0.8</sub>Fe<sub>0.55</sub>Ti<sub>0.45</sub>O<sub>3</sub> (LSFT) was 13 S/cm at 500°C. The net hole concentration calculated from the Seebeck measurements agrees with the theoretical calculation from the composition used; p = 0.8-0.45 = 0.35. Therefore, the LSFT formulation maintained its original composition after the sintering process. The activation energy for mobility was about 0.2 eV which suggested small polaron conduction. According to the electrical conductivity and Seebeck coefficient measurements as a function of oxygen activity, LSFT exhibited p-type to n-type conductivity transition at about 1x10<sup>-8</sup> and 1x10<sup>-6</sup> atm of oxygen activity at 1000 and 1200°C. However, the electrical conductivity measurement of LSFT showed a p-type to ntype transition at about 1x10<sup>-10</sup> and 1x10<sup>-6</sup> atm of oxygen activity at 1000°C and 1200°C, The difference between the two measurements may be due to differences in the carrier mobilities. Mössbauer Spectroscopy also confirmed that the oxygen vacancy density increases as temperature increases with the ratio of Fe<sup>3+</sup>/Fe<sup>4+</sup> ions increases. More details are discussed in this report.

To investigate the structure, composition and bonding changes that occur within grains, at grain boundaries, at domain boundaries and within ordered structures in the ceramic membrane materials, advanced atomic resolution techniques in scanning transmission electron microscopy (STEM) were used. In particular, Z-contrast imaging is used to provide

a direct image of the atomic structure and as a map to position the probe for electron energy loss spectroscopy (EELS). EELS is sensitive to both composition and bonding, allowing us to correlate the structure with changes in composition and valence state for the transition metal elements in the structure. We used these techniques to develop strategies to detect and characterize vacancy creation, dopant segregations and defect association in the oxygen conducting membrane material.

The program at Houston and Toronto was aimed at measuring the transport properties of ferrites with the perovskite structure under different conditions to determine the variation in properties expected across an operating membrane. The stability, thermal expansion and conductivity data that are also important membrane parameters have been obtained over a wide pressure range ( $1 \ge pO_2 \ge 10^{-18}$ ) by using sealed electrochemical cells. Isotope infusion techniques were used to separate the surface activation and bulk mobility contributions to the movement of oxygen into and through the materials. Conductivity relaxation studies were performed on the materials also to complement the isotope experiments. These experiments provide higher data rates and allow multiple experiments on each sample, but the results do not completely separate the surface and bulk terms.

At UH, we investigated the  $pO_2$  and temperature dependence of the conductivity, non-stoichiometry and thermal-expansion behavior of compositions with increasing complexity of substitution on the perovskite A and B sites. The complete set of compounds that we have studied is given below:

SrFeO <sub>3-x</sub>	SFO
$La_{0.2}Sr_{0.8}FeO_{3-x}$	LSFO
$La_{0.5}Sr_{0.5}FeO_{3-x}$	LSFO
$La_{0.2}Sr_{0.8}Fe_{0.8}Cr_{0.2}O_{3-x}$	LSFCO
$La_{0.5}Sr_{0.5}Fe_{0.8}Ga_{0.2}O_{3-x}$	LSFGO
$La_{0.6}Sr_{0.4}Fe_{0.8}Co_{0.2}O_{3-x}$	LSFCoO
$La_{0.2}Sr_{0.8}Fe_{0.55}Ti_{0.45}O_{3-x}$	LSFTO

The most detailed measurements of the thermodynamics and the ionic and electronic transport were made for  $La_{0.5}Sr_{0.5}FeO_{3-x}$ ,  $La_{0.2}Sr_{0.8}Fe_{0.8}Cr_{0.2}O_{3-x}$ , and  $La_{0.2}Sr_{0.8}Fe_{0.55}Ti_{0.45}O_{3-x}$ .

These and other recent studies of ferrites with the perovskite structure show anomalous behavior at low oxygen partial pressures (<10<sup>-5</sup> atm). The anomalies are due to non-equilibrium effects and can be avoided by using very strict criteria for the attainment of equilibrium. The slowness of the oxygen equilibration kinetics arises from two different mechanisms. In the first, a two phase region occurs between an oxygen vacancy ordered phase such as brownmillerite SrFeO<sub>2.5</sub> and perovskite SrFeO<sub>3-x</sub>. The slow kinetics are associated with crossing the two phase region. The width of the miscibility gap decreases with increasing temperature and consequently the effect is less pronounced at higher temperature. Both SrFeO<sub>3-x</sub> and La<sub>0.2</sub>Sr<sub>0.8</sub>Fe<sub>0.8</sub>Cr<sub>0.2</sub>O<sub>3-x</sub> show this behavior; La<sub>0.5</sub>Sr<sub>0.5</sub>FeO<sub>3-x</sub> and La<sub>0.5</sub>Sr<sub>0.5</sub>FeO<sub>3-x</sub> were not studied in detail.

In contrast, in  $La_{0.2}Sr_{0.8}Fe_{0.55}Ti_{0.45}O_{3-x}$  deviations between equilibrium and non-equilibrium behavior become larger with increasing temperature suggesting that cation rearrangements or phase separation must take place. The preferred kinetic pathway to reduction of perovskite ferrites when the vacancy concentration corresponds to the formation of significant concentrations of  $Fe^{2+}$  is via the formation of a Ruddlesden –Popper (RP) phases as clearly observed in the case of  $La_{0.5}Sr_{0.5}FeO_{3-x}$  where  $LaSrFeO_4$  is found together with Fe. In more complex compositions, such as LSFTO, iron or iron rich phases are observed locally with no evidence for the presence of discrete RP phase.

## Chapter 1 Development of Ceramic Membrane/Metal Joints

Prof. Thomas W. Eagar, Dr. Harold R Larson, Mr. Raymundo Arroyave and Ms. Jocelyn L. Wiese

Massachusetts Institute of Technology, Dept. of Material Science and Engineering

### 1.1. INTRODUCTION

The development of reliable ceramic/metal (C/M) seals is fundamental to the development of gas-to-liquid Electropox® technologies. These seals are needed to form a leak-tight interface between the oxygen-conductive ceramic membrane (OCCM) (Perovskites) and a nickel-base super alloy. The expected reactor design for this technology requires the existence of two regions of very different oxygen partial pressure, which will require isolation from each other. Both process-related and safety issues require a leak-tight seal around the OCCM in the reactor. During normal operation, these seals will be subjected to high temperatures under cyclic oxidizing/reducing conditions. Although conventional mechanical seals have been used for relatively low-temperature ceramic/metal seal applications, it is believed that a braze-type sealing technique is a potentially successful sealing strategy, capable of enduring higher operating temperatures and thermal cycling in addition to providing a reliable leak-tight seal.

In all industrial C/M joining applications, two essential aspects of the joint must be addressed. One is the fact that molten metals usually do not wet ceramic surfaces. Since wettability is related to the effectiveness of the joining technique, non-wetting constitutes a major obstacle in the development of C/M seals. The second problem is that ceramics and metals generally have very different thermo-mechanical properties. Since the joining process takes place at high temperature, significant heating and cooling of the joint during bonding is unavoidable. As this takes place, large thermal stresses can be generated across the C/M interface, making the joint physically unstable. In order to address both problems, a research program focused on studying both the chemical and mechanical interactions between perovskites and nickel-based alloys was undertaken.

Although good progress was achieved, there are still many important aspects regarding the development and design of reliable C/M joints that have not been resolved. Nickel-based

brazing alloys are capable of wetting the ceramic surface in question, however, considerable improvement of these alloys is needed in order to achieve practical and reliable seals. From the mechanical point of view, numerical simulations and joint strength experiments on C/M joints have been made for a model system. So far, no mechanical experiments have been made on perovskites/metals seals. However, the evaluation techniques and criteria developed so far are expected to hold when applied to the particular perovskite/metal system we are studying.

In this report, we present the work completed in a chronological order. We begin by presenting some related experiments with zirconia-based ceramics and later we present results obtained from wetting and reaction experiments on the perovskite/braze system. Additionally, the mechanical behavior of dissimilar material joints are discussed based on the results obtained from experimental and computational methods. Implications of these results on the final joint design are also addressed.

## 1.2 Experiments using Zirconia-based ceramics

During the first stages of this project, zirconia-based ceramics were used as model systems, because perovskite samples were not yet available. Since the majority of the ceramic oxides are thermodynamically stable under most conditions, they are not easily wetted by regular braze alloys. In these cases, the addition of reactive elements (such as titanium, zirconium, etc.) promotes the reaction between the ceramic and the braze, creating a stable interface, along with a series of interfacial reaction products. At this stage of the project, it was believed that perovskite-based ceramics would react in a way similar to zirconia-based ceramics

Therefore, a series of experiments using zirconia-based ceramics and copper-based reactive brazes was devised. These experiments had the objective of determining the different parameters that influence the reactivity of the braze, as well as to gain information on the morphology and chemistry of the interfacial reaction products. For these experiments, copper-based brazing alloys with zirconium or titanium additions were investigated. Powder mixtures were pressed and put between the ceramic and metallic parts. The arrangement was then put into a vacuum furnace and the temperature was increased until the braze alloy

melted. From this work, several important aspects of ceramic/metal reactive brazing were verified:

It was found for example, that there is a maximum Ti content that can be added to a copper braze. If this maximum content is exceeded, the joint tends to break apart at very small stresses. This composition is around 20% (wt.) Ti. The probable cause for this brittleness seems to be the formation of a thick reaction layer on the ceramic's surface.

On the other hand, copper alloys with 5% and 10% Ti proved to have enough toughness to resist the cutting action needed to prepare the samples for optical and electronic microscopy analysis:

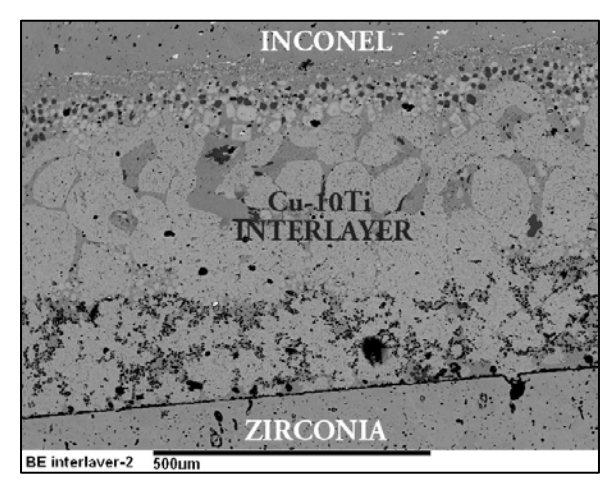


Figure 2 Zirconia/Metal Joint using Cu-10Ti Braze Alloy

Figure 2 corresponds to a Cu-10% Ti brazing alloy that was held at 1050° C for 1 hr. The extremely complex microstructure across the interlayer is evident. Interdiffusion between the Inconel plate and the Cu-10Ti interlayer was observed. As the brazing temperature increases, interdiffusion becomes more pronounced, which has implications for the cases in which perovskite-based ceramics are to be brazed to metallic parts: if the metallic part is dissolved by the braze alloy (which is likely, specially when the braze alloy and the metallic part are nickel-based alloying systems) then the chemistry of the interfacial reactions can vary.

It is evident that the titanium present in the brazing alloys reacted with the zirconia surface. Using techniques such as backscattering electron microscopy and EDS it was possible to identify Ti<sub>2</sub>O<sub>3</sub> as an interfacial reaction product. The thickness of this reaction product

increased, and the rate of growth seemed to follow a parabolic law (diffusion-controlled) although conclusive evidence of this was not obtained.

Another important feature of the experiments seen on zirconia-based ceramics was the observation that the braze ceramic parts presented a discoloration zone that advanced from the ceramic/braze interface outwards. This indicates a reaction that takes place due to the displacement of oxygen ions from the bulk of the ceramic to the ceramic/braze interface where they react with the reactive element dissolved in the brazing alloy.

To complement these experiments, reactive brazing alloys with zirconium additions were prepared and tested under similar experimental conditions. In these cases the reaction between the reactive braze and the ceramic was not similar to the one observed during the experiments using titanium-containing brazing alloys. In the case of zirconium reactive brazing alloys, the morphology of the interface was very irregular, with no clear indication of a reaction product formed at the ceramic/braze interface as shown in Figure 2. This difference in interfacial morphology may influence the mechanical behavior of ceramic/metal joints.

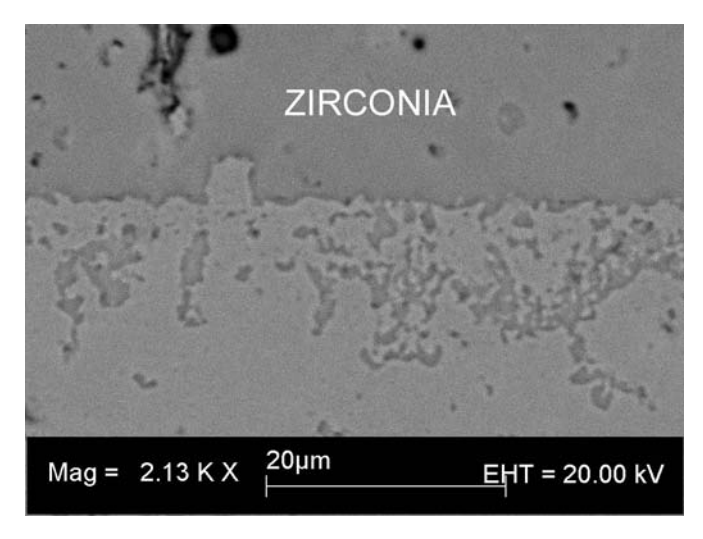


Figure 2. Zirconia - Cu-Zr Interactions

## 1.2.1 Other Metallization Approaches

Despite its effectiveness in ceramic/metal bonding applications, copper-based alloys are not good options for joints operating above 800° C. Since Ni-based alloys have proven to be ineffective reactive brazing solvents, new strategies to produce ceramic/metal bond were

tested. Pre-metallization of the ceramic surface with a reactive element (Ti or Zr) and later brazing to the metal using conventional nickel-based brazing alloys seems to be a promising approach for obtaining joints capable of enduring high operating temperatures under oxidizing atmospheres.

Once the ceramic has reacted with the coating, the temperature can be raised above the solidus of the Ni-based brazing alloy. At that temperature, a liquid phase forms and wets the coated ceramic surface as shown in Figure 3. Once wetting has been achieved, it is possible to hold the temperature for a time sufficient for the melting point depressant (boron) to diffuse away from the interlayer into the parent metal. This raises the re-melting temperature of the interlayer and higher re-melting temperatures may be achieved.

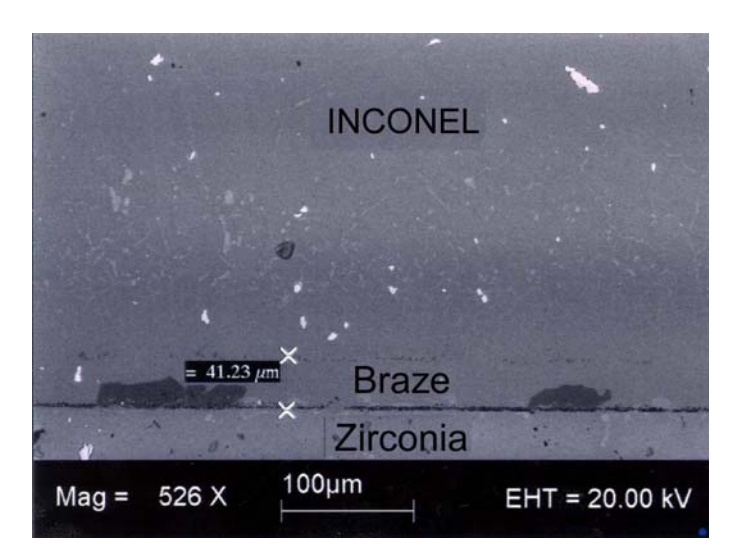


Figure 3. Use of alternative metallization techniques: Reactive coating with Ni-based brazing alloys

#### 1.2.2 Mechanical Properties of the Joints

Mechanical testing techniques were developed to measure the mechanical properties of concentric C/M joints. A model system of alumina (Al<sub>2</sub>O<sub>3</sub>) tubes brazed to nickel- and iron-based alloy rods, using commercially available Ticusil<sup>TM</sup> brazing alloy was chosen for the preliminary studies. These materials were chosen because the brazing of alumina with this alloy is well documented in the literature, and because the metal rods were available with a range of thermo-elastic properties (Table 1). Although it is not expected that the perovskite/metal seals will have the same mechanical properties, the development of a

reliable testing technique is essential for the project. As part of this effort to understand the mechanical behavior of concentric ceramic/metal joints, a finite element model was created. This model has been able to qualitatively predict the mechanical strength of such joints, as a function of the total strain energy stored at the joint.

Material	Room Temperature		Joining Temperature		
		(20° C)	(780° C)		
	CTE (ppm/°C)	E (GPa)	CTE* (ppm/C)	E (GPa)	
Alumina	7.8	366	7.8	366	
Invar 36	1.3	141	11.5	105	
Hastelloy	9.3	217	14	167	
B2					
Inconel 600	11.6	214	16	164	
304	14.7	205	19	135	
Stainless					
1		I		I	

Table 1 Selected Thermo-Physical Properties of Materials Used in Experiments

#### 1.2.3 Measurement of Shear Strength

The geometry of the brazed rod-in-tube samples is shown schematically in Figure 4. The inner diameter of the ceramic tube was 0.257". Two different rod diameters – which result in two different braze thicknesses - were used: 0.250" and 0.247", giving braze thicknesses of 0.0035" and 0.005" respectively. The ceramic tubes were 0.75" long, and the length of the metal rod was systematically varied between 0.50" and 0.75" in order to vary the length of the lap joint between 0.2" and 0.35". Thus, from these experiments, the influence of braze-alloy thickness, joint overlap, and thermo-elastic property mismatch on the shear strength of a C/M concentric lap joint can be investigated.

<sup>\*</sup> Total CTE at  $780^{\circ}$  C calculated by: CTE =  $\epsilon_{th}$  /  $(780^{\circ}$  C- $20^{\circ}$  C )

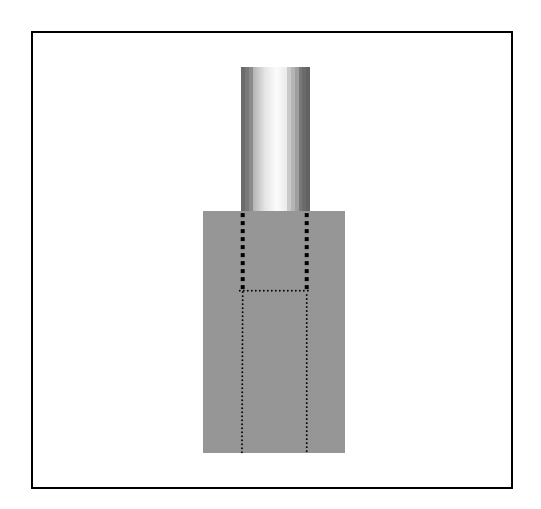
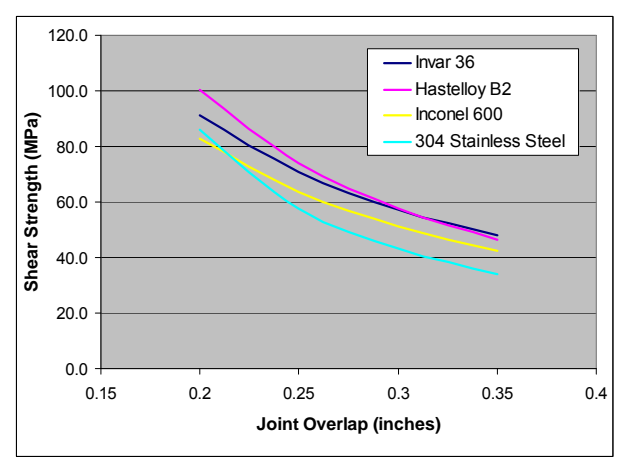


Figure 4. Mechanical tests specimens

The shear strength of a joint is measured by loading the samples in compression using an Instron testing machine. The strength of the joint is defined as the maximum load the joint can support, and the braze shear strength is calculated by normalizing the maximum load by the lap joint area.

Figure 5 depicts results from the large collection of data obtained from the mechanical strength measurements from which the following conclusions could be reached:

- Joints with greater CTE mismatch between the metal and ceramic generally exhibited lower shear strengths. The primary exception to this were the Hastelloy B2 joints which exhibited higher strengths than the Invar 36 joints for a braze thickness of 0.0035" and overlaps smaller than 0.30". Also, at short joint overlaps (<0.22"), the 304 stainless steel joints were stronger than those made with Inconel 600.
- The joints with a thicker braze (0.005") were slightly stronger than those with thinner brazes (0.0035")
- The braze shear strength decreased as the joint overlap increased for all materials and braze thicknesses.



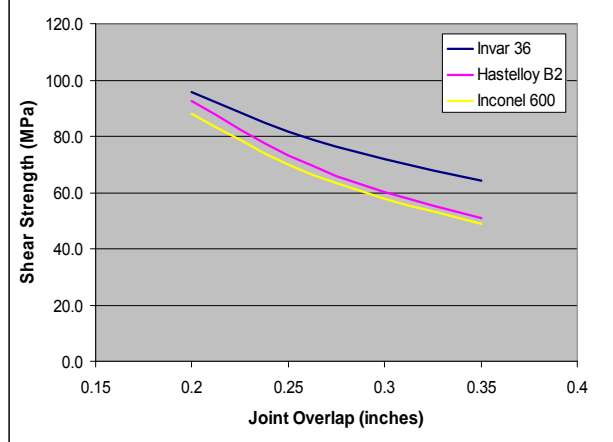


Figure 5. Relationship between joint overlap length and joint shear strength. (L) 0.0035" braze thickness. (R) 0.005" braze thickness

## 1.2.4 Finite Element Modeling

Finite element models for C/M joints were developed using the ABAQUS commercial software package. Residual stresses develop in these joints during cooling. The system was considered to be stress-free at the solidus temperature of the braze alloy (780°C for Ticusil<sup>TM</sup>). However, as the joint cools, one member often contracts more than the other, which results in high residual stresses when the joint is at room temperature.

The model system analyzed had the same geometry as the samples used for mechanical testing. The model takes in to account temperature-dependant materials properties in predicting the stresses developed upon cooling from 780°C to 20°C. It was assumed that both the alumina and base metal are perfectly elastic, and the Ticusil<sup>TM</sup> layer is perfectly plastic. The finite elements were 8-node axisymmetric elements with reduced integration, and the nodes lying on the Z-axis were constrained in the radial direction.

The magnitude of thermo-elastic property mismatch between the ceramic and metal greatly influences the residual stresses present after cooling. The magnitude of residual stress in a system can be quantified by using the scalar quantity strain energy.

Figure 6 shows how the total strain energy of the concentric C/M joints used in the shear strength experiments increases both with increasing joint overlap and CTE mismatch.

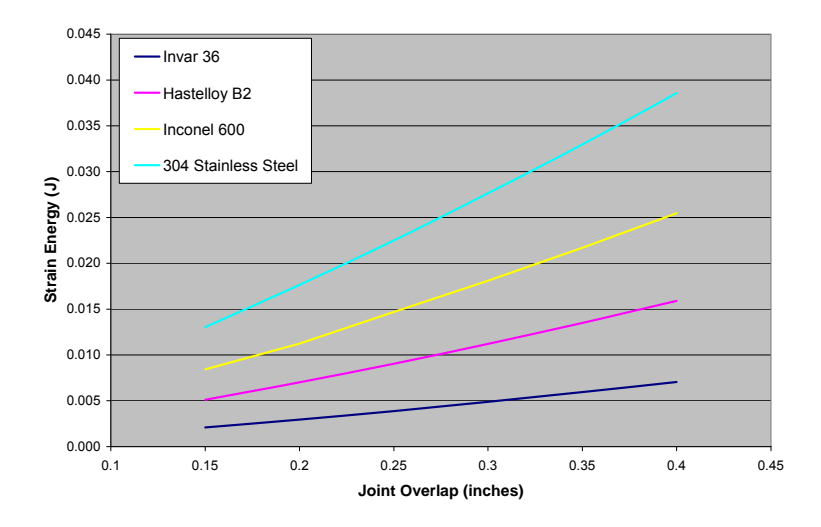


Figure 6. Relationship between joint overlap and total joint strain energy

# 1.2.5 Correlation between Strain Energy and Joint Shear Strength

Since it is the residual stresses in a metal-to-ceramic brazed joint that degrade the strength of the joint, existence of a correlation between strain energy and joint shear strength may be anticipated. Furthermore, since residual stresses are a function of joint geometry and materials, this correlation should hold for joints made with different substrates. The strain energy – joint strength data for all samples were plotted together, and R<sup>2</sup> values calculated (Figure 7). Both the calculated plastic strain energy in the filler metal correlate quite well with the calculated joint shear strength.

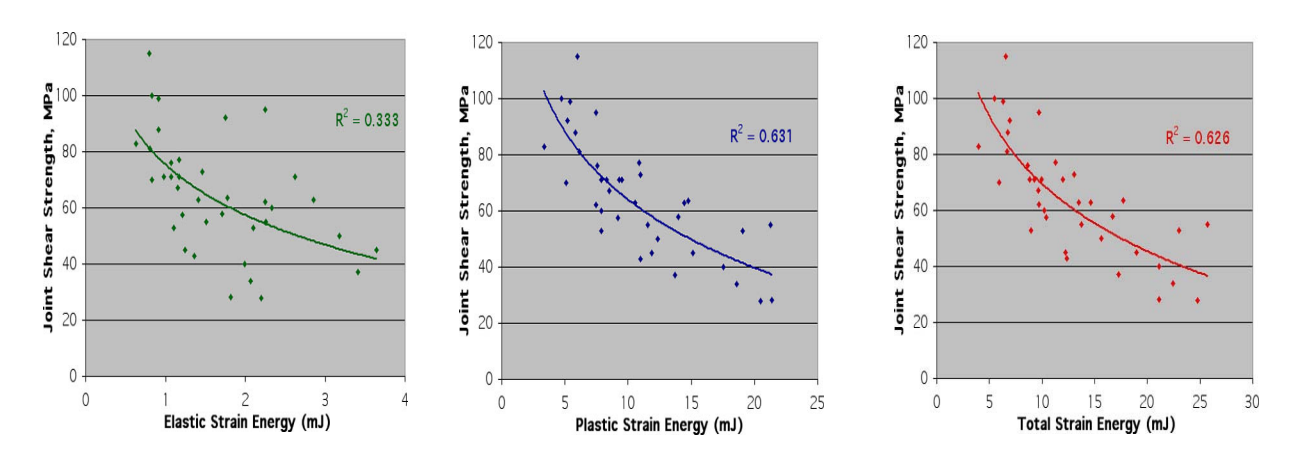


Figure 7: Correlations between measured joint shear strength and calculated elastic, plastic, and total strain energy in the filler metal.

The correlation between joint strength and strain energy depicted in Figure 7 indicates that it is possible to predict joint strength of ceramic/metal seals once the mechanical properties of the components of the joints are known.

From the work on the mechanical strength of ceramic/metal interfaces, the following key conclusions can be drawn that have applicability for the particular case of perovskite/metal seals:

- The plastic deformation of the interlayer plays a significant role in determining the mechanical strength of a ceramic/metal interface. For the particular case of perovskite/metal seals, it can be inferred that by properly selecting the interlayer material, the strength of the seal can be maximized.
- The total strain energy of the ceramic/metal system appears to be a good indicator for the comparison of the influence of different base metals on the final mechanical strength of ceramic/metal systems.
- The difference in the coefficient of thermal expansion between the base metal and ceramic is the most important physical property influencing the strain energy in the filler metal and the theoretical strength of the joints. The yield stress of the base metal is of secondary importance.

The morphology of the filler metal in joints varied with the base metal. Nickel from the base metal tended to dissolve into the filler metal, altering the microstructure. This is particularly important when applied to the perovskite/metal systems, as the rate of the reaction between nickel-based alloys and perovskite substrates is such that large reaction zones develop at the ceramic/metal interface. The chemical nature and morphology of these zones have been observed to play an important role in the nucleation of cracks that eventually lead to joint failure.

#### 1.2.6 Perovskite-Metal Interactions

The main objective of this part of the Oxygen Transport Ceramic Membranes project is the development of reliable ceramic/metal techniques that would be used for the creation of perovskite/metal seals. The perovskite/metal seals must be able to isolate two systems at

extremely different oxygen partial pressures at very high temperatures (possibly around 1000° C). Additionally, the ceramic/metal seals must be able to endure thermal cycling, as well as other transient mechanical loads under normal industrial operations.

Although mechanical seals have been used in other ceramic/metal sealing applications, it is our belief that brazed joints may offer superior sealing performance, as well as higher operating temperatures. This can only be possible with a good understanding of the chemical interactions between perovskite-based ceramics and metallic brazes. With this aim, a series of designed experiments were conducted. In these experiments, the interfacial reactions were studied and some flat joints were created.

## 1.2.7 Reaction Bonding Experiments with La-Sr-Fe-O Perovskites

Several experiments were performed using ceramic oxygen membrane (La<sub>6</sub>Sr<sub>4</sub>FeO<sub>3</sub>) and Haynes 230® discs. The first series of studies, using "conventional" reactive brazing alloys (with titanium or zirconium additions) showed excessive reactivity between the ceramic membrane and the braze. It was in fact observed that the reactive element additions to the brazing alloys were chemically reducing the ceramic discs. According to measurements on electrical conductivity of perovskite membranes done by other groups in the consortium, irreversible decomposition of the ceramics takes place at oxygen partial pressures below 10<sup>-16</sup> atm. Therefore, it is inferred that the interfacial conditions during these experiments produced at least these oxygen potentials.

With more stable ceramic oxides (zirconias, for example) the additions of reactive elements to the brazing alloy are necessary. Since the surfaces of such stable ceramics tend to be very stable themselves, when a molten metal is made to contact such a surface no wetting occurs, and therefore no stable interface is created. By adding reactive elements, the interfacial energies are reduced (due to the formation of reaction products, for example) and stable interfaces can be created. In this particular case, however, the ceramic appeared to be too unstable, and therefore, it was necessary to explore the use of less reactive metallic systems.

Preliminary experiments, found that conventional amorphous nickel-based alloys were capable of wetting the perovskite's surface, something not possible in the case of zirconia-

based ceramics. Nickel-based brazing alloys also have the advantage of having relatively low brazing temperatures (1090° C). This brazing temperature is achieved by the additions of boron or silicon to the nickel-based alloy. Additionally, the fact that boron can diffuse away from the braze, providing that the joint is held at high temperature for long enough time, constitutes an additional advantage since it becomes possible (in theory) to braze at one temperature, while operating at a higher temperature.

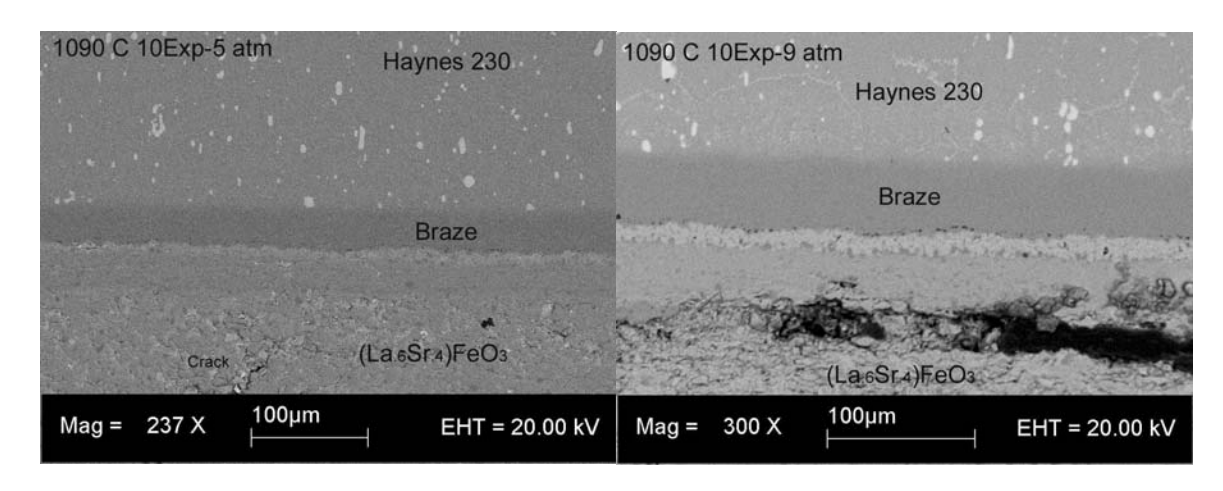


Figure 8a. Ceramic Membrane/Braze/Metal Interface

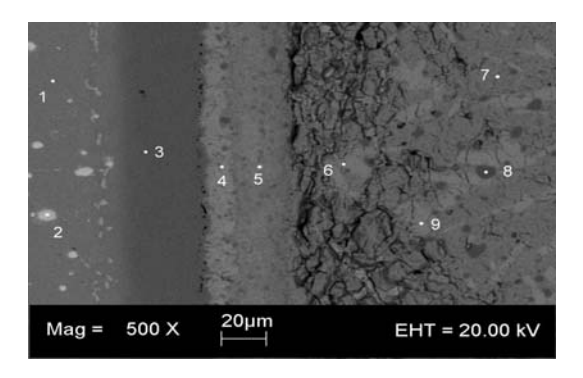
Figure 8a shows a typical interface created with this technique. It is observed that while a joint was created, the reactions taking place at the ceramic/braze interface were so intense that the chemical changes undergone by the ceramic reached depths in the order of tens of microns. The chemical changes and reaction products precipitated are evident from changes seen in contrast in Figure 8a (right micrograph) with the formation of extremely connected porosity possibly due to localized ceramic decomposition.



Figure 8b. Perovskite/Metal Joints Using Ni-based Brazing Alloys

Figure 8b presents typical flat joints created using the Ni-based brazing approach. As can be seen, it was possible to create large contact area (disc diameter of approx. 0.8 in) joints, which is, by itself, quite remarkable. However, it was observed that cracks appeared in a direction parallel to the ceramic/metal interface. From experimental results, it was observed that these cracks tended to appear when the furnace atmosphere went below 10<sup>-5</sup> atm. It is possible that the crack formation might be as a result of decomposition reactions occurring at the ceramic/braze interface.

From these experiments, it was evident that despite the relatively low chemical reactivity of these nickel-based brazing alloys, extensive reactions between the brazing alloy and the ceramic membrane occur when brazing. Figure 9 shows a typical braze/ceramic interface, with the corresponding chemical compositions obtained by EDS analysis.



	1	2	3	4	5	6,9	7	8
Ni	56	21	70	0	0	0	0	0
Cr	25	30	9	0	0	0	0	0
W	13	40	0	0	0	0	0	0
Mo	1	0	0	0	0	0	0	0
Ti	0	0	0	0	0	0	0	0
Si	0	0	3	0	0	0	0	0
Fe	2	1	7	1	1	14	15	69
La	0	0	0	23	12	13	15	1
Sr	0	0	8?	1	15	8	8	2
O	0	0	0	76	71	65	62	29
Mn	4	4	0	0	0	0	0	0

Figure 9. Ceramic/braze interface

Compositions obtained using EDS.

The EDS composition analyses of points 4 through 8 in Figure 9 show the extent of the reaction between the ceramic membrane and the brazing alloy. It can be observed that the first zone in contact with the brazing alloy has been depleted of both iron and strontium, while the next layer has been only iron-depleted. The formation of iron-rich "islands" are also observed, which are not normally observed in the pre-brazing ceramic membrane. From profile analyses, it was also observed that iron tended to diffuse out of the ceramic into the brazing alloy, possibly due to the low Fe activity within the braze alloy.

Figure 10 compares the spectrum obtained from a perovskite sample before the brazing procedure takes place (green) with the spectrum observed after the braze has reacted with the ceramic surface (red). As can be seen, the composition of the ceramic close to the braze/membrane interface is significantly modified.

The true nature of the reactions and their sequence has not been entirely elucidated, but it is clear that excessive reaction caused detrimental effects on the flat joints created during these preliminary experiments. We believe that by controlling the reactivity of the braze with the perovskite surface, the reliability of the seals could improve. Further experiments were aimed at studying ways of reducing the chemical interfacial reactions between perovskite-based ceramics and Ni-based brazing alloys.

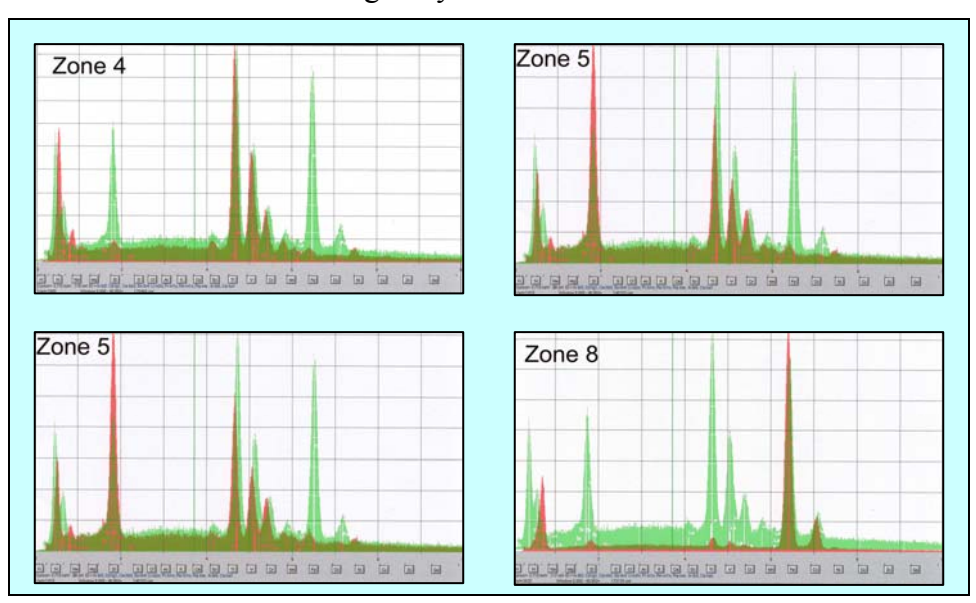


Figure 10. EDS spectra of different zones in Figure 9.

## 1.2.8 Reaction Bonding Experiments with La-Sr-Cr-Fe-O Perovskites

Experiments confirmed the good wetting behavior of Ni-based brazing alloys on perovskite discs. Because of their solidus and liquidus range, these brazing alloys provided a promising option for the creation of high-temperature seals. However, the problem of excessive reactivity remained. Since excessive interfacial reaction was shown to be detrimental to the integrity of the ceramic membrane, it was decided that a new direction in the research was necessary.

A series of experiments were devised to determine the potential use of diffusion barrier materials to limit the extent of the reaction at the ceramic/metal interface. External factors caused the ceramic used for these tests to be different from the first series of experiments, so no direct comparison between previous and new results was possible. For the diffusion-barrier experiments, the ceramic used was La<sub>0.2</sub>Sr<sub>0.8</sub>Cr<sub>0.2</sub>Fe<sub>0.8</sub>O<sub>3</sub>. A nickel-based super alloy was used as the metal substrate and the same Ni-B brazing alloy was used as the bonding interlayer.

The samples were cut in 0.5" dia x 0.1" thick disks, and polished to 600 GRIT. Then the samples were ultrasonically cleaned in isopropyl alcohol. The ceramic disks were conditioned in a  $N_2$  atmosphere at  $500^{\circ}$  C for 2 hours before the experiments. For the actual joining experiments, the same high-temperature vacuum furnace used in previous experiments was used. Up and down temperature ramping was controlled to minimize joint failure due to thermal shock. To keep the joint in place while joining, a slight pressure was applied.

To test the concept of diffusion barriers, a Cr layer was deposited on top of the ceramic substrate using a magnetron-sputtering unit. A layer of 10 microns was deposited on the perovskite disks. For the experiments, three different cases were studied:

In the first case, a two-step brazing operation was performed in which the joint at first was brought to a temperature (950° C) lower than the solidus of the Ni-B interlayer and leaving the joint at that temperature for about 15 minutes to allow time for the reaction between the perovskite disk and the Cr layer to occur so that a stable Cr<sub>2</sub>O<sub>3</sub> layer could be formed. After this step, the temperature was raised to 1100° C, a temperature high enough to allow the

melting of the Ni-B interlayer. After 15 minutes at this temperature, the sample was cooled to room temperature at a rate low enough to limit thermal shock (10 degrees per minute).

The second option explored was to form the chromium oxide ( $Cr_2O_3$ ) layer before the joining experiment took place. For this, perovskite disks with Cr layers were held in a slightly oxidized atmosphere at 550° C for 2 hours. An oxide layer was observed to form on top of the perovskite disks. The purpose of this experimental approach was to take advantage of the fact that  $Cr_2O_3$  is usually insoluble in other oxides as well as in liquid metals. Once the oxide layer was formed, the joint was raised to  $1100^{\circ}$  C in the vacuum furnace for 15 minutes, as in the experiments described above.

Finally, to establish a base case for comparison, a perovskite disk without any sputtered Crlayer was joined to a Ni-based base metal using the same Ni-B interlayer. The same heating and cooling rates were used. Below we present the results concerning these experiments:

# **Cr-Based Diffusion Barrier**

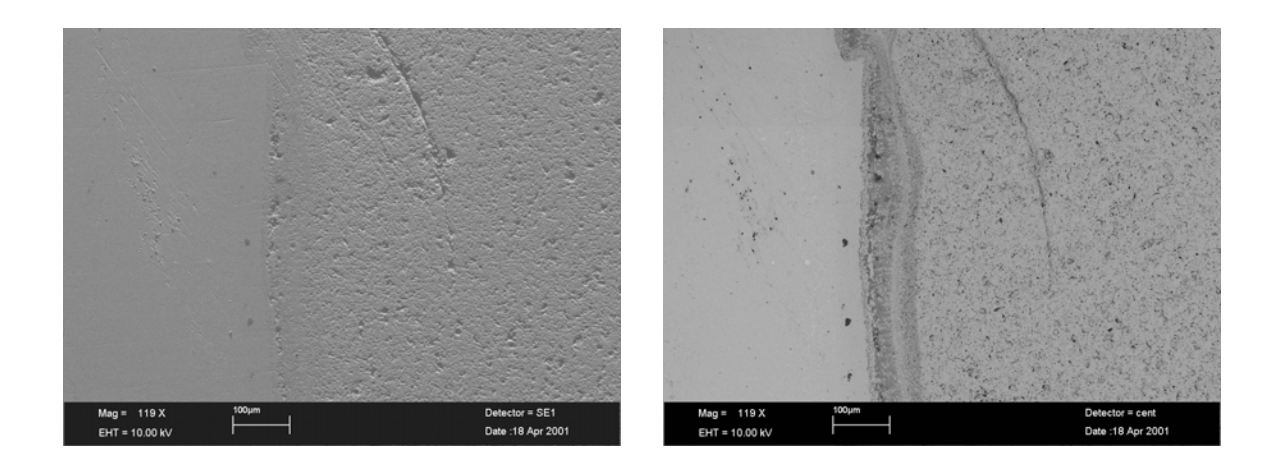
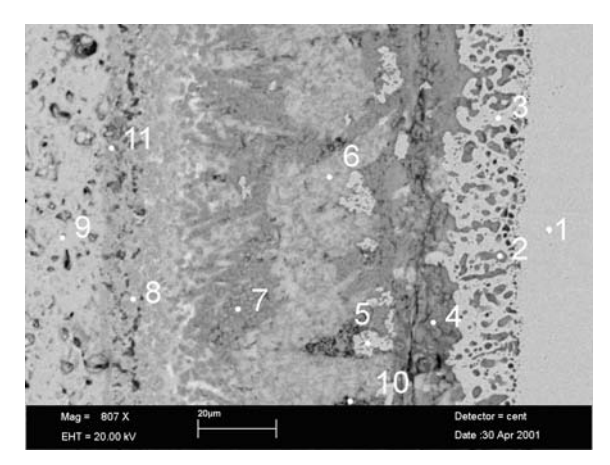


Figure 11. Perovskite/Cr/Ni/Inconel Joint. Secondary and Backscattered Image

From Figure 11, it can be observed that an interface was formed between the braze metal and the perovskite surface. Contrary to our expectations, though, the Cr layer sputtered on the

ceramic surface dissolved in the braze and the reaction with the ceramic was rather extensive (the reaction zone was almost as wide as in the previous series of experiments). Excessive porosity was also observed at the ceramic/braze interface. It was also noted that the nature of the interactions between the ceramic and the braze were different from those observed with the La<sub>0.6</sub>Sr<sub>0.4</sub>FeO<sub>3</sub> perovskite:



	1	2	3	4	5	6	7	8	9	10	11
Ni	81.6	96.5	25.5	4.7	4.0	17.3	4.0	1.1		4.1	1.5
Cr	8.2	1.3	11.6	9.8	3.4	2.9	2.4	8.0	3.1	3.0	3.2
Fe	4.6	2.1	6.0	12.4	9.2	8.2	9.5	4.8	12.6	9.0	12.3
Sr				13.8	9.4	6.5	10.7	15.6	16.3	9.7	11.4
La					0.1	2.6	1.4	5.7	4.2	3.5	3.0
0			56.9	59.4	73.9	62.4	72.0	72.1	63.8	70.7	68.6
Si	5.4										

Figure 12. Perovskite/Ni-B/Inconel Joint SEM 807x Compositions obtained using EDS

Another important difference between the reactions observed in the previous experiments with La<sub>0.6</sub>Sr<sub>0.4</sub>FeO<sub>3</sub> perovskites and those observed in theseLa<sub>0.2</sub>Sr<sub>0.8</sub>Cr<sub>0.2</sub>Fe<sub>0.8</sub>O<sub>3</sub>/Metal joints was the absence of a La-O layer in direct contact with the braze. When La is the major component in the A sites of the perovskite structure, the formation of La-O compounds appears very likely. When this is not the case, however, La appears to segregate towards the perovskite (see micrograph & EDS table in Figure 12). Another important difference is the formation of a complex Ni-Cr-O (point 3) layer in direct contact with the braze. This implies that local reduction of the perovskite surface is taking place. The local oxygen chemical potential at the interface must thus be such that decomposition of the perovskite structure is favorable (pO<sub>2</sub> around 10<sup>-16</sup>). A very interesting feature of this layer is the presence of highly metallic precipitates with Ni (point 2) as the major component (96%). As we go deeper into the reaction zone, Sr appears as a major component of the reaction products. La, on the other hand, does not appear at all in this region (point 4). It has been observed that this region is

most likely to be the nucleation site of cracks that run parallel to the ceramic/metal interface and further characterization of the reaction products in this area appears to be necessary.

At approximately 30 microns from the ceramic/metal interface, no noticeable changes in composition can be observed. In fact, it is not unreasonable to infer that the only difference between this region and the bulk perovskite ceramic is the presence of brazing alloy inside the pores of the material:

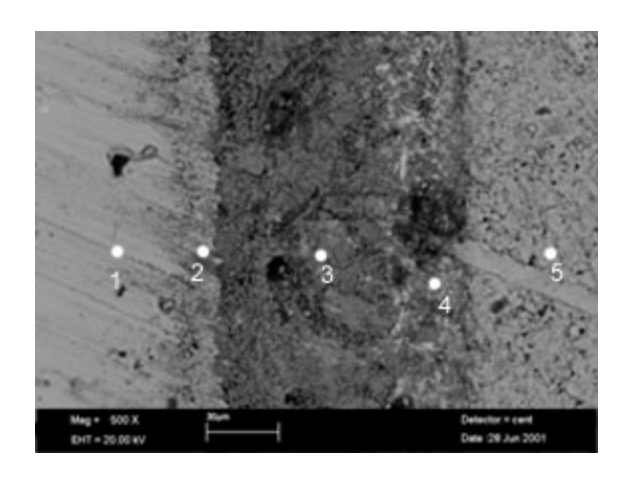
When comparing the results of both series of experiments, it is evident that Ni appears to be playing a major role in the these La<sub>0.2</sub>Sr<sub>0.8</sub>Cr<sub>0.2</sub>Fe<sub>0.8</sub>O<sub>3</sub>/Metal experiments, which is not the case in the La<sub>0.6</sub>Sr<sub>0.4</sub>FeO<sub>3</sub> /Metal reactions. Ni has been observed to be present at a depth of 60 microns into the reaction zone. This could be explained by the fact that the La<sub>0.2</sub>Sr<sub>0.8</sub>Cr<sub>0.2</sub>Fe<sub>0.8</sub>O<sub>3</sub> perovskite samples presented an extremely high porosity. The braze, therefore, was able to infiltrate the ceramic to a large extent. The porosity is thus "healed" by the presence of this liquid metal. The problem with this, though, is that the difference in expansion coefficients between the porous matrix and the filling medium can lead to a weakening of the matrix, as cooling and heating cycles occur.

# Perovskite / TiO / Ni-B / Inconel:

It had been observed that Cr-based diffusion barriers were not able to stop the extensive reaction occurring at the perovskite/braze interface. In fact, it was inferred from the results that the nickel-based brazing alloy effectively dissolved the Cr deposited on top of the ceramic surface.

In some preliminary experiments, Ti-sputtered layers were deposited on top of zirconia-based ceramic substrates. The aim of these experiments was to explore the possibility of using these reactive layers in conjunction with a non-reactive brazing alloy (Ni-based). It was observed that the Ti-sputtered layer reacted with the zirconia substrate to form a titanium oxide (presumably TiO). The Ni-based brazing alloy would in turn wet the oxide and a ceramic/metal interface would be created, as can be seen in Figure 3. The Ti-O layer was proved to be insoluble in the nickel-based brazing alloy, besides its ability to be wetted by it, forming a relatively stable and strong ceramic/metal interface. This particular characteristic made these layers a natural choice for the experiments conducted with the perovskite substrates.

In those experiments, however, it was observed that the reaction between the ceramic substrate and the brazing alloy were not halted at all. In fact, the nature and morphology of the reaction layers was observed to be the same as that present in previous experiments. As in the previous work, no Fe-segregation was observed. However, localized reduction of the perovskite was evident at the interface with the Ni-based alloy. Figure 13 illustrates the nature and morphology of the reaction products formed:



	1	2	3	4	5
Ni	80	22	4	1.0	0
Cr	7.2	10.1	3.1	2.1	2.9
Fe	6.1	0.6	8.4	10.2	11
Sr	0	0.8	9.2	11.1	14
La	0	0	2.4	2.5	3.8
0	0	62	72.9	73.1	67
Ë	0.1	0.5	0	0	0
Si	6.6	4	0	0	0

Figure 13. Interface between Perovskite and Ni-based brazing alloys with Ti-based diffusion barrier

Compositions obtained using EDS

As in the previous experiments, it was again observed that Ni infiltrated the ceramic substrate through numerous pores present in the system as fabricated. This infiltration, we believe, has several detrimental effects on the strength of perovskite/metal seals:

First, extensive infiltration increases the rate of the reaction between the ceramic substrate and the brazing alloy, exposing more area to the localized reduction that takes place when the Cr contained in the alloy reacts with the perovskite substrate to form  $Cr_2O_3$  or other complex oxides. Additionally, as the infiltrated metal cools down, large thermal stresses build up in the porous area close to the ceramic/metal interface, due to the different thermal expansion rates of the ceramic and the infiltrated metal.

Despite the fact that Ni-based brazing alloys do not normally dissolve Ti-O layers (as evident from previous experimental results), excessive porosity prevented the Ti-O layer from acting as an effective diffusion barrier. As the infiltrated metal attacked the ceramic immediately below the Ti-O layer, the reactions undergone diminished the adherence of the barrier and further attack was promoted.

#### 1.2.9 Zirconia Ceramics as Diffusion Barriers

In this project several approaches have been investigated in order to develop an effective way to prevent the excessive interfacial interactions that occur occurring when attempting to create perovskite/metal seals using liquid alloys. Many of these approaches were based on the creation of a diffusion barrier directly on top of the perovskite substrate. In order to do this, physical vapor deposition techniques were used to deposit thin films of metals that could be easily oxidized and form protective barriers that would limit the reduction of the perovskite substrate. Although the thin films could be easily deposited on the substrate, it was found that the transient liquid phase bonding (TLPB) alloy was able to penetrate through the film and attack the perovskite substrate.

Given the limitations of the diffusion barriers that were investigated in earlier stages of the project, it was decided that it was necessary to explore other alternative barriers that were more stable and thus capable of protecting the perovskite membrane in a better way. Given their thermodynamic stability and their relatively large coefficient of thermal expansion (compared to that of other oxides such as alumina), zirconia-based ceramics were considered as a possible solution to the problem in question.

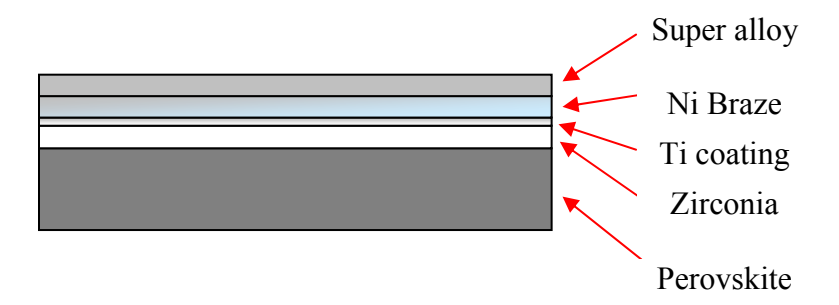


Figure 14. Interfacial modification of perovskite substrates.

Figure 14 shows the basic idea behind the use of a zirconia thin layer that would serve as a protective coating for the perovskite substrate. Since zirconia is one of the most stable ceramic oxides, conventional Ni-based alloys would not be able to wet it. In order to promote wetting, it was found that the zirconia layer needed to be modified. To this effect, a relatively

thin layer (5  $\mu$ m) of Ti was deposited through sputtering on the zirconia surface. Due to the strong thermochemical interaction between Ti and Ni and Ti and ZrO<sub>2</sub>, it was expected that the addition of this layer would promote adhesion between the Ni-based alloy and the zirconia substrate.

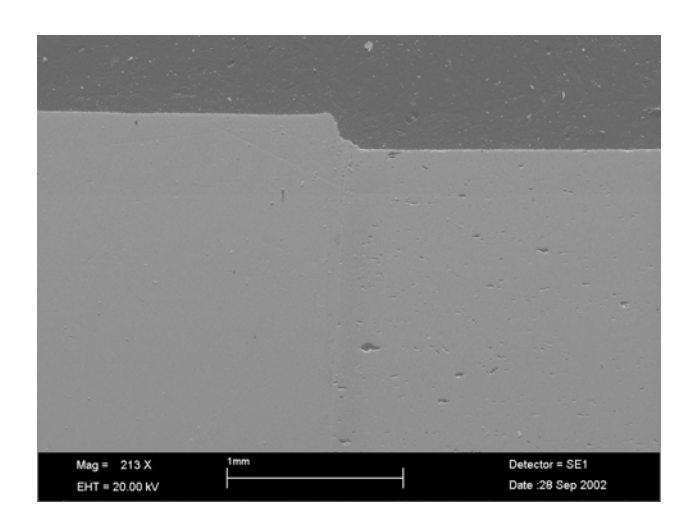


Figure 15. Zirconia/Ni-TLPB Alloy/Ni-based Super Alloy Interface.

Figure 15 shows that, by using Ti coatings over zirconia substrates it is possible to obtain full adhesion between the Ni-based TLPB alloy and the zirconia substrate. In order to understand the zirconia/Ti interfaces formation process, it was decided to develop a model that would describe the thermodynamic and kinetic aspects of the zirconia/Ti interactions.

#### 1.2.10 Modeling of Zirconia/Ti Interactions

As zirconia reacts with Ti, oxygen vacancies are created according to the reaction:

$$2Zr_{Zr}^X + O_O^X \Rightarrow 2 \cdot Zr_{Zr} + V_O^{\bullet \bullet} + \frac{1}{2}O_2(g)$$

$$\tag{1}$$

Because of the high chemical affinity between O and Ti, a large oxygen chemical potential gradient is created across the C/M interface as soon as the ceramic oxide is put in contact with Ti. This gradient constitutes the driving force necessary to carry out joining. As oxygen vacancies are created, oxygen atoms diffuse towards the zirconia/Ti interface. As zirconia reacts with Ti, a sequence of titanium oxides is formed at the interface and the complex layering grows with time until chemical equilibrium is reached.

According to experimental results the titanium reaction layer often found at zirconia/Ti interfaces is  $TiO_{1-x}$ . The nature of the first-forming titanium-oxygen compound at the C/M interface is determined by the interfacial oxygen chemical potential, which can be fixed by additional chemical reactions occurring in the system.

In general, for zirconia/Ti interfacial reactions involving active metal brazing, it can be assumed that:

As soon as the Ti thin film over the zirconia interface is put in contact with the zirconia substrate, oxygen vacancies will be formed in the latter. The freed oxygen ions will diffuse towards the Ti film, due to the large oxygen chemical potential gradient across the zirconia/Ti interface.

As oxygen diffuses out of the zirconia lattice, unsaturated bcc (body centered cubic)-Ti(O) forms. As oxygen continues to flow across the zirconia/Ti interface a second phase, hcp (hexagonal close packed)-Ti(O) precipitates and becomes increasingly saturated with oxygen until it reaches the saturation composition Ti<sub>2</sub>O. If the oxygen chemical potential at the interface is fixed at a suitable value, the TiO<sub>1-x</sub> phase may precipitate (See Figure 16, horizontal arrow), provided there are no kinetic barriers for its nucleation and growth. When cooling the sample, solid-state transformations can take place, transforming the reaction layer to oxide phases stable at low temperatures.

It has been shown that it is possible to model the Ti/zirconia thermochemical interactions through the solution of the so-called Cahn-Hilliard equation,

$$\frac{dc}{dt} = -\nabla \cdot M \cdot \nabla \left( \frac{\partial f}{\partial c} - 2k \nabla^2 c(x) \right)$$

$$= M \left( \nabla^2 \left( \frac{\partial f}{\partial c} \right) - 2k \nabla^4 c(x) \right)$$
(2)

where c is the composition, M is the atomic mobility, and  $\frac{\partial f}{\partial c}$  corresponds to the oxygen chemical potential at any region of the system.

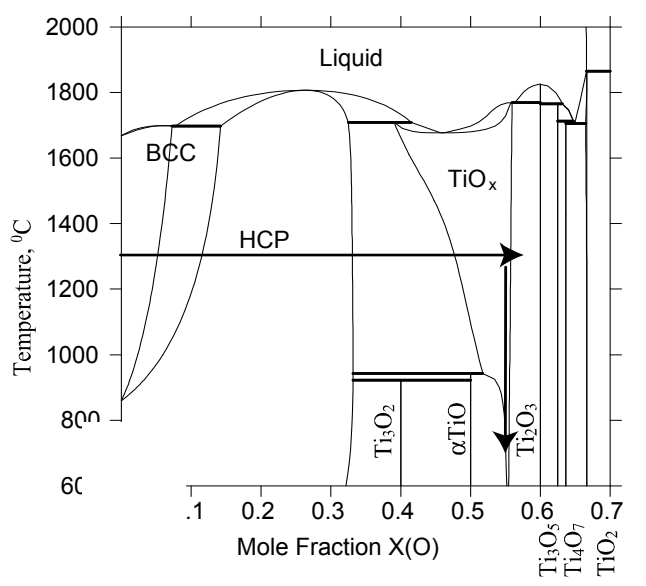


Figure 16 Ti-O Phase Diagram.

Through the numerical solution of equation 2 it has been possible to describe the evolution of zirconia/Ti interactions. In figure 17 some of the results are shown. As can be seen, the reaction sequence through which bcc-Ti is transformed into a Ti-oxide, as was observed in the experiments corresponding to figure 15, is correctly represented through the solution of the Cahn-Hilliard Equation.

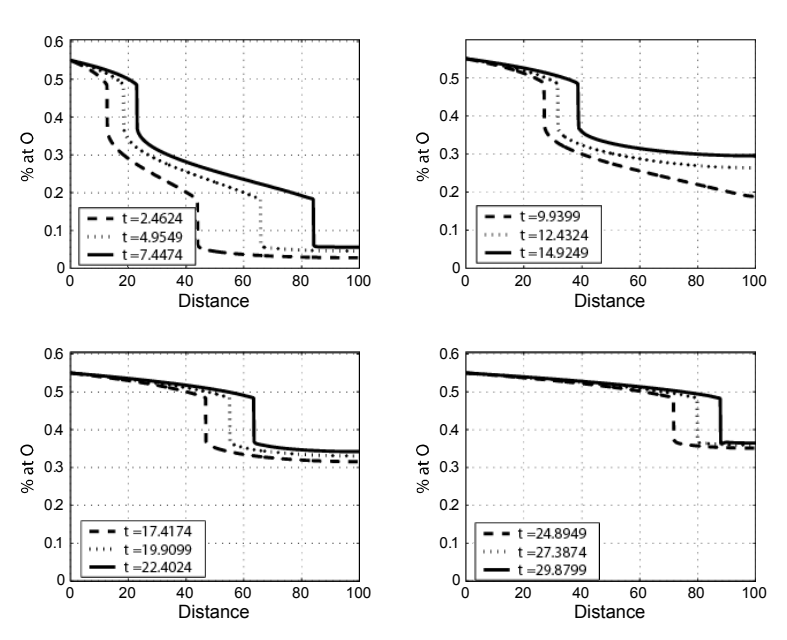


Figure 17. Concentration profile of a Ti layer in contact with a zirconia substrate, according to the solution of the Cahn-Hilliard equation.

#### 1.3 CONCLUSIONS

Considerable progress was made in the understanding of the main factors that affect the reliability of perovskite/metal seals. A mechanical testing procedure has been developed. This model was tested with model ceramic/metal systems but it is expected to be useful for testing concentric perovskite/metal seals. A finite element model of the concentric joint has been developed. Although it has been actually tested with data corresponding to alumina-based ceramics, the model was used in conjunction with the experiments to establish a reliable relationship between the strength of dissimilar material joints and the total strain energy stored in the system. It was found that this basic model helps to predict to a first approximation the strength of a ceramic/metal joint, provided the total energy stored in the system can be calculated.

The objective of this part of the project is the development of reliable perovskite/metal seals. Therefore, several possible brazing systems to be used in perovskite/metal seals were investigated. It was concluded that Ni-based brazing alloys provided the best option in terms of brazing temperature and final operating conditions. Although it was possible to create flat perovskite/metal seals, it was observed that there was an excessive reaction at the ceramic/braze interface. Observed cracks parallel to the perovskite/metal interface were attributed to this interfacial decomposition of the perovskite. In order to limit the extent of interfacial reactions, diffusion barriers were tested.

In order to get a better understanding of the thermochemical interactions between zirconia-based ceramics (possible diffusion barrier materials) and titanium, a kinetic model based using Phase-Field techniques was developed during this project. A better model for the thermochemical interactions between zirconia layers and Ti thin films allows a better estimation of the processing times necessary to obtain a stable interface in perovskite/metal applications where zirconia-based diffusion barriers are used to decrease the interaction between the TLPB alloy and the substrate itself. Furthermore, the model developed in this work may eventually be applied to describe the detrimental liquid metal/perovskite interactions that prevent the creation of reliable perovskite/metal interfaces without the use of protective diffusion barriers.

# Chapter 2: Determine material mechanical properties under conditions of high temperature and reactive atmosphere

Prof. S. Bandopadhyay, Prof. Robert H. Trent, Dr. Nagendra Nagabhushana, Dr. Thangamani Nithyanantham and Dr. Somnath Biswas

University of Alaska Fairbanks, AK 99775

#### 2.1 Introduction

The objective of the proposed research program is to develop a fundamental understanding of high temperature deformation and fracture of ceramic membrane and other materials and to generate a high temperature mechanical property database for use in the design of structural ceramic membrane based synthesis gas reactors for the gas to liquids program. In addition to experimental investigations, another objective of the program is to develop extensive modeling of deformation, fracture and micro-structural aspects of these material systems.

The overall research program included:

- (a) Mechanical testing of materials in several regimes to include elastic tension and compression, fatigue, creep and fracture.
- (b) Detailed micro-structural characterization of materials prior to and after deformation to include grain size and defect distribution.
- (c) Developing physically based micro-mechanical analytical as well as computational models to describe deformation and failure mechanisms in such materials.

The overall approach of the proposed study was to develop a fundamental understanding of the influence of micro-structure on performance, and to assess the influence of processing variables on high temperature mechanical behavior. In addition, the fundamental understanding gained would enable the development of constitutive equations to predict the mechanical behavior of the ceramic membrane materials under the high temperature operating conditions.

# 2.2 Experimental Methods and Materials Characterized

## 2.2.1 X-Ray Diffraction

The samples were powdered and analyzed in a XRD for phase composition and analysis using a Rigaku diffractometer with 0.15418 nm Cu  $K_{\alpha}$  radiation. The interpretation of the data has to be backed by simulation of the XRD profiles and physical evidence of the ordering or phase transitions. In order to do this, we used X-ray diffraction programs such as FULLPROF to refine the possible structures and crystal geometry.

# 2.2.2 Scanning Electron Microscopy

The fractured samples were sectioned using a low speed saw and the surfaces sputtered with gold or platinum prior to examination in an electron microscope.

## 2.2.3 Thermal Analyses

The OTM membranes were cut into small pieces and the thermal analysis were carried out in the air and in the N<sub>2</sub> atmosphere with the heating rate of 20°C/min using a TGDTA (Perkin Elmer Instruments). The change in weight and endothermic and exothermic process corresponding to different oxygen desorption and structural changes were examined.

## 2.2.4 Expansion Studies

Thermal expansion behaviors of the OTM bars were studied using a commercially available dilatometer (Netzsch DIL 402 PC). The rectangular samples were cut and used for the analysis. Sapphire standard was used to run the correction runs and a heating rate of  $3^{\circ}$ C/ min was used for all analysis. N<sub>2</sub> was used as a purge gas in some studies and a flow rate 0f 150ml/min was used with an outlet pressure of 0.5bar.

## 2.2.5 Moduli Studies

Room temperature elastic properties (Young's and shear moduli) of the membranes were determined by the impulse excitation technique using the commercially available Buzz-o-

sonic nondestructive testing system (BuzzMac International, Glendale, WI) which measures the fundamental vibration frequencies. Young's moduli of the materials were also evaluated at elevated temperatures using a custom designed high temperature module of the testing system. A cylindrical alumina base was used as a stage on which the test specimen (50x15x0.6mm) was suspended on a thin wire support. A computer controlled impulse tool which fired an alumina rod onto the sample, was used to give mechanical impulse at the bottom of the rectangular bar and the vibration frequencies were transferred to a microphone through a sound guide. Delivering mechanical impulse in a definite time interval (1 min) and data acquisition was managed by the Buzz-o-sonic testing system and the whole experimental setup was housed inside a furnace and the temperature was controlled by a programmable controller.

## 2.2.6 Hardness and Fracture Toughness

The fractured samples tested at four different conditions (Air at RT and 1000°C,  $N_2$  at 1000°C and 90%CO<sub>2</sub>/10%CO at 1000°C) were mounted and polished to 0.25µm finish. The Vickers hardness (H) and the fracture toughness ( $K_c$ ) were measured by applying varying loads (.98 N – 9.8 N) for 15 seconds. The diameters and crack lengths of twenty indents in each of the materials were evaluated using the formula:

where 2a is the indent diameter and l is the crack length measured from the indent tip to the crack tip and E is the Young's modulus.

For LSFT, SLFT-CGO we used the formula:

Niihara et al. (1982)[1] equations for the Palmqvist cracks (0.25  $\leq$  1/a  $\leq$  2.5) and for the median cracks (c/a  $\geq$  2.5) are given in equations 1 and 2 respectively.

$$\begin{array}{c|c}
\hline
K_{IC} \varnothing \\
\hline
H \sqrt{a}
\end{array}
\qquad
\begin{array}{c}
H \\
\hline
E\varnothing
\end{array}
\qquad
\begin{array}{c}
0.4 \\
\hline
0.035(I/a)^{-0.5}
\end{array}$$

$$\begin{array}{c|c}
\hline
K_{IC} \varnothing \\
\hline
H \sqrt{a}
\end{array}
\qquad
\begin{array}{c}
H \\
\hline
E\varnothing
\end{array}
\qquad
\begin{array}{c}
0.4 \\
\hline
E\varnothing
\end{array}
\qquad
\begin{array}{c}
0.129 (c/a)^{-1.5}
\end{array}$$

where,

 $K_{IC}$  is the Mode I critical stress intensity factor (MPa.m  $^{1/2}$ ) Ø is the constraint factor ( $\approx 3.0$ ) H is the Vickers hardness (GPa) E is the Young's modulus (GPa) a is the half diagonal of the Vicker's indent (m) c is the radius of the surface crack (median) (m) and l is the crack length (Palmqvist) (m)

For comparison the  $K_{IC}$  values were calculated by using the following formula (eqn. 4 suggested by Evans and Charles [2] which does not include the elastic modulus of the membranes.

$$K_{IC} = 0.16 \text{ H}_{v} \text{ a}^{\frac{1}{2}} (c/a)^{-3/2}$$

#### 2.2.7Strength of Materials

# 2.2.7.1Strength Determination at Elevated Temperature and reducing Atmosphere

The operating environment was determined to be mixtures of CO, CO<sub>2</sub>, H<sub>2</sub> and steam at temperatures of up to 1000°C and 600 PSI. The autoclave was designed to fit into a MTS hydraulic test frame (MTS bionics). The skin of the autoclave (Fig 18) was Haynes 30 super alloy and the casing was lined with porous alumina refractory. The autoclave had a controlled three zone heating and the temperatures were controlled and monitored externally. The loading pedestals were made of high-density recrystallized alumina rods of 1 inch diameter and were designed to be loaded by super alloy spring baffles. This was done to

ensure no leakage of the corrosive gases from the autoclave chamber during application of load. The whole set up was enclosed in an environmental chamber (figure 19) which was connected to a heavy duty filter pump for evacuating any leaks as well as to prevent any rise in temperature inside the chamber. The reactant gases were designed to be mixed externally by digitally controlled mixing apparatus and provision was also made to inject steam through the line by means of a controlled syringe pump. The injection line was designed to be preheated to 250°C prior to be let into the autoclave chamber.

To determine strength at elevated temperatures, the autoclave was flushed with ultra high purity (UHP)  $N_2$  till a steady state was established and a positive chamber pressure of 0.17 MPa was maintained. The chamber temperature was then raised at  $10^{\circ}$ C/min to the final temperature of  $1000^{\circ}$ C. The test conditions correspond to a slightly reducing (oxygen equilibrium partial pressure =  $\log$  -4) environment. For testing in  $CO_2/CO$  environment, initial heating was done in UHP  $N_2$  and the environment then changed at  $900^{\circ}$ C by letting in premixed gas mixtures ( $CO_2/CO = 90/10$ ). The reducing environment at  $1000^{\circ}$ C and 0.17 MPa corresponded to oxygen equilibrium partial pressure of  $\log$  (-12.1). The rings were soaked for a period of 15 minutes at the test temperature prior to application of load.

For evaluating the rectangular bars, they were evaluated in-situ in an autoclave mounted on a servo-electric loading frame (Figure 20) and fixtures designed with specification as described by ASTM standard were used (Figure 18).



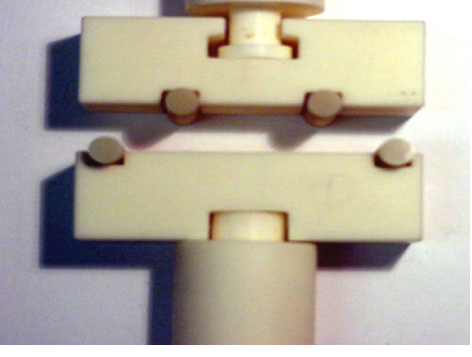


Figure 18. Autoclaves and Fixtures used for strength test.



Figure 19 Laboratory set up for testing strength of ceramic membranes for tubes



Figure 20 Laboratory set up for testing strength of ceramic membranes for bars

## 2.2.7.2 C-ring tests for fracture strength of Ceramic Tubes

C-ring tests were chosen for strength evaluation of oxide membrane tubes. For a C-ring test, the specimen preparation is simple and since the maximum tensile stress is generated along the outer diameter, results are sensitive to surface flaws or changes in surface flaw distribution induced by environmental factors.

The maximum fracture strength of the C-Ring specimens were calculated from the equation:

$$\sigma_{\theta \max} = \frac{PR}{btr_o} \left[ \frac{r_o - r_a}{r_a - R} \right]$$
 -----5

where where P is the failure load,  $r_o$  is the outer c-ring radius,  $r_i$  is the inner c-ring radius,  $r_a$  is the average of  $r_o$  and  $r_i$ , b is width, t is thickness or  $r_o$ - $r_i$ , and  $R = (r_o$ - $r_i)/ln(r_o/r_i)$ . However, the actual fracture strength is calculated from the measured angle of fracture from the mid plane.

The actual schematic of the test configuration is shown in Fig. 22. The C-ring specimens were placed between the alumina platens and monotonically loaded in compression under displacement loading at 0.5 mm/min. Zirconia cloth pads (~ 0.5 mm thick) were used to reduce friction between the platen and the test specimen.

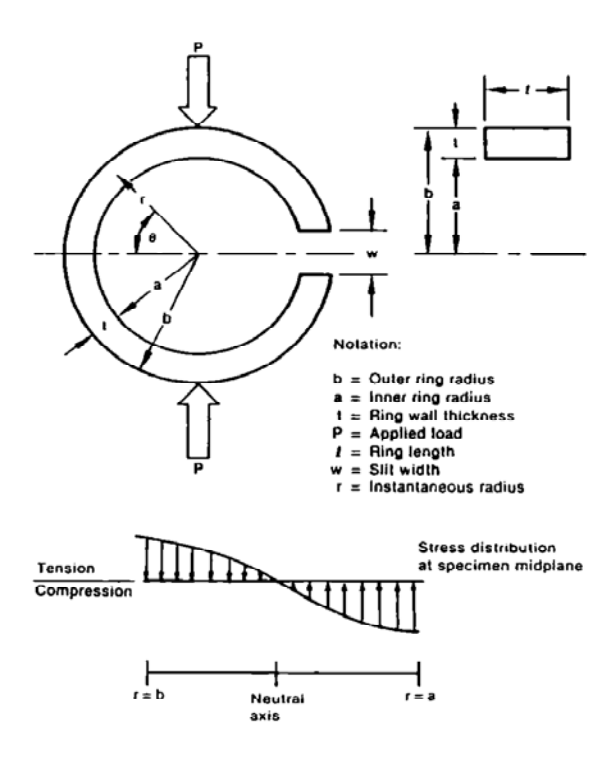


Figure 21. Stress distribution in a C-ring specimen subjected to uniaxial compressive load. The stress is tensile on the outer skin of the tube  $(r_o)$  and compressive at the inner surface  $(r_1)$ 

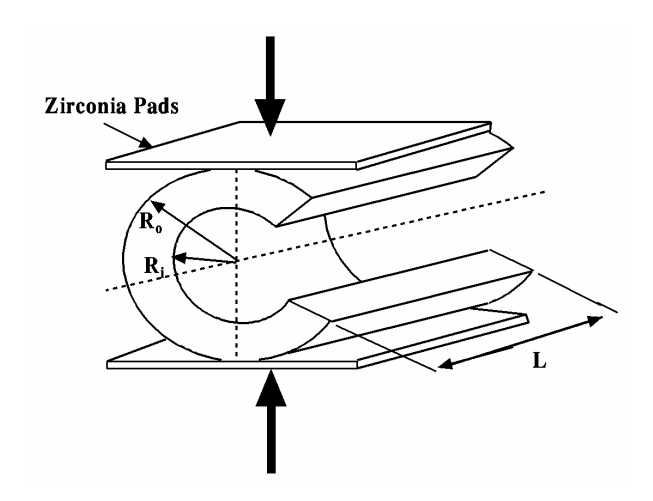


Figure 22. Schematic of the C-ring test adapted for the tubular OTM materials.

# 2.2.7.3 4- point bend Method

Flexural strength test specimens of dimensions (3x4x48 mm) were used for the study. They were evaluated in-situ in an autoclave mounted on a servo-electric loading frame. Loading was done in an in-house designed 4-point flexure with an outer span of 38.1 mm and inner span of 19.05 mm (ASTM-B). The specimens were ground and the edges barreled. All flexural strength tests were done by monotonic loading to fracture at a constant cross head speeds such as 6,60,600 µm/min in room temperature.

For testing in reducing conditions, the autoclave chamber was flushed with Ultra High Purity (UHP)  $N_2$  till a steady state was established and a positive chamber pressure of 25 PSI was established. The chamber temperature was raised at a rate of  $10^{\circ}$ C/ min to the final temperature of  $1000^{\circ}$ C. The specimens were soaked for a period of 1 hr at the reducing conditions (log pO<sub>2</sub> = -4) prior to application of any load. All flexural strength tests were done by monotonic loading to fracture at a constant cross head speeds such as 6,60,600 µm/min. The fracture strength  $\sigma_f$  of the OTM bars in 4-point flexure was calculated using the simple beam formula,

$$\sigma_f = \frac{3PL}{4BW^2}$$
 where P = Fracture Load, L = Outer Span, B = thickness and W = width of the beam respectively.

# 2.2.8 Weibull Analysis

The probability of failure  $P_f$  for the C-ring specimen subjected to a stress distribution  $\sigma$  was estimated from the two-parameter Weibull equation

$$P_f = 1 - \exp \left[ -\int_{V} \left( \frac{\sigma}{\sigma_o} \right)^m dV \right] \qquad -----6$$

Where m is the Weibull modulus (*shape parameter*) and  $\sigma_o$  is the characteristic strength (*scaling parameter*). The strength data can be graphically represented by the equation

$$\ln \ln \left(\frac{1}{1 - P_f}\right) = m \ln \left(\frac{\sigma}{\sigma_o}\right) + \ln KV$$

where KV is the effective volume of the material being tested. The effective volume expression is a function of the Weibull modulus and the geometry of the specimen configuration and is used to predict the strength distribution of one type of specimen from that of another.

#### **Slow Crack Growth Studies**

From the individual load-displacement traces of the specimen tested, the rate of stress increase was calculated as function of time from the equation:

Where P is the load rate, P is the specimen thickness, W is the specimen width and  $S_o$  (38.1 mm) and  $S_i$  (19.05 mm) are outer and inner spans respectively.

The Slow Crack Growth parameters n and D were then determined by a linear regression analysis using log strength values over the complete range of individual log strain rates, based on the following equation.

$$\log \sigma_f = \frac{1}{n+1} \log \dot{\sigma} + \log D$$
The slope of the linear regression line can be calculated as:

Where  $\alpha =$  slope, **K** is the total number of specimens tested (=8),  $\sigma_j$  is the stress rate and fracture strength of the individual test specimen respectively.

The SCG parameter n is calculated as

$$n = \left(\frac{1}{\alpha}\right) - 1$$

The intercept of the linear regression line is calculated as

$$\beta = \frac{\left(\sum_{j=1}^{K} \log \sigma_{j}\right) \sum_{j=1}^{K} \left(\log \overset{\bullet}{\sigma}_{j}\right)^{2} - \left(\sum_{j=1}^{K} \log \overset{\bullet}{\sigma}_{j} \log \sigma_{j}\right) \left(\sum_{j=1}^{K} \log \overset{\bullet}{\sigma}_{j}\right)}{K \sum_{j=1}^{K} \left(\log \overset{\bullet}{\sigma}_{j}\right)^{2} - \left(\sum_{j=1}^{K} \log \overset{\bullet}{\sigma}_{j}\right)^{2}} - \left(\sum_{j=1}^{K} \log \overset{\bullet}{\sigma}_{j}\right)^{2}} - \left(\sum_{j=1}^{K} \log \overset{\bullet}{\sigma}_{j}\right)^{2}$$

## 2.3 Materials Characterized

- i. OTM tubes
  - two sets of tubes: 20572-25PX and 20572-25T
  - six identical tubes 20573 (a-f) La<sub>0.2</sub>Sr<sub>0.8</sub>Fe<sub>0.8</sub>Cr<sub>0.2</sub>O<sub>3-δ</sub>
- ii. OTM bars
  - $La_{0.6}Sr_{0.4}FeO_{3-\delta}$  (LSF)
  - La<sub>0.8</sub>Sr<sub>0.2</sub>CoO (LSC)
  - $La_{0.2}Sr_{0.8}Co_{0.8}Fe_{0.2}O_{3-\delta}$  (2882)
  - $La_{0.6}Sr_{0.4}Co_{0.2}Fe_{0.8}O_{3-\delta}$  (6428)
  - $La_{0.8}Sr_{0.2}Co_{0.8}Fe_{0.2}O_{3-\delta}(8282)$
  - $La_{0.2}Sr_{0.8}Fe_{0.8}Cr_{0.2}O_{3-\delta}$  (LSFCO-3)
  - LSFT ( $La_{0.2}Sr_{0.8}Fe_{0.6}Ti_{0.4}O_{3-\delta}$ )
  - LSFT  $(La_{0.2}Sr_{0.8}Fe_{0.6}Ti_{0.4}O_{3-\delta})$   $Ce_{0.9}Gd_{0.1}O_{2-\delta}$  (CGO)

# iii. YSZ support

#### 2.4 Results and Discussion

#### 2.4.1 OTM Tubes 20572-25PX and 20572-25T

# **2.4.1.1 Specimen Preparation**

Samples for strength evaluation were cut from the given tubes by a low speed precision diamond saw. The cut surfaces of the rings were ground with SiC powder and polished with

diamond paste to  $\sim 1 \mu m$ . The edges of the samples were chamfered to  $\sim 45^{\circ}$  to ensure that failures do not originate from them. The polished rings were notched with a diamond saw to form a C-ring for strength evaluation. The dimensions of the C-rings were measured for strength calculation [ASTM].

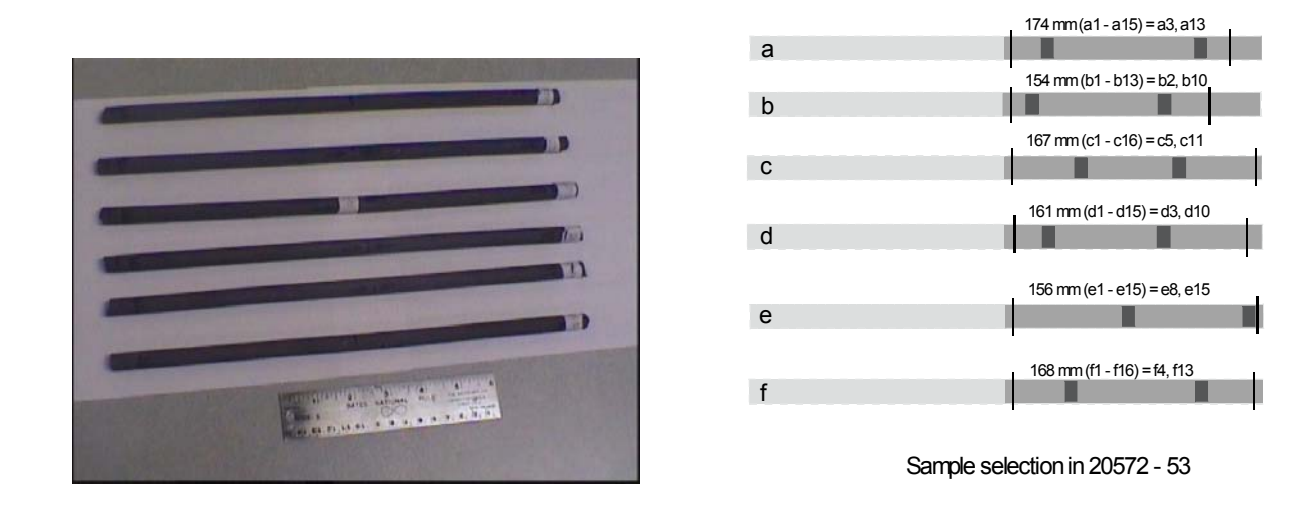


Figure 23. Sampling procedure for random sampling of specimens for strength evaluation

## **2.4.1.2** Results

# 2.4.1.2.1 Validation of experimental tests: Alumina

To validate the experimental set up and the testing procedure, tests were initially done on recrystallized alumina tubes (CoorsTek). The alumina tubes were of uniform dimensions and surface machined. Testing of the tubes yielded a 'm' value of 16 which is within the realistic estimates for alumina ceramic.

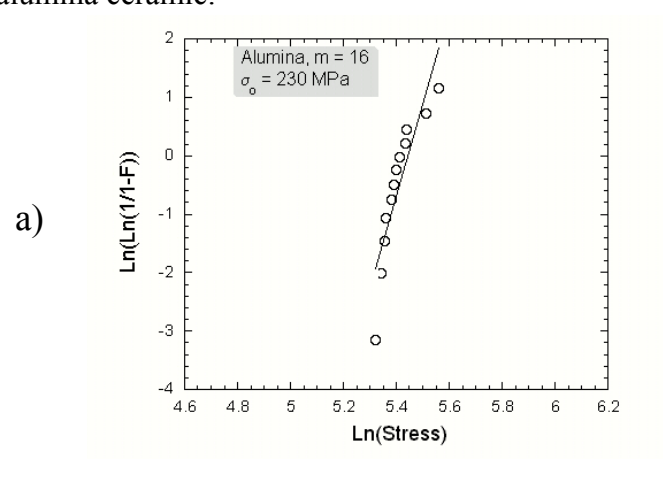


Figure 24. Weibull studies on reference material: 99.8% alumina

Initially two set of tubes 20572–25PX and 20572-25PT were provided for strength evaluation. The tubes provided were not uniform throughout the length and C-ring specimens showed variations in the wall thickness. As shown in the fig. 25, C-rings from 20576-25 PX had uniform outer diameter, but showed a large variation in the wall thickness. On the other hand, 20572-25 PT showed fewer scatter in the wall thickness but was not uniform in the outer diameter. These variations were expected to be reflected in the strength distribution. Hence as a standard procedure, strength values were calculated for every specimen.

	20572-25 PX	20572- 25 PT
Minimum, MPa	114.47	175.53
Maximum, MPa	210.43	429.18
Points	11	12
Mean, MPa	167.23	307.79
Median, MPa	188.47	302.05
Std Deviation	35.62	86.95
Variance	1269 19	7561 61

Table 2 Strength of 20572 tubes determined by C-ring tests.

The measured strengths of the 20572 tubes are as shown in table 2. The maximum strength of 429 MPa observed in 20572-25 PT was twice of that observed in 20572-25 PX (210 MPa). However, the standard deviation in the strength values of 20572-25 PT was higher than that observed in 20572-25 PX. This could possibly be attributed to the variation observed in the specimen geometry.

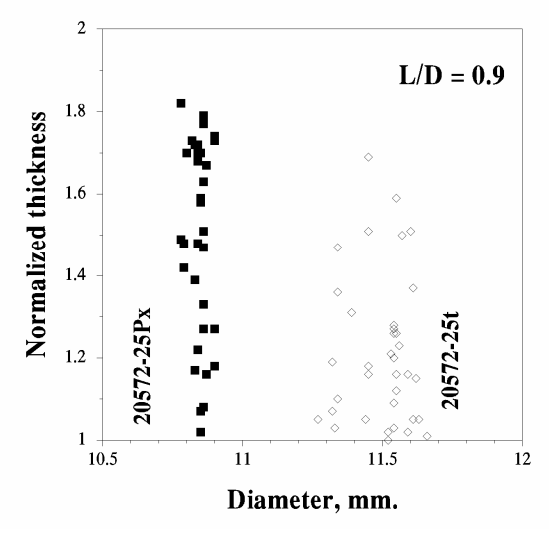


Figure 25. Dimensional variation observed in C-ring specimens for Weibull Modulus study

Macroscopic observation as shown in Fig. 26 indicated a distinctive difference in fracture morphology of 20572-25 PX and 20572-25 PT. In 25 PX, fractures in all the specimens tested occurred at midplane. The fracture surfaces were smooth and seemingly dominated by surface flaws. On the other hand, specimens of 25 PT shattered during testing and very often the fracture plane was at an angle from the midplane. The fracture morphology was predominantly jagged with interspersing planes of smooth fracture.

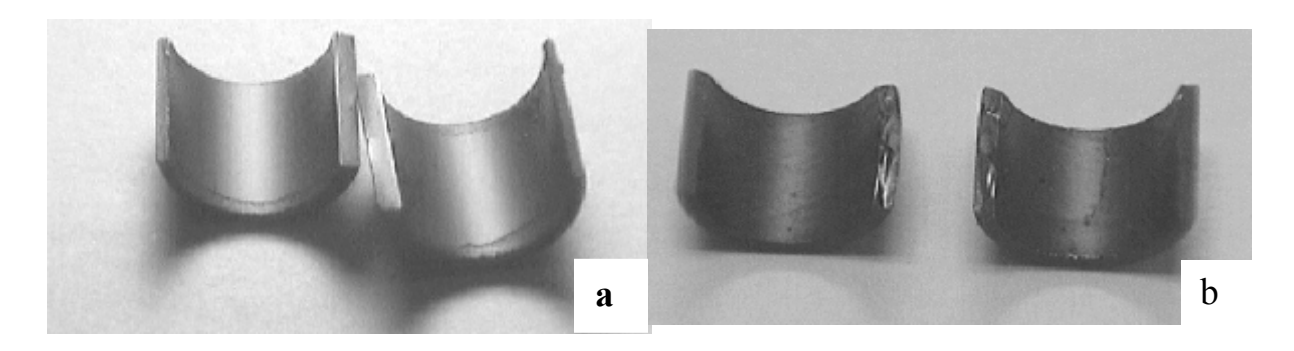


Figure 26. Macro-fracture observed in 20572 tubes: a) Smooth fracture in 20572-25PX and b) Jagged fracture in 20572-25T

Subsequent microscopic analysis (Fig. 27) indicated that the fracture in both the sets of tubes was controlled primarily by surface and volume flaws. The volume flaws were approximately of the order of  $10\text{-}25\mu\text{m}$  and occurred randomly in the microstructure. Microscopic studies (Fig. 28) also indicated that although the fracture in both the sets were by cleavage, they were of distinctively different morphology. In set A (Fig. 28a), the surfaces were smooth with apparent lack of features while in set B (Fig. 28b) microscopic cleavage planes were observed with evidence of 'pull out' of precipitates at triple point grain boundaries. Based on the macroscopic and microscopic fracture observations, a simple two-parameter Weibull plot was generated to characterize the strength and the observed variation in wall thickness of individual C-rings. The Weibull plot indicated a decreased Weibull modulus (m) in the 25T samples as compared to 25PX specimens. However, the characteristic fracture stress,  $\sigma_0$ , was higher in 25T samples at 372 MPa as compared to 183 MPa for 25 PX samples. A complete Weibull plot was generated from microscopic observation of fracture and the observed angle of fracture.

The observed variation in strength for the two set of tubes were plotted on a Weibull graph as shown in figure 28 a & b. The higher Weibull parameter, m = 5.2 for the 20572-PX as compared to m = 4 for 20572-25T, complement the observations for deviations in the materials strength values at room temperatures. The lower value of 'm' in both the sample sets signifies the influence of specimen geometry and flaw distribution on the overall strength distribution. The observed variation in the Weibull parameters and strength values can thus be attributed to the following factors:

- i) factors such as: additives added (distribution of volume pores arising from binder burn out), die used (surface flaws distribution) in processing of the tube
- ii) variations observed in the wall thickness and circular geometry of the tubes provided C- rings from 20572-25PX were generally less uniform in thickness while in rings from 20572-25T, variations in outer diameter were observed

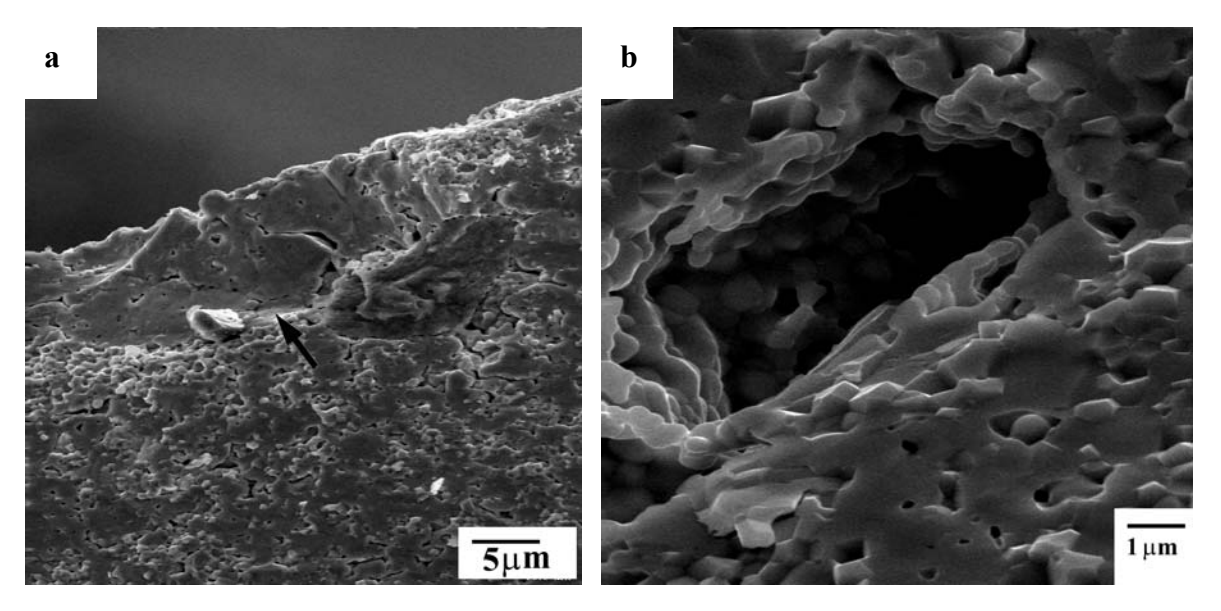


Figure 27. Transgranular fracture in: a) 20572-PX and b) 20572-PT. Instances of micro-cleavage are evident in 20572-25T

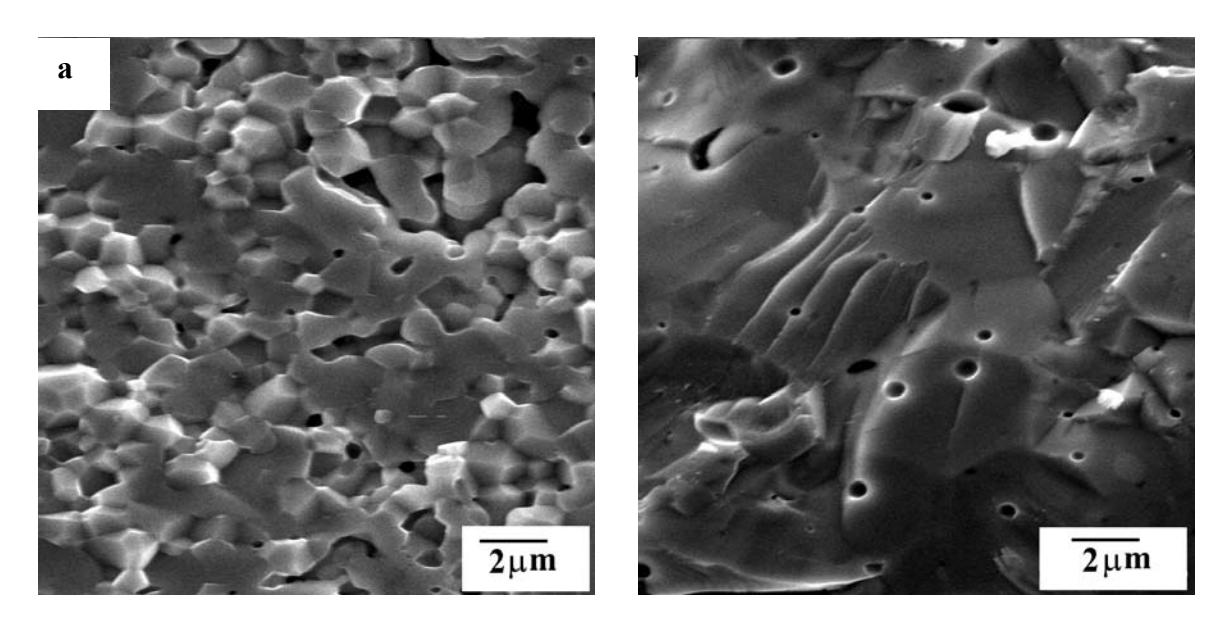


Figure 28. Transgranular fracture in: a) 20572-PX and b) 20572-PT. Instances of micro-cleavage are evident in 20572-25T

- iii) orientation of the fracture plane with respect to the loading axis or to the axis of the tube variations in dimension of the C-ring can significantly alter the stress distribution in the ring. Specifically in 20572-25T, although fracture was not at the mid-plane, the measured angles of fracture were not too high necessitating a detailed stress distribution. The equivalency from a computed stress profile for a C-ring test indicates that the fiber strains are nearly equivalent over a region described by  $\theta = 30^{\circ}$  and maximum stresses are not limited to the exact mid-plane of the specimen
- iv) inherent strength of the material

The first three factors affecting the strength distributions are invariably related to the processing route employed for processing the tubes. However, the fourth factor can be correlated to the inherent strength of the material and should be seen as a function of the composition and characteristics of the base powder. This is well reflected in the apparent difference between the two sets of tubes with respect to their fracture morphology. 20572-25PX is relatively fine grained and fracture is purely cleavage with total absence of any

feature indicative of a very brittle fracture. On the other hand, 20572-25T is coarser grained and the fracture exhibits additional features such as micro-cleavage of grains, pull out of grain and grain boundary precipitates indicating activation of toughening related mechanisms.

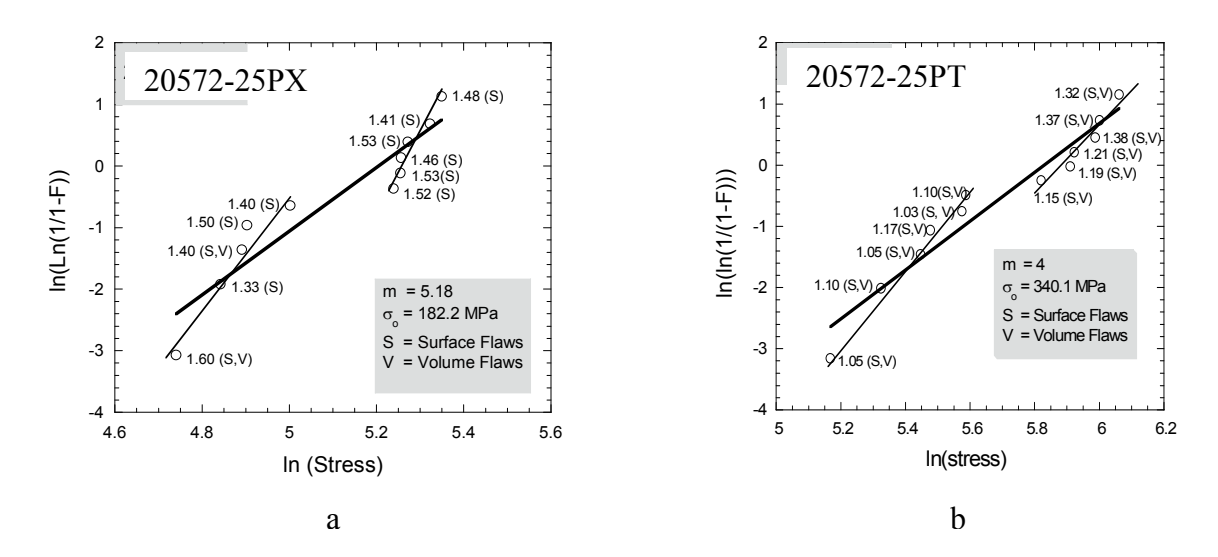


Figure 29. Weibull graphs on 20572 tubes. a) and b) 20572-25T

# 2.4.1.2.1 Effect of Temperature, Pressure and Environment

The perovskite tubes 20573 (a-f) (LSFCO) were evaluated for their strength as a function of temperature and pressure in air and in  $N_2$  environment. The average strengths (from 3 tests) are plotted graphically in figure 30.

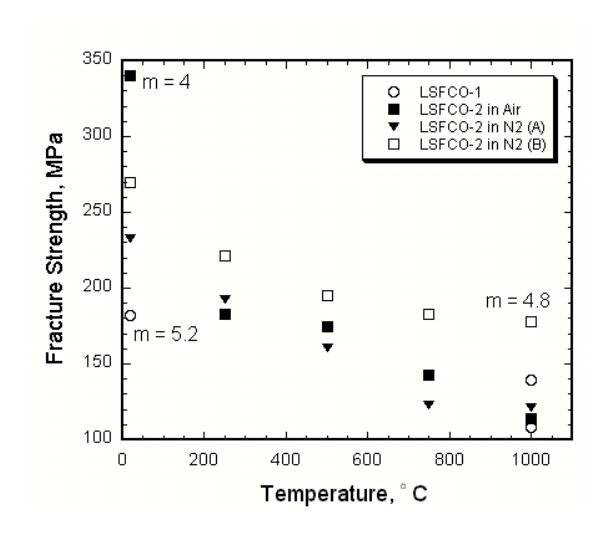


Figure 30. Influence of temperature, pressure and environment on the fracture strength of perovskite tubes

The perovskite tubes showed a slight change in fracture strength in air and in UHP nitrogen (with or without pressure). However, the strength values were within the acceptable range in comparison with the reported strength in Weibull modulus studies (in air). In air, the perovskite tubes showed a big drop in strength value from ~350 MPa at RT to 180 MPa at 250°C. Another drop in strength to 140 MPa occurred at 750°C followed by fracture at 120 MPa at 1000°C. In N<sub>2</sub>, the strength gradually decreased till up to 750°C and evened out at 1000°C. In N<sub>2</sub> with a pressure of 25 PSI (0.17 MPa), the strengths of the tubes were consistently higher than the corresponding strengths in air or in N<sub>2</sub> (no pressure) at all temperatures. The degradation in strength had a similar trend to that with out pressure. For comparison, the strength values of 20572 tubes are plotted in the graph (fig 30). The tubes showed lower strength than the 20573 tubes and in introspection were higher in N<sub>2</sub> as compared to in air. Fracture at lower temperature in air or in N2 did not show any dramatic changes in comparison with fracture at room temperature. However more incidences of particle pullouts were observed. Instances of material degradation were observed at 750°C, but were markedly more severe at 1000°C. Fracture and fracture morphology at 1000°C will be discussed in much detail in later sections.

### 2.4.1.2.2 Weibull modulus as a function of environment

The specimens chosen for testing indicated variation in wall thickness. Variation was observed to be severe at the center as compared to at the edges and deviation from circular cross-section was observed in some of the samples. The variation in wall thickness plotted as a function of the outer diameter of the tube is as shown in figure 31.

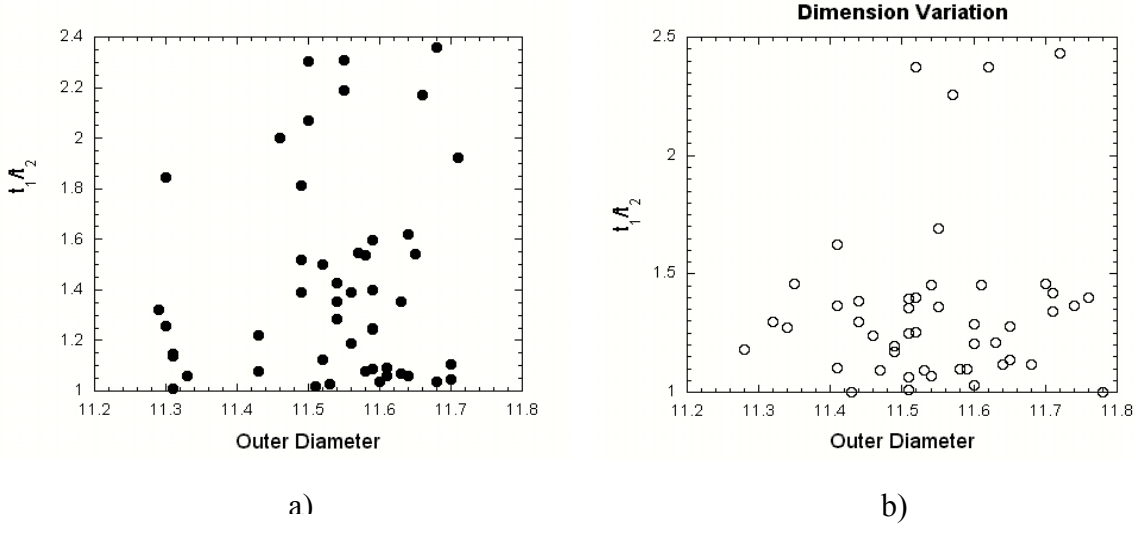


Figure 31. Dimensional variations recorded in the `as-processed' tubes for evaluation of fracture strength for Weibull Analysis. a) for N<sub>2</sub> and b) for CO<sub>2</sub>/CO environment

The Weibull plots as a function of environment are as shown in fig 32. Twelve samples were tested in each environment to generate the plots. The plots indicated no significant influence of the sampling procedure. This effectually meant that the processing techniques did not influence the strength of the tube or that the flaws in the tubes were not specific to the position in the tube from where the rings were drawn.

The characteristic strength ( $\sigma_o$  = 188 MPa) of the perovskite membrane tube at 1000°C in N<sub>2</sub> (fig. 32 a) was nearly half its value (340 MPa) at ambient condition. The decrease in strength was accompanied with a slight increase in the Weibull parameter as compared to that at ambient conditions (from 4 to 4.8). Although this increase is not significant (the values may possibly converge with large number of tests), there is a possibility that the environmental conditions may have actually blunted the strength controlling surface flaws (that dominate at room temperature) and the overall strength distribution then being controlled by the processing related volume flaws. The volume flaws distribution can also be expected to be augmented by the additional pores formed due to pull out of chromate phase precipitates at the grain boundaries. In the case of CO<sub>2</sub>/CO environment (fig. 32 b), a further drop in the characteristic strength ( $\sigma_o$ ) to 89 MPa was observed. A slight drop in the Weibull parameter (m = 3.8) was observed and could be attributed to the increased porosity in the fractured surface.

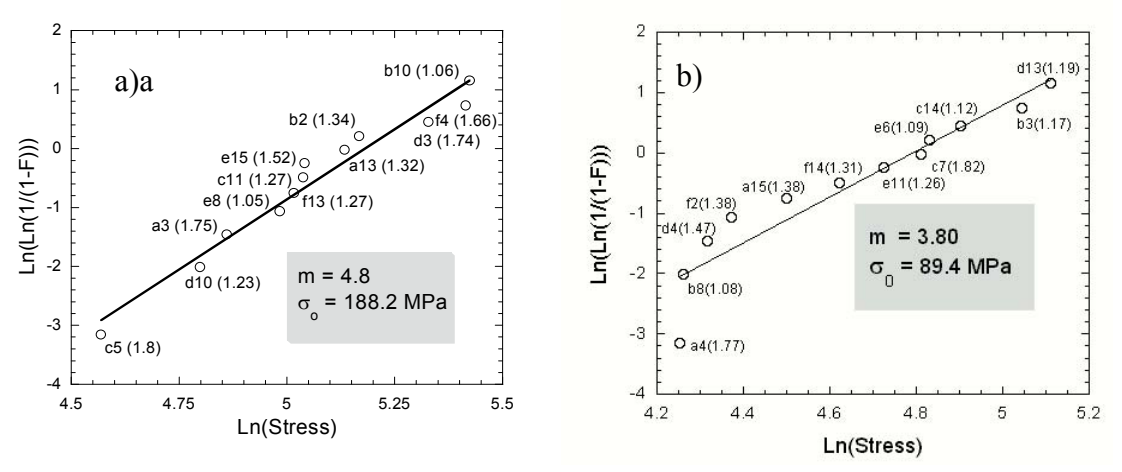


Figure 32. Weibull plots of `as-processed' in: a) N<sub>2</sub> and b) CO<sub>2</sub>/CO environment

### 2.4.1.2.3 Fracture and Fracture Mechanisms

All specimens tested in the present study exhibited brittle fracture. The macroscopic fracture morphology at ambient temperature was transgranular and predominantly jagged with interspersing planes of smooth fracture. Subsequent microscopic analysis indicated that surface and volume flaws controlled the fracture origins. The volume flaws were approximately of the order of 5-10μm and occurred randomly in the microstructure. In samples tested at 1000°C in N<sub>2</sub> and CO<sub>2</sub>/CO environment, the fracture surface as also the outer surface of the tube appeared to have significantly roughened. The measured surface roughness (Average roughness-Ra) increased to 5.6μm Ra from an initial value of 4.3μm Ra at room temperature. Microscopic analysis suggested that volume flaws were dominating the fracture origins.

Fractured surfaces of samples tested in both the reducing conditions showed that the material was composed of equiaxed grains. The microscopic analysis of fracture at ambient temperature indicated characteristic transgranular fracture with evidences of flat cleavage planes of brittle fracture and increased formation of pores at the grain boundaries (Fig. 33 b). The additional pores formed could probably be due to pull out of precipitates of the chromate phase at triple point grain boundaries. However, the exact contribution of the chromate phase at the grain boundary to the fracture strength of the material was not clear. Micro-cleavage planes in the grains pointed towards activation of additional energy dissipative process during crack growth and thus promoting small scale toughening in the material. Samples tested at 1000°C in N<sub>2</sub> showed a dramatic effect of the environment and temperature on the fracture morphology (fig. 33). The fracture surfaces showed increased density of pores at grain-boundary triple points and grain-boundary cavitations (fig. 33b). Moreover, the larger grains appeared to have broken down to finer particles and accentuated relief between the grains and the grain boundaries were observed (Fig. 33b). The grain boundaries were approximately ~0.5µm thick and the accentuated relief appeared to be similar to those observed in thermally etched surfaces of a similar oxide. The relief between the grain and the grain boundary seemed unlikely to be the effect of thermal etching since the test temperature was at least 500°C lower than the sintering temperature, and the residence time after fracture

was only a few seconds before the test furnace was switched off. The accentuated grain boundary could be due to the segregation of impurities or chemical inhomogeneity at the

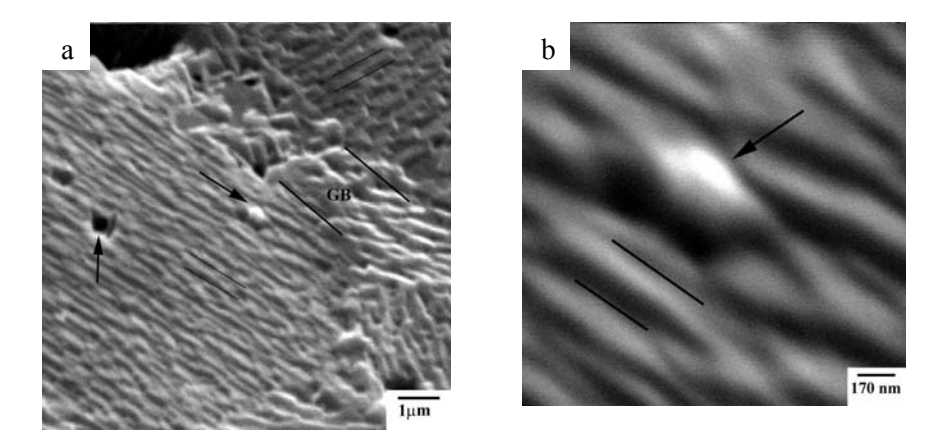


Figure 33. Transgranular fracture observed in samples tested in N<sub>2</sub> at 1000°C illustrating a) grains with accentuated grain boundary relief and b) Grain boundary cavitations.

grain boundary. A higher magnified view of a single fractured grain shows clear evidence of precipitate formation and their pull out inside a grain (Fig. 33 a and b). These precipitates were approximately 100 nm and appeared to have randomly formed between bands of grain matrix (Fig. 33b). The bands inside the grain were approximately 150nm with an average band spacing of 100 nm and indicated an orientation unique to the individual grain (Fig. 3 a). The accentuated grain boundaries also exhibited bands but they did not have the same orientation as inside the grains.

Energy dispersive X-ray (EDS) line scan profiles across fractured grains indicated significant variation of the elements La, Sr, Fe and Cr. As a rule, the dominant peaks were from Sr and Fe; La concentration was coupled with Sr and Cr with Fe concentration respectively. At ambient conditions, the grain boundaries tended to be richer in Strontium and leaner in Iron. In grains fractured at higher temperature (Fig. 34b), the dark bands were richer in Sr and Fe as compared to the brighter bands. Within each band, two distinct zones were noted: In the first zone, any increase in Sr, La and Cr concentration was accompanied with a decrease in Fe concentration. In contrast drop in La accompanied with increase of Fe and Cr and Sr concentration is observed in

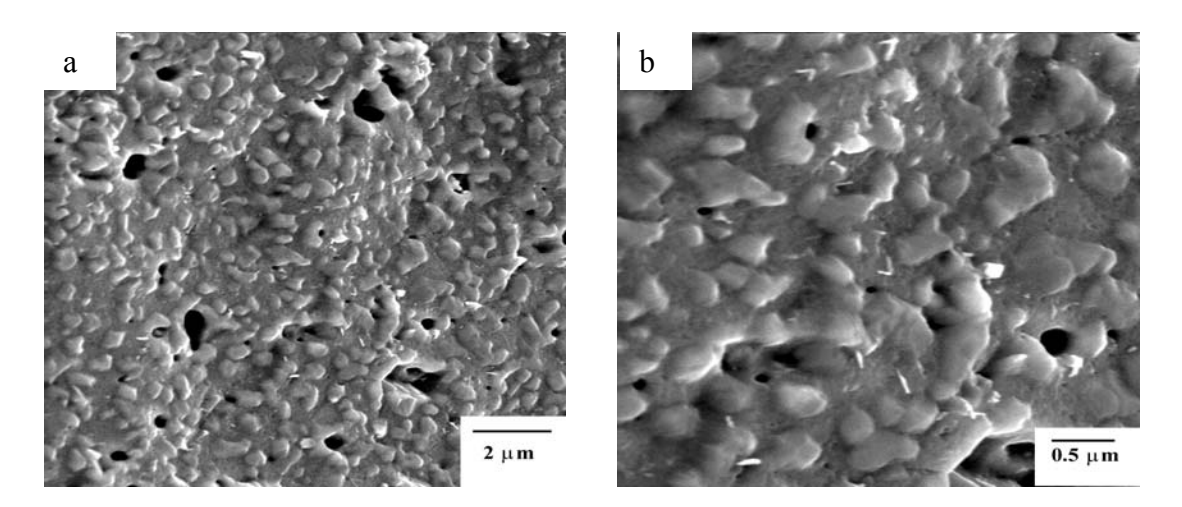


Figure 34. Transgranular fracture in a single grain indicating: a) Precipitation and pull out in the grains and b) Banded structure in the grain

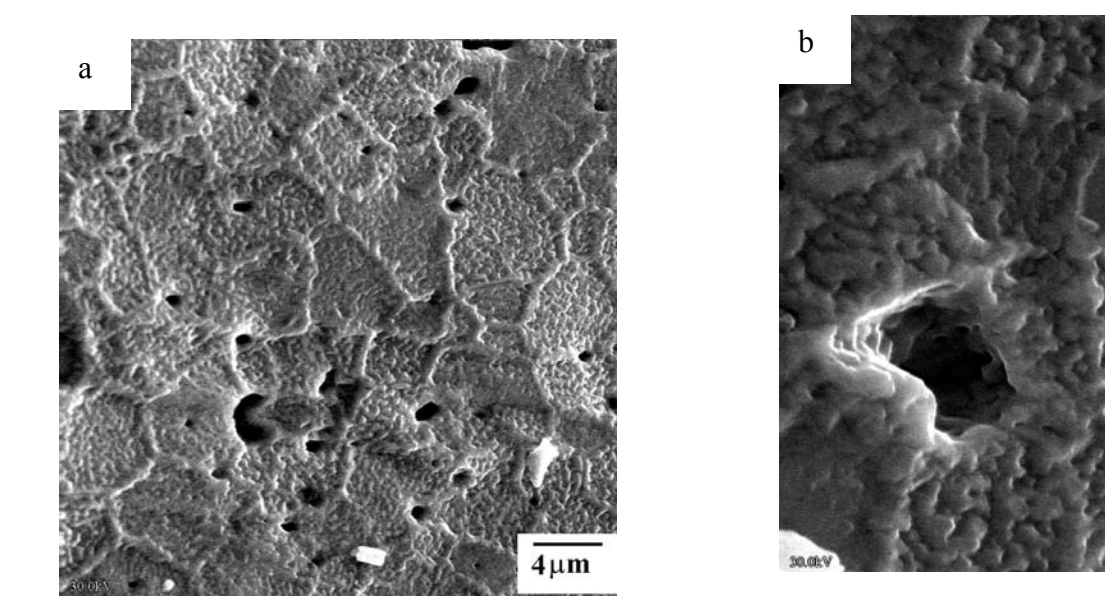


Figure 35. Fracture observed in samples tested in 90%CO<sub>2</sub>/10%CO.

second zone. In contrast, the first zone in the bright band indicated an uniform rise in La, Sr, Fe and Cr concentration and was followed by zone in which any rise in Fe concentration was accompanied by a drop in Cr, La and Sr concentration. The particles between the bands were observed to be richer in La, Sr and Fe as compared to the bands in the grains. This could

probably be the (La, Sr) Fe<sub>12</sub>O<sub>12</sub> phase. The grain boundaries were richer in Sr, while the grains tended to be Sr deficient. Within, the grain boundary any increase in Sr was accompanied with an increase in La and a corresponding drop in both Fe and Cr. The increased Sr at the grain boundary corresponded well with previous observations indicating a build up of strontium at the grain boundaries with the strontium deficient grains acting as acceptors. The enrichment of strontium probably via high diffusive paths at the grain boundaries could lead to the formation of point defects. The formation of point defects could then enhance the diffusion of oxygen or metal component via grain boundary and often govern the oxygen permeation, reaction and degradation of materials.

Sample fractured in  $CO_2/CO$  gas mixture, the fracture was essentially transgranular. Similar features as those observed in fracture in  $N_2$  were observed. However, the features were relatively coarsened and the grain boundaries showed lesser relief. At lower magnification (fig 35a), increased porosity and cavitations wer observed. At higher magnification (fig 35b), it seemed plausible that the bands as observed in (fig 34b) had coarsened. Also additional precipitates were observed.

### 2.4.1.3 Conclusions

- (1) Perovskites have been investigated to provide directly pertinent information on strength and fracture mechanism when processed as tubular membranes for application in separation reactors. The strength of the single phase perovskite tube in slightly reducing conditions decreases to nearly half—the value at ambient conditions (186 MPa and 307 MPa respectively). Fracture at both the conditions is primarily controlled by processing related defects such as surface flaws, pores etc. However, the flaw population does not significantly alter the high temperature strength distribution (Weibull parameter `m') in the oxide tubes.
- (2) Fracture in the tubular membranes is by transgranular cleavage of the equiaxed grains. Micro cleavage planes observed in individual grains indicates activation of small scale toughening process. Also evidences of precipitate (chromate phase) pull out at triple point grain boundaries are seen. Samples tested in reduced conditions, indicate roughening of the surface. Subsequent microscopic analysis reveals accentuated relief between the grains and

the grain boundaries probably due to segregation of elements and internal stresses. In addition, secondary phases at the phase junctions are formed during the heating and reduction process. The secondary phases formed inside the grains could probably be (La,Sr)Fe<sub>12</sub>O<sub>12</sub>.

- (3) The active diffusion mechanisms in LSFCO are observed to be controlled by the oxygen vacancies in the bulk. The oxygen vacancies are created by the acceptor A-site doping and are accompanied by the reduction of Fe and Cr at the B-site.
- (4) The possible ordering of the oxygen vacancies into the Brown-millerite phase leads to lattice expansion in one dimension. This may introduce additional stress at the grain boundaries.
- (5). The interactions between the dopant ions, oxygen vacancies, structure and/or phase transitions significantly influence the strain in the lattice. The interaction influences the fracture morphology and probably manifests in the formation of bands in the fractured grains.
- (6). The preferred fracture paths in the LSFCO membrane are possibly controlled by phase transition aided by reducing conditions and applied stress. The concentration of the oxygen vacancies in the membranes could significantly alter the stress distribution in the tubular membrane

# 2.4.2 OTM Tubes 20573 (a-f) $La_{0.2}Sr_{0.8}Fe_{0.8}Cr_{0.2}O_{3-\delta}$

The perovskite tubes 20573 (a-f) were evaluated for their strength as a function of temperature and pressure in 90%CO<sub>2</sub>/CO environment. The mechanochemical stability of the perovskites was examined by X-ray diffraction studies. The hardness and fracture toughness of the materials were evaluated as a function of reducing conditions and related to the observed mechanochemical degradation.

### 2.4.2.1 Experimental procedure

LSFCO membranes of the general composition  $La_{0.2}Sr_{0.8}Fe_{0.8}Cr_{0.2}O_{3-8}$  were evaluated in three different environments: air at room temperature, 0.17 MPa N<sub>2</sub> at 1000°C and 0.17 MPa CO<sub>2</sub>/CO (90/10) at 1000°C. The test conditions corresponded to oxygen partial pressures of  $log_{PO_3} = (-0.7)$ ,  $log_{PO_3} = (-4)$  and  $log_{PO_3} = (-12.1)$  respectively. The rings were

soaked for a period of 15 minutes at the test temperature prior to application of load. To evaluate the crack growth characteristics in the membranes, tests were done with a Vickers indent as a starter flaw. The indent formed with 9.8N load was placed on the polished outer surface (tensile mid-plane) of the ring and corresponded to a flaw size of  $157\mu m$ .

To study the effect of flaw size, indents with different loads were placed in two different conditions: i) individually and ii) in a profile as shown in figure 36. The cracked specimens were then placed in the chamber and loaded to fracture at a constant crosshead speed of 0.5 mm./min. respectively.

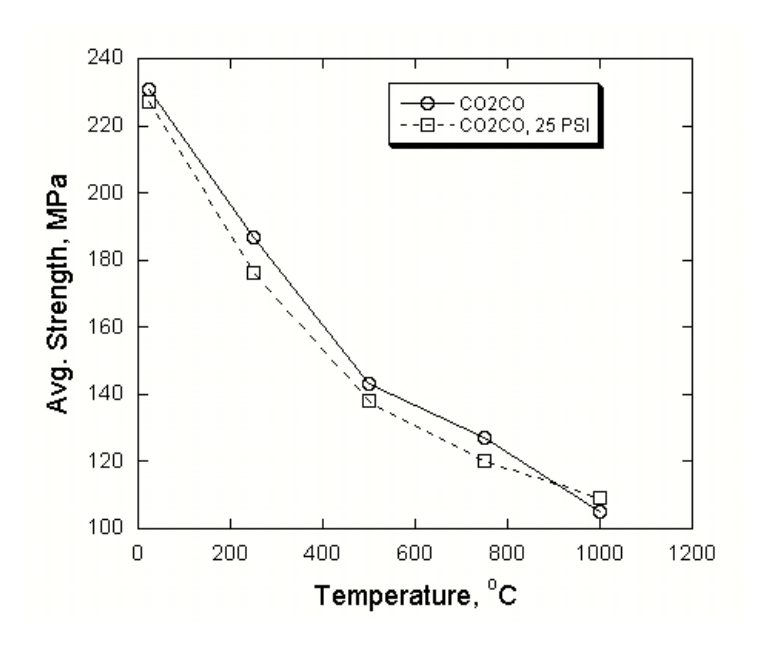


Figure 36. Influence of temperature, and pressure on the fracture strength of perovskite tubes

# 2.4.2.2 Effect of Temperature, Pressure and Environment

The average strengths (from 3 tests) are plotted in figure 37. A big drop in strength value occurred up to 500°C and thereafter the rate of strength degradation lowered. The strength

degraded to nearly 50% of its value at room temperature in the same environment. With a chamber pressure of 25 PSI (0.17 MPa), the strength of the tubes were consistently lower at all temperatures except at 1000°C, where a slight increase was observed. Fracture at lower temperature in 90%CO<sub>2</sub>/10%CO did not show any dramatic changes in comparison with fracture in air and N<sub>2</sub>. Material degradation were observed to occur at 750°C, that markedly became more severe at 1000°C. Fracture and fracture morphology at 1000°C have been discussed in much detail in earlier sections.

As seen in figure 37, the strength of the perovskite tubes decrease with reducing partial pressure. The strength degradation is rapid at very low reducing conditions (air at  $1000^{\circ}$ C corresponds to  $\log Po_2 = -0.7$ ). However, the strength degradation is less drastic in  $N_2$  and very high in  $90\%CO_2/10\%CO$ . The strength degradation was examined by analyzing the outer surfaces of the tubes exposed to the environment in a Seimens D5000  $\theta/\theta$  diffractometer using Cu radiation at 40kv/30 Milliamps to determine any phases formed after the tests. The samples were tested in a parallel beam arrangement to minimize the displacement errors caused by the curved surfaces. The X-ray plots as shown in figure 38 (a-c) indicate that the perovskite is stable at all temperatures up to  $750^{\circ}$ C where after it decomposes forming additional phases such as  $SrCrO_3$ ,  $SrFe_{12}O_{12}$  and SrO.

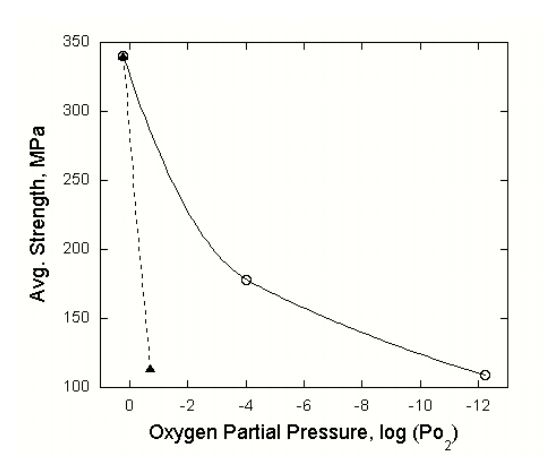
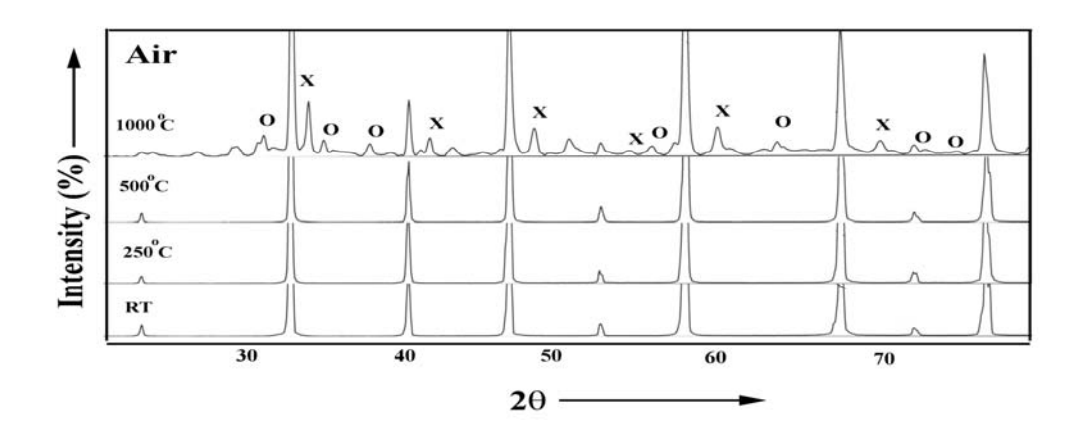


Figure 37. Effect of oxygen partial pressure on the strength of Perovskite tubes



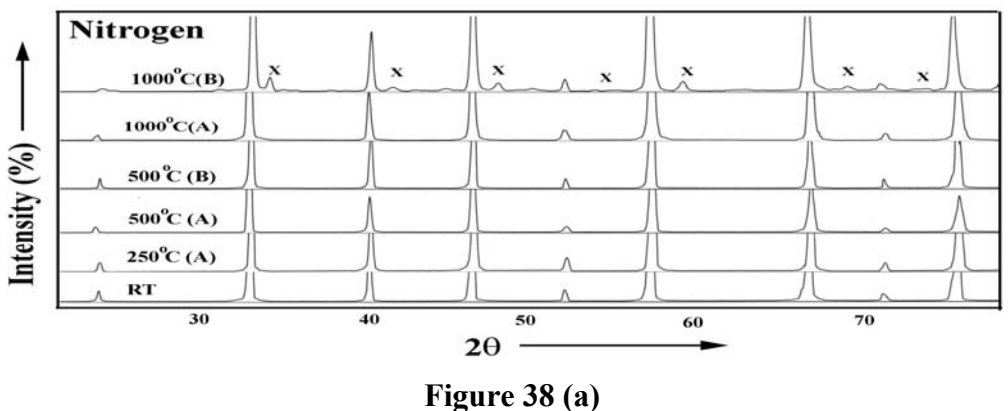


Figure 38 (b)

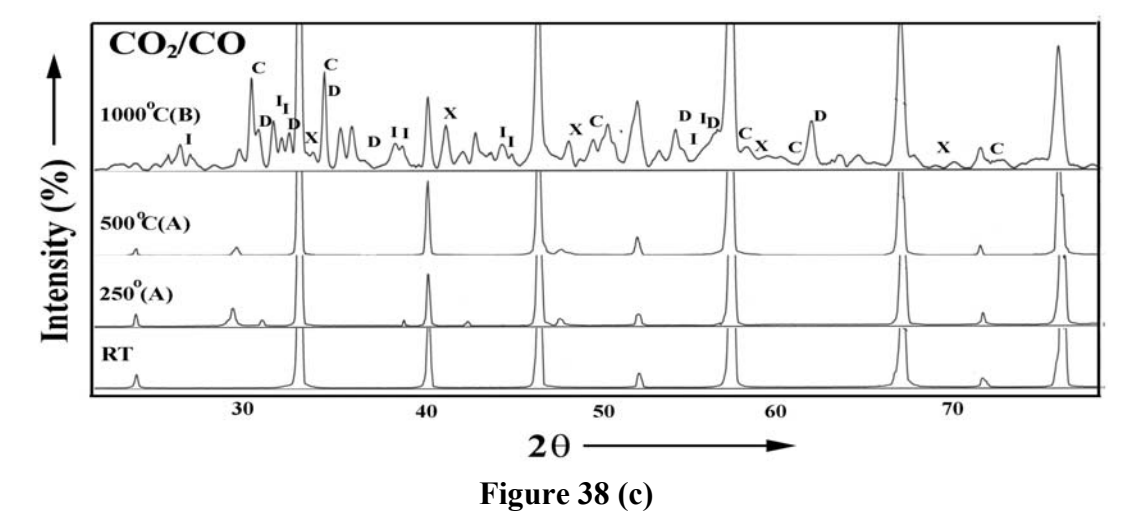


Figure 38. X-ray plot of the Perovskites after exposure to the environment. The phases formed are: (X)  $SrCrO_3$ ; (O)  $SrFe_{12}O_{12}$ ; (C) SrO and (D)  $CrFeSr_2O5.6$ 

As seen from Figure 38 a and b, the perovskite is more stable in  $N_2$  than in air. This corresponds well with the recorded loss of strength in air in comparison with  $N_2$ . Similarly, the perovskite decomposes to a larger extent in  $90\%CO_2/10\%CO$  than in  $N_2$  which explains the loss of strength in the environment.

# 2.4.2.3 Hardness and Indentation Fracture toughness of membranes

The fractured samples tested at four different conditions (Air at RT and  $1000^{\circ}$ C,  $N_2$  at  $1000^{\circ}$ C and 90%CO<sub>2</sub>/10%CO at  $1000^{\circ}$ C) were mounted and polished to  $0.25\mu m$  finish. The Vickers hardness (H) and the fracture toughness ( $K_c$ ) were measured by applying varying loads (.98 N – 9.8 N) for 15 seconds. The diameters and crack lengths of twenty indents in each of the materials were evaluated using the equation 1. A typical micrograph of the indent with lateral cracks extending from the tips of the indent is shown in figure 39. The measured hardness and fracture toughness are tabulated in Table 3.

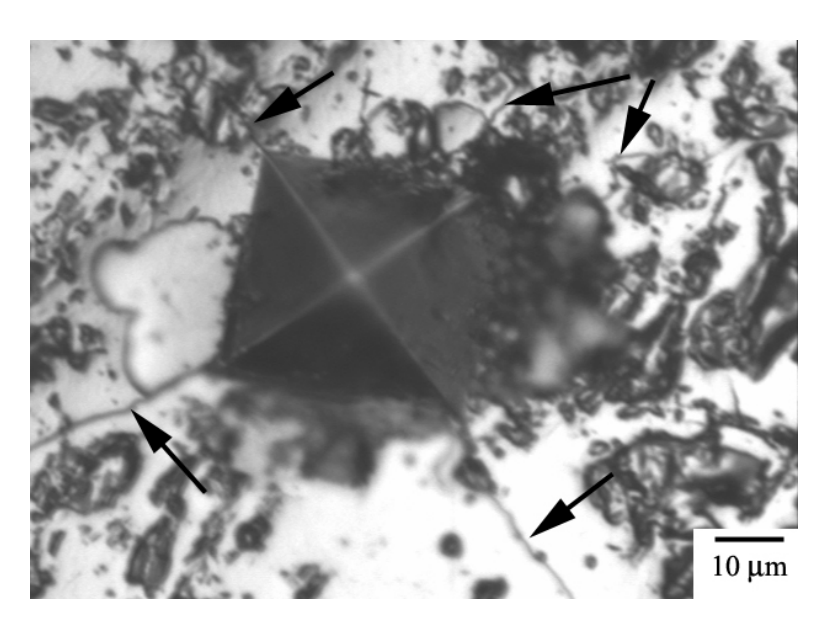


Figure 39. Vickers indent in the material for fracture toughness studies. The arrows mark the crack extending from the indent tip and used for computing fracture toughness

Table 3. Hardness and Fracture toughness as a function of reducing conditions

Test conditions	Hardness	Toughness (K <sub>c</sub> )	Normalized
	GPa	MPa√m	Toughness
As received	4.34±0.18	1.2 ±0.3	1
Air, RT	5.52±0.15	0.9±0.3	0.75
Air , 1000°C	5.43±0.22	0.1±0.015	0.08
N <sub>2</sub> at1.7 MPa and	4.02±0.10	0.14±0.01	0.11
1000°C			
CO <sub>2</sub> /CO at1.7 MPa	4.24±0.13	0.12±0.012	0.1
and 1000°C			

The hardness of the perovskite membrane in the as received condition was  $4.34\pm0.18$  GPa. Well-formed lateral crack extended from the tips of the indent at loads of 4.8 N. At higher loads 9.8 N a transition to the damage mode was observed. The fracture toughness was measured as  $1.2\pm0.3$  MPa $\sqrt{m}$ . The membrane after testing and fracture showed an increase in hardness to 5.52 GPa and a marginal decrease in fracture toughness.

Sample tested in Air at 1000°C indicated a similar change in hardness (5.43±0.22 GPa) in comparison with as–received samples although, increased variations were noticed in the measured values. However, the fracture toughness showed a drastic drop to nearly 8% of its room temperature value. The cracks emanating from the indent tip were larger and were observed to be predominant at lower loads of 1.96 N. Upon exposure to more reducing conditions (N<sub>2</sub> and CO<sub>2</sub>/CO at1.7 MPa and 1000°C), a decrease in hardness was observed. The hardness and its variation were relatively lower in samples tested in N<sub>2</sub> compared to those tested in CO<sub>2</sub>/CO. The measured fracture toughness was however higher in N<sub>2</sub> although it was drastically reduced form its initial value at room temperature.

The changes in hardness and fracture toughness are probably due to the decomposition of the parent perovskite phase. The decomposition products and the changes in fracture mechanisms upon exposure to varied reducing conditions have been thought to be the reason behind different hardness and toughness degradation observed in the membranes.

# 2.4.2.4. Fracture of membranes in oxygen chemical gradients

In a membrane reactor, the oxygen partial pressure (chemical potential) of the gas atmospheres on the two sides of the membrane typically varies from 0.21atm on the air side to as low as  $10^{-17}$ atm on the methane side. As shown in Fig. 40, the oxygen chemical potential at any point in or on the solid under steady state operating conditions is the result of dynamic balancing of the rates of each sequential oxygen transfer process along the path. Oxygen molecules are activated at the surface of the membrane on the air side and move through the membrane via coupled transport of oxide ions and electron holes. On the low partial pressure side of the membrane, oxide ions are available for direct oxidation of methane to synthesis gas or for recombination to form oxygen molecules, which may then subsequently react with the various gas species present on the fuel side. Thus in principle, any part of the oxide membrane can experience oxygen activities which cover the entire range. The entire solid will experience the conditions of the air side if the reaction of surface oxygen at the fuel side is rate limiting. In this case, all regions of the membrane (towards the air side) can be in partial equilibrium with air. At the other extreme, if oxygen activation is rate limiting, the entire solid operates under the reducing conditions of the fuel side. If oxygen transport through the solid is rate limiting, then a gradient across the solid between the two extremes is present. In all cases, the key kinetic parameters, surface reaction rates, oxygen diffusion, and electronic conductivity depend on the oxygen activity.

The results of our studies on mechanical strength, stability and fracture behavior of the membranes upon exposure to reducing conditions indicate an inherent dependence of strength on the stability of the microstructure due to changes in oxygen content in the structure. However, in gradient conditions, the resultant oxygen gradient can create a lattice mismatch across the ceramic bulk due to oxygen enrichment (air side) or depletion (reducing side), with concurrent expansion or contraction of the lattice, respectively. Failures arising from these conditions have been reported in studies on discs exposed to gradient conditions. In the present study, fracture evolution in LSFCO membranes has been characterized in partially gradient conditions. A partially gradient condition has been created by insulating one of the membrane surfaces with Platinum foils and the oxygen partial pressure (p<sub>O2</sub>) varied on the reducing side. The resultant

fracture morphology is characterized by Scanning Electron Microscopy [SEM] and correlated with earlier observations on phase transition, defect structure and oxygen fluxes.

# **Experimental Procedure**

Tests were conducted on LSFCO membranes C-rings insulated by Platinum foils such that only the tensile surfaces were exposed to the atmosphere. After testing, the fractured surfaces were examined under a Scanning Electron Microscope with an attached Electron Dispersive X-ray analysis (EDX) to characterize the dominating flaws and fracture mechanisms.

### **2.4.2.5 RESULTS**

Unique strength values for the material in the insulated specimen geometry could not be determined due to significant contribution from the Platinum foils. At room temperature, the strength values were consistently higher by approximately 50% and similar values were observed at elevated temperatures. Fracture analysis as shown in Fig. 41 indicated a gradient morphology with three distinct fracture regions. In  $N_2$  (Fig. 41a), a region ( $\sim 25 \mu m$ ) very close to the surface exhibits entirely transgranular fracture and is followed by a region (~250µm) with a mix of transgranular and intergranular fracture. The interior of the membrane is entirely transgranular cleavage and extends up to ~ 600µm. This region is again followed by a mix of inter- and transgranular fracture leading to complete transgranular failure at the inner wall surface. In CO<sub>2</sub>/CO (Fig. 41b), similar features are observed. The first region extends to only ~ 100µm and is followed by a mid region with a mix of inter- and trans- granular fracture extending over larger distance (~750 µm). Transgranular fracture dominates in the beginning of the region leading to a more pronounced intergranular fracture. This is followed by a third region (~150 µm) which shows a small area of transgranular fracture at the surface. Using a higher magnification study, comparative effect of environment on the fracture morphology in the three region is shown in figure 42.

**Regime I:** In N<sub>2</sub>, the initial region of transgranular mode is characterized by enrichment of Sr at the grain boundaries. With appearance of grains fracture in intergranular mode (Fig. 42a), a concurrent change in elemental distribution is observed. In CO<sub>2</sub>/CO, significant precipitation of second phase is observed in grains fracture in a transgranular mode (Fig. 42b). The precipitates

are relatively coarse with a size distribution varying from 0.25- $1.5\mu m$ . The precipitation is high near the surface (fully transgranular fracture mode) and reduces away from the surface. Single grains fractured in an intergranular mode in  $N_2$  (Fig. 43a) indicated a clear breakdown in structure. On the other hand, grains fractured intergranularly in  $CO_2/CO$  (Fig. 43b) showed clean surfaces and edges. Precipitate formations on the surfaces were clearly evident.

Regime II: In  $N_2$ , characteristic transgranular fracture of the perovskite grains was observed (Fig. 42c). The grain indicated the beginning of formation of a banded structure. However, the conspicuous thickening of the grain boundaries as seen in earlier studies on fracture was absent. In  $CO_2/CO$ , grains fractured in a transgranular mode and indicated precipitation of a second phase at the grain boundaries (Fig. 42d)

Regime III: In N<sub>2</sub>, although the fracture was a mix of trans- and inter-granular fracture, it was characteristically different from region I. The grains appear to have broken down aided by formations of very coarse precipitates (Fig. 42e). Overall, the structure appear similar to that of fracture in air with the coarse particles corresponding to the brittle (La,Sr)Fe<sub>12</sub>O<sub>12</sub> phase. In CO<sub>2</sub>/CO, the region is dominated by intergranular fracture (Fig. 42f). Second phase precipitation, which shows both intra- and trans granular fracture modes of failure, is markedly reduced in grains.

### 2.4.2.6 Discussions

At 1000°C, strength degradation is severe in air followed by CO<sub>2</sub>/CO and N<sub>2</sub> environment respectively. The strength degradation is accompanied by decomposition of the parent perovskite. The decomposition products are formed as precipitates either at the grain boundaries and/or inside the grains aiding in fracture of the grains and the membranes. Fracture is observed to be transgranular and has been argued to be assisted by transformation to the Brownmillerite or Laves phases depending on the test temperature. In the evaluation of fracture in the partially gradient conditions, two important issues are of merit:

i) Stresses in the membrane arising due to tubular geometry and oxygen transport; and, ii) Stresses arising due to differential decomposition of the parent perovskite structures. These two

factors are observed to be synergistic with a fair degree of complexity. The contributions from these two factors are discussed in subsequent sections.

# 2.4.2.6.1. Stresses arising due to Specimen geometry and Oxygen transport:

Perovskite are characterized by oxide ion transport through vacancy mechanism. Assuming that at a given oxygen chemical potential gradient the phase composition of the oxide is constant, the partial ionic and electronic conductivities under isothermal conditions can be expressed as

where  $[V_O]$  and  $c_o$  stand for the fraction of vacant and occupied sites in the oxide ion sub lattice; N is the concentration of oxide ion sites;  $h \times (N/3)$  is the concentration of holes (h is a relative concentration of holes);  $K_o$  and  $K_e$  are constants. In accordance with the equation for oxygen entering and leaving the crystal lattice

with h<sup>•</sup> being an electron hole, the concentration of oxide ions and vacancies in terms of point defects model are related by the expression

$$K_g = \frac{h}{3} + 2[V_O] \qquad ---- 17$$

Where  $K_p$  and  $K_g$  are constants; p is the partial pressure of oxygen. The density of the molecular oxygen flow passing through a ceramic material under the action of the chemical potential difference can be expressed as follows:

Where  $K_m = (RT)/(16F^2d)$ ,  $c_1$  and  $c_2$  are the values of  $c_0$  in the surface layers of the membrane

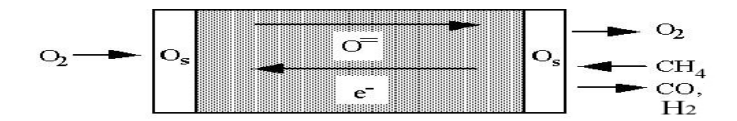
Published models have assumed constant properties (for example, a simple first order rate constant for oxygen surface activation and a single value of the diffusion coefficient). Clearly, if the surface and bulk transport rates have a strong dependence on the oxygen activity, these models will contain significant errors and will not provide reliable predictions especially when the  $po_2$  gradient is large as is the case for syngas generation. The distribution of the  $po_2$  gradient depends on the relative rates of the surface and bulk processes and consequently kinetic data for the whole range of partial pressures is relevant. In case B, the left hand surface is neither at the oxygen potential of the bulk or of the gas phase and the surface exchange kinetics may exhibit different behavior from either of the bilk phases. To model this results for  $La_{0.2}Sr_{0.8}Fe_{0.8}Cr_{0.2}O_{3-x}$ , initial values of  $D_{chem}$  and  $b_{chem}$  of  $b_{chem}$  of  $b_{chem}$  and  $b_{chem}$  of  $b_{chem}$ 

# 2.4.2.6.2. Stresses due to decomposition of the parent perovskite

The perovskite structure, with the general formula ABO<sub>3</sub>, is a simple cubic system having one formula unit per unit cell. The B cation is octahedrally coordinated to six oxygen ions, and these octahedra are corner-shared. The A cation occupies the space between eight octahedra and has twelve nearest-neighbor oxygen ions. Thus, there are many possible distortions of the perovskite structure depending on the relative sizes of the A and B cations. Replacement of the A cation with cations of lower charge (A') begins to distort the perovskite crystal structure through the introduction of oxygen vacancies into the lattice. Likewise, replacing the B cation with B' affects the crystal structure. The resulting material is an intergrowth of perovskite and a material termed

brownmillerite (AA'BB'O<sub>5</sub>) in which (due to oxygen vacancies) some of the B cations are tetrahedrally bound to oxygen rather than octahedrally bound. The transformation of the crystal structure from the cubic perovskite structure to the orthorhombic perovskite-brownmillerite intergrowth results in a change of structural dimensions. Changes in temperature results in additional mechanical stresses since the cubic perovskite structure undergoes uniform isometric changes in all dimensions, whereas the brownmillerite pseudomorph undergoes anisotropic changes due to its orthorhombic crystal structure. Replacement of La<sup>+3</sup> on the A sites by divalent ions such as strontium (Sr<sup>+2</sup>) results in materials with increased oxygen permeability. Increase in strontium content, however, has detrimental structural effects upon the crystal lattice.

The thermal expansion increases with increasing strontium content, which is consistent with the theory of cubic perovskite to orthorhombic brownmillerite transformation. The B site cations (Cr, Fe) in these substituted perovskites frequently exhibit unusually high oxidation states, which have been stabilized by the unique crystal structure. Therefore, chromium can exist as Cr<sup>+3</sup>, Cr<sup>+4</sup>, and Cr<sup>+6</sup>, iron as Fe<sup>+3</sup> and Fe<sup>+4</sup>. Since, a trivalent ion is required for charge satisfaction in LaMO<sub>3</sub>, reduction to a lower oxidation state will result in a brownmillerite structure, and hence oxide conduction. As the atomic number increases, the stability of the trivalent state decreases. Therefore, the trivalent oxidation states of Cr and Fe can be considered fairly stable. The crystal structures of many of the solid solutions of (LaA')(B'B")O<sub>3</sub> compounds indicate phase transformations from cubic to orthorhombic/tetragonal/rhombohedral as the crystal lattice is subjected to temperature profiles. Likewise, a large number of CTE have been determined for these systems. Slight changes in crystal structure can thus introduce point defects into the material matrix and, mismatches in CTE could further aid in failure.



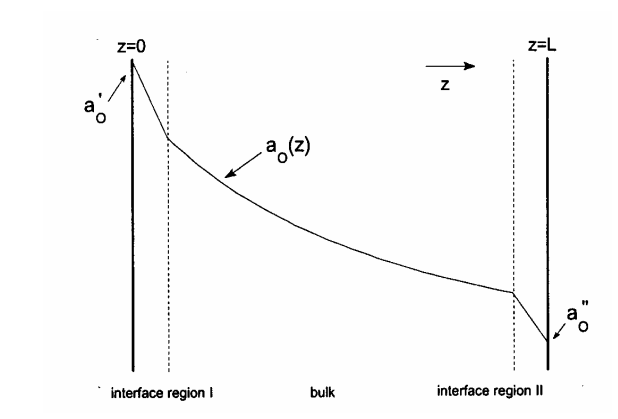


Figure 40. A schematic diagram of a membrane

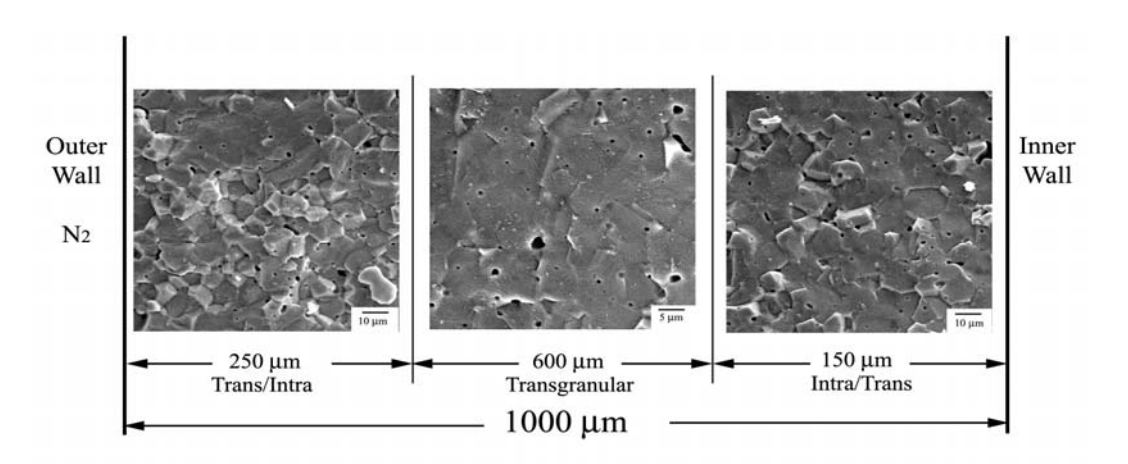


Figure 41a. Gradient Fracture in N2 at 1000°C

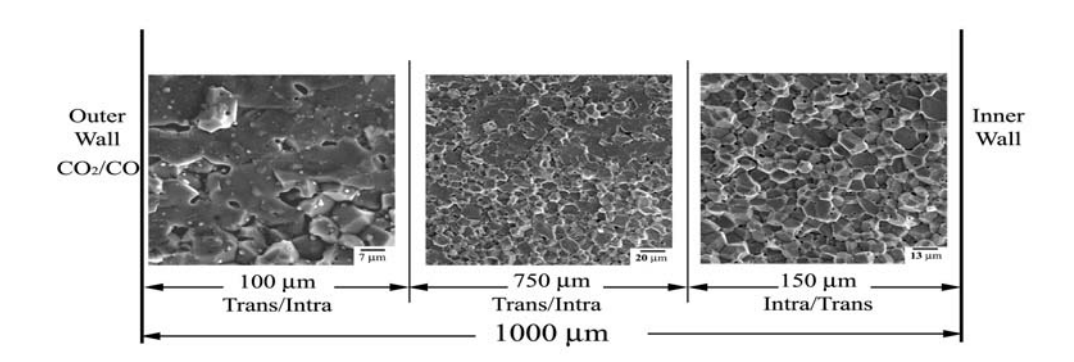


Figure 41b. Fracture gradient in CO<sub>2</sub>/CO at 1000°C

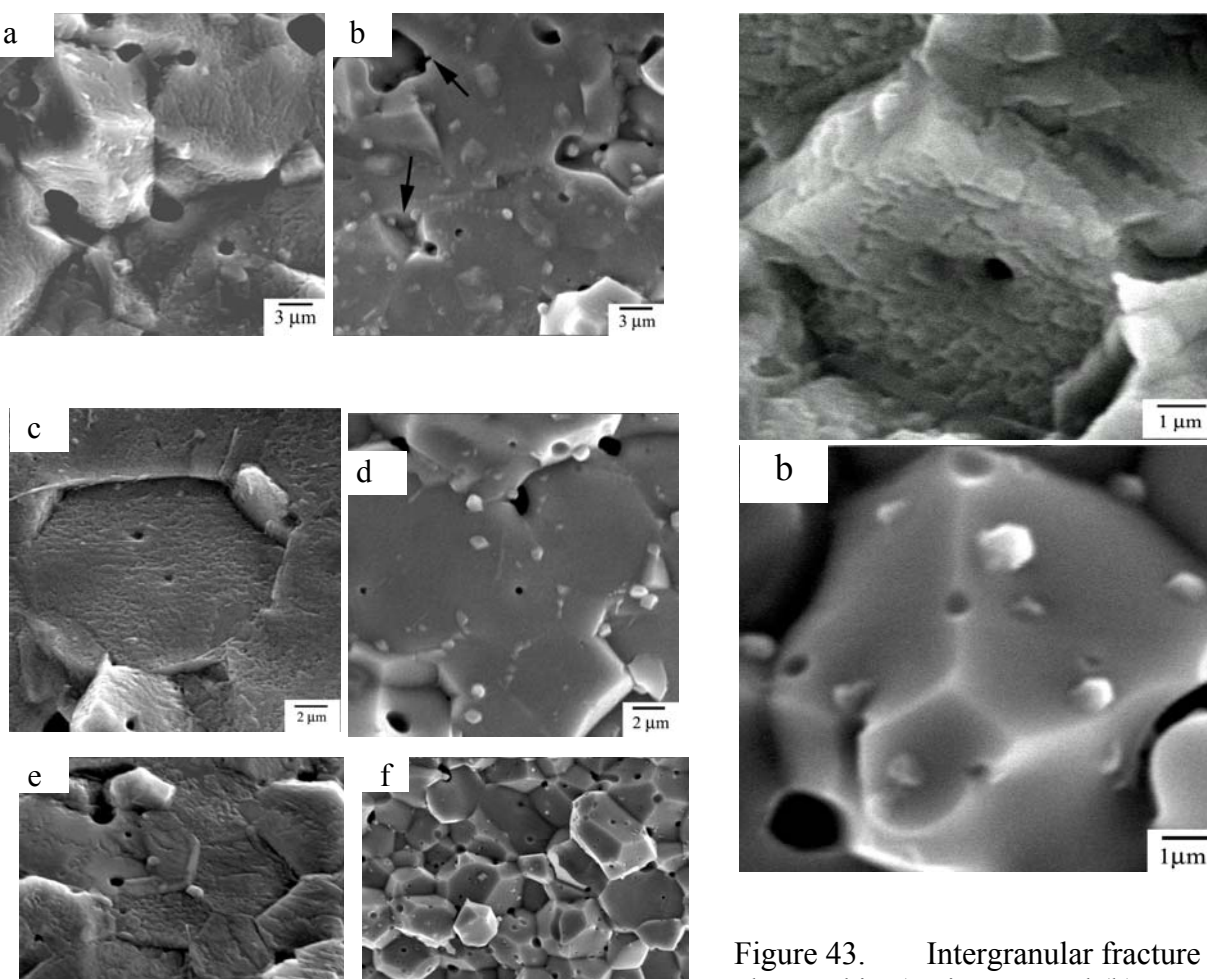


Figure 42. Higher magnification viewgraphs of gradient fracture in reducing conditions. (a), (c) and (e) are in Nitrogen and (b), (d) and (f) are in 90%CO<sub>2</sub>/CO atmosphere.

observed in a) Nitrogen and (b) 90%CO<sub>2</sub>/CO environment. In Nitrogen, the grains are broken down while in CO<sub>2</sub>/CO fine precipitates of SrO are formed on the surfaces of the grain

# 2.4.3. Evaluation of OTM Bars

Emphasis was also placed on evaluating the strength of membranes in a flexure geometry. In accordance, 4 –point bend fixtures were designed and fabricated.

### 2.4.3.1 EXPERIMENTAL PROCEDURE

# Fabrication of test bars of LSF and related composition

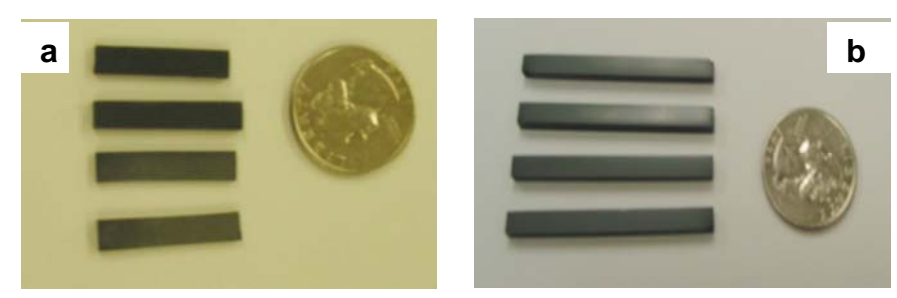
Perovskites of the composition listed in Table 4, were acquired from Praxair Specialty Ceramics. The materials were processed by combustion spray pyrolysis. The average particle size ' $d_{50}$ ' was 0.6 µm. The materials were analyzed by X-ray to determine the lattice structure. Green samples of dimension 50 x 6.7x 10 mm were fabricated by mixing with PVA (polyvinyl alcohol) as binder and cold pressing in a steel die at pressure of 28 MPa. The samples were sintered at 1350°C for 2-3 hours to the final density of ~ 90-95% of theoretical values.

No.	Composition	Particle size d <sub>50</sub>	Major Phase	Sintering Conditions	Sintered Density g/cc	Theoretical Density g/cc
1	LaSrFeO (LSF)	0.6	Perovskite	1250/4 h	6.66	
2	La <sub>0.8</sub> Sr <sub>0.2</sub> CoO (LSC)	0.6	Perovskite	1250/4 h	6.3	
3	$\begin{array}{c} La_{0.2}Sr_{0.8}Co_{0.8}Fe_{0.2}O_{3-\delta}\\ (2882) \end{array}$	0.6	Perovskite	1250/4h	6.2 (?.)	
4	La <sub>0.6</sub> Sr <sub>0.4</sub> Co <sub>0.2</sub> Fe <sub>0.8</sub> O <sub>3-δ</sub> (6428)	0.6	Perovskite	1300/4h	6.06	6.37
5	La <sub>0.8</sub> Sr <sub>0.2</sub> Co <sub>0.8</sub> Fe <sub>0.2</sub> O <sub>3-δ</sub> (8282)	0.6	Perovskite	1350/4h	6.58	6.68

The samples were thermally etched in air at 1150°C for 0.5h for microstructure analysis. In addition, samples were analyzed by XRD (x-ray diffraction) after sintering and characterized for porosity and final density before proceeding to mechanical strength measurements as a function of environment. Our studies on LSFCO membranes indicated preferential segregation of cations upon exposure to environment and stress. For this reason, the membranes need to be well characterized for segregation prior to exposure to the environment. A major question that needs to be addressed is environmental effects on crack initiation vs. crack propagation. For this, the characterized membrane materials will be indented at various loads and along with a control sample, exposed to the environment of study. Post exposure and comparative studies (XRD, EDS etc.) on existing and new indents would indicate the extent of cation segregation, decomposition of the perovskite and their influence on crack propagation.

### 2.4.3.2 RESULTS AND DISCUSSIONS:

La<sub>0.2</sub>Sr<sub>0.8</sub>Fe<sub>0.8</sub>Cr<sub>0.2</sub>O<sub>3-δ</sub> (LSFCO-3) composition provided by the OTM alliance was studied along with model La<sub>x</sub>Sr<sub>1-x</sub>Fe<sub>1-y</sub>Co<sub>y</sub>O<sub>3-δ</sub> compositions fabricated in the laboratory. The dimensions of the bars and their compositions fabricated in the lab and those provided by Praxair are shown in figure 44 a and b respectively. Our studies on LSFCO membranes had indicated preferential segregation of cations upon exposure to environment and stress. Studies on the well characterized LSCF in terms of defect chemistry and stability would thus provide an excellent point of study for comparison. For this purpose, the compositions were so selected that the B site in the perovskite was varied from fully Co to fully Fe cation occupation. Along with the Co/Fe ratio on the B site, the La/Sr ratio on the A site were also varied. The bars were fabricated for tests in the fixture designed in the laboratory according to ASTM test specifications.



a) ASTM standard type A samples of LSF, LSC and LSCF compositions to study strength degradation with environment and b) ASTM standard type B samples of LSFCO provided by Praxair.

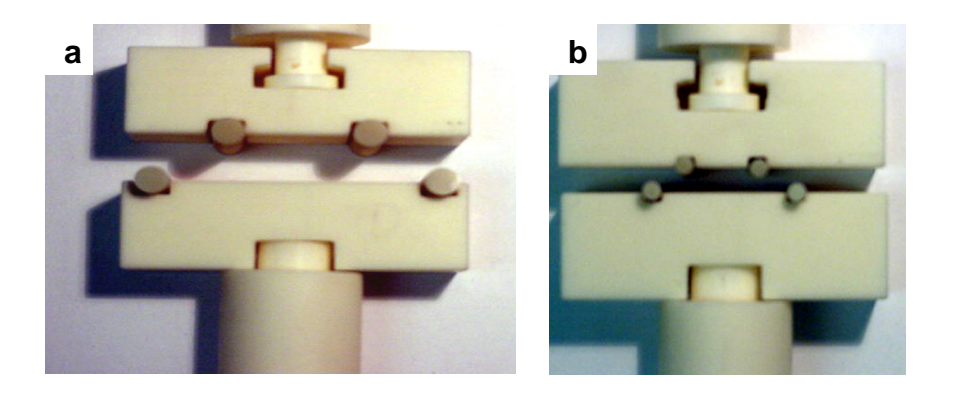


Figure 45. ASTM fixtures designed for 4-Point flexure testing of membrane bars. A) ASTM D and b) ASTM A

XRD analysis of the membranes fabricated in the lab indicated retention of the perovskite phase composition. A typical XRD plot for one such composition LSCF 8282 is shown in figure 46.

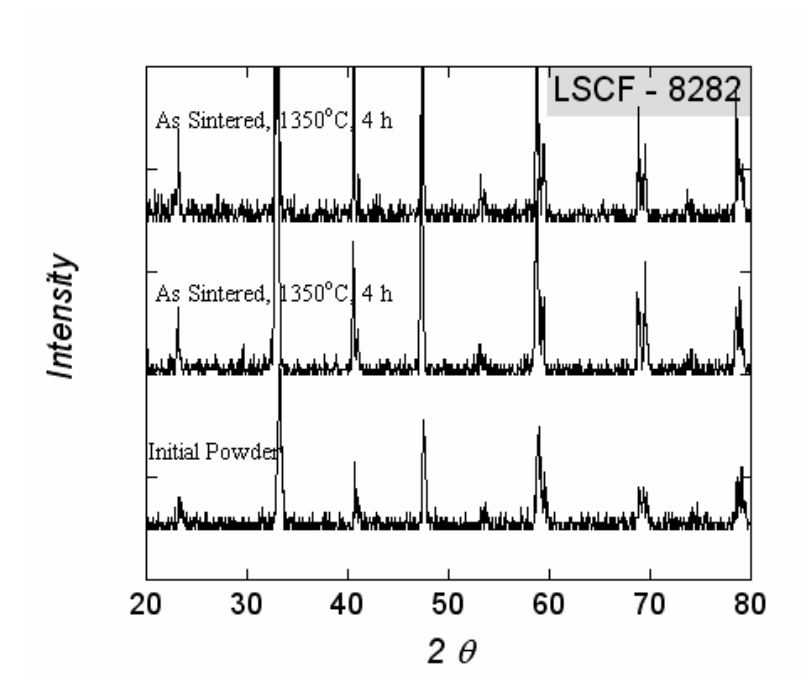


Figure 46. XRD analysis of LSCF- 8282 prior to and after sintering indicating retention of parent perovskite structure.

## 2.4.3.2.1 Hardness and Fracture Toughness

The results of the indentation hardness and toughness studies on Lanthanum based compositions are tabulated in table 3. The B site was varied from fully Co to fully Fe cation occupation. The Co/Fe ratio on the B site and the La/Sr ratio on the A site were also varied. The hardness and toughness were measured as a function of indentation load and corresponded to measured values reported in the literature. As shown in the table 5, no perceptible changes were observed with the indentation load. However, at higher loads lateral cracks were observed that were well defined. At higher loads, incidences of damage accumulation in the materials were observed.

A typical micrograph of the indent with lateral cracks extending from the tip of the indent is shown in figure 47. A graphical representation of the variation in hardness and toughness for the composition  $La_{0.2}Sr_{0.8}Co_{0.8}Fe_{0.2}O_{3-\delta}$  is shown in figure 48.

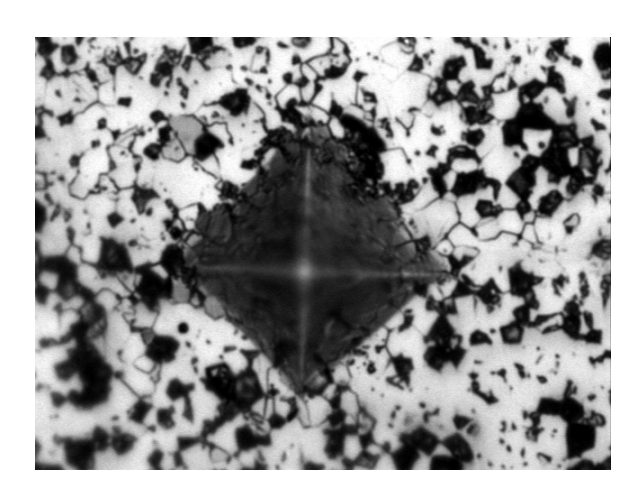


Figure 47. Vickers indents on LSCF - 8282 for fracture toughness and crack growth studies

The results of the indentation hardness and toughness studies on Lanthanum based perovskite compositions are tabulated in table 3. With increasing load, there was a corresponding increase in the crack length and in some instances (for ex: LSFCO) damage accumulation was observed around the indent.

Indentation toughness was also measured at elevated temperature in two different environments: i) in Air and ii) in a cycle of heating in  $N_2$  and slowly switching the gas to air (from  $N_2$  to air at high temperature). As shown in table 6, the test samples indicated changes in toughness values after exposure to the environment. In air, samples of all compositions tested indicated degradation of  $\sim 25\text{-}35$  % in toughness values. However, exposure to the cycle ( $N_2$ /Air) indicated mixed results. A gradual recovery was observed in LSFCO composition (1.06 MPa.m<sup>0.5</sup> as compared to 0.84 MPa.m<sup>0.5</sup> in air but still less than the RT value) while in LSC, LSCF 6428 and 8282 an increase in toughness over room temperature values were observed.

Table 5.Room temperature Indentation hardness and toughness values for the composition being evaluated.

Material	Lood (gree)	Hardness, GPa	Fracture Toughness, MPa.m <sup>0.5</sup>	
	Load (gms)	(STD Dev)	(STD Dev)	
	50	8.73 (±0.92)	1.03 (±0.23)	
$La_{0.8}Sr_{0.2}C_0O_{3-\delta}$	100	8.93 (±0.40)	1.28 (±0.42)	
	200	8.25 (±0.60)	1.10 (±0.18)	
	300	8.27 (±0.56)	1.16 (±0.17)	
	500	$7.56 (\pm 0.53)$	1.07 (±0.23)	
	1000	7.07 (±0.47)	1.17 (±0.13)	
	50	8.19 (± 1.86)	$1.59 (\pm 0.72)$	
$La_{0.6}Sr_{0.4}Co_{0.2}Fe_{0.8}O_{3-\delta}$	100	$7.42 (\pm 0.60)$	$1.46 (\pm 0.30)$	
	200	$7.44 (\pm 0.95)$	$1.38 (\pm 0.44)$	
	300	$7.44 (\pm 0.36)$	$1.10 (\pm 0.52)$	
	500	$6.48 (\pm 0.99)$	$1.10 (\pm 0.31)$	
	1000	$6.56 (\pm 0.58)$	$0.91 (\pm 0.14)$	
	50	7.77 (±1.27)	2.25 (±0.27)	
$La_{0.8}Sr_{0.2}Co_{0.8}Fe_{0.2}O_{3-\delta}$	100	9.15 (±0.69)	2.56 (±0.31)	
	200	8.41 (±1.011)	2.48 (±0.23)	
	300	8.7 (±0.91)	2.43 (±0.5)	
	500	7.79 (±0.57)	2.25 (±0.57)	
	1000	6.61 (±0.45)	1.71 (±0.47)	
La <sub>0.6</sub> Sr <sub>0.4</sub> FeO <sub>3-δ</sub>	50	10.50 (±1.06)	1.73 (±0.44)	
	100	9.52 (±0.56)	1.98 (±0.60)	
	200	9.02 (±0.29)	1.27 (±0.39)	
	300	9.05 (±0.24)	1.70 (±0.45)	
	500	8.80 (±0.80)	1.57 (±0.58)	
	1000	7.82 (±0.43)	$1.05 (\pm 0.16)$	

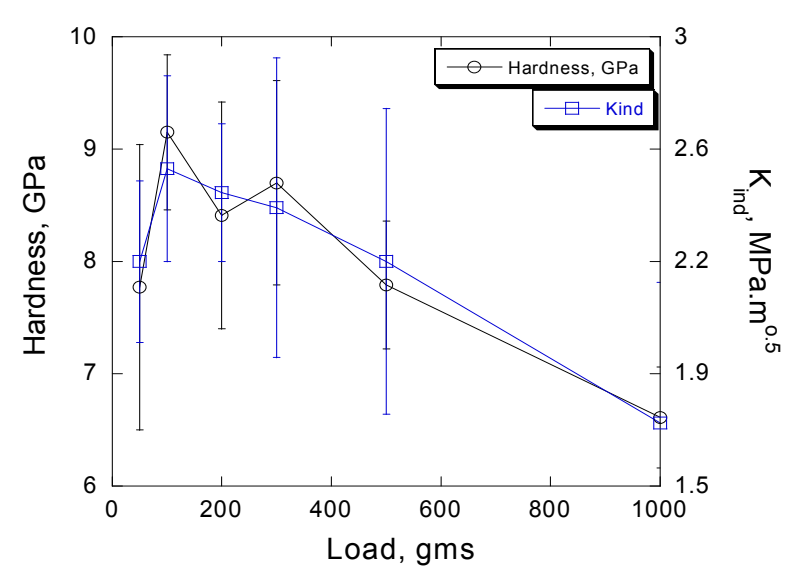


Figure 48. Hardness and toughness variation in  $La_{0.2}Sr_{0.8}Co_{0.8}Fe_{0.2}O_{3-\delta}$ 

Table 6. Indentation hardness and toughness of the composition in different environment

Composition		In Air, 1000 °C K <sub>c</sub> , MPa.m <sup>0.5</sup>	In N <sub>2</sub> /Air 1000°C K <sub>c</sub> , MPa.m <sup>0.5</sup>
$La_{0.2}Sr_{0.8}Cr_{0.2}Fe_{0.8}O_{3-\delta}$ (LSFCO)		0.84 (± 0.08)	1.06 (± 0.21)
$La_{0.6}Sr_{0.4} FeO_{3-\delta} (LSF)$	1.3 (± 0.12)	1 (±0.11)	-
La <sub>0.8</sub> Sr <sub>0.2</sub> Co <sub>0.8</sub> Fe <sub>0.2</sub> O <sub>3-δ</sub> (LSCF- 8282)	$1.2 (\pm 0.05)$	0.87 (± 0.05)	1.62 (± 0.38)
La <sub>0.6</sub> Sr <sub>0.4</sub> Co <sub>0.2</sub> Fe <sub>0.8</sub> O <sub>3-δ</sub> (LSCF- 6428)	1 (± 0.12)	0.87 (± 0.11)	1.51 (± 0.32)
$La_{0.8}Sr_{0.2}CoO_{3-\delta}$ (LSC)	1 (± 0.1)	$0.65 \ (\pm \ 0.12)$	1.09 (± 0.25)

# 2.4.3.2.2 Development of Reliability Model for OTM's

To understand the behavior of flaws and their initiation and propagation, initial studies were performed on samples with flaws generated by Vickers indent. The stress distribution in a Vickers indent in a brittle material can be well defined. Studies were initiated to correlate the stress distribution in a well characterized Vickers indent flaw, with effects coming from stresses generated by cation movement, degradation of the material etc.

### 2.4.3.2.3 Indentation flaw characterization in La<sub>0.2</sub>Sr<sub>0.8</sub>Fe<sub>0.8</sub>Cr<sub>0.2</sub>O<sub>3-x</sub>

The cation distribution in the stress field around an indented flaw was analyzed in  $La_{0.2}Sr_{0.8}Fe_{0.8}Cr_{0.2}O_{3-x}$  composition (figure 49). Initial studies were done on the  $La_{0.2}Sr_{0.8}Fe_{0.8}Cr_{0.2}O_{3-x}$  (LSFCO-2) composition (which we have studied before), that indicated changes to the cation distribution along the distance away from the indent (Fig 49 b-c).

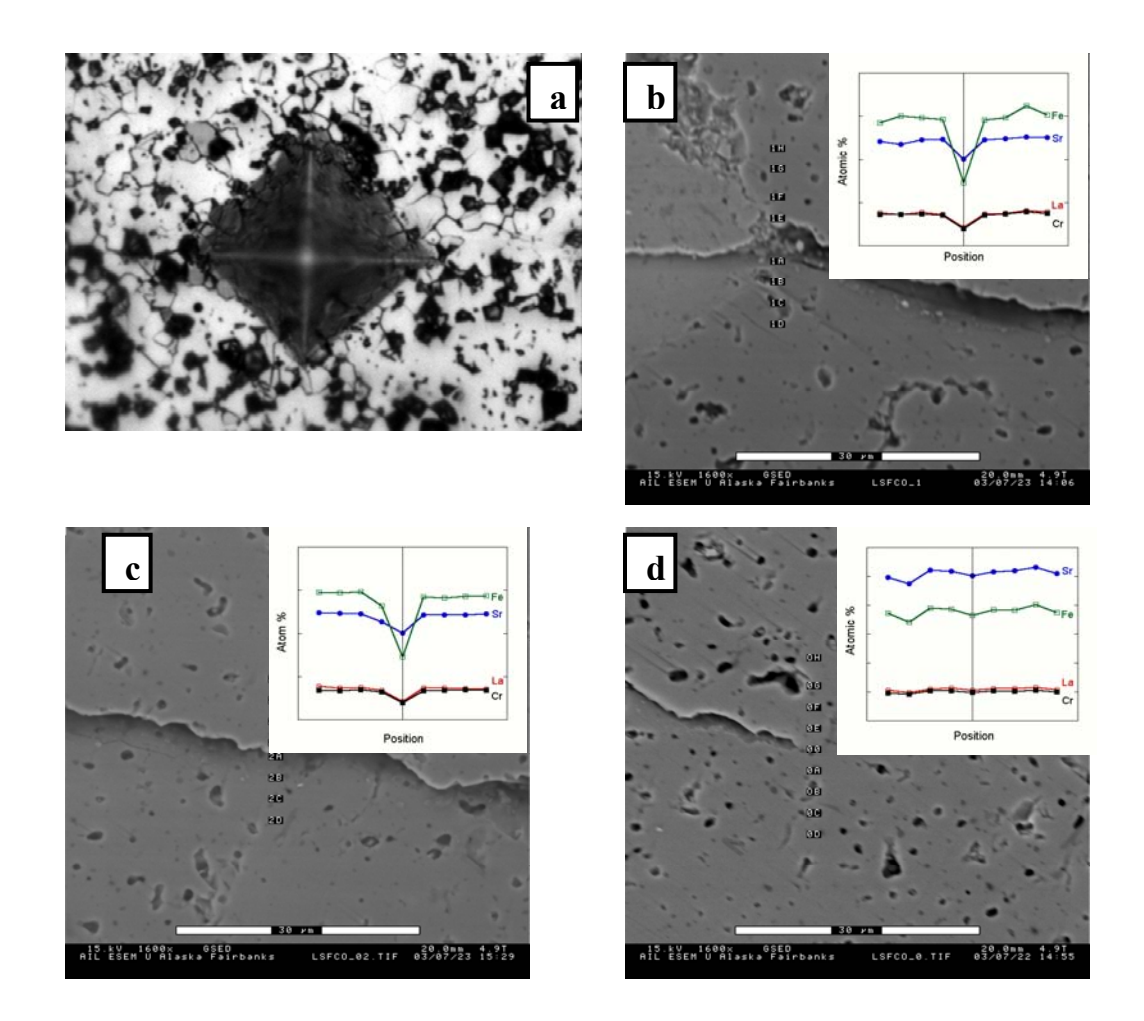


Figure 49. Cation distribution along a growing crack from an indentation in the La<sub>0.2</sub>Sr<sub>0.8</sub>Fe<sub>0.8</sub>Cr<sub>0.2</sub>O<sub>3-x</sub> system: a) an indented sample b) close to the indent; c) at half distance from the indent and d) at the crack tip

# 2.4.3.2.4 Indentation flaw characterization in a model La<sub>06</sub>Sr<sub>0.4</sub>FeO<sub>3-x</sub> system

In parallel to studies on the  $La_{0.2}Sr_{0.8}Fe_{0.8}Cr_{0.2}O_{3-x}$  system, indents were characterized in the samples of composition listed in table 2. The indents were later exposed to air at 1000°C in order to study the interaction of the cracks with the environment. The interaction of a crack with the microstructure in a  $La_{06}Sr_{0.4}FeO_{3-x}$  is shown in figure 50.

# A) LSCF 2882 Before exposure After exposure Air, 1000°C B) LSF Before exposure After exposure Air, 1000°C

Figure 50. An indented flaw exposed to air at 1000°C in the A) LSCF and B) La<sub>06</sub>Sr<sub>0.4</sub>FeO<sub>3-x</sub> system. Upon exposure, the crack tip shows healing (in red) as well as areas of more damage (in blue)

Upon exposure to air at 1000°C, the crack in the indented flaws (10 N) shows healing (highlighted in red) and also increased damage accumulation (highlighted in blue).

Studies to understand the behavior of flaws (their initiation and propagation) were conducted with flaws generated in the samples by Vickers indent. The cross sections of the indents were polished to reveal sub-surface cracks beneath the indent. Of importance is the knowledge of the

median crack. In the median-radial indentation crack system, the radial cracks are shallow surface cracks and do not promote strength degradation. On the other hand, median cracks propagate by further application of stress  $\sigma_{app}$  and can be correlated to the degradation in strength values. By characterizing the median crack, it is also possible to characterize the stress field around the flaw. The indentation load controls the length of the median crack, while the generation of the crack by itself is a function of the elastic properties of the indenter and the test material and its microstructure. The cross sections of LSCF 8282 and LSFCO indentation cracks are shown in figure 51. In LSCF – 8282 (Fig. 51a), the indentation load of 9.8 N produced a median-radial-lateral crack system and as reported in literature the fracture was intergranular. In LSFCO-2 (Fig. 51b) the indentation load of 9.8 N produced a median-radial-lateral crack system and according to our previous observations, fractured in a transgranular mode. In brittle solids, the lateral cracks are formed upon unloading the indenter which grow progressively from the median to the radial crack. Although the lateral cracks are not strength governing, they interact with the radial crack and lead to a transition to damage mode of fracture. This corresponds to our observations that at higher loads (ex.: 9.8N), damage is seen around surface indents and results in increased scatter in measured hardness and toughness values.

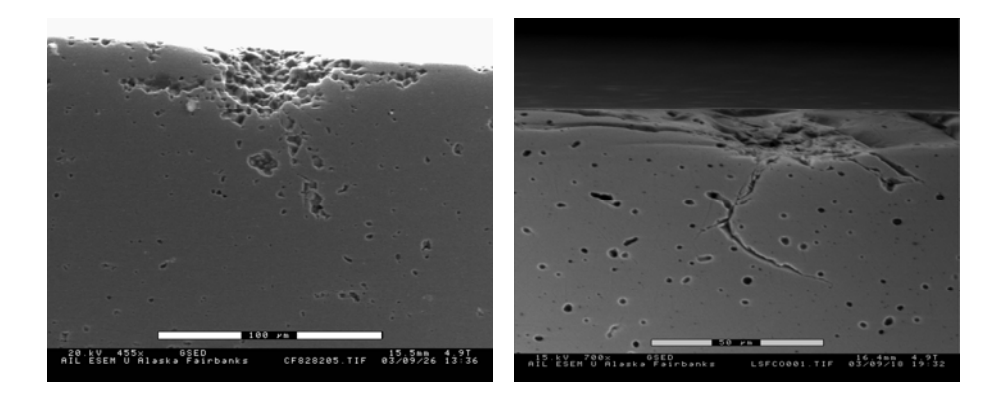


Figure 51. Cross section of an indent flaw formed at load P = 9.8 N in a) LSCF -8282 and b) LSFCO-2. Fracture in LSCF-8282 is intergranular compared to transgranular mode in LSCFO-2

The stress field around the median crack is linked to the indentation load by the relation:

$$\sigma_{ij} = \frac{P}{\pi R^2} f_{ij}(\varphi) \qquad ----- 20$$

where P is the indentation load, R the median crack length and the function  $f_{ij}$  relates the Poisson's ratio of the material,  $\varphi$  the angle to the crack to define the stress field around the indent. The radial  $(\sigma_{rr})$ , tangential  $(\sigma_{\theta\theta})$  and shear forces  $(\sigma_{zz}, \sigma_{rz})$  around the indent were calculated for LSFCO-2 assuming a Elastic modulus of 123 GPa and a Poisson's ratio of 0.22. With the knowledge of these stresses, it is possible to compute the principal stresses  $\sigma_{11}$ ,  $\sigma_{22}$  and  $\sigma_{33}$  respectively. The distribution of the stresses around the indent are shown in figure 52.

Initial attempts were also made to measure the crack tip parameters. As shown in figure 53, the crack opening displacements, u(r), were measured behind the crack tip and related to the stress intensity for the linear-elastic median crack tip from the following equation:

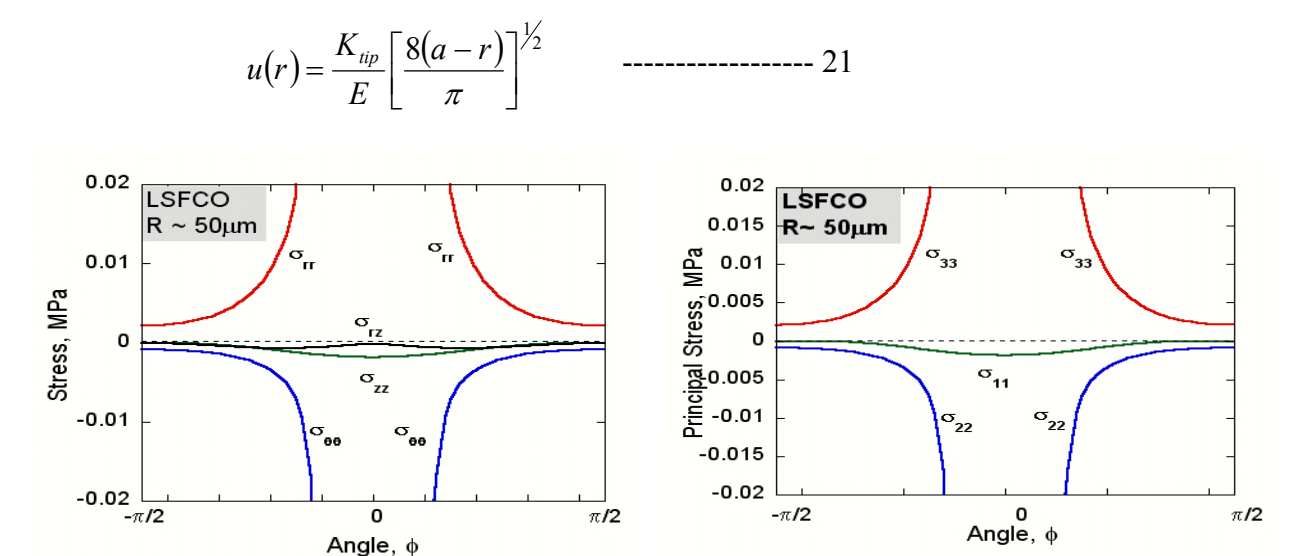


Figure 52. Stress fields around an indent flaw formed at load P = 9.8 N in LSFCO-2. The median crack was  $\sim 50 \mu m$  as compared to  $\sim 100 \mu m$  in LSCF-8282

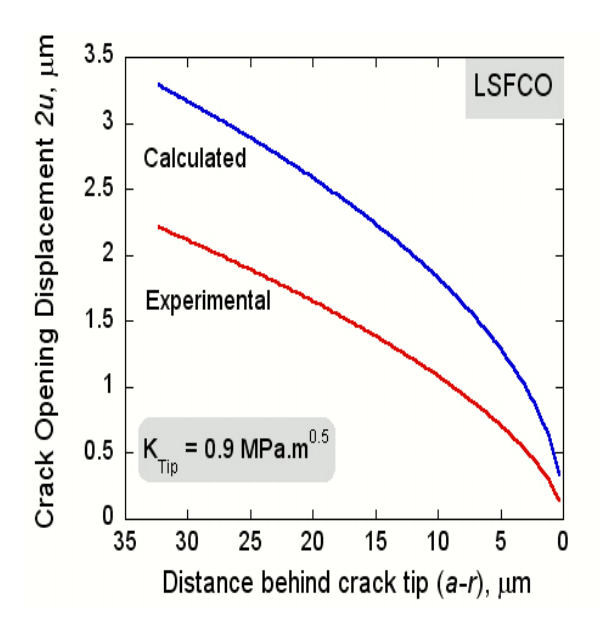


Figure 53. Crack opening displacement as a function of distance behind the crack tip for LSFCO-2. The profile provided a value of  $K_{tip} = 0.9$ 

where E= Young Modulus = 123 GPa, a is the crack length and r is the distance behind the crack tip. The stress intensity at the crack tip  $K_{tip}$  computed from the equation was 0.9 MPa $\sqrt{a}$ . From the Von Mises criterion,  $\sigma^{max}$ , is given according to the equation:

$$\sigma^{\text{max}} = \frac{1}{\sqrt{2}} \sqrt{(\sigma_{11} - \sigma_{22})^2 + (\sigma_{22} - \sigma_{33})^2 + (\sigma_{33} - \sigma_{11})^2 + (\sigma_{12}^2 + \sigma_{13}^2 + \sigma_{23}^2)}$$
 22

An accurate description of the localized stresses and stress intensity are necessary for prediction of microscopic fracture origins such as stress induced segregational effects, precipitation etc.

# 2.4.3.2.5 Residual stresses effects in La<sub>0.2</sub>Sr<sub>0.8</sub>Fe<sub>0.8</sub>Cr<sub>0.2</sub>O<sub>3-x</sub>

In some of the model MIEC perovskites studied, the crack lengths from starter indentation flaws were reduced after exposure to air at 1000°C. This has an important bearing in evaluating crack growth parameters at elevated temperatures as the starting flaw is no longer what was characterized at room temperature. The flaw can interact with the environment, get blunted or possibly grow some distance and thus affecting the crack calibrations.

To characterize and study the interaction of the cracks with the environment, the indents of LSFCO-2 were exposed to air at  $1000^{\circ}$ C and also to a complex schedule of heating in  $N_2$  up to  $1000^{\circ}$ C prior to introduction of air. The latter schedule as recommended by the research group at Praxair is designed to equilibrate the composition in  $N_2$  prior to exposing it to air (the materials are fabricated by cooling in  $N_2$ ).

Upon exposure to air at 1000°C (Fig. 54b) the indented flaws (10N) shows considerable crack healing when compared to that at room temperature (Fig. 54a). The reduction in crack length is more apparent when the indent is annealed in the environment of N<sub>2</sub> prior to switching to air (Fig. 54 c and d).

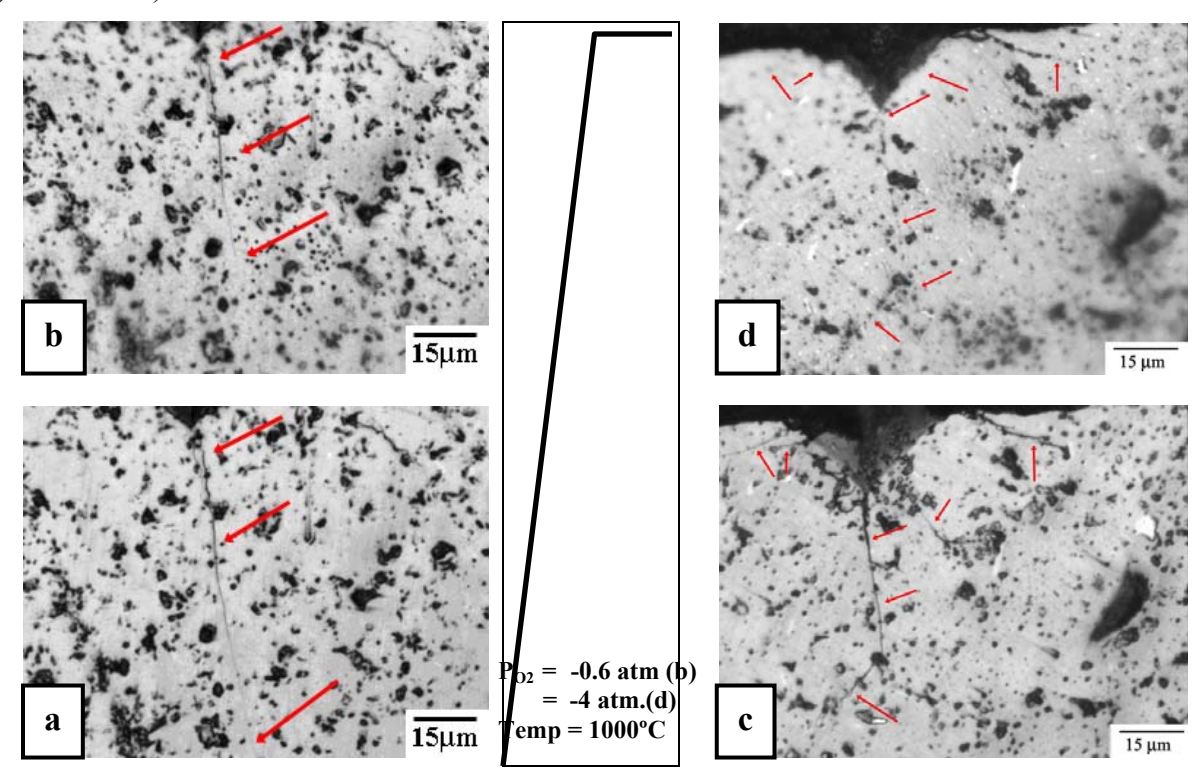


Figure 54. An indented crack exposed to environment and elevated temperature shows reduction of radial crack lengths. a) In air at  $1000^{\circ}$ C ( $P_{O2} = -0.7$  atm.) and b) in  $N_2$ /Air at  $1000^{\circ}$ C ( $P_{O2} = -4/-0.7$  atm.)

In explaining the reasons, it can be argued that the reduction of the crack length is just the thermal relief from the tensile residual stresses. Since, the stress produced by the indent

decreases with distance from the indent, the crack propagated by the applied stress (indentation load) initially grows rapidly, then slows, and finally stops growing. Crack growth stops when the stress intensity  $K_I$  drops to the critical stress intensity  $K_{Ic}$ . The effect of an applied stress is to change the length of the crack emanating from the indent. Tensile stress raises  $K_I$  value, increasing the crack length and conversely, a compressive stress shortens the crack. The compressive stress for closing the cracks can be derived from fracture mechanics based on the assumption that the crack growth stops when the stress intensity  $K_I$  at the crack tip reaches  $K_{Ic}$ . The net stress intensity, which includes contributions from the residual stress at the indent and the stress  $\sigma_s$  present from other sources and closing the crack can be expressed as:

where  $\chi_r$  is the residual stress parameter,  $\Phi$  is a parameter accounting for the geometry of the crack and c is the crack length.

Rearranging the equation and denoting the initial toughness and crack length as  $K_I$  (initial) and  $c_i$  respectively and the final crack length as  $c_f$ , the stress can be expressed as:

$$\sigma_{S} = (K_{Ic} - K_{I}(initial)c_{i}^{3/2}/c_{f}^{3/2})/\Phi c_{f}^{1/2} \qquad ------ 24$$

Assuming that the crack system is half penny ( $\Phi = 0.30$ ) and there is no subcritical crack growth,  $K_{I, initial}$  and  $K_{Ic}$  can be assumed to be equal. The surface stress can then be calculated and is observed to be compressive.

In air:  $\sigma_s \sim -7 \text{ MPa}$ 

In  $N_2/Air$ :  $\sigma_s \sim -60$  MPa.

### 2.4.3.2.6 Strength degradation and slow crack growth studies:

Slow crack growth studies were begun on the new set of bar samples. The OTM samples with dimensions of 3 x 4 x 48 mm termed LSFCO-3 were provided by Praxair. Small samples were sectioned from one of the bars and analyzed for microstructure, phase composition, hardness and indentation toughness. As with studies on LSFCO-2 (tube), the indents on the polished samples were exposed to environment and the radial, lateral and median cracks characterized.

The microstructure of LSFCO-3 (fig. 55b) was approximately  $\sim 3\mu m$  compared to  $\sim 6\mu m$  for LSFCO-2 (fig. 55a). Some surface cracks were observed and we were advised by Praxair that

they were shallow thermal relief cracks. The test samples were chamfered before testing in 4-point flexure.

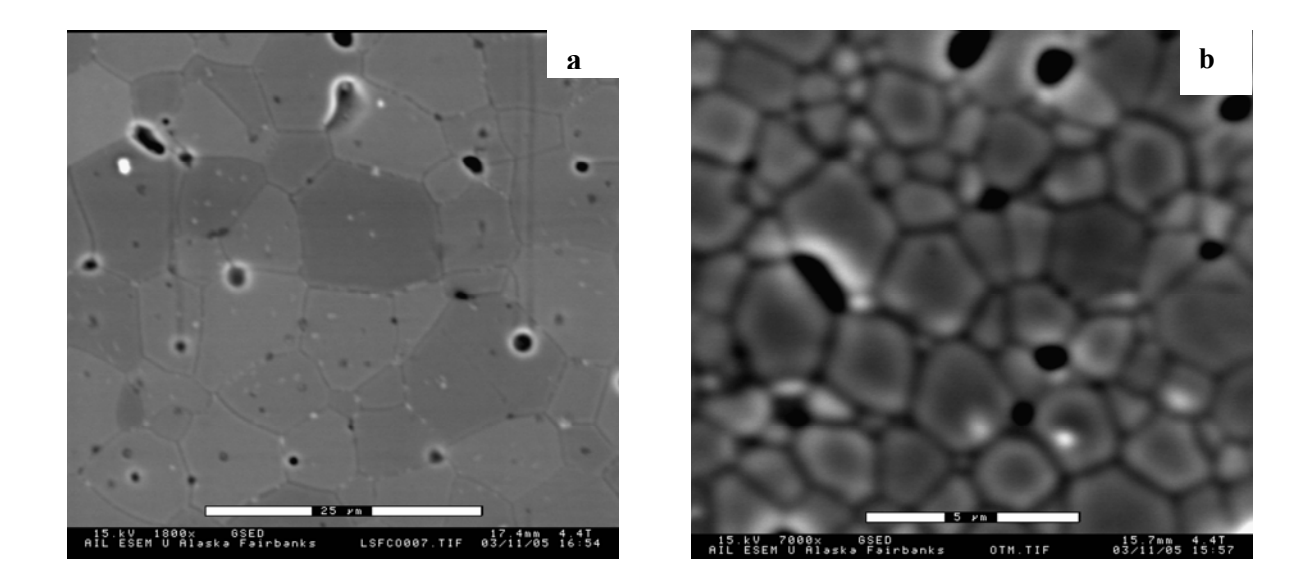


Figure 55. Thermally etched microstructure of a) LSFCO-2 and b) LSFCO-3

Initial studies were done at room temperature. The samples were tested by monotonic loading in displacement control mode at 4 different crosshead speeds. The crosshead speeds of  $3\mu m$ ,  $6\mu m$ ,  $60\mu m$  and  $600\mu m$  were chosen so as to give a wide scale of loading spectrum. The fracture loads were recorded and the fixture unloaded immediately upon fracture.

The fracture strength of the bars were calculated from peak loads as:

$$\sigma_f = \frac{3Pl}{4bd^2} \qquad -----25$$

where P is the fracture load, l is the outer support span = 38.1 mm, b is the specimen width and d is the specimen thickness. The fracture strength of the bar tested at room temperature is shown in figure 56. Slow crack growth at room temperature appears to be a probable reason for changes in strength values. This will be characterized by plotting fracture strength as a function of stress or strain rates calculated from individual tests.

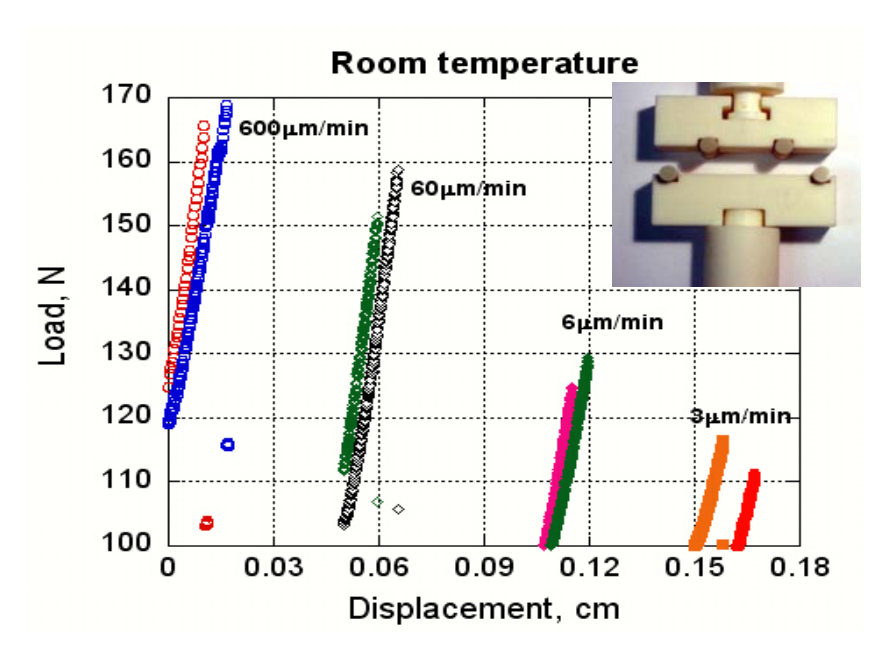


Figure 56. Load-displacement trace of OTM bars tested in flexure at varying strain rates.

#### **OTM Bars for Slow Crack Growth Studies:**

Dense OTM bars were evaluated for slow crack growth (SCG). XRD analyses were carried out on the fractured samples exposed to different atmospheres. TGA (Thermogravimetric analysis) and DTA (Differential thermal analysis) studies were also conducted on post fractured samples.

#### **EXPERIMENTAL**

The edges of twentyone OTM bars of dimensions 3 x 4 x 48 mm provided by Praxair were chamfered prior to testing. The tests were done in-situ in an autoclave mounted on a servo-electric loading frame. Flexural tests were conducted using an in-house designed 4 – point bending fixture with an outer span of 38.1 mm and an inner span of 19.05 mm span (ASTM D). Nine samples were loaded at varying strain rates at room temperature in air and eight samples at 1000°C in an atmosphere of N<sub>2</sub>/Air respectively. The strain rates were so chosen as to provide a minimum of two decades in loading rates and two samples were tested at each loading rates. Stable crack growth in the OTM samples was achieved by loading a notched beam to fracture (Single Edge Notched Beam - SENB) and also by loading a beam with Vickers indents on the

surface to fracture (Indentation Fracture – IF). Samples from failed surfaces were taken for fracture analysis using SEM after gold sputtering. In addition, samples were cut near to fracture, then powdered and analyzsed in XRD to obtain information on possible phase retention or precipitation of secondary phases. Two conditions were used for XRD analysis – a fast scan to provide complete data and a slow scan with a step angle of 0.01 degrees and a dwell time of 2 secs. For both conditions, the XRD was operated at 30 KV and 20 mA with a Cu target.

#### **RESULTS AND DISCUSSIONS**

The fracture strength  $\sigma_f$  of the OTM bars in 4-point flexure was calculated using the simple

beam formula, 
$$\sigma_f = \frac{3PL}{4BW^2}$$
 where P = Fracture Load, L = Outer Span, B = thickness and W

= width of the beam respectively. The fracture strength of the bars tested at room temperature in air is listed in table 7 and the load-displacement traces are graphically shown in Fig. 57.

Table 7. Slow Crack Growth tests in air at Room Temperature

		Avg,	Avg.	Avg.	Span,	Load	Strength	Cross Head
No	Code	cm	m	m	m	(N)	(MPa)	Speed
2	1b	4.828	0.004	0.003	0.0381	165	114.36	0.01mm/s
3	1c	4.817	0.004	0.003	0.0381	169	111.06	0.01mm/s
4	1d	4.813	0.004	0.003	0.0381	163.6	117.23	0.01 mm/s
5	1e	4.840	0.004	0.003	0.0381	151.6	103.71	0.001mm/s
6	2a	4.839	0.004	0.003	0.0381	157.2	102.76	0.001mm/s
7	2b	4.828	0.004	0.003	0.0381	124.7	92.09	0.0001mm/s
8	2c	4.833	0.004	0.003	0.0381	128.5	92.52	0.0001mm/s
18	3g	4.832	0.004	0.003	0.0381	111	86.09	0.00005mm/s
19	3h	4.838	0.004	0.003	0.0381	116.5	90.70	0.00005mm/s

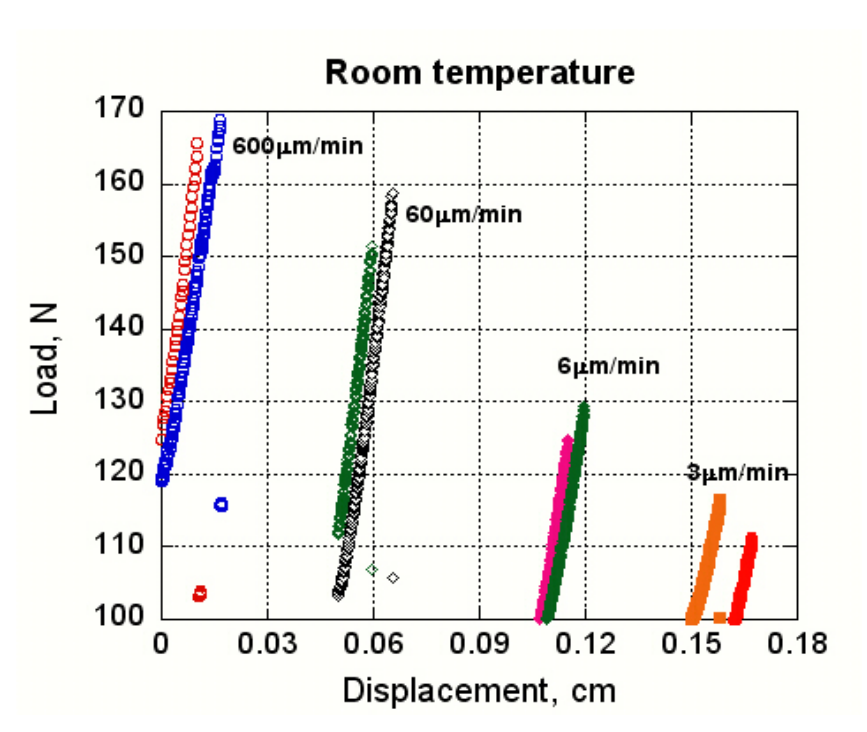


Figure 57. OTM flexural strength in varying strain rates at RT in air

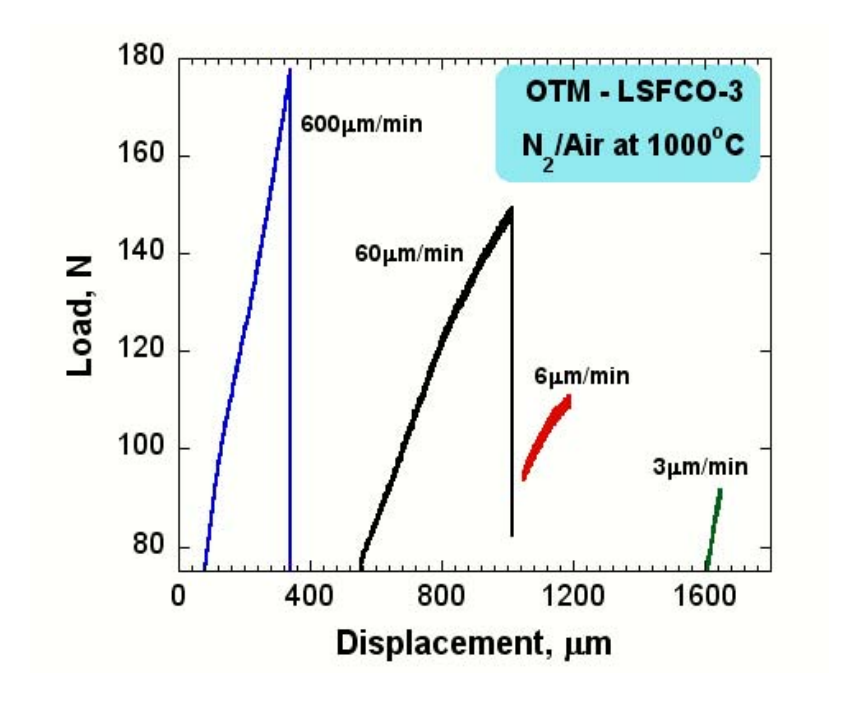


Figure 58: OTM flexural strength at varying strain rates in  $N_2/Air$  at  $1000^{\circ}C$ .

The highest strength of 115 MPa was recorded at the highest cross-head speed of 0.01 mm/s. Thereafter the strength continuously decreased with decreasing cross-head speeds and a low strength value of 86 MPa was recorded at a cross-head speed of 0.00005 mm/s.

# Flexural strength in environment:

The OTM bars were loaded in the fixture and heated in flowing nitrogen up to 1000°C. Thereafter, the nitrogen flow was shut off with the outlet fully open. The bars were soaked for 1 hour prior to application of any load. The bars were loaded at the same cross head speeds as at room temperature. The furnace power was completely shut off after fracture of the samples. A typical test had a heating up period of  $2\frac{1}{2}$  hours, soaking of 1 hour, loading rates as specified and a cool down period of 45 min. from 1000 to 700°C and  $1\frac{1}{2}$  hrs from 700 to 200°C for a sum total of 6-7 hours.

The flexural strength calculated from the fracture load and is presented in table 8 and the load-displacement curves are graphically plotted in Fig. 58. At high cross-head speeds (0.01 mm/s), the strength (110 and 118 MPa) recorded was comparable to that at room temperature (so called 'inert' strength). Thereafter the strength decreased much steeper as indicated by a recorded strength of 69 MPa at 0.00005 mm/s.

Table 8 Slow Crack Growth tests in N<sub>2</sub>/Air at 1000°C

		Avg	Avg	Avg	Span	Load	Strength	<b>Cross Head</b>
No	Code	m	m	m	m	(N)	(MPa)	speed
12	3a	0.049	0.0041	0.0032	0.0381	156.6	110.75	0.01mm/s
13	3b	0.049	0.0042	0.0032	0.0381	176.84	118.92	0.01mm/s
14	3c	0.048	0.0041	0.0031	0.0381	126	91.57	0.001 mm/s
\15	3d	0.049	0.0042	0.0032	0.0381	148.6	98.49	0.001mm/s
16	3e	0.048	0.0040	0.0031	0.0381	105.7	80.13	0.0001mm/s
17	3f	0.049	0.0041	0.0031	0.0381	110.6	79.78	0.0001mm/s
20	3i	0.049	0.0041	0.0031	0.0381	89.7	66.03	0.00005mm/s
21	3f	0.049	0.0040	0.0031	0.0381	90.2	69.03	0.00005mm/s

# Slow Crack Growth analysis in RT (Air) and at 1000°C (N<sub>2</sub>/Air)

From the individual load-displacement traces of the specimen tested, the rate of stress increase was calculated as function of time from the equation:

$$\dot{\sigma} = \frac{3P(S_o - S_i)}{2RW^2} \qquad ----- 26$$

Where  $\vec{P}$  is the load rate,  $\vec{B}$  is the specimen thickness, W is the specimen width and  $S_o$  (38.1 mm) and  $S_i$  (19.05 mm) are outer and inner spans respectively.

The Slow Crack Growth parameters n and D were then determined by a linear regression analysis using log strength values over the complete range of individual log strain rates, based on the following equation.

$$\log \sigma_f = \frac{1}{n+1} \log \overset{\bullet}{\sigma} + \log D$$
The slame of the linear magnesian line can be calculated as:

The slope of the linear regression line can be calculated as:

Where  $\alpha$  = slope, **K** is the total number of specimens tested (=8),  $\dot{\sigma}_j$  is the stress rate and fracture strength of the individual test specimen respectively.

The SCG parameter n is calculated as

$$n = \left(\frac{1}{\alpha}\right) - 1$$

The intercept of the linear regression line is calculated as

#### (Note: 'n' decreases by more than 50% in the environment tested)

The plot of the log of e flexural strength as a function of log stress rate is shown in fig 59. The SCG parameters n and D were calculated as 23.57, 94.71 and 11.28, 80.2 in air at room temperature and in  $N_2$ /Air at 1000°C respectively.

The high value of n = 23.6 at RT, air indicates that the OTM material is not very susceptible to slow crack growth. However, the value of n decreases drastically to 11.3 in N<sub>2</sub>/Air (less than 50% at RT) indicating that the OTM material is prone to SCG. A value of  $n \approx 5$  or less indicates a brittle ceramic which is affected by SCG.

# **Crack Growth Studies on Indented Samples:**

In establishing reliability estimates for a ceramic component, it is very important to have inputs on the structural parameters such as strength and strength distribution (Weibull plots), slow crack growth (SCG) and fracture toughness in the environment. Attempts were made to record fracture toughness in the same environment as in slow crack studies. Two fracture toughness measurement techniques, one based on indentation fracture (IF or IS) and the other based on single edge notched beam (SENB) were selected based on their simplicity and ease of testing (fig. 60).

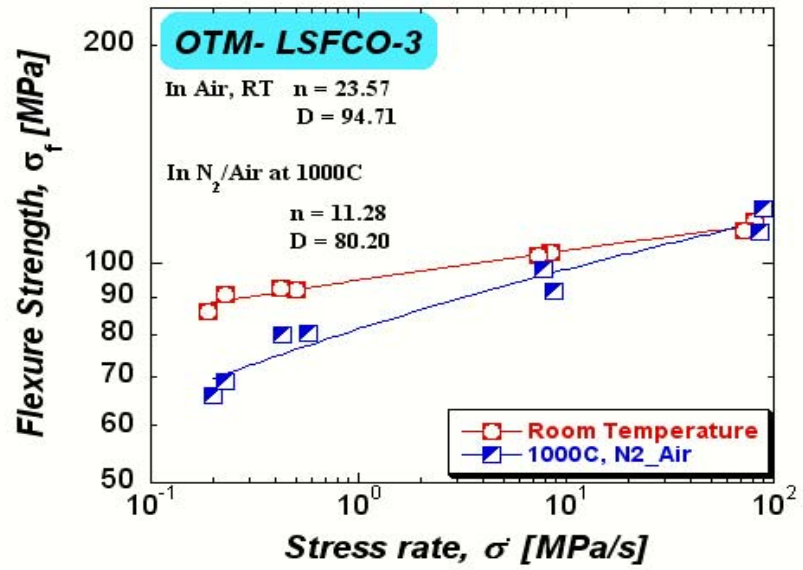


Figure 59: Flexure strength as a function of stress rate (log/log

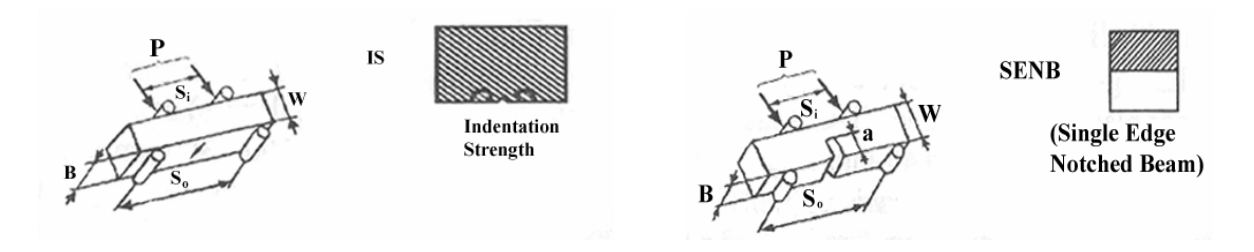


Figure 60: Testing configuration for crack growth studies.

The crack healing effects were suspected in the OTM type material and testing by IF method would help in better understanding of the reasons for these effects. The SENB method relies on a notch being introduced in the bar specimen and accordingly a fine notch was created by a 0.075 mm diamond wafering blade.

The fracture toughness,  $K_{IF}$ , for the IF method is calculated using the equation:

$$K_{IF} = \frac{3P_{max}(S_o - S_i)}{2BW^2} \bullet Y \sqrt{a} MPa \sqrt{m}$$
------31

where P is the load, W is the specimen width, So and Si are <u>outer and sinner spans</u>, B is the specimen thickness, 2a is the indent diameter and Y is the stress intensity factor for the Vickers indent flaw at the surface. Value for  $Y_{max}$  is assumed to be 1.59.

Two tests were conducted on the OTM bar specimen. In the first test, the specimen with a Vickers's indent produced by 9.8 N on the surface was loaded to fracture. As shown in fig. 61, the test was stopped intermittently and the specimen was unloaded. In the second test, the indent introduced on the surface was polished on a diamond wheel to remove residual surface flaw if any. As in the first test, the sample was frequently unloaded to ensure stable crack growth.

The fracture toughness for the-SENB- specimen tested in four-point bending,  $K_{INB}$  is calculated using equations 32 and 33. These equations are valid under the condition 0 < a/W < 1.

where  $Y_m$  is the stress intensity factor for the notch of length 'a' as given by:

$$Y_{m} = 1.9887 - 1.326 \frac{a}{W} - \frac{\left(3.49 - 0.68 \frac{a}{W} + 1.35 \frac{a^{2}}{W^{2}}\right) \frac{a}{W} \left(1 - \frac{a}{W}\right)}{\left(1 + \frac{a}{W}\right)^{2}} - \dots 33$$

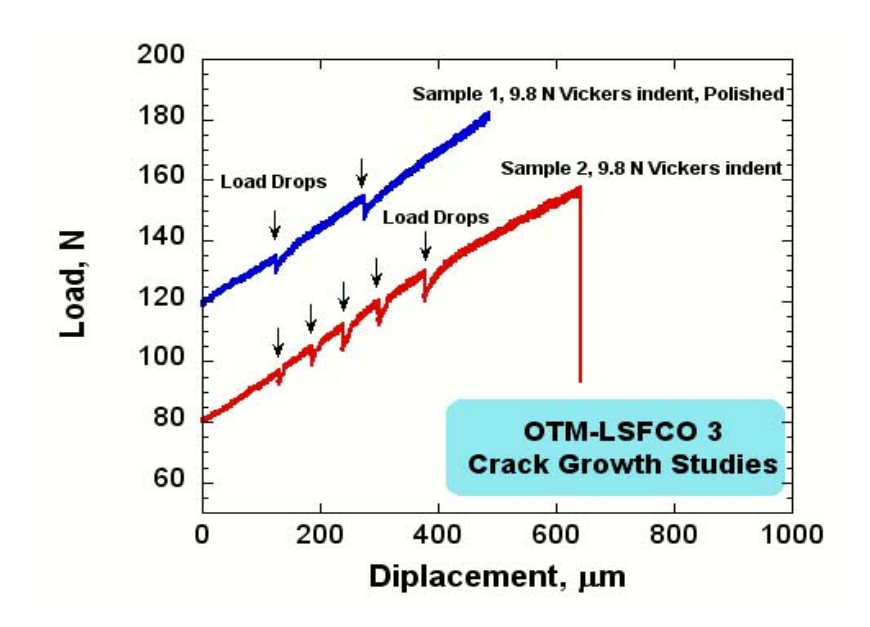


Figure 61: Load-displacement plots for fracture toughness studies in nvironment

Fatigue pre-cracking (fig. 62) of the notched sample was attempted in order to convert the SENB test to a more widely accepted single edge pre cracked beam (SEPB) test for ceramics. However, the test frame and the fixture set up were observed to be unsuitable for SEPB test due to the low strength OTM materials.

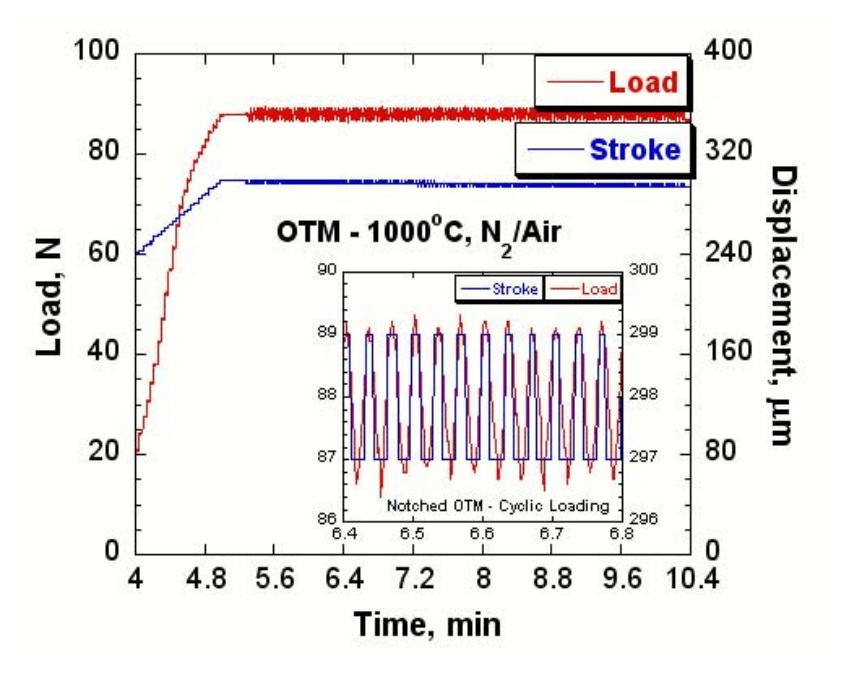


Figure 62: Load-displacement plots for fatigue pre-cracking studies in environment

The fracture toughness of the LSFCO-3 as calculated from the two methods is tabulated in table9:

Table 9. Fracture toughness ( $K_c$ ) of OTM (LSFCO-3) in N<sub>2</sub>/Air at 1000°C

Sample No and	Load	OuterS	InnerS	В	W	a	a/W	$K_{C,}$
Configuration	N	pan	pan	mm	mm	mm		MPa.m <sup>0.5</sup>
		mm	mm					
No. 9 – 2d								
<b>Surface Crack</b>	157.6	38.1	19.05	3.18	4.24	0.15	0.035	1.53
in Flexure								
No. 10 – 2e								
<b>Surface Crack</b>	182.4	38.1	19.05	3.25	4.22	0.15	0.035	1.75
in Flexure –								
indent Polished								
No. 11 – 2f								
Single Edge	92	38.1	19.05	4.04	4.11	1.15	0.28	1.42
Notched Beam								

At a first glance, the fracture toughness of the material recorded from various techniques appear very similar. However for proper determination of toughness values, careful measurements of the initial crack lengths are needed which will be acquired from SEM analysis.

#### **Design of Bridge-cracking fixture**:

In previous studies for evaluating the fracture toughness, it was necessary to have a stable crack growth as a pre-requisite for fracture mechanics calculations. Studies on bar samples with a Vickers indent or a sharp notch were inconclusive due to the absence of stable crack growth features. A pre-cracking fixture termed as "Bridge-compression technique" was fabricated. The rationale behind the technique is that the application of small and controlled tensile forces on a Vickers indent would start a stable pre-crack. Upon release of the load, the pre-crack is arrested. This pre-cracked sample could then be used for 4-point flexure testing. As shown in Fig. 63a, Vickers indents were placed along the center line of the polished dense OTM bar sample. Vickers indent at the center of the line was created with a 9.8 N load and the indents with a lower load (4.9N) were placed at a distance of 0.5mm from the indent at the center. The indented sample was loaded into the bridge fixture (Fig. 63b) such that the indents were on the tensile surface. A pre-load was applied and released through the top rod for "n" number of times to

ensure a uniform pre-crack from the indents. The pre-cracked specimens were tested at room temperature in 4-point flexure.. As shown in fig. 63c, the indented flexure bar did fail at the pre-cracked point and stereo microscope image (fig. 63d) clearly indicates an indented region, a regime of slow and stable crack growth, fast fracture and compression curl.

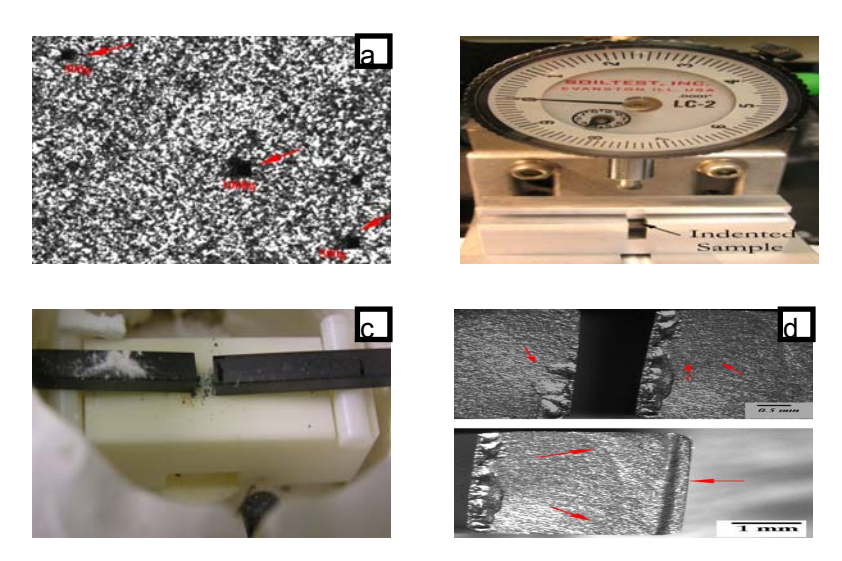


Figure 63: Pre-cracking fixture and stable crack growth in indented dense OTM samples. a) Vickers indent along the center line; b) Bridge Cracking fixture; c) 4-Point failure at the pre-cracked point; d) Stereo micrograph indicating stable crack growth and fast fracture.

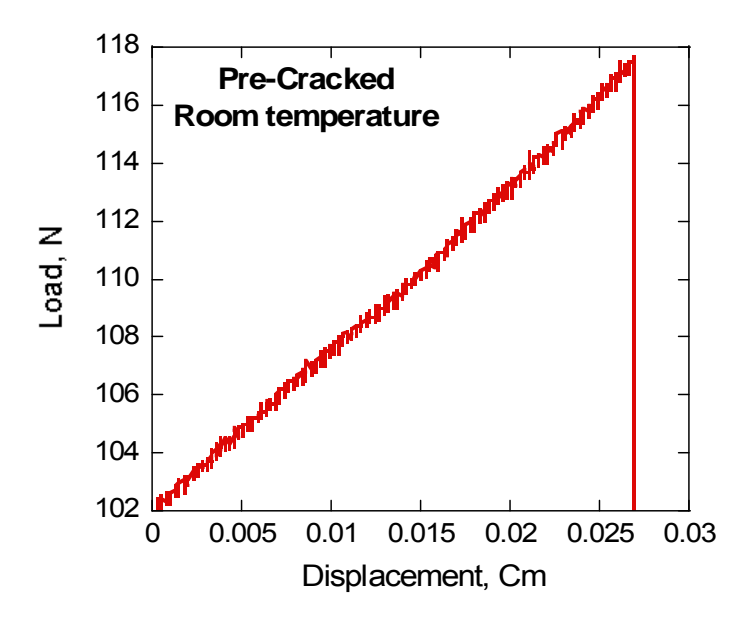


Figure 64 OTM bar loaded to fracture after pre-cracking by Bridge-Compression technique.

This result is indicative of a "good-test run". Since the method is very simple, it will also be used for testing samples subjected to various environmental conditions (temp, pressure and chemical).

## Fracture analysis

The fractured samples were sectioned using a low speed saw and the surfaces sputtered with gold prior to examination in an electron microscope.

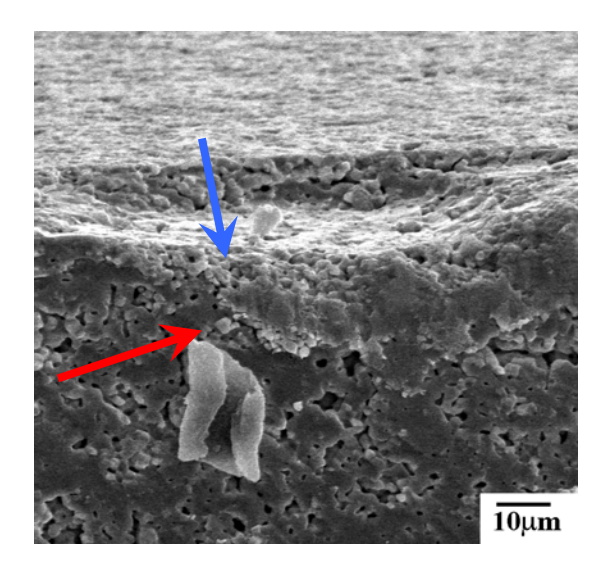


Fig. 65:Surface flaw as fracture origin

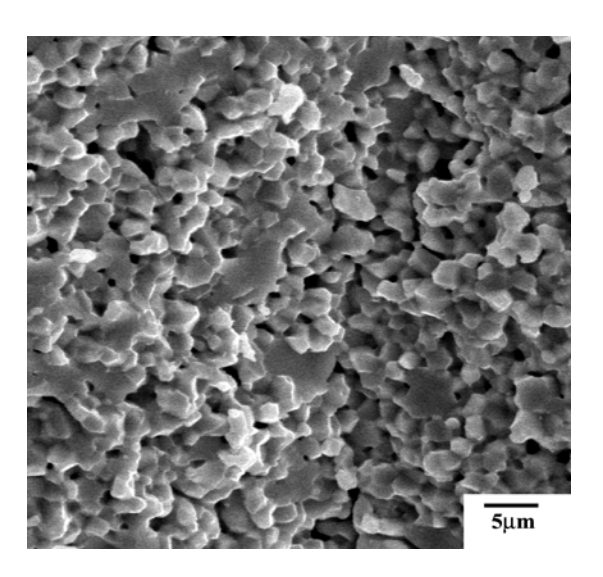


Fig. 66:Intergranular fracture in OTM bars

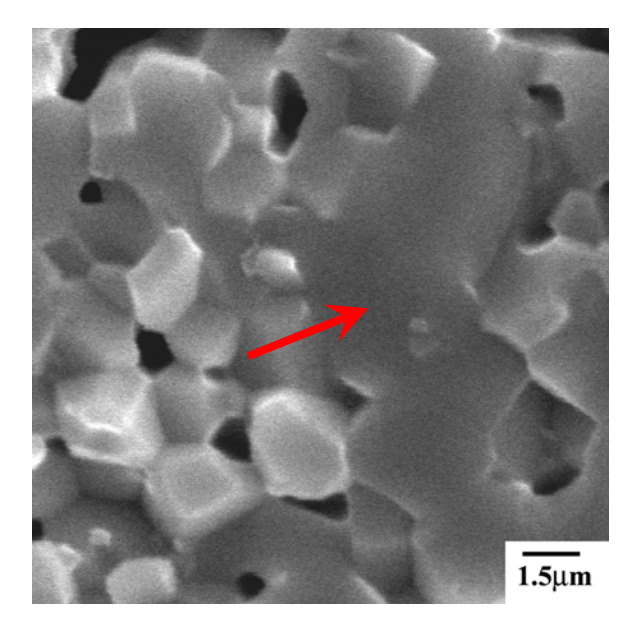


Fig.67a: Intergranular fracture of grains along OTM with presence of fine precipitates

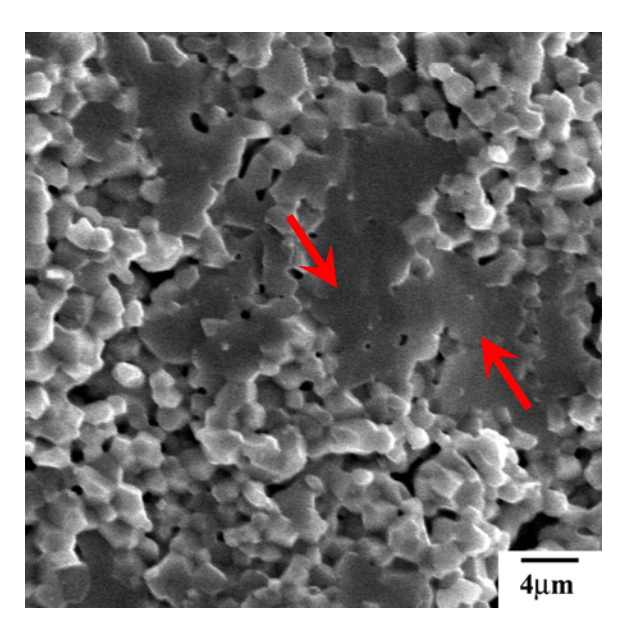


Fig.67b:Trans/Intergranular fracture in and formation of fine precipitates

In all the samples analyzed, the origins of fracture were consistently from the surface (Fig. 65) which led to a conclusion that fracture strength was controlled by surface condition. The fractured sample surfaces were ground and finished by researchers at Praxair.

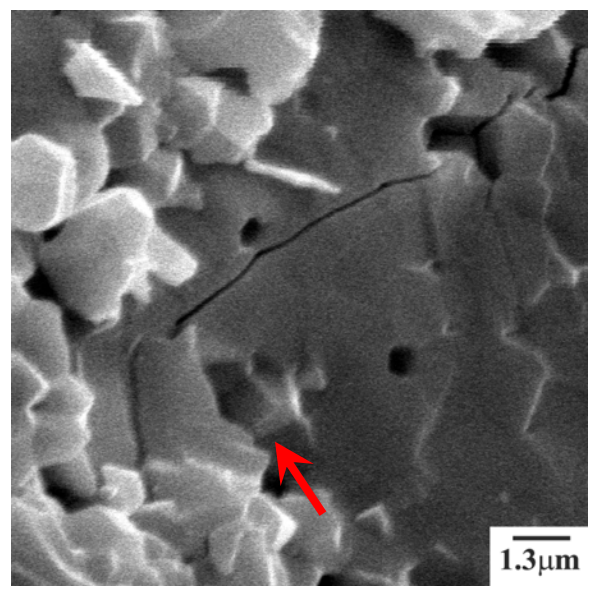


Fig.68: Interaction of microstructure with secondary cracks. Increased formation of precipitates is observed

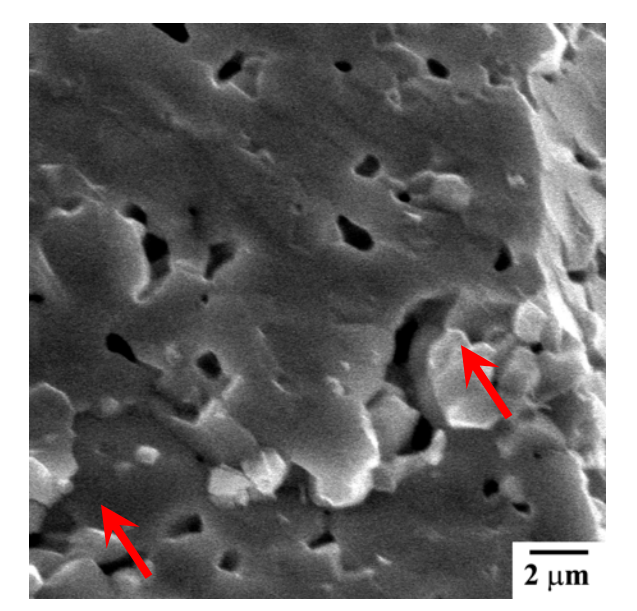


Fig. 70: Slow transgranular crack growth with increased formation of two types of precipitates

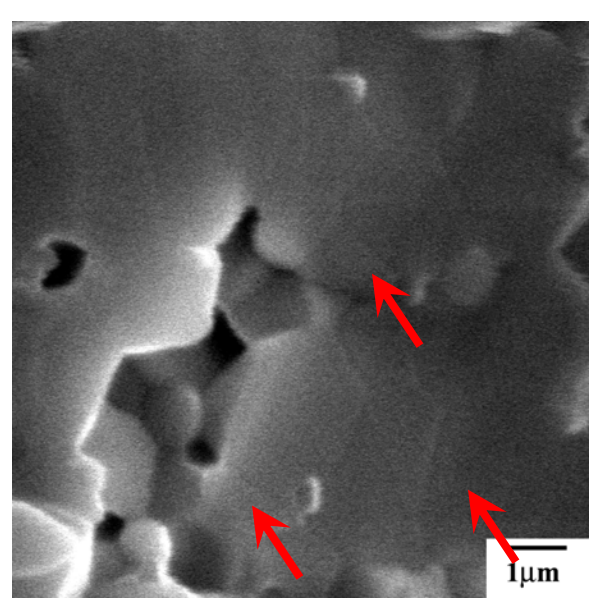


Fig.69: Transgranular fracture and presence of two types of precipitates

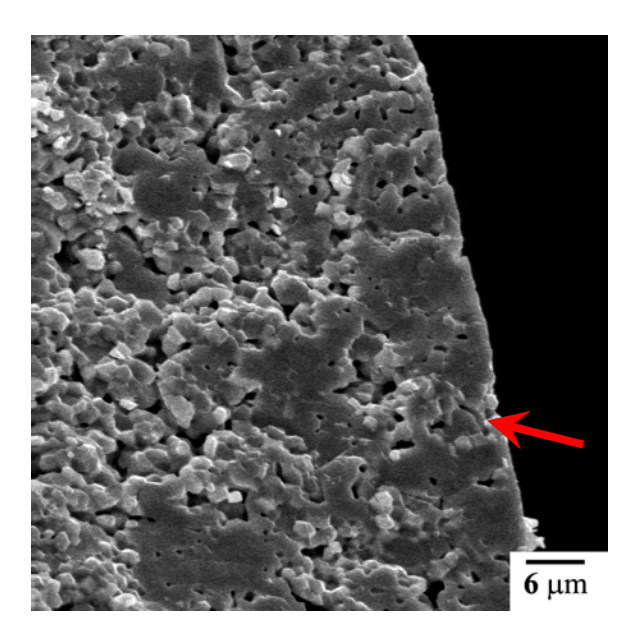


Fig.71: Fast Transgranular fracture at the edge. The so called compressive curl consistently leads to transgranular Fracture

Initial scanning of the fracture surfaces indicated an intergranular mode of fracture. However, several nuances were observed depending on the position in the fractured samples.

- 1. The area very near (~5-10 micron in Fig. 65) to the tensile surface of the flexure bar was predominantly of intergranular fracture. The fracture originated from surface flaws (blue arrow) and proceeded along the grain boundaries. The cracks coalesced and proceeded in a transgranular mode through the OTM grains (red arrow). Precipitation of secondary phases were also observed (Fig. 67). A mixed mode of intergranular and transgranular fracture was observed away from the tensile surface. (Fig. 67b). The area of transgranular failure region increased at slower strain rates accompanied by increased formation of fine precipitates.
- 2. The interaction of the crack with the microstructure was better illustrated in the secondary cracks. As shown in Fig. 68, the secondary cracks followed a transgranular mode through the OTM grains. The secondary cracks were observed very close to the transition from intergranular to transgranular mode of fracture and indicated the possible presence of localized residual stresses. Residual stresses can alter the trajectory of the crack paths in the OTM structures. Regions of transgranularly fractured grains also indicated increased formation of precipitates. As shown in Fig 69, two distinct precipitates, a coarse (~ 0.5 -0.8μm) and a very fine (0.1-0.25μm), were observed to form at the grain boundary and grain boundary junctions.
- 3. I the present OTM materials, crack growth was a mix of intergranular and transgranular mode. In the region from the tensile to the neutral axis, crack growth was predominantly intergranular with isolated pockets of transgranular fracture. In the areas away from the neutral axis and extending toward the compressive side, increased pockets of transgranular fracture along with increased formation of secondary precipitates were observed (Fig. 70). Interestingly as shown in Fig. 71, grains at the compressive side failed in a transgranular mode. Moreover, these were also the regions of fast fracture and correlated well with increase in area of transgranular fracture with a decrease in applied strain rates.

### **2.4.3.2.7 XRD Analysis**

The full scale XRD analysis and the relevant peaks are shown in figure 72 and 73 respectively. The following observations were made from the data:

- 1. The as-received OTM samples belong to a primitive cubic perovskite structure with a lattice parameter of 3.9105*A*°.
- 2. Samples exposed to environment of N<sub>2</sub> with a switch to Air at 1000°C indicated that the major XRD peaks had a small but perceptible shift towards the left. In the sample exposed to air at 1000°C, the shift was to the right.
- 3. There were no significant decomposition peaks in the samples exposed to N<sub>2</sub>/Air or to air at 1000°C
- **4.** In the samples fractured in the environment, the major XRD peaks shift towards the left. The shift (to the left) was higher in samples fractured with slower strain rates.
- **5.** Slow XRD scan rates of fractured samples indicated that the major peaks were no longer single and had decomposed to several peaks. In addition, several additional peaks were observed that were becoming dominant.
- 6. Many of the peaks were indexed with the International Centre for Diffraction Data ( ICDD) and Inorganic Crystal Structure Database (ICSD) databases and had a close match corresponding to La<sub>2</sub>SrFe<sub>2</sub>O<sub>7</sub>, LaSrFeO<sub>4</sub>, LaSr<sub>3</sub>Fe<sub>3</sub>O<sub>9.9</sub>, LaFeO<sub>3</sub>, SrCrO<sub>3</sub> Sr<sub>3</sub>Cr<sub>2</sub>O<sub>7</sub>, CrFeSr<sub>2</sub>O<sub>5.544</sub>, Sr<sub>3</sub>Fe<sub>2</sub>O<sub>6</sub>, Sr<sub>2</sub>FeO<sub>4</sub>, Sr<sub>3</sub>Fe<sub>2</sub>O<sub>6.93</sub> and Sr<sub>2</sub>Fe<sub>2</sub>O<sub>5</sub> phases. However, there were also some peaks which couldn't be indexed at all.
- 7. Some of the unexplained peaks were indexed with Powder X-ray analysis program which indicated Brownmillerite (or Sr<sub>2</sub>Fe<sub>2</sub>O<sub>5</sub> type phases) and Aurivilius type of structures. In earlier electron microscopy studies on LaSrFeCrO at UIC, these structures were analyzed to be of the following lattice parameters

Phases: P = Perovskite, B = Brownmillerite, A = Aurivilius

Lattice Parameter of Perovskite ( $a_c$ ) = 3.9105 $A^o$ 

## Brownmillerite Phase

$$a_0 = a_c^* (2)^{\frac{1}{2}}$$
 = 5.5352  
 $b_0 = 3a_c$  = 11.742  $c_0 = a_c^* (2)^{\frac{1}{2}}$  = 5.5352

Aurivilius phase:

$$a_0 = a_c * (20)^{\frac{1}{2}} = 17.4878$$
  
 $b_0 = a_c * 0.97 = 3.7930$   $c_0 = a_c * (20)^{\frac{1}{2}} = 17.4878$ 

8. In sample fractured at very slow strain rates (~3micron/min), the brownmillerite (Sr<sub>2</sub>Fe<sub>2</sub>O<sub>5</sub> type) peaks became more dominant.

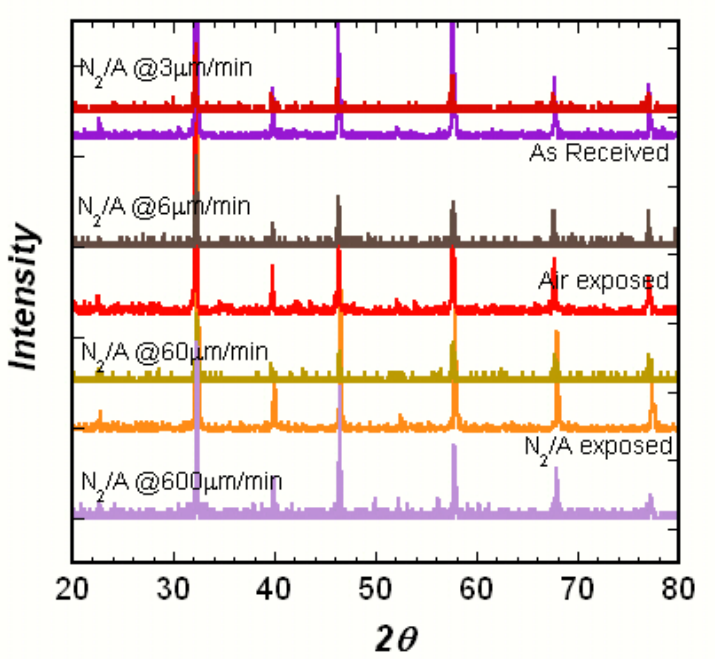


Figure 72. XRD plots of the OTM samples in a) as received, b) exposed to Air at 1000°C; c) exposed to N<sub>2</sub>/Air at 1000°C and fractured at varying strain rates in N<sub>2</sub>/Air at 1000°C

The X-Ray data and the observations point to non-equilibrium decomposition of the LSFCO OTM membrane. The non-equilibrium conditions could probably be due to the nature of the applied stress field (strain rates) which leads to transition in crystal structures and increases kinetics of decomposition. The formation of Brownmillerite or Sr<sub>2</sub>Fe<sub>2</sub>O<sub>5</sub> type structures, which are orthorhombic, are attributed to the ordering of oxygen vacancies. The transition from cubic to orthorhombic structure leads to 2.6% increase in strain. Thus residual stresses generated could influence the fracture behavior of the OTM membrane.

On a cautious note, the interpretation of the data has to be backed by simulation of the XRD profiles and physical evidence of the ordering or phase transitions. In order to do this, we started using X-ray diffraction programs such as FULLPROF to refine the possible structures and crystal geometry.

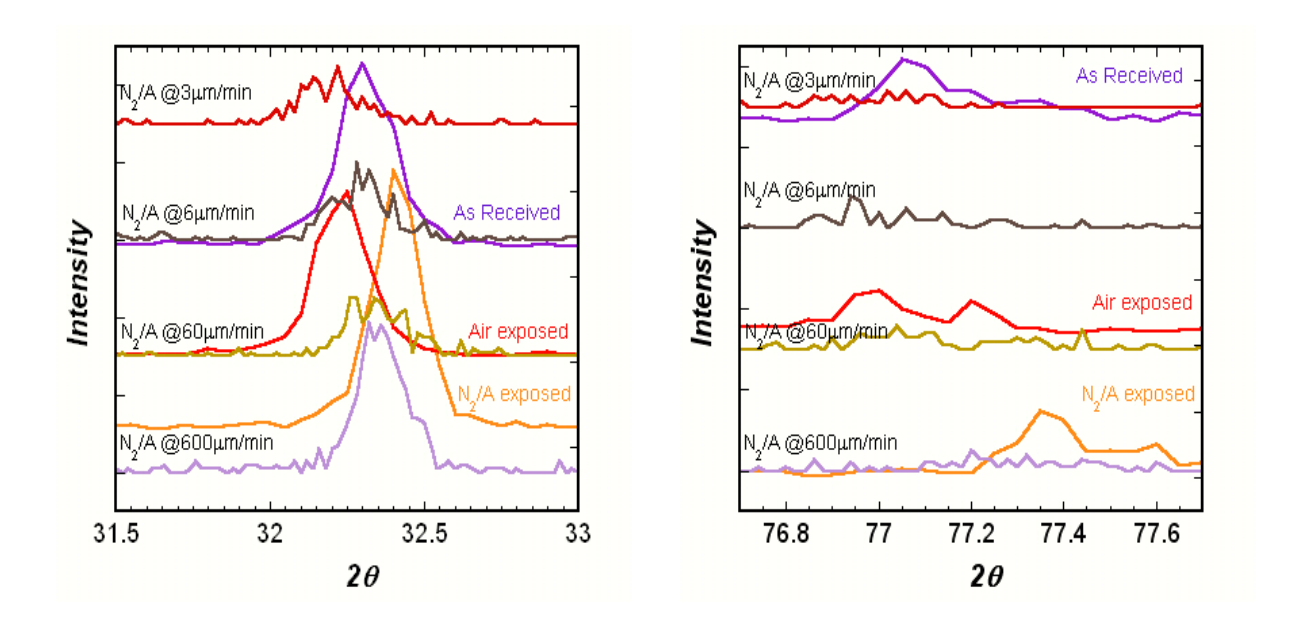


Figure 73: Major peaks  $(2\theta = 32 \text{ and } 77)$  from XRD analysis indicating a perceptible shift and decomposition of the single peaks.

Based on the data available from the X-ray analysis of OTM fractured samples, a flow chart depicting a possible decomposition route of the parent perovskite is shown in figure 74. The significance of this on fracture and crack growth behavior is studied.

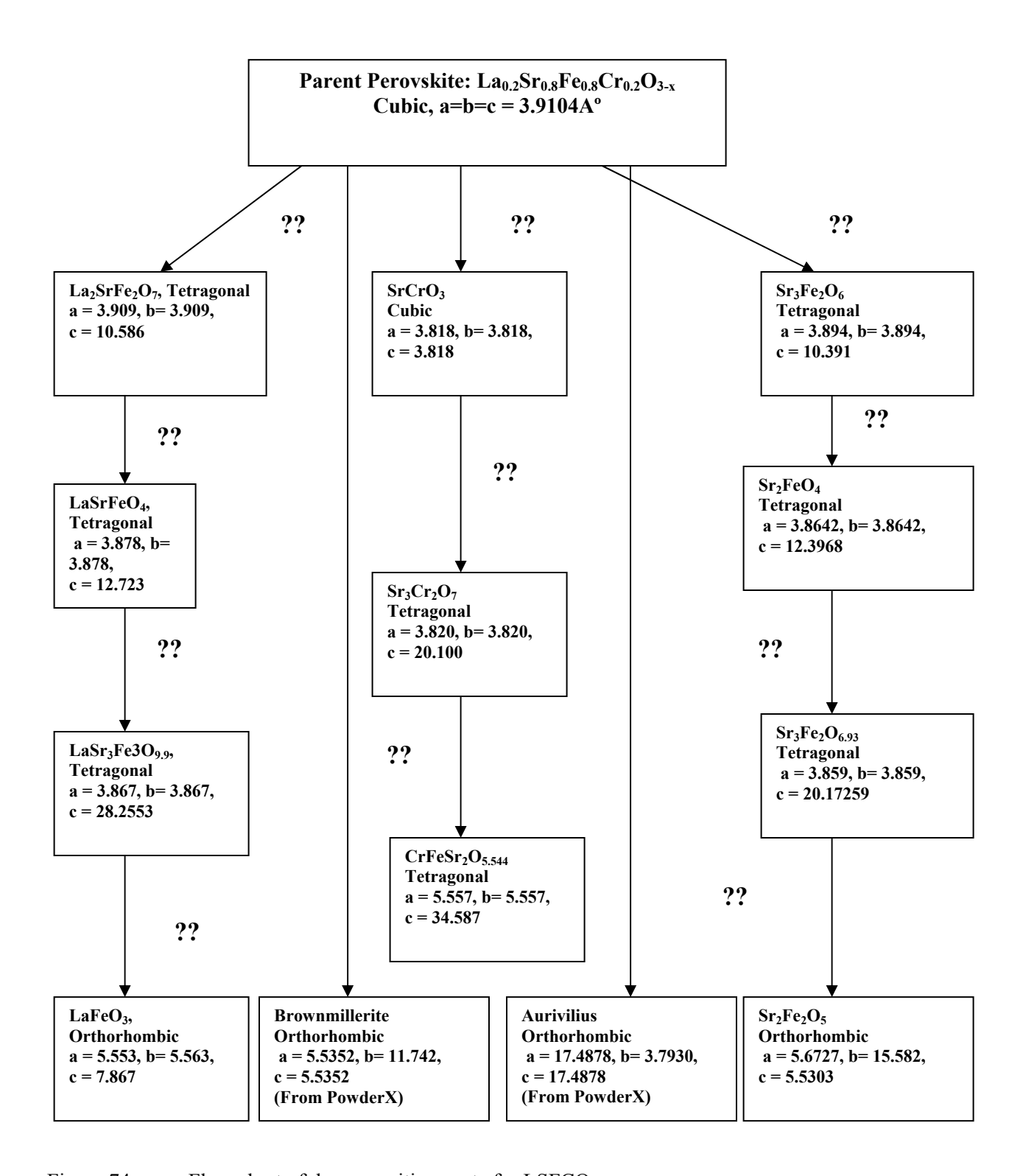


Figure 74: Flow chart of decomposition route for LSFCO

### Refinement of X-ray data:

To understand the decomposition process in the dense OTM material after exposure to a combination of stress and environment, it is very important to refine the raw X-ray data in order to define the crystal parameters.

The major peaks from the XRD data were selected and refined by FULLPROF Code. The major peaks ( $2\theta = 22.94$ , 32.5, 39.91, 46.25, 52.56, 57.32, 67.69 and 77.17) were chosen based on the literature data available and indexed to the cubic structure of the LSFCO material. The results of the refinement are plotted in Figure 75, 76 and 77 respectively and the resulting lattice parameters listed in Table 10

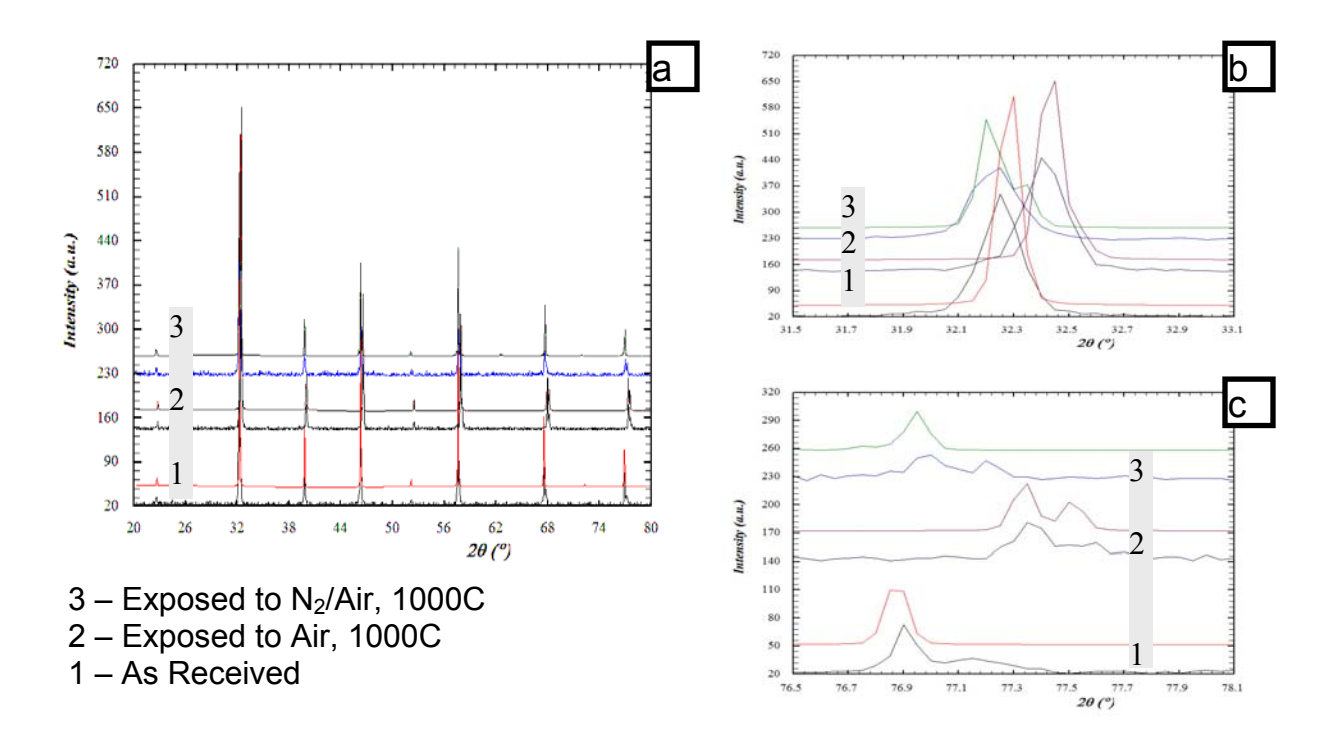


Figure 75: Refinement of OTM material in as received, as exposed to air, and  $N_2$ /air at 1000°C. Insets b and c, indicate the observed shift in 20 values

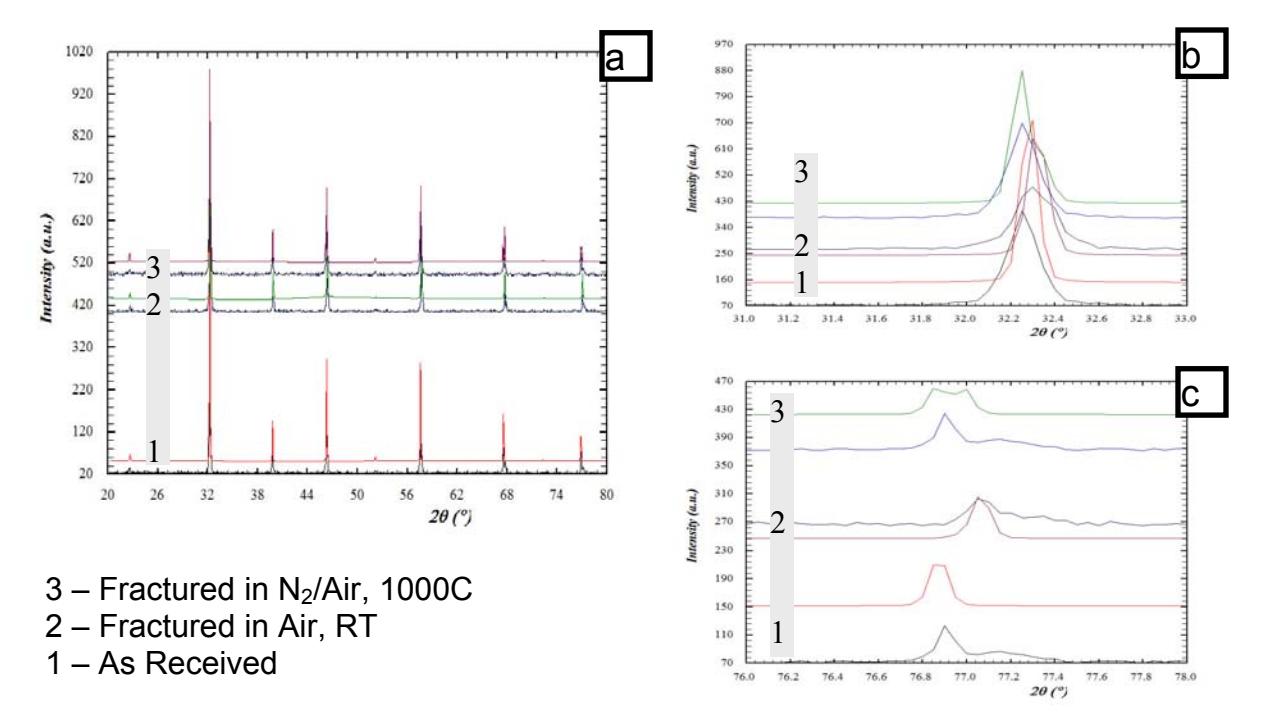


Figure 76: Refinement of OTM material in as received, fractured in air (RT), and  $N_2$ /air at 1000°C. Insets b and c, indicate the observed shift in 20 values

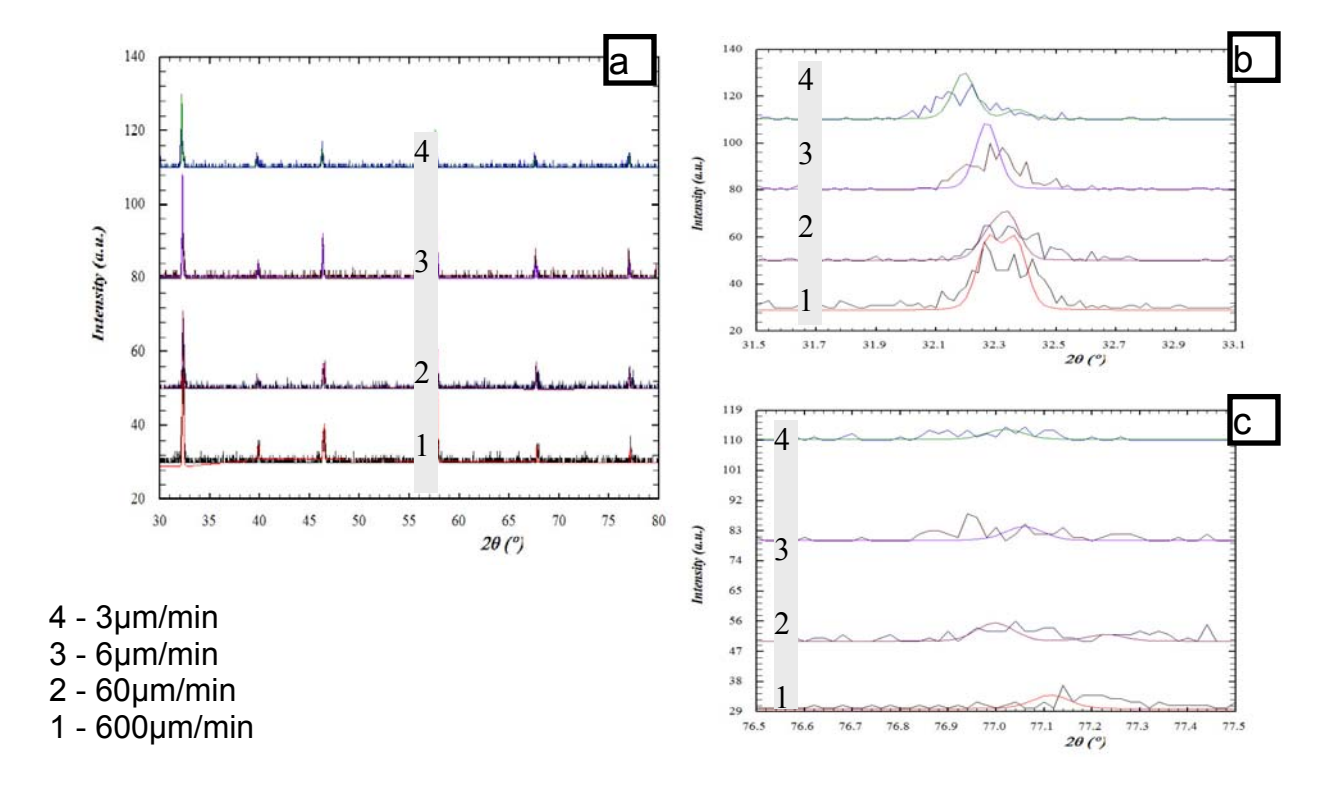


Figure 77: Refinement of OTM material fractured in  $N_2$ /air at 1000°C at different strain rates. Insets b and c, indicate the observed decomposition of the major peak and shift in  $2\theta$  values

Table 10. Crystal Symmetry and lattice parameters obtained from refinement of XRD data.

Condition	Symmetry	$a_c$	b	С	α=β=γ
As received	Pm3m	3.9104	3.9104	3.9104	90
Air exposed	Pmmm	3.8991 (~a <sub>c</sub> )	2.758	2.7497	90
(1000°C)			$b \sim a_c/\sqrt{2}$	$c \sim a_c/\sqrt{2}$	
N <sub>2</sub> /Air exposed	Pmmm	3.9362 (~a <sub>c</sub> )	3.9174 (~a <sub>c</sub> )	2.7634	90
(1000°C)				$c \sim a_c/\sqrt{2}$	
D	70	2.0124 ( )	2.0005 ( )	2.545	0.0
Fracture, RT	Pmmm	$3.9134 (\sim a_c)$	$3.9085 (\sim a_c)$	2.7647	90
Fracture	Pmmm	3.9294 (~a <sub>c</sub> )	3.9175 (~a <sub>c</sub> )	$c \sim a_c/\sqrt{2}$ $2.7656$	90
N <sub>2</sub> /Air,	1 111111111	3.7274 ( u <sub>c</sub> )	3.7173 ( u <sub>c</sub> )	$c \sim a_c/\sqrt{2}$	70
(1000°C)				0 40 12	
Fracture	Pmmm	3.9340 (~a <sub>c</sub> )	3.9052 (~a <sub>c</sub> )	2.7640	90
N <sub>2</sub> /Air,			, ,	$c \sim a_c/\sqrt{2}$	
600µm/min					
Fracture	Pmmm	3.9278 (~a <sub>c</sub> )	3.9033 (~a <sub>c</sub> )	2.7606	90
N <sub>2</sub> /Air,				$c \sim a_c/\sqrt{2}$	
60μm/min					
Fracture	Pmmm	3.9233 (~a <sub>c</sub> )	2.7783	2.7634	90
N <sub>2</sub> /Air,			$b \sim a_c/\sqrt{2}$	$c \sim a_c/\sqrt{2}$	
6μm/min					
Fracture	Pmmm	$3.9155 \ (\sim a_c)$	2.7385	2.7719	90
N <sub>2</sub> /Air,			$b \sim a_c/\sqrt{2}$	$c \sim a_c/\sqrt{2}$	
3μm/min					

The results from the refinement indicate that the parent perovskite with a primitive cubic perovskite structure (a=b=c = 3.9104A°) undergoes a slight distortion to orthorhombic structure (Pmmm) with reduced crystal symmetry. Although slight changes are observed in the a axis, the distortion is primarily in the c and b axes. Interestingly, samples tested under stress and environment showed increasing distortion with decreasing strain rates. Although major peaks were refined, broader reflections and splitting of several peaks observed indicate the possible presence of secondary phases. Further refinement of the data will be done considering various phase composition determined by XRD.

Although, the XRD analysis indicated phase instability and decomposition of the parent perovskite upon exposure to the environment and strain rates, the possibility of vacancy ordering and structure change in micro-domains need to be examined. To do this, studies were done using a TGA-DTA (Perkin Elmer Instruments) analyzer to obtain relevant information on endothermic and exothermic processes corresponding to different oxygen desorption processes and structural

changes (e.g.; vacancy order-disorder transitions and reversible structural stability of the materials).

Initial TGA studies were done by retaining the thermal history of the materials tested. For these, the tested bar samples were sectioned and heated in N<sub>2</sub> up to 1000°C with a equilibration time of 1 hr. As shown in Fig.78, the weight loss and the DTA signal were monitored for further analysis.

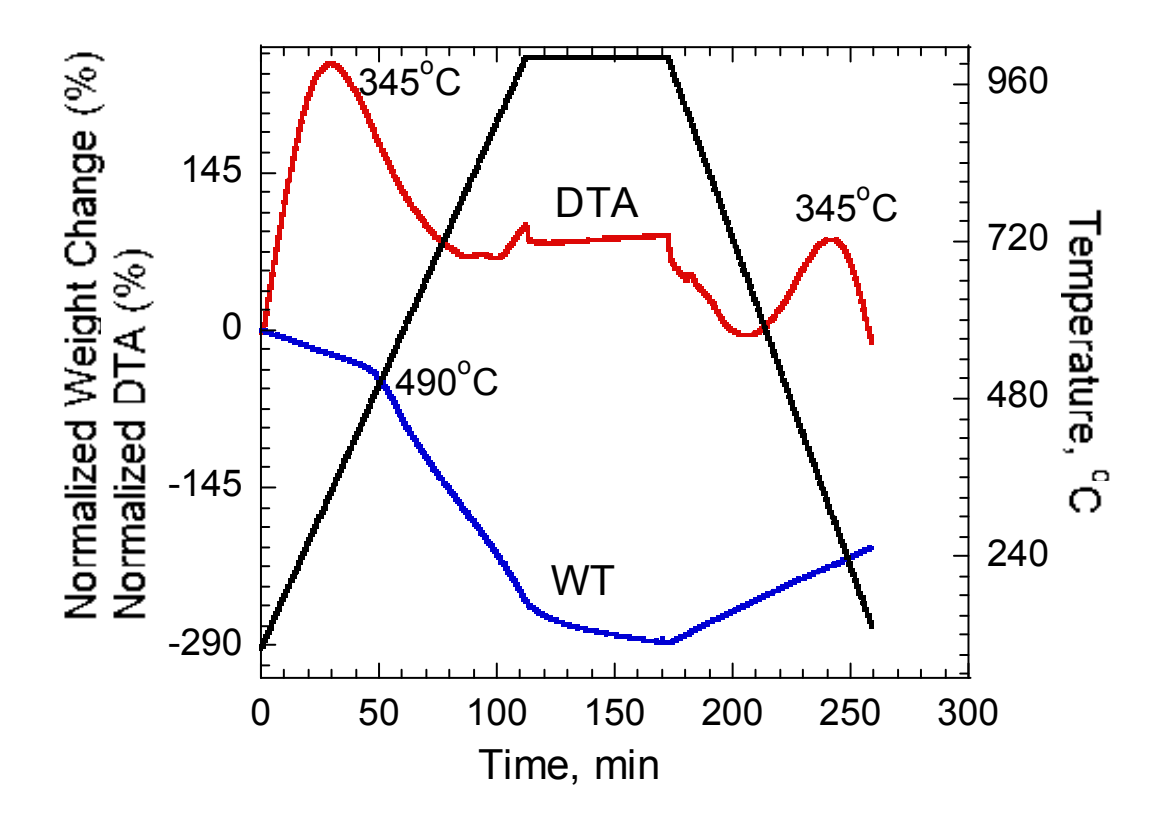


Figure 78: Weight change, DTA and temperature data as a function of time.

As shown in Fig. 79-80 and Table 11, post-fracture thermal analysis studies on the sample indicated significant changes in weight and DTA response signal. The as-received sample indicated a continuous change in weight with increasing temperature till around 235°C and thereafter a plateau wherein no change in weight was observed. A second weight loss was observed around 850°C. On the other hand, sample exposed to an environment of N<sub>2</sub> changing to air at 1000°C and fractured in the same environment indicated a drastic weight loss at higher

temperature. The onset temperature for the drastic weight loss varied depending on the stress history [Table 11].

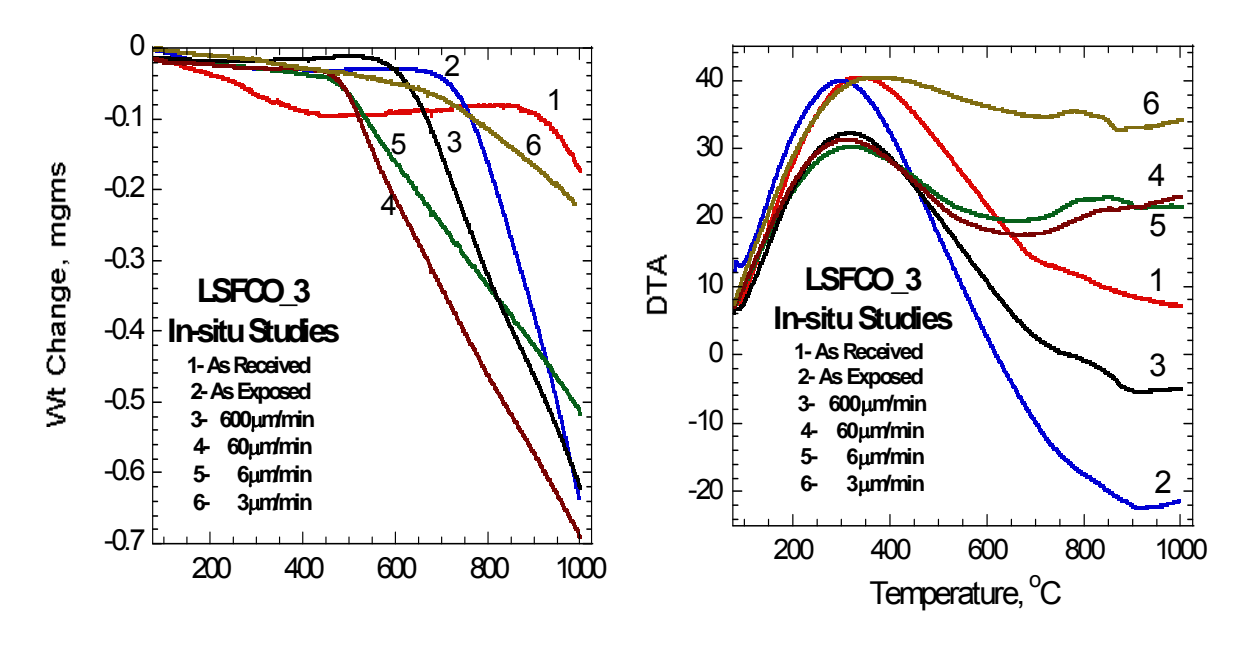


Figure 79-80: Post-fracture thermal analysis of LSFCO-3 OTM material.

The DTA signal (Fig 80) also indicated changes and depending on the sample history, showed the presence of highly exothermic peak in the temperature range of 310- 350°C. In samples fractured in the environment, a second peak prominent was also observed in the temperature region of 775-800°C. This peak was of low intensity and was masked by the as-received sample

Table 11: Thermal analysis of LSFCO-3 samples.

		Wt loss at Temp., °C	DTA (peak 1) °C	DTA (peak 2) °C
As received	235	850	336	801
Exposure N <sub>2</sub> /Air 1000°C		680	300	805
600μm/min N <sub>2</sub> /Air 1000°C		542	311	777
60μm/min N <sub>2</sub> /Air 1000°C		455	316	802
6μm/min N <sub>2</sub> /Air 1000°C		450	333	847
3μm/min N <sub>2</sub> /Air 1000°C		670	348	777

The stoichiometry ( $\delta$ ) of the samples were determined from weight change measurements and calculated as:

$$W_{i} = \text{initial weight}$$

$$W_{s} = \text{equilibrium Weight}$$

$$W_{o} = \text{atomic weight of oxygen}$$

$$W_{i}/M_{w,0} = \text{molecular weight of sample}$$

$$\delta_{o} = 0.2379 \text{ at } 800^{\circ}\text{C in } 10^{-4}$$

 $\delta_{o}$  for the calculation were obtained from Prof. Jacobson's work on La<sub>0.2</sub>Sr<sub>0.8</sub>Fe<sub>0.8</sub>Cr<sub>0.2</sub>O<sub>3-x</sub> apart of the present program.

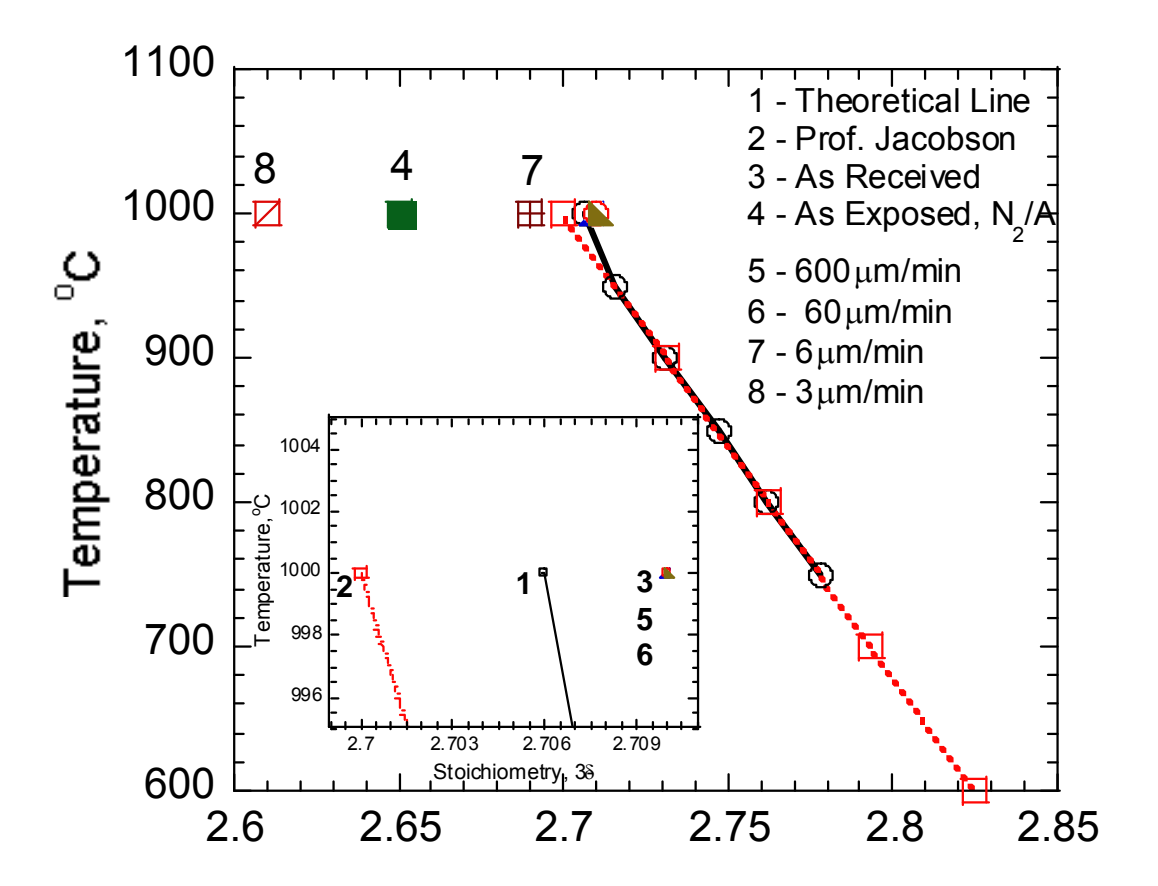


Figure 81: Stoichiometry (3-δ) of the fractured samples calculated from weight change measurements in a TGA

The results indicate that there is a perceptible change in the stoichiometry of the fractured OTM membrane as compared to related studies on non-fractured samples.

Results from the TGA/DTA studies were assumed to be artifacts of prior thermal/stress history in the specimen. Based on discussions with the group at University of Houston, a thermal profile was added in the test run to negate the so-called history effects.

For this, the specimens were rapidly heated in N<sub>2</sub> up to 1000°C and cooled to 100°C. For comparative purpose, test runs similar to earlier studies were also done.

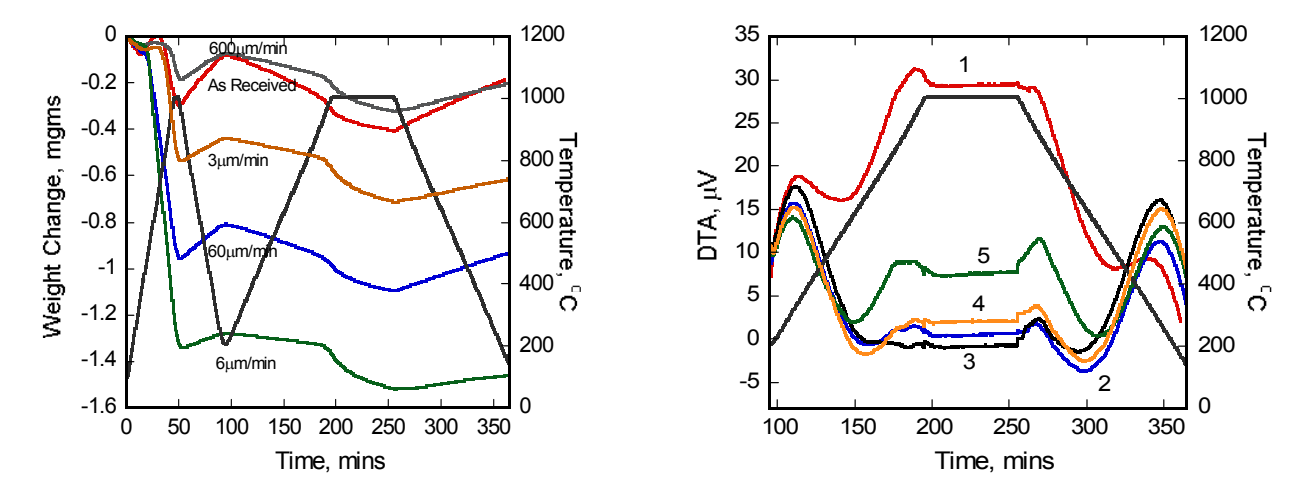


Figure 82: TGA/DTA runs on samples with prior thermal/stress history negated by initial heating in  $N_2$ .

1. As received, 2. 600µm/min, 3. 60µm/min, 4. 6µm/min and 5. 3µm/min

Results from the new test runs confirmed the expected presence of residual effects in the sample due to prior thermal/stress history. As shown in Fig. 82a and b, the first heat up cycle indicated significant weight loss in earlier studies and the second cycle showed the weight change which is an expected behavior for these classes of materials. However, the TGA/DTA signal still reflected on possible irreversible changes in the material.

#### **Crack Growth studies under elevated temperature and pressure:**

Studies were done on evaluating crack growth in OTM membranes under combined temperature, pressure and environment loading.

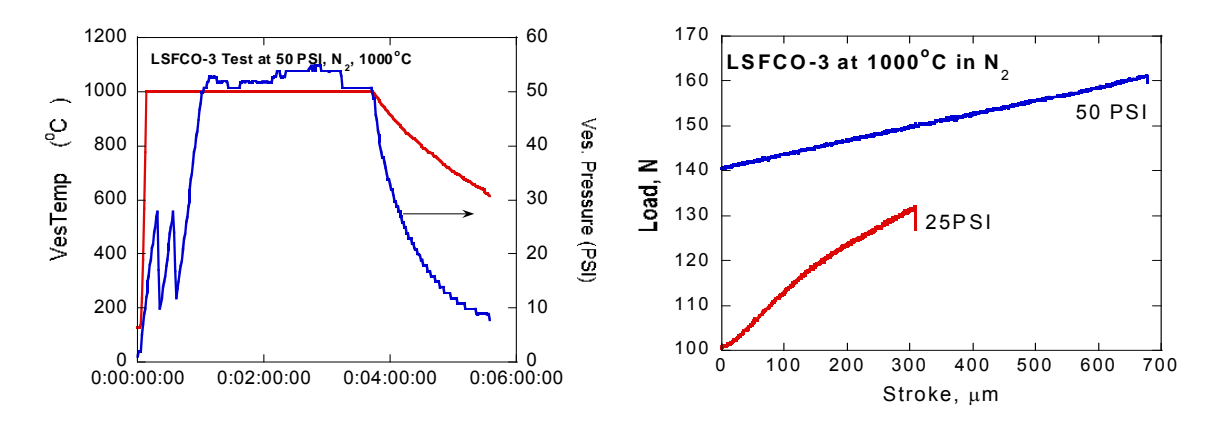


Figure 83: a) Combined Temperature/Pressure test run to evaluate crack growth in OTM membranes. b) Increase in hydrostatic pressure leads to increased stress for crack growth and final fracture.



Figure 84: Fracture in OTM membranes under combined elevated temperature and pressure loading. The fracture origins are at the multiple indents placed on the tensile surface.

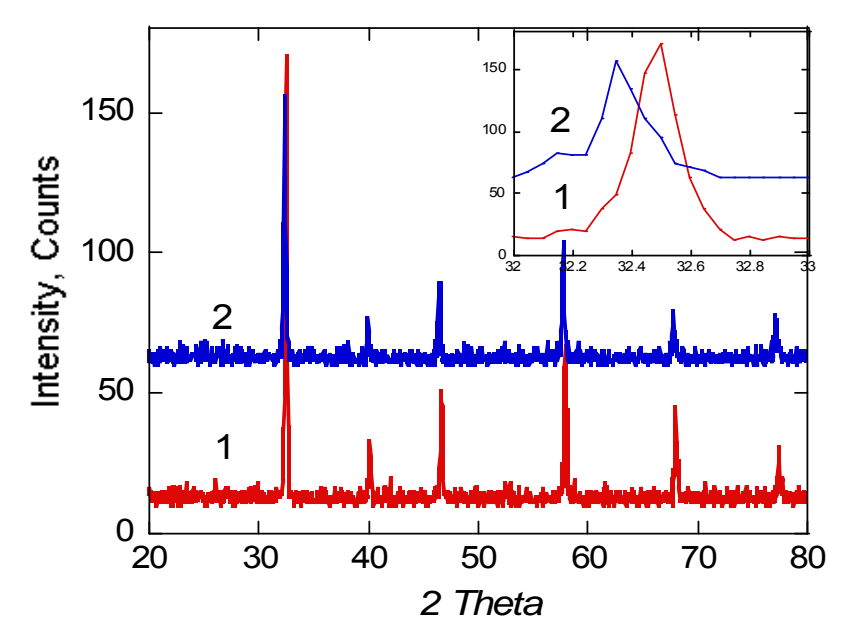
As shown in Fig 84, the methodology used for crack growth and fracture studies at room temperature is fairly reproduced at elevated temperature and pressure conditions. This is an important aspect as the safety and alignment procedures are very critical for studies under such

conditions. This is also the first set of data points ever generated on these classes of materials under more practical operating conditions.

Under the conditions mentioned above, the fracture stress of the OTM membrane materials appear to increase under elevated hydrostatic pressure. Previous studies have indicated that the surface cracks may blunt or often close upon exposure to reducing environment ( $N_2 \sim 10^{-4}$  atm and above). This effect may be further magnified in the presence of hydrostatic pressure resulting in increased strength and changes in crack growth behavior.

# X-Ray analysis:

The fractured samples were powdered and analyzed in a XRD for phase composition and analysis. The analysis indicated that the powder retained the perovskite (pseudo?) structure.



However, there was a minor shift towards the left in the major peak angle as shown in figure 85 Figure 85 – X-ray analysis of fractured OTM membranes under combined elevated temperature and pressure loading. 1) 25 PSI and 2)50 PSI.

Slow scan analysis (not shown here) did reveal that the major peak was composed of several minor peaks indicating possible decomposition and phase transitions.

## 2.4.3.2.8 TGA/DTA analysis

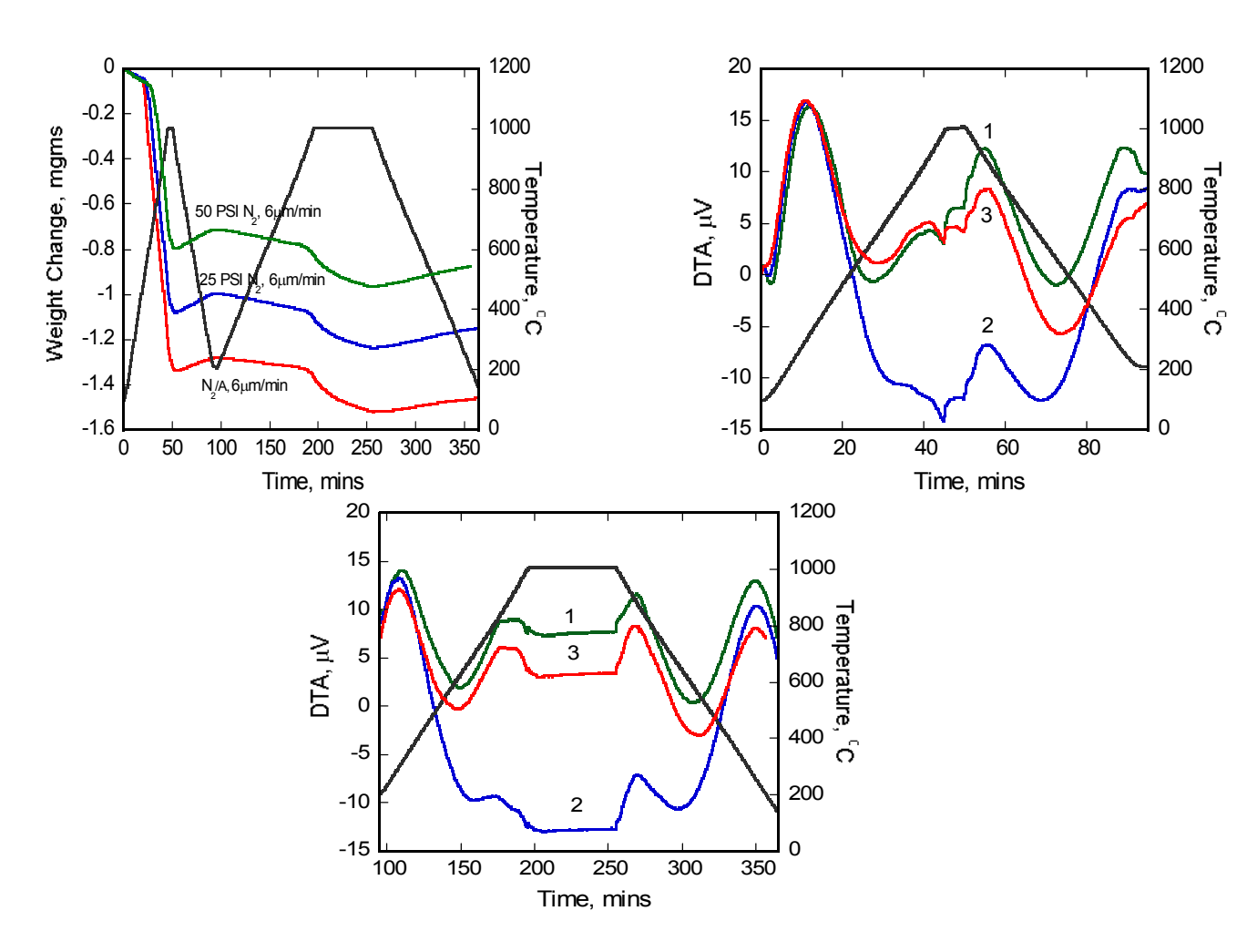


Figure 86: TGA/DTA analysis of fractured OTM membranes under combined elevated temperature and pressure loading. 1) 25 PSI, 2)50 PSI, 3) N2/Air

As from earlier studies, the samples were analyzed in a TGA to determine stoichiometry and also to check for transitions if any. As shown in Fig 86, the second peak indicating a secondary transition ( $\sim$ 915-950°C) was stronger in materials fractured in N<sub>2</sub> at 25 PSI and 50 PSI respectively.

The change in the material stoichiometry as calculated from weight change measurements, are indicated in table 12. Further change in stoichiometry is reflected by changes in 3- $\delta$  values to 2.64 and 2.63 from a equilibrium value of 2.7.

Table 12: Weight loss and DTA peaks in sample fractured in  $N_2$  at elevated temperature and pressure.

	Wt loss at Temp., °C	DTA (peak 1) °C	DTA (peak 2) °C	3-δ
6µm/min N2/Air 1000°C	450	333	847	2.69
Fractured in N2 at 25 PSI, 1000°C	625	314	916	2.64
Fractured in N2 at 50 PSI, 1000°C	645	295	944	2.63

Fracture analysis in combination with X-ray/DTA/TGA analysis indicates a possible correlation with expansion, decomposition or structural transition of the unit cell of the cubic perovskite structure. The expansion/decomposition and transitions indicate the possibility of residual stresses which influence crack growth and fracture in the OTM material. This needs to be further examined by careful experimentation and modeling of the residual stresses.

#### 2.4.4 Evaluation of OTM Bars - LSFT and LSFT/CGO

#### 2.4.4.1 Introduction

Dense dual-phase OTM bars and dense LSFT samples fabricated at Praxair facility by the Coprincipal investigator who spent 6 weeks on this program at Praxair research facilities in New York. Both the samples were analyzed for microstructure and density. For both the membrane materials, the hardness values were measured for different loads and fracture toughness were calculated. Thermal analyses and X-ray diffraction analyses were also carried out on these samples. The effect of strain rate on the flexural strength of dual phase membranes was studied to understand the slow crack growth. The effect of temperature and the reducing environment on the strength of dual phase samples are estimated by four point bend method and the fractography was used to understand the fracture behavior. Thermal and chemical expansion behavior of the dual phase membranes were studied using dilatometry.

## 2.4.4.2 Experimental

LSFT (La<sub>0.2</sub>Sr<sub>0.8</sub>Fe<sub>0.6</sub>Ti<sub>0.4</sub>O<sub>3-8</sub>) powder was obtained from Praxair Specialty Ceramics. The LSFT powder was prepared as dense membrane and also mixed with CGO (Ceria doped Gandolium Oxide) in the ratio of 60/40 vol%. The mixing of the powders was done in a polycarbonate lined ball mill with Zirconia as milling media. The powders were uniaxially pressed in hardened steel die at 5000 PSI and later iso-statically cold pressed at 20KSI. The dimension of the green samples was 20 x 65 mm. The samples were sintered in air at  $1400^{\circ}$ C for 4 hours (LSFT) and  $1350^{\circ}$ C for 4 hours (LSFT/CGO) respectively. Figure 87 shows the as-sintered bars of LSFT-CGO ( $40/60 - 1^{st}$  batch).



Figure 87. Fully sintered and dense dual phase membranes

#### 2.4.4.3 Microstructure

### Microstructure analysis of LSFT membrane

The sintered LSFT samples were polished down to 3µm and thermally etched at 1350°C for 30 minutes. The etched samples were sputtered with gold for 3 minutes prior to SEM analysis.

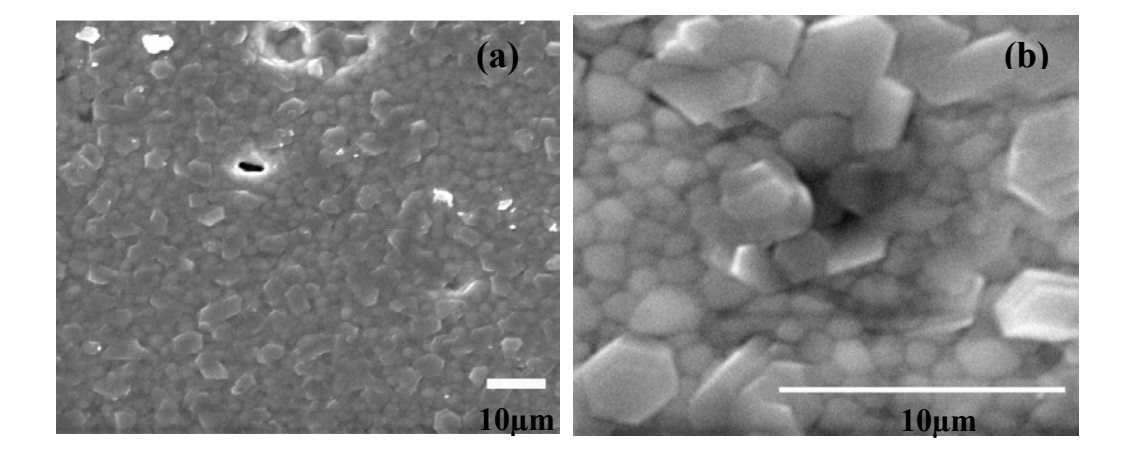


Figure 88. SEM microstructure of LSFT sintered at 1400°C. Microstructure (a) shows a densely packed grain structure and the closer observation (b) reveals the presence of two types of grains, platy hexagonal grains and closely packed fine grains

The image analysis was carried out using Sigmascan pro 4 and average grain size and grain size distributions were measured. The SEM micrograph and the image analysis showed that about 90% of the grains were less than 3.0 $\mu$ m with an average grain size of 2.07 $\mu$ m as indicated in figure 89 (a). The grain size distribution was bimodal with a peak at 4 $\mu$ m as shown in figure 89 (b).

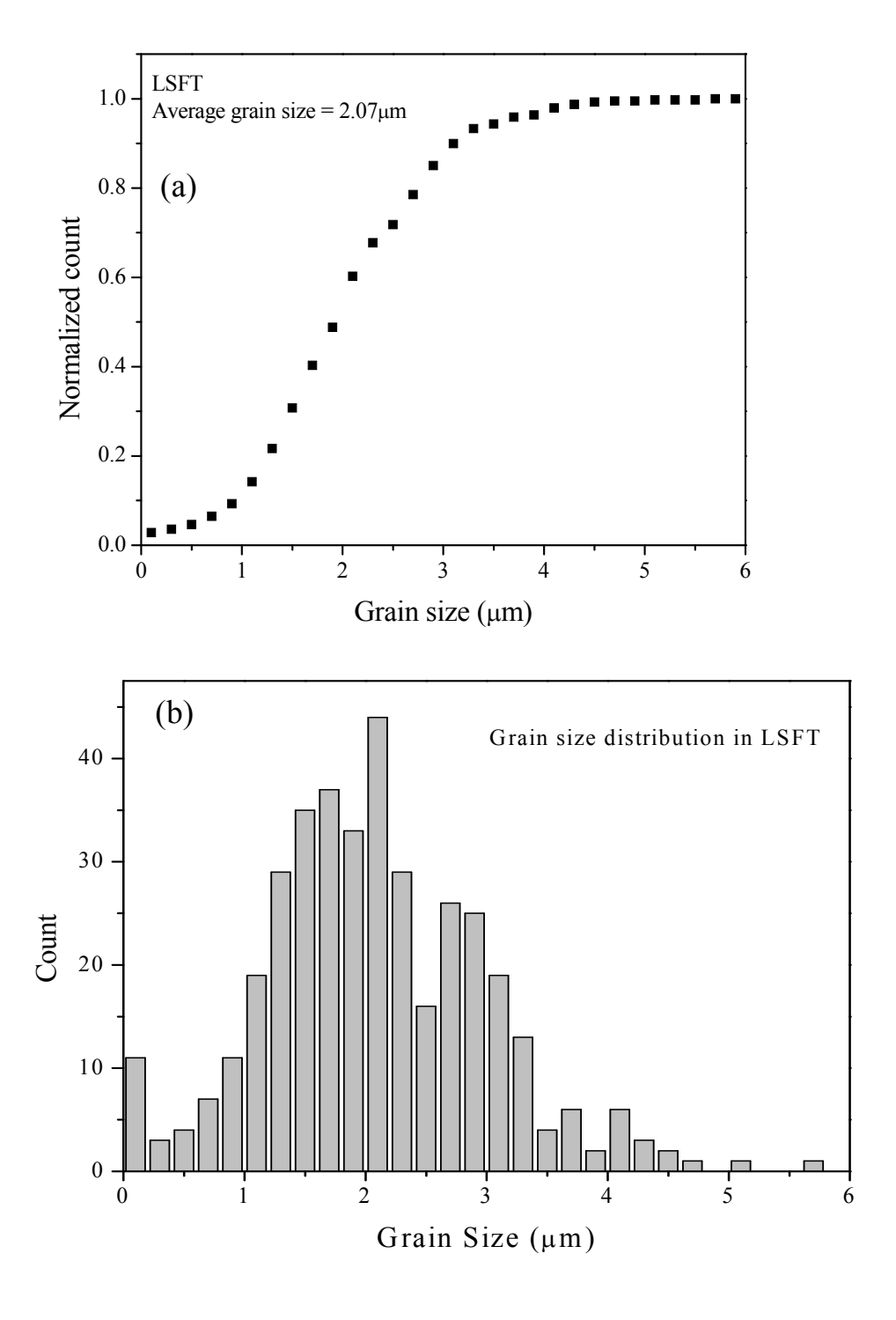


Figure 89. Grain size and distribution in sintered LSFT; (a) shows average grain size and (b) grain size distribution. The bimodal distribution of grains is clearly seen in the plot as well as in the microstructure.

### 2.4.4.3.2 Microstructural analysis of dual phase membranes (40-60vol%)

The microstructure of the dual phase membranes (1<sup>st</sup> batch bars from Praxair) was analyzed using SEM. The dual phase membrane samples were cut and ground down to 600 grade SiC paper. Further polishing of the surface did not improve the surface finish. Rather it marred the surface finish. The polished samples were thermally etched at 1300°C for 1hr and were subjected to gold coating before the SEM analysis. The SEM micrographs of dual phase membrane are shown in Figure 90. It is evident from the micrograph that the microstructure is composed of dual phases. The dense circular regions are enclosed by the less dense, continuous phase which accommodates most of the pores. The pores are normally aggregated and found clustered along the dense region boundaries. The dense regions, however, do not have pores.

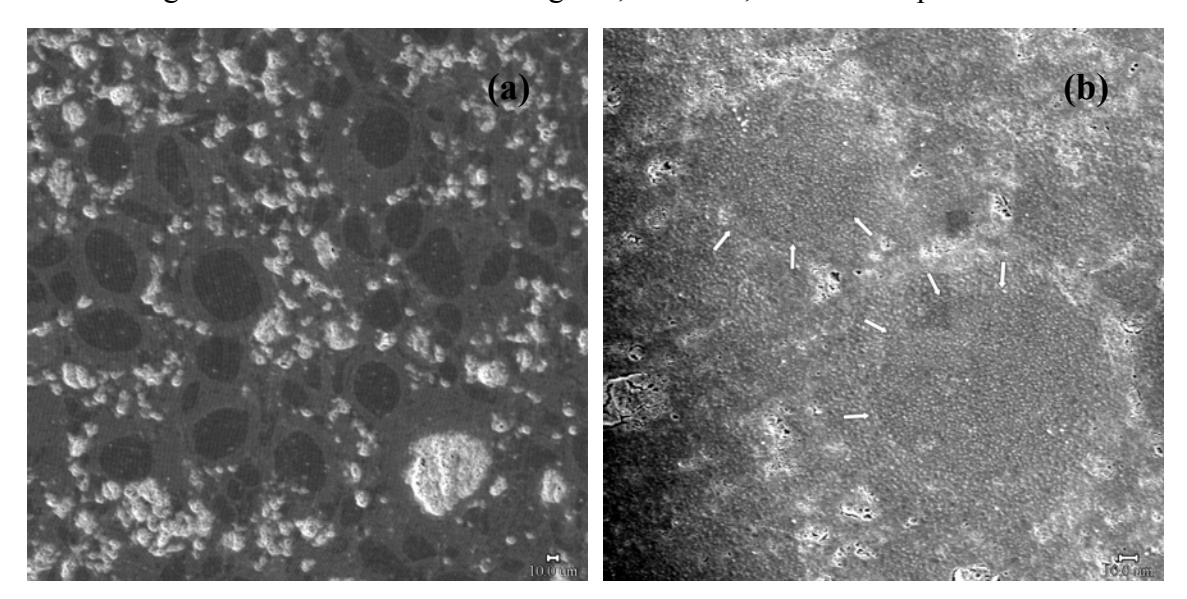


Figure 90. SEM micrographs of dual phase membrane. The dense spherical regions (dark in color in Figure 90a) are enclosed by the less dense, continuous phase which accommodates the pores. On closer observation (Figure 90b), the dense regions appear to have clear circular boundaries or cracks. The white arrows point to the circular cleavages.

The size distribution of the dense, circular region in the microstructure was examined using image analysis. The dense regions are clearly distinguishable from the surrounding porous, continuous phase. Hence the dense regions in micrographs were layered with a color marker which were later used to analyze the size distribution. The total area of the dense region was also calculated and found to be 26% of the microstructure.

Figure 91(a) shows the size distribution of the dense, discontinuous regions. Size distribution ranges from 5 to 20  $\mu$ m with a  $D_{50}$  of 15  $\mu$ m. Another important thing that one can observe from the micrographs is that the discontinuous regions are mostly near circular in shape. This shape factor can be used to understand the nature of the regions and may allow postulating a theory for the formation of those regions. Upon closer observation of the micrograph it can be seen that the dense regions have clear circular cleavages or cracks as their boundaries. The white arrows in Figure 90 (b) point to the circular cleavages. This unique microstructure is more clearly revealed in the higher magnification image shown in Figure 92(a). The circular cleavage clearly encompasses a dense region with no pores or visible flaws present. The cleavages appear to be transgranular in nature.

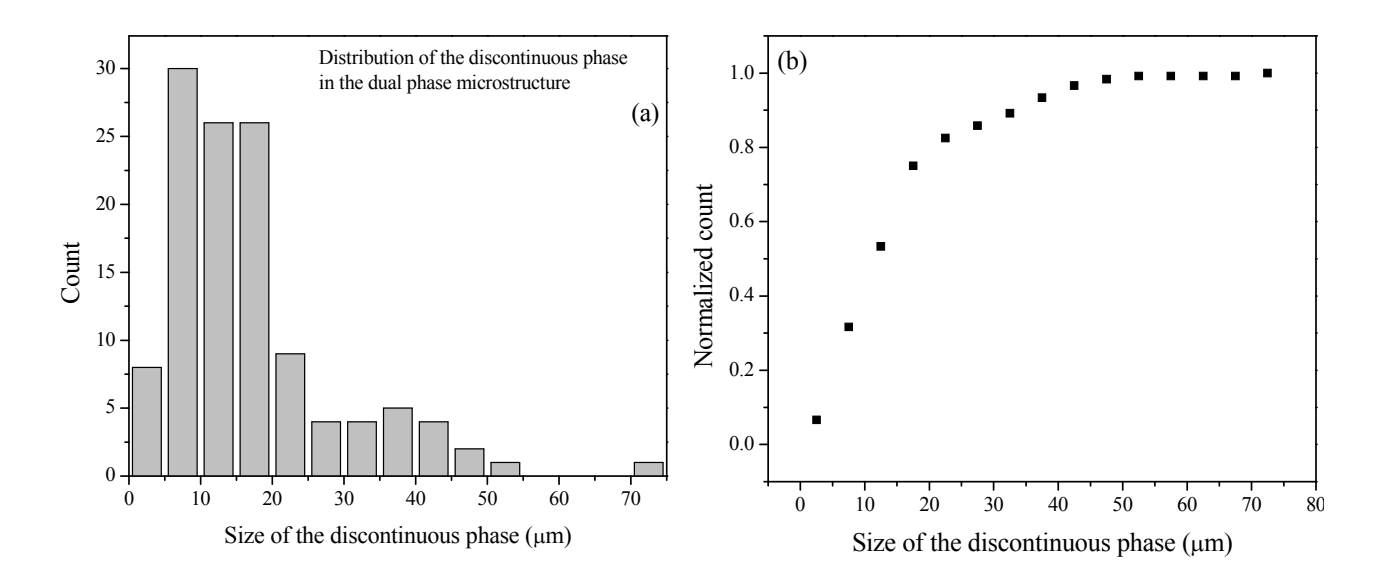


Figure 91. Size distribution of the discontinuous phase in the dual phase membrane microstructure.

These cracks clearly separate the less dense continuous regions which accommodate pores from the dense regions. Figure 92 (b) shows the micrograph of the dense region in which the grains are well fused and contain no pores. The spherical nature of the dense region in a three dimensional network is associated with the segregation of pores along the boundaries. The segregation of the pores may have been caused by the pore formers which were added during processing or as a result of the sintering process. The formation of cleavage around the dense regions can be explained by the differential shrinkage of the pore free regions caused by the

sintering process. The highly dense regions shrink more than the rest of the surrounding phase due to different sintering rates which eventually lead to the formation of cleavages or cracks.

The microstructure of the dual phase membrane is shown in Figure 93. The microstructure clearly shows that the pores are clustered together. The grain growth in the non-porous region is favored by the increased diffusion channels which are formed as a result of better packing during compaction or due to particle rearrangement during initial stages of sintering. The pores hinder the grain growth that results in the formation of fine grains in the porous region.

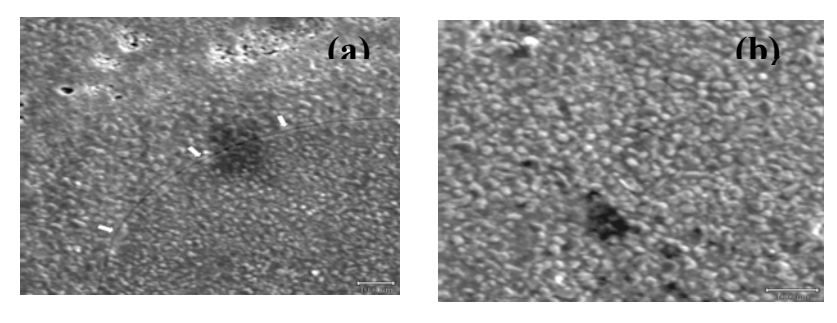


Figure 92. (a) The circular crack or cleavage at higher magnification. The crack is transgranular and encompasses a dense region; (b) Micrograph of the dense region.

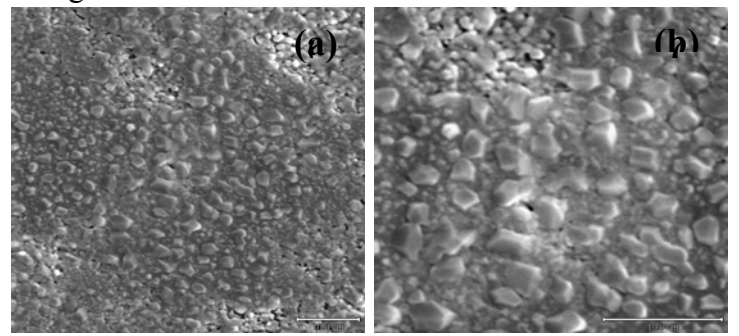


Figure 93. Microstructures of the dual phase membrane. Figure (a) shows the presence of pores which are clustered together. A closer view of the microstructure shown in Figure (b) reveals that the grain growth is controlled in the porous region.

Apart from the pores and circular cracks in the microstructure, the next significant flaws that were observed were the craters. These were formed mostly due to the burnout of the organic additives (like the binder) that were added during the processing of the membranes. One such crater is shown in the Figure 94. The size of the craters varied between 10 to 30µm and was bigger than the grain boundaries or pores. The craters can reduce the flexural strength of the

membranes to a greater extent. The formation of carters could be avoided by refinement of processing methods and selection and use of suitable organic additives.

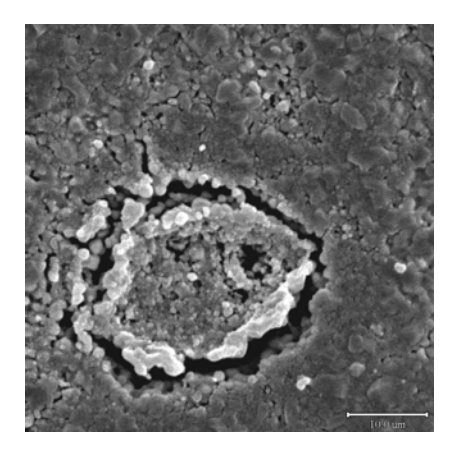


Figure 94. Illustration of a crater which might have formed due to the burn out of organic additives during sintering

The grain size distribution was estimated using image analysis and is shown in Figure 95. It showed a unimodal distribution (Figure 95 a) with an average grain size of 1.99  $\mu$ m (figure 95 b). The finer grains which are less than  $1\mu$ m are mainly observed in the porous region caused by the hindered diffusion process.

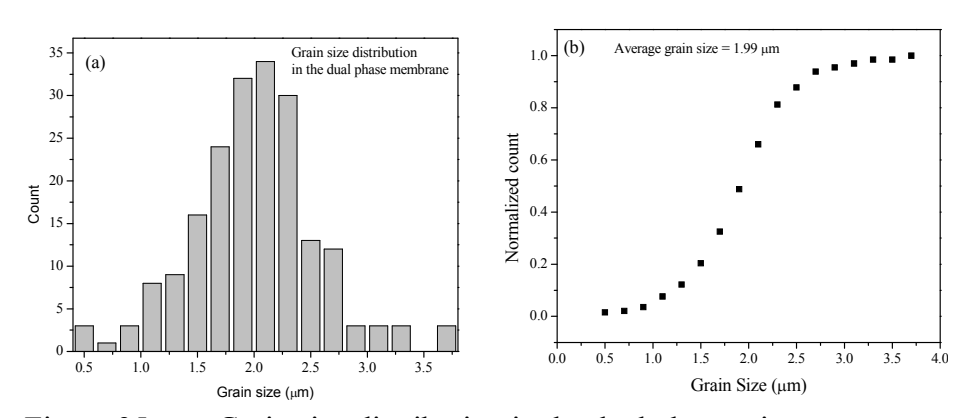


Figure 95. Grain size distribution in the dual phase microstructure.

The EDX analysis was also carried out independently in the circular, dense region and the continuous porous region in order to verify any possible element segregation or evaporation during this phase formation. The EDX patterns taken from the dense regions as well as from the porous regions were identical and all the relevant elements were found to be there in both

patterns. The analysis showed that there was no segregation or evaporation of elements within the detection limits of this EDX instrument.

#### 2.4.4.4 Density measurements of LSFT and dual phase (LSFT-CGO) membranes:

The bulk densities of the membranes were determined using the Archimedes method. The membranes were cut into small pieces and their dry weights were measured. The sample pieces were then immersed in distilled water and boiled for 5 hrs and allowed to cool overnight. The sample weights were measured suspended in water. Their wet weights were also measured after they were cleaned with wet cloth to remove the adsorbed water from the surface. The bulk densities were calculated using the measured weights and the results are presented in Table 13. The bulk densities of the LSFT membrane and the dual phase membrane were found to be 5.029 g/cc and 5.57 g/cc respectively.

Table 13. Densities of the membranes

	Bulk Density (g/cc)	Apparent Specific Gravity	Volume of the impervious material (cc)	Mean Bulk Density (g/cc)
LSFT	4.9305 4.99433 5.16073	4.98982 5.03557 5.19103	0.2161 0.4723 0.6643	5.029
LSFT-CGO	5.4 5.62998 5.67944	5.76667 5.94777 5.98951	0.081 0.2374 0.3242	5.57

#### 2.4.4.5 Xray – Diffraction Analyses

#### 2.4.4.5.1 Energy Dispersive X-ray analysis (EDXA)

The presence of impurities in the chemical composition of the membranes can affect the structural and mechanical properties the materials significantly. Hence EDX analysis was carried out on the LSFT (figure 96) and dual phase membrane samples (figure 97) to determine the elemental compositions. The elements identified were Sr, La, Fe, Ti, and Au. The presence of Au is due to the gold coating applied to the sample prior to SEM analysis. No other impurities were detected.

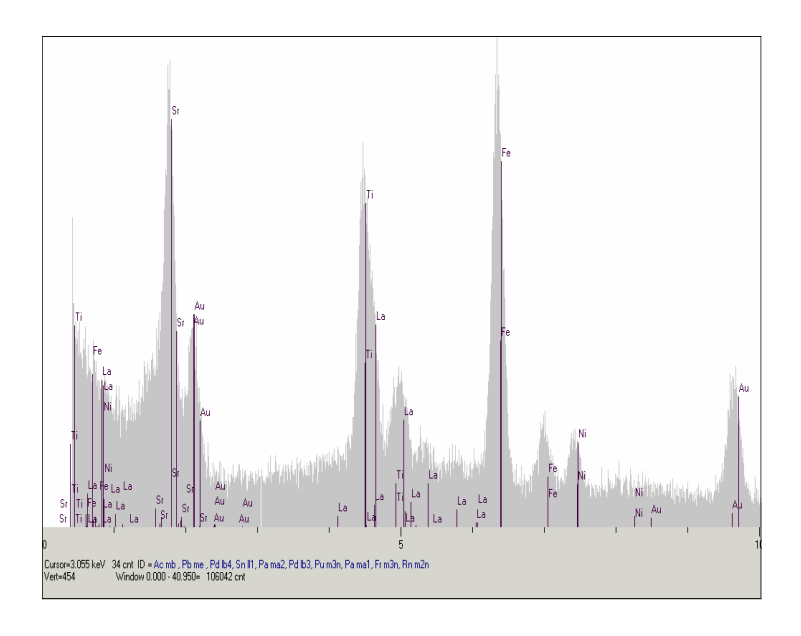


Figure 96. EDX analysis spectrum of LSFT membrane

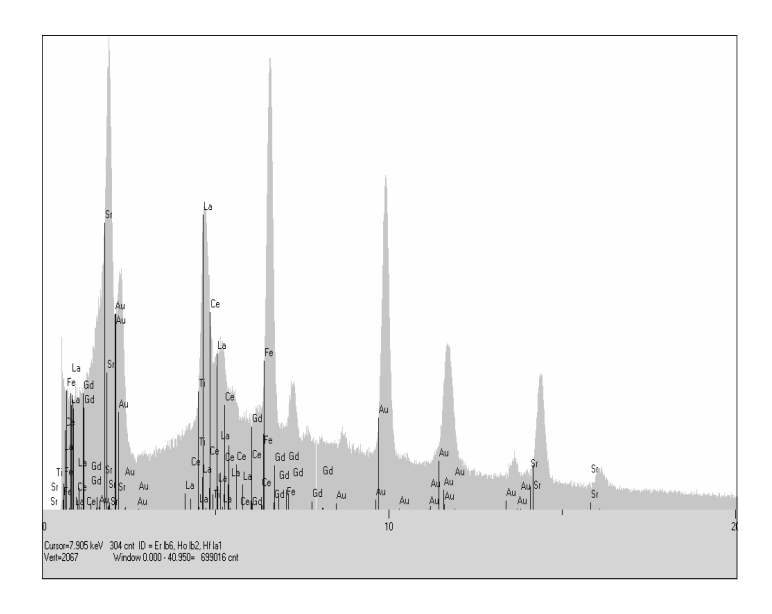


Figure 97. EDX analysis spectrum of dual phase membrane

## 2.4.4.5.2 X-ray diffraction analysis of the membranes

The x-ray diffraction analyses were carried out for the LSFT and dual phase membranes to identify the crystal systems and to conduct phase analysis. The membranes were crushed into fine powders and analyses were done at a very slow scan rate. The x-ray diffraction analyses of the LSFT and dual phase membranes were performed using the "as received" and heat treated samples in a powder form. The refinement of the XRD data was carried out and the results are summarized in Table 14. The x-ray diffraction patterns are shown in Figure 98. The crystal structure was found to be orthorhombic. Interestingly, samples tested under environment (N<sub>2</sub>) showed some shift in the higher angles (Figure 98). The x-ray diffraction analysis of the as received and heat treated dual phase membranes are shown in Figure 99. The crystalline phases are identified and marked. An orthorhombic LSFT and cubic CGO are the two identified crystalline phases observed. A clear shift in the peaks of the N<sub>2</sub> exposed samples is observed. This suggests phase instability and a possible decomposition of the parent structure upon exposure to the N<sub>2</sub> environment and high temperature. However, the possibility of the structural changes needs to be examined. Hence, complete thermal analysis and refinement of the XRD data will be helpful to understand the structural changes associated in the samples exposed to the N<sub>2</sub> environment.

Table 14. Lattice parameters obtained from refinement of XRD data

Condition	Crystal	a	b	c	α=β=γ
	Structure				
LSFT-as	Orthorhombic	3.92	3.908	3.92	90
received					
LSFT- exposed	Orthorhombic	3.92	3.908	3.92	90
to Air, 1000°C					
LSFT- exposed	Orthorhombic	3.92	3.908	3.92	90
to N <sub>2</sub> , 1000°C					

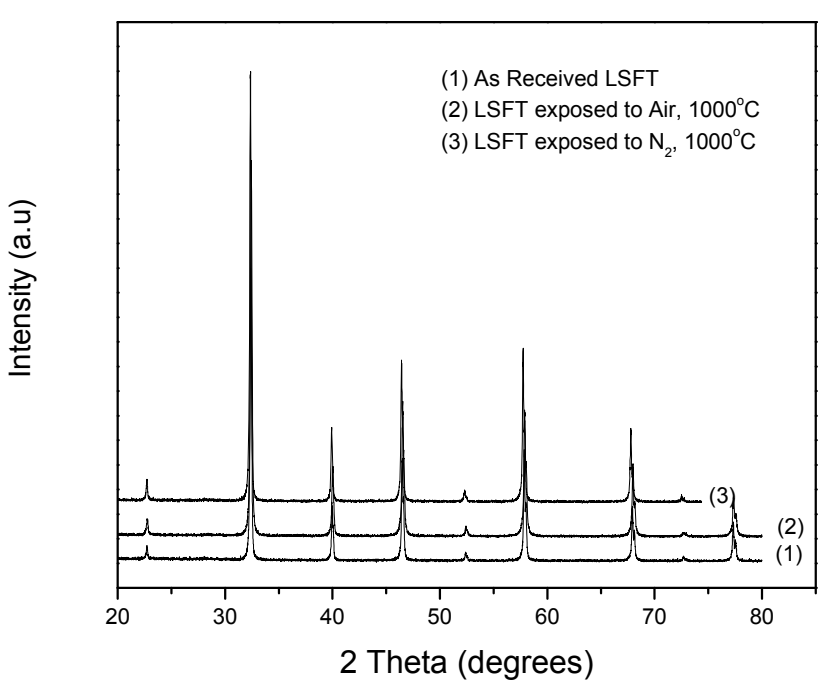


Figure 98. XRD plots of the LSFT membranes.

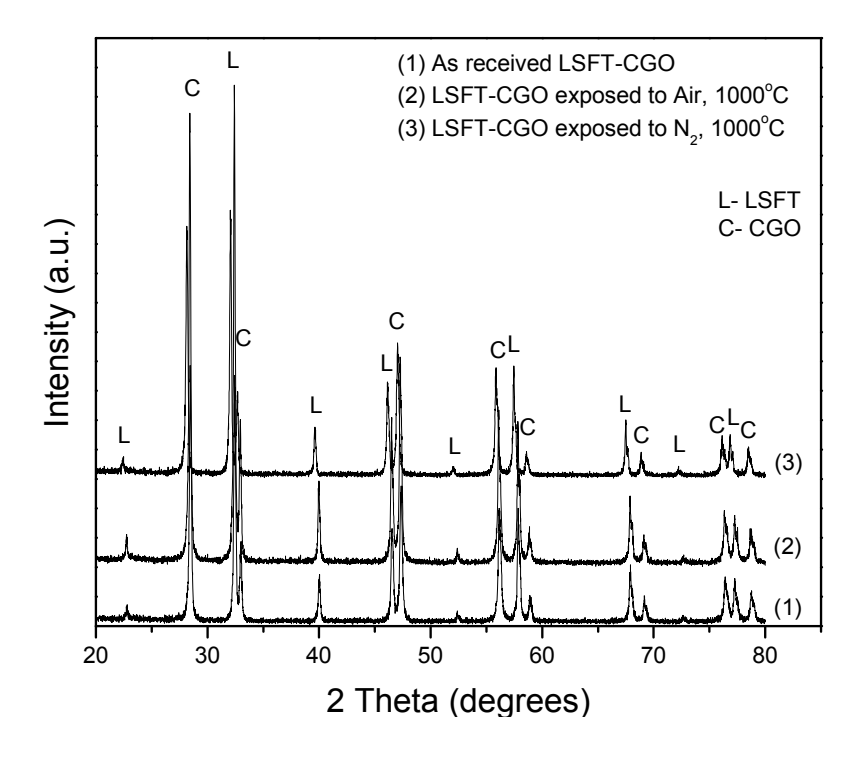


Figure 99. XRD plots of the dual phase membranes.

## 2.4.4.6 Hardness and Fracture Toughness

#### 2.4.4.6.1 Hardness of the LSFT and dual phase membranes

The polished samples of the membranes were used for hardness measurements. A Vickers indenter was used for characterization and the indentations were made at various loads for 10 sec. The hardness was measured on the surface of the membranes using loads at 300g, 500g and 1000g respectively. The cross section of the samples were also subjected to the hardness analysis. A load of 500g was applied at various places along the cross section to study the hardness profile in the cross section. It is interesting to note the scatter in the hardness values reduces with increasing load. The indentation that formed at 300g load was very small and shallow. Hence it cannot represent the hardness of the membrane in which the pores are distributed evenly. At 1000g load, the indentation area is sufficiently large enough to contain both the dense regions and the pores and therefore the scatter in the hardness values is relatively less.

A maximum hardness value of 6.0 GPa for LSFT (figure 100) and 6.2 GPa (figure 101) for dual phase membrane at 500 gm load respectively was observed. In LSFT, the scatter in hardness values decreased with increasing load which confirms the uniform distribution of pores in the membrane. In the dual phase membrane this behavior, however, was not observed. In comparison, the hardness at the cross section in both the materials was slightly lower than that at the surface. Also, there was no specific trend was noted in hardness profile along the cross section.

In order to understand the mechanical properties of the membranes it is essential to know the microstructure and chemical composition of membranes. The mechanical properties of the membranes are greatly dependent on grain size, grain size distribution and the kind of flaws that are present. While the fracture toughness of the membrane is influenced by the microstructure of the membrane, the flexural strength is controlled by the critical flaw size in the membrane.

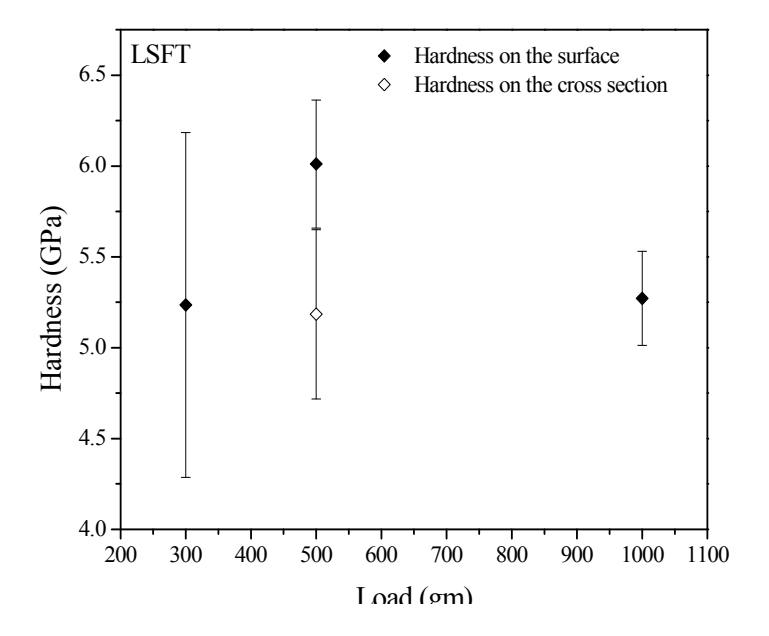


Figure 100. Hardness of the LSFT membrane

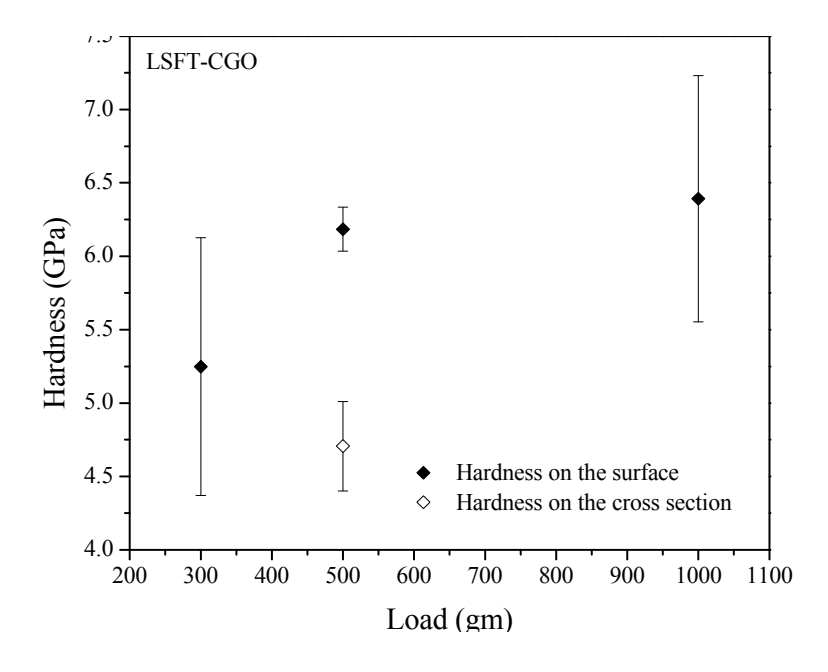


Figure 101. Hardness of the dual phase membrane.

Fracture toughness is defined as the resistance of a material to arrest an advancing crack. Fracture toughness generally depends on temperature, environment, loading rate, the composition of the material and its microstructure.

The LSFT and dual phase membranes were cut and ground down to 600 grade SiC paper prior to analysis. Indentations were made using loads starting from 0.98N to 9.8N to initiate cracks. The duration of indentation was for 10 sec under all loads. The cracks were generated only at the load of 9.8N, the maximum achievable load the machine could generate. No observable cracks were produced at lower loads. The indentations were immediately analyzed using SEM instead of optical microscope since measuring the crack lengths using the latter was difficult. The development of Vicker's indentation cracks is illustrated in Figure 102. It can be seen that below the Vickers pyramid a deformation zone develops.

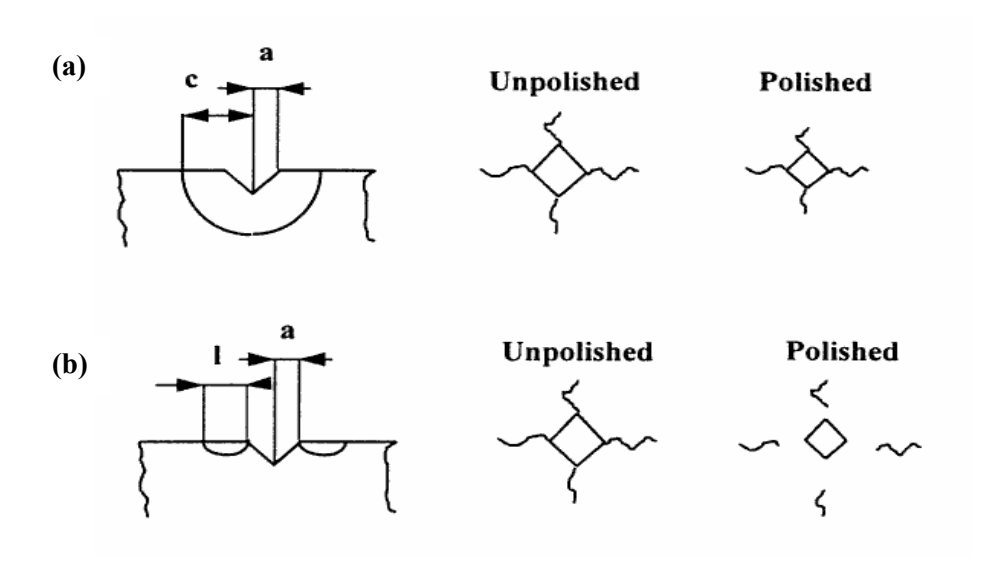


Figure 102. (a) Median and (b) Palmqvist crack systems induced by Vicker indentation.

During loading and unloading two perpendicular cracks are initiated starting at the deepest location of the deformation zone which propagate to the specimen surface. The final crack has nearly a half penny shape (median cracks). The crack length at the surface is 'c' (from the center of the indentation diagonal) and the length of the indentation diagonal is 2a. For some materials

(with relatively high toughness), a different crack system develops. They exhibit radial shallow cracks which occur directly below the surface. These cracks are called Palmqvist cracks. The length of the Palmqvist cracks '1' is measured from the ends of the impression diagonals (Figure 102-b). Therefore, the crack length, c, can be written as (a+1). The hardness of the membranes was calculated from the diagonal length (equation 35) and the Young's modulus of the materials was assumed to be 123GPa, where as, Ø is the constraint factor which is approximately 3.0 for ceramics. Figure 103 shows the impression of the indentation with cracks emanating from the corners.

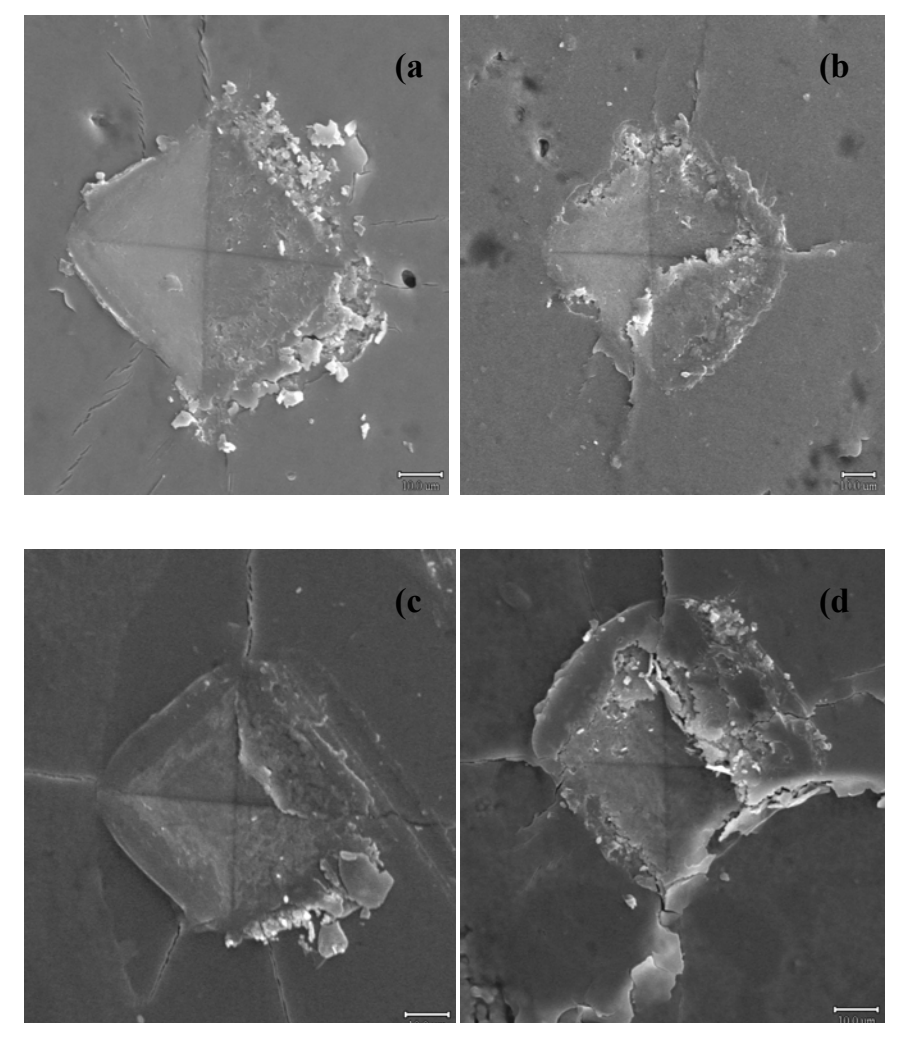


Figure 103. Vicker's indentations in (a-b) LSFT membrane and (c-d) in dual phase membrane. Note in the LSFT-CGO the crack patterns are mainly median cracks. In dual phase the Palmqvist cracks are also seen (in Figure 103-a). In Figure 103-c the indentation is in the dense region where as in Figure 103-d the indentation is on porous region.

Crack lengths were measured and the l/a and c/a values were calculated to verify the crack types. Appropriate formulas were used to calculate fracture toughness and the results were compared. Niihara et al. (1982)[1] equations for the Palmqvist cracks (0.25  $\leq$  1/a  $\leq$  2.5) and for the median cracks (c/a  $\geq$  2.5) are given in equations 35 and 36 respectively.

where,

 $K_{IC}$  is the Mode I critical stress intensity factor (MPa.m  $^{1/2}$ )

Ø is the constraint factor ( $\approx 3.0$ )

H is the Vickers hardness (GPa)

E is the Young's modulus (GPa)

a is the half diagonal of the Vicker's indent (m)

c is the radius of the surface crack (median) (m) and

1 is the crack length (Palmqvist) (m)

For comparison the  $K_{IC}$  values were calculated by using the following formula suggested by Evans and Charles [2] which does not include the elastic modulus of the membranes.

$$K_{IC} = 0.16 \text{ H}_{v} \text{ a}^{\frac{1}{2}} (\text{c/a})^{-3/2}$$

The fracture toughness values of the LSFT and dual phase membranes are tabulated in Table 15 and Table 16 respectively. In the LSFT membrane, the cracks emanating from the indentation

impression were mainly Palmqvist type. Hence, the fracture toughness values calculated using the equation 2.1 are relatively higher than those calculated using the two other methods. The difference in fracture toughness values calculated from equations 2.1 and 2.2 is not significant. In the dual phase membrane, the cracks are predominantly median ( $c/a \ge 2.5$ ) type. In the dual phase membrane, the crack length is controlled by the microstructure. In Figure 103-c, the indentation is made on a dense region as also in Fig 104. In figure 103-b, the indentation has fallen on a porous region. The heterogeneity of the microstructure causes a scatter in the hardness values (Table 16). Initiation and propagation of cracks are also significantly affected by this microstructural inhomogeneity (Figure 104).

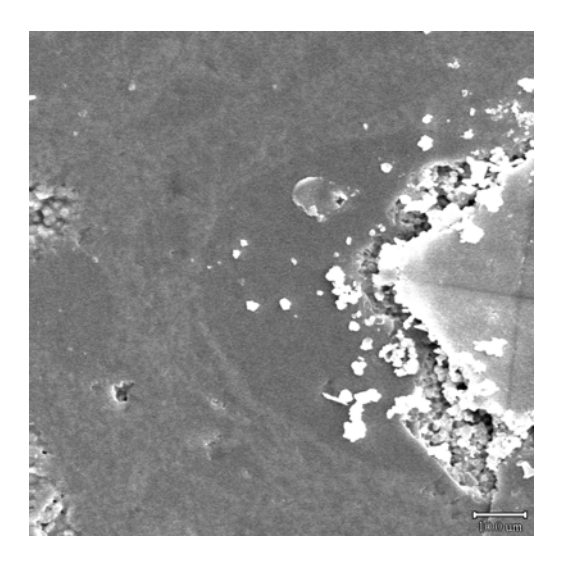


Figure 104. Influence of microstructural heterogeneities on initiation and propagation of cracks. The indentation is made on the dense region in the dual phase microstructure. While the crack has not formed in the dense region, a crack has emanated from the diagonal that is closer to the porous region.

The fracture toughness of the LSFT-CGO is slightly inferior to the LSFT. The factors influencing fracture toughness reduction in the dual phase material can be analyzed by studying the crack propagation behavior. In general, the fracture toughness of the LSFT membranes was low and slightly higher than the window glass. In the case of LSFT membrane, the cracks were mainly Palmqvist type. But the cracks that were generated in the dual phase membrane were Median type. The fracture toughness values of dual phase membrane that were calculated from the crack length also support the Median type of cracks. The c/a ratio of the cracks was  $\geq 2.5$  in the LSFT-CGO membrane and the  $K_{IC}$  values were inferior to the  $K_{IC}$  values of LSFT membrane. The  $K_{IC}$  values of both the membranes calculated without using the Young's modulus were significantly inferior to the rest of the values.

Table 15. Fracture toughness of the LSFT membrane

Crack Length				a (m)	H <sub>v</sub>	K <sub>IC</sub> <sup>1</sup>	K <sub>IC</sub> <sup>2</sup>	K <sub>IC</sub> <sup>3</sup>	
L1	L2	L3	L4	L (m)	E-5	(GPa)	(MPa.m <sup>1/2</sup> )	(MPa.m <sup>1/2</sup> )	$(MPa.m^{1/2})$
(µm)	(µm)	(µm)	(µm)	E-5		(31)	(1/11 )	(1/11 )	(1/11 )
39.3	42.76	73.45	31.94	4.68625	2.881	5.47	1.45	1.59	1.1
63.18		32.02	45.46	4.68867	2.54525	7.01	1.48	1.55	1.19
33.78	31.96	50.66	38.02	3.8605	3.05925	4.85	1.58	1.92	1.26
35.96	40.88	40.23	32.1	3.72925	3.0595	4.85	1.6	1.97	1.3
41.01	56.25	34.16		4.38067	2.817	5.72	1.5	1.69	1.19
41.36	67.43		39.71	4.95	2.8545	5.57	1.41	1.52	1.05
48.37	63.42	36.46		4.94167	2.86475	5.53	1.41	1.52	1.05
66.78	65.39	47.62	34.69	5.362	3.1115	4.69	1.33	1.44	0.93
44.25	56.88	44.6	26.58	4.307	2.78525	5.85	1.52	1.72	1.22
37.13	57.82	37.67	44.41	4.425	3.048	4.89	1.47	1.7	1.12
<b>69.7</b>	59.34	53.76		6.09333	2.90175	5.39	1.26	1.24	0.85
59.14	69.12	45.28	43.22	5.419	3.0835	4.77	1.33	1.42	0.93
		50.48		5.048	3.1827	4.48	1.37	1.53	0.97
54.69	48.44	47.26	36.25	4.666	2.939	5.26	1.46	1.61	1.1
36.77	28.3	50.01	46.56	4.041	2.8202	5.71	1.56	1.82	1.28
43.71	55.68			4.969	3.0935	4.74	1.39	1.54	1.0
41.01	46.21	29.35	49.15	4.143	2.8707	5.51	1.54	1.79	1.24
52.07	56.17	47.11	42.11	4.936	2.78	5.87	1.42	1.51	1.07

<sup>&</sup>lt;sup>1.</sup> Equation 35 <sup>2.</sup> Equation 36 <sup>3</sup>.Equation 37

Table 16. Fracture toughness of the Dual Phase LSFT-CGO membrane

$ \begin{array}{c ccccccccccccccccccccccccccccccccccc$	(GPa)  175 6.32  575 5.9  025 6.67  55 6.69  4 6.04  475 5.86  85 8.17	K <sub>IC</sub> <sup>1</sup> (MPa.m <sup>1/2</sup> )  1.22 1.46 1.35 1.48	K <sub>IC</sub> <sup>2</sup> (MPa.m <sup>1/2</sup> )  1.07 1.53 1.36 1.47	0.78 1.14 0.98 1.19
$ \begin{array}{c ccccccccccccccccccccccccccccccccccc$	175 6.32 575 5.9 025 6.67 55 6.69 4 6.04 475 5.86 85 8.17	1.22  1.46 1.35	1.07  1.53 1.36	0.78   1.14 0.98
2.77 2.61 46.43 42.29 48.68 54.37 4.79425 2.60 48.52 61.87 53.18 55.45 5.4755 2.74 2.78 43.16 43.75 43.42 62.71 4.826 2.35 64.47 58.06 45.21 71.92 5.9915 2.38 72.96 93.85 40.73 57.07 6.61525 2.18 89.68- 58.16 54.5 45.58 5.27467 2.37 58.77 101.03 50.92 42.44 6.329 2.45	575   5.9 025   6.67 55   6.69 4   6.04 475   5.86 85   8.17	 1.46 1.35	 1.53 1.36	  1.14 0.98
2.61           46.43         42.29         48.68         54.37         4.79425         2.60           48.52         61.87         53.18         55.45         5.4755         2.74              2.78           43.16         43.75         43.42         62.71         4.826         2.35           64.47         58.06         45.21         71.92         5.9915         2.38           72.96         93.85         40.73         57.07         6.61525         2.18           89.68-         58.16         54.5         45.58         5.27467         2.37           58.77         101.03         50.92         42.44         6.329         2.45	025   6.67 55   6.69 4   6.04 475   5.86 85   8.17	 1.46 1.35 	1.53 1.36	 1.14 0.98 
46.43     42.29     48.68     54.37     4.79425     2.60       48.52     61.87     53.18     55.45     5.4755     2.74          2.78       43.16     43.75     43.42     62.71     4.826     2.35       64.47     58.06     45.21     71.92     5.9915     2.38       72.96     93.85     40.73     57.07     6.61525     2.18       89.68-     58.16     54.5     45.58     5.27467     2.37       58.77     101.03     50.92     42.44     6.329     2.45	55 6.69 4 6.04 475 5.86 85 8.17	1.46 1.35	1.53 1.36	1.14 0.98 
48.52     61.87     53.18     55.45     5.4755     2.74           2.78       43.16     43.75     43.42     62.71     4.826     2.35       64.47     58.06     45.21     71.92     5.9915     2.38       72.96     93.85     40.73     57.07     6.61525     2.18       89.68-     58.16     54.5     45.58     5.27467     2.37       58.77     101.03     50.92     42.44     6.329     2.45	4 6.04 475 5.86 85 8.17	1.35	1.36	0.98
2.78       43.16     43.75     43.42     62.71     4.826     2.35       64.47     58.06     45.21     71.92     5.9915     2.38       72.96     93.85     40.73     57.07     6.61525     2.18       89.68-     58.16     54.5     45.58     5.27467     2.37       58.77     101.03     50.92     42.44     6.329     2.45	475   5.86 85   8.17		-	
43.16     43.75     43.42     62.71     4.826     2.35       64.47     58.06     45.21     71.92     5.9915     2.38       72.96     93.85     40.73     57.07     6.61525     2.18       89.68-     58.16     54.5     45.58     5.27467     2.37       58.77     101.03     50.92     42.44     6.329     2.45	85 8.17			
64.47     58.06     45.21     71.92     5.9915     2.38       72.96     93.85     40.73     57.07     6.61525     2.18       89.68-     58.16     54.5     45.58     5.27467     2.37       58.77     101.03     50.92     42.44     6.329     2.45		1.48	1.47	1.19
72.96     93.85     40.73     57.07     6.61525     2.18       89.68-     58.16     54.5     45.58     5.27467     2.37       58.77     101.03     50.92     42.44     6.329     2.45				1.1/
89.68-     58.16     54.5     45.58     5.27467     2.37       58.77     101.03     50.92     42.44     6.329     2.45	1 8.01	1.33	1.18	0.95
58.77   101.03   50.92   42.44   6.329   2.45	6 9.50	1.29	1.02	0.88
	2 8.07	1.42	1.35	1.09
(1.0) 52.54 72.27 01.00 (.00277 2.42	42 7.54	1.29	1.13	0.88
61.96   53.54   72.37   91.88   6.99375   2.43	6 7.65	1.23	1.01	0.79
64.88   72.16   65.09     6.73767   2.83	42 5.65	1.21	1.11	0.78
69.34   61.54   48.02   50.18   5.727   2.51	95 7.16	1.35	1.26	0.97
60.84 6.084 2.57	6.88	1.30	1.19	0.9
90.07   75.56   53.79   50.35   6.74425   2.34	8.3	1.26	1.03	0.84
67.77   63.27     70.79   6.72767   2.45	675 7.53	1.25	1.05	0.83

<sup>1.</sup> Equation 35

## 5.4.6.2 Crack Propagation behavior

Enhancing the toughness of non-transforming ceramics (other than stabilized zirconias) depends primarily on the events which occur beyond rather than at or ahead of the advancing crack. It has been acknowledged that several toughening events may take place simultaneously and that the net effect is not necessarily a simple liner combination of the individual effects. In the present investigation, in order to understand the strengthening mechanisms involved in the non-transforming La based ceramic composites, cracks were generated using Vicker's indenter. Even though the crack evolutions that are shown in the figures are representations of LSFT and dual phase membranes, they need not be considered as characteristic crack patterns of the respective membrane or loading conditions since the cracks could not be exactly reproduced.

<sup>2.</sup> Equation 36

<sup>3.</sup> Equation 37

#### **Crack propagation in the LSFT membrane:**

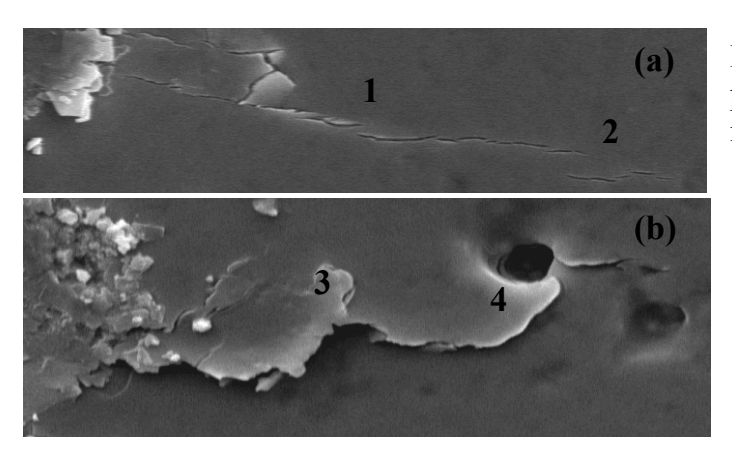


Figure 105. Crack propagation in the LSFT membrane

- (a) grain bridging
- (b) crack deflection by boundaries and pores

The predominant toughening mechanisms are grain bridging, crack branching and crack deflection. Figure 105 shows apparently isolated segments at site 1 and 2 which get connected together in a common crack interface. In site 3, it can be noted that the lower crack segment enclosing the bridging grain has over-linked up with a crack branch to lead a rupture of the bridging grain. Another crack front that advanced further was deflected by a pore and eventually got arrested (at site 4).

Figure 106 (a and b) shows the several discontinuous (segmented) crack traces on the membrane surface. However the crack segments connect beneath the surface into a common, primary crack interface. In the discontinuous crack, the bridging ligaments (at site 1) exert closing forces which reduce the stress intensity at the crack tip and hence additional stress is needed to break the interfacial bonding. Site 2 (in Figure 106.b) shows a particularly large bridging behind the tip of an extended crack. It is evident that this bridging has consumed most of the crack energy and thus stopped the crack growth. The final rupture of the bridging grain can be seen at site 3.

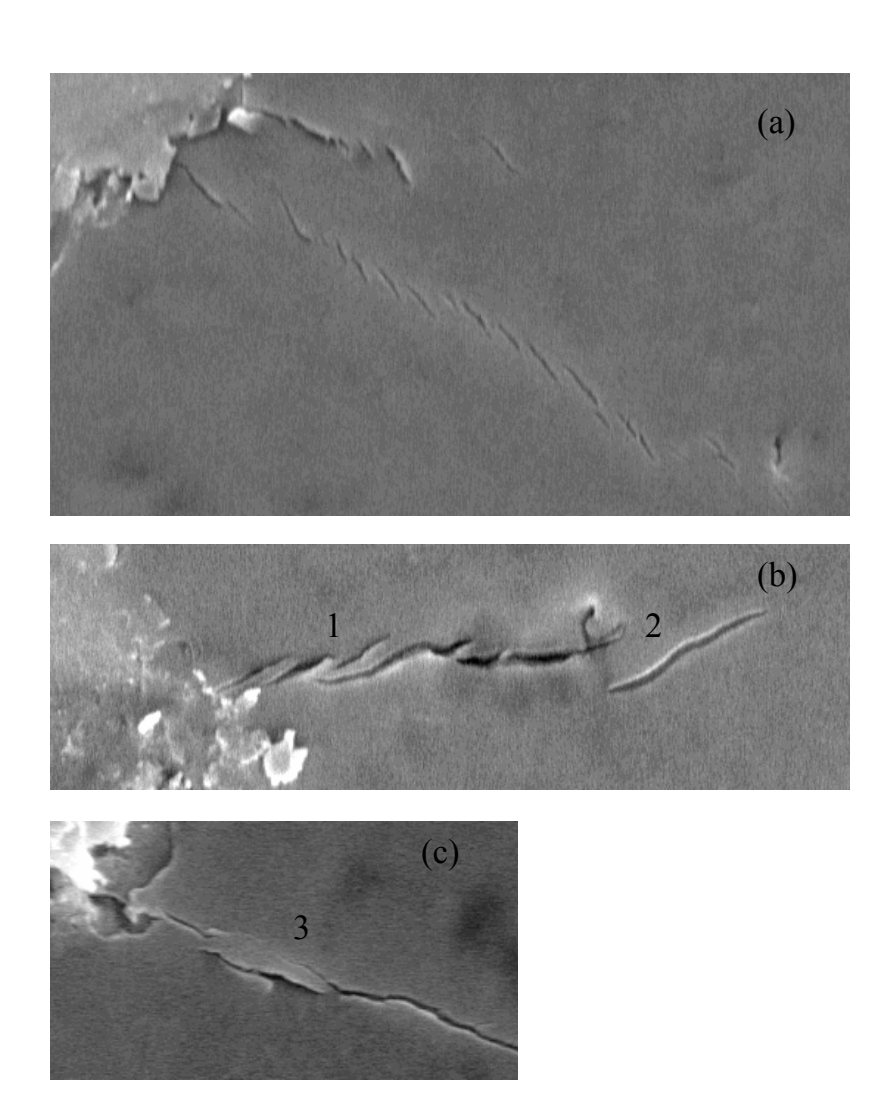


Figure 106. Discontinuous crack and rupture of bridging grain. Note the extensive grain bridging all along the crack length (a). A closer observation of the other crack reveals the effect of bridging ligaments on closing the crack propagation (b). Final rupture of the grain (c)

Figure 107 shows the frictional interlocking of grains along the fracture causes surface tractions. Each source of traction acts to shield the crack tip from the applied stress, by expending the energy needed for crack propagation.

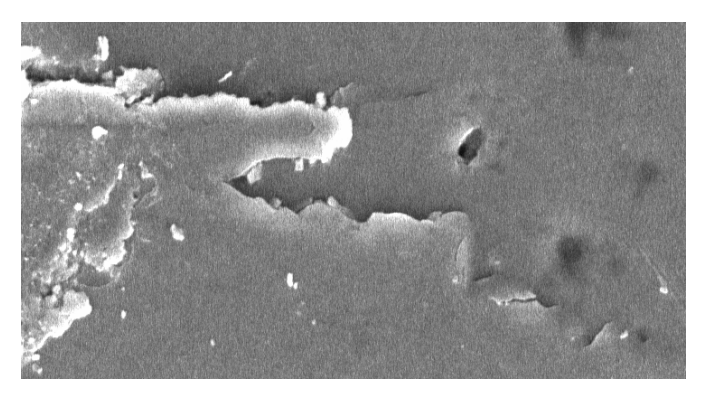


Figure 107. Surface traction in an advancing crack caused by frictional interlocking of grains

This frictional interlocking tries to 'trap' the growing crack. Hence, more energy is needed to advance the crack front.

#### **2.4.4.6.2** Crack propagation in the dual phase membrane:

All the common toughening mechanisms that are involved in the single phase membrane are also active in the dual phase. Furthermore, in the dual phase membrane, the inherent microstructural feature is due to the distribution of discrete dense regions in the continuous porous region. Crack deflection is an important toughening mechanism which contributes to approximately  $\approx 40\%$  of fracture resistance in the composite. The crack is likely to be deflected at the interface when it approaches a dense region or cluster.



Figure 108. Crack bridging by dense region in the dual phase membrane.

Figure 108 shows the crack bridging caused by a dense region. The crack appears very weak after the bridging event since it has traveled a long distance along the dense region's interface.

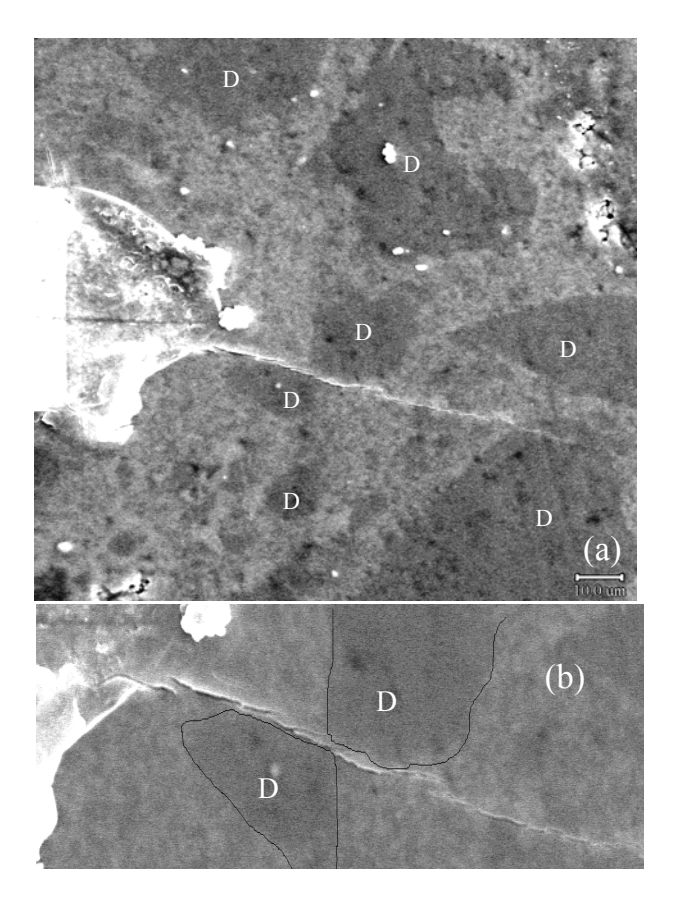


Figure 109. Crack propagation behavior in the dual phase membrane. Crack deflection by the dense regions.

Figure 109 shows a typical crack propagation behavior in the dual phase membrane. The crack emanating from the indentation was deflected by a dense aggregate which then took the path along the boundary of the aggregate and exactly passed between two dense regions. Normally the interfacial region around a dense region or an aggregate will be weak due to the thermal expansion mismatches or differential shrinkage of the constituent phases. Hence the crack propagation will be always favored along the interface. In the LSFT-CGO membrane, the crack has continued its propagation in the less dense region rather than proceeding along the boundaries of the dense region. This indicates that the discontinuous dense regions and the surrounding porous region have a strong interface.

Figure 110 shows crack branching and interlocking of grains. The crack experiences-bridging (site 1) and eventually halts. The growth of the other branch of the crack has been arrested by a strong frictional interlocking mechanism (site 2) that has taken place behind the crack tip.

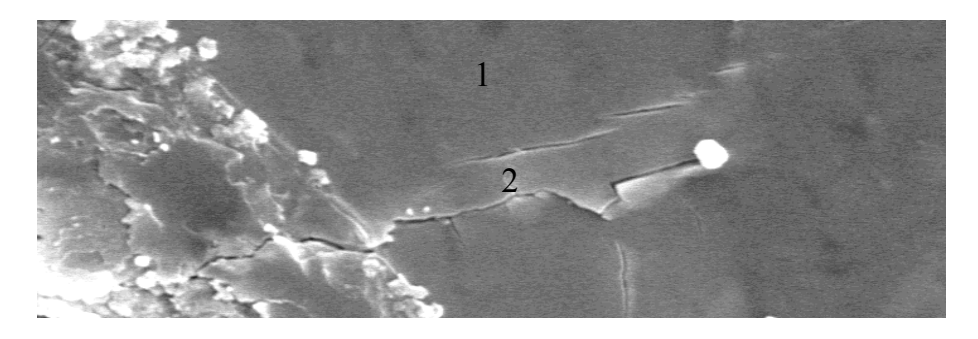


Figure 110. Crack branching and frictional interlocking of grains

The fracture toughness of the LSFT and LSFT-CGO (dual phase) membranes at room temperature was already studied (Table 15,16). The membranes that were exposed to high temperatures at inert and reactive atmospheres undergo many structural changes which in turn affect the mechanical properties to a greater extent. The membranes (LSFT and Dual phase) were heat treated at  $1000^{\circ}$ C in air and  $N_2$  atmosphere and the hardness and fracture toughness of the membranes were studied after the heat treatment. The indentation method was used to determine the fracture toughness.

Closer observation of the load-Vicker's hardness curves suggests a transition where hardness changes from being load dependent to being load independent. At lower loads, the indentation work is absorbed by volume deformation and by fracture surface formation processes. As the load increases, the indentation becomes larger and more energy is consumed in both volume deformation and fracture surface generation process. Numerous cracks of various types like median, radial and lateral cracks are formed during the indentation process depending upon indenter geometry, load, elasticity and microstructural behavior. In a brittle material like LSFT, after some critical load, the fracture surface generation process consumes more energy and the volume deformation process is left unchanged. Hence the hardness remains almost constant after the critical load. The dependence of L/a of LSFT heat treated in air and N<sub>2</sub> atmosphere on indentation load is shown in Figure 111.

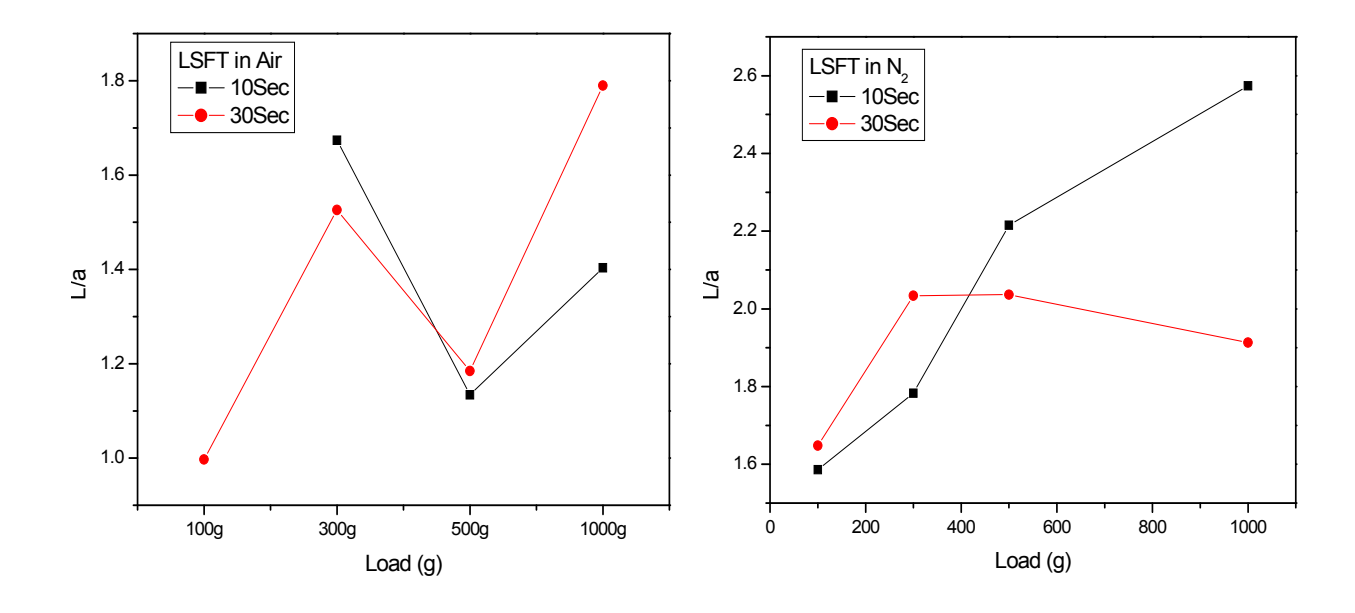


Figure 111. Dependence of L/a of LSFT on indentation load

The membranes treated in air show no meaningful change with increasing indentation load but the L/a of the  $N_2$  treated membrane increases with increasing indentation load. Moreover the L/a values for the  $N_2$  treated samples are significantly higher than the air treated samples. Hence one may conclude that the treatment of LSFT in  $N_2$  significantly alters the microstructure of the membranes. The structural and microstructural changes associated with the heat treatment were analyzed using x-ray diffraction and SEM. In general, the fracture toughness values of the membranes increase with increasing indentation load. The fracture toughness of the LSFT heat treated in air reaches a maximum value and remains mostly unchanged. Also the fracture toughness value is higher than that of  $N_2$  treated sample. Even though the increment in the fracture toughness is consistence with the increasing load, the fracture toughness of the membrane is reduced in  $N_2$  atmosphere.

The dependence of L/a of dual phase membrane treated in air and  $N_2$  on the indentation load is shown in Figure 112. The effect of loading time on the development of cracks is very much significant in the air treated samples, where as no such influence is observed in the  $N_2$  treated samples. The L/a increases with increasing load for the samples heat treated in  $N_2$  atmosphere.

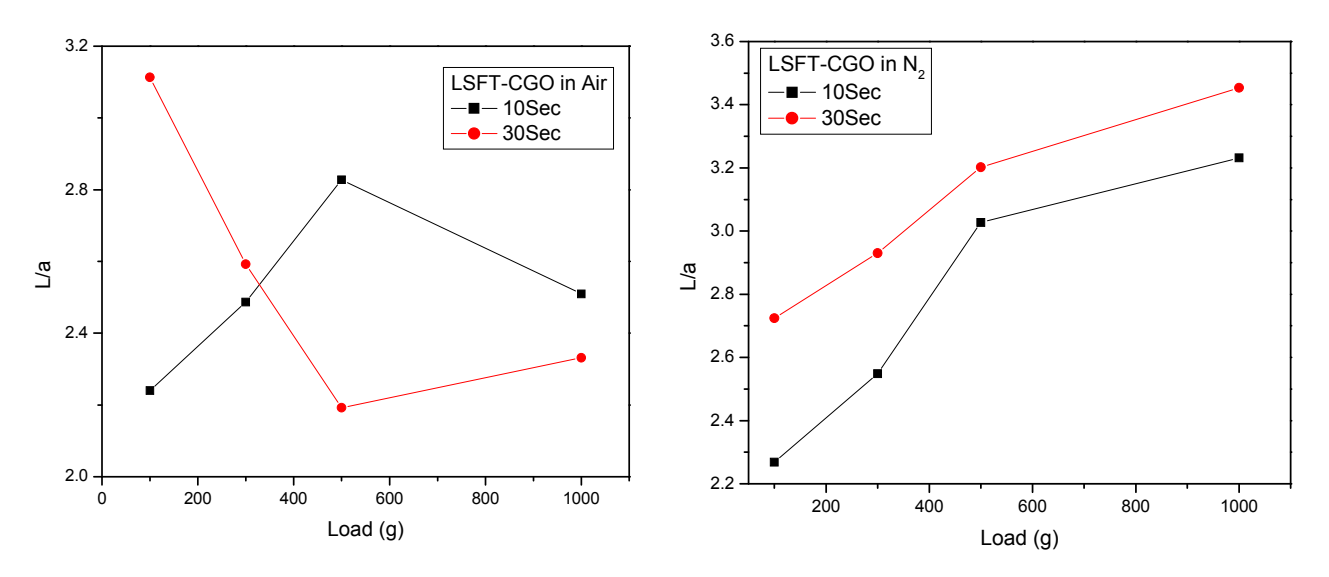


Figure 112. Dependence of L/a of dual phase membrane on indentation load.

## 2.4.4.6.3 Fracture Toughness of LSFT and dual phase membranes

The fracture toughness values of the membranes are shown in Figure 113. Two important observations can be made from this figure.

- 1. In both (LSFT and dual phase) the membranes, the fracture toughness value increases with increasing load. This trend is not affected by the heat treatment environment of the specimens.
- 2. The fracture toughness value of the LSFT exposed to N<sub>2</sub> is less than that exposed to air at 1000°C. This behavior can be observed under all test loads. Also, it is evident that the fracture toughness of the "as received" LSFT exposed to air at 1000°C does not change at the maximum test load.

The change in the fracture behavior of the membranes due to the heat treatment in  $N_2$  atmosphere is mainly due to the changes occurring in the microstructure or in the crystal structure. The change in the hardness (Figure 114) of the LSFT membranes heat treated in air and  $N_2$  environment under the test loads indicate that the samples exposed to  $N_2$  favor an extensive crack growth.

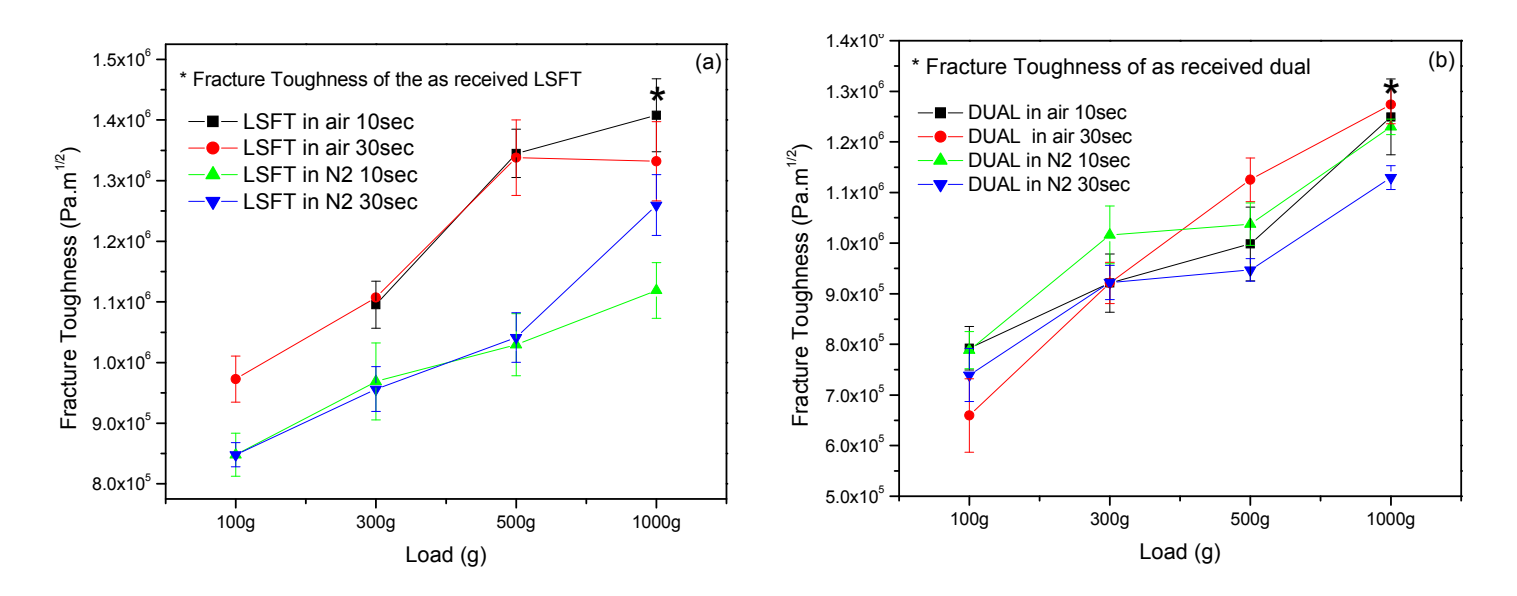
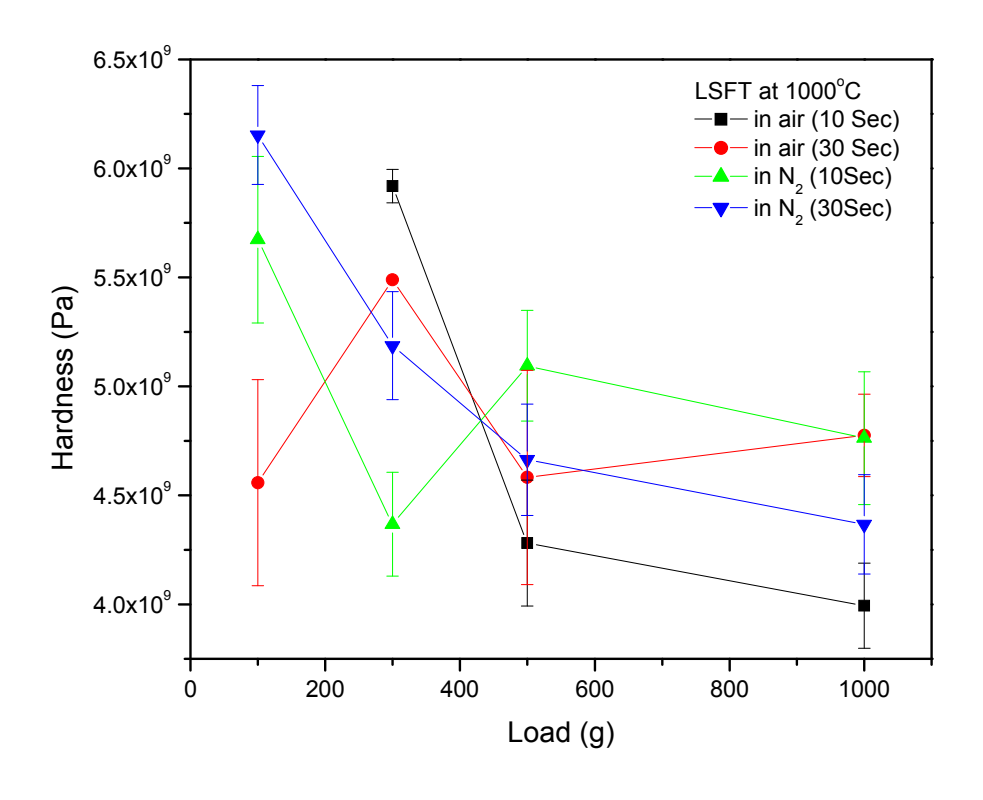


Figure 113. Fracture toughness of the LSFT and dual phase membranes

The L/a of the  $N_2$  exposed samples are higher under most of the test loads than those exposed to air. The increase in L/a means the crack generated at a given load is longer as the hardness values are slightly higher than the samples exposed to air.

The structural changes occurring in the samples exposed to the  $N_2$  atmosphere might altered the elastic/plastic properties of the membrane. The energy imparted during the indentation process is mostly used for the generation new surfaces rather than the plastic deformation of the membrane. In order to understand the fracture behavior of the heat treated samples, the fractured surfaces of the membranes were analyzed using SEM.

The SEM micrographs of the as received LSFT are shown in the Figure 115. The fracture is predominantly transgranular in nature and the pores are distributed evenly along the fractured plane. This shows that the crack growth has not occurred through the grain boundaries which indicates that the grain boundaries have no weaker bonds or interactions.



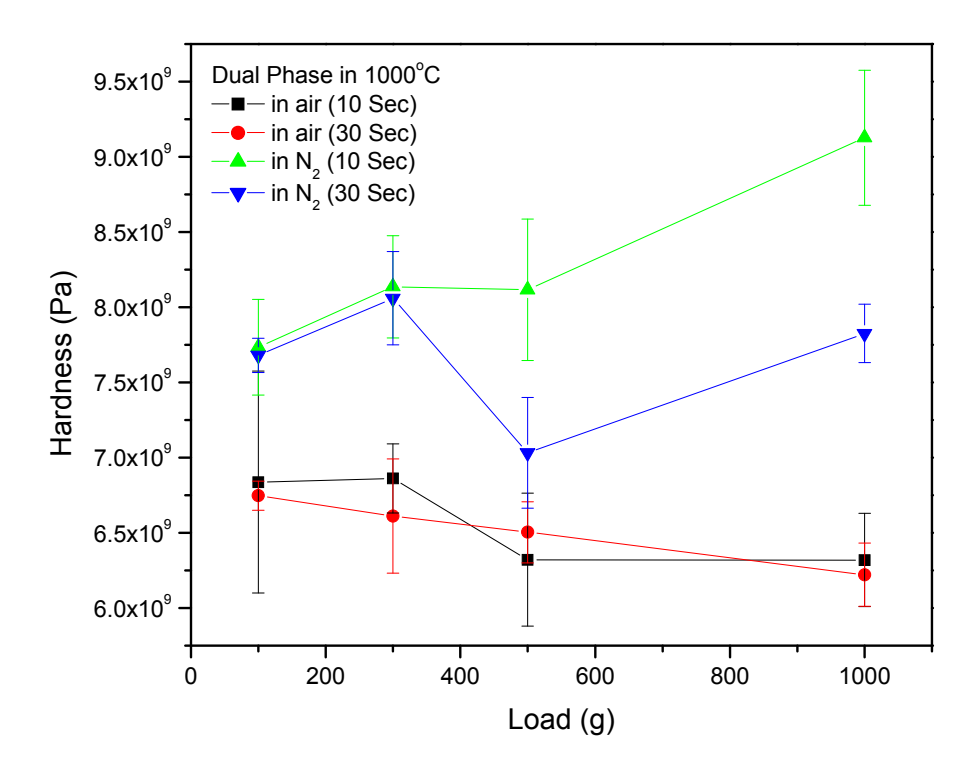
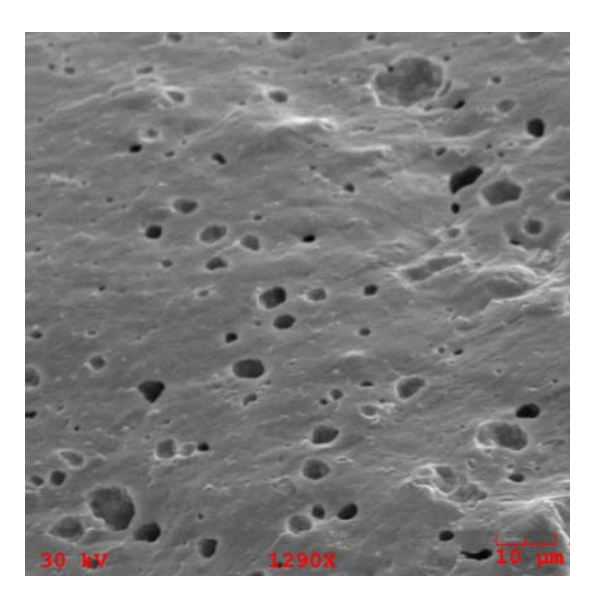


Figure 114. Hardness of the LSFT and dual phase membranes



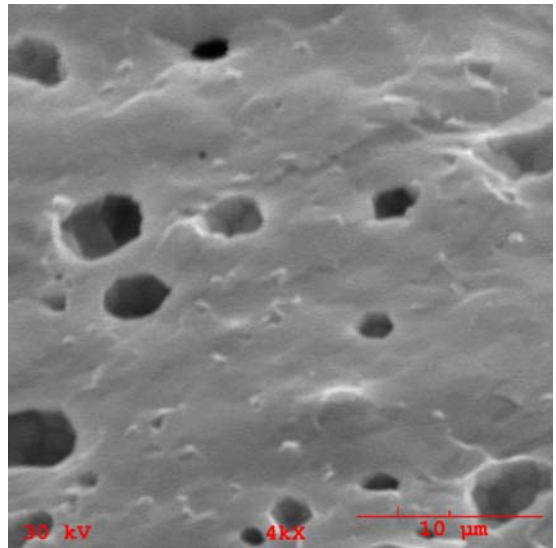


Figure 115. SEM micrographs of the as received LSFT. The fracture surface shows a transgranular fracture behavior.

The fracture surfaces of the LSFT exposed to air show a transgranular fracture and also a tendency for an intergranular fracture in some locations. This may be due to the weakening of the grain boundaries as a result of the high temperature treatment in air. The effect of  $N_2$  on the fracture behavior is clearly intergranular without a single trace of transgranular fracture. This transformation in the fracture behavior is significant. Closer observation of the fracture surface shows large grain pull outs and the absence of any grain boundary precipitates. There is no significant grain growth in the  $N_2$  exposed LSFT. This intergranular fracture behavior is mainly facilitated by structural changes that occurred on exposure to the  $N_2$  atmosphere.

## 2.4.4.7 Flexural strength and Fractography:

#### **Experimental:**

The LSFT-CGO specimens were cut from the as sintered bars and used for the evaluation of Mechanical Properties after polishing. The figure 116 shows the photograph of the as-sintered and test specimen. Test specimens of dimensions (3x4x48 mm) were cut from the bulk, as-sintered bars provided by Praxair. The tests were done in-situ in an autoclave mounted on a servo-electric loading frame. Loading was done in an in-house designed 4-point flexure with an outer span of 38.1 mm and inner span of 19.05 mm (ASTM-B).



Figure 116. Photographs of as-sintered and test specimens.

The experiments were carried out in room temperature and at  $1000^{\circ}$ C in inert (N<sub>2</sub>) atmosphere. The specimens were polished in all 4 sides and the tensile side was polished using diamond paste of 1 µm prior to the test. The edges of the specimens were also trimmed. In the inert atmosphere, the specimen was loaded in the fixture and heated to  $1000^{\circ}$ C for 1 hr prior to application of any load. The furnace power was completely shut off after the fracture of the specimen and allowed to cool. A typical flexural strength test usually have a heating period of 2 hrs, dwelling of 1 hr, loading rate as specified and a cool down period of  $1000-700^{\circ}$ C in 60 min and a  $700-200^{\circ}$ C in 2 hrs for a sum total of 6-7 hrs.

For testing in reducing conditions, the autoclave chamber was flushed with Ultra High Purity (UHP) N2 till a steady state was established and a positive chamber pressure of 25 PSI was established. The chamber temperature was raised at a rate of 10°C/ min to the final temperature of 1000°C. The specimens were soaked for a period of 1 hr at the reducing conditions (log pO2 = -4) prior to application of any load.

The effect of strain rate on the flexural strength of the LSFT-CGO test specimens was studied. Three strain rates 6, 60 and 600  $\mu$ m/ min were chosen for this study. The samples were mounted in 4-point bend test fixture and the load was applied with the strain rate mentioned until the

specimen fractures. The load-deflection data was plotted and analyzed. The fracture surfaces after the test was secured for further analysis using SEM, XRD and thermal analysis.

High density alumina test specimens with the same dimensions were also prepared with a notch in the middle of the bars and used for calibration purposes.

The flexural strength was calculated using the simple beam formula,

#### Results

Figure 117 shows the LSFT-CGO specimen on the 4-point fixture before and after strength test at room temperature.

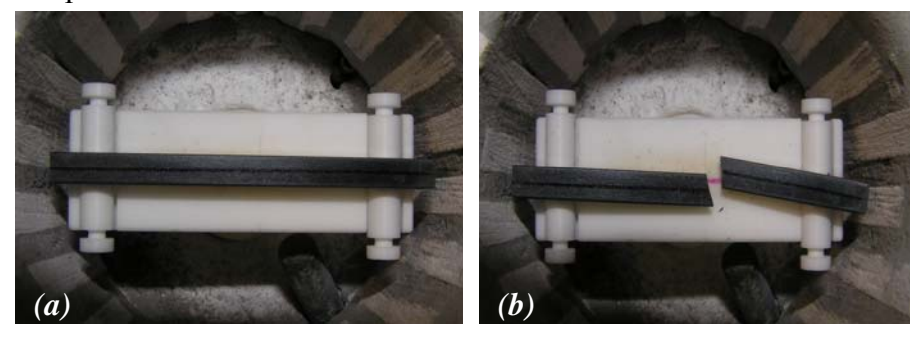


Figure 117. LSFT-CGO specimen on the 4-point fixture (a) before (b) after strength test at room temperature

The flexural strength results are summarized in the Table 17 and load-displacement curves of three selected specimens were shown in Figure 118. It is observed from the results that with increasing cross head speed the membrane takes higher loads to fail. This kind of fracture behavior is quite normal in the brittle materials which contain flaws.

Table 17. LSFT-CGO (40/100 vol% Batch 1) Flexural strength tests at RT and at 1000°C in  $N_2$  atmosphere.

No.	<b>Experimental Conditions</b>	<b>Cross Head Speed</b>	Maximum Load (N)	Maximum Strength (MPa)
1.	RT, Air	6 μm/min	157	82.3
2	RT, Air	6 μm/min	133	53.2
3.	RT, Air	60 μm/min	182	104.8
4.	RT, Air	600 μm/min	219	90.8
5.	RT, Air	600 μm/min	201	94.1
6.	1000°C, in N <sub>2</sub>	60 μm/min	120	51.2

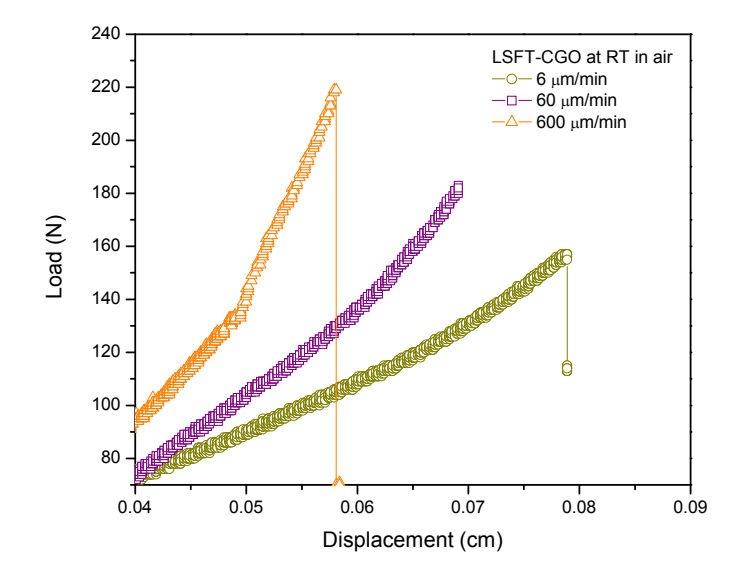


Figure 118. Effect of strain rate on the fracture load.

The presence of a flaw such as a crack, pore, or inclusion in a ceramic material results in stress concentration. Griffth proposed an equation for the form

$$\sigma_{\rm f} = A \left( \begin{array}{c} E \gamma \\ \hline c \end{array} \right)$$
 ----- 39

for relating the fracture stress to the material properties and the flaw size, where  $\sigma_f$  is the fracture stress, E the elastic modulus,  $\gamma$  the fracture energy, c the flaw size, and A a constant that depends on the specimen and flaw geometries. In the slower strain rate the crack growth is relatively easier by linking up with the grain boundaries and neighboring flaws which eventually increase the size of the critical flaw and reduce the fracture stress. In the slower strain rate the slow crack growth facilitates the fracture at the lower applied stress itself. In the rapid loading, materials fail at higher fracture stress due to the absence of slow crack growth. Hence, the stress needed to fracture the LSFT-CGO at 600  $\mu$ m/min is 25% higher than to fracture the membrane at 6 $\mu$ m/min.

# Bend strength LSFT-CGO (40/100 vol% Batch 1) in $N_2$ atmosphere at elevated temperatures:

The LSFT-CGO test specimen was loaded in the 4-point bend fixture and the  $N_2$  was purged during heating of the autoclave. The temperature was maintained at 1000°C for 60min prior to apply any load. The specimen was loaded with a rate of 60  $\mu$ m/min. The furnace power was switched off after the fracture of the sample. The flexural strength analysis of the LSFT-CGO in room temperature and at 1000°C in  $N_2$  atmosphere is shown in figure 119. The strain rate was maintained as  $60\mu$ m/min for both the tests and the strength values obtained at the room temperature and at  $N_2$  atmosphere are 104.8 MPa and 51.2 MPa respectively.

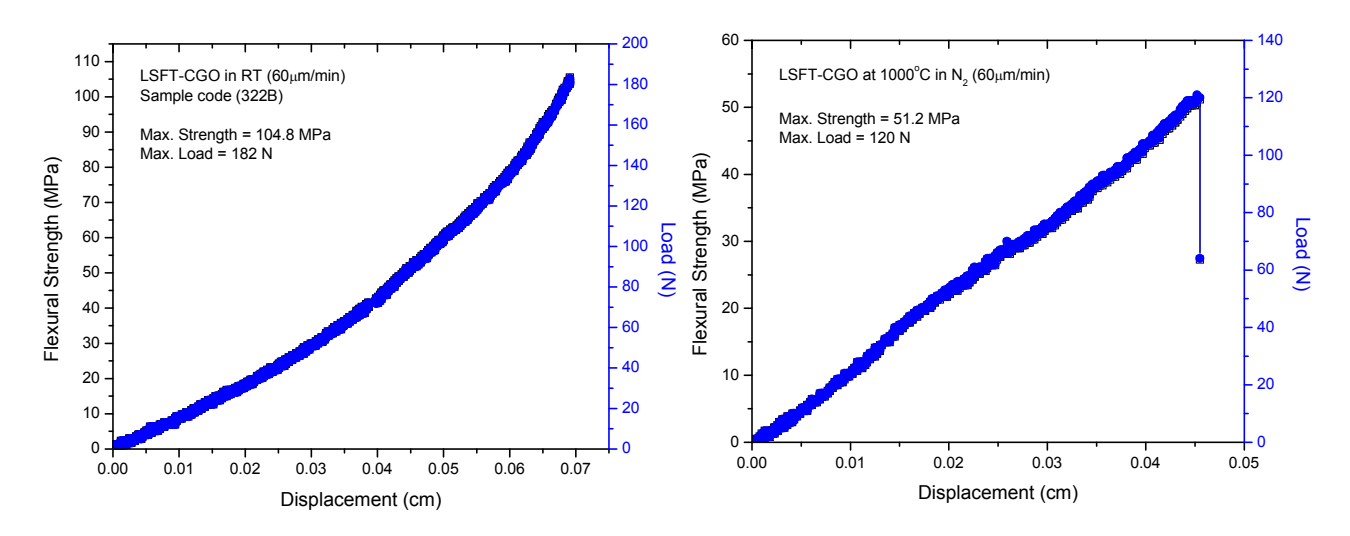


Figure 119. Effect of temperature and environment on flexural strength of the LSFT-CGO membranes.

The reduction in the strength can be attributed to the formation of new flaws or enlargement of existing flaws at the high temperature. The perovskite membranes experience the oxygen non-stoichiometry  $\delta$  for a doped perovskite type ceramic as a function of temperature and oxygen partial pressure. By changing the temperature or the oxygen partial pressure, the oxygen stoichiometry, or the oxygen content in the solid changes. Within the certain range of temperature and oxygen partial pressure, the change of the oxygen nonstoichiometry does not affect its perovskite structure and the change in the oxygen content is reversible. Hence, studying the effect of high temperature and environment can help to understand the fracture mechanism involved in the process. The LSFT-CGO test specimens fractured at room temperature and  $1000^{\circ}$ C in  $N_2$  were characterized using TGDTA. The as-received LSFT-CGO was also calcined at  $1000^{\circ}$ C in air and  $N_2$  and characterized using thermal analysis. In order to understand the reversible oxygen content, few samples were calcined at  $1250^{\circ}$ C in air prior to the thermal analysis. The results were compared with the results of the as received LSFT-CGO membranes.

In order to study the effect of environment and temperature in detail, more samples of LSFT-CGO dual phase membranes were obtained from Praxair with 3 different compositions. They were LSFT-CGO 40/60 vol%, LSFT-CGO 50/50 vol% and LSFT-CGO 60/40 vol%. All the membranes except LSFT-CGO 60/40 vol% were machined to the size of the four point test specimen and evaluated for their flexural strength. The LSFT-CGO 60/40vol% was too brittle to machine any rectangular bars suitable for the flexural strength. Hence, only LSFT-CGO 40/60 vol% and LSFT-CGO 50/50 vol% were evaluated for their strength.

Flexural strength test specimens of dimensions (3x4x48 mm) were cut from the assintered bars and tested in-situ in an autoclave mounted on a servo-electric loading frame. Loading was done in an in-house designed 4-point flexure with an outer span of 38.1 mm and inner span of 19.05 mm (ASTM-B). The specimens were ground and polished to 3 µm finish using successive grades of SiC paper and finally with a diamond paste and the edges barreled. In addition, the tensile side was polished using diamond paste of 1µm prior to the test. All flexural strength tests were done by monotonic loading to fracture at a constant cross head speed of 60 µm/min. The flexural strength was calculated using the simple beam formula.

Rectangular sample bars prepared from the 'as-received' LSFT and LSFT-CGO were used for dilatometry measurements (Netzsch, DIL 402PC) in air and UHP N2 with a heating rate of 5 Kmin-1. The post fractured dual phase membranes were characterized by thermogravimetric analysis, X-ray diffraction and scanning electron microscopy to understand the fracture behavior.

#### **Results:**

Figure 120 shows a typical SEM micrograph of LSFT-CGO (40/60 vol %Batch 2) dual phase composite. The micrograph (Fig 120a) shows the percolation of both the phases constituting the composite ceramics. No decomposition or reaction products were observed from the X-ray diffraction patterns of the 'as-received' composites.

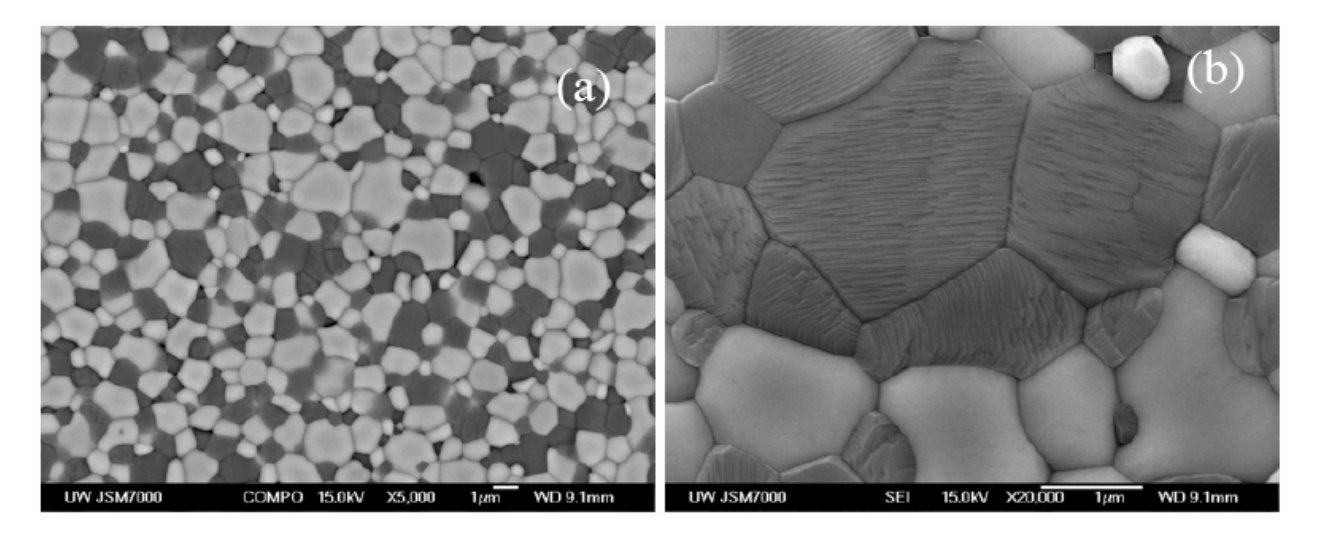


Figure 120. SEM micrographs of the 'as-received' LSFT-CGO membranes. The dark phase is LSFT and the bright phase is CGO. Percolation of the two-phases is clearly observed in (a) and no micro cracks and any other flaws caused by the thermal expansion mismatch are visible at the grain boundaries (b).

Fig 121 shows the typical displacement- strength curves of the dual phase membrane at different temperatures and environment. The mean flexural strength values of the membrane at every test condition are given in the parenthesis.

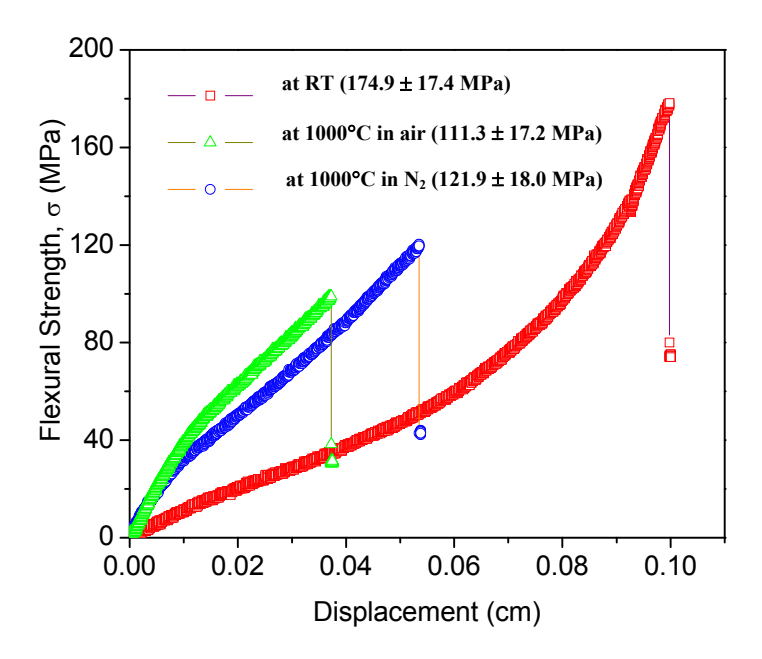


Figure 121. Effect of temperature and environment on the flexural strength of the dual phase membrane

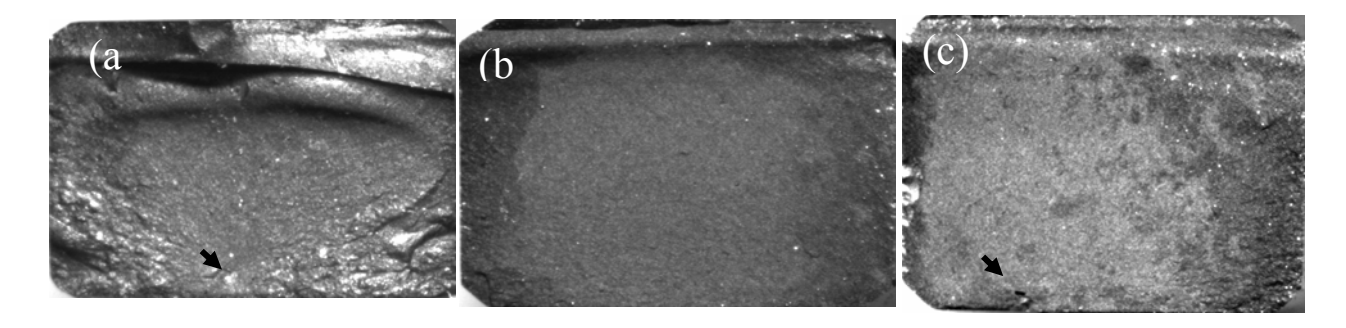


Figure 122. Stereo micrographs of fracture surfaces: (a) room temperature, (b) at 1000°C in air, (c) at 1000°C in N2. The volume flaw (in a) and the surface flaw (in c) are marked by arrows.

Figure 122 shows the stereo micrographs of the fracture surfaces. At room temperature, a medium-high energy failure was observed for the dual phase membrane which is reflected by the fracture surface. The secondary fractures surface shows compression curls and the surface and volume flaws. The SEM micrographs of the fracture surfaces show that there is a difference in the mode of fracture (Fig 123) between the membranes fractured at room temperature and at 1000°C in air and N2.

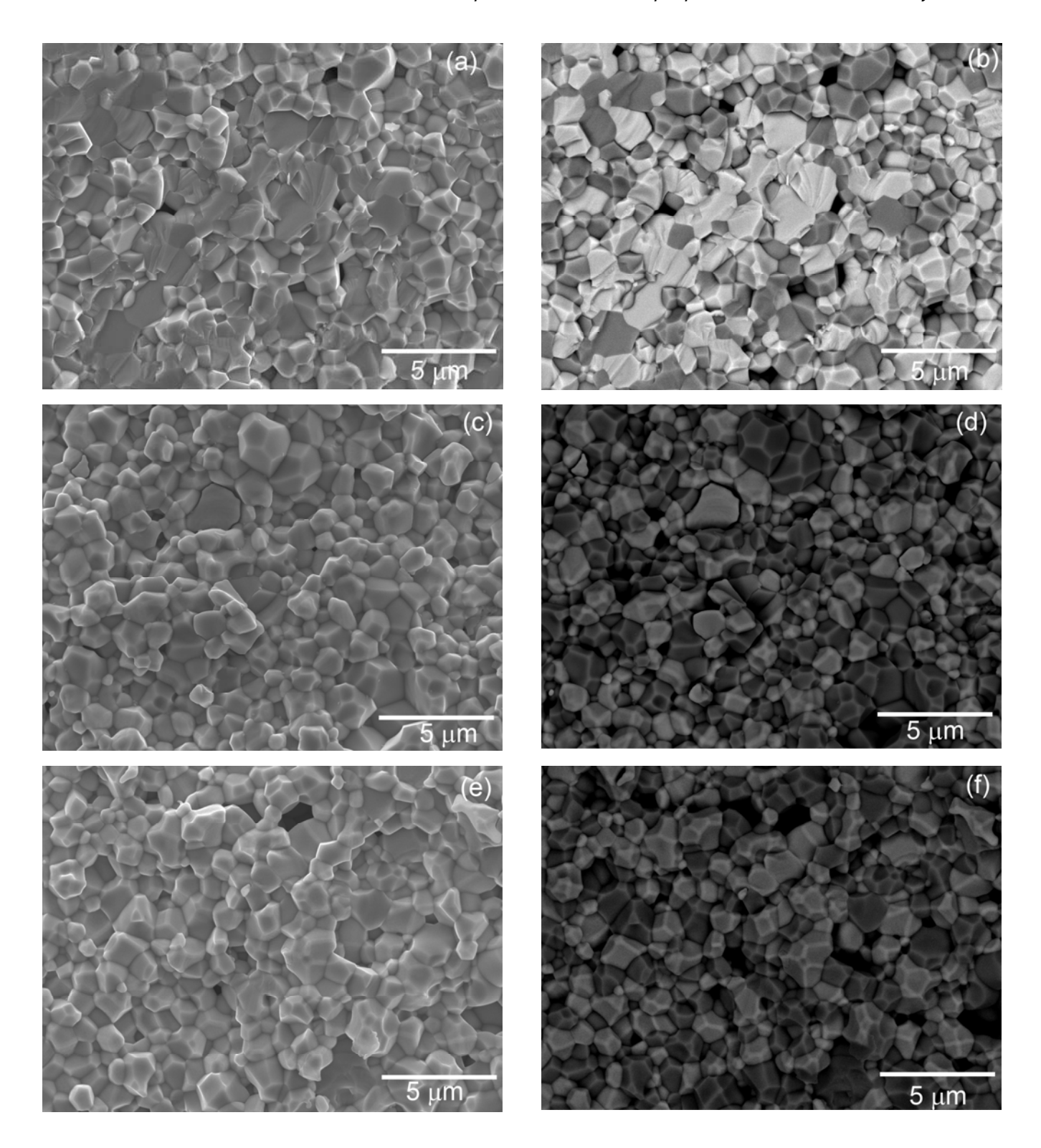


Figure 123. SEM micrographs of fracture surfaces at room temperature (a,b) at  $1000^{\circ}$ C in air (c,d) and at  $1000^{\circ}$ C in  $N_2$  (e,f). Fracture was mainly transgranular at the room temperature and intergranular at  $1000^{\circ}$ C in air and  $N_2$  atmosphere.

The fracture cleaved most of the grains during the high energy failure which suggests a preferred tendency for some crack paths. The membranes fractured at 1000°C showed mostly intergranular fractures (Fig 123b and 163c), which suggests a crack path mostly along the boundaries. The fracture-path transition from transgranular to intergranular can be associated to probable tensile stresses at the grain boundaries that promote the interfacial debonding at the wake of advancing crack tip. Hence, the fracture mode transition can be correlated largely to the thermally induced chemical expansion of the LSFT and CGO.

Normally in a two phase composite, the crack path is controlled by the stress fields from mismatches in the thermal and elastic constants of different phases. When a crack that is approaching a reinforcement encounters the stress field from thermal and elastic mismatches, it follows the path that leads to maximum elastic energy dissipation. The path taken influences the bulk fracture properties i.e., the fracture toughness and the fracture strength.

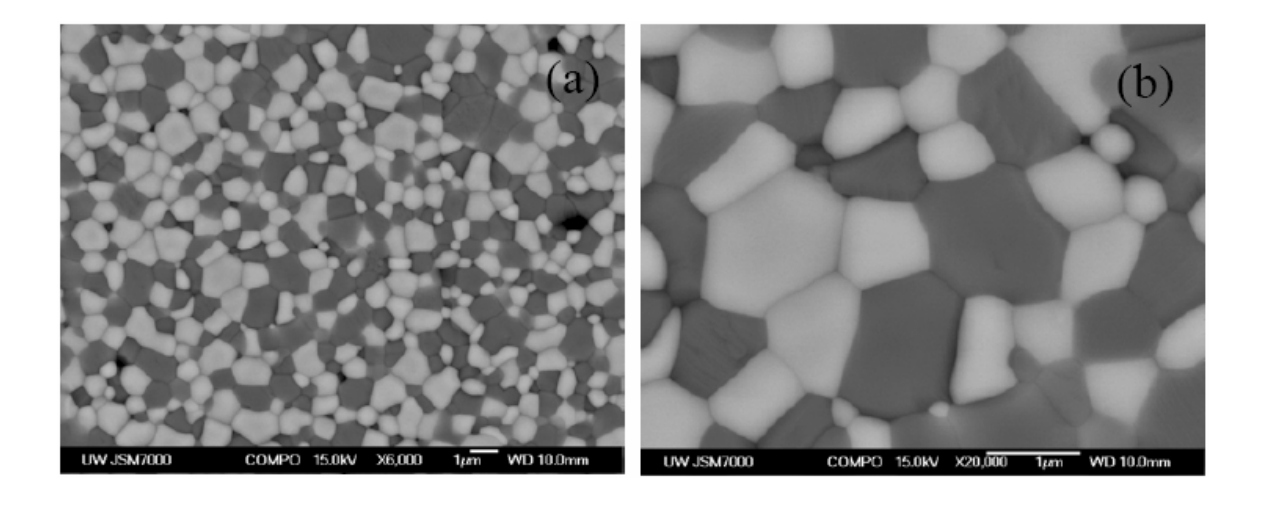


Figure 124. SEM micrographs of the 'as-received' LSFT-CGO (50/50 vol%) membranes. The dark phase is LSFT and the bright phase is CGO. Percolation of the two-phases is clearly observed in (a) and no micro cracks and any other flaws caused by the thermal expansion mismatch are visible at the grain boundaries (b).

It is known from the theoretical calculations that the cracks are attracted to lower Young's

modulus (E) and/ or lower TEC ( $\alpha$ ) reinforcements [4-7]. The crack path tendency is predictable if the TEC ( $\alpha$ ) and the E values of the reinforcement have a tendency to drive the crack in a similar manner; the crack path, however, is less predictable if they have a tendency to drive the crack differently.

Figure 124 shows a typical SEM micrograph of LSFT-CGO (50/50 vol %) dual phase composite. The micrograph (Fig 124a) shows the percolation of both the phases constituting the composite ceramics.

Fig 125 shows the typical displacement- strength curves of the dual phase membranes. The flexural strength of the LSFT-CGO (50/50 vol%) is significantly affected by the temperature and the environment. At room temperature the strength of the membrane is approx. 180 MPa whereas at  $1000^{\circ}\text{C}$  the strength has decreased to 110 MPa. The slightly reducing environment ( $N_2$ ) has increased the strength of the membrane.

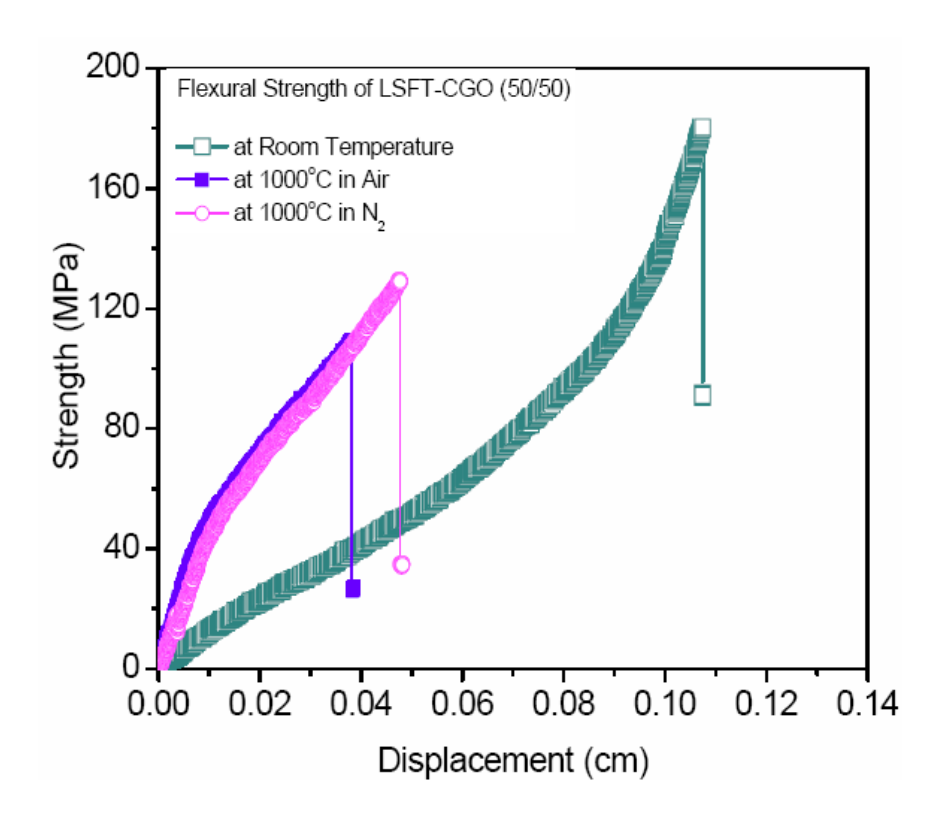


Fig. 125 Effect of temperature and environment on flexural strength of the LSFT-CGO (50/50 vol%)

This increasing strength caused by the  $N_2$  atmosphere can be attributed to the thermal/ chemical expansion of the constituent phases. The thermal and chemical expansion behaviors of the LSFT-CGO membranes are investigated to understand the fracture behavior in the reactive environment and elevated temperatures. The effect of temperature and environment on displacement-strength curve pattern is also significant which suggests the change in elastic properties of the membranes when they are exposed to the reducing atmospheres at the elevated temperatures.

The SEM micrographs of the fracture surfaces show that there is a difference in the mode of fracture (Fig 126) between the membranes fractured at room temperature and at 1000°C in air and N<sub>2</sub>. While the secondary electron images are presented to illustrate the mode of fracture, the back scattered image of the fractured surfaces were shown to analyze the role of constituent phases in fracture behavior. The membranes fractured at room temperature showed mostly transgranular torturous fractures. The fracture cleaved most of the grains (both LSFT and CGO) during the high energy failure which suggests a preferred tendency for some crack paths. Particularly, the crack path has cleaved the larger grains irrespective of the phase and smaller grains are either debonded or circumvented during the course of the crack propagation.

Also a strained or torturous fracture is observed with the CGO grains. Fig 127 shows the strained fracture happened at the CGO grains. The membranes fractured at 1000°C showed mostly intergranular fractures (Fig 126b,c,d&f), which suggests a crack path mostly along the boundaries. The fracture-path transition from transgranular to intergranular can be associated to probable tensile stresses at the grain boundaries that promote the interfacial debonding at the wake of advancing crack tip. Hence, the fracture mode transition can be correlated largely to the thermally induced chemical expansion of the LSFT and CGO. Normally in a two phase composite, the crack path is controlled by the stress fields from mismatches in the thermal and elastic constants of different phases. When a crack that is approaching a reinforcement encounters the stress field from thermal and elastic mismatches, it follows the path that leads to maximum elastic energy dissipation.

The path taken influences the bulk fracture properties i.e., the fracture toughness and the fracture strength. It is known from the theoretical calculations that the cracks are attracted to lower

Young's modulus (E) and/ or lower TEC ( $\alpha$ ) reinforcements (25-28). The crack path tendency is predictable if the TEC ( $\alpha$ ) and the E values of the reinforcement have a tendency to drive the crack in a similar manner; the crack path, however, is less predictable if they have a tendency to drive the crack differently.

The elastic modulus of the CGO is approximately twice that of the LSFT. Hence, from the elastic mismatch stresses standpoint the LSFT will attract the crack than the CGO when a load is applied which will eventually leads to the debonding of LSFT/CGO interface. Thus, in LSFT-CGO composite, thermal and elastic modulus mismatch stresses will have a tendency to drive the crack in opposite paths. The crack path is determined by the combined stress fields that result from thermal expansion and elastic modulus mismatches. Therefore, in room temperature, the fracture leads to medium-high energy failure which fractures the CGO grains due to the crack path prefers more interaction with the CGO rather than LSFT.

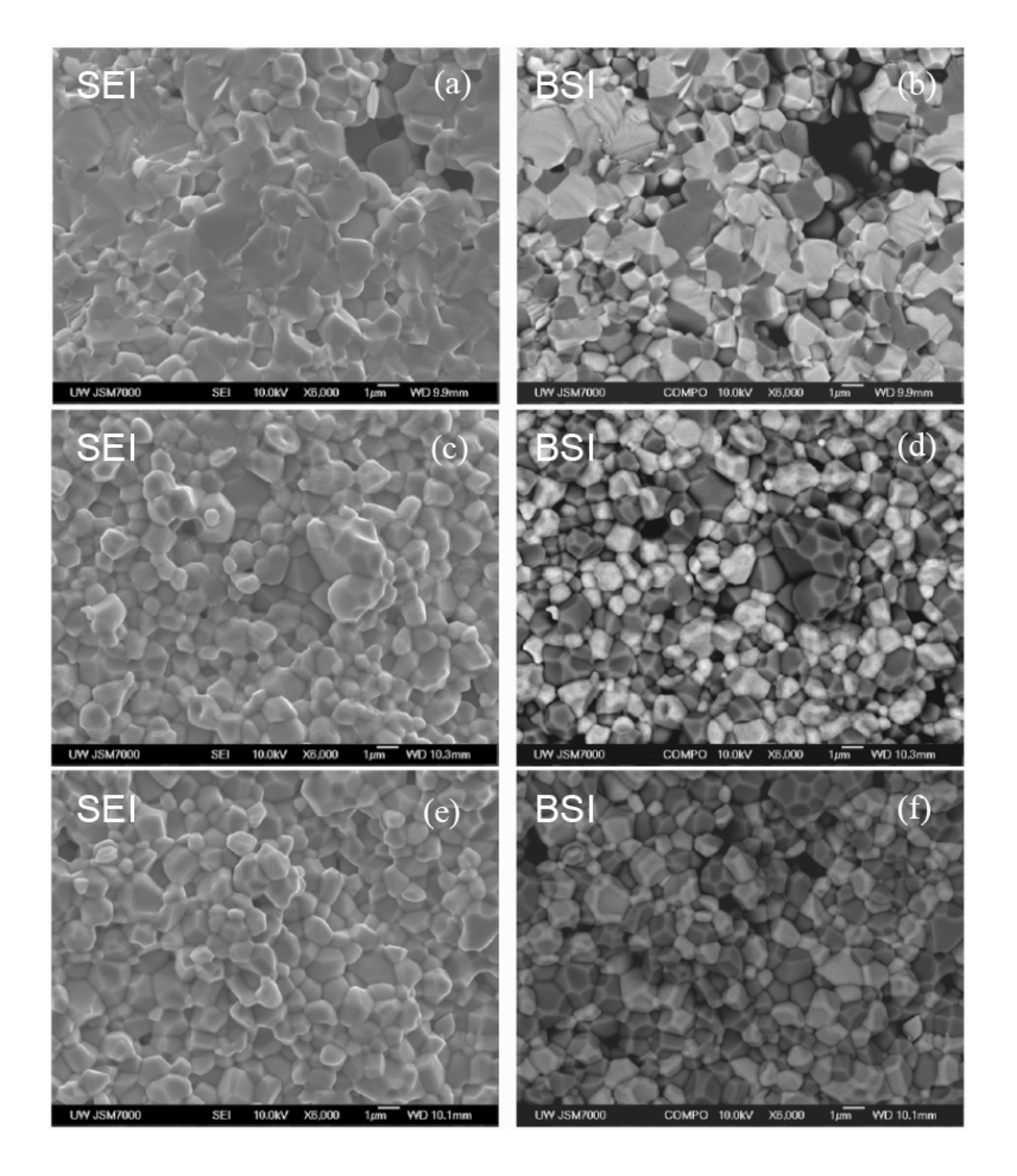


Fig. 126. Secondary electron and back scattered electron images of the fracture surfaces: LSFT-CGO (50/50) fractured at room temperature (a-b); LSFT-CGO (50/50) fractured at 1000°C in air (c-d) and LSFT-CGO (50/50) fractured at 1000°C in N<sub>2</sub> (e-f).

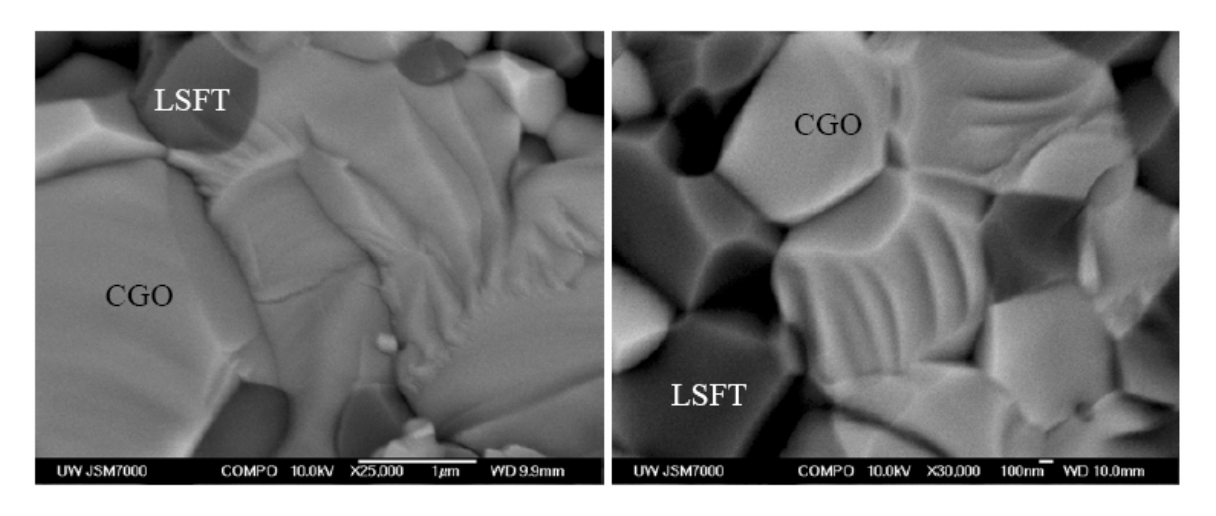


Fig. 127. The room temperature failure of the LSFT-CGO (50/50). Note the torturous failure of CGO grains

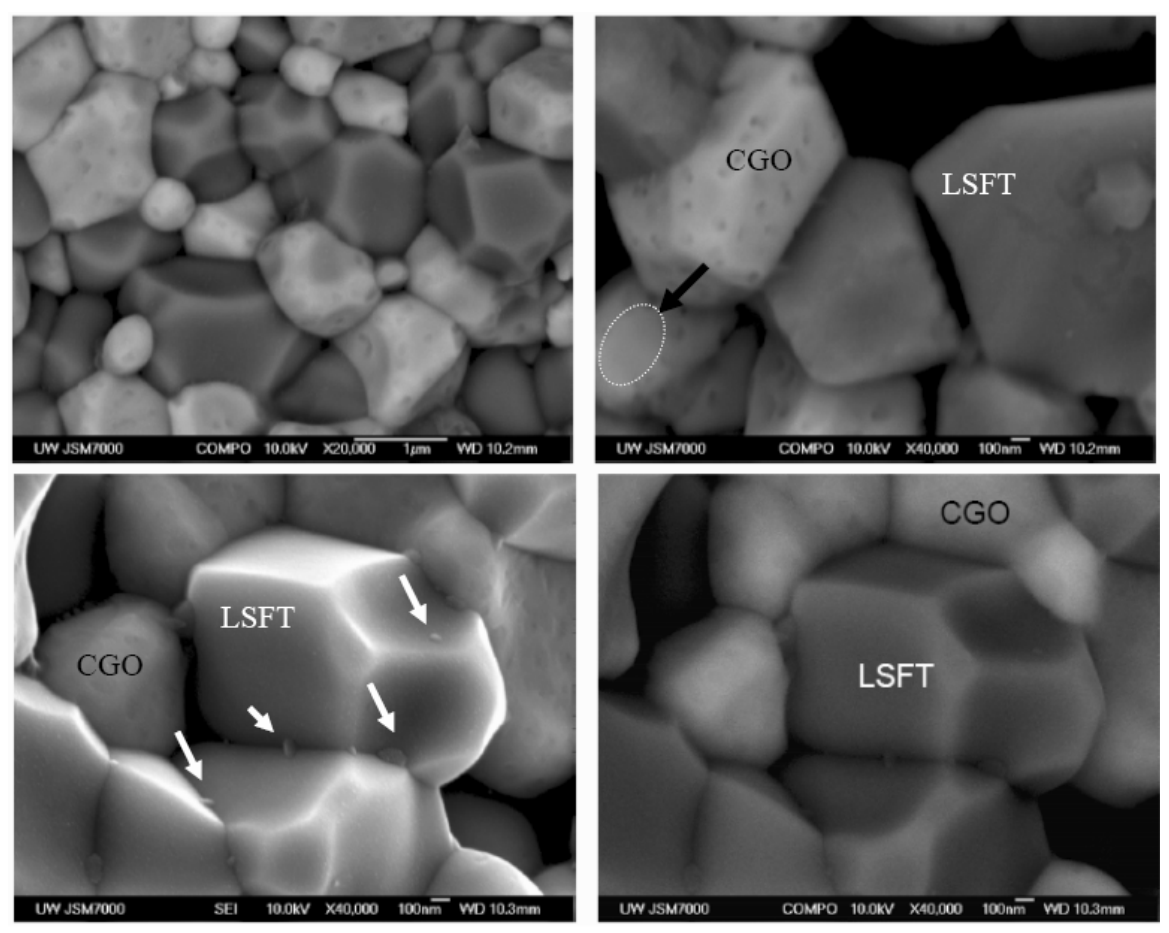


Fig. 128. LSFT-CGO (50/50) fractured at 1000°C in air (a-b) and  $N_2$  (c-d).

The analysis of the fracture surfaces also revealed the presence of precipitates in the grain boundaries and junctions. Fig. 128 shows the presence of precipitates in the grain boundaries of LSFT (shown by the white arrow marks) and their impression marks on the CGO grains. The precipitates are formed on the surfaces of the LSFT and they leave the impression marks on the CGO grains. The EDS analyses of the precipitates were carried out and an EDS spectrum is shown in Fig. 129. The precipitates are strontium or iron rich LSFT particles segregated along the boundaries.

The precipitates leave the impression marks on the CGO (brighter grains) grains. The white arrows are marking the precipitates and the black arrow is marking a place where there is no impression marks on the CGO grains. This suggests a pullout of a CGO grain from that place.

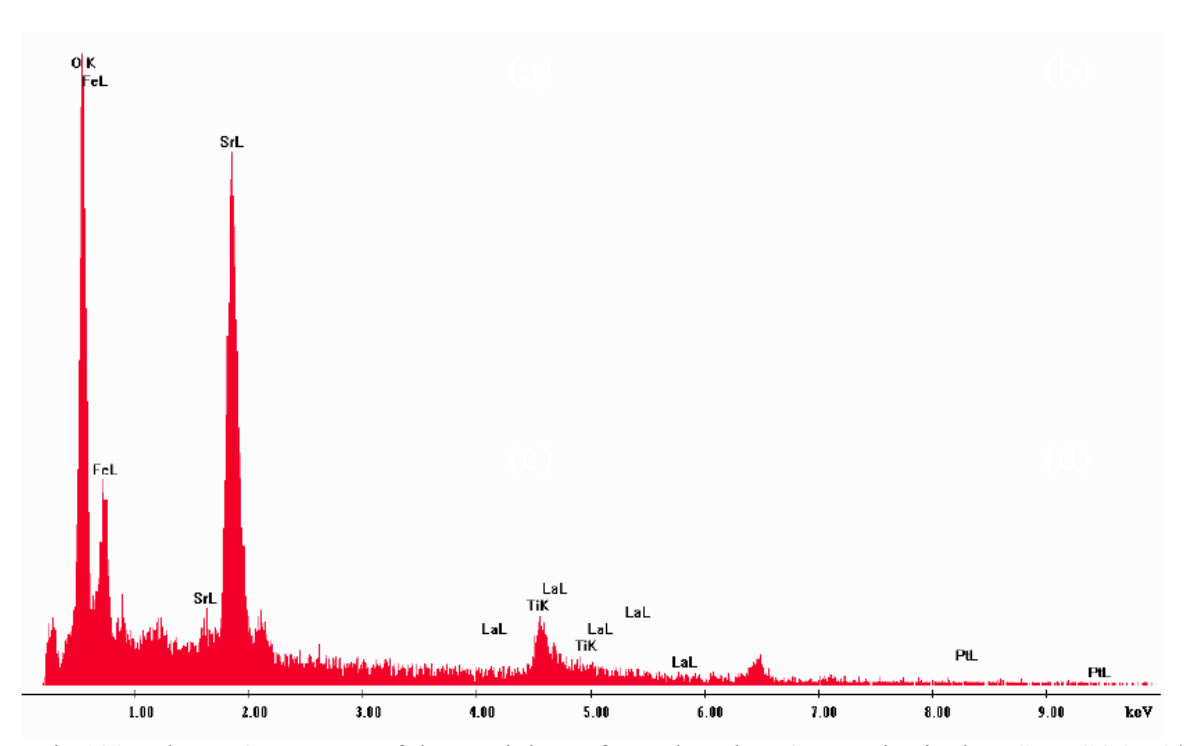


Fig.129. The EDS spectrum of the precipitates formed on the LSFT grains in the LSFT-CGO 50/50) fractured at 1000°C in  $N_2$ 

The black arrow mark is used in Fig. 128 to note the CGO grain face (marked by white circle) which doesn't have any impression marks caused by the precipitates. The other sides of the same grain are clearly marked with the impression marks left by the precipitates. This suggests a

pullout of a CGO grain from that space which has no precipitates to leave impression on that CGO grain shown in the figure.

It can be considered that the precipitates that are formed at the grain boundaries have no or minimal impact on the crack propagation behavior as the precipitates are observed on samples fractured both at room temperature and at  $1000^{\circ}$ C in  $N_2$  atmosphere. Also there is no reaction product was observed between the LSFT and CGO in any of the samples fractured which confirms the precipitates are not the reaction product of the constituent phases.

# 2.4.4.8 Thermal analyses

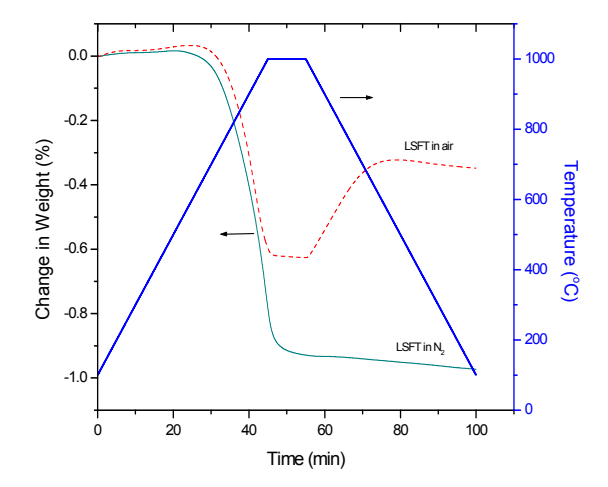
## **Experimental:**

Thermal analysis on the samples was carried out using Perkin Elmer-Pyris Diamond TG/DTA. The N<sub>2</sub> was used as purge gas (200ml/min) and the analysis were carried out in the air also. Some of the LSFT samples were calcined at 1000 and 1250°C prior to the thermal analysis in air and N<sub>2</sub> atmosphere and annealed to 1000°C for TGA. The as-received LSFT and dual phase membranes were cut into small pieces and the thermal analysis were carried out in the air and in the N<sub>2</sub> atmosphere with the heating rate of 20°C/min. The change in weight and endothermic and exothermic process corresponding to different oxygen desorption and structural changes were examined.

Figure 130 shows the change in weight, DTA and temperature data as a function of time for LSFT in air and N<sub>2</sub> environment. The temperature and corresponding weight changes are tabulated in Table 18. With increasing temperature, the samples exposed in air gained a marginal weight before a major weight loss starting from 723°C. A maximum weight loss 0.62% was observed during the heating of the sample at 1000°C. There was no significant weight loss during dwelling at 1000°C in air. A significant amount of this weight loss is reversible mainly due to the absorption of oxygen. This is reflected by the weight gain (Figure 130a). The reversible weight loss is observed till the temperature reaches 575°C during cooling. The exothermic and endothermic reactions are shown in Figure 130a.

Table 18. Change in weight and corresponding temperatures of OTM membranes in air and  $N_2$  environment

		LSFT			LSFT-CGO				
		Temperature		Wt Cha	nge (%)	Temper	ature	re Wt Change (%)	
		(°C)				(°C)			
		Air	N <sub>2</sub>	Air	N <sub>2</sub>	Air	N <sub>2</sub>	Air	N <sub>2</sub>
Heating		233	233	0.02	0.01	211	239	0.01	-0.02
		612	523	0.03	0.02	515		0.02	
		723	624	0.0	0.0				
		1000	1000	-0.62	-0.93	1000	1000	-0.23	-0.51
ij		575	452	-0.33	-0.95	500	500	-0.07	-0.58
Cooli	$\mathbf{g}_{\mathbf{u}}$	100	100	-0.35	-0.97	100	100	-0.09	-0.6



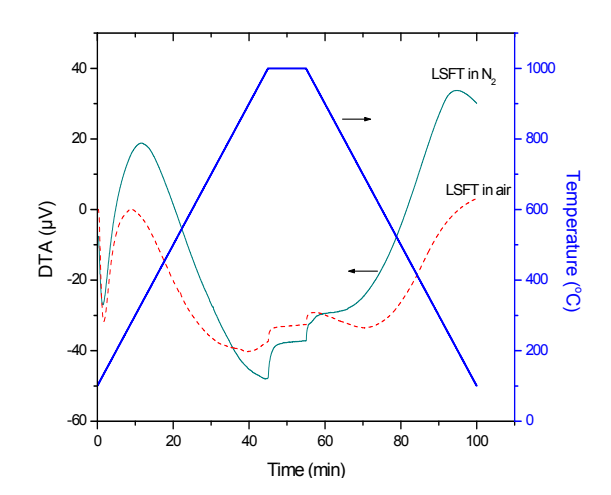


Figure 130(a). Change in Weight (b) DTA and temperature data as function of time for LSFT in air and  $N_2$  environment

The reversible weight loss of 0.29% is observed for LSFT in air which is slightly lesser than the weight loss value obtained for annealed LSFT in air as reported [3]. An irreversible weight loss of 0.33% was observed during the present analysis. This irreversible weight loss may be due to the volatile organic substances. Calcination of the membrane at 1200°C can be helpful in minimizing the irreversible weight loss, caused by the volatile species.

The total weight loss in the N<sub>2</sub> atmosphere is significantly higher than the weight loss occurred in air. The maximum weight loss at 1000°C in N<sub>2</sub> is 0.93%. The flow of N<sub>2</sub> has caused more oxygen desorption. Also absorption of oxygen during cooling was not possible. This has resulted a continuous weight loss even during cooling after dwelling at 1000°C, even though the rate of weight loss has decreased significantly during cooling cycle. The major weight loss has started 100°C earlier during heating with the flow of N<sub>2</sub>. This behavior has raised questions about the early decomposition products which may need to be studied in detail.

The change in weight with the function of time in the LSFT-CGO membrane in air and N<sub>2</sub> environment is shown in Figure 131. In air a maximum weight loss of 0.23% was observed at the maximum temperature, 1000°C. Prior to this significant weight change, two small events of weight gains were observed. There is no noticeable weight loss after the temperature has reached the steady state during dwelling. The cooling has resulted in the positive weight change which lasts till 500°C. The reversible weight loss was about 0.07% and the remaining weight loss caused during heating can be considered as irreversible. The higher percentage (69.56%) of reversible weight loss observed for dual phase membrane suggests the presence of volatile substances in the dual phase membrane and comparatively lesser than the LSFT.

In the nitrogen atmosphere the major weight change during heating was started earlier than in air and the total weight loss also higher (0.58%) for the dual phase membrane. There was no reversible weight change with flowing  $N_2$  and the weight loss is continuous even in the cooling cycle like that of LSFT.

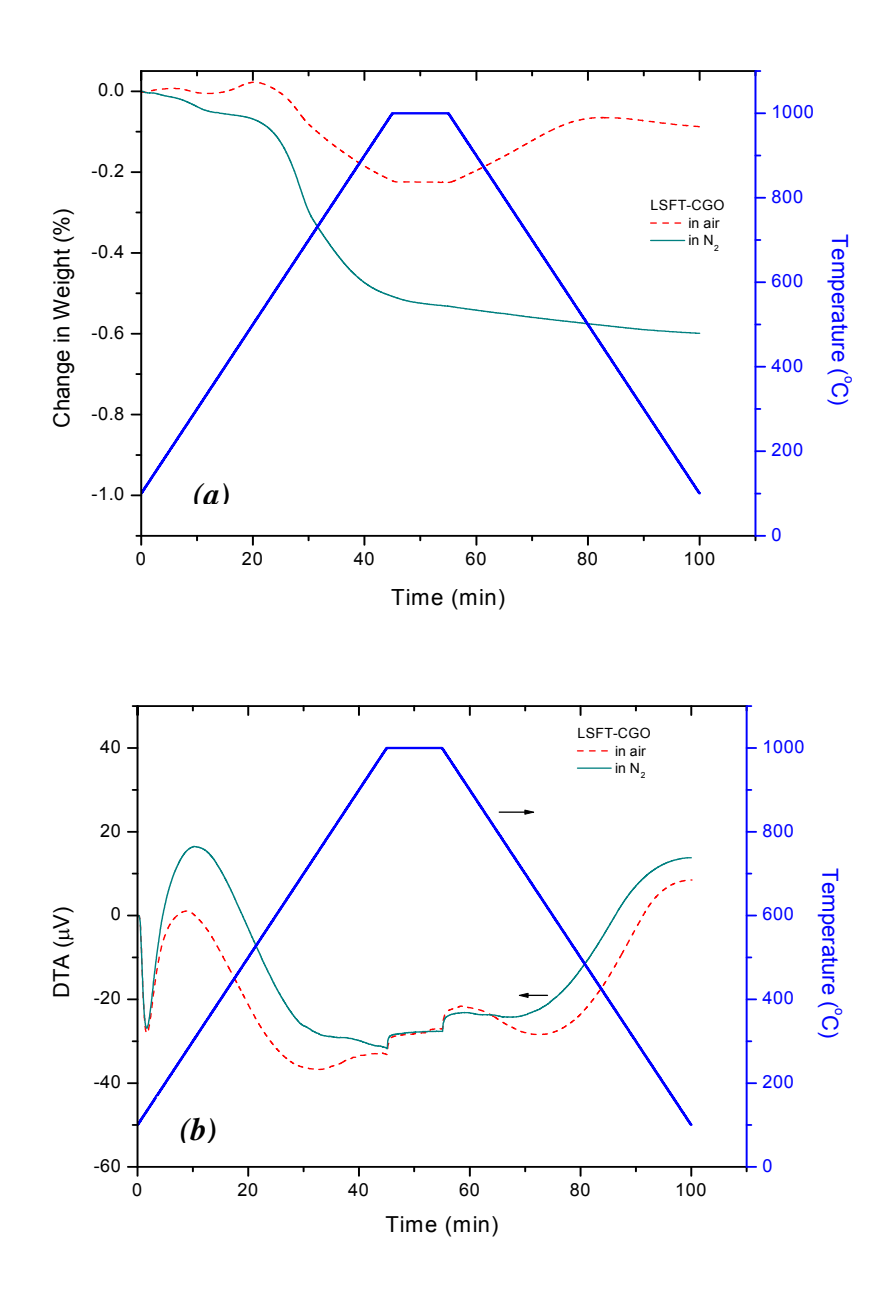


Figure 131. (a) Change in weight (b) DTA and temperature data as function of time for LSFT-CGO in air and N2 environment

In general, the weight loss during heating (in both environments) is higher for LSFT than the dual phase membrane and the reversible weight change during cooling is higher for the dual phase membrane.

The fractured samples after the flexural strength test were analyzed using TGDTA in air and  $N_2$ . The change in weight during the exposure of as received LSFT-CGO in  $N_2$  and air is shown in Figure 132. The weight loss is reversible in the air and it is, however, irreversible in the  $N_2$  atmosphere. The reversible weight loss in air was approx. 0.2 % and the maximum weight loss in the  $N_2$  atmosphere is about 0.6%.

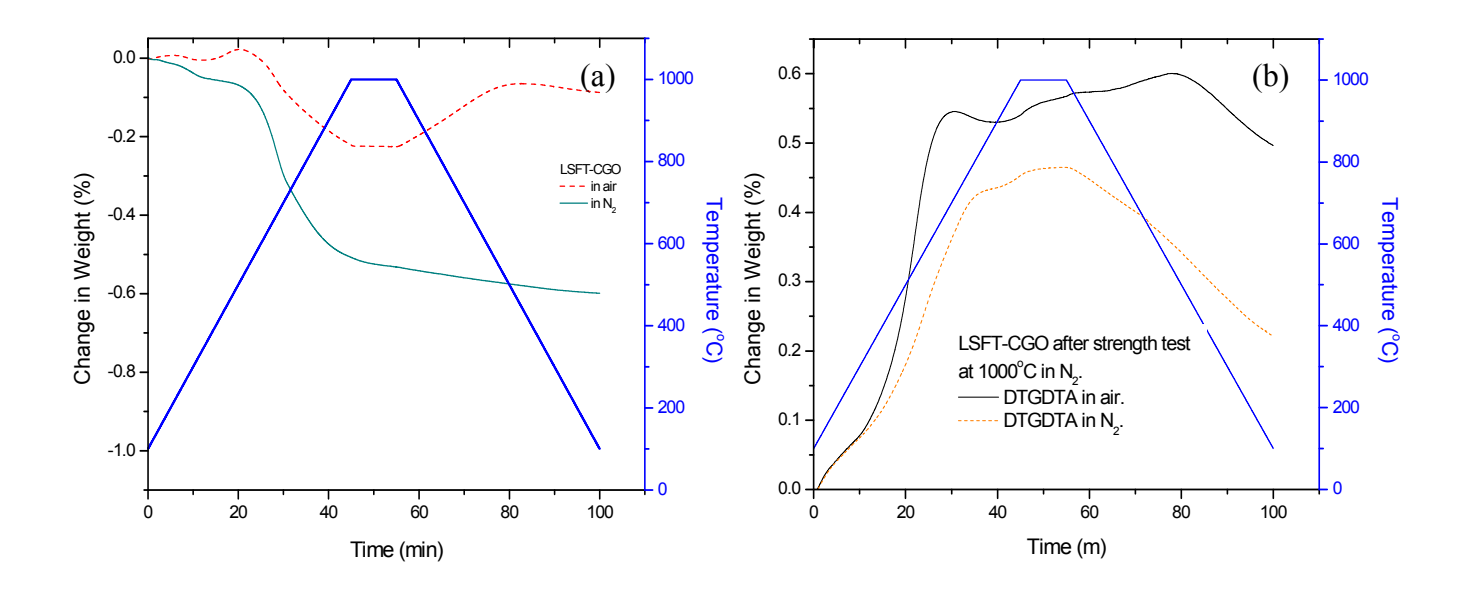


Figure 132. The weight change during annealing of LSFT-CGO measured by TGA

It can be observed from figure 132 that the fractured sample in  $N_2$  gains a weight of 0.6 % during annealing as indicated in the thermal analysis. Figure 132(b) shows the weight gain during heating of the membrane and the weight gain almost stabilizes at 500°C. The weight gain in the  $N_2$  rich atmosphere is comparatively less and in both experiments desorption of oxygen is recorded during cooling.

The change in weight during annealing of the LSFT-CGO which was calcined at 1000 and 1250°C in air is shown in figure 133.

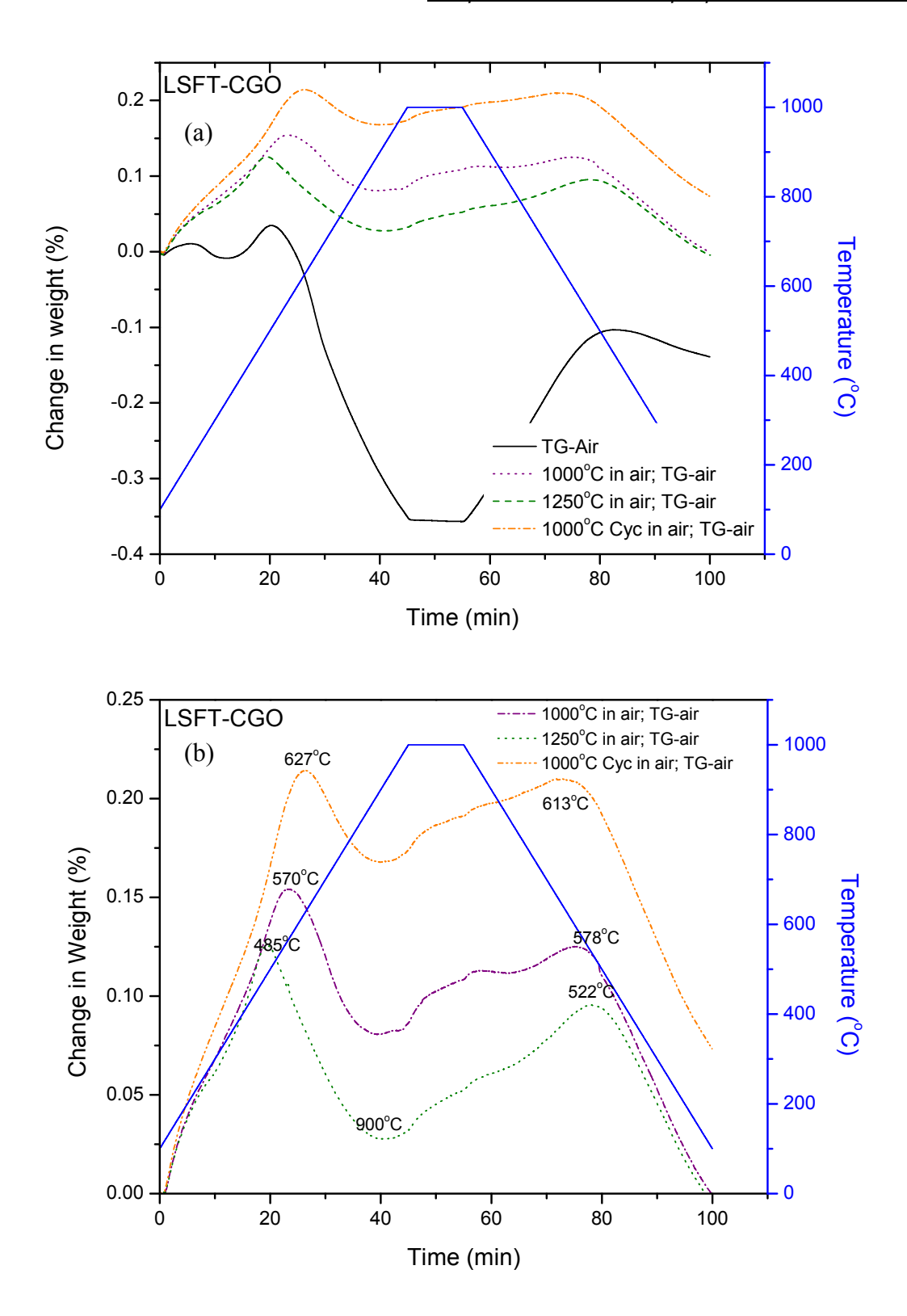


Figure 133. The weight change during annealing of LSFT-CGO calcined at 1000°C and 1250°C measured by TGA at 1000°C.

All the calcined samples gained weight during annealing and they lost weight during cooling. Since the change in weight is reversible, it ensures that the oxygen loss is the reason for the weight change. A thermal cycle was employed on few LSFT –CGO at 1000°C in air prior to annealing at 1000°C for thermal analysis. The thermal cycled sample gains a weight of 0.2% and looses the weight during cooling. Figure 133(b) shows the temperatures at which the weight gain saturates during annealing and the temperatures at which the weight loss is started. For the samples calcined at 1000°C, the weight changes are marked around 570°C. As the sample was annealed after the thermal cycling at 1000°C, the temperatures at which the weight losses are marked have increased. It may be interesting to note that a similar pattern in the TGA curves during annealing for all the samples calcined or thermal cycled at 1000°C and 1250°C in air. This clearly confirms the LSFT-CGO undergoes a structural change or change in the nonstoichiometry at high temperature. The LSFT-CGO specimens fractured at 1000°C in N<sub>2</sub> and CO/CO<sub>2</sub> atmosphere were annealed at 1000°C for TGA in air and N<sub>2</sub> atmosphere and the results are shown in figure 134.

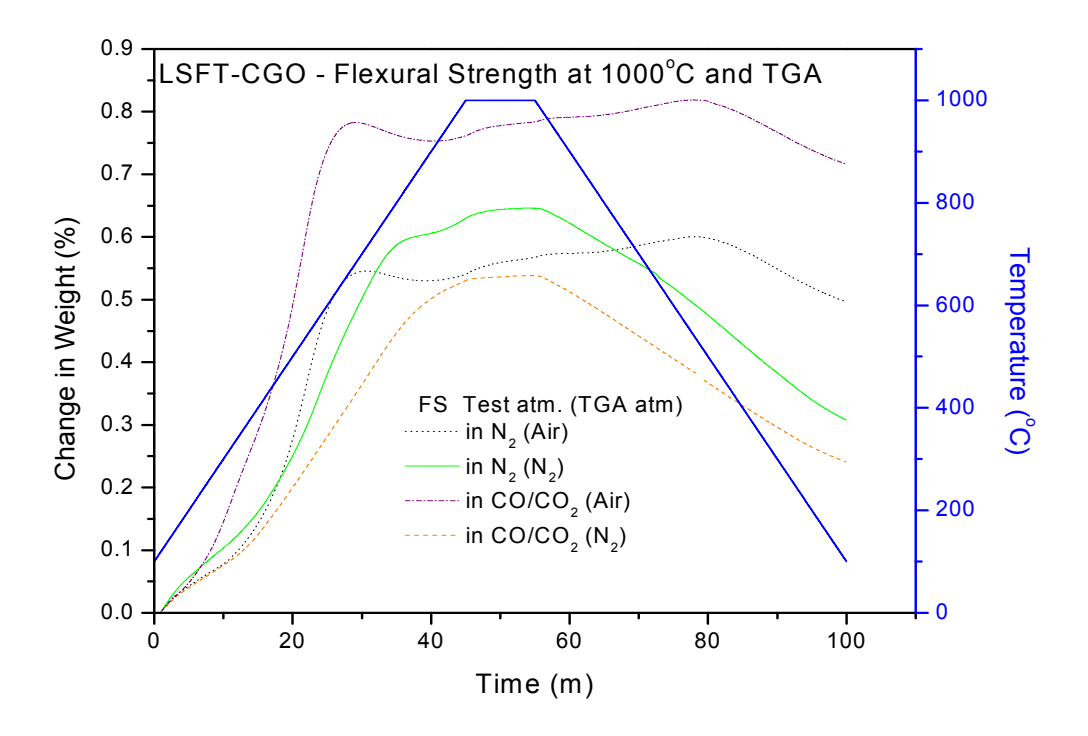


Figure 134. Effect of flexural test atmosphere on the weight change of the LSFT-CGO.

The LSFT-CGO membranes fractured at the  $1000^{\circ}$ C in  $N_2$  gains a weight of 0.5% when they are annealed at  $1000^{\circ}$ C during TGA. The same LSFT-CGO membranes gain about 0.6% of weight when it was annealed at  $N_2$ , but unlike in the air, the membrane looses the weight during cooling. The membranes fractured at  $CO/CO_2$  environment at  $1000^{\circ}$ C also gains a weight of 0.8% saturates at the weight even during cooling. This result is quite obvious when the membrane is exposed to an environment in which the partial pressure of oxygen is less at the high temperature.

This study confirms the nonstoichiometry of the oxygen at high temperatures in an inert and reducing atmosphere. X-ray diffraction analysis of the membranes fractured at these test conditions may be able to elucidate the changes associated with the crystal structure of the membranes.

# 2.4.4.9 Thermal Expansion studies

The thermal expansion of the membranes is very important to material phenomenon to be studied, particularly for materials at high temperatures. In the dual phase membranes the thermal expansion mismatch could be a potential source for nucleating new flaws and reducing the strength of the material. The dilatometer was installed and the correction runs were carried out for the standard (sapphire) rods. Figure 135 shows the photograph of the dilatometer installed at the ceramic membrane lab and the sample holder with the LSFT-CGO membrane (inset). N<sub>2</sub> can be used a purge gas and the heating rates can be varied to a desired condition. The thermal expansion can be measured and plotted in the PC using the data accusation system.

# 2.4.4.9.1 Chemical Expansion

The thermal expansion of the LSFT was studied in the air and N<sub>2</sub> atmosphere and shown in the figure 136. The thermal expansion is almost similar for the LSFT in the air and N<sub>2</sub> atmosphere. Also, thermal expansion of the membranes was not monotonic and the coefficient of thermal expansion changes around 500°C in both the environments. It is interesting to note from TGA around this temperatures the membranes experiences a change in the oxygen content.

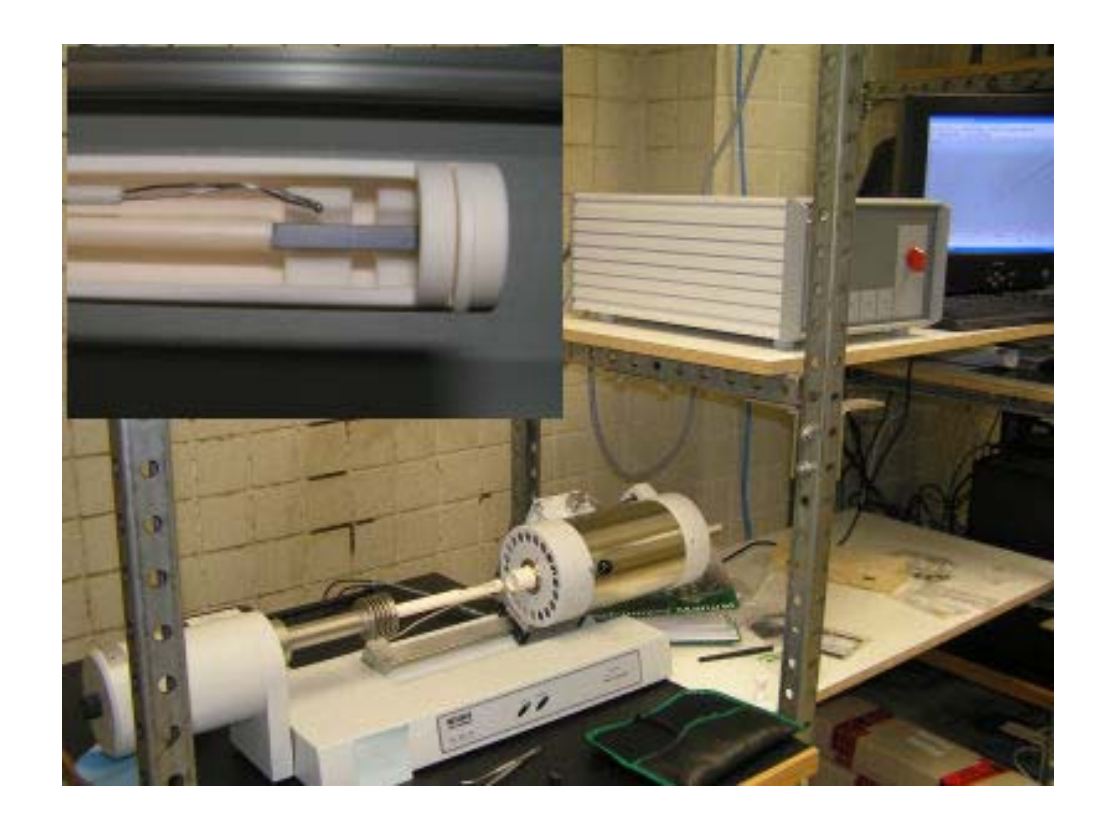


Figure 135. The dilatometer installed at the ceramic membrane lab and the sample holder with a LSFT-CGO membrane is shown in the inset.

The thermal expansion was done for the thermal cycled membranes and no significant change was observed with the dual phase membranes.

The thermal expansion coefficient of the LSFT and dual phase membranes measured from dilatometry is given in the Fig 136. The TEC of LSFT was found to be  $16.1 \times 10^{-6} \text{K}^{-1}$  at 950°C in air. It is interesting to note the change in the TEC at 550°C when it is measured in N2 atmosphere. A positive difference of  $0.8 \times 10^{-6} \text{K}^{-1}$  is observed in the TEC value at 950°C when the LSFT is heated in the slightly reducing atmosphere.

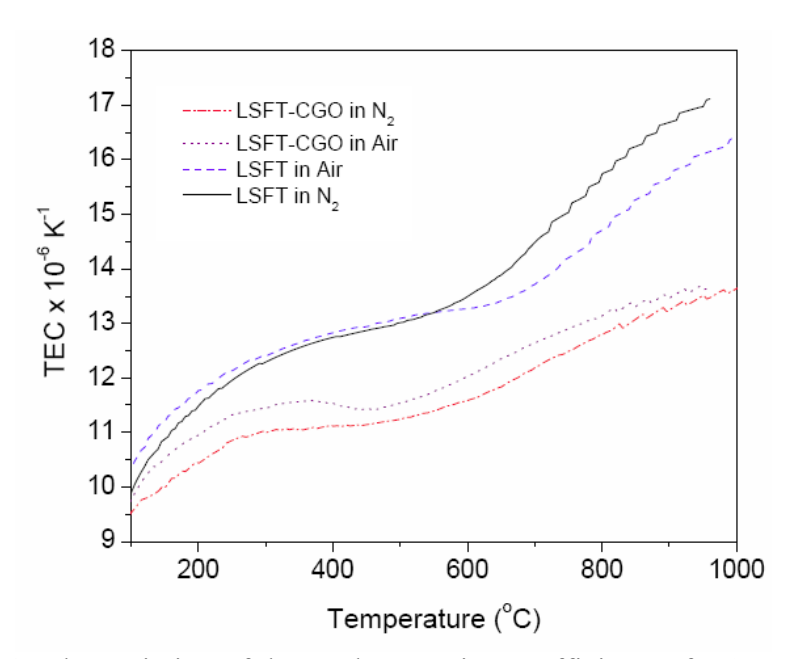


Fig 136. The variation of the total expansion coefficients of LSFT and LSFT-CGO on heating in air and at N<sub>2</sub> at 5k min<sup>-1</sup>.

The equations developed by Hsueh and Taya et al [8-9] can be rearranged to calculate the internal stresses introduced during post-sintering cooling as a result of thermal expansion mismatch between the CGO and the LSFT.

$$\sigma_{\rm p} = \Delta T \Delta \alpha \left[ (1-2\upsilon_{\rm p})/E_{\rm p} + (1+2f+\upsilon_{\rm m} (1-4f))/(2E_{\rm m} (1-f)) \right]^{-1}$$
 ------41

Where,  $\Delta T$  is the temperature range over which the internal stresses develop, and  $\Delta \alpha = \alpha_p - \alpha_m$ , is the difference in the coefficients of thermal expansion. The termso, E and f refer to Poisson's ratio, Young's modulus and the particle volume fraction, respectively and the subscripts p and m refer, respectively to the particle and the matrix. The average hydrostatic stresses in the matrix are related to those in the particle through the relation

$$f \sigma_{\rm p} + (1-f) \sigma_{\rm m} = 0$$
 ------42

Equation (41) represents the solution for the thermal expansion mismatch stresses when CGO is matrix (subscript m) and LSFT exist as a particle (subscript p) and the  $\sigma_p$  and  $\sigma_m$  were calculated for all three test conditions as shown in table 19. Here, the smaller magnitude of  $\alpha$  in CGO

versus  $\alpha$  in LSFT yields residual circumferential compressive and radial tensile stresses in the CGO matrix, where as the LSFT particles and the LSFT/CGO interface are in tension. If these residual thermal stresses influence the crack path, it is expected, from the above-mentioned stress state, that the crack will be deflected from the LSFT particles more frequently than would occur from random intersections, because the crack will see an increasing circumferential compressive stress field as it approaches the CGO/LSFT interface.

Table 19. The average internal stresses in the dual phase membranes at all test conditions

	$RT(\Delta T = 1400-25^{\circ}C)$	$1000^{\circ}$ C AIR ( $\Delta$ T = $1400-1000^{\circ}$ C)	$1000^{\circ}$ C N <sub>2</sub> ( $\Delta$ T = $1400-400^{\circ}$ C)
	$\alpha_{\rm CGO} = 12.2  \text{x} 10^{-6} \text{K}^{-1}$	$\alpha_{\rm CGO} = 12.2  \text{x} 10^{-6} \text{K}^{-1}$	$\alpha_{\rm CGO} = 12.2  \text{x} 10^{-6} \text{K}^{-1}$
	$\alpha_{LSFT} = 16.1 \times 10^{-6} \text{K}^{-1}$	$\alpha_{LSFT} = 16.25 \times 10^{-6} \text{K}^{-1}$	$\alpha_{LSFT} = 17.1 \times 10^{-6} \text{K}^{-1}$
σ <sub>p</sub> (MPa)	387.5	112.7	141.3
σ <sub>m</sub> (MPa)	-258.3	-75.1	-94.2

The elastic modulus of the CGO is approximately twice that of the LSFT. Hence, from the elastic mismatch stresses standpoint the LSFT will attract the crack than the CGO when a load is applied which will eventually leads to the debonding of LSFT/CGO interface. Thus, in LSFT-CGO composite, thermal and elastic modulus mismatch stresses will have a tendency to drive the crack in opposite paths. The crack path is determined by the combined stress fields that result from thermal expansion and elastic modulus mismatches. Therefore, in room temperature, the fracture leads to medium-high energy failure which fractures the CGO grains due to the crack path prefers more interaction with the CGO rather than LSFT. In order to make a stereological analysis of this crack path, a crack was produced in the as received LSFT-CGO membrane which was polished and thermally etched. A typical crack pattern is shown in the Fig 137.

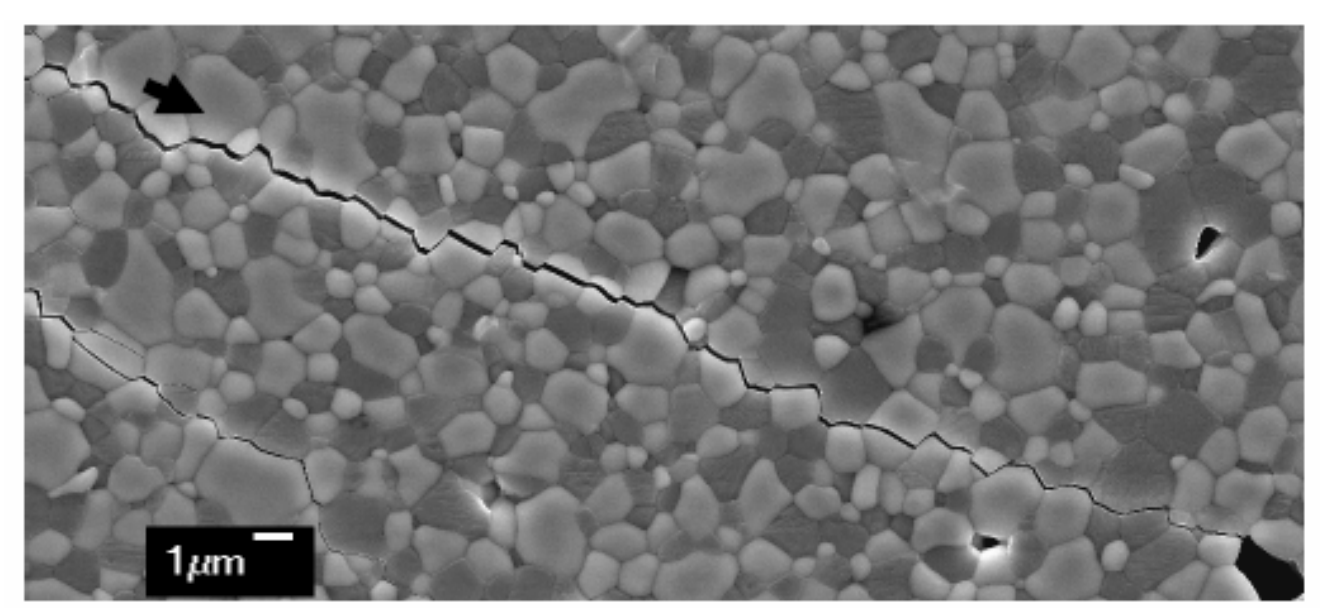


Fig. 137. A typical indentation crack produced on the membrane at room temperature. Arrow mark indicates the direction of crack path.

# 2.4.5 Evaluation of OTM Supports- Yttria Stabilized Zirconia supports

#### 2.4.5.1 Experiment

Yttria Stabilized Zirconia (YSZ Sample A, B and C) flexural strength test specimens of dimensions (3x4x48 mm) were received from Praxair. They were evaluated in-situ in an autoclave mounted on a servo-electric loading frame. Loading was done in an in-house designed 4-point flexure with an outer span of 38.1 mm and inner span of 19.05 mm (ASTM-B). The specimens were already ground and the edges barreled. All flexural strength tests were done by monotonic loading to fracture at a constant cross head speed of 60 µm/min in room temperature. The flexural strength was calculated using the simple beam formula.

Room temperature elastic properties (Young's modulus) of the as-received YSZ samples were determined by the impulse excitation technique with the Buz-o-sonic software by measuring the fundamental vibration frequencies. Young's modulus of the high density, highly pure alumina bars of the same dimensions were also estimated for comparison. The surfaces of the as-received YSZ supports and the post fractured YSZ pieces were characterized by stereo microscope and optical microscope (OM) respectively.

# 2.4.5.2 Flexural strength and Fractography

Table 20 shows the flexural strength and Young's modulus values of the YSZ supports at room temperature. At room temperature the strength of the YSZ-A, YSZ-B and YSZ-C are 179.78 MPa, 164.9 MPa and 113.85 MPa respectively.

Table 20. The flexural strength and Young's modulus values of the YSZ supports

	YSZ-A	YSZ-B	YSZ-C	Al <sub>2</sub> O <sub>3</sub>
Flexural Strength (MPa) (SD)	179.78 (4.87)	164.9 (4.15)	113.85 (7.5)	-
Young's modulus (GPa) (SD)	57.56 (0.44)	40.2 (0.26)	19.7 (0.16)	366.7 (0.67)

YSZ-A exhibits the highest flexural strength value among all YSZ supports. The YSZ-C exhibits the lowest strength among the supports. It is also interesting to note that the elastic properties of the supports are significantly different from each other. The YSZ-A has the Young's modulus of 57.56GPa which is higher than values obtained for the rest of the supports. The elastic properties of this porous YSZ supports are closely matching with the published results for the porous Ce-TZP using Dynamic Mechanical Analysis.

The fracture surfaces of the YSZ supports were studied initially by the Stereo microscope for understanding the fracture origin. Normally surface or volume flaws act as a fracture origin. In YSZ-B and YSZ-C the compression curls are slightly noticeable. In all 3 samples the pores are uniformly distributed and no significant machining flaws could be observed.

#### **Experiment:**

Yttria Stabilized Zirconia (YSZ Sample A, B and C) flexural strength test specimens of dimensions (3x4x46.6 mm) were received from Praxair. The crystal structure in the YSZ samples was analyzed with x-ray diffraction (XRD) studies, using a Rigaku diffractometer with 0.15418 nm Cu  $K_{\alpha}$  radiation. Hardness of the samples was measured by the Vicker's indentation method with a load of 1 kg for 10s.

The strength of the specimens was evaluated in-situ in an autoclave mounted on a servo-electric loading frame. Loading was done in an in-house designed 4-point flexure with an outer span of 38.1 mm and inner span of 19.05 mm (ASTM-B). The specimens were already ground and the edges barreled. All flexural strength tests were carried out by monotonic loading to fracture at a constant cross head speed of  $60 \text{ }\mu\text{m/min}$ . The effect of temperature on strength was studied by breaking the samples at elevated temperatures. The sample was allowed to rest at a specific temperature for 1 hr prior to the application of the load. The flexural strength was calculated using the simple beam formula.

Thermal expansion of the YSZ samples is important to analyze high temperature mechanical properties such as modulus of elasticity. Hence, thermal expansion behaviors of the YSZ supports were studied and the coefficient of thermal expansion was estimated in air using a dilatometer (Netzsch 402PC dilatometer).

#### **Results:**

## *X-ray diffraction:*

Fig. 138 compares the x-ray diffractograms observed for the pulverized YSZ samples. All the three samples show strong peaks of YSZ in the tetragonal (P42/nmc) crystal structure. The lattice parameters, a and c and lattice volume,  $V_0$  observed in the three samples are given in Table 21.

Table 21. Lattice parameters and lattice volume of YSZ supports

Samples	a (nm)	c (nm)	$V_o (nm^3)$
Composition A	0.3614	0.5191	0.0678
Composition B	0.3602	0.5171	0.0671
Composition C	0.3606	0.5178	0.0673

The sample A, having a porosity of  $\sim 35\%$ , shows tetragonal YSZ peaks with a = 0.3614 nm and c = 0.5191 nm ( $V_o = 0.0678$  nm<sup>3</sup>). The sample B with a higher porosity of  $\sim 36\%$  shows YSZ peaks with slightly reduced lattice parameters a = 0.3602 nm and c = 0.5171 nm ( $V_o = 0.0671$  nm<sup>3</sup>). Sample C with a still higher porosity value of  $\sim 55\%$  shows YSZ peaks with a = 0.3606 nm and c = 0.5178 nm ( $V_o = 0.0673$  nm<sup>3</sup>).

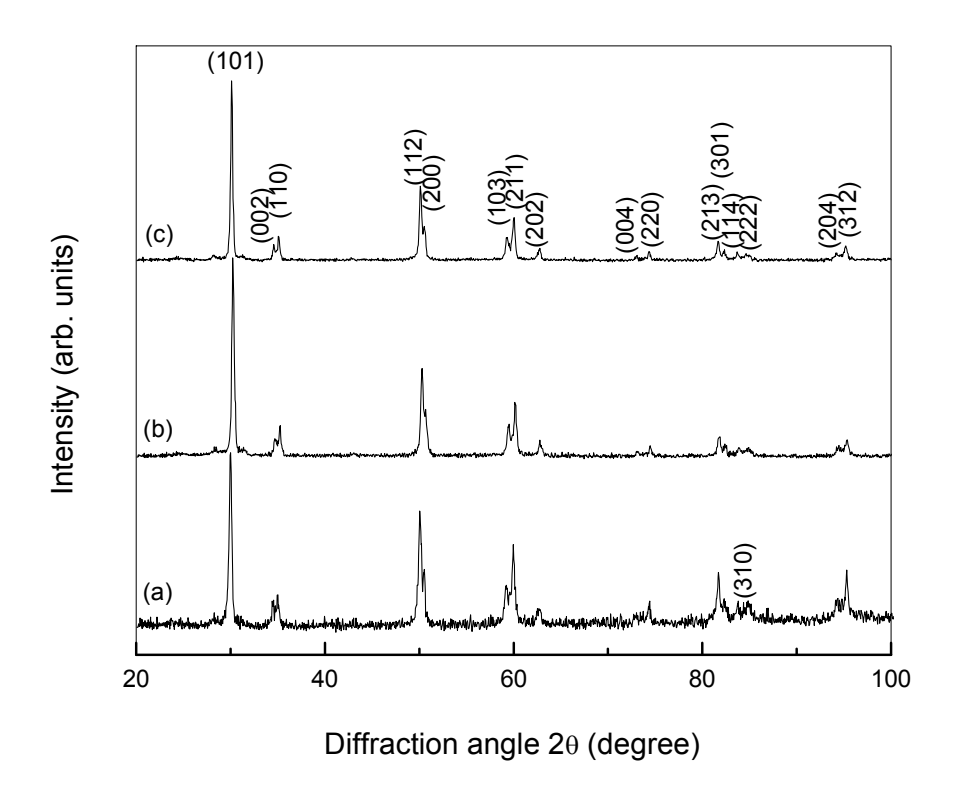


Figure. 138. The X-ray diffractograms of the pulverized YSZ supports: (a) Composition A, (b) Composition B and (c) Composition C.

The average hardness values of YSZ supports measured by the Vicker's indentation method are given in Table 22.

Table 22. Hardness values of the YSZ porous supports

Samples	Hardness (GPa)	Standard deviation (GPa)
Composition A	1.31	0.341
Composition B	0.71	0.140
Composition C	0.56	0.081

As expected, the less porous sample A has the highest hardness value. It is also observed that the scattering in the hardness values decreases significantly in the highly porous samples B or C.

# **Flexural Strength:**

The flexural strengths of the YSZ-composition C supports were estimated at 500°C and 900°C in air. The strengths of the composition B and C were estimated only at 900°C in air and the results were compared with the respective room temperature flexural strengths of the supports.

Fig. 139 shows the effect of temperature on the strength of the YSZ-C supports. Typical strength-displacement curves of the Composition C -YSZ supports at three different test temperatures are shown in Fig. 139a. The loading curves did not show any evidence of non-linear deformation before fracture even at high temperature. However, the failure occurred catastrophically. The flexural strength of the YSZ-C decreases drastically with increasing test temperature. The average strength values are summarized in Table 22. At 500°C, the strength decreases almost to half of its room temperature value. At 900°C, the support is very fragile and fails at a very low load. Porosity of the YSZ-C support is  $\approx 55\%$  with a median pore diameter of 8 $\mu$ m. This higher percentage of porosity with large median pore size causes failure at comparatively lower loads at elevated temperatures. Fig. 140 shows the typical strength-displacement curves of YSZ-A (a) and YSZ-B (b) at room temperature and at 900°C in air. The average strength values of these supports are summarized in Table 22.

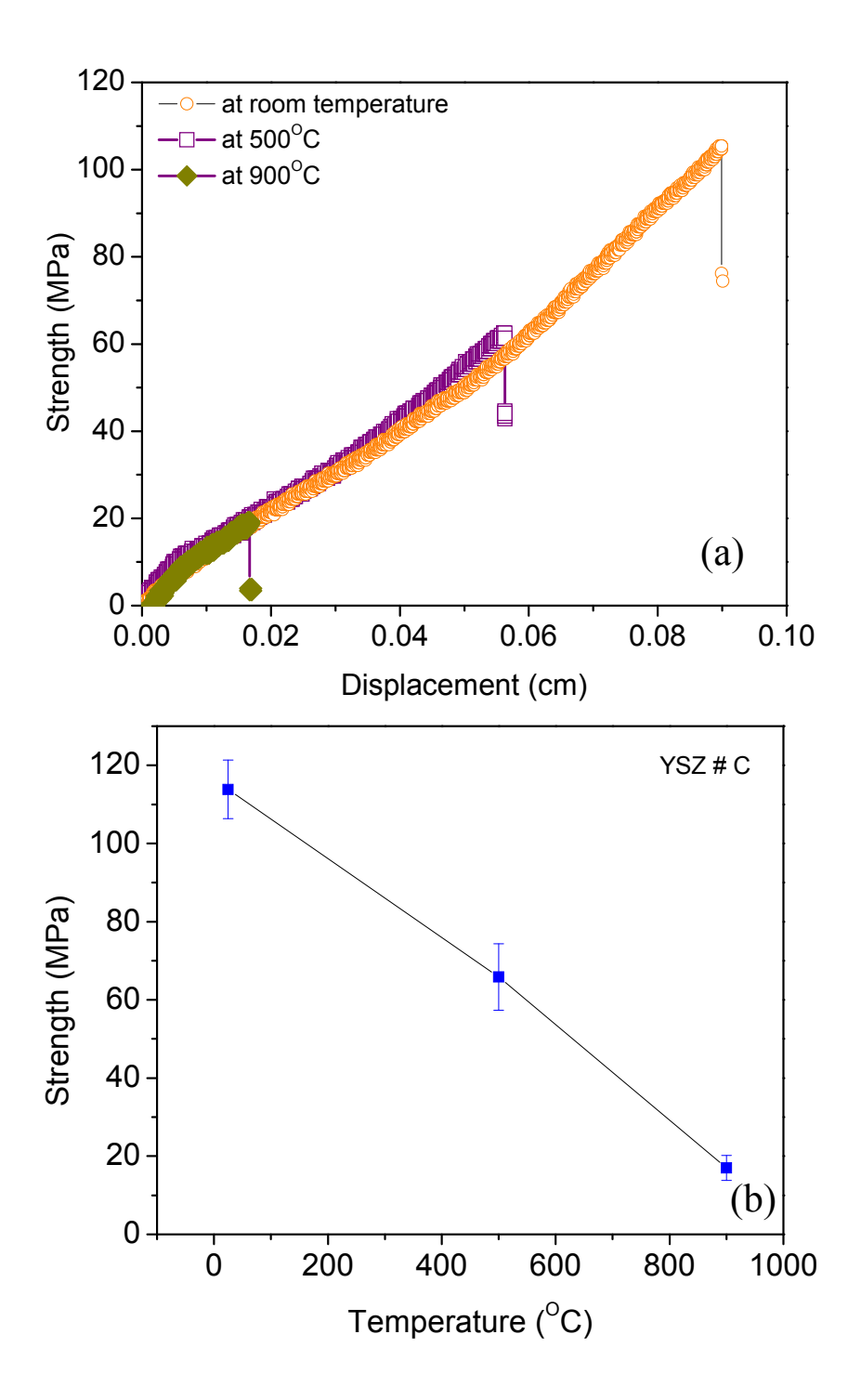
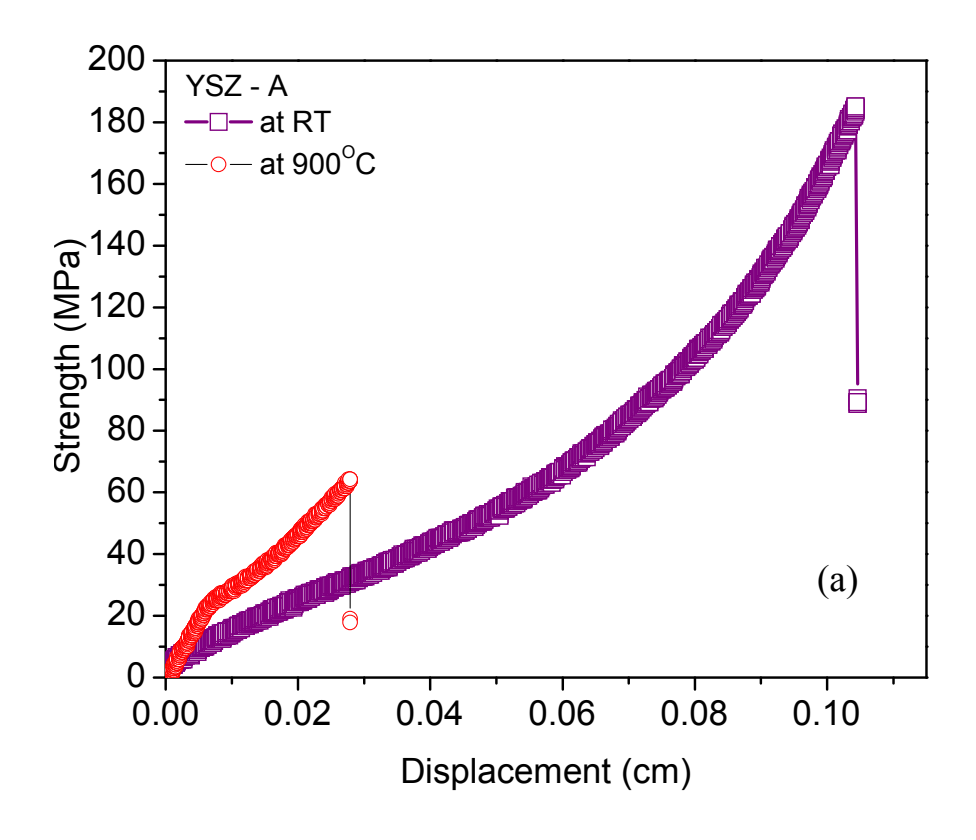


Figure 139. Effect of temperature on strength of YSZ-C supports; typical strength- displacement curves (a) and strength of YSZ-C as a function of test temperature.



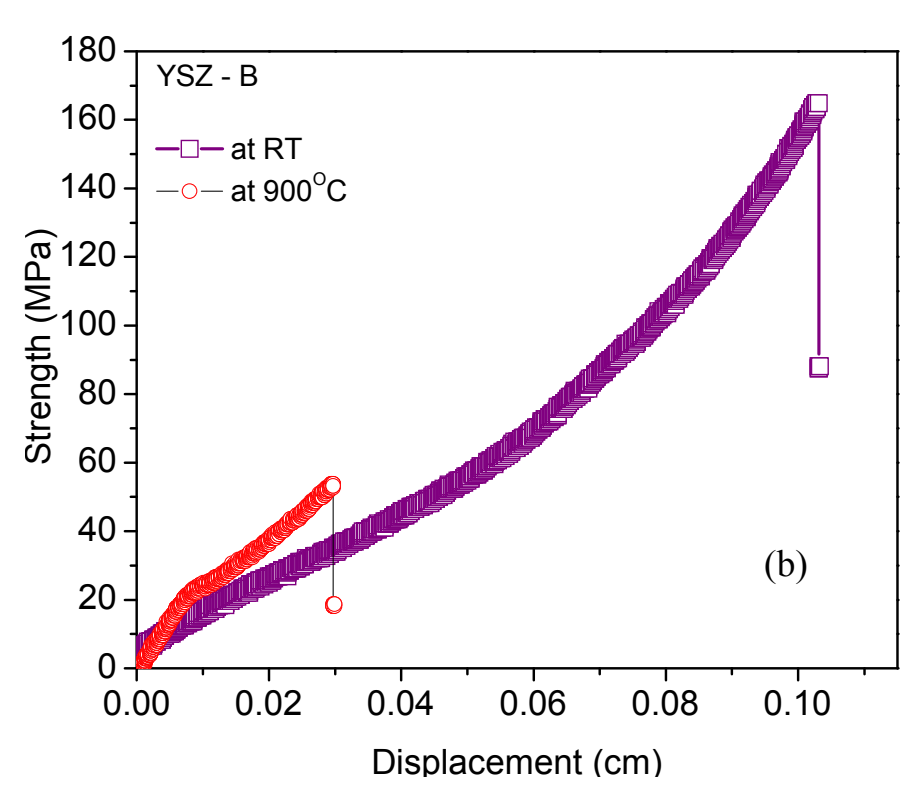


Figure 140. Strength- displacement curves of YSZ- A (a) and YSZ- B (b) at room temperature and at 900°C in air.

Table 23. Average flexural strength values of the YSZ supports at room temperature and elevated temperatures.

Composition	Flexural Strength, MPa (SD)			
	RT	500°C	900°C	
YSZ - A	179.78 (4.8)	-	60.71 (7.8)	
YSZ - B	164.9 (4.2)	-	53.96 (9.4)	
YSZ - C	113.85 (7.5)	65. 86 (8.5)	16.99 (3.2)	

The strength of the YSZ - A and B are also significantly affected by the temperature. The supports were not evaluated at 500°C, however, they exhibit a severe reduction in their strength values when they are tested at 900°C in air.

The thermal expansion behaviors of the all three YSZ supports are shown in Fig 141. The experiments were conducted in air from room temperature to 1300°C. The coefficient of thermal expansion at 1200°C is approximately 12.5x 10<sup>-6</sup>K<sup>-1</sup> and all three supports exhibit almost a similar TEC values. The coefficient of thermal expansion curves of YSZ- A and B exhibit a shrinkage above 1300°C which may be due to sintering of the materials.

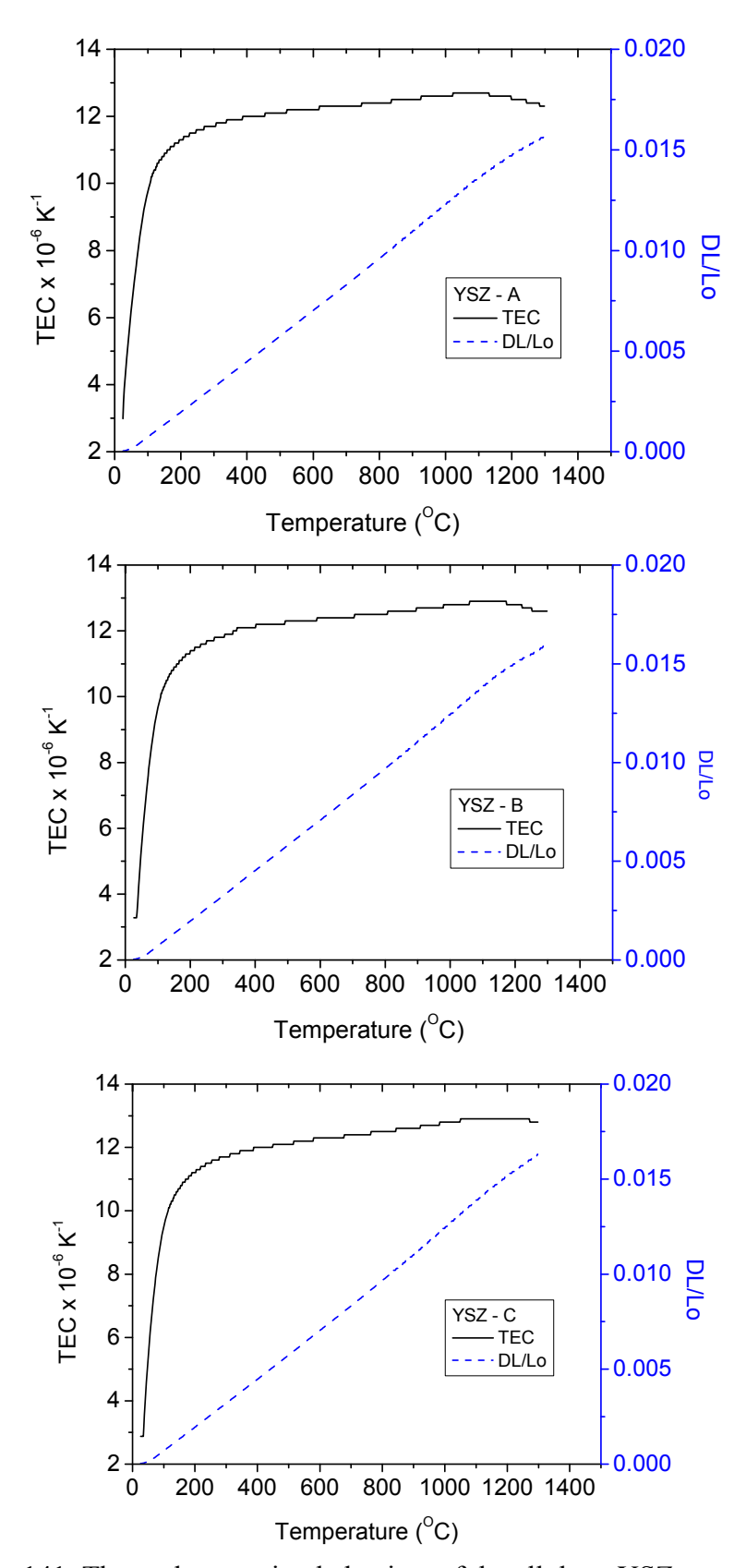


Figure 141. Thermal expansion behaviors of the all three YSZ supports in air.

# 2.4.5.3 Slow crack growth studies:

Measuring the static fatigue (SCG) for specimens containing natural flaws is presumably the closest one can get to mimic the real service application. In principle the test involves applying a mode I, plan strain static stress in an appropriate environment and measuring the time to failure. By repeating the measurement for a different applied stress, the υ-K curve can be established using fracture mechanics. However, the disadvantage of this method is that it can be extremely time consuming. Dynamic fatigue principally generates the same results except the testing time is shortened by testing at several constant stress rates and fracture mechanics may be used to back out the υ-K relationship. In this study the samples were fractured at various loading rates such as 6, 60, 600 μm/min and 1.2 mm/min at room temperature. Loading was done in an inhouse designed 4-point flexure with an outer span of 38.1 mm and inner span of 19.05 mm (ASTM-B). The specimens were already ground and the edges barreled. All flexural strength tests were carried out by monotonic loading to fracture at a constant cross head speeds mentioned above. The flexural strength was calculated using the simple beam formula. The fracture surfaces and the microstructures of the YSZ supports were studied using SEM. The asreceived samples were sputtered with gold prior to the analysis.

#### **Results:**

Figures 142 – 144 show the effect of loading rate on the 4-point bend strength of the YSZ supports. The composition-A was studied at 3 different loading rates such as 600, 60 and 6μm/min. The YSZ-A exhibits a relatively strength when the loading rate is very slow. Similarly, all 3 materials fractures at higher load and exhibit a higher strength value when the loading rate is higher. The decreasing strength values with decreasing loading rate may be interpreted as the result of SCG in the YSZ. At the same time, only the loading rates that are lower 1.2 mm/min reveal the SCG behavior in all 3 compositions. In Composition A and C the loading rate, 1.2 mm/min was not shown as it can not be correlated to the SCG behavior. The SCG is better revealed in Composition A from the loading rates plotted. This may be due to the porosity of the YSZ-A which is lesser compared to the other supports. The highly porous

Composition C with porosity of 55% shows a marginal strength reduction as the loading rate decreases. In the highly porous microstructure even a small event of SCG can lead to the formation critical flaw that causes the failure.

Fig. 145 shows the microstructures of all 3 compositions. The YSZ-C exhibits a highly porous structure made up of poorly sintered particles. Even the donut shaped spray dried YSZ particles could be observed in the microstructure (Fig. 145d) randomly. The average grain size of the YSZ-C is 100nm which is finer than the other 2 compositions. It may be either by lower sintering temperature or finer stating powders used for the preparation of YSZ-C supports.

The 4 point bend experimental conditions and the corresponding strength values are listed in Table 23 and the fracture surfaces are shown in Fig. 146 to Fig. 148. Even though the test temperatures had a significant influence on the flexural strengths of the supports studied in this work, it was not reflected in the fracture morphology in general. The higher magnification fracture morphologies show (shown in Fig. 149 and 150) the collapse of porous network and fracture of agglomerates to some extent. This is quite normal for these type of materials. Fig. 150 early shows the fracture of necks that were formed between the spherical or donut shaped agglomerates.

In all 3 compositions the fracture originated mostly from the surface flaws developed during machining. In most of the YSZ-C samples tested, the strength limiting flaws are of surface of the samples developed during processing of the samples.

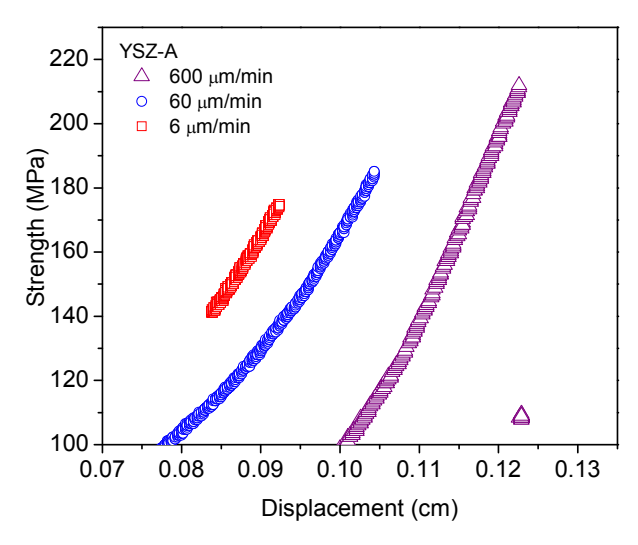


Fig. 142. Effect of loading rate on the flexural strength of the YSZ-A supports

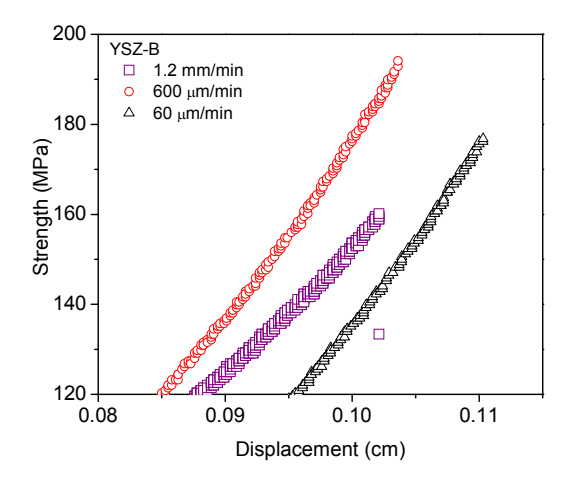


Fig. 143. Effect of loading rate on the flexural strength of the YSZ-B supports

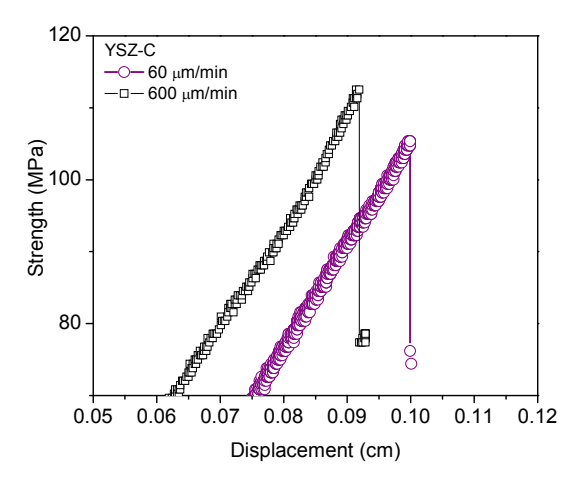


Fig. 144. Effect of loading rate on the flexural strength of the YSZ-C supports

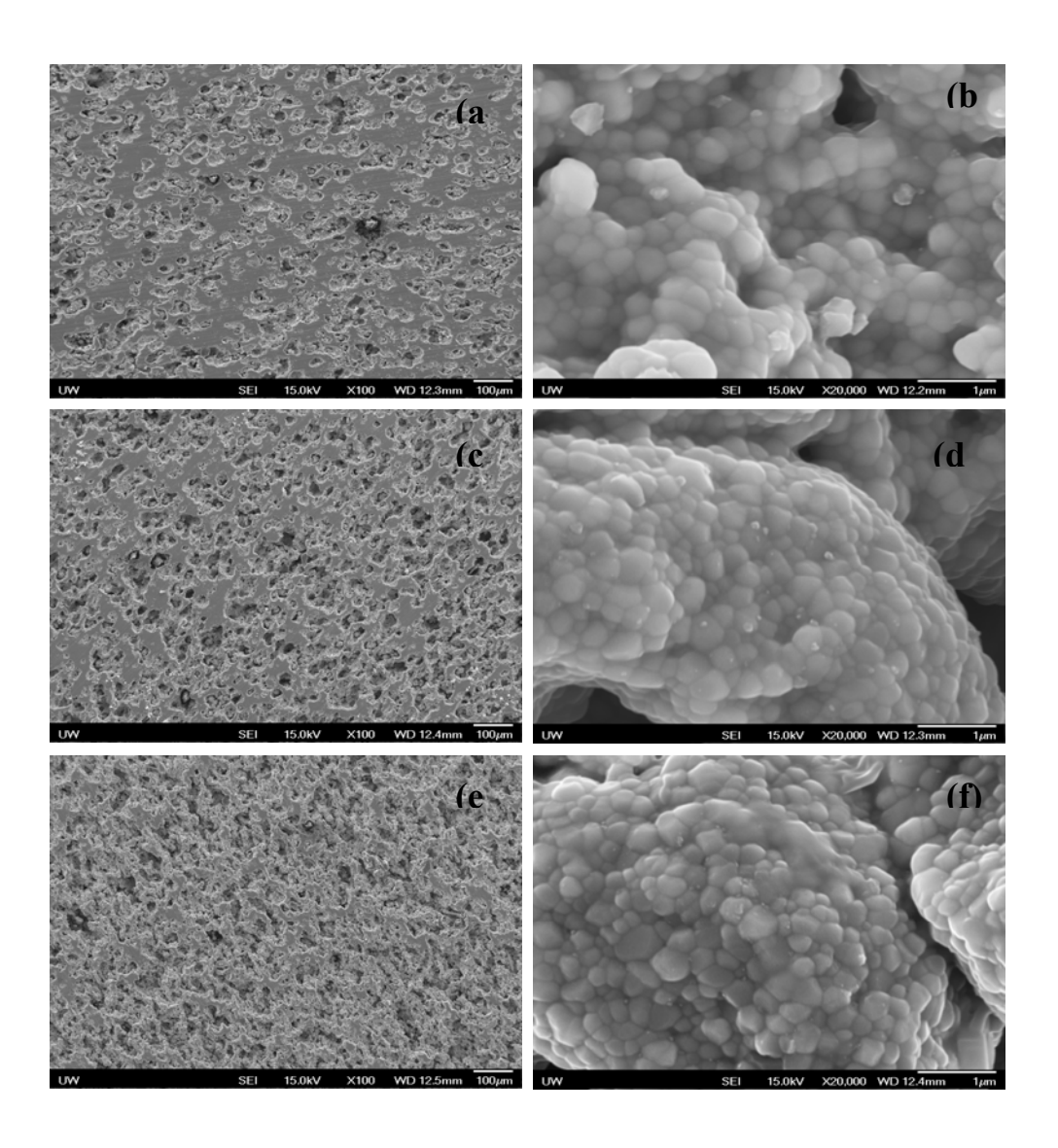


Fig. 145. Microstructure of the YSZ supports; Composition A (a and b), Composition B (c and d) and Composition C (e and f).

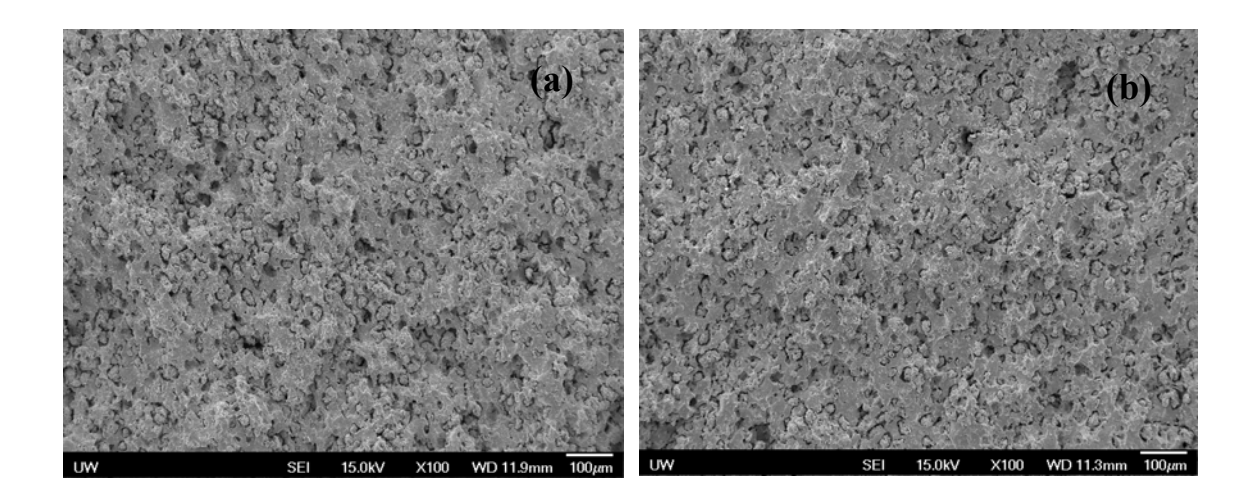


Fig. 146. Fracture surfaces of YSZ-A at room temperature (a) and at 900°C (b) in air

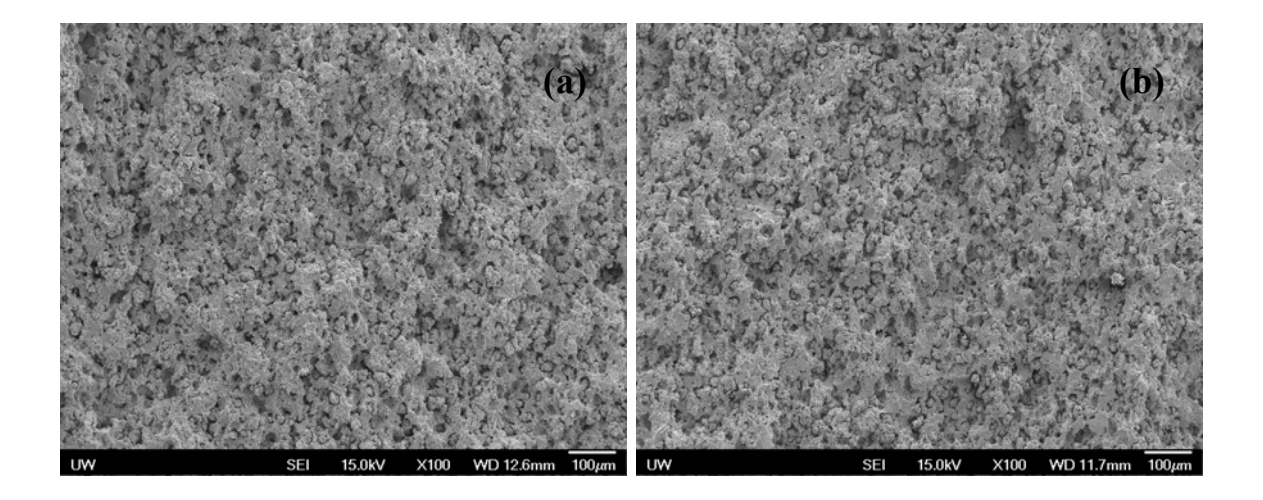


Fig. 147. Fracture surfaces of YSZ-B at room temperature (a) and at 900°C (b) in air

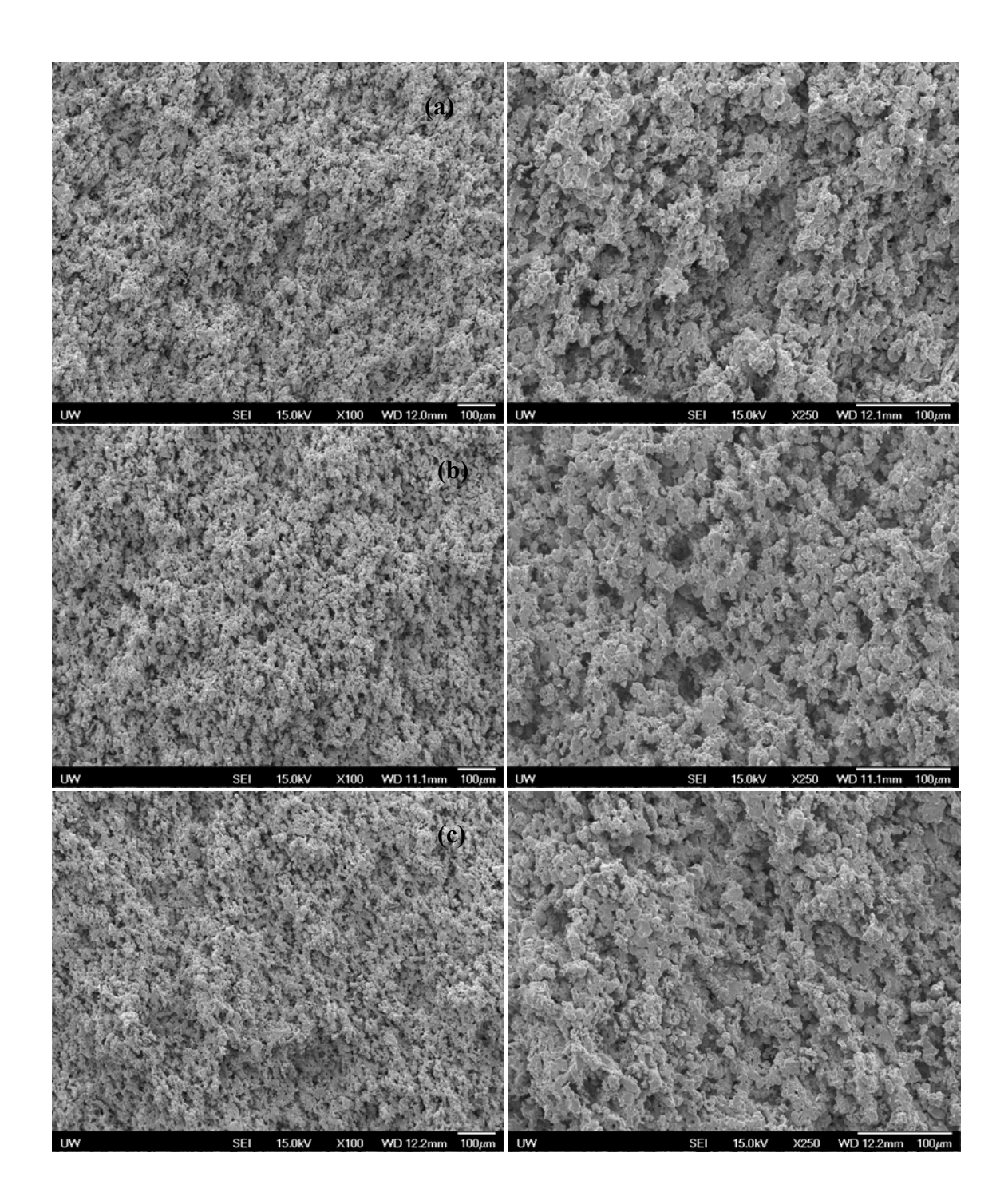


Fig. 148. Fracture surfaces of YSZ-C at room temperature (a), at  $500^{\circ}$ C (b) and at  $900^{\circ}$ C (c) in air

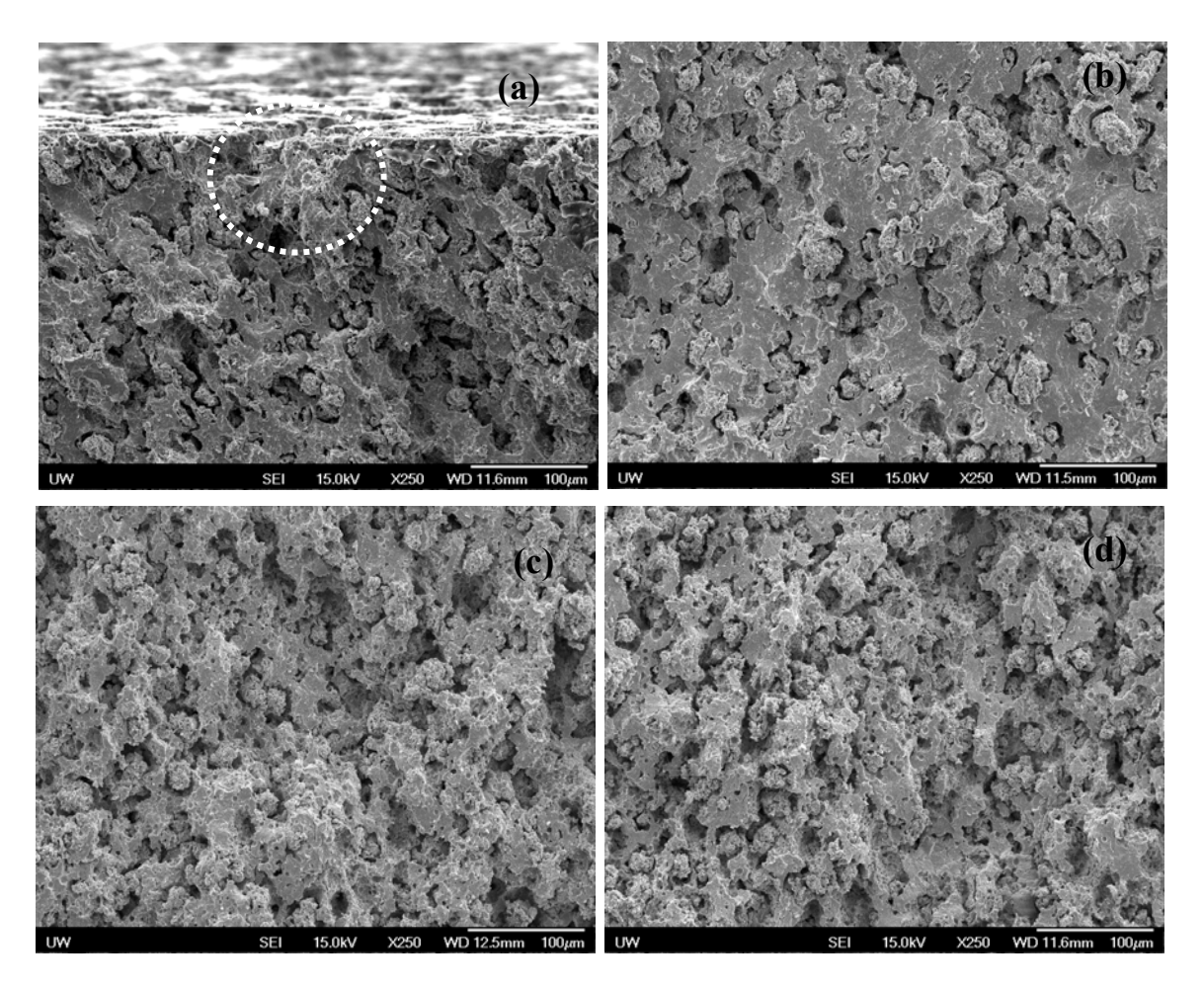


Fig. 149 Fracture behavior of YSZ- A in room temperature (a) and at 900°C (b); YSZ-B in room temperature (c) and at 900°C (d). The fracture origin is marked in Fig. (a).

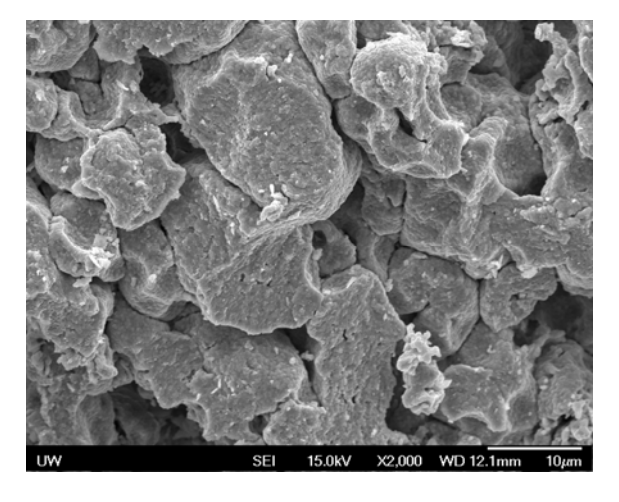


Fig. 150. Fracture behavior of agglomerates at YSZ-C at 900°C in air

#### 2.5 CONCLUSIONS

Progress of task on mechanical properties in chemical environment has been made on two important fronts: a) fundamental understanding of the mechanical behavior of the parent perovskite compositions and b) evaluation of OTM under operating conditions desired by the industry. The studies are aimed at generating important parameters for developing a comprehensive model in reliability estimates for the membranes. On exposure to specific environment (Air, N<sub>2</sub>/Air), marked changes in toughness, hardness and strength were observed. In addition, healing of the radial cracks emanating from the indent was observed in some materials. The healing was attributed to the reduction in residual stresses and also onset of compressive stresses generated due to chemical expansion of the lattice in some materials.

Decrease in oxygen occupancy in LSFT at the reducing conditions was observed from TGA which in turn favored a chemical expansion and induced a stress in the matrix. The marginal decrement in the toughness for the membranes exposed to reducing conditions was correlated to the increased hardness and decreased elastic modulus. The severe degradation in strength of the membranes at 1000°C and in reducing conditions and the transition in the fracture behavior in the dual phase (LSFT-CGO) composite were discussed in the light of residual stresses that arise due the thermal and elastic mismatch of the constituent phases. Although no decomposition was observed in the LSFT, Fe rich precipitates were observed along the boundaries which have no apparent influence on the mechanical properties of the dual phase membranes.

The flexural strengths of the porous YSZ supports were evaluated at room temperature and at elevated temperatures. At elevated temperatures the strength of the supports decreases drastically. The composition C exhibits a very inferior strength value at 900°C in air among all the three supports. For all three compositions the porosity significantly affects the flexural strength of the supports at elevated temperatures.

#### 2.6 LIST OF ACRONYMS AND ABBREVIATIONS

 $\begin{array}{ll} LSF & La_{0.6}Sr_{0.4}FeO_{3-x} \\ LSC & La_{0.8}Sr_{0.2}CoO \end{array}$ 

 $\begin{array}{lll} LSFCO\text{-}3 & La_{0.2}Sr_{0.8}Fe_{0.8}Cr_{0.2}O_{3\text{-}x} \\ LSFT & La_{0.2}Sr_{0.8}Fe_{0.6}Ti_{0.4}O_{3\text{-}x} \end{array}$ 

LSFT-CGO  $La_{0.2}Sr_{0.8}Fe_{0.6}Ti_{0.4}O_{3-x}$  -  $Ce_{0.9}Gd_{0.1}O_{2-\delta}$ 

YSZ yttria stabilized zirconia

XRD X-ray diffraction

TGA thermogravimetric analysis
TEC thermal expansion coefficient

#### 2.7 REFERENCES FOR CHAPTER 2

- 1 Niihara K., Morena R., and hasselman D.P.H. (1982), 'Evaluation KIC of brittle solids by the indentation method with low crack-to-indent ratios,' J. Mater.Sci.Lett., 1 (1982) 13-16.
- 2 A. G. Evans and E. A. Charles, "Fracture Toughness Determinations by Indentation," J. American. Ceram. Soc., 59 [7-8] 371-372 (1976).
- 3 Zhou et al, OTM annual report 2005, page 10
- 4 Faber K.T., "Toughening of Ceramic Materials by Crack Deflection Processes", Ph.D. Dissertation; pp 15-25. University of California, Berkeley, CA, 1982.
- 5 Krstic V.V and Nicholson, P.S. "Toughening of Glasses by Metallic Particles," *J.Am.Ceram.Soc.*, **64(9)** 499-504 (1981)
- 6 Evans. "The role of inclusions in the fracture of ceramic materials". *J.Mater. Sci.* **9(7)**,1145-52, 1974.
- 7 Tirosh, J and Tetelman, A.S., "Fracture Conditions of Crack Approaching a Disturbance," *Int. J. Fract.* **12[1]** 187-99 (1976).
- 8 Hsueh, C.H., "Sintering Behavior of Powder Compacts With Multiheterogeneities," *J.Material, Sci.*, **21**, 2067-72 (1986)

# 2.8 Publications out of this part of work (chapter 2)

1. Nagendra, N. and Bandopadhyay, S., Strength and Fracture Characterization of Perovskite Tubes *in Program and Abstracts of PACRIM 4*, An International Conference on Advanced Ceramics and Glasses. Maui Hawaii, The American Ceramic Society, 2001, p 138.

- 2. Nagendra, N. and Bandopadhyay, S., Strength and Fracture Characterization of Perovskite Oxide Tubes in The Fourth Pacific Rim International Conference on Advanced Materials and processing (PRICM4). Ed. By S. Hanada, Z. Zhong, S.W. Nam and R.N. Wright, The Japan Institute of Metals 2001, pp 2803-06.
- 3. N. Nagendra, R.F. Klie, N.D. Browning, and S.Bandopadhyay, "Fracture characterization in tubular LSFCO ceramic membranes", *Mater. Sci. Eng. A.*, 341 (1-2) (2003) 236-246.
- 4. N. Nagendra, and S.Bandopadhyay, "Strength and toughness of LSFCO membranes exposed to reducing conditions," *Scripta mater.*, 48(1), 37-42(2003).
- 5. N. Nagendra, and S.Bandopadhyay, "Room and elevated temperature strength of perovskite membrane tubes", *J. Eur. Ceram. Soc.*, 23(9), 1361-1368 (2003).
- 6. Nagendra, N. and Bandopadhyay, S., Fracture Strength and Crack Growth In Tubular Perovskite Membranes, In the Proceeding of the 26<sup>th</sup> Annual International Conference on Advanced Ceramics and Composites, American Ceramic Society, 2002, **23(3)**, 775 782.
- 7. Thangamani Nithyanantham and S. Bandopadhyay, "Effect of Temperature and Environment on the Mechanical Properties of LSFT-CGO Membranes" Advances in Solid Oxide Fuel Cells III, Ceramic Engineering and Science Proceedings, Volume 28, Issue 4, 2007, Jonathan Salem and Dongming Zhu, General Editors; Narottam P. Bansal, Editor. Page 377-388
- 8. Nagendra Nagabhushana, Jing Zhang, Thangamani Nithyanantham, Sukumar Bandopadhyay "Slow Crack Growth Analyses of Oxygen Transport Ceramic Membranes" in Functional Nanoscale Ceramics for Energy Systems, edited by E. Ivers-Tiffee and S. Barnett (Mater. Res. Soc. Symp. Proc. Volume 1023E, Warrendale, PA, 2007), 1023-JJ08-03
- 9. Thangamani Nithyanantham and S. Bandopadhyay, "Strength and Fracture characterization of Dual-phase (LSFT-CGO) Membranes" Communicated to Materials Science & Engineering A
- 10. Nagendra Nagabhushana, Jing Zhang, Thangamani Nithyanantham, Sukumar Bandopadhyay, "Fracture Gradient in Tubular LSFCO Ceramic Membranes under Graded Reducing Conditions" Communicated to Materials Science & Engineering A

# Chapter 3: Preparation and Characterization of Dense Ceramic oxygen Permeable Membranes

Yong-Wook Sin, H. U. Anderson Materials Research Center, University of Missouri-Rolla, Rolla, MO 65401

#### 3.1 Introduction

The search for the new generation of oxygen transport membrane (OTM) materials and an understanding of the mechanisms of oxygen vacancy generation and oxygen reduction are of great importance to increase energy efficiency and improve long term stability. One technique to improve the materials' properties is to tailor its microstructure, for example its porosity, tortuosity, composite connectivity etc; the other technique is to design the OTM to be a mixed ionic and electronic conductor (MIECs) [1]. The University of Missouri at Rolla (UMR) studied high temperature structural and electrical properties of the new materials selected for the OTM in order to improve oxygen flux of membranes, with an emphasis on thin film membranes. After extensive studies of candidate materials, lanthanum ferrites were selected and considered as the favorite materials for oxygen transport membrane and of particular interest in fundamental and practical research, partly because this series possesses a wide range of solid solutions. This report includes the electrical conductivity, neutron diffraction, Mössbauer spectroscopy, Seebeck coefficient, thermogravimetric measurements on La<sub>1-x</sub>Sr<sub>x</sub>FeO<sub>3</sub> (LSF) and La<sub>0.2</sub>Sr<sub>0.8</sub>Fe<sub>1-y</sub>Ti<sub>y</sub>O<sub>3</sub> (LSFT).

#### 3.2 Experimental

#### 3.2.1. Electrical Conductivity

The D.C. four point probe electrical conductivity measurement method was used. A Keithley Model 2400 Series Source Meter was used as a constant current source and a Keithley 195A Digital Multi-meter was interfaced with a personal computer that was used to collect the potential difference between two inner platinum wires wrapped around the samples. Electrical conductivity and Seebeck coefficient of LSFT were measured in air as a function of temperature.

## 3.2.2. Thermogravimetric Analysis (TGA)

The thermogravimetic apparatus used in the current experiment is a Cahn balance (Model TG-171) which is located in the Electronic Materials Applied Research Center in University of Missouri - Rolla. The reliable accuracy limit of Cahn balance in UMR is approximately ±0.4 milligrams or ±7.5 x 10<sup>-4</sup> moles oxygen even though the minimum detection limit is ±1 microgram or ±1.8 x 10<sup>-6</sup> moles oxygen for La<sub>0.2</sub>Sr<sub>0.8</sub>Fe<sub>0.55</sub>Ti<sub>0.45</sub>O<sub>3-δ</sub> (LSFT). The TGA consists of a balance from which up to 100 grams of sample can be suspended in a vertical furnace that is sealed from the atmosphere. The atmosphere is controlled by using mixtures of different gases such as oxygen, air, argon, carbon monoxide and carbon dioxide. The gas flow rate is also controlled by using MFC (mass flow controller by MKS) and MKS 244A muti-channel analog controller. A personal computer and TGA operation program from Cahn controls temperature schedule and collect data for weight change and draw plots as a function of time.

In the current experiment, a 5 grams sample of La<sub>0.2</sub>Sr<sub>0.8</sub>Fe<sub>0.55</sub>Ti<sub>0.45</sub>O<sub>3-δ</sub> powder was used for thermogravimetic measurement. The same sample was used for all the experiments in this report. The ratios of carbon monoxide and carbon dioxide gases were maintained by a gas mixing apparatus which allowed the mixtures to flow into the furnace tube to produce the desired oxygen activity.

The gas flow rate of 0.2 cm/sec of was used to minimize the buoyancy effect caused by the positive gas pressure due to the gas flow from the bottom of the alumina tube that is vertically mounted in the TGA furnace system. The powder sample was placed into an alumina bucket that was suspended inside of the vertical furnace tube with a sapphire wire. The other end of the wire is attached to the balance located on the top of the TGA apparatus. The CO and  $CO_2$  gases were separately delivered from their cylinders at a certain flow rate into a gas mixing chamber filled with hundreds of small hollow glass tubes (the length of the glass tubes is  $0.5 \sim 1$  cm) and were thoroughly mixed with argon in the same gas mixing chamber to dilute the  $CO/CO_2$  gas mixture before entering the furnace tube. The dilution ratio of the  $CO/CO_2$  mixture and argon is

10% / 90%. The oxygen activities were monitored by using a zirconia oxygen sensor in a separate furnace with air as the reference gas. The relationship for oxygen activity is

$$E_{v} = -\frac{RT}{4F} \ln \frac{PO_{2}^{'}}{PO_{2}^{"}}$$

where  $PO_2$  and  $PO_2$  are the oxygen activity in the measuring cell and in air, respectively, and T is the absolute temperature of the specimen. Thermodynamically calculated oxygen partial pressures are listed in Table 23.

Table 23. The oxygen partial pressure used in this experiment at 1000°C

	$E_{v}$	PO <sub>2</sub> at 1000°C
Air		0.21
0.01% O <sub>2</sub> – Balance Ar	0.187	1.19E-4
CO/CO <sub>2</sub>	0.690	2.48E-12
CO/CO <sub>2</sub>	0.771	1.29E-13
CO/CO <sub>2</sub>	0.831	1.45E-14

#### 3.2.3. Neutron Diffraction

Neutron diffractometry is a powerful tool for studies of crystal structures of materials containing elements of very dissimilar atomic number or neighboring elements in the periodic table, particularly on the ceramic materials in OTMs with heavy cations and light oxygen anions [2-4]. Neutron-diffraction techniques have proven to be useful methods to analyze thermal motion and disorder because of (1) the lack of electronic interference and because (2) the neutron form factor is independent of the scattering angle. In addition, neutron diffraction has an added advantage at non-ambient temperatures over conventional X-ray analysis. A high temperature furnace for neutron-diffraction measurements, designed and developed at UMR was used for in situ study of the OTM materials. Mössbauer spectroscopy was also used to characterize the perovskite type ferrites, in terms of the crystal structure, oxygen occupancy, magnetic moment, and Fe valence state.

# 3.2.4. Mössbauer Spectroscopy

Mössbauer spectroscopy can reveal information on chemical bonding, valence state and magnetic properties of Fe-containing systems (ferrites). Therefore, this method can provide direct information on the electron density at the nucleus and can often be interpreted to give unequivocal information about the valence state of the Fe ion.

#### 3.2.5. XRD

Phase purity and crystalline structure of each composition were examined by X-ray powder diffraction (XRD) using Cu-Ka radiation. The crystalline phases in various cathodes were determined by XRD (XRD – 2000. Scintag Inc.)

## 3.2.6 Impedance Spectroscopy

The ASR of each part of the SDC symmetrical cells (for example, electrolyte, cathode, current collector and interfaces between those layers) was evaluated using an impedance analyzer (Solartron Analytical 1470 Cell Test) in the frequency range of  $0 - 10^6$  Hz. This test was very important to estimate how the cell performed during the test.

#### 3.3 Results and Discussion

# 3.3.1. Studies of Ferrites for OTM using Electrical Conductivity, Neutron Diffractometry and Mössbauer Spectroscopy

# 3.3.1.1. Electrical Conductivity of La<sub>1-x</sub>Sr<sub>x</sub>FeO<sub>3-δ</sub>

Electrical conductivity ( $\sigma$ ) is determined by carrier concentration (N), carrier mobility ( $\mu$ ) and charge of the carrier (q) as:

 $\sigma = N \mu q$ 

Carrier concentration in the LSF system is dependent on the acceptor dopant level ( $[Sr_{La}^{\dagger}]$ ) and oxygen vacancy density ( $[V_0^{\bullet \bullet}]$ ) as:

$$N = [Sr_{La}] - 2[V_O^{\bullet \bullet}]$$

In the LSF system, Fe<sup>4+</sup> locates on Fe<sup>3+</sup> sites; therefore, carrier concentration can also be calculated from the Fe valence state. For example, the average Fe valence state is 3.4 in La<sub>0.60</sub>Sr<sub>0.40</sub>FeO<sub>3</sub> (L6SF) thus the carrier density would be 40% of total Fe sites. It will be straightforward to achieve a carrier density of 20% in La<sub>0.80</sub>Sr<sub>0.20</sub>FeO<sub>3</sub> (L8SF) and 45% in La<sub>0.55</sub>Sr<sub>0.45</sub>FeO<sub>3</sub> (L55SF). The highest electrical conductivity is expected in La<sub>0.55</sub>Sr<sub>0.45</sub>FeO<sub>3</sub> because of the highest carrier concentration. Figure 151 shows plots of electrical conductivity of these three compounds measured in air from 200 to 1200°C. The results from Figure 151 are twofold: (1) the electrical conductivity is primarily determined by carrier concentration in the measured temperature regime as ( $\sigma_{L8SF}$  <  $\sigma_{L6SF}$  <  $\sigma_{L55SF}$ ) (2) there exists a maximum conductivity for each compound at a different temperature.

Figure 152 are plots of  $\ln(\sigma T)$  vs. 1/T for L8SF, L6SF and L55SF. Small polaron conduction was proposed for these p type conductor systems, similar to other transition metal perovskites, such as chromites, manganate, and cobaltites. The mobility term can be achieved over the regime where  $\ln(\sigma T)$  is linearly proportional to 1/T (Table 24). Mobility values are similar for the compounds in this study, indicating a similar conduction mechanism in the ferrite system. Co doped ferrites possess a much lower mobility, thus LSCF often has a higher conductivity value than LSF.

Table 24 Activation for mobility of LSF and LSCF

	La <sub>1-x</sub> Sr <sub>x</sub> FeO <sub>3-δ</sub>			$La_{1-x}Sr_xFe_{0.80}Co_{0.20}O_{3-\delta}$			
	x=0.2	x=0.4	L55SF	x = 0.4	x = 0.3	x = 0.2	x = 0.1
$E_h$ (eV)	0.28	0.24	0.23	0.087	0.13	0.16	0.18

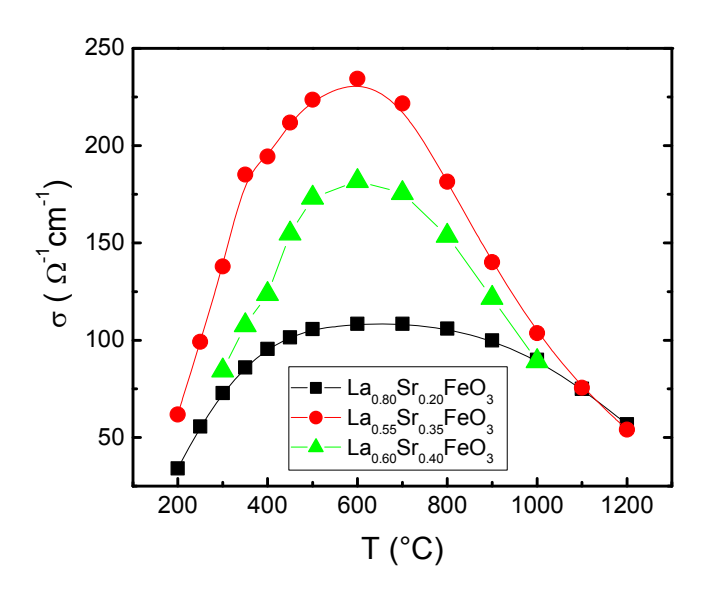


Figure 151 A plot of conductivity ( $\sigma$ ) vs. temperature ( $^{\circ}$ C) for La<sub>0.80</sub>Sr<sub>0.20</sub>FeO<sub>3</sub>, La<sub>0.60</sub>Sr<sub>0.40</sub>FeO<sub>3</sub> and La<sub>0.55</sub>Sr<sub>0.45</sub>FeO<sub>3</sub> measured in air.

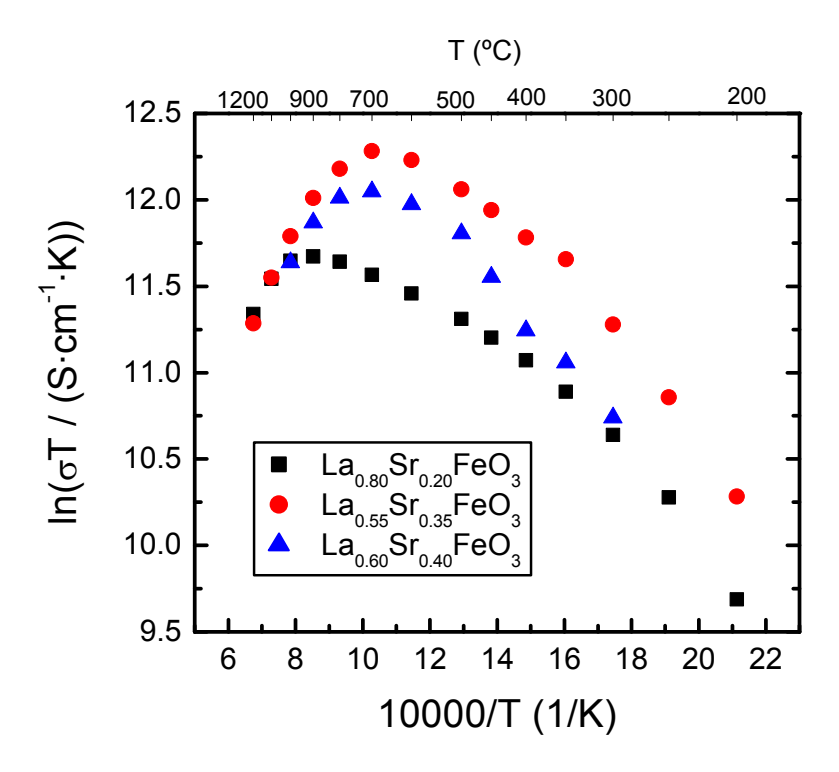


Figure 152 A plot of conductivity  $ln(\sigma T)$  vs. 1/T for  $La_{0.80}Sr_{0.20}FeO_3$ ,  $La_{0.60}Sr_{0.40}FeO_3$  and  $La_{0.55}Sr_{0.45}FeO_3$  measured in air. Activation energy can be calculated from the slope over relative low temperature regime (200 – 500°C)

The maximum conductivity represents the temperature at which the oxygen vacancy concentration starts to influence the carrier concentration. It does not mean that the oxygen vacancy concentration is negligible at this temperature, but that the influence of oxygen vacancy concentration on total carrier concentration is negligible below this temperature and the concentration of oxygen vacancies is so small that their contribution to transport processes becomes minimal. Since oxygen vacancies are required for lower cathodic overpotentials, this temperature also represents the temperature below which, when used as a cathode in solid oxide fuel cells, high overpotentials will be observed. In addition, the maximum in conductivity should indicate the lowest temperature the material can be used as an oxygen permeable membrane.

# 3.3.1.2. Neutron Diffraction and Mössbauer Spectroscopy Study for LSF

#### 3.3.1.2.1 Neutron diffraction pattern and refinement

Figure 153 illustrates typical room temperature neutron diffraction patterns of  $La_{0.60}Sr_{0.40}FeO_{3-8}$  (L6SF) quenched from 1500°C. The most obvious difference between the two patterns is a much stronger low angle (~ 19°) peak, which is caused by the magnetic interaction only. In order to achieve detailed information about the magnetic moment and crystal structure, neutron diffraction data was refined using the FULLPROF program. One study showed that refining the data using the  $R\bar{3}c$  space group could resolve oxygen content. The other study found that refinement in the trigonal space group P-3C1 on the same data resulted in an improvement of the fit parameters, which in turn gave more realistic oxygen occupancy. For example, an observed peak at about 41° for the specimen quenched from 1000°C is not modeled in  $R\bar{3}c$ , which can be fitted in P-3C1. The magnetic moment and unit cell volume however, are found to be essentially independent of the choice of crystallographic model.

# 3.3.1.2.2 Crystallographic Structure

From all the quenched samples, similar patterns to that shown in Figure 153 were observed, showing them to be single phase. Crystal structure at various quenching temperatures is shown in Figure 154, in which a\* represents  $a/\sqrt{2}$  and c\* is  $c/2\sqrt{3}$ . The symmetry of L6SF quenched from 600-1200°C to room temperature remains as rhombohedral (space group R $\bar{3}$ c). The rhombohedral splitting of the peaks becomes not obvious for the specimens quenched from T > 1200°C, which indicates a significant lattice distortion from the rhombohedral cell to the cubic cell. This distortion becomes small (~0.06°) in samples quenched from T > 1300°C. The unit cell volume increases monotonically as the quenching temperature increases. This determination suggests that increasing the unit cell volume (~1.1%) resulted from increasing the oxygen vacancy concentration and ionic radius of Fe ion.

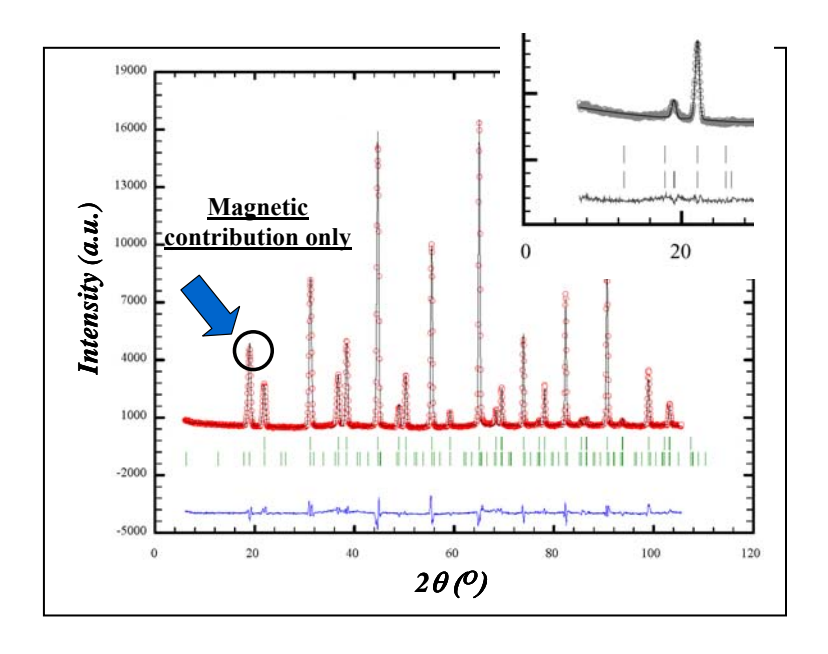


Figure 153 Neutron diffraction of La<sub>0.60</sub>Sr<sub>0.40</sub>FeO<sub>3-δ</sub> quenched from 1500°C. The inserted figure is the low angle part of the sample without quenching.

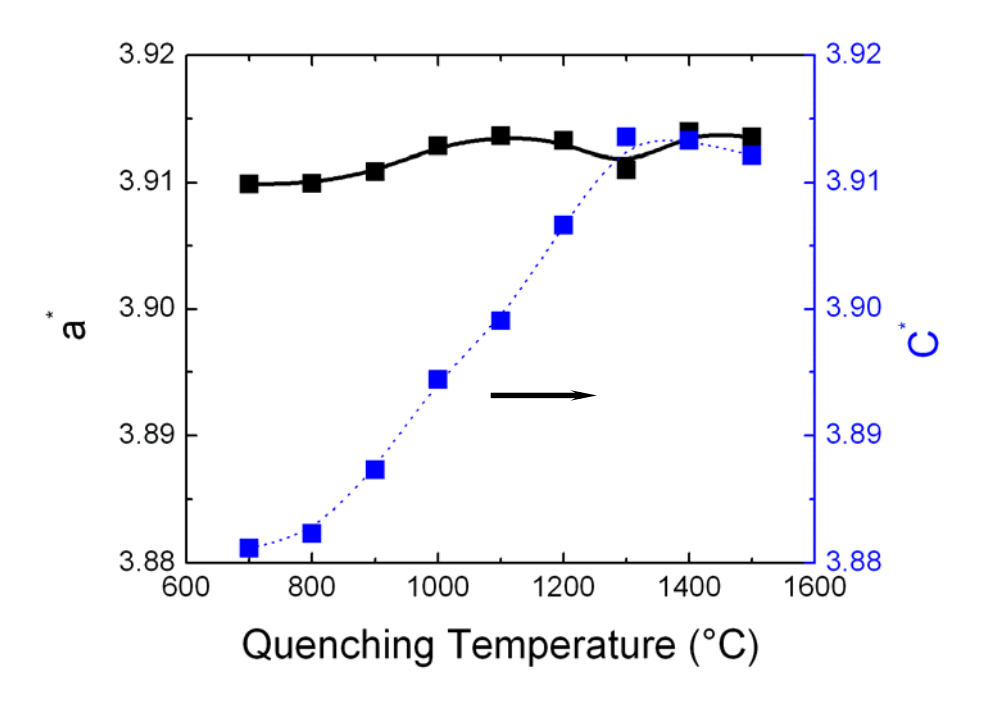


Figure 154 Lattice parameter of La<sub>0.60</sub>Sr<sub>0.40</sub>FeO<sub>3-δ</sub> quenched from various temperatures.

#### 3.3.1.2.3 Local Chemistry of Fe and Magnetic moments

#### Magnetic interaction

 $La_{0.60}Sr_{0.40}FeO_{3-\delta}$  exhibits an antiferromagnetic – paramagnetic transition, hence the magnetic moments on the two Fe sites are constrained to be equal, and the room temperature moment was found to increase from  $1.3\mu_B$  for the sample without quenching to  $3.4\mu_B$  for the  $1500^{\circ}C$  specimen. The reason for the increased magnetic moment is mainly due to the distribution of 3+ and 4+ ions. Since the  $Fe^{4+}$  ions have small or zero moments, the exchange interactions in this system are expected to be dominated by the  $Fe^{3+}$  -  $Fe^{3+}$  interactions. These will obviously increase markedly as the  $Fe^{3+}$  concentration increases with increasing oxygen vacancies. The magnetization of  $La_{0.60}Sr_{0.40}FeO_{3-\delta}$  as a function of temperature follows the Brillouin curve: saturated at low temperature and decreasing slowly up to about 70% of  $T_N$  and more rapidly as  $T_N$  is approached. Thus, for unquenched L6SF, where the Fe-O-Fe angle is small, and the  $Fe^{4+}$  concentration large,  $T_N$  is low and the room temperature moment is small.  $T_N$  increases to  $\sim$ 410°C for the specimen quenched from 1500°C, therefore the room temperature moment is

little affected by the change in superexchange and  $T_N$ . However, the same effect that leads to the variable saturation moment (the ratio of low moment  $Fe^{4+}$  and high moment  $Fe^{3+}$ ) will dominate the room temperature moment when the ordering temperature is high. Since the Fe atoms are antiferromagnetically ordered, this effect cannot be observed using bulk magnetic measurements, but can easily be seen with the neutron diffraction measurements. When the composition reaches  $La_{0.6}Sr_{0.4}FeO_{2..8}$ , it is expected that the system will reach its maximum average moment. Beyond this point  $Fe^{2+}$  is expected to appear, also with a smaller moment than  $Fe^{3+}$ , and the room temperature moment would then be expected to decrease. This trend was in fact seen in the  $CO/CO_2$  reduced samples.

# Fe valence state

The relative ratio of  $Fe^{3+}$  and  $Fe^{4+}$  ions for  $La_{0.60}Sr_{0.40}FeO_{3-\delta}$  without quenching obtained from relative areas of the Mössbauer spectra is 64:36, indicating a nearly zero oxygen vacancy in these compounds. This ratio changes to 70:30 for the specimen quenched from 800°C, showing an increase of oxygen vacancy concentration. As the quench temperature becomes higher than 900°C, the  $Fe^{4+}$  spectrum disappears ( $Fe^{4+}$  is normally non-magnetic with a single line) and the magnetic sextets become dominant (Figure 155). The spectra of the specimens quenched from T > 1200°C are particularly sharp, which represents an increase in the Fe magnetic ordering temperature and suggests a structural transformation in the sample. It was found that the valence state of Fe changes from 3.36 to 3.04, suggesting that the Fe valence states change from a mixture of  $Fe^{3+}$  and  $Fe^{4+}$  to about 96%  $Fe^{3+}$  as quenched at 1500°C. The change in the valence state of Fe results in an increase in both the hyperfine field and magnetic moment for the quenched samples. The oxygen content  $\delta$  changes from 0.02 to 0.18 per formula after quenching at 1500°C. The oxygen contents  $\delta$  obtained from Mössbauer spectra are again consistent with those obtained from the neutron diffraction refinements (Figure 156).

Since the isomer shift (IS) provides direct information about the electron density at the nucleus, we have attempted to derive information about the valence states of Fe ions in these compounds. By using the average IS  $^7$  of the quenched La<sub>0.60</sub>Sr<sub>0.40</sub>FeO<sub>3- $\delta$ </sub>, the average valence states of Fe is shown in Figure 157.

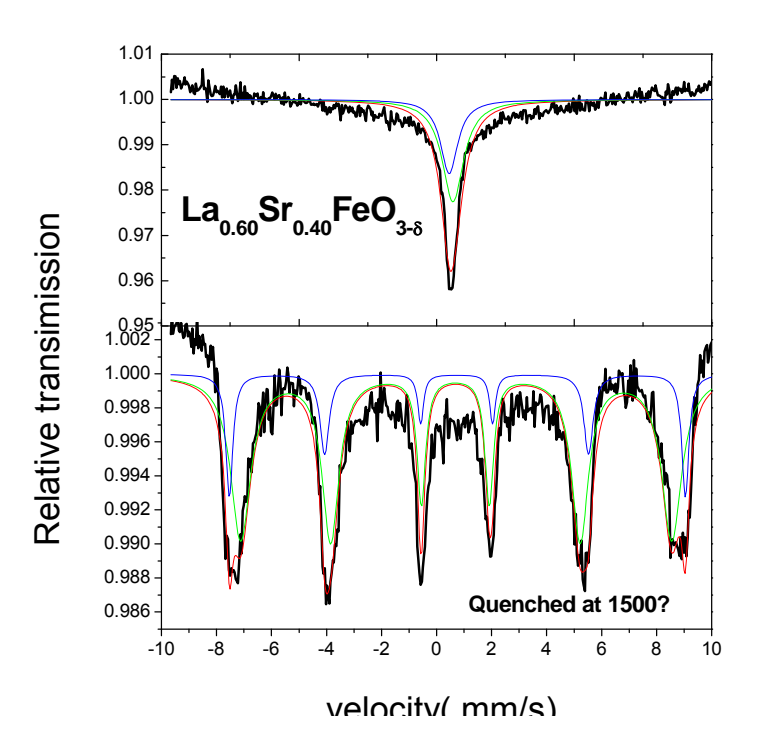


Figure 155 Comparison of Mossbauer spectra of LSF samples between unquenched and quenched from  $1500^{\circ}\mathrm{C}$ 

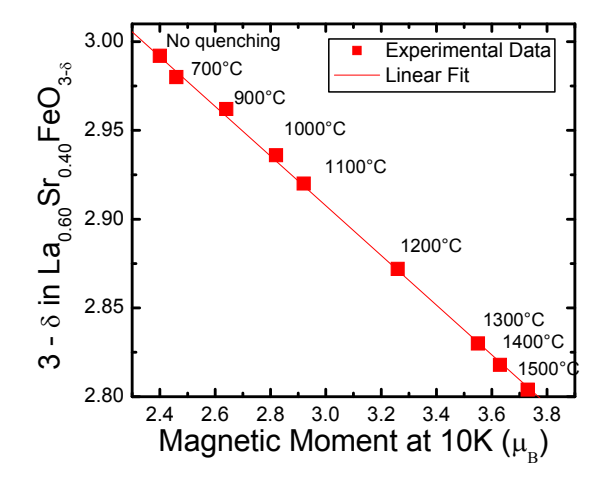


Figure 156 Correlation between oxygen vacancy and magnetic moment of  $La_{0.60}Sr_{0.40}FeO_{3-\delta}$  using neutron diffractometry

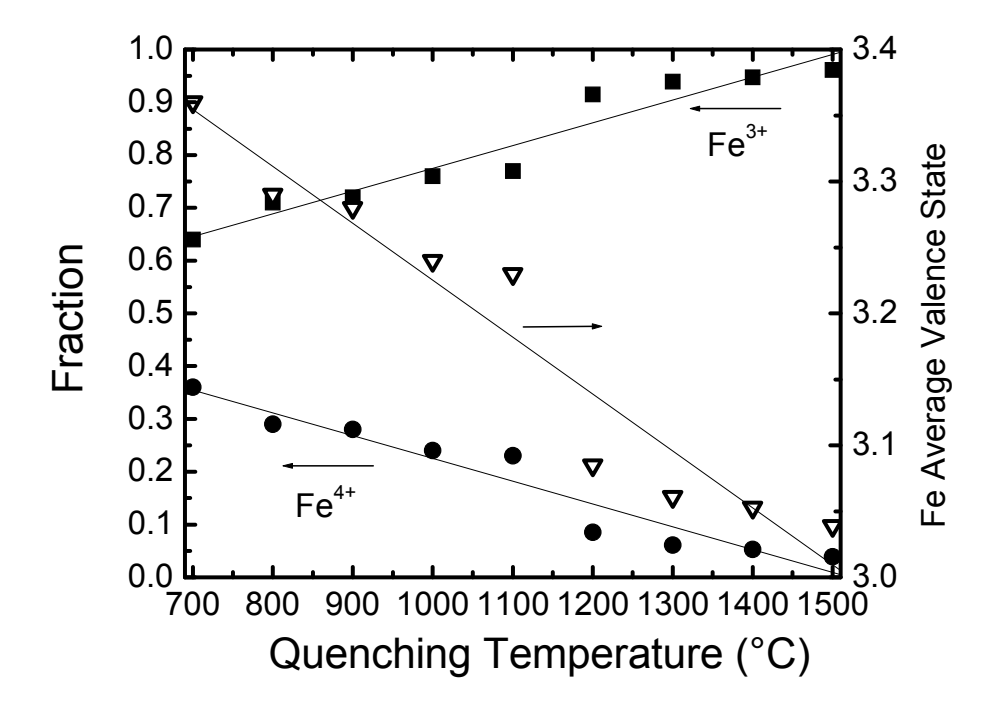


Figure 157 Plot of Fe average valence state and fraction of  $Fe^{3+}$  and  $Fe^{4+}$  in  $La_{0.60}Sr_{0.40}FeO_{3-\delta}$  quenched from various temperatures.

# 3.3.2 Study of $La_{0.2}Sr_{0.8}Fe_{0.55}Ti_{0.45}O_{3-\delta}$ (LSFT) for OTM using Electrical conductivity, Seebeck coefficient and Mössbauer Spectroscopy

#### **3.3.2.1. Ti doped LSF**

Ti doping on  $La_{1-x}Sr_xFeO_{3-\delta}$  (LSF) tends to increase the oxygen equilibration kinetics of LSF in lower oxygen activity environment because of the high valence state of Ti. However, the addition of Ti decreases the total conductivity because the acceptor ([Sr'\_{La}]) is compensated by the donor ([Ti^{\bullet}\_{Fe}]) which decreases the carrier concentration. The properties of  $La_{0.2}Sr_{0.8}Fe_{1-x}Ti_xO_{3-\delta}$  (LSFT, x=0.45) have been experimentally and theoretically investigated to elucidate (1) the dependence of oxygen occupancy and electrochemical properties on temperature and oxygen activity by thermogravimetric analysis (TGA) and (2) the electrical conductivity and carrier concentration by Seebeck coefficient and electrical measurements.

SrTiO<sub>3</sub> (perovskite, ABO<sub>3</sub>), an n-type conductor, has thermodynamic stability, but exhibits low electronic and ionic conductivity at high temperature and high oxygen activity. La doping on the A-site of SrTiO<sub>3</sub> does provide increased electrical conductivity in highly reducing atmospheres (Figure 158). Acceptor doping such as Fe on the B-site of SrTiO<sub>3</sub> provides p-type conduction and decreases electrical conductivity. On the other hand, ferrite such as (La, Sr)FeO<sub>3- $\delta$ </sub> (LSF) which is known as a mixed ionic and p type electronic conductor is currently being widely used because of its high electronic conductivity in oxidizing conditions, but in low oxygen activity its conductivity is suppressed (Figure 159). When high valence state elements like Ti are added as a donor on the B site of LSF, the electrical conductivity at lower oxygen activity tends to be increased. Therefore, Ti doped (La, Sr)FeO<sub>3- $\delta$ </sub>, may attain high electronic and ionic conductivity as well as improved stability in highly reducing atmospheres. As shown in Figure 160 [5], according to the XRD results, the perovskite structure in LSFT was also preserved very well after 12 hours at  $1000^{\circ}$ C in  $10^{\circ}$  H<sub>2</sub> /  $90^{\circ}$  N<sub>2</sub>.

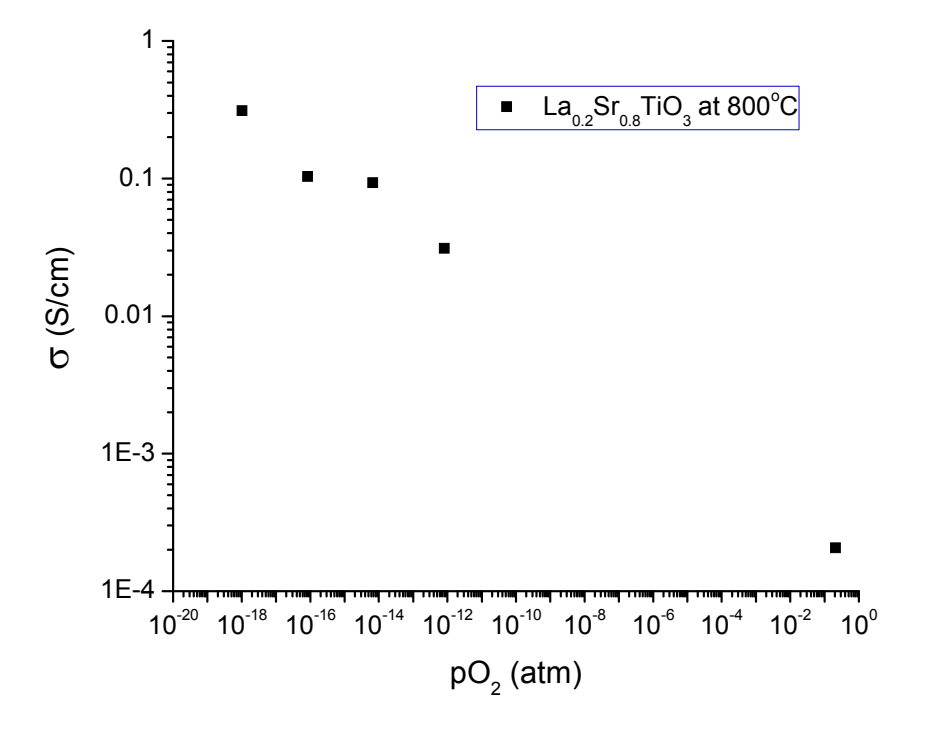


Figure 158  $\sigma$  vs. pO<sub>2</sub> of La<sub>0.2</sub>Sr<sub>0.8</sub>TiO<sub>3</sub> at 800°C (annealing temperature was 1200°C)

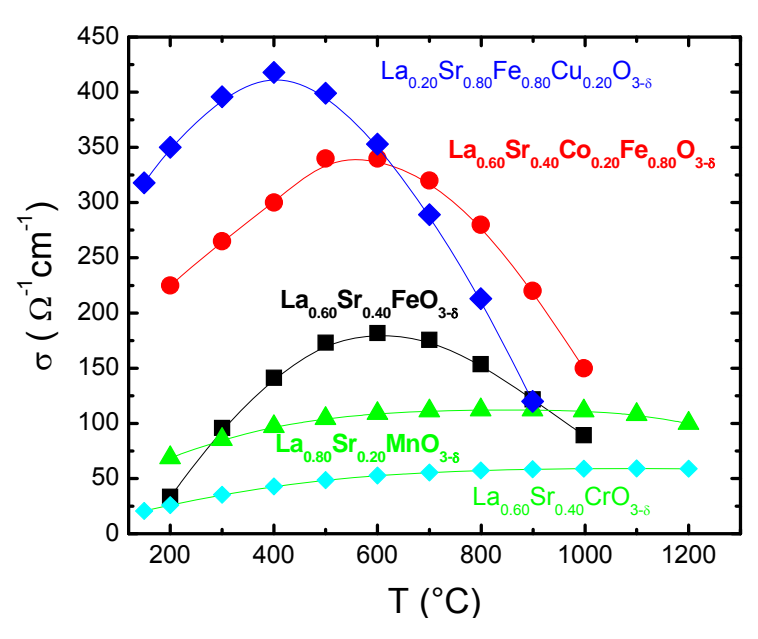


Figure 159 Conductivity of LSF as a function of temperature in air

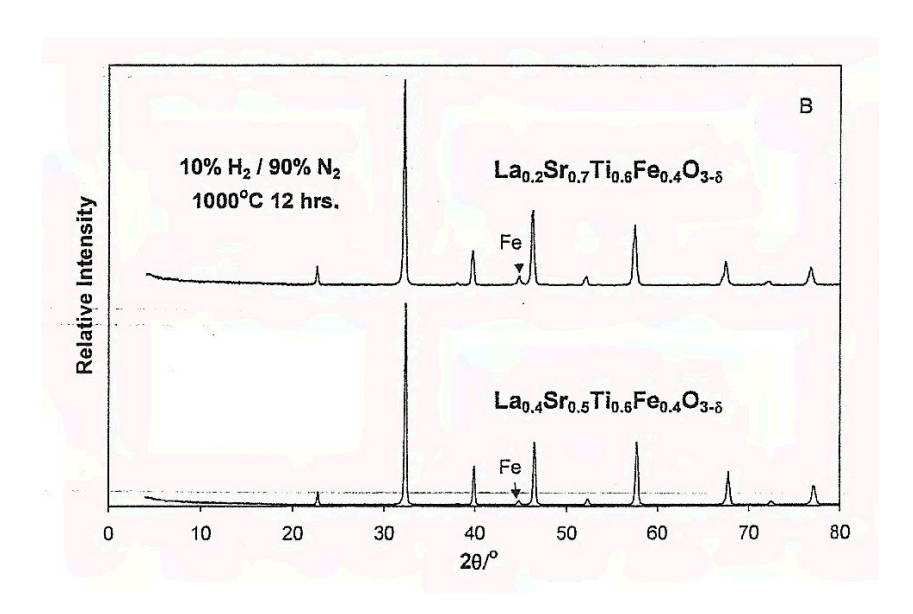


Figure 160 XRD profiles of LSFT annealed in forming gas  $(10\% H_2 / 90\% N_2)$  at  $1000^{\circ}$ C [5]

# 3.3.2.2 LSFT Powder Preparation

The first objective was to fabricate well dispersed and nano-sized LSFT powder. To achieve this goal, the development of powder preparation technologies to fabricate non-agglomerated, nano-sized powder was required. Several water based solution processes were investigated to

prepare the required powder. Among them, the method using ethylene glycol and nitrates was selected as the best route for power preparation. LSFT powder samples were annealed at 600, 1200, 1300 and 1400°C and characterized using XRD. As can be seen in Figure 161, the XRD profiles show that the resulting LSFT was single phase with the perovskite structure.

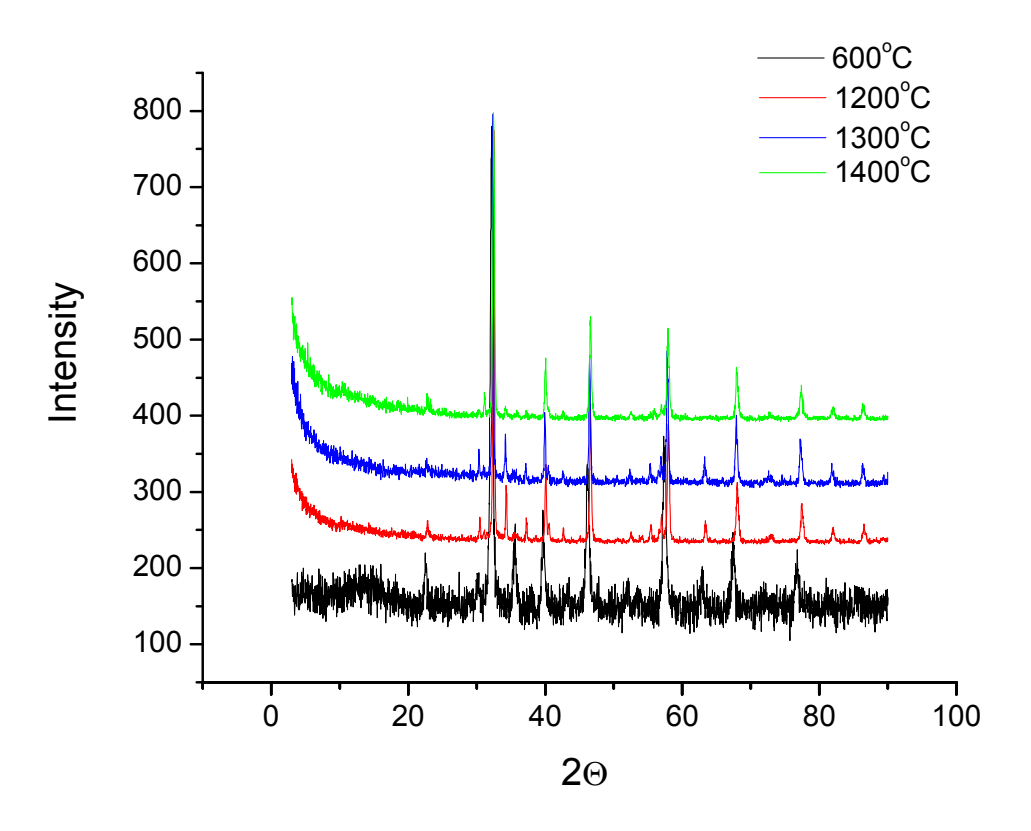


Figure 161 XRD profiles of LSFT annealed at 600, 1200, 1300, and 1400°C

# 3.3.2.3. Oxygen Occupancy Study

Based on the assumption that the structure had full oxygen occupancy at room temperature in air, the oxygen occupancy (3- $\delta$ ) as a function of oxygen activity was estimated by thermogravimetric analysis (TGA). This assumption yielded the oxygen occupancy (3- $\delta$ ) at  $1200^{\circ}$ C to be 2.92 in air, and 2.86 in 1 x  $10^{-12}$  atm (Figure 162).

These data agree with that found at the University of Houston (Figure 163) [6]. As shown in Figure 164, below 1 x  $10^{-13}$  atm of oxygen activity at  $1200^{\circ}$ C, the LSFT lost weight due to dissociation. However, upon re-oxidation, the weight loss was found to be fully reversible.

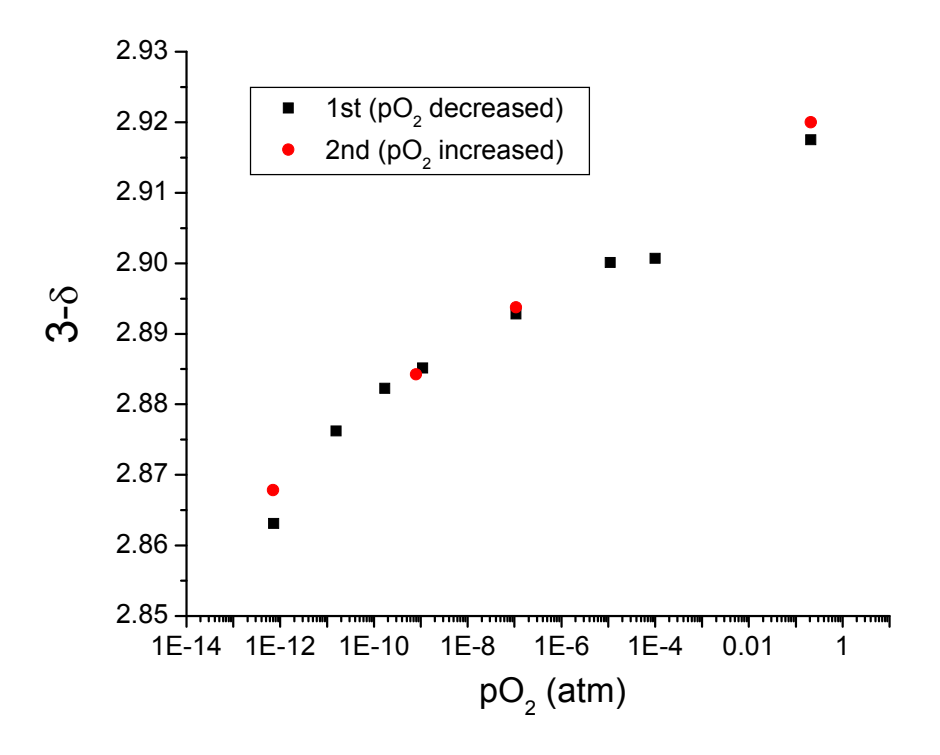


Figure 162 Oxygen occupancy (3-δ) of LSFT as function of oxygen activity at 1200°C

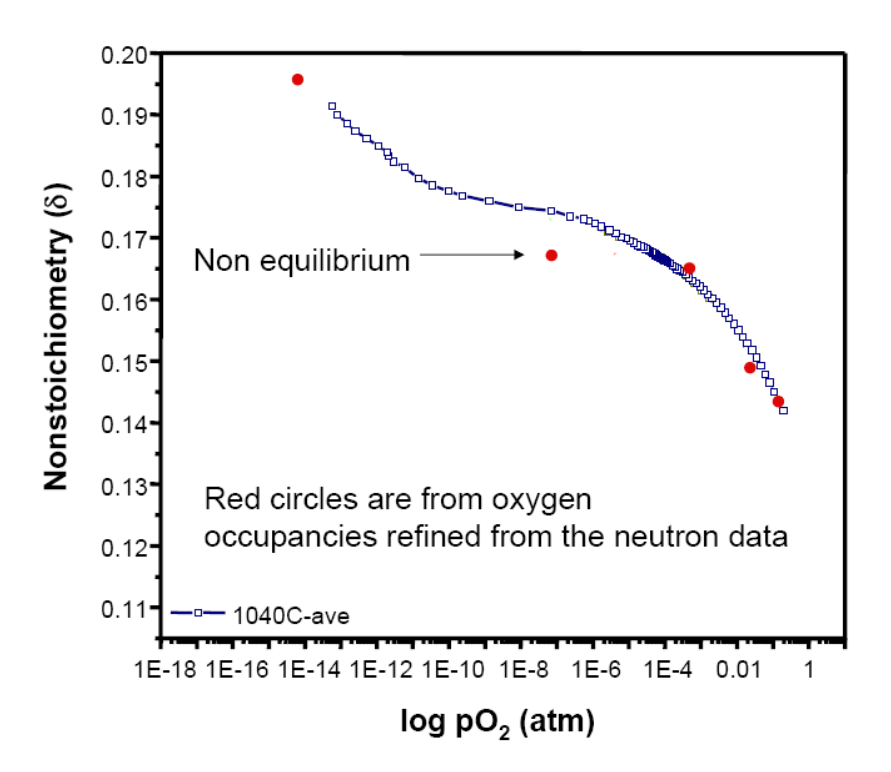


Figure 163 Stoichiometry of La<sub>0.2</sub>Sr<sub>0.8</sub>Fe<sub>0.55</sub>Ti<sub>0.45</sub>O<sub>3-δ</sub> (LSFT) [6]

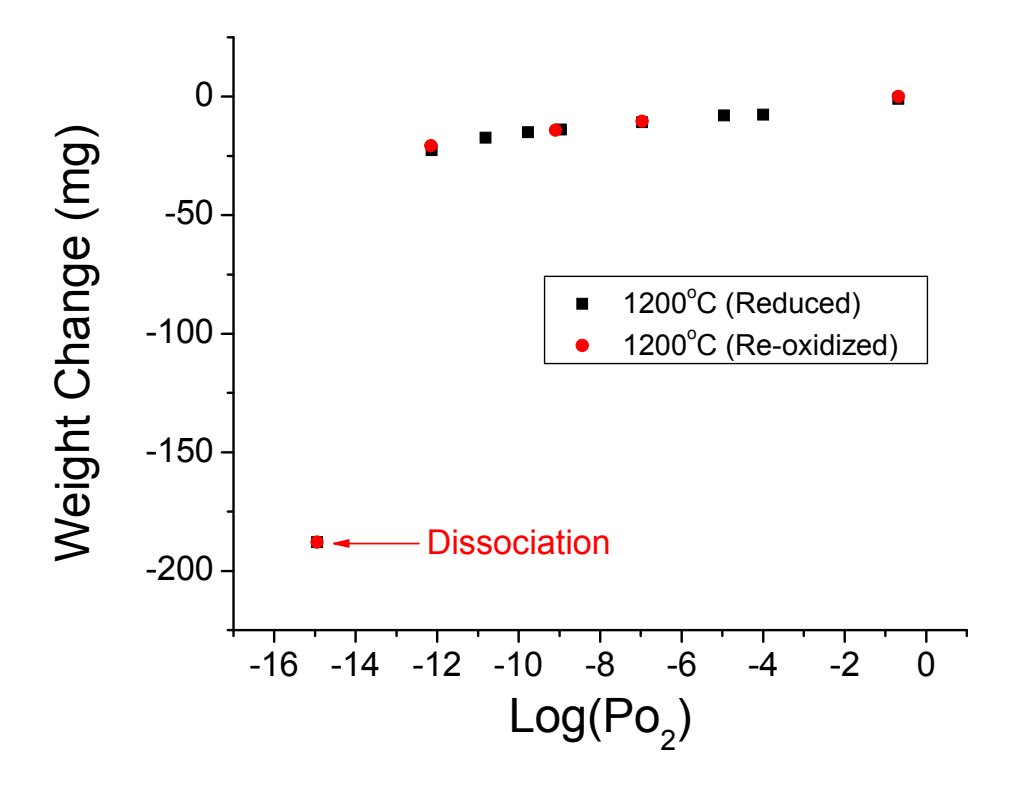


Figure 164 Weight changes of LSFT as a function of oxygen activity at 1200°C

### 3.3.2.4. Electrical Conductivity and Seebeck Coefficient of LSFT in Air

The electrical conductivity and Seebeck coefficient were measured on dense LSFT (>90% of theoretical density) as a function of temperature and oxygen activity. The electrical conductivity in air was about 2 S/cm at  $200^{\circ}$ C and reached a maximum value of 13 S/cm at  $500^{\circ}$ C and then decreased to 4 S/cm at  $1200^{\circ}$ C (Figure 165). The Seebeck coefficient is inversely related to the electrical conductivity. It decreased from 30 to 20  $\mu$ V/K between 200 and  $500^{\circ}$ C and then increased to about  $150~\mu$ V/K at  $1200^{\circ}$ C.

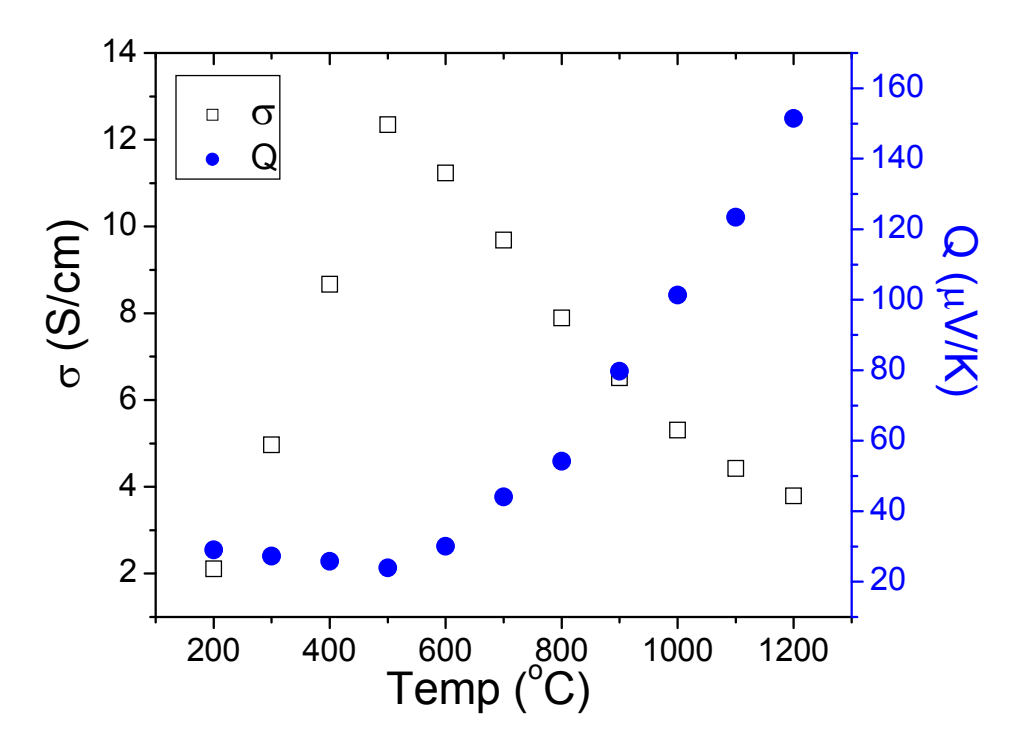


Figure 165 Total conductivity and Seebeck coefficient of LSFT as a function of temperature.

The Seebeck Coefficient and charge carrier concentration are also inversely related through the relationship

$$Q = \pm \frac{k}{e} [\ln(\frac{1-c}{c})]$$

where Q is the Seebeck Coefficient in  $\mu V/K$  or  $\mu V/C$ , k is Boltzmann's constant, and c is the ratio of charge carriers to available conduction sites. This equation was used to evaluate the charge carrier and acceptor dopant concentration. As can be seen in Figure 166, the charge carrier concentration was initially about  $8x10^{21}/cm^3$  at  $500^{\circ}C$  and then decreased to  $2x10^{21}$  at  $1200^{\circ}C$  as Q increased. Figure 167 shows that the value of the net acceptor dopant concentration as function of temperature. As can be seen, the average value was found to be about 0.35. In  $La_{0.2}Sr_{0.8}Fe_{0.55}Ti_{0.45}O_{3-8}$  (LSFT), the acceptor ([Sr'<sub>La</sub>]) is compensated by the donor ([Ti\*<sub>Fe</sub>]), thus if the dopants are homogenously distributed in the lattice and are fully ionized, the hole concentration is given by the relation  $p = [Sr'_{La}] - [Ti*_{Fe}]$ . Thus for the composition used in this study, the net hole concentration should be, p = 0.8-0.45 or 0.35, which agrees with that calculated from the Seebeck measurements. This suggests that both the donors and acceptors were completely ionized and were homogeneously incorporated into the perovskite lattice.

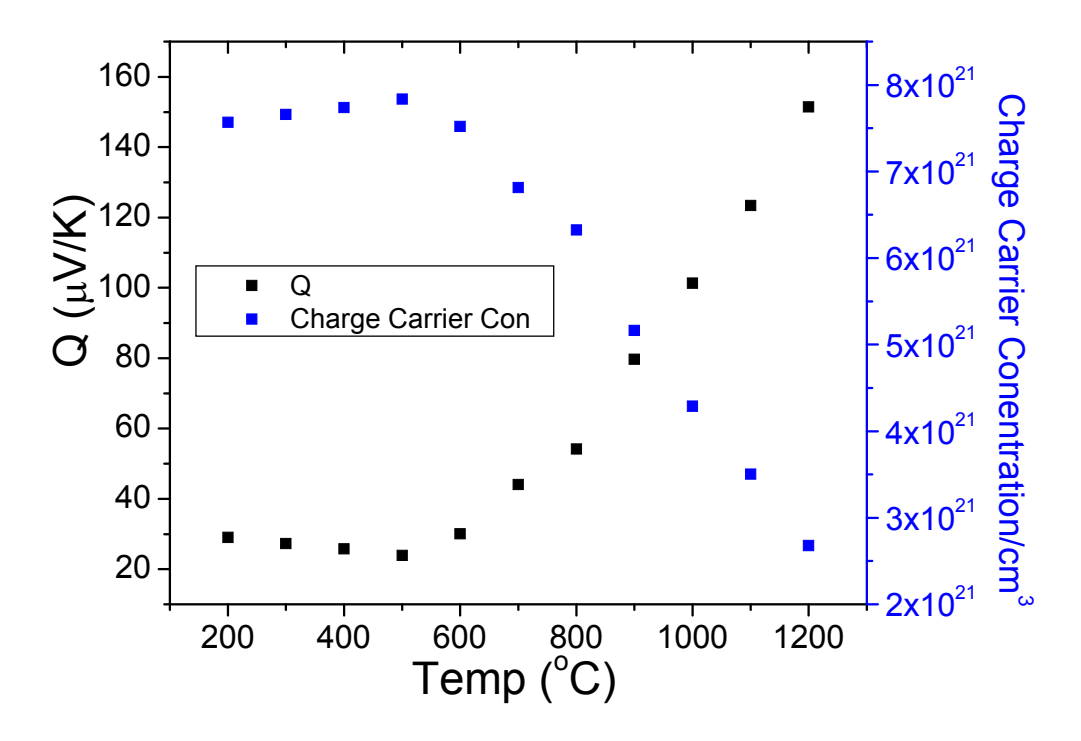


Figure 166 Charge carrier concentration and Seebeck coefficient of LSFT as a function of temperature

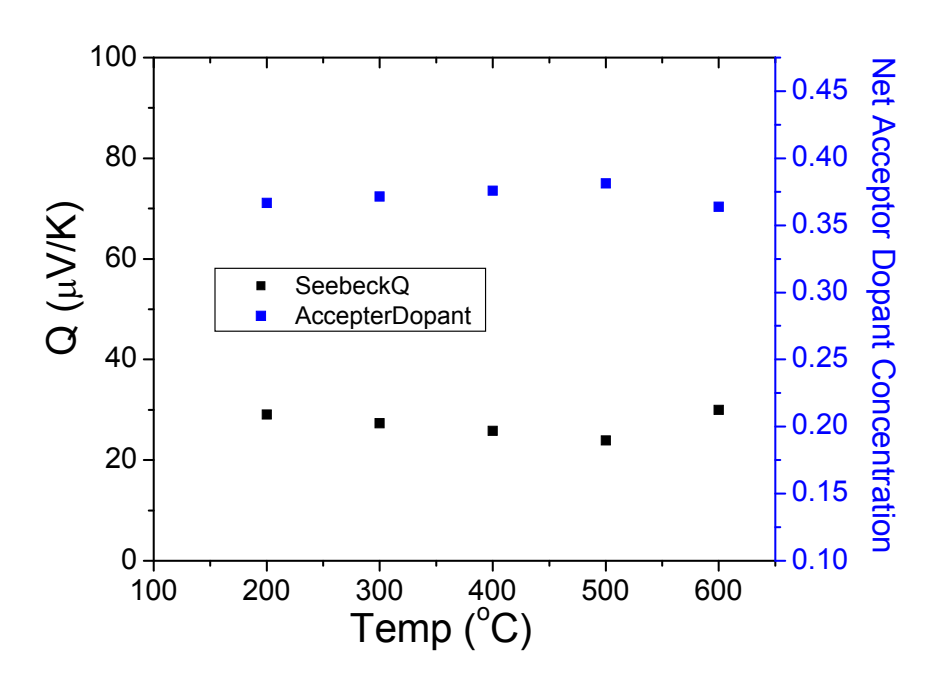


Figure 167 Net acceptor dopant concentration and Seebeck coefficient of LSFT as a function of temperature

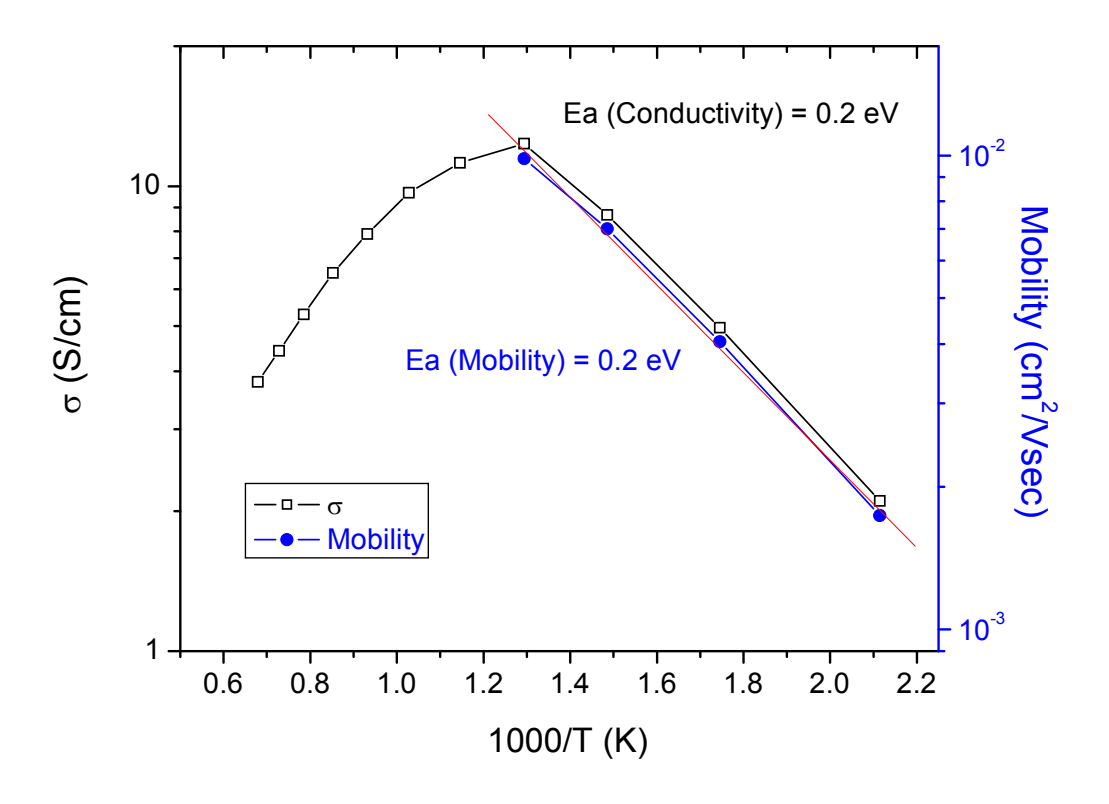


Figure 168  $\,$   $\sigma$  vs. 1/T of LSFT and corresponding mobility measured in air as a function of temperature

As shown in Figure 168, the activation energy of conduction for LSFT was about 0.2 eV. The hole mobility was also calculated using the electrical conductivity and carrier concentration data; the results along with the electrical conductivity of the LSFT samples are shown in the Figure 168. The activation energy for the mobility is 0.2 eV which implies that LSFT conducts via the small polaron conduction mechanism.

# 3.3.2.5. Electrical Conductivity and Seebeck Coefficient as a function of oxygen activity

The *in situ* electrical conductivity and Seebeck coefficient measurements were made on LSFT at 1000 and 1200°C over the oxygen activity range from air to 10<sup>-15</sup> atm. As can be seen in Figure 169, the LSFT shows a p-type to n-type transition as the oxygen activity dcreases from that in air to 10<sup>-15</sup> atm. The p-type to n-type transition occurred at an oxygen activity of 1x10<sup>-10</sup> at 1000°C and 1x10<sup>-6</sup> at 1200°C. The whole plot including the minimum point (the electrical conductivity at the p-type to n-type transition) in Figure 169 was shifted to higher oxygen activity range when the temperature was increased from 1000 to 1200°C which is typical of p-type oxides. This shift is related to the fact that the oxygen vacancy concentration is higher at the higher temperature which tends to compensate the p type carriers at higher oxygen activity.

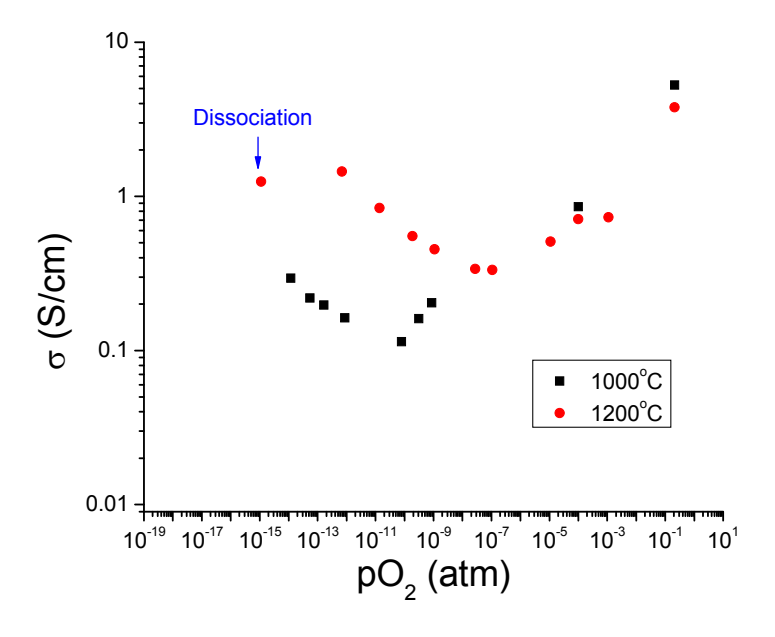


Figure 169 Electrical conductivity as a function of oxygen activity of LSFT at 1000 and 1200°C.

This phenomenon is because  $p = [Sr'_{La}] - 2[V"_O]$  in the p type conduction region. Since the concentration of oxygen vacancy,  $[V"_O]$ , is higher at  $1200^{\circ}$ C than at  $1000^{\circ}$ C, the electrical conductivity of LSFT at  $1200^{\circ}$ C is lower in the p-type regime because the holes resulting from the acceptor concentration,  $[Sr'_{La}]$ , are compensated by the oxygen vacancies. As the oxygen activity continues to decrease, LSFT enters the n-type conductivity regime when sufficient oxygen vacancies have been generated to totally compensate the acceptors. At this point, the conductivity starts to increase with further decreases in oxygen activity as p-type carriers are increasingly compensated by oxygen vacancies. This results in the n-type conductivity at  $1200^{\circ}$ C being higher than that observed for  $1000^{\circ}$ C because of the higher oxygen vacancy concentration at  $1200^{\circ}$ C. Further decrease of the oxygen activity below  $1x10^{-13}$  atm appeared to cause dissociation or phase changes. The increase of  $[V"_O]$  and evidence of dissociation in n-type regime was verified by TGA study shown in Figure 162 and 164. These results agreed with the experimental results from the University of Houston (Figure 170) [6].

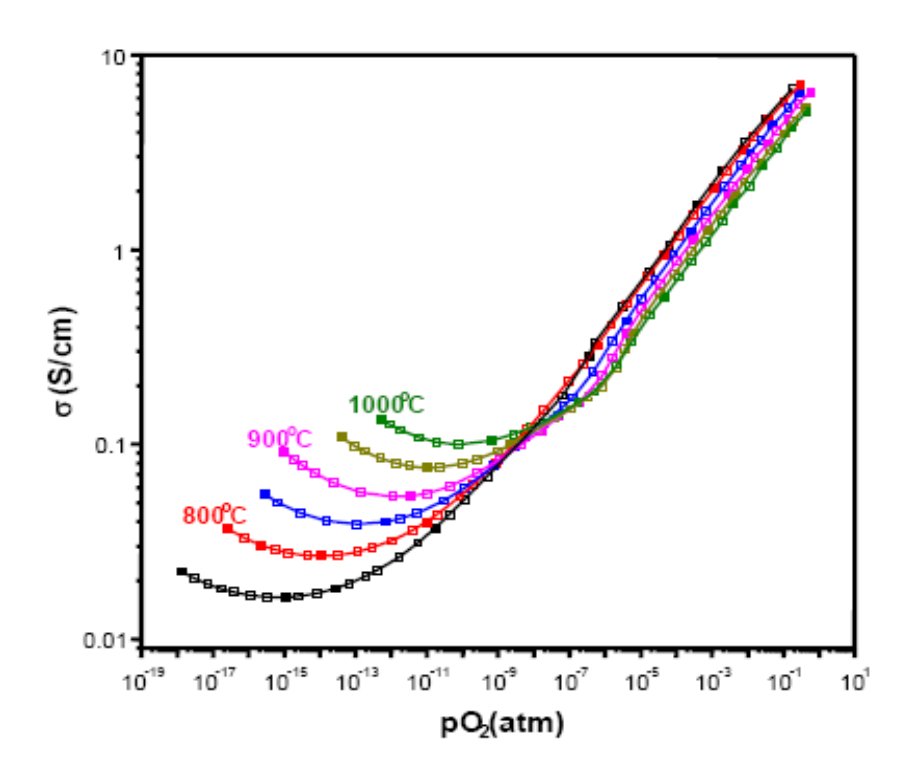


Figure 170 Log  $\sigma$  vs. Po<sub>2</sub> of dense Sr<sub>0.9</sub>Ti<sub>0.6</sub>Fe<sub>0.4</sub>O<sub>3- $\delta$ </sub> (sintered at 1600°C) at 800°C [6]

Seebeck coefficients were also measured as a function of oxygen activity at 1000 and 1200°C (Figure 171). As can be seen in Figure 171, the Seebeck coefficient verified that LSFT has ptype conductivity in the high oxygen activity regime and n-type conductivity in the low oxygen activity regime. The Seebeck coefficient also indicated that the LSFT exhibits a p-type to n-type transition at about  $1x10^{-8}$  and  $1x10^{-6}$  atm of oxygen activity at 1000 and  $1200^{\circ}$ C. However, the electrical conductivity measurement of LSFT showed a p-type to n-type transition at about  $1x10^{-10}$  and  $1x10^{-6}$  atm of oxygen activity at  $1000^{\circ}$ C at  $1200^{\circ}$ C. The difference between the two measurements may be due to differences in the carrier mobilities.

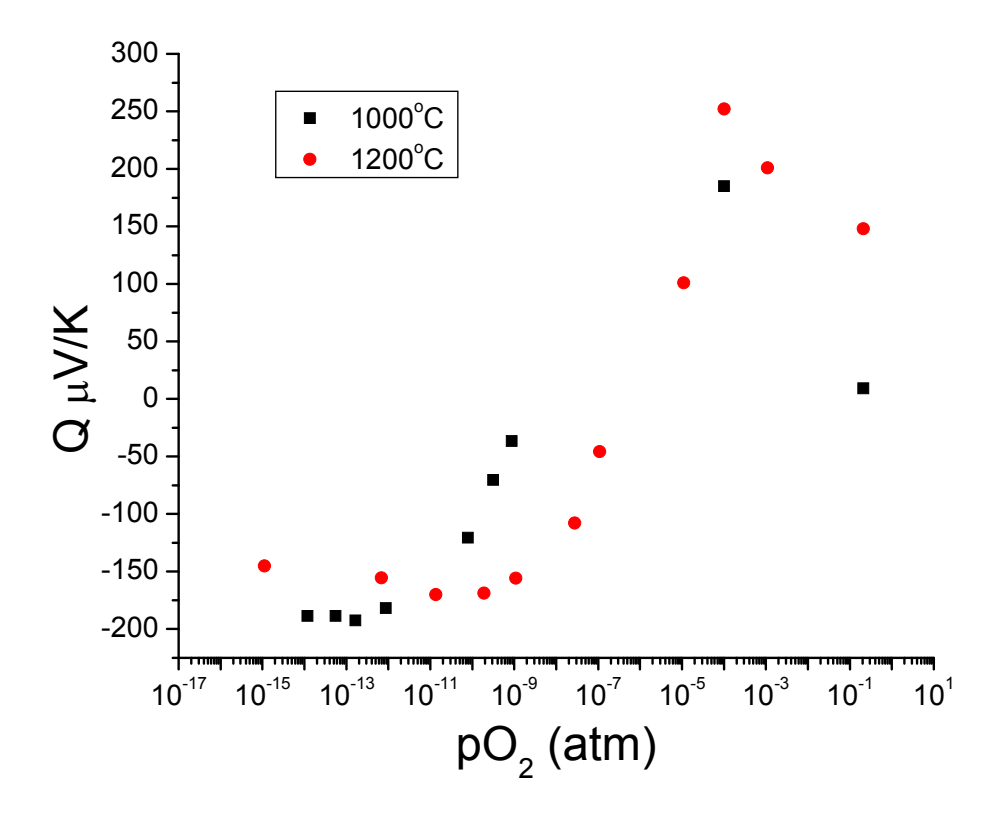


Figure 171 Seebeck coefficient vs. Log Po<sub>2</sub> of  $\sim 50\%$  dense La<sub>0.2</sub>Sr<sub>0.8</sub>Fe<sub>0.55</sub>Ti<sub>0.45</sub>O<sub>3- $\delta$ </sub> (LSFT) at  $900^{\circ}$ C

#### 3.3.2.6. Mössbauer Spectroscopy

Figure 172 (a) and (b) show the Mössbauer spectra of LSFT specimens quenched to room temperature from annealing temperatures ranging from 1100 to 1500°C. Included in Figure 172 (a) is a spectrum of the sample cooled from 1400°C at 3°C/min to room temperature. All of the spectra possess two singlet peaks, which indicate the paramagnetic interaction at room temperature for these materials. We know that the isomer shift arises from the interaction energy of the part of the electronic cloud, inside the nucleus, with the nuclear charge. Thus, Mössbauer spectra can provide direct information on the electron density at the nucleus and this can often be interpreted to give unequivocal information about the valence state of the Fe ion. Hence, these two sets of singlet spectra in Figure 172 show that there exist two distinguished local environments for Fe ions in LSFT, which is often interpreted as valence state.

We anticipated these two valence states are in 3+ and 4+. Figure 173 illustrates a detailed analysis of isomer shift as a function of quenching temperature for LSFT. Figure 174 shows a plot of the fraction of the two Fe ions in quenched LSFT. The oxygen vacancy density increases with increasing quenching temperature, which reduces the fraction of Fe 4+ ions. This implies that Fe ions responsible for isomer shift labeled Fe(1) in Figure 174 should correspond to Fe 4+ and Fe(2) represents Fe 3+ in Figure 174.

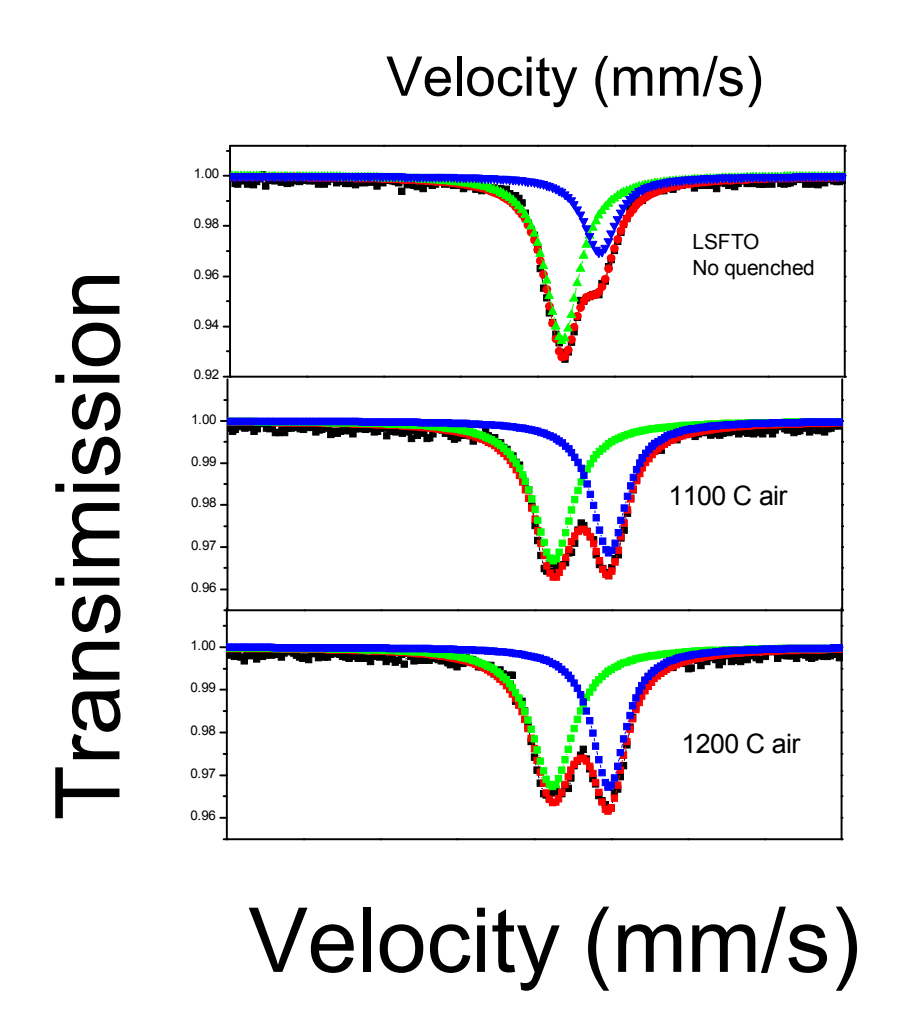


Figure 172 (a) Mössbauer spectra of LSFT samples quenched from 1100°C and 1200°C to room temperature.

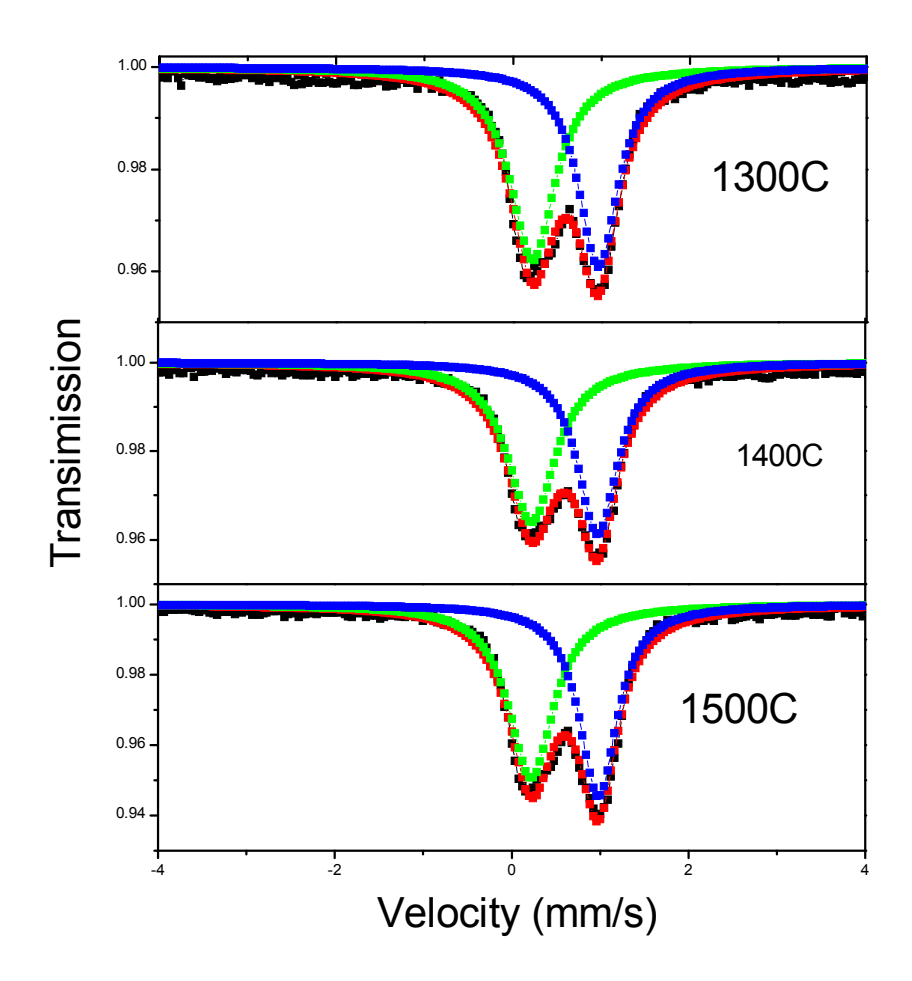


Figure 172 (b) Mössbauer spectra of LSFT samples quenched from 1300°C, 1400°C and 1500°C to room temperature.

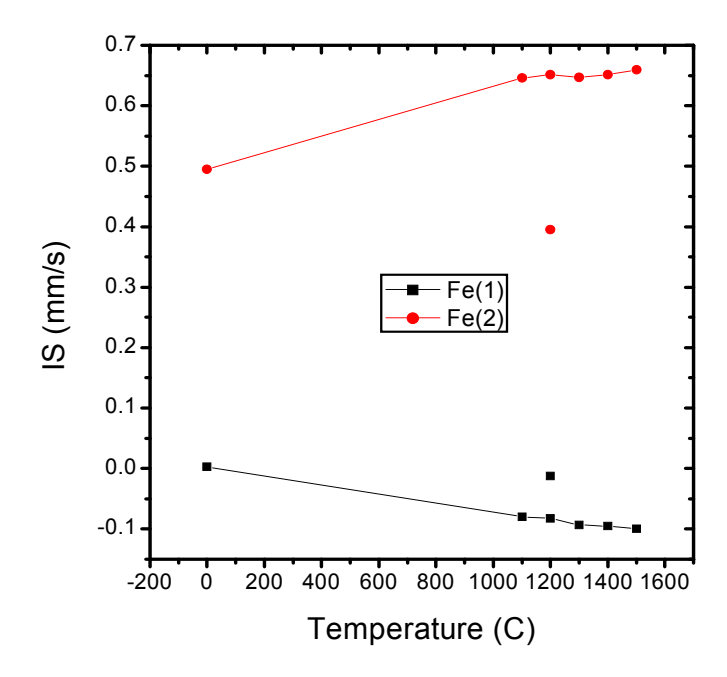


Figure 173 Isomer shift of two types of Fe ions in LSFT quenched to room temperature from the temperatures ranging between 1100 and 1500°C. Included is the isomer shift of the specimen, which was annealed at 1400°C and then cooled to room temperature at 3°C/min.

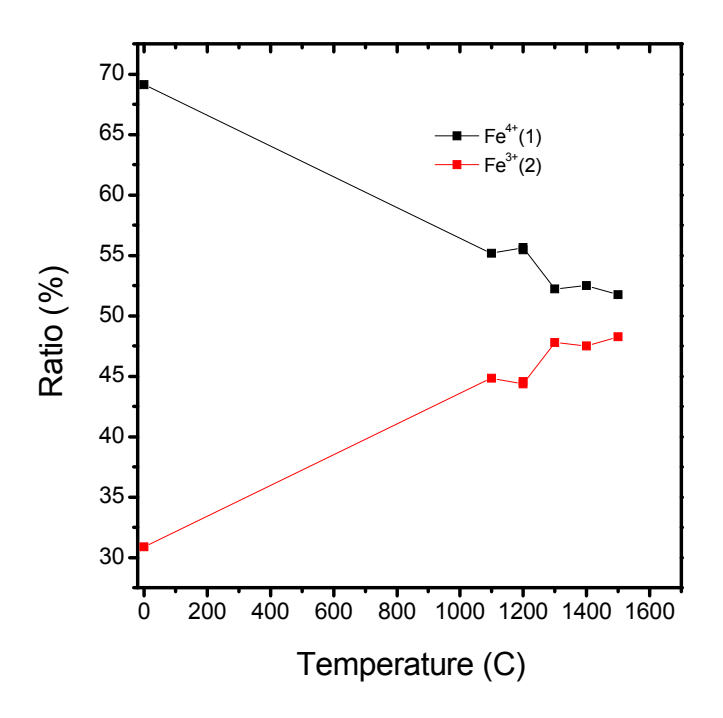


Figure 174 The fraction of the two types of Fe ions in LSFT quenched to room temperature from the temperatures ranging between 1100 and 1500°C. Included is the Fe ion fraction in the specimen which was annealed at 1400°C and then cooled to room temperature at 3°C/min.

#### 3.4 Conclusions

- 1. After extensive studies of candidate materials, lanthanum ferrites (LSF and LSFT) were selected as the favored materials for the oxygen transport membrane (OTM).
- 2. The efficiency of lanthanum ferrites as OTMs can be evaluated by analysis of the total conductivity and oxygen vacancy concentration, which depend on the concentration of acceptor dopant.
- 3. Oxygen occupancy of LSF can be evaluated by measuring the magnetic moment with neutron diffractometry
- 4. Mössbauer spectroscopy also enables the estimation of oxygen occupancy in LSF by measuring both the hyperfine field and magnetic moment.
- 5. LSF is a very good material for an OTM because of its high electronic and oxygen ionic conductivity if long term stability and mechanical strength are improved.
- 6. LSFT not only exhibits p-type behavior in the high oxygen activity regime, but also has n-type conduction in reducing atmospheres.
- 7. Higher concentrations of oxygen vacancies in the low oxygen activity regime may improve the performance of LSFT as an OTM.
- 8. The hole concentration is related to the difference in the acceptor and donor concentration by the relation  $p = [Sr'_{La}] [Ti^{\bullet}_{Fe}]$ . The chemical formulation predicts that the hole concentration is, p = 0.8-0.45 or 0.35. Experimental measurements indicated that p is about  $\sim 0.35$ .
- 9. The activation energy of conduction is 0.2 eV which implies that LSCF conducts via the small polaron conduction mechanism.
- 10. LSFT has excellent chemical and mechanical strength in reducing and oxidizing atmospheres but its electrical and ionic conductivity needs to be improved and further investigation on LSFT is recommended.

# 3.5 References (for Chapter 3)

- 1. B. C. H. Steele, J. Mater. Sci., 36, 1053 (2001).
- 2. H. U. Anderson, X.-D. Zhou and F. Dogan, *Proceeding of the Electrochem. Soc.* (2002)
- 3. J. B. Yang, W. B. Yelon, W. J. James, Z. Chu, M. Kornecki, Y. X. Xie, X. D. Zhou, H. U. Anderson, A. G. Joshi and S. K. Malik, *Phys. Rev. B*, **66**, 184415 (2002).
- 4. D. E. Cox, *IEEE Trans. Magn.*, **MAG 8**, 161 (1972).
- 5. D.P. Fagg et al., "Stability and mixed ionic-electronic conductivity of (Sr,La)(Ti,Fe)O<sub>3-δ</sub> perovskites", *Solid State Ionics*, 156 (2003) 45-57
- 6. A J. Jacobson and C. A. Mims.,"Transport properties and phase stability of mixed conducting oxide membranes", Oxygen Transport Ceramic Membrane Annual Project Review at University of Houston, December 11, 2006

# 3.6 Publication from Program (for Chapter 3)

- 1. X.D. Zhou, L.R. Pederson, Q. Cai, J. Yang, B.J. Scarfino, M. Kim, W.B. Yelon, W.J. James, H.U. Anderson and C. Wang, "Structural and magnetic properties of LaMn<sub>1</sub>-xFe<sub>x</sub>O<sub>3</sub> (0<x<1.0)", J. of Appl. Physics **99** 08M918 (2006).
- 2. X.D. Zhou, E. Thomsen, Q. Cai, J. Yang, B. Scarfino, W. James, W. Yelon, H.U. Anderson and L.R. Pederson, "Electrical, thermoelectric, and structural properties of La(Fe,M)O<sub>3</sub> (M = Mn, Ni and Cu)", J. of Electrochem. Soc. **153**, J133-J138 (2006).
- 3. X.D. Zhou, Q. Cai, J. Yang, B. Scarfino, W. James, W. Yelon, H.U. Anderson, Y. Shin and L.R. Pederson, "Electrical and structural properties of La(Fe,M)O<sub>3</sub> (M = Mn, Ni and Cu)", The Electrochem. Soc. Trans., **Vol. 1**, 211 (2006).
- 4. X.D. Zhou, B.J. Scarfino, Q. Cai, J. Yang, M. Du, Y. Ma, W.J. James, W.B. Yelon and H.U. Anderson, "Transport properties of Cr excess of p type perovskite conductors", Electrochem. Solid-State Lett. (submitted 2006).
- 5. X.D. Zhou and H.U. Anderson, "Defect chemistry in ternary compounds", in "Materials for Energy Conversion Devices", C.C. Sorrell, J. Nowotny and S. Sugihara, Ed., Woodhead Publishing Ltd., p. 235-257 (2005).
- 6. J. Cheng, A. Navrotsky, X.D. Zhou and H.U. Anderson, "Enthalpies of formation of LaMO<sub>3</sub> perovskites (M = Cr, Fe, Co and Ni)", J. Mater. Res. **20**, 191-200 (2005).

- 7. J. Cheng, A. Navrotsky, X.D. Zhou and H.U. Anderson, "Thermochemistry of La<sub>1</sub>.  $_x$ Sr<sub>x</sub>FeO<sub>3- $\delta$ </sub> solid solutions (0.0 $\le$ x $\le$ 1.0, 0.0 $\le$  $\delta$  $\le$ 0.5)", Chemistry of Materials **17**, 2197-2207 (2005).
- 8. X.D. Zhou, J.B. Yang, Q. Cai, M. Kim, W.B. Yelon, W.J. James and H.U. Anderson, "Coupled electrical and magnetic properties in (La,Sr)FeO<sub>3-δ</sub> by *in situ* studies", J. of Appl. Physics **97**, 10C314-316 (2005).
- 9. J.B. Yang, S.K. Malik, X.D. Zhou, M.S. Kim, W.B. Yelon, W.J. James and H.U. Anderson, "Magnetic and Transport Properties of Nanocomposite Fe/Fe<sub>3-δ</sub>O<sub>4</sub> Films Prepared by Plasma-Enhanced Chemical Vapor Deposition", J. Phys.: D Appl. Phys., **38** (2005) 1215.
- 10. J.B. Yang, M.S. Kim, Q. Cai, X.D. Zhou, W.B. Yelon, W.J. James and H.U. Anderson, "Study of the Electronic Structure of CaFeO<sub>3</sub>", J. Appl. Phys. **97** (2005) 10A312.
- 11. X.D. Zhou, J.B. Yang, Q. Cai, M. Kim, W.B. Yelon, W.J. James and H.U. Anderson, "Role of Oxygen Deficiency on Electrical and Magnetic Properties of (La, Sr)FeO<sub>3-δ</sub> by *in Situ* Studies", J. Appl. Phys. **97**, (2005) 10C314.
- 12. X.D. Zhou, Q. Cai, Z. Chu, J. Yang, W.B. Yelon, W.J. James and H.U. Anderson, "Utilization of neutron diffraction and Mössbauer spectroscopy in the studies of the cathode for SOFCs", Solid State Ionics 175, 83-86 (2004).
- 13. W.B. Yelon, Q. Cai, W.J. James, H.U. Anderson, J.B. Yang, X.D. Zhou and H.A. Blackstead, "Neutron Diffraction Studies of Magnetic and Superconducting Compounds", Phys. Status Solidi (a) **201**, (2004) 1428.
- 14. R. Smith, X.D. Zhou, W. Huebner and H.U. Anderson, "Novel yttrium-stabilized zirconia polymeric precursor for the fabrication of thin films", J. Mater. Res., 19, 2708-2713 (2004).
- 15. W.B. Yelon, Q. Cai, W.J. James, H.U. Anderson, J.B. Yang, X.D. Zhou and H.A. Blackstead, "Neutron diffraction studies of magnetic and superconducting compounds", Physica Status Solidi **201**, 1428-1435 (2004).
- 16. J.B. Yang, X.D. Zhou, Q. Cai, W.B. Yelon, W.J. James and H.U. Anderson, "Charge ordering and disproportionation of La<sub>1/3</sub>Sr<sub>2/3</sub>FeO<sub>3</sub>", J. Phys. Cond. Matt. **15**, 5093-5102 (2003).
- 17. J.B. Yang, W.B. Yelon, W.J. James, Y.X. Xie, X.D. Zhou, H.U. Anderson, Z. Chu and M. Kornecki, "Crystal structure, magnetic properties, and Mössbauer studies of La<sub>0.6</sub>Sr<sub>0.4</sub>FeO<sub>3</sub> prepared by quenching in different atmospheres", Phys. Review, B **66**, 184415 (2002).

- 18. J.B. Yang, W.B. Yelon, W.J. James, X-D. Zhou, Y.X. Xie, H.U. Anderson and Z. Chu, "Magnetic and Mössbauer studies on the oxygen deficient perovskite La<sub>0.6</sub>Sr<sub>0.4</sub>FeO<sub>3</sub>", J. Appl. Phys., **91**, 7718-7720 (2002).
- 19. Z. Chu, W.B. Yelon, J.B. Yang, W.J. James, H.U. Anderson, Y.X. Xie and S.K. Malik, "Effect of Oxygen Vacancies on the Magnetic Structure of the La<sub>0.6</sub>Sr<sub>0.4</sub>FeO<sub>3-δ</sub> Perovskite: A Neutron Diffraction Study", J. Appl. Phys. **91**, (2002) 7938.

#### **Reviewed Proceedings/Book Chapters**

- 1. X.D. Zhou and H.U. Anderson, "Some aspects of defect chemistry in p-type perovskite conductors", The Electrochem. Soc. Proceedings Series, **Vol. PV2005-07**, Solid Oxide Fuel Cells IX, Ed. S.C. Singhal and J. Mizusaki, 1479-1486 (2005).
- 2. X.D. Zhou and H.U. Anderson, "Defect chemistry of p-type perovskite conductor used in solid oxide fuel cells", Preprints of Symposia American Chemical Society, Division of Fuel Chemistry, **49**, 749-750 (2004).
- 3. H.U. Anderson, X.D. Zhou and F. Dogan, "Defect chemistry of mixed ionic/electronic p type oxides", NATO Science Series, II: Mathematics, Physics and Chemistry, **173** (Mixed Ionic Electronic Conducting Perovskites for Advanced Energy Systems), 303-312 (2004).
- 4. H.U. Anderson, X.D. Zhou and F. Dogan, "Intermediate solid oxide fuel cells, challenges and opportunities for the materials scientists", Proc. of Electrochem. Soc. (Solid State Ionic Device III) **2002-26**, 16-17 (2003).

Chapter 4: Assessment of Microstructure of the Membrane Materials to Evaluate the Effects of vacancy-Impurity Association, defect Clusters, and Vacancy Dopant Association on the Membrane Performance and Stability

Professor Niegel Brown, University of Illinois Chicago

#### 4.1 Introduction

Perovskite oxide ceramics of the structure ABO<sub>3</sub> developed in recent years is one of the main functional materials for both industrial applications and basic materials research. [1-8]. This functionality ranges from electronic and ionic conductivity to superconductivity, ferromagnetism, ferroelectricity, dielectricity and magneto resistance. The multitude of potential industrial applications that have arisen from these properties has led to many micro-structural evaluations of different perovskite oxide materials being performed in an effort to understand the structure-property relationships of these crystalline solids. [1-6]. While the results of these studies are often specific to the system under investigation, it has become increasingly clear that point defects in the bulk and at internal interfaces are responsible for many of the interesting mechanical, chemical and electronic properties.

(La, Sr)FeO<sub>3-δ</sub> is a perovskite material that is primarily used as an oxygen separating membrane in ionic and electronic conductivity applications (i.e. fuel cells, syngas reactors)[9]. Under steep oxygen pressure gradients it exhibits properties such as high temperature stability, high mechanical stability, and high point defect acceptance, which makes it highly suited to these applications. Electrochemical measurements have shown that the point-defects present under heavy reducing conditions are oxygen vacancies and decreased valence cation substitutions [7,10,11]. Furthermore, detailed studies revealed that under these highly reducing conditions, instead of randomly distributed point defects in the bulk, the majority of the oxygen vacancies are surrounded by localized electrons that lower the valence of the neighboring transition metals, thereby forming defect clusters. [11] Ab-initio calculations indicate that lower valence dopants on the A- as well as on the B-site enhance the formation energy and the mobility of such defect clusters. [12] This means that careful control of dopant atoms can optimize the oxygen and electron mobility at the elevated operating temperature of these ceramic membranes [13]. Of particular importance from a micro-structural point of view is the presence of ordering or

interaction between these defect clusters. As ionic conductivity occurs via hopping of the oxygen atoms to adjacent unoccupied lattice sites, these effects will confine their mobility along the ordering direction and may reduce the overall bulk ionic conductivity.

Conventional high resolution phase contrast imaging studies by Alario-Franco et al [14] on reduced Ca<sub>x</sub>La<sub>1-x</sub>FeO<sub>3-y</sub> powders highlighted randomly oriented domains with a brownmillerite-like structure as a result of the intergrowth between Ca<sub>2</sub>Fe<sub>2</sub>O<sub>5</sub> and Ca<sub>2</sub>LaFe<sub>3</sub>O<sub>8</sub> under reducing conditions. Grenier et al [10] used these results for studies on the high temperature phase of Sr<sub>2</sub>Fe<sub>2</sub>O<sub>5</sub> by X-ray diffraction, Differential Thermal Analysis (DTA), and magnetic measurements. They concluded that the ordered micro domains above a certain transition temperature would shrink and orient randomly throughout the bulk until the final cubic perovskite phase is reached (cubic perovskite can also be regarded as an ordered brownmillerite phase with infinitely small domains). Several other high-resolution microscopy studies were also used to characterize these systems, but none of the results were obtained on an atomic level and the interpretation was made only in the context of bulk defect chemistry models and macroscopic transport measurements [3,8]. As such, the fundamental atomic scale origins of the properties were not investigated and a full understanding of the effects of cluster ordering and interactions was not developed.

In this study we characterize the previously observed micro domains in (La, Sr)FeO<sub>3-δ</sub> through a combination of Z-contrast imaging and electron energy loss spectroscopy (EELS) in the scanning transmission electron microscope (STEM)[15-17]. In-situ specimen heating is used to characterize oxygen vacancy ordering and investigate the development of the different phases and domains at conditions close to the membrane operating temperature in syngas reactors. These results show that ordered domains progressively grow with increasing temperature until the reduction of the cubic perovskite crystal structure cause some areas to collapse, thereby forming Aurivillius phases in the bulk that may restrict oxygen conductivity.

#### 4.2. Experimental Techniques

The experimental results presented in this report were obtained using a JEOL 2010F STEM/TEM [15-16], having a Schottky FEG-source and being operated at 200 kV. It is equipped with a standard UHR ("ultra high resolution") objective lens pole piece, a JEOL annular dark-field detector, a post column Gatan imaging filter (GIF) [15-16]. The oxygen partial

pressure in the column is 5\*10<sup>-8</sup> Pa. The lens conditions in the microscope were defined for a probe-size of 0.2 nm, with a convergence angle of 13 mrad and a collection angle of 52 mrad. With these settings, the probe current is sufficient (40 pA) to obtain statistically significant information and the Z-contrast image is essentially incoherent, i.e. a direct image of the structure is acquired. Furthermore, if the atomic spacing in a zone-axis orientation is larger than the probe size, an atomic resolution image can be obtained [15-16].

The experimental setup of this microscope allows us to use the low-angle scattered electrons that do not contribute to the Z-contrast image for EELS [18]. As the two techniques do not interfere, Z-contrast images can be used to position the electron probe at the desired spot in the sample to acquire spectra [18-20]. The physical principle behind EELS relates to the interaction of the fast electrons with the sample to cause either collective excitations of electrons (plasmons), or discrete transitions between atomic energy levels [19].

For (La, Sr)FeO<sub>3</sub>, investigated in this study and for other perovskite oxides, we are primarily interested in the bonding between oxygen and the B-site transition metal atoms. To investigate this, the near edge fine structure of the oxygen K-edge contains valuable information about the nearest neighbor bonding (O 2p with metallic 3d) and the hybridization with the metal sp band [21]. For example, the iron core-electron transitions from  $2p^63d^m$  to  $2p^53d^{m+1}$ , which indicate the number of available orbitals for hybridization with the oxygen bands, also lie in the sensitive part of the energy loss spectrum.

The formal valence-state of the transition metal elements in the structure can be determined from the analysis of the  $L_2$  and  $L_3$  white lines that are visible due to the spin-orbit interaction. More specifically, the  $L_3$  and  $L_2$  lines are the transition of  $2p^{3/2} \rightarrow 3d^{3/2}3d^{5/2}$  and  $2p^{1/2} \rightarrow 3d^{3/2}$ , respectively. Wang and Kang [4] have described a method of using the  $L_3/L_2$  white line intensity ratio to determine the numerical value for the valence. However, it needs to be stated that the computed ratios must be compared either with results from the literature or parametric fits calculated from well known materials under similar conditions in order to convert the intensities into numerical ionization values [6]. Here, the  $L_3/L_2$  ratio is determined by measuring the intensity of the  $L_3$  and  $L_2$  peaks in the second difference of the spectrum (so as to be insensitive to the thickness) [22]. The second difference spectra are obtained using the numerical filter

available in the Gatan EL/P software [23], with a 4.1 eV positive and a 1.7 eV negative window width. Using such a window width, small channel-to-channel fluctuations are averaged out. Furthermore, the maximum amplitude in this method is proportional to the white line intensity and can therefore be used to compare these intensities in different spectra.

This method of calculating the corresponding transition metal valences directly from the white line ratios does not take the magnetic moment of the compound into consideration. Pease et al. [24] have developed parameterization algorithm that linearizes the relationship between the local magnetic moment and the 3d white line ratio. In the course of this parameterization, we are able to correct the white line ratios for the local magnetic moments, and therefore calculate the corrected valence from the initial L<sub>3</sub>/L<sub>2</sub> white line ratios. For the correction of the magnetic moment of the different Fe-O compounds, a moment of 5 for Fe<sub>2</sub>O<sub>3</sub>, 3.43 for FeO and 4.5 for Fe<sub>3</sub>O<sub>4</sub> was assumed [24]. All the Fe-valences reported in this study, will be corrected for the local magnetic moment, without explicitly mentioning this fact further.

The in-situ heating experiments performed here utilize a double tilt heating stage with a miniature, encapsulated heater, which is attached to the two terminal posts in the specimen tip. A SmartSet Hot Stage Controller is used for temperature control of the heating stage, which gives us a variable temperature range between 293° K and 1273°C K. If the holder is operated above 773° K a water recirculation must be connected, to prevent heat transfer through the rod of the stage. Turbulent flow of water through the recirculation system makes it impossible to achieve atomic resolution for temperatures higher than 773° K. The piezo-electric stage drift control compensates for continuous drift of the heating holder, which will be caused by the temperature gradient in the stage. This enables us to acquire images and EEL spectra with longer acquisition times and therefore increase the signal to noise ratio. The oxygen partial pressure in the microscope column is  $P_{O_2^{\rm gus}} \sim 5*10^{-8}$  Pa during the experiment, which means that at 724° K the oxide samples are in a highly reducing environment.

The key to obtaining detailed information on the structure, composition and bonding at interfaces and defects is linked to the ability of the STEM to form a small electron probe. Figure 175 shows a schematic of the detector arrangement in the STEM demonstrating that all the signals of interest for materials characterization can be acquired simultaneously, relative to the probe

position on the surface of the sample. The starting point for the analysis is the Z-contrast image, which is formed by collecting the high-angle scattering on an annular detector (Figure 175). Detecting the scattered intensity at these high-angles and integrating over a large angular range effectively averages coherence effects between neighboring atomic columns in the specimen. Thermal vibrations reduce the coherence between atoms in the same column to residual correlations between near neighbors, a second order effect. This allows each atom to be considered as an independent scatterer. Scattering factors may be replaced by cross sections, and these approach a Z<sup>2</sup> dependence on atomic number. This cross section effectively forms an object function that is strongly peaked at the atom sites, so for very thin specimens where there is no dynamical diffraction, the detected intensity consists of a convolution of this object function with the probe *intensity* profile. The small width of the object function (~0.02 nm) means that the spatial resolution is limited only by the probe size of the microscope. For a crystalline material in a zone-axis orientation, where the atomic spacing is greater than the probe size, the atomic columns are illuminated sequentially as the probe is scanned over the specimen. An atomic resolution compositional map is thus generated, in which the intensity depends on the average atomic number of the atoms in the columns.

This result also holds true for thicker specimens. In this case, the experimental parameters cause dynamical diffraction effects to be manifested as a columnar channeling effect, thus maintaining the thin specimen description of the image as a simple convolution of the probe intensity profile and an object function, strongly peaked at the atom sites. The phase problem associated with the interpretation of conventional high-resolution TEM images is therefore eliminated. In thin specimens, the dominant contribution to the intensity of a column is always its composition. However, due to the higher absorption of the heavy strings the contrast does decrease with increasing specimen thickness and in very thick crystals there is no longer a high-resolution image. The effect of changing focus is also intuitively understandable as the focus control alters the probe intensity profile on the surface of the specimen. For defocus less than the optimum Scherzer condition, the probe broadens causing the individual columns not to be resolved. For higher defocus values the probe narrows with the formation of more intense tails, causing sharper image features but compositional averaging over several columns. The optimum focus condition therefore represents a compromise between high resolution (narrow probe profile) and

the desire for a highly local image (no tails to the probe). This focus condition also corresponds to the optimum probe for microanalysis.

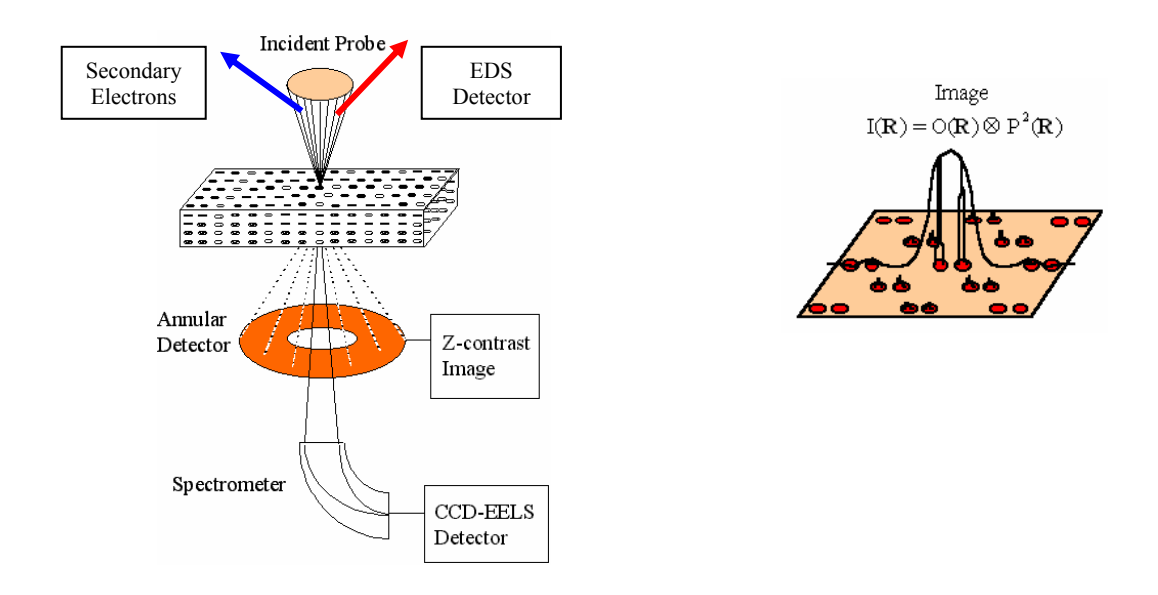


Figure 175 (a) Schematic of the STEM. (b) The Z-contrast image and energy loss spectrum can be interpreted as a simple convolution of the experimental probe and the object function. With lower spatial resolution, the EDS spectrum can also be interpreted in this manner.

As can be seen from Figure 175, the annular detector used for Z-contrast imaging does not interfere with the low-angle scattering used for EELS. This means that the Z-contrast image can be used to position the electron probe over a particular structural feature for acquisition of a spectrum. The physical principle behind EELS relates to the interaction of the fast electron with the sample to cause either collective excitations of electrons in the conduction band, or discrete transitions between atomic energy levels, e. g.  $1s\Box 2p$  transitions. The ability to observe discrete atomic transitions allows compositional analysis to be performed by EELS (the transitions occur at characteristic energy losses for a given element). Furthermore, the transitions to unoccupied states above the Fermi level allows the degree of hybridization between atomic orbitals to be determined, i.e. information on local electronic structure (bonding) changes can be ascertained. To be able to correlate these features of the spectrum precisely with a structural feature of interest, it is essential that the spectrum has the same atomic resolution as the Z-contrast image. In order to achieve this atomic resolution, the range over which a fast electron can cause an excitation event must be less than the inter-atomic spacing. Hydrogenic models show that for the majority of edges accessible by conventional energy-loss spectrometers  $\Delta E < 2$  keV) the

object functions are localized within 0.1 nm of the atom cores. Hence, like the Z-contrast image, we have an object function localized at the atom cores and an experimental probe of atomic dimensions. For crystalline materials in zone-axis orientations, providing we maintain a large collection angle, the description of the spectrum (Figure 175) in terms of a convolution of the probe with an object function is valid.

#### 4.3 Results

In figure 176a) the Z-contrast image of the atomic structure of the sintered but untreated material is shown. The cubic symmetry is clearly visible and the brightest spots represent the mixed (La, Sr), whereas the less bright spots are the Fe-O columns. The pure O-columns are not visible in the image due to the low scattering amplitude of oxygen compared to La, Sr, and Fe. In the bulk of the grains we could not detect any sign of ordering, which confirms their ideal stoichiometry of this starting structure. The corresponding EEL spectrum is displayed in figure 176b). The spectrum includes the La M<sub>4,5</sub>, Fe L<sub>3,2</sub> and the O-K edges. The Sr core loss peaks are located beyond the detector range of this spectrometer. The spectrum is background subtracted, corrected for multiple scattering [19] and normalized to the La M<sub>4,5</sub> edge intensities. The calculated average Fe valence state for this untreated membrane material is 2.6±0.1. Lower magnification images that depict a different grain oriented along a major zone axis ([001]) show some additional features (figure 177a).

Upon investigation at higher magnification, the atomic structure of these planar defects, which run irregularly through the grains, can be identified. The regular lattice above and below the dark line is shifted by half a unit-cell along the direction of this dark feature. EEL spectra taken from the center of the dark line and the adjacent bulk exhibit a significantly lower La M-edge signal but higher O-edge intensity (figure 178). Therefore the spectra are in this case normalized to the Fe-L<sub>3,2</sub> intensities. In addition to the decrease of La-M edge intensities, the Fe-L<sub>3,2</sub> ratio as well as the oxygen K-edge pre-peak is decreased in the planar defect column. The measured Fe valence in the dark lines of 2.4±0.1, as well as the changed O K-edge fine structure originates from the different local atomic environment, rather than from an oxygen vacancy ordering.

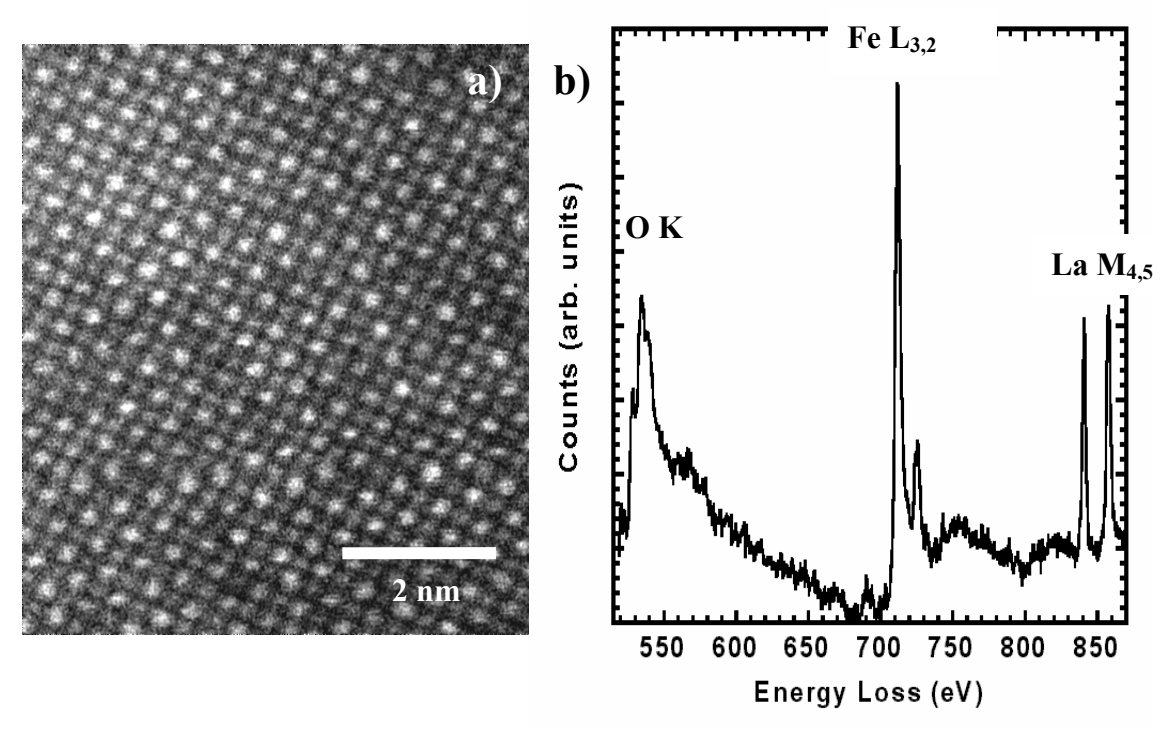


Figure 176.

a) Z-contrast micrograph of sintered (La, Sr)FeO<sub>3</sub> [001] showing the cubic perovskite structure, with the brighter (La, Sr) columns, and the less bright Fe-O columns. b) EEL-spectra nano-meter scale probe-diameter. The spectra are a sum of 14 individual spectra with an acquisition time of 2 sec and show the O K-, the Fe L- and the La M-edges.

Figure 179 shows a Z-contrast micrograph of the material after it was reduced at 1023 K and  $P_{O_2} = 10^{-2}$  Pa for 27 h at room temperature with ordered structures in the form of contrast variations in every second column. For this material, the average measured iron valence is  $+(2.7 \pm 0.1)$ . The weak change in contrast and the extremely low count rates make it very difficult to distinguish between the spectra taken at the different columns. Nevertheless the results show that the dark columns represent the reduced valence columns ( $\sim$ 2.6), whereas in the bright columns the valence is close to +2.8. The results show, that the point-defect concentration is higher, as the reduced average iron valence indicates a increased number of vacancy clusters.

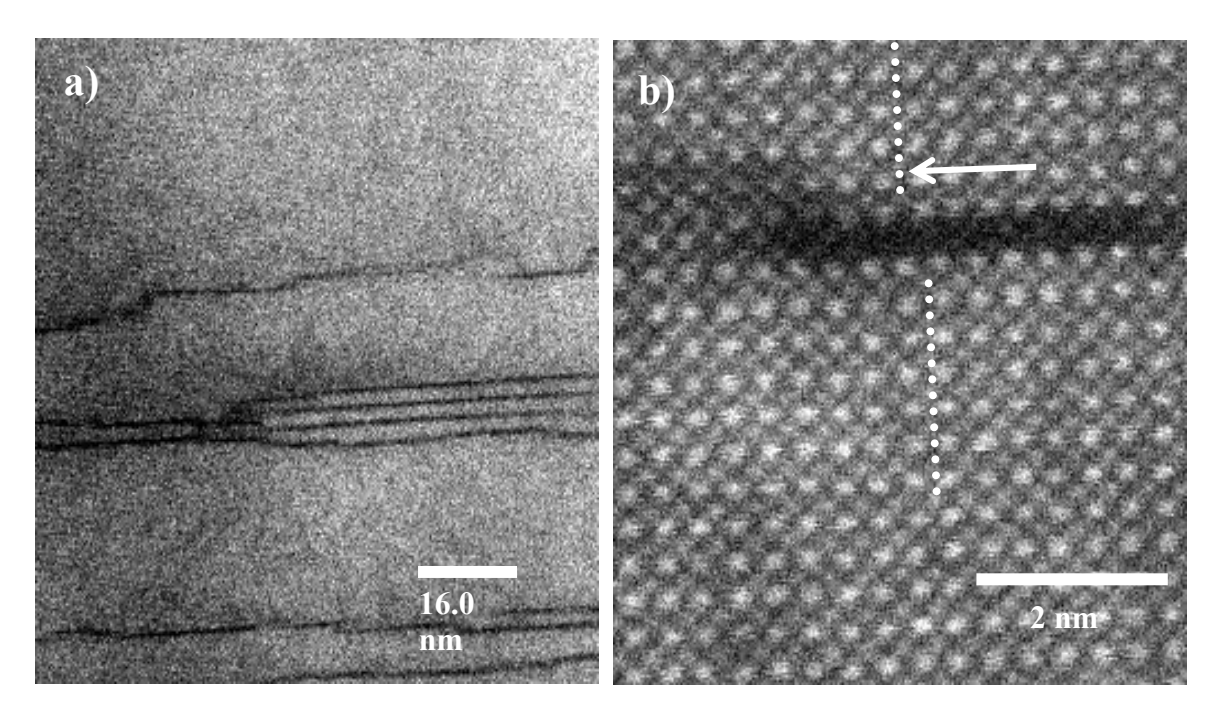


Figure 177. a) Low magnification dark field image of the bulk of a sintered LSFO grain exhibiting dark features. b) Atomic resolution of one dark line, showing the internal structure of this feature and the shift between the adjacent bulk crystal structures.

After the type 1 sample was heated and allowed to stabilized at 724° K for 12 hours in the

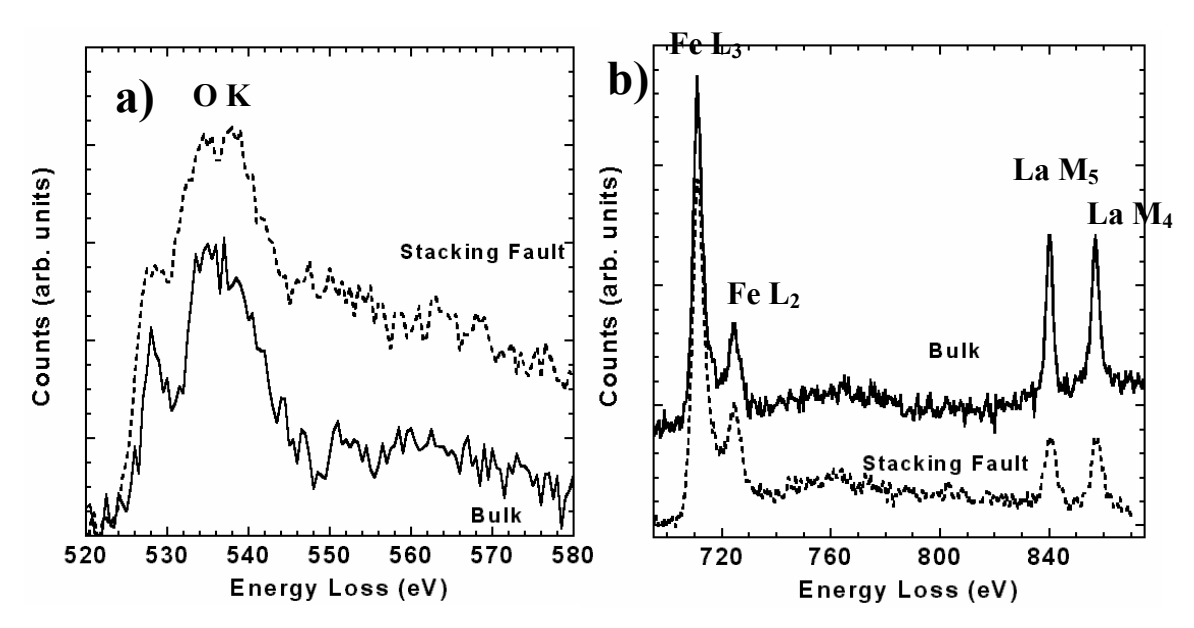


Figure 178.

a) Atomic resolution EELS of one dark line, showing the internal structure of this feature and the shift between the adjacent bulk crystal structures. b) O K-edge from the stacking fault and from the bulk, showing the differences in the fine-structure and the higher intensity in the stacking fault. e) Fe L- and La M-edges from the same positions.

microscope the contrast changes appear more distinct in the sample, and can be clearly identified in the power spectrum of the acquired image (figure 180a). We can now observe small microdomains of 8-16 unit cells width (2.4 nm - 4.8 nm); the orientations and boundaries seem to be

random. Note that the EEL spectra at elevated temperatures from the dark and the bright FeO<sub>2</sub> columns (figure 180c), normalized to the intensity of the La M-edges, display different fine structures and intensities of the O K- and Fe L-edges. The pre-peak of the O K-edge (figure 181 b) in the dark columns of the domains is reduced with respect to the bright ones, indicating a decreased number of available O 2p - Fe 3d orbits, and therefore a lower valence. Also the Fe white line intensity ratios reveal a reduction of the transition metal valence from  $+(2.8 \pm 0.1)$  in the bright to  $+(2.3 \pm 0.1)$  in the dark columns respectively. Additionally, the intensity ratio of

the iron L-edge to the oxygen K-edge is increased in the dark lines by 10% with respect to the bright line ratio, showing the lower oxygen content in the dark columns.

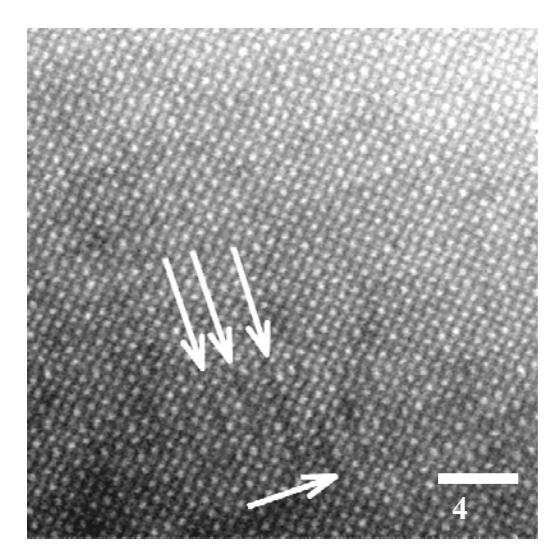


Figure 179 Z-Contrast image with marked change in contrast in

Following this characterization, the reducing conditions were increased by heating the specimen to 1074° K for 3 hours at an constant oxygen partial pressure of  $P_{O_2} = 5*10^{-8}$  Pa. Figure 181 a) shows a Z-contrast image (after the temperature is reduced to 724° K) of the material after it was quenched in the microscope column. Here the ordered domains, as well as the interwoven domain-boundaries can be seen very clearly. The picture appears blurred due to the increased contamination layers from the heating process. Although the overall contrast of this micrograph is lower and the sample vibrates slowly due to the heating process, the ordered structures can bee seen easily here. Both pictures suggest that the size of the micro domains is increased dramatically in this environment (~20 nm), and also the domain boundaries are more clearly defined after the increase in temperature. The stronger distinction between the bright and dark columns suggests that the difference in the oxygen concentration between the bright and the dark lines is even higher than before the reducing process. Analysis of the EEL spectra at 724° K

reveals that the already reduced, dark columns have an even lower iron valence of  $+(2.0\pm0.1)$ , whereas the bright columns remain at a constant valence of  $+(2.9\pm0.1)$ .

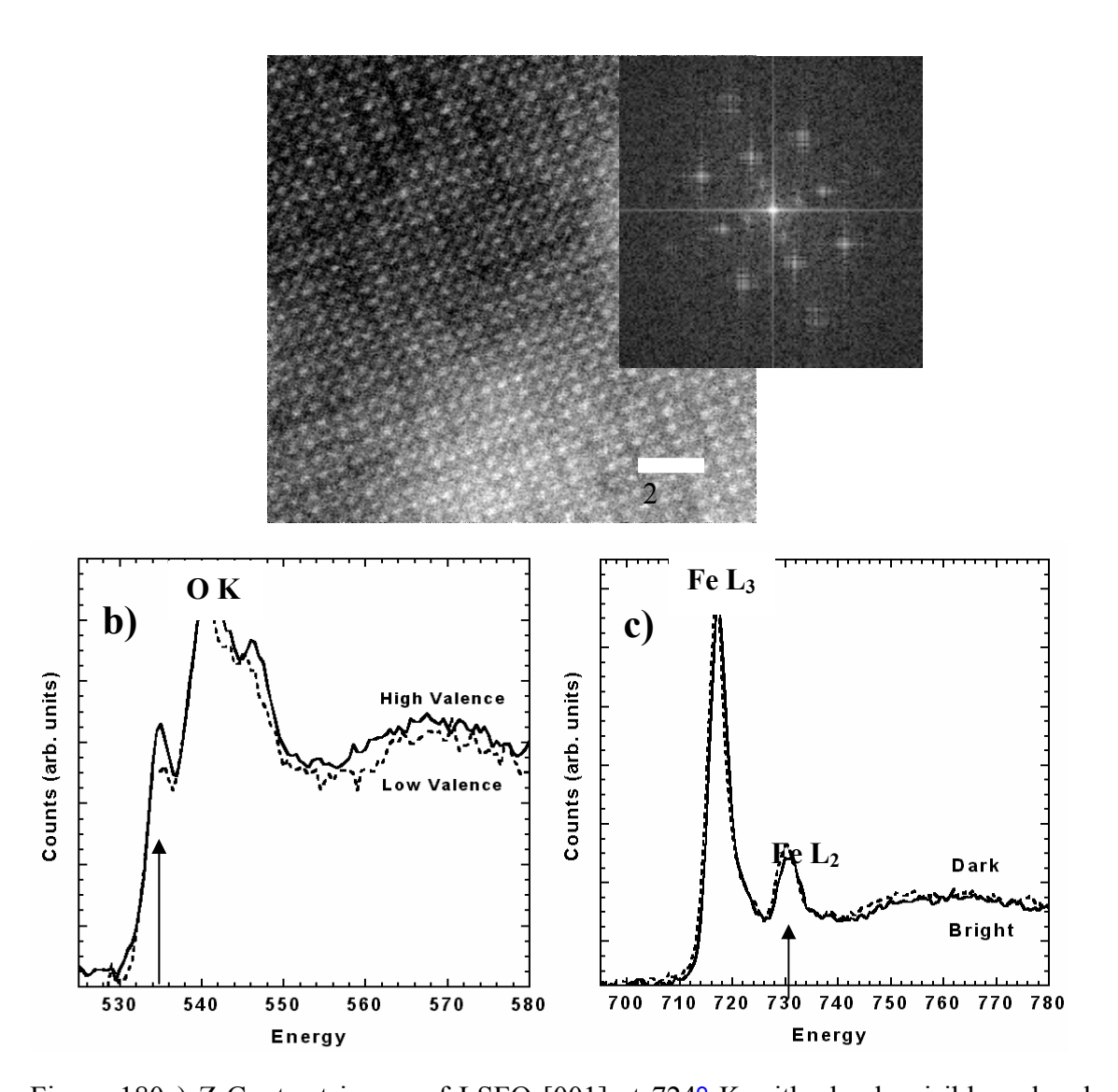


Figure 180a) Z-Contrast image of LSFO [001] at 724° K with clearly visible ordered domain, inlet shows diffraction pattern with additional spot. EELS of bright and dark columns in (La.Sr)FeO<sub>3</sub> at 724° K b) O K-edge c) Fe L-edges with arrows marking the differences.

Figure 182 shows the micrographs at room temperature of the sample in the [001] direction that was previously reduced at  $1073^{\circ}$  K and  $P_{O_2} = 10^{-10}$  Pa until a stable equilibrium with its surrounding was reached. The image displays some features that were not observed in the bulk of the untreated or lesser-reduced samples before. Two dark lines of one unit cell width, separated by one bright line in the center (see figure 182b) are oriented along the [010] direction. The EEL data acquired from the dark feature and from the surrounding bulk material is shown in figure 183, and all the spectra are normalized to the O K-edge intensities. The most striking difference between the bulk spectra and the spectra taken from the defect structure is the drastic decrease in

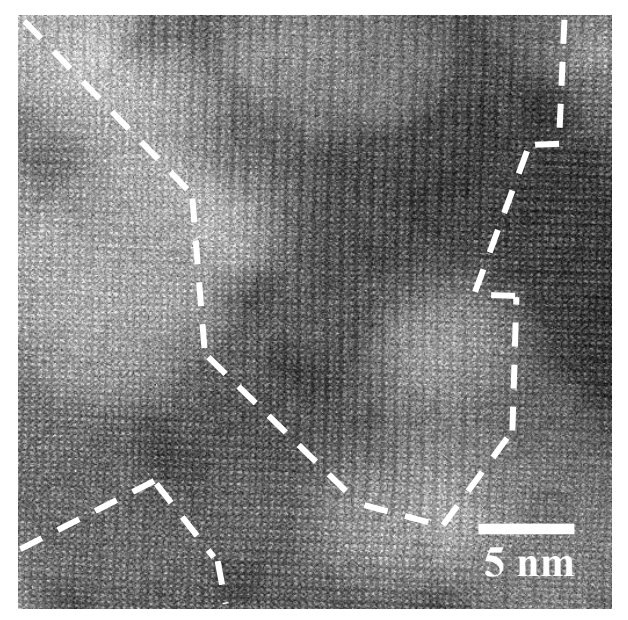


Figure 181 Z-Contrast image of LSFO at 724° K after heating at 1073° K, showing the change in contrast very clearly. The white spots in the image are caused by contamination built up on the surface during the heating process.

the La M-edge intensity. Hence, it appears to be most likely that the dark lines are caused again by a stacking fault, containing a double layer of FeO<sub>2</sub>, as the La M-edge intensity is nearly halved in these columns. The different atomic environment in the stacking fault also gives rise to the observed difference in the O K-edge fine structure. Parallel to these stacking faults the reduced columns form huge domains in this kind of sample. In general, the ordered domain size is dramatically increased in the type 2 sample, but so far no other phases, such as LaFeO<sub>3</sub> or SrO have been found.

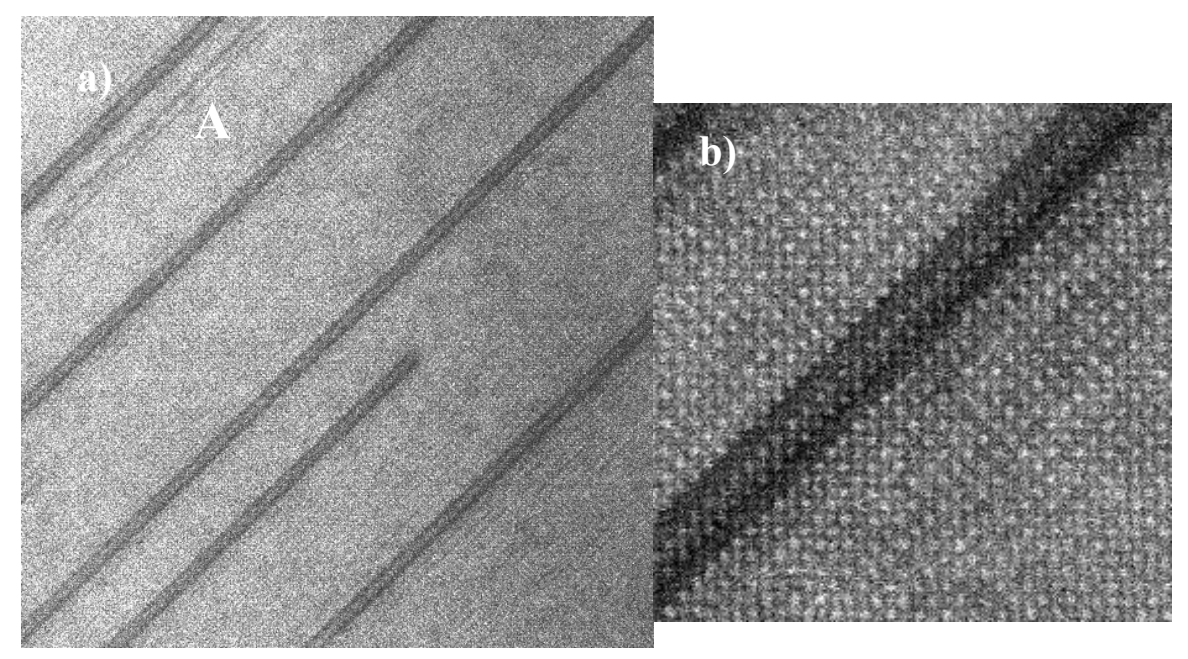


Figure 182 Z-Contrast image of (La,Sr)FeO<sub>3</sub>, previously treated at 1024° K in 10<sup>-10</sup> Pa showing stacking faults and ordered structure parallel to them.

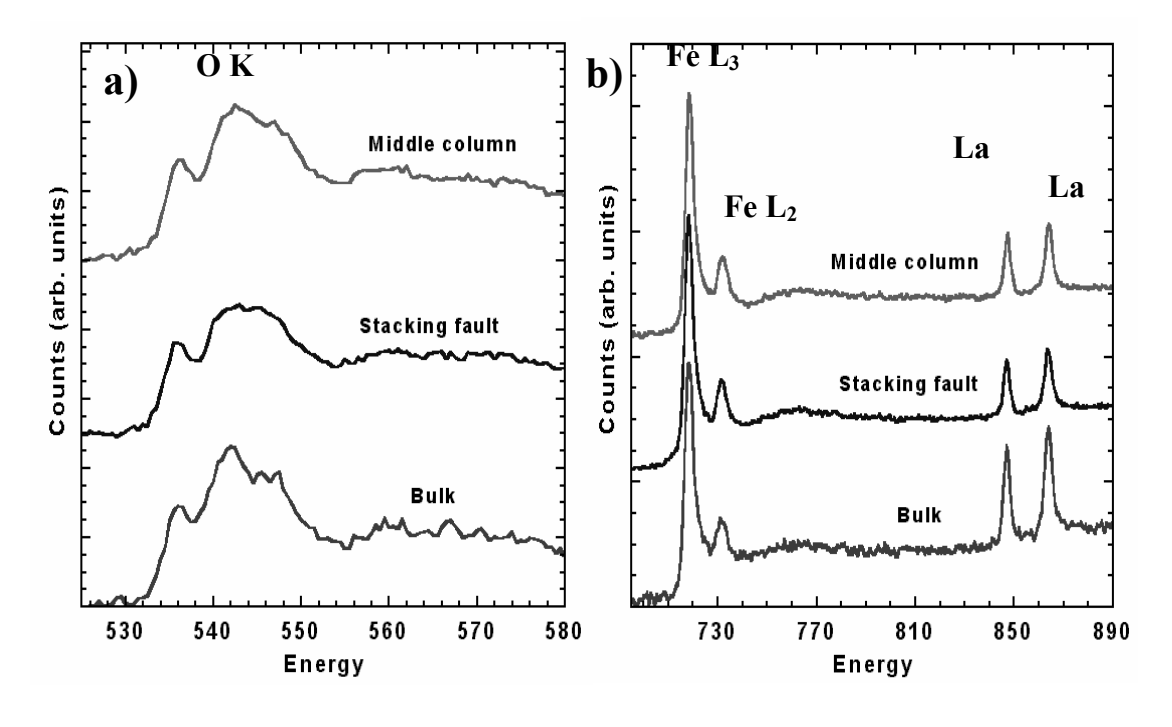


Figure 183 EELS of (La, Sr) FeO3 from the bulk, the stacking fault and the brighter middle column, normalized to the iron core loss edge intensities. a) Oxygen K-edge b) Fe L-and La Ma-edges.

Figure 184 shows images obtained from a representative area of the membrane material. One of the advantages of the JEOL 2500SE used to obtain these images is that it permits a secondary electron image of the sample surface to be obtained. By comparing this image to the bright field (thicker regions are darker) and dark field (thicker regions are brighter) we can identify several key features in the sample. The most obvious features of the sample are the precipitates that can be clearly observed in all the images. The changes in contrast indicate that these precipitates may be thinner than the matrix in which they are embedded or be of a different composition. The contrast in the three images gives some indication of a thickness change, but the composition cannot be verified without obtaining EDS spectra from the sample.

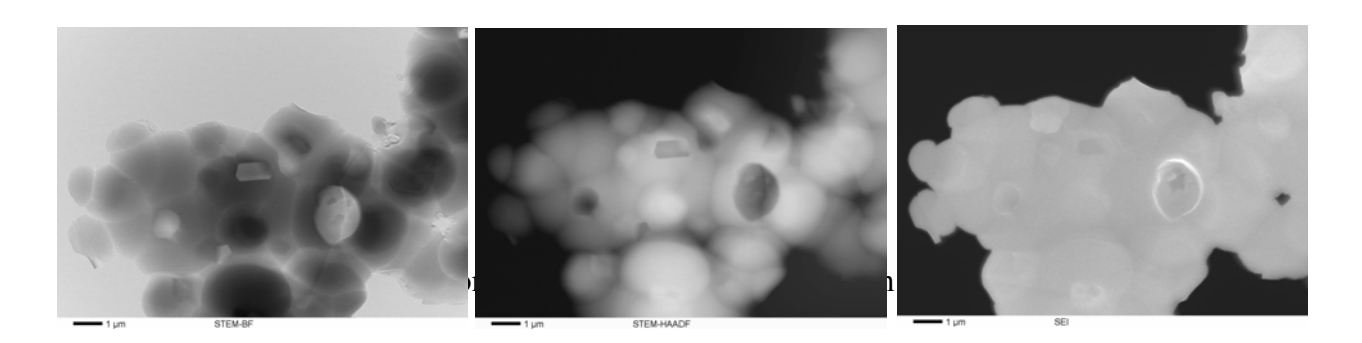


Figure 184 Secondary electron (bright field) images indicating presence of precipitates in the matrix

Figure 185 shows the results of the X-ray maps obtained from the area of sample shown in figure 184. Here, a full EDS spectrum is acquired at each pixel in the scan across the sample and then this complete scan is used to provide an intensity map of a given peak. In the case of the sample here, the Fe, Cr, La, Sr, O and Mg peaks were found to have a major presence in the spectra, and so these peaks were used to form the images. From these scans, some of the features from the images can be understood. The large irregular patches in the bright field and dark field images are shown to be thinner areas. In these cases, it is likely that the grains that occupied these spaces fell out during processing. Other features in these spectral images show that there are regular facetted secondary phases existing. In both cases, these phases appear to be composed of FeCrMgO. It is not immediately clear where the Mg comes from, but this will be addressed in future work. Another interesting result of these images, is that all the spectral maps show the same intensity changes at the grain boundaries, indicating that there is no significant enrichment of the grain boundaries by any particular element.

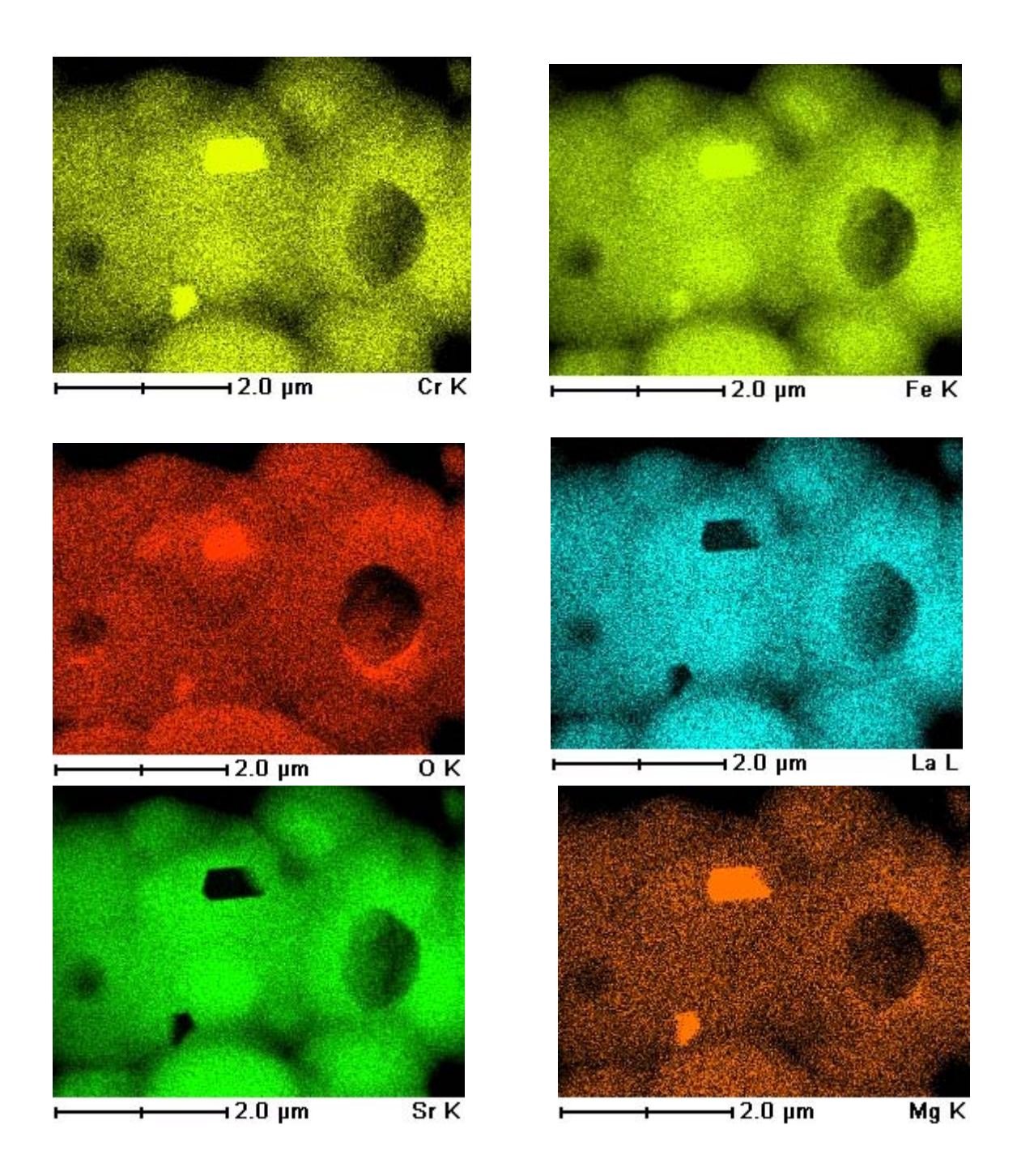


Figure 185 Elemental profiles of the area shown in figure 184.

The lack of segregants at the grain boundaries has been investigated further using the atomic resolution imaging and spectroscopy techniques. The initial findings suggest that the major effect that occurs at the grain boundaries is an increase in the number of oxygen vacancies.

# 4.4 Discussion

The atomic scale analysis of (La, Sr)FeO<sub>3</sub> under various ambient pressure and temperature conditions, illustrates the formation and evolution processes of ordered vacancy structures in the reduced perovskite oxides. The freshly sintered samples exhibit the ideal cubic perovskite structure in the majority of the grains, which indicates a stoichiometric composition for the bulk material. However, some grains contain linear stacking faults (Fig. 177), which can be identified as a Ruddelsden-Popper phase. A schematic drawing of the atomic structure of the Ruddelsden-Popper phase is shown in figure 186a. These planar defects (first discovered in SrTiO<sub>3</sub>-like structures by Ruddelsden and Popper [25] ) are usually formed in connection with the planartype accommodation of excess alkaline-earth oxides by interleaving slabs of the rock-salt structure within the perovskite structure. The structures observed here are similar to those reported by Suzuki [26] where the growth of hetero-epitaxial non-stoichiometric BaTiO<sub>3</sub> led to the formation of layered Popper-Popper phases (RP) of the general formula BaO-(BaTiO<sub>3</sub>)<sub>n</sub> with n=1,2,.... Here the images suggest that the planar defect formed in the (La, Sr)FeO<sub>3</sub> ceramic is the interleaving a single-layered FeO<sub>2</sub> block within the perovskite structure with a shear vector ½ [110] [27] Therefore, the occurrence of these RP-phases is always closely linked to a deviation from the ideal *cation* stoichiometry of the bulk matrix. The rock salt intergrowth layer functions as a buffer layer that compensates for the local non-stoichiometry. Although this compensation mechanism is only reported for A-site excess [26,28] it seem conceivable to expect a similar compensation mechanism for any kind of B-site non-stoichiometry. Most importantly, these defects are not related to oxygen vacancies and are found not to exist in the subsequently annealed samples.

The formation of the Popper-Popper phase in the as sintered materials is clearly not related to changes in ionic conductivity at elevated temperatures. In fact, the conductivity of the reduced materials appears to be controlled by the formation of the Brownmillerite phase. The Z-contrast and EELS results clearly demonstrate that the ordering of oxygen vacancy clusters in every second FeO2 column causes the planar structures observed under reducing conditions. We therefore confirm earlier results [10] that the ordered structures appear in reduced perovskite oxides, such as (Ca, La)FeO<sub>3</sub> [14], (La, Sr)(Fe, Cr)O<sub>3</sub> or SrCoO<sub>3</sub>. [29]. The results presented

here, rule out other suggested reasons for the observed 1-dimensional ordering, such as a segregation of La and Sr in every second column [29], as this would cause the bright (La, Sr)O columns rather than the FeO<sub>2</sub> columns to vary in contrast.

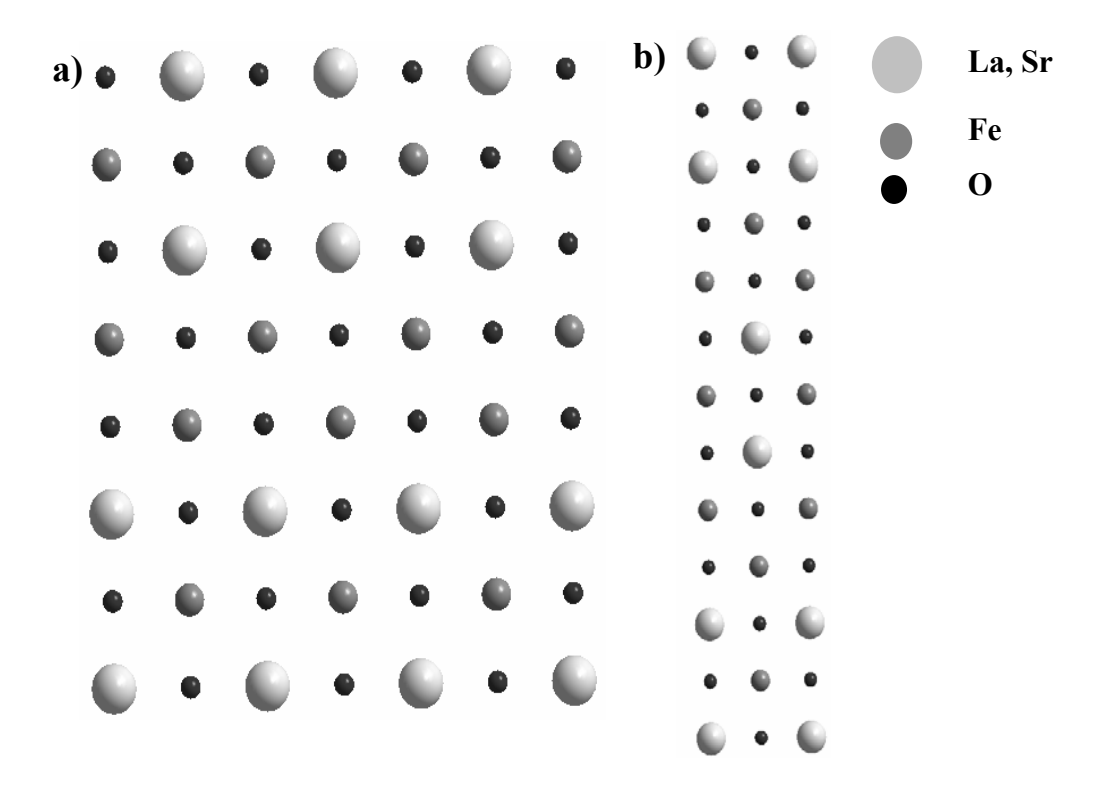
At temperatures below 1073° K and  $P_{O_2} = 1*10^{-6}$  Pa, the oxygen vacancy ordered domains are randomly oriented throughout the bulk. Due to the arbitrary direction of this ordering, with no preferential orientation or clustering into larger ordered domains, the overall diffusion performance of the material should be very high (as the reduced planes act as conductivity channels [12]. A disordered arrangement (on the scale of a few nm) of the ordered vacancies is therefore essential for the high oxygen transport material performance. Under higher reducing conditions (lower oxygen partial pressure and higher temperatures) more oxygen vacancies are created. However, the formation of these vacancies does not occur in every position with identical probability. It seems that the already reduced (dark) columns have an increased vacancy formation rate, or from the opposite point of view, a lower vacancy formation energy. The iron valence data for this situation show a decrease in the iron valence from +2.6 to +2.3. The bright columns on the other hand remain mostly unchanged or even a slight increase in the iron valence (i.e. oxygen content) is measured. This means that the two atomic layers in the same material have a completely different thermodynamic behavior.

A further increase in temperature causes even more oxygen to diffuse out of the material and leave behind continuously growing micro domains of ordered vacant oxygen lattice sites. The oxygen of the already reduced columns is decreased even further, as the iron valence drops from +2.3 to +2.0, while the unreduced columns (bright) keep their original oxygen content (iron valence +2.8). The dark lines represent a further reduction of the Brownmillerite phase.

At this point the micro domains start to exhibit a distinct bulk and boundary behavior. In the center of the domains, all the dark columns are aligned in one direction, whereas at the interfaces a small interwoven domain-boundary layer is observed, similar to the features in SrCoO<sub>3</sub> [29]. Under these conditions the huge ordered domains are assumed to not act as high conductivity paths anymore, as oxygen flow is only possible in one direction. Rather than flowing along the shortest line of the concentration gradient, the oxygen atoms must move in the direction of the ordered domains. The grains oriented perpendicular to the oxygen gradient do not contribute to

the overall oxygen current across the membrane and the oxygen ions must flow along a percolative path. Four probe conductivity measurements seem to confirm this hypothesis.

At temperatures of 1350° K and pressure around 10<sup>-9</sup> Pa, the concentration of oxygen vacancies in the dark (vacancy containing) columns reaches a critical value. Here the already highly reduced columns cannot host any more oxygen vacancies without losing their structural integrity. Consequently these columns collapse and form the observed stacking faults of double FeO<sub>2</sub> layers, or the Aurivillius phase. A schematic drawing of the atomic structure of the Aurivillius phase is shown in figure 186b.



a) Schematic drawing of the proposed secondary Ruddelsden-Popper phase in a perovskite oxide material, which compensates for the local anion non-stoichiometry. The rock-salt layer consists of two atomic layers of Fe-O. b) Schematic drawing of the Aurivillius phase, which consists of a perovskite layer sandwiched between two layers of Fe-O.

The Aurivillius phase (first detected by Aurivillius [30] Bi<sub>2</sub>O<sub>2</sub>)[A<sub>n-1</sub>B<sub>n</sub>O<sub>3n-1</sub>]) is a lamellar material derived from the perovskite structure. Its structure is composed of n layers of ABO<sub>3</sub> perovskite units, sandwiched between (Bi<sub>2</sub>O<sub>2</sub>)<sup>2+</sup> layers. It has been found that this structure is very difficult to crystallize because of the chemical complexity [31]. However, several cases have been reported where a transformation of the RP-phase into the Aurivillius phase has been A similar effect occurs here in the membrane materials, where a observed [32,33]. transformation of the RP-phase into the Aurivillius phase via the oxygen ordered Brownmillerite phase is seen. These second phases then act as nucleation sites/barriers to preferentially orient the ordered domains, thereby forming gigantic ordered domains. Four-probe conductivity measurements under these conditions indicate a sudden drop in the ionic and electronic conductivity, consistent with this effect. The decrease in conductivity can be explained by the preferential flow direction in the bulk of a single grain and that fact that practically no oxygen transport occurs perpendicular to the stacking faults. The appearance of the stacking faults in such high concentration, could also give rise to the measured shift towards lower angles and the small additional peak intensities in the X-ray diffraction spectra, taken from the type 2 sample, rather than the segregation of different phases in the material as previously proposed.

#### 4.5 CONCLUSIONS

In conclusion, the ability to observe the structure, characterize the composition and to map valence state changes at atomic resolution in various thermodynamic environments provides an unparalleled capability to understand the effects of oxygen vacancy ordering in electronic and ionic conducting perovskites. Although we are not able to acquire atomic resolution images at temperatures higher than 724° K, we now have the opportunity to test the predictions of conventional defect chemistry on the atomic scale. The results presented here clearly show that the oxygen formation energy is not constant from one atomic column to another: the defect chemistry differs dramatically from one FeO<sub>2</sub> layer to the next. These results are also contrary to previous suggestions regarding the vacancy ordering low and high temperature phases [10,14]. It was previously concluded that at elevated temperatures (below a specific order-disorder transition temperature) ordered micro-domains progressively grow and asymptotically reach a stable equilibrium concentration [3]. The reason for this difference in the results lies in the fact

that X-ray diffraction methods cannot detect the Brownmillerite phase and none of the previous studies acquired the high temperature phase data above room temperature. It is also conceivable, that the high temperature phase is unstable and was not investigated at all by those studies [10]. It should be noted that another explanation could be that at the specific (La, Sr) doping level in these samples, the decomposition temperature of the material is lower than the actual disorder-order transition temperature. Therefore the sample decomposed before a transition from the brownmillerite to the perfect cubic perovskite phase was observed. Future work will investigate the effect of composition on the nucleation and growth of vacancy ordered domains and phases in these membrane materials. The group of Professor H. Tuller at MIT initially treated all the membrane samples.

We used advanced atomic resolution techniques in scanning transmission electron microscopy (STEM) to investigate the structure, composition and bonding changes that occur within grains, at grain boundaries, at domain boundaries and within ordered structures in the ceramic membrane materials. In particular, Z-contrast imaging is used to provide a direct image of the atomic structure and as a map to position the probe for electron energy loss spectroscopy (EELS). EELS is sensitive to both composition and bonding, allowing us to correlate the structure with changes in composition and valence state for the transition metal elements in the structure. We used these techniques to develop strategies to detect and characterize vacancy creation, dopant segregations and defect association in the oxygen conducting membrane material. We could assess the microstructure of the membrane material to evaluate the effects of vacancy-impurity association, defect clusters, and vacancy dopant association on the membrane performance and stability.

# 4.6 References (for Chapter 4)

- 1. Huang K, Tichy R S, and Goodenough J B (1998) Superior Perovskite Oxide-Ion Conductor; Strontium and Magnesium-Doped LaGaO<sub>3</sub>: I, Phase Relationships and Electrical Properties. *J. Am. Ceram. Soc.* **81**, 2565-75
- 2. Mazanec T J (1994) Prospects for ceramic electrochemical reactors in industry. *Solid State Ionics*, **70/71**, 11-19.
- 3. Kruidhof H, Bouwmeester H J M, von Doorn R H E, and Burggraaf A J (1992) Influence of order-disorder transactions on oxygen permeability through selected nonstoichiometric perovskite type oxides. *Solid State Ionics*, **63-65**, 816-822.
- 4. Z.L. Wang, Z L and Kang, Z C (1998) Functional and smart materials. (Plenum Press)
- 5. Rao C N R, Gopalakrishnan J, and Vidyasagar K (1984) Superstructures, Ordered Defects & Nonstoichimetry in Metal Oxides of Perovskite & Related Structures. *Indian J. Chem.*, **23A**, 265-284.
- 6. Wang Z L, and Zhang J (1996) Tetragonal domain structure and magnetoresistance of La<sub>1-x</sub>Sr<sub>x</sub>CoO<sub>3</sub>. *Phys. Rev. B*, **54**, 2, 1153-58.
- 7. Ling S (1994) High-concentration point-defect chemistry: Statistical-thermodynamic approach applied to nonstoichiometric cerium dioxides. *Phys. Rev. B*, **49**, 2, 864-880.
- 8. Chiang, Y M, Birnie, D and Kingery, W D (1997) Physical Ceramics. (MIT Series)
- 9. Balachandran U, Dusek J T, Sweeney S M, Poeppel R B, Mieville R L, and Maiya P S (1995) Methane to Syngas via Ceramic Membranes. *Am. Cer. Soc. Bul.*, **74**, 1, 71-75.
- 10. Grenier J C, Ea N, Pouchard M, and Hagenmuller P (1997) Structural Transitions at High Temperature in Sr<sub>2</sub>Fe<sub>2</sub>O<sub>5</sub> . *J. Solid State Chem.*, **58**, 243-252, 1985.
- Lankhorst M H R., Bouwmeester, H J M and Verveij, H (1997) J. Am. Ceram. Soc, 80
   [9], 2175-98.
- 12. Islam M. S. (2000) Ionic transport in ABO<sub>3</sub> perovskite oxides: a computer modeling tour. *J. Mat. Chem.*, 10 (5), 1027-1038
- ten Elshof J E, Bouwmeester H J M, Verweij H (1995) Oxygen transport through
   La<sub>1-x</sub> Sr<sub>x</sub>FeO<sub>3-δ</sub> membranes. I. Permeation in air/He gradients. *Solid State Ionics*, 81, 97-109.

- 14. Alario-Franco M A, Gonzalez-Calbet J M, and Vallet-Regi M (1983) Brownmillerite-type micro domains in the calcium lanthanum ferrites: Ca<sub>x</sub>La<sub>1-x</sub>FeO<sub>3-y</sub>. *J. Solid State Chem.*, **49**, 219-231.
- 15. James E M, and Browning N D (1999) Practical aspects of atomic resolution imaging and analysis in STEM. *Ultramicroscopy* **78** 125-139.
- 16. James E M, Browning N D, Nicholls A W, Kawasaki M, Xin Y, and Stemmer S (1998) Demonstration of atomic resolution Z-contrast imaging by a JEOL JEM-2010F scanning transmission electron microscope. *J. Electr. Micr.*, **47(6)**, 561-574.
- 17. Nellist P D and Pennycook S J (1998) Incoherent imaging using dynamically scattered coherent electrons. *Ultramicroscopy* **78**, 111, 124.
- 18. Jesson D E, and Pennycook S J (1995) Incoherent imaging of crystals using thermally scattered electrons. *Proc. R. Soc. Lond. A*, **449**, 273-293.
- 19. Egerton, R F (1986) Electron Energy Loss Spectroscopy in the electron microscope. (Plenum, New York)
- 20. Browning N D, Chrisholm M F, and Pennycook S J (1993) Atomic Resolution Chemical Analysis Using a Scanning Transmission Electron Microscope. *Nature*, **366**, 143-146.
- 21. Browning N D, Buban J P, Moltaji H O, Duscher G, Pennycook S J, Rodrigues R P, Johnson K, and Dravid V P (1999) The influence of atomic structure on the formation of electrical barriers at grain boundaries in SrTiO<sub>3</sub>. *Applied Physics Letters* **74**, 2638-2640.
- 22. Botton G A, Appel C C, Horsewell A, and Stobbs W M (1995) Quantification of the EELS near-edge structures to study Mn doping in oxides. *Journal of Microscopy*, **180**, 211-216.
- 23. Kundman M, Chabert X, Truong K, and Krivanek O L (1990) *EL/P software for Macintosh II computer*, Gatan Inc.
- 24. Pease, D M, Fasihuddin, A, Daniel, M, Budnick, J I(2001) Method of linearizing the L<sub>3</sub>/L<sub>2</sub> white line ratio as a function of magnetic moment. *Ultramicroscopy*, **88**, 1-16
- 25. Ruddlesden S N, and Popper P (1958) Acta Crystallogr., 11, 54.
- 26. Suzuki T, Nishi Y, and Fujimoto M (2000) Ruddlesden-Popper Planar Faults and Nanotwins in Heteroepitaxial Nonstoichiometric Barium Titanate Thin Films. *J. Am. Ceram. Soc.*, **83**, 3185-95.

- 27. Eibl O, Pongratz P, Skalicky P, and Schmelz H (1998) Dislocations in BaTiO<sub>3</sub> Ceramics *Phys. Status Solidi*, A, **108**, 495-502.
- 28. Fujimoto M, Suzuki T, Nishi Y, Arai K (1998) Calcium-Ion Selective Site Occupation at Ruddlesden-Popper-Type Faults and the Desultant Dielectric Properties A-Site-Excess Strontium Calcium Titanate Ceramics. *J. Am. Ceram. Soc.*, **81**, 33-40.
- 29. Klie R F, Ito Y, Stemmer S and Browning N D (2001) Observation of oxygen vacancy ordering and segregation in Perovskite oxides. *Ultramicroscopy*, 86, 289-302.
- 30. Aurivillius, B (1950) Ark. Kemi, 2, 519,.
- 31. Du X and Chen I-W (1998) Ferroelectric Thin Films of Bismuth-Containing Layered Perovskites: Part II, PbBi<sub>2</sub>Nb<sub>2</sub>O<sub>9</sub>. *J. Am. Ceram. Soc.*, **81**, 3260-64.
- 32. Gopalakrishnan J, Sivakumar T, Ramesha K, Thangadurai K, and Subanna G N (2000) Transformations of Ruddlesden-Popper Oxides to New Layered Perovskite Oxides by Metathesis Reactions. *J. Am. Chem. Soc.*, **122**, 6237-41.
- 33. Sugimoto W, Shirata M, Sugahara Y, Kuroda K (1999) New Conversion Reaction of an Aurivillius Phase into the Protonated Form of the Layered Perovskite by the Selective Leaching of the Bismuth Oxide Sheet. *J. Am. Chem. Soc.*, **121**, 11601-02.

#### 4.7 Publication resulted from this research:

- N.D. Browning, I. Arslan, Y. Ito, E.M. James, R.F. Klie, P. Moeck, T. Topuria and Y. Xin: Application of atomic scale STEM techniques to the study of interfaces and defects in materials. *J. Electron Microscopy*, **50** (3), 205-218 (2001)
- Y. Ito, R.F. Klie, N.D. Browning and T.J. Mazanec: Atomic-resolution analysis of the defect chemistry and micro-domain structure of brownmillerite-type strontium cobaltite. *Journal of the American Ceramics Society* (submitted)
- R.F. Klie, Y. Ito, S. Stemmer and N. D. Browning: Observation of oxygen vacancy ordering and segregation in perovskite oxides. *Ultramicroscopy*, **86**, 289-302 (2001)
- R.F. Klie and N. D. Browning: Atomic Scale Characterization of Oxygen Vacancy Segregation at SrTiO<sub>3</sub> Grain Boundaries. *Proceedings MRS Fall meeting 2000 AA: Structure-*Property relationships of Oxide Surfaces and Interfaces (2000)

- R.F. Klie, Y. Ito, S. Stemmer, N.D. Browning and T.J. Mazanec: Atomic scale characterization of oxygen-deficient ceramic membranes by EELS and Z-contrast imaging. *Inst. Phys. Conf. Ser. No 165:* **Symposium 6**, 241-242
- R.F. Klie and N.D. Browning: Atomic Scale Characterization of Oxygen Vacancy Segregation at SrTiO<sub>3</sub> Grain Boundaries. *Appl.Phys.Let.*, 77, 23, 3737-3739 (2000)
- S. Stemmer, A. Sane, N. D. Browning & T. J. Mazanec: Characterization of oxygen-deficient SrCoO<sub>3-∂</sub> by electron energy-loss spectroscopy and Z-contrast imaging. *Solid State Ionics* **130**, 71-80 (2000).
- Y. Ito, R. F. Klie, N. D. Browning, S. Stemmer, A. Sane and T. J. Mazanec: Analysis of the atomic scale defect chemistry in oxygen deficient materials by STEM. *Proceedings MRS Fall meeting 1999*

#### **Presentations:**

- R. F. Klie: "Nano-Scale Characterization of Oxide Material by Atomic Resolution Z-Contrast Imaging and EELS." (invited) National Center of Electron Microscopy, Lawrence Berkley National Laboratory, Berkeley, July 19, 2001
- R. F. Klie: "Nano-Scale Characterization of Oxide Material by Atomic Resolution Z-Contrast Imaging and EELS" (invited) Argonne National Laboratory, Argonne, July 10, 2001
- N. D. Browning, J. P. Buban, Y. Ito, R. F. Klie and Y. Lei: "Atomic Scale Analysis of Oxygen Vacancy Segregation at Grain Boundaries in Ceramic Oxides." (invited) *Microscopy and Microanalysis Meeting 2001*, Long Beach, August 5-9, 2001
- R.F. Klie, N. D. Browning: "Atomic Scale Characterization of Oxygen Vacancy Ordering in Oxygen Conducting Membranes." *Microscopy and Microanalysis Meeting 2001*, Long Beach, August 5-9, 2001
- R.F. Klie and N.D. Browning: "Atomic scale characterization of oxygen vacancy segregation at SrTiO<sub>3</sub> grain boundaries." MRS Fall Meeting 2000 (Boston)
- Y. Ito, R. F. Klie, N. D. Browning, and T. J. Mazanec: "Atomic Scale Analysis of Domain Boundaries in Vacancy–Ordered Brownmillerite-type SrCoO<sub>3-d</sub>." MRS Fall Meeting 2000 (Boston)
- R.F. Klie, and N. D. Browning: "Atomic level investigation of oxygen vacancy segregation at a SrTiO<sub>3</sub> grain boundary with Z-contrast imaging and EELS." FEMM2000 Meeting (Matsue, Japan)

- Y. Ito, S. Stemmer, R.F. Klie and N.D. Browning: "Analysis of the atomic scale oxygen ordering by EELS and Z-contrast imaging." MSA 2000 (Philadelphia) and EUREM2000 (Brno, Czech Rep.)
- R.F. Klie, Y. Ito, S. Stemmer, N.D. Browning and T.J. Mazanec: "Atomic scale characterization of oxygen-deficient ceramic membranes by EELS and Z-contrast imaging." MSA Meeting 2000 (Philadelphia)
- R.F. Klie, Y. Ito, S. Stemmer and N. D. Browning: "Observation of oxygen vacancy ordering in perovskite oxides." IUMAS Meeting 2000 (Hawaii)
- R.F. Klie, N.D. Browning, Y. Ito, S. Stemmer, A. Sane and T.J. Mazanec: "Atomic scale investigation of oxygen-vacancy ordering in the Perovskite (La, Sr)FeO<sub>3</sub>." *102nd Annual Meeting and Exposition of the American Ceramic Society*, St Louis, April 28-May 3, 2000
- Y. Ito, R.F. Klie, N.D. Browning, S. Stemmer, A. Sane and T.J. Mazanec: "Analysis of the atomic-scale defect chemistry in SrCoO<sub>3-x</sub> by electron energy loss spectroscopy." *102nd Annual Meeting and Exposition of the American Ceramic Society*, St Louis, April 28-May 3, 2000
- Y. Ito, R.F. Klie, S. Stemmer, N.D. Browning and T.J. Mazanec: "Quantified atomic scale analysis of vacancy ordering and defect chemistry in ceramic oxides." *APS March meeting*, Minneapolis, March 20-26, 2000
- R.F. Klie, Y. Ito, S. Stemmer, N.D. Browning and T.J. Mazanec: "Characterizing the atomic scale defect chemistry in Perovskite oxides by EELS." Spectroscopy Workshop in Schloss Ringberg (Munich, Germany), 1999
- Y. Ito, S. Stemmer, N. D. Browning, A. Sane, T. J. Mazanec: "Analysis of the atomic scale defect chemistry in oxygen deficient materials by scanning transmission electron microscopy." MRS Fall meeting, Boston, November 1999.
- S. Stemmer, S. K. Streiffer, A. Sane, T. J. Mazanec and N. D. Browning: "Atomic scale characterization of interfaces and defects in non-stoichiometric multicomponent oxides." (Invited) 57th Annual Meeting of the Microscopical Society of America, Portland, August 1-5, 1999.

# Chapter 5: Measurement of Surface Activation/Reaction Rates in Ion Transport Membranes using Isotope Tracer and Transient Kinetic Techniques.

Prof. Alan Jacobson and Prof. C.A. Mims University of Houston/University of Toronto

## 5.1. INTRODUCTION

Mixed ionic electronic conductors (MIECs) with the ABO<sub>3</sub> perovskite or related structures have been widely studied because of their practical applications in ion-transport membranes, pressure-driven oxygen generators, partial oxidation reactors, and as electrodes for solid oxide fuelcells (SOFCs)[1]. A number of materials problems remain outstanding for the application of ion transport membrane reactors in the high oxygen partial pressure gradients found, for example, in  $syn\ gas$  generation by partial oxidation of methane. The membrane composition must simultaneously provide the necessary oxygen flux and have stability over a wide  $pO_2$  range and appropriate mechanical properties.

The La<sub>1-x</sub>Sr<sub>x</sub>FeO<sub>3-x</sub> (LSFO) series has high mixed conductivity and better stability than the La<sub>1-x</sub>Sr<sub>x</sub>CoO<sub>3-x</sub> (LSCO) series but still exhibits limited stability in low-pO<sub>2</sub> environments. Additional substitution on the B-site by metal ions that are more difficult to reduce solves some of these problems but issues remain concerning both kinetic and thermodynamic stability and the effects of composition changes that result from partial decomposition or surface segregation on the membrane surface catalytic properties.

The program at Houston and Toronto was aimed at measuring the transport properties of ferrites with the perovskite structure under different conditions to determine the variation in properties expected across an operating membrane. These experiments use isotope infusion techniques that can unambiguously separate the surface activation and bulk mobility contributions to the movement of oxygen into and through the materials. Conductivity relaxation studies were performed on these materials also to complement the isotope experiments. These experiments provide higher data rates and allow multiple experiments on each sample, but the results do not completely separate the surface and bulk terms. Stability and conductivity data have been obtained over a wide pressure range ( $1 \ge pO_2 \ge 10^{-18}$ ) by using sealed electrochemical cells.

In our studies of membrane materials, we have investigated the  $pO_2$  and temperature dependence of the conductivity, non-stoichiometry and thermal-expansion behavior of compositions with increasing complexity of substitution on the perovskite A and B sites. The complete set of compounds that we have studied is given below:

SrFeO <sub>3-x</sub>	SFO
$La_{0.2}Sr_{0.8}FeO_{3-x}$	LSFO
$La_{0.5}Sr_{0.5}FeO_{3-x}$	LSFO
$La_{0.2}Sr_{0.8}Fe_{0.8}Cr_{0.2}O_{3-x}$	LSFCO
$La_{0.5}Sr_{0.5}Fe_{0.8}Ga_{0.2}O_{3-x}$	LSFGO
$La_{0.6}Sr_{0.4}Fe_{0.8}Co_{0.2}O_{3-x}$	LSFCoO
$La_{0.2}Sr_{0.8}Fe_{0.55}Ti_{0.45}O_{3-x}$	LSFTO

The most detailed measurements of the thermodynamics and the ionic and electronic transport were made for La<sub>0.5</sub>Sr<sub>0.5</sub>FeO<sub>3-x</sub>, La<sub>0.2</sub>Sr<sub>0.8</sub>Fe<sub>0.8</sub>Cr<sub>0.2</sub>O<sub>3-x</sub>, and La<sub>0.2</sub>Sr<sub>0.8</sub>Fe<sub>0.55</sub>Ti<sub>0.45</sub>O<sub>3-x</sub>, [2 3 4 5 6].

#### **5.2. EXPERIMENTAL**

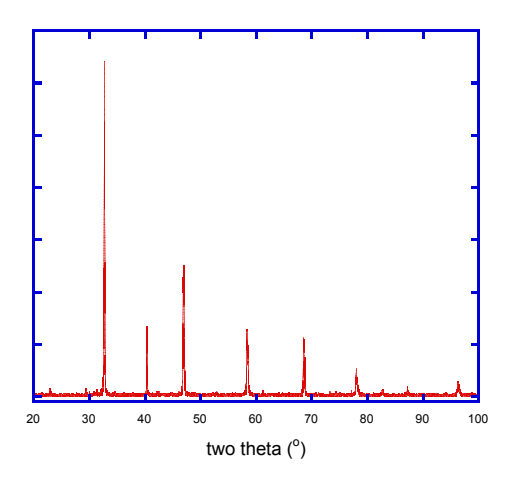
The following compositions were investigated during the program:

$SrFeO_{3-x}$	SFO
$La_{0.2}Sr_{0.8}FeO_{3-x}$	LSFO
$La_{0.5}Sr_{0.5}FeO_{3-x}$	LSFO
$La_{0.2}Sr_{0.8}Fe_{0.8}Cr_{0.2}O_{3-x}$	LSFCO
$La_{0.5}Sr_{0.5}Fe_{0.8}Ga_{0.2}O_{3-x}$	LSFGO
$La_{0.6}Sr_{0.4}Fe_{0.8}Co_{0.2}O_{3-x}$	LSFCoO
$La_{0.2}Sr_{0.8}Fe_{0.55}Ti_{0.45}O_{3-x}$	LSFTO

#### **5.3.a SAMPLE PREPARATION**

#### 5.3.1 SrFeO<sub>3-x</sub>

The SrFeO<sub>3-x</sub> was synthesized by the self-propagating high temperature synthesis (SHS) technique. The reactants, SrO<sub>2</sub> (Aldrich) and Fe powder (Alfa Aesar, 99.998%), were mixed by using zirconia balls for 24 h. Three wt. % of NaClO<sub>4</sub> (Sigma, 99.6%) was added to the mixture as an internal source of O<sub>2</sub> and heat for the initial combustion. The final mixture was pressed into a pellet. The pellet was preheated at 250 °C to increase the ignition temperature and ignited with a match. The ignition product was heat-treated at 1400 °C for 1 h and then cooled to room temperature at the rate of 5 °C/min. The finely powdered product was pelletized and sintered at 1250 °C for 12 h.



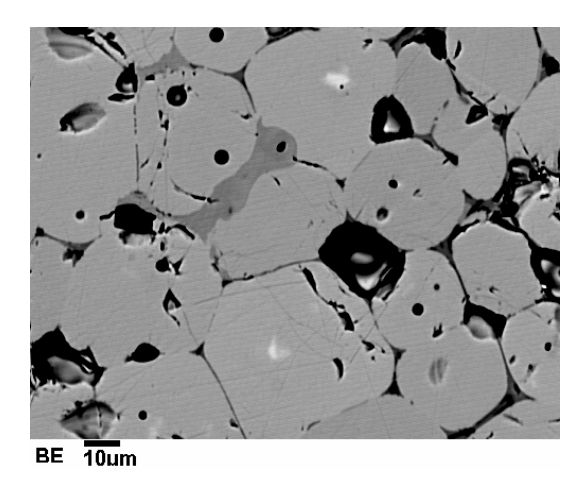


Figure 187. X-ray powder diffraction pattern (left) and a back scattered electron micrograph (right) of SrFeO<sub>3-x</sub> prepared by the SHS method.

X-ray powder diffraction (Scintag XDS 2000, Cu K $\alpha$  radiation) and electron microprobe analysis (JEOL JXA-8600) (Figure 187) were used to confirm the phase purity of SrFeO<sub>3-x</sub>. The sample was single phase by powder X-ray diffraction and by microprobe analysis.

#### 5.3.2 $La_{0.5}Sr_{0.5}FeO_3$

The starting material, La<sub>0.5</sub>Sr<sub>0.5</sub>FeO<sub>3</sub>, was prepared by self propagating high temperature synthesis. La<sub>2</sub>O<sub>3</sub> and Fe powder were first separately ground using zirconia balls for 48 h. The green mixture was prepared by dry mixing the reactants in a ball mill for 24 h. A cylindrical pellet with a diameter of 2.54 cm was formed from the powder by uniaxial pressing at 6000psi. The pellet was preheated at 250°C for 30 min. The preheated pellet was then placed in a quartz tube and ignited using a match. The SHS product was immediately transferred to a furnace and heated to 1400°C, held for 1h and then cooled down to ambient temperature at the rate of 5°C/min. The product was ball milled for 24 h in iso-propanol and then dried in the air. The dry powder was pressed to form a disc (2.54 cm in diameter and 0.25 ~0.52 cm thick) and sintered at 1300°C for 12 h with a heating and cooling rate of 2°C/min. Electron microprobe analysis indicated that the doped sample was compositionally homogeneous and was found to be single phase by X-ray diffraction.

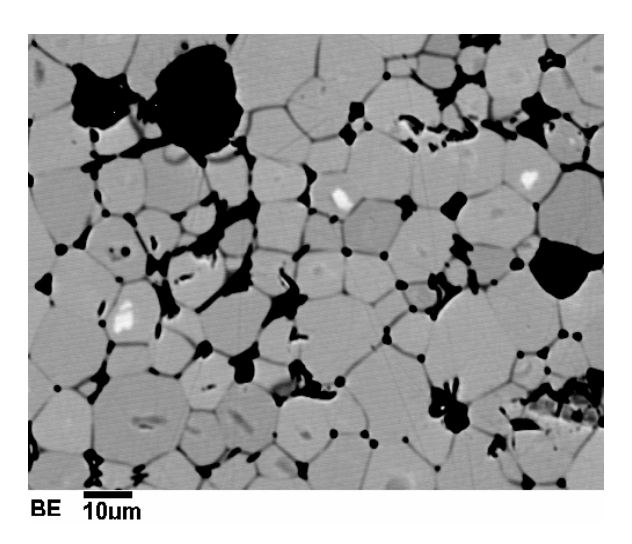


Figure 188. Back Scattered Electron Image (BEI) of LSF prepared by SHS.

A sample of La<sub>0.2</sub>Sr<sub>0.8</sub>FeO<sub>3</sub> was supplied to us and was single phase by X-ray diffraction. The first batch of disks were evaluated by electron microprobe analysis and were found to contain significant amounts of (La,Sr)FeO<sub>4</sub> suggesting that the starting powder composition was off-stoichiometry.

#### 5.3.3 $La_{0.6}Sr_{0.4}Fe_{0.8}Co_{0.2}O_{3-x}$

The first isotope transient/membrane experiments at UT used a well characterized material, La<sub>0.6</sub>Sr<sub>0.4</sub>Fe<sub>0.8</sub>Co<sub>0.2</sub>O<sub>3-x</sub>. The La<sub>0.6</sub>Sr<sub>0.4</sub>Fe<sub>0.8</sub>Co<sub>0.2</sub>O<sub>3-x</sub> powder was made by combustion spray pyrolysis and obtained from Praxair with 99.9% chemical purity. The chemical purity was verified using electron microprobe analysis. The powder was first calcined at 1325 °C for 10 h to remove any residual carbonate, and then ball-milled in 2-propanol (99.5% anhydrous, Aldrich) for 48 h. The ball-milled powder was dried at 110 °C overnight, and pressed uniaxally at 2000 psi and then pressed using cold isostatic pressing (CIP) at 40,000 psi. The sample was then sintered at 1250 °C for 4h with heating and cooling rates of 1°C/min. The density of the final sample was  $\geq$  95% of its theoretical density. In Figure 189a, a representative example of a tube isostatically pressed and sintered is shown. The outside diameter is 6 mm and the wall thickness is 0.5 mm. Approximately 1 cm sections of this tube were used in the UT permeation apparatus.

# 5.3.4 $La_{0.2}Sr_{0.8}Fe_{0.8}Cr_{0.2}O_{3-x}$

La<sub>0.2</sub>Sr<sub>0.8</sub>Cr<sub>0.2</sub>Fe<sub>0.8</sub>O<sub>3- $\delta$ </sub> powder was purchased from Praxair specialty ceramics (lot number: 03-P3102DM). A combustion spray pyrolysis process was used to synthesize the powder, which had 99.9 % chemical purity. The powder was pressed to form a 25.4 mm diameter pellet with 2.5 ~ 5.0 mm thickness. The pellet was cold isostatically pressed at 40,000 psi. The sample was then sintered at 1150 °C for 8 h with heating and cooling rates of 1 °C/min. Finally rectangular sample bars, with dimensions 18 mm × 2.2 mm × 2.5 mm for conductivity measurements and 21 mm × 2.2 mm × 1.8 mm for electrical conductivity relaxation (ECR) experiments, were cut from the sintered. The sample was compositionally homogeneous and single phase with a density of  $\approx$  93 % of the theoretical density. A tubular ceramic sample of La<sub>0.2</sub>Sr<sub>0.8</sub>Fe<sub>0.8</sub>Cr<sub>0.2</sub>O<sub>3-x</sub> was synthesized for use in the membrane reactor at UT (see Figure 189b).

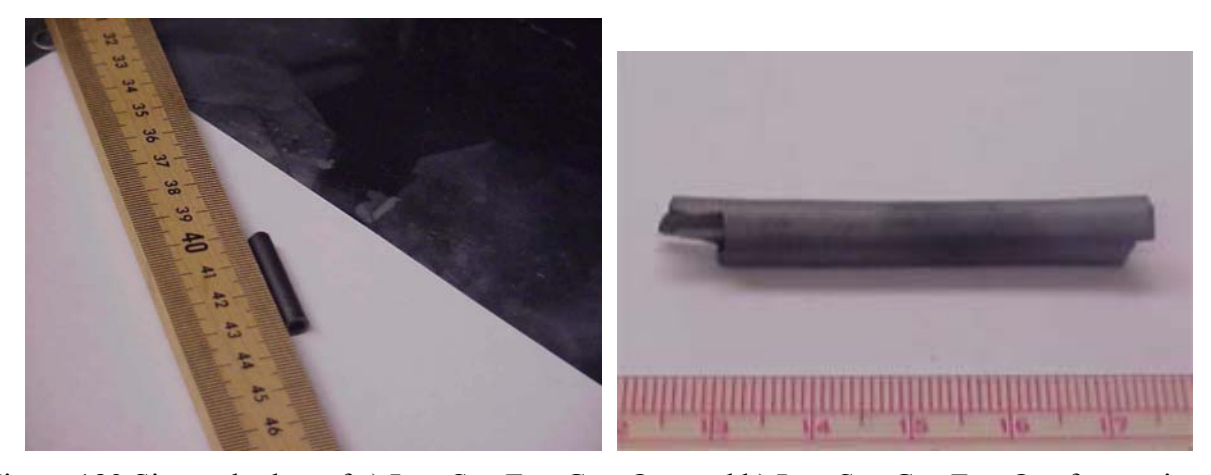


Figure 189 Sintered tubes of a)  $La_{0.6}Sr_{0.4}Fe_{0.8}Co_{0.2}O_{3-x}$  and b)  $La_{0.2}Sr_{0.8}Cr_{0.2}Fe_{0.8}O_{3-x}$  for use in isotopic transient measurements.

# 5.3.5 $La_{0.5}Sr_{0.5}Fe_{0.8}Ga_{0.2}O_{3-x}$

La<sub>0.5</sub>Sr<sub>0.5</sub>Fe<sub>0.8</sub>Ga<sub>0.2</sub>O<sub>3-x</sub> was prepared by a freeze-drying route using La<sub>2</sub>O<sub>3</sub> (Aldrich, 99.991%), SrCO<sub>3</sub> (Aldrich, 99.995%), Fe metal powder (Aldrich, 99.991%), and Ga metal (Alfa, 99.999%) as starting materials. The predried starting materials (La<sub>2</sub>O<sub>3</sub>, 3 h at 1100 °C and SrCO<sub>3</sub>, 24 h at 120 °C) were dissolved in nitric acid with Fe metal powder (Aldrich, 99.991%) and Ga metal (Alfa, 99.999%) in the required stoichiometric ratio. The nitric solution was then sprayed into liquid nitrogen at a rate of 2.5 mL/min using an atomizer (Sonotek). The resulting nitrate "snow" was transferred to an FTS Dura-Dry II MP freeze-dryer. The dried nitrate powder was gradually

heated from 100 to 300 °C to remove residual acid and then heated at 600 °C for 1 h to decompose the nitrates. The powder was cooled to room temperature by quenching in air. Finally the powder was fired in a platinum crucible in air at 1400 °C for 17 h and air quenched to room temperature. The resulting powder was shown by X-ray powder diffraction to be a single phase perovskite with a slightly distorted cubic structure. In addition to XRD, the microstructures of the ceramic samples for both membrane and conductivity relaxation experiments were characterized by electron-probe microanalysis (EMPA, JEOL JXA-8600). Backscattered electron (BSE) imaging and X-ray microanalysis of the ceramic samples showed a single phase.

## 5.3.6 $La_{0.2}Sr_{0.8}Fe_{0.55}Ti_{0.45}O_{3-x}$

Powders of La<sub>0.2</sub>Sr<sub>0.8</sub>Fe<sub>0.55</sub>Ti<sub>0.45</sub>O<sub>3-x</sub> synthesized by using the spray pyrolysis method, were obtained from Praxair Specialty Ceramics (Woodinville, WA). The La<sub>0.2</sub>Sr<sub>0.8</sub>Fe<sub>0.55</sub>Ti<sub>0.45</sub>O<sub>3-x</sub> powder was calcined at a series of temperatures (1200 °C, 1250 °C and 1300 °C in air to investigate phase purity and densification behavior. The X-ray data are shown in Figure 190. The sample is apparently single phase after hting at 1220 C though some line broadening is apparent. At 1300 °C the lines become sharper and the pattern can be completely indexed with a tetragonal unit cell with lattice parameters a = 5.506(9) Å and c = 7.787(9) Å. The density measured by the Archimedes method was 96% of the theoretical value after annealing the sample for 10 h at 1300 °C or at 1350 °C for 10 h. The sample densified at 1350 °C was more brittle than that at 1300 °C sample and the latter was used for conductivity measurements.

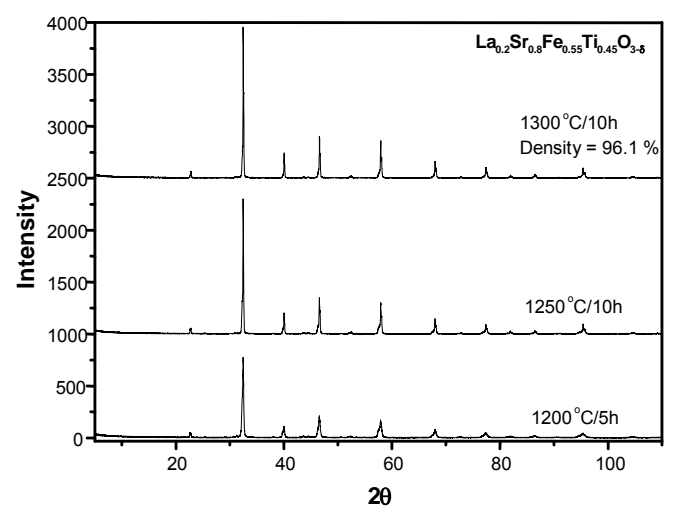


Figure 190. X- ray diffraction data for La<sub>0.2</sub>Sr<sub>0.8</sub>Fe<sub>0.55</sub>Ti<sub>0.45</sub>O<sub>3-x</sub> samples annealed at different temperatures – batch #1.

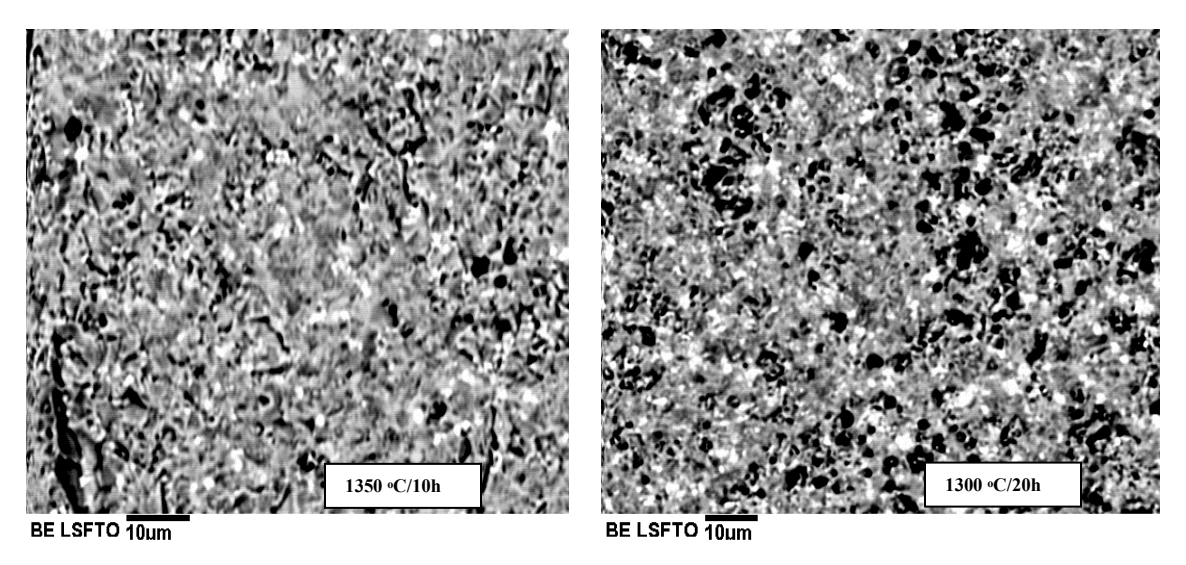


Figure 191. Back-scattered electron images of La<sub>0.2</sub>Sr<sub>0.8</sub>Fe<sub>0.55</sub>Ti<sub>0.45</sub>O<sub>3-x</sub>.

Samples were mounted and polished for electron microprobe analysis using a JEOL JXA-8600 Electron Microprobe. Backscattered electron images taken in the microprobe are shown in Figure 191. Elemental compositions were determined with the probe placed at different spots on the sample and the composition ratios determined from the average data to be La: Sr = 0.2:0.87 and Fe: Ti = 0.55:0.43 in reasonable agreement with the nominal composition.

A second larger batch of La<sub>0.2</sub>Sr<sub>0.8</sub>Fe<sub>0.55</sub>Ti<sub>0.45</sub>O<sub>3-x</sub> powder was calcined at a series of temperatures (1250 °C, 1300 °C and 1400 °C in air to investigate phase purity and densification behavior. The X-ray data are shown in Figure 192. The sample is apparently single phase after heating at 1250 °C though some line broadening is apparent. At 1400 °C the lines become sharper and the pattern can be completely indexed with a tetragonal unit cell with lattice parameters a = 5.523(7) Å and c = 7.811 Å (cf. 5.506(9) Å and 7.787(9) Å for batch#1 sintered at 1300 °C). The density measured by the Archimedes method was 90% of the theoretical value after annealing the sample for 10 h at 1400 °C.

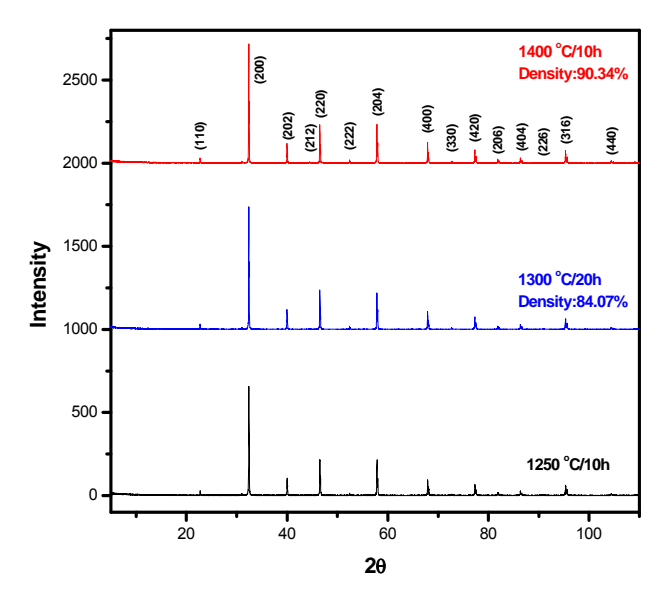


Figure 192. X- ray diffraction data for  $La_{0.2}Sr_{0.8}Fe_{0.55}Ti_{0.45}O_{3-x}$  samples annealed at different temperatures – batch #2.

Samples were mounted and polished for electron microprobe analysis using a JEOL JXA-8600 Electron Microprobe. Elemental compositions were determined with the probe placed at different spots on the sample and the composition ratios determined from the average data to be La: Sr = 0.2:0.80 and Fe: Ti = 0.55:0.45 in agreement with the nominal composition. Some small variations in composition were observed due to the roughness of the sample surfaces.

**Table 25.** The composition of  $La_{0.2}Sr_{0.8}Fe_{0.55}Ti_{0.45}O_{3-x}$  batch #2

Point		Atomic %				
#	La	Sr	Fe	Ti	O	
1	3.948	16.104	11.567	9.412	58.970	
2	3.961	16.522	11.695	9.475	58.348	
3	3.977	16.338	11.560	9.615	58.510	
4	3.979	16.181	11.673	9.553	58.614	
5	4.021	16.331	11.749	9.634	58.265	
Average	3.977	16.295	11.649	9.538	58.541	
S. D.	0.028	0.161	0.083	0.094	0.276	
Composition	0.196	0.804	0.550	0.450	3.00-x	

# 5.4. Experimental Methods

# 5.4.1. Electrical Conductivity Measurements using Electrochemical Cells

The variation of the electrical conductivity with pO<sub>2</sub> was monitored with electrochemical cells for the various materials. The walls of the cells are built by stacking alumina rings (OD = 12 mm, thickness = 1.5 mm, and height =  $3 \sim 10$  mm) and Pyrex glass rings (OD = 12 mm, thickness = 1.5 mm, and height =  $0.5 \sim 1$  mm) one by one (Figure 193). Polycrystalline yttriastabilized zirconia discs were prepared by using 8-mole % Y<sub>2</sub>O<sub>3</sub>-doped ZrO<sub>2</sub> powder (TOSOH -Zirconia, TZ-8Y). The powder was pressed into a disc using 1"-diameter die. The disc was cold isostatically pressed at 40,000 psi and then sintered at 1450 °C for 4 h with heating and cooling rates of 2 °C / min. Thereafter, Pt paste (Engelhard 6926) was painted on both faces of the TZ-8Y disc. Pt wires (0.004" diameter) were then contacted to the disc by using Pt meshes (150  $\times$ 150 mesh, 0.002" wire diameter, Unique Wire Weaving Co., Inc.). The resulting disc was heattreated at 1000 °C for 10 min. Both the top and the bottom of the cell were closed with TZ-8Y discs. The top YSZ disc was used as a sensor monitoring pO<sub>2</sub> inside the cell with air as the reference gas on the outside; the bottom YSZ cell was used as a pump to control the oxygen flux into the cell and thereby the pO<sub>2</sub>. As TZ-8Y is a pure oxide ion conductor, it can be used to remove or supply oxygen quantitatively down to very low pO<sub>2</sub>s. Four Pt wires were linked to the rectangular sample bar that was placed in the middle of the cell. The Pt wires inside the cell were brought out through the glass rings. A thermocouple (type-R) was placed just above the cell to monitor the temperature. The cell became gas-tight when the temperature was raised above 821°C and the glass rings melted. The EMF of the sensor was measured by using Keithley 2000-20 multimeter. A Keithley 2400 SourceMeter was used as the pump current source. The experiments were controlled by Labwindow software through a GPIB communicator.

To minimize the current flow through the sample, an ac four-point probe technique was used to monitor the conductivity of the sample with a lock-in amplifier (Stanford Research Systems: Model SR 830 DSP). The electrical conductivity measurements were performed as a function of pO<sub>2</sub> and temperature. The lock-in amplifier enabled us to measure very low voltages without

noise problems. In order to provide constant current, an outer resistance more than 100 times larger than that of the sample was connected to the input current lead.

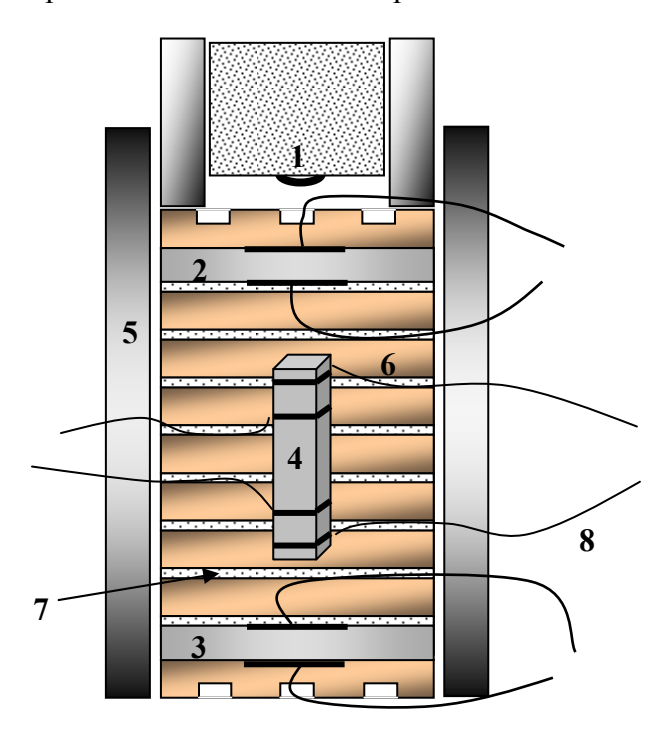


Figure 193. A cell for conductivity measurements. 1: thermocouple, 2: YSZ sensor, 3: YSZ pump, 4: sample, 5: alumina tube, 6: alumina ring, 7: glass ring, 8. Pt wires.

#### **5.4.2** Solid-state coulometric titrations

The solid-state coulometric titrations were carried out with the cell schematically shown in Fig. 194. The wall of the cell was built by stacking 2 alumina tubes, where one is one-end closed and the other is both-sides open (OD = 12 mm, thickness = 1.5 mm, and height =  $3 \sim 10$  mm), and Pyrex glass rings (OD = 12 mm, thickness = 2 mm, and height =  $0.5 \sim 1$  mm). The top of the cell was covered with the electroded TZ-8Y disc, which served as both an oxygen sensor reading pO<sub>2</sub>, and an oxygen pump controlling the oxygen flux. The cell was then installed in the coulometric titration apparatus shown in Figure 194. The cell was spring loaded at the top of the apparatus in order to help the sealing process. A thermocouple (type-R) was placed just above the cell to monitor the temperature. The cell became gas-tight when the glass rings melted above 821 °C. The *EMF* of the sensor was measured by using a Keithley 2000-20 multimeter. A Keithley 2400

SourceMeter was used as the current source for the oxygen pump. The experiments were controlled by Labview software.

The non-stoichiometry change ( $\Delta x$ ) was recorded as a function of pO<sub>2</sub> in the range of  $10^{-18} \sim 0.5$  atm at 750, 800, 850, 900, 950, 1000, and 1040 °C. The  $\Delta x$  values were measured step-by-step. At the beginning of the experiment, the sample was allowed to equilibrate with the pO<sub>2</sub> in the cell. A known amount of oxygen was pumped into (or out of) the cell. When the new equilibrium is attained, the pO<sub>2</sub> inside the cell and  $\Delta x$  were determined after correction for the free volume inside of the cell. A variation in the sensor voltage by less than 0.1 %/min was used as the criterion for equilibrium. Then the procedure was repeated. To remove the possibility of any unexpected leakage through microcracks or open pores, every titration isotherm was determined twice on both increasing and decreasing the pO<sub>2</sub>.

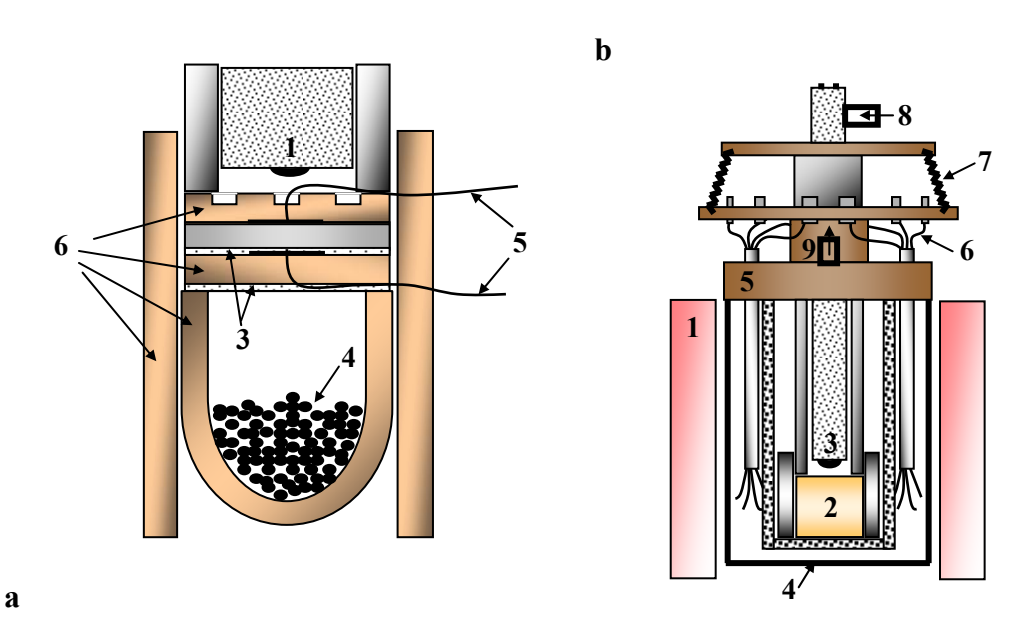


Figure 194a. Coulometric titration cell: 1. thermocouple, 2.YSZ, 3. pyrex sealant, 4. sample powder, 5. Pt electrodes and wires, 6. alumina. Figure 194b. Coulometric titration system: 1. Furnace, 2. electrochemical cell, 3. thermocouple, 4. quartz tube, 5. metal frame, 6. Pt wires, 7. spring, 8. gas in, 9. gas out.

A tightly sealed cell is crucial for the success of the coulometric titration technique. Even when a sealed cell is prepared, however, oxygen leakage through solid electrolyte limits the accuracy of data, especially in the lower pO<sub>2</sub> region. According to previous work [7], the oxygen leakage flux

 $(J_o)$  of 8-mole %  $Y_2O_3$ -doped  $ZrO_2$  is dependent on both temperature and  $pO_2$  gradient according to:

$$J_{o} = \frac{RT}{FL} \cdot \left[ \sigma_{h} \left( pO_{2(ref)} \right) \cdot \left\{ \left( \frac{pO_{2(cell)}}{pO_{2(ref)}} \right)^{0.25} - 1 \right\} + \sigma_{e} \left( pO_{2(ref)} \right) \cdot \left\{ I - \left( \frac{pO_{2(cell)}}{pO_{2(ref)}} \right)^{0.25} \right\} \right]$$

where L is the thickness of the 8-mole %  $Y_2O_3$  doped  $ZrO_2$ , and  $\sigma_e(pO_2)$  and  $\sigma_b(pO_2)$  are  $pO_2$ -dependent conductivities of the electrons and holes, respectively:

$$\sigma_e(pO_2) = 1.31 \times 10^7 \cdot exp\left(\frac{-3.88 \, eV}{kT}\right) \cdot pO_2^{-0.25}$$

$$\sigma_h(pO_2) = 2.35 \times 10^2 \cdot exp\left(\frac{-1.67 \, eV}{kT}\right) \cdot pO_2^{0.25}$$

The experimental results were corrected for leakage through the YSZ pump using these relationships.

#### **5.4.3** Polarization Measurements

The electrochemical cell for polarization measurements is shown schematically in Figure 195. The sample disc (0.05-inch thickness) is located between two YSZ electrodes (1/2-inch diameter, 0.04-inch thickness). The outside surface of two YSZ discs were connected to Pt wires (0.004-inch diameter) using Pt meshes (150 × 150 mesh, 0.002-inch wire diameter, Unique Wire Weaving Co., Inc) and Pt paste (Engelhard 6926). In order to avoid any side reaction between the sample and YSZ, the inside surface of the YSZ was covered with Pt paste. The YSZ discs covered with Pt were annealed at 1300 °C for 30 min. Thin porous platinum layers were formed on the YSZ and the porosity was determined to be ~ 29% by scanning electron microscopy (JEOL JSM-6330F) as shown in Figure 195b. The sample was sealed with Pyrex glass to prevent oxygen ingress from air. The voltage across the cylindrical sample and two YSZ disks was monitored by 2000-20 multimeter (Keithley). Data acquisition was controlled by the LabView program.

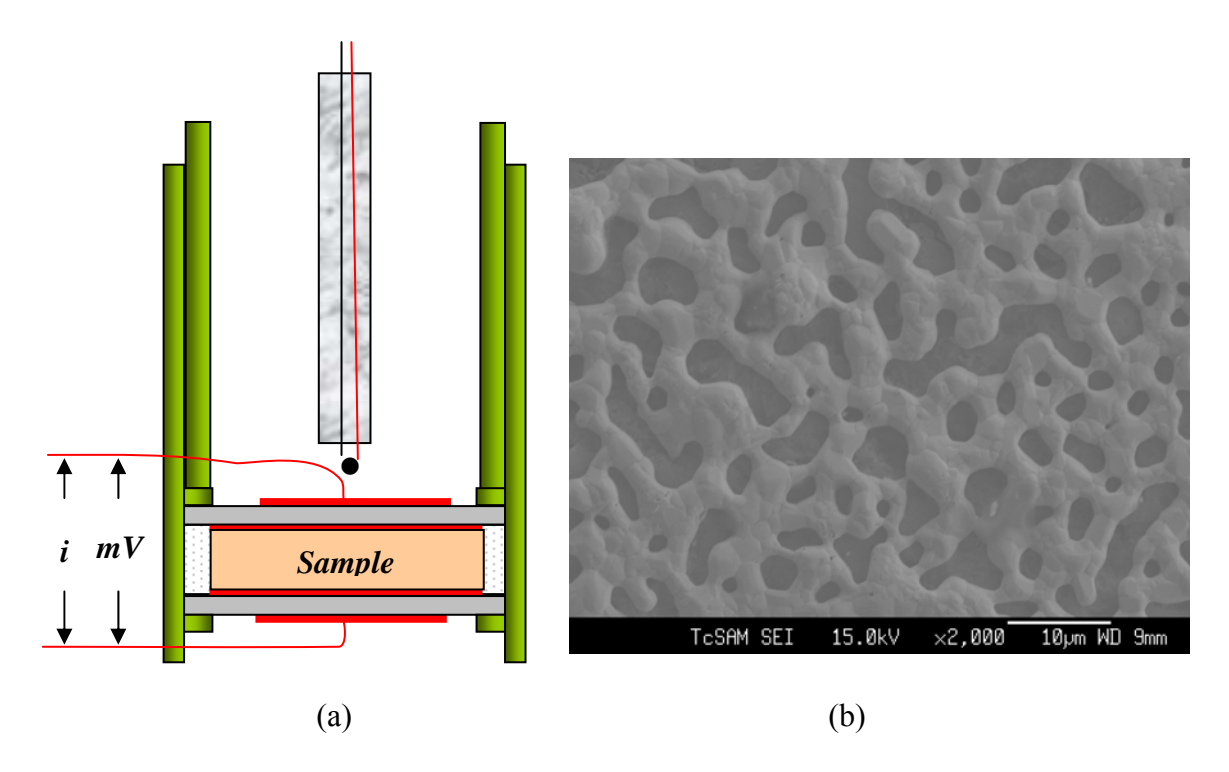


Figure 195 (a) The symmetric electrochemical cell for polarization measurement and (b) scanning electron micrograph of YSZ covered with Pt after annealed at 1300 °C for 30 min.

#### **5.4.4** Seebeck Measurements

The electrochemical cell for Seebeck measurements is shown schematically in Figure 196. The top and bottom parts of the cell were composed of a pure ionic conductor, 8-wt% polycrystalline yttria-stabilized zirconia (YSZ, TZ-8Y) disc. The top YSZ disk was used for monitoring the pO<sub>2</sub> and the bottom one was used for pumping the oxygen in/out of the cell. Air was used as the reference gas. The Pt wires connected to the rectangular sample bar were brought out via the glass rings. The gas- tight seals were made by heating the cell above the softening temperature (821 °C) of the glass rings. The total height of the cell was less than 45 mm after sealing.

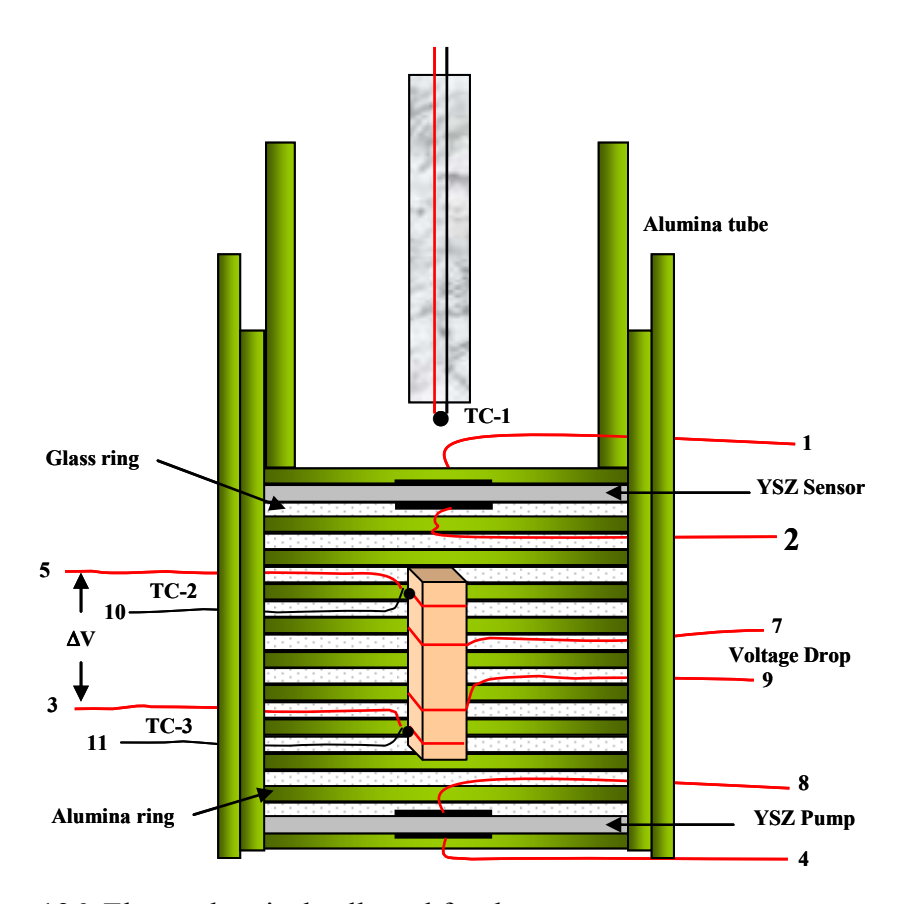


Figure 196. Electrochemical cell used for thermo-power measurements

A rectangular bar with dimensions  $0.17 \times 0.18 \times 1.98$  cm was cut from a sample that was sintered at 1400 °C. The pump current was introduced by a 2400 SourceMeter (Keithley) and the EMF of the sensor and pump were monitored by a 2000-20 multimeter (Keithley). Three R-type thermocouples were used to monitor the temperature. One thermocouple is for the vertical furnace and other two were attached to both ends of the sample in the electrochemical cell. Cold junction compensators are connected to R-type thermocouples in order to read an accurate temperature difference. We used the natural temperature gradient along the cell. Normally this is  $\sim 3$  °C/cm but can be varied by shifting the cell along the furnace. The EMF values between two Pt wires of the thermocouples were monitored by 2182 nano-voltameter (Keithley) with the equilibrium criteria of  $\leq 5 \times 10^{-5} \,\mu\text{V/min}$  and less than a half order difference between sensor and pump pO<sub>2</sub>.

# 5.4.5 Thermal Expansion

Rectangular sample bars with dimensions typically 15 mm  $\times$  5 mm  $\times$  5 mm) were used for dilatometry measurements (NETZSCH, DIL 402C). Thermal expansion measurements were performed at  $25 \le T \le 1200$  °C with a heating and cooling rate of 3 °C per minute. Purified air was flowed through the dilatometer furnace at  $\sim$ 80 ml/min. Chemical expansion data for the sample were obtained by switching the gas from air to pure argon or to a specific gas mixture (5% H<sub>2</sub>/N<sub>2</sub>, CO<sub>2</sub>, and argon) in the temperature range between 800 and 1000 °C. The flow rate of the each gas was controlled by using mass flow controllers (MKS 247C). An oxygen analyzer (AMETEK, TM-1B) was connected to the dilatometer. The oxygen partial pressures (pO<sub>2</sub>) were recorded every minute by measuring the emf reading of an oxygen analyzer using an HP 3468A multimeter.

## **5.4.6 Conductivity Relaxation Studies**

Theory: In an electrical relaxation experiment, the time dependent response of electrical conductivity is monitored after imposing a stepwise change of the chemical potential of oxygen in the ambient. For a rod sample with a  $2l_1$  by  $2l_2$  cross-section, and a length much greater than the sides, the time dependence of the normalized conductivity is written as Eq (1). We assume that the oxygen concentration at the surface is proportional to that in the bulk and that the conductivity change of the material is linear with its oxygen concentration change.

$$g(t) = \frac{\sigma - \sigma_1}{\sigma_2 - \sigma_1} = 1 - \sum_{n=1}^{\infty} \sum_{m=1}^{\infty} \frac{2C_1^2 \exp(-\alpha_{1m}^2 D_{chem} t/l_1^2)}{\alpha_{1m}^2 (\alpha_{1m}^2 + C_1^2 + C_1)} \frac{2C_2^2 \exp(-\alpha_{2n}^2 D_{chem} t/l_2^2)}{\alpha_{2n}^2 (\alpha_{2n}^2 + C_2^2 + C_2)}$$
(1)

Where  $D_{chem}$  is the chemical diffusion coefficient. The coefficients  $a_{1m}$  and  $a_{2n}$  are roots of the transcendental equations:  $\alpha_{1m} \tan \alpha_{1m} = C_1$  and  $\alpha_{2m} \tan \alpha_{2m} = C_2$  with  $C_1 = l_1/L_d$  and  $C_2 = l_2/L_d$ , where  $L_d = D_{chem}/k_{chem}$  is the surface exchange coefficient in a relaxation process. For the case of surface limited transport (C  $\rightarrow$ 0), Eq. 1 reduces to  $g(t) = 1 - \exp(-t/\tau)$ , where  $\tau = \frac{1}{K} \frac{l_1 l_2}{l_1 + l_2}$ 

Experimental: In typical experiments, rectangular samples were used for conductivity relaxation experiments. These were cut from the sintered disk and wound with 4 gold wires (0.025 mm, Alfa), which serve as electrodes. The 4-probe dc conductivity relaxation experiments were carried out as follows. Current was supplied to the sample with a Keithley 200 constant current

source. The voltage was measured with a Keithley 2000 DMM interfaced to a computer. The sample was first equilibrated in an atmosphere of  $O_2$  ( $O_2/N_2$  mixture with  $CO_2 < 1$ ppm, Trigas) at a flow rate of 310 ml/min. The oxygen atmosphere was then changed abruptly to a new partial pressure of  $O_2$  and the conductivity change with time was recorded using a LabVIEW acquisition program. The sample was protected from exposure to  $CO_2$  and water by maintaining a constant flow of dry  $O_2$  when no measurement was made. The apparatus has a switching time of 0.3 sec and a lock-in amplifier ac technique was used in order to measure very small changes in the resistance of the sample. This method permits data acquisition over a wider range of pressure switches on the same sample and measurements with only small departures from equilibrium.

## 5.5 RESULTS AND DISCUSSION

## 5.1 SrFeO<sub>3-x</sub>

#### 5.5.1.1Introduction

High electronic and ionic conductivity and structural stability in reducing atmospheres are critical requirements for the use of mixed conductors in membrane reactors used for the generation of synthesis gas (CO+H<sub>2</sub>) from methane. These requirements have led to a focus on the more stable iron-based systems for this particular application. In order obtain fundamental information on the transport properties and thermodynamic stability of the iron compounds in low partial pressures of oxygen, we reinvestigated the simplest system, SrFeO<sub>3-x</sub>, as part of our studies of more complex systems substituted with other metals.

Many studies have been performed to understand the structural characteristics of SrFeO<sub>3-x</sub> because of interest in the order-disorder transition, ordered defect structures, and the high oxygen deficiency. The non-stoichiometry and phase behavior of bulk SrFeO<sub>3-x</sub> at  $900 \ge T \ge 400$  °C and for  $1 \ge pO_2 \ge 10^{-5}$  atm were determined by thermogravimetric analysis.[8] A phase diagram based on a combination of X-ray diffraction data and thermogravimetric data is shown in Fig. 197 adapted from Takeda *et al.*[9] At high temperature, SrFeO<sub>3-x</sub> adopts the cubic perovskite structure with disordered oxygen vacancies for the entire stoichiometry range. On lowering the temperature, phase transitions occur from the disordered cubic perovskite structure to vacancy-ordered phases. Depending on the value of x, three different ordered phases have been reported. They are SrFeO<sub>2.5</sub> with the orthorhombic brownmillerite structure (BR), an orthorhombic phase

with a composition centered at SrFeO<sub>2.75</sub> (O-P) and SrFeO<sub>2.875</sub> with a tetragonally distorted perovskite structure (T-P). Each of the three single phases exists over a composition range and they are separated by two-phase regions.

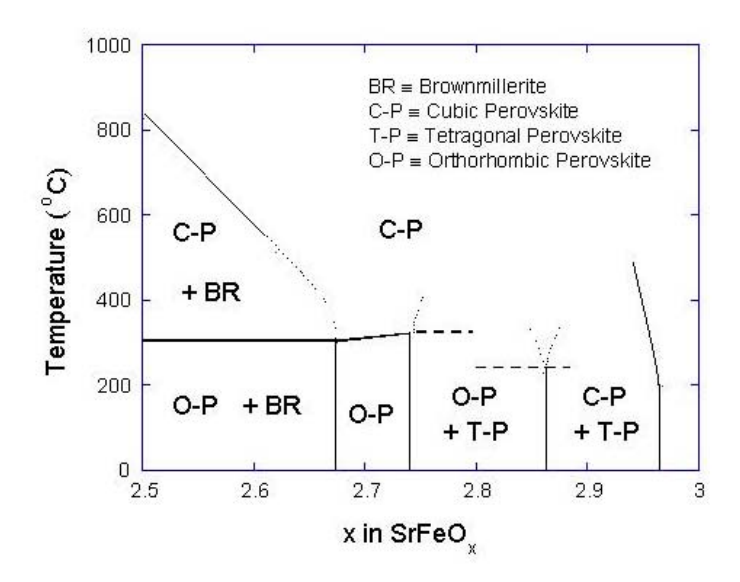


Figure 197. Phase Diagram of SrFeO<sub>3-x</sub> after Takeda et al. [9]

Following the previous work, we have determined the equilibrium non-stoichiometry of oxygen in SrFeO<sub>3-x</sub> by the solid-state coulometric titration technique in the temperature range  $1040 \ge T \ge 750$  °C and at  $1 \ge pO_2 \ge 10^{-18}$ , where SrFeO<sub>3-x</sub> forms with the cubic perovskite structure. The experimental technique enables us to accurately control  $pO_2$  and thereby determine the  $pO_2$  dependence of the non-stoichiometry. Defect models for the  $pO_2$  dependence of the stoichiometry have been investigated and the data compared with recent results on the electrical conductivity and thermopower of SrFeO<sub>3-x</sub> measured at  $1 \ge pO_2 \ge 10^{-16}$  atm and from 700 to 950 °C.

# 5.5.1.2 Coulometric titration measurements of the oxygen non-stoichiometry

The  $pO_2$  dependence of the oxygen non-stoichiometry (x) for the perovskite  $SrFeO_{3-x}$  was determined from the coulometric titration measurements. A typical example of experimental data in the form of a plot of  $log pO_2$  vs. nonstoichiometry is given in Figure 198. The data are reproducible, irrespective of the direction of measurement, but in the lower  $pO_2$  region, a small gap exists between the data measured in the two directions because of oxygen leakage through the zirconia disc, which becomes increasingly significant as the temperature increases and the  $pO_2$ 

decreases. The experimental data were corrected for leakage taking into account the equilibrium time at each step and the  $pO_2$  inside the cell.

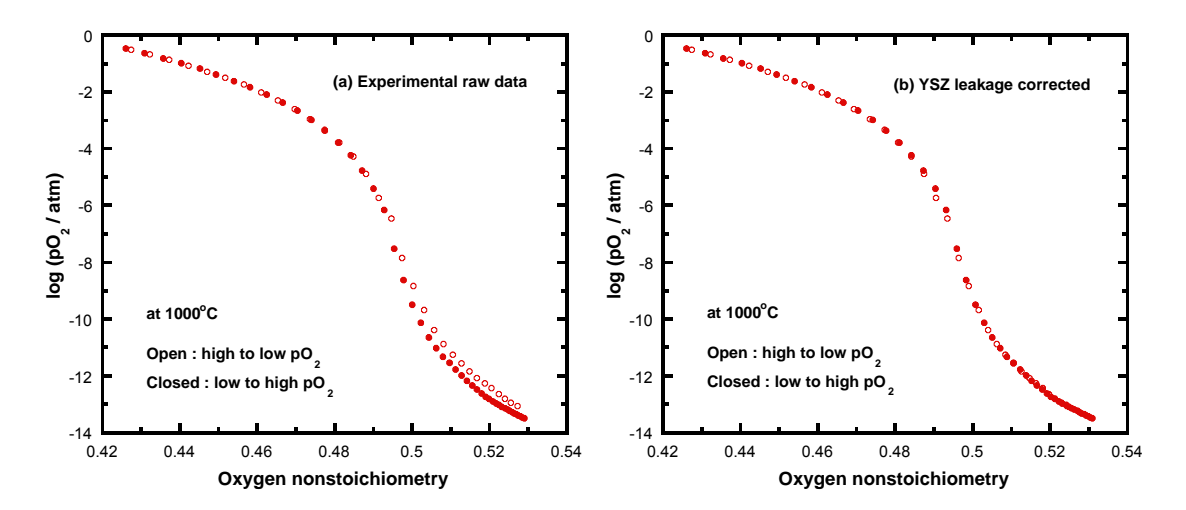


Figure 198. Coulometric titration data for the pO<sub>2</sub> dependence of the oxygen non-stoichiometry of SrFeO<sub>3-x</sub> at 1000 °C, (a) raw data and (b) after leakage correction. After correction the data measured on increasing and decreasing pO<sub>2</sub> agree over the entire pO<sub>2</sub> range, as shown in Figure 198 (b). Similar results were observed at the other temperatures.

The absolute x-value at temperatures of  $750 \le T \le 1040$  °C and pO<sub>2</sub> = 0.21 atm was taken from the previous work, [8] where it was determined by both chemical titration and thermogravimetric analysis (TGA). The validity of the absolute x-value was confirmed by inserting a reference x value at 900 °C into both our TGA data at  $0.15 \le pO_2 \le 1$  atm, and the current coulometric titration results. In the whole temperature range, the normalized x-values from both experiments showed good agreement with less than 1% difference with the literature values. At temperatures ≥ 900 °C, the stoichiometry over the whole range of pO<sub>2</sub> was determined but at lower temperatures, only the higher partial pressures (pO<sub>2</sub> >  $10^{-6}$  atm) are reported. At temperatures  $\leq 850$  °C, the separation into two phases, perovskite and brownmillerite, is apparent in the isotherms. For example, in the 800 °C data discontinuities are observed and significant differences in the results are obtained depending on whether pO<sub>2</sub> is increasing or decreasing. Equilibrium is very difficult to achieve in this region and allowing longer equilibration times compromises the precision of the stoichiometry measurements because of the larger corrections that are necessary. Consequently, only the high-pressure equilibrium data are reported. The results for the variation of the oxygen non-stoichiometry with pO<sub>2</sub> are shown in Figure 199 for different temperatures. All the isotherms were corrected for leakage and then an average of the data measured on increasing and decreasing  $pO_2$  was taken as the equilibrium value of x.

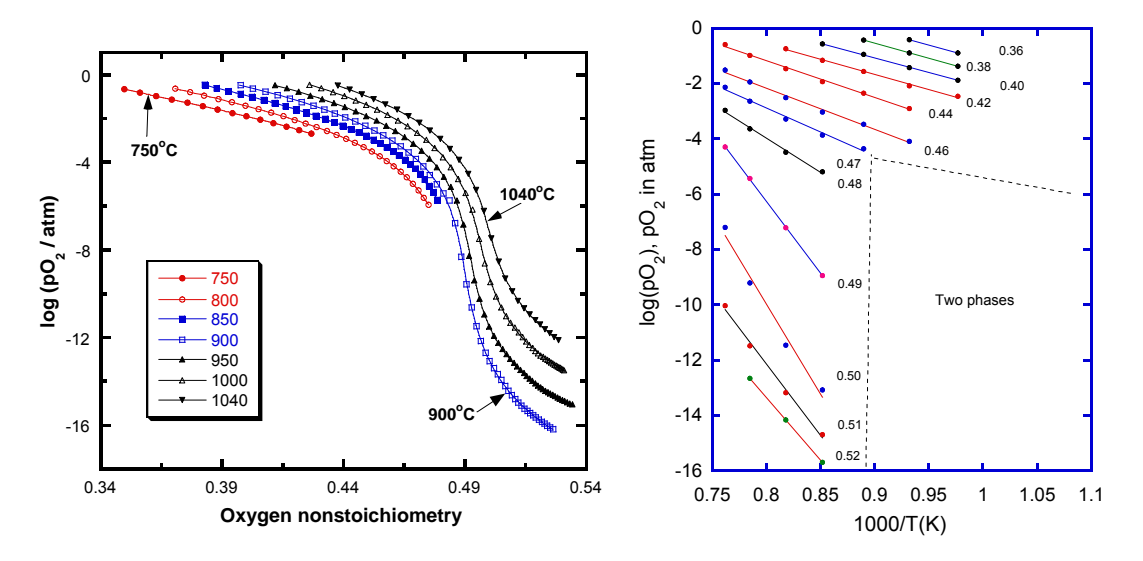


Figure 199. (left) The dependence of the equilibrium non-stoichiometry x in  $SrFeO_{3-x}$  on  $pO_2$  at different temperatures. Lines are to guide the eye only. (right) The temperature and  $pO_2$  dependence of the non-stoichiometry x, in  $SrFeO_{3-x}$ , shown as lines of constant composition.

In previous work, Mizusaki *et al.* [8] determined the non-stoichiometry of SrFeO<sub>3-x</sub> from  $1 \ge pO_2$   $\ge 10^{-5}$  atm and  $900 \ge T \ge 400$  °C by thermogravimetric analysis. The range of the previous measurements partly overlaps the present data. A comparison of the two sets of measurements shows good agreement apart from a small composition offset (0.02). Misuzaki *et al.* set the stoichiometry at the plateau in the plot of 3-x versus  $pO_2$  to 3-x = 2.5 at both 900 and 1100 °C whereas in the present data a lower value was used. The difference in the choice of reference point most likely accounts for the difference and the two sets of data agree within this uncertainty.

#### 5.5.1.3 Point defect model

A simple point defect model has been used to describe the non-stoichiometry in  $SrFeO_{3-x}$ . With  $SrFeO_3$  as an ideal stoichiometric formula, the predominant point defect species are  $V_O$ ,  $Fe_{Fe}$ ,  $Fe_{Fe}$ ,  $Fe_{Fe}$  and  $Fe_{Fe}$  are randomly distributed and non-interacting, and that only doubly ionized oxygen vacancies exist, the equilibrium constants for the oxidation of  $Fe^{3+}$  and the disproportionation reactions:

$$1/2O_2 + V_O^* + 2Fe_{Fe}^{\prime} \rightarrow O_O^x + 2Fe_{Fe}^x$$
 and  $2Fe_{Fe}^{\prime} \Leftrightarrow Fe_{Fe}^x + Fe_{Fe}^{\prime\prime}$ 

can be defined assuming dilute defects as:

$$K_{O} = \frac{[O_{O}^{x}] \cdot [Fe_{Fe}^{x}]^{2}}{pO_{2}^{1/2} \cdot [V_{O}^{\bullet \bullet}] \cdot [Fe_{Fe}^{\prime}]^{2}} \quad K_{D} = \frac{[Fe_{Fe}^{\prime\prime}] \cdot [Fe_{Fe}^{x}]}{[Fe_{Fe}^{\prime\prime}]^{2}}$$

In addition, site relations and electroneutrality provide three more equations.

$$[Fe_{Fe}^{x}] + [Fe_{Fe}^{y}] + [Fe_{Fe}^{y}] = I$$
  
 $[O_{O}^{x}] + [V_{O}^{\bullet \bullet}] = 3$   
 $[Fe_{Fe}^{y}] + 2[Fe_{Fe}^{y}] = 2[V_{O}^{\bullet \bullet}]$ 

A least squares fit of this simple model to the pO<sub>2</sub> dependence of the non-stoichiometry at 1040  $^{\circ}$ C gave good agreement with values of  $K_O$  and  $K_D$  of 0.231 and 1.60 × 10<sup>-5</sup>, respectively. The experimental data and the model calculation are shown in Figure 200

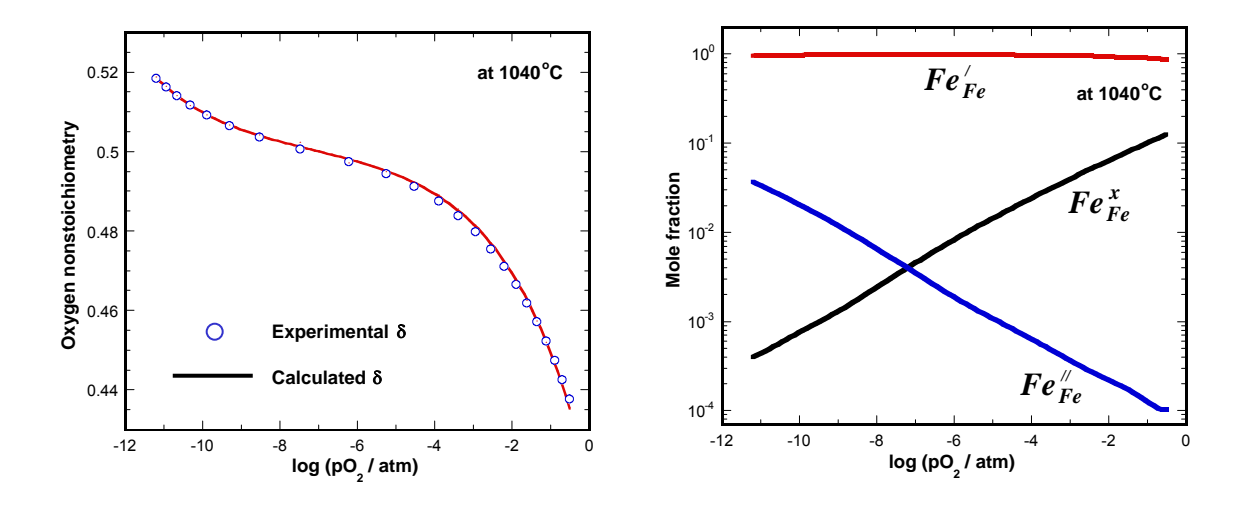


Figure 200. Experimental and calculated non-stoichiometry and defect concentrations.

At lower temperatures,  $1000 \ge T \ge 750$  °C, however, the simple defect model cannot describe the data and the model must include additional terms that describe the interaction between defects.

#### **5.5.1.4** Conductivity Measurements

Recently Kozhevnikov *et al.* [10] measured the electrical conductivity and the Seebeck coefficient of SrFeO<sub>3-x</sub> in the temperature range  $700 \ge T \ge 950$  °C and at  $0.3 \ge pO_2 \ge 10^{-18}$  atm. The results they obtained are shown in Figure 201 as a log-log plot of conductivity versus pO<sub>2</sub> from 700 to 950 °C at 50 °C increments. The data show the expected p and n type behaviour at

high and low oxygen partial pressures, respectively. The  $\pm 1/4$  dependence is expected from a simple defect model with doubly ionized defects. Surprisingly, a pronounced discontinuity is observed in the conductivity at pO<sub>2</sub> values below  $10^{-4}$  atm. A plateau is observed over a wide pO<sub>2</sub> range at 700 °C that decreases in width as the temperature is raised. Similar discontinuities were also observed in thermopower measurements. The measurements were made in one direction only with a criterion for equilibrium that the conductivity changed by less than 0.0005 S/min.

The results obtained by Kozhevnikov *et al.* [10] are surprising and not consistent with the data that we have obtained previously. Consequently, we repeated the measurements using our own cell design. In initial experiments, Pt leads were used but problems were observed at very low oxygen partial pressures due to reaction of Pt with  $SrFeO_{3-x}$  as illustrated by the results shown in Figure 202a. The filled circles correspond to measurements made with decreasing partial pressure of oxygen whereas the data represented by the open circles were obtained by first pumping the cell down to  $pO_2 = \sim 10^{-11}$  atm and then increasing  $pO_2$ . A significant discrepancy in the conductivity values observed below  $10^{-8}$  atm, which we attribute to problems with the voltage probes. Subsequent experiments used Pt13%Rh voltage and current leads to avoid the problem.

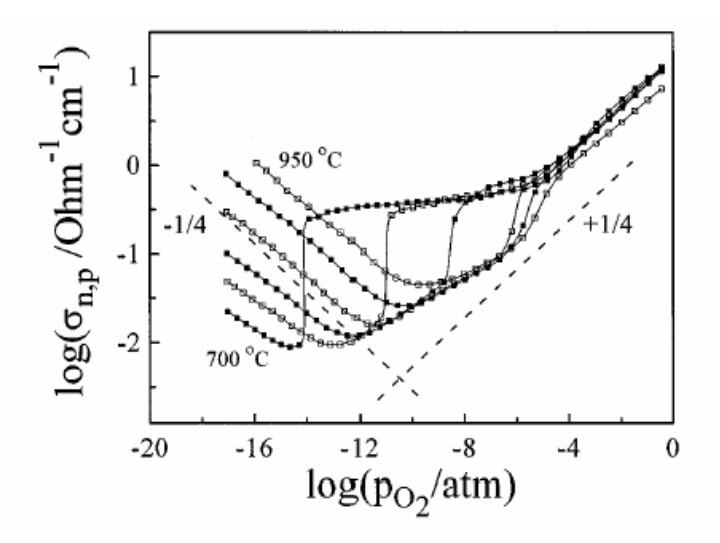


Figure 201. Conductivity isotherms for SrFeO<sub>3-x</sub> as a function of log(pO<sub>2</sub>) taken from reference 10.

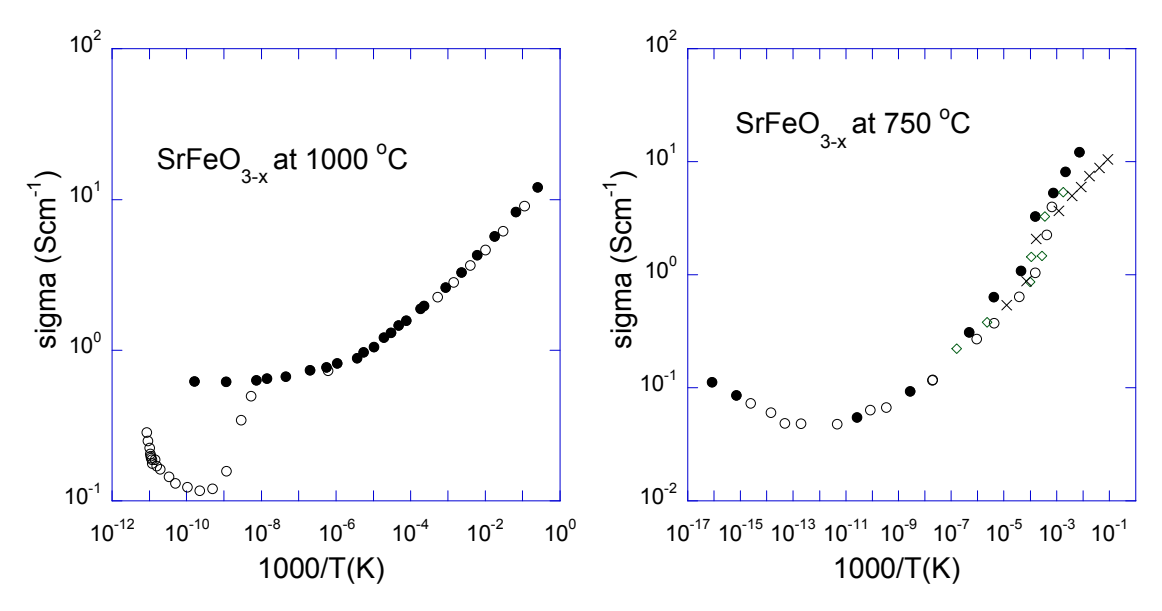


Figure 202 a) Conductivity of SrFeO<sub>3-x</sub> at 1000 °C, filled and open circles represent measurements made on decreasing and increasing pO<sub>2</sub>, respectively; b) Conductivity of SrFeO<sub>3-x</sub> at 750 °C, the filled circles correspond to measurements from high to low pO<sub>2</sub>, data with the other symbols were obtained from low to high pO<sub>2</sub>.

The results for 750 °C are shown in Figure 202b where the filled circles correspond to measurements from high to low pO<sub>2</sub>, and the data with the other symbols were obtained from low to high pO<sub>2</sub>. In general, the magnitude of the conductivity is closely similar to that found in previous measurements but the shape is quite different. The shape of our 750 °C isotherm most closely resembles the previous data obtained at 950 °C. The present results were obtained using a criterion for equilibrium of  $\sim 5 \times 10^{-5}$  Smin<sup>-1</sup>, an order of magnitude slower than that used by Kozhevnikov *et al.* [10] and show no evidence for the plateau reported previously. Even with long equilibration times, at 750 °C some scatter in the data is apparent in the region where phase separation occurs.

The low pressure data at 750 and 850 °C were fit to a model in which the conductivity dependence on oxygen partial pressure is represented by a pressure independent ionic component and  $\pm 1/4$  dependences for the n and p branches according to  $\sigma = \sigma_0 + {\rm ApO_2}^{+1/4} + {\rm BpO_2}^{-1/4}$ . The data for the two temperatures were least squares fit to extract the constants and the results are compared with the data of (1) in Figure 203. The agreement is generally satisfactory.

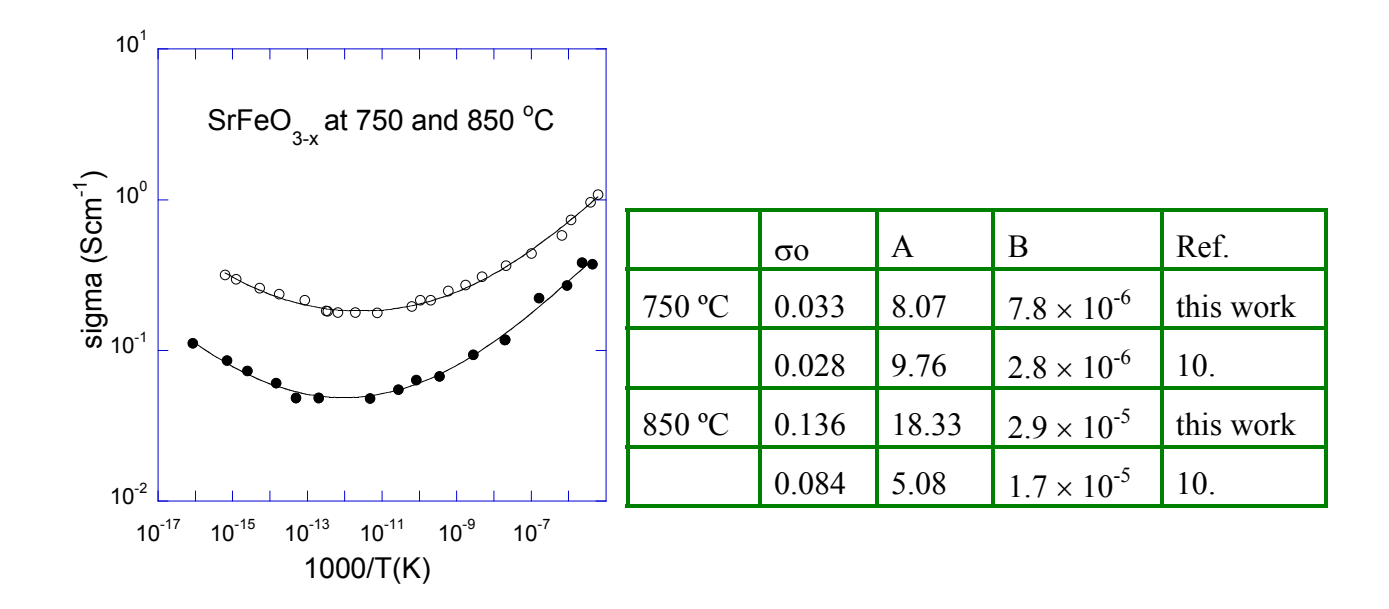


Figure 203. The low pressure conductivity of SrFeO<sub>3-x</sub> at 750 and 850 °C.

### 5.5.2. La<sub>0.5</sub>Sr<sub>0.5</sub>FeO<sub>3-x</sub> and La<sub>0.2</sub>Sr<sub>0.8</sub>FeO<sub>3</sub>

Electrical conductivity relaxation measurements on  $La_{0.2}Sr_{0.8}FeO_3$  were made with pressure switches from 1% to 2%  $O_2$  in the temperature range 850°C to 955°C. Values of  $D_{chem}$  = 7.4 x  $10^{-6}$  to 9 x  $10^{-5}$  cm<sup>2</sup>/s and  $k_{chem}$ .= 3 x  $10^{-4}$  cm/s to 9 x  $10^{-3}$  were obtained by fitting the experimental relaxation curves at 850°C and 955°C. Conductivity relaxation experiments were made on  $La_{0.5}Sr_{0.5}FeO_3$ . Three samples were prepared in the form of small rectangular bars with dimensions of 15.9 mm x 0.2 mm x 0.46 mm, 8.4 mm x 0.56 mm x 2.38 mm, and 13 mm x 0.96 mm x 1.12 mm. The measurements were made on samples with different sizes in order to confirm that the correlation between D and k is not influencing the values in any significant way.

The results for the two iron compounds are compared with earlier results for  $La_{0.5}Sr_{0.5}CoO_{3-x}$  and  $La_{0.6}Sr_{0.4}Fe_{0.8}Co_{0.2}O_{3-x}$  in and Figures 204 and 205 for D and k.

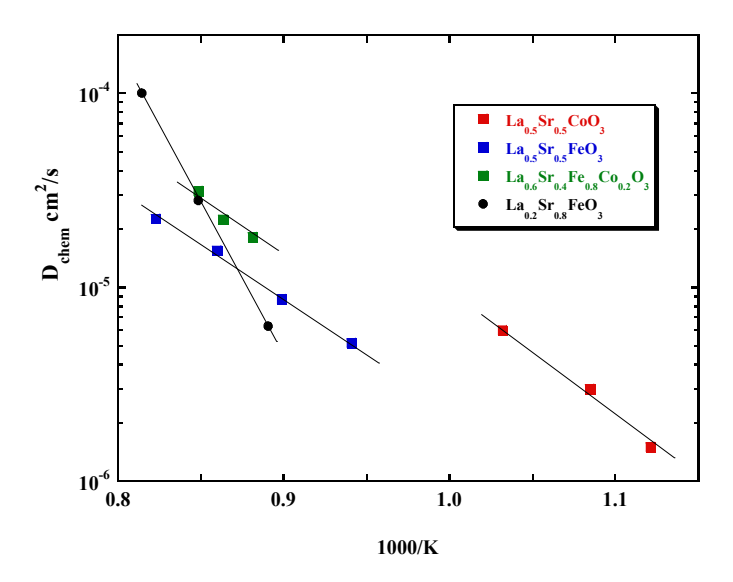


Figure 204 Comparison of D<sub>chem</sub> values measured by electrical conductivity relaxation.

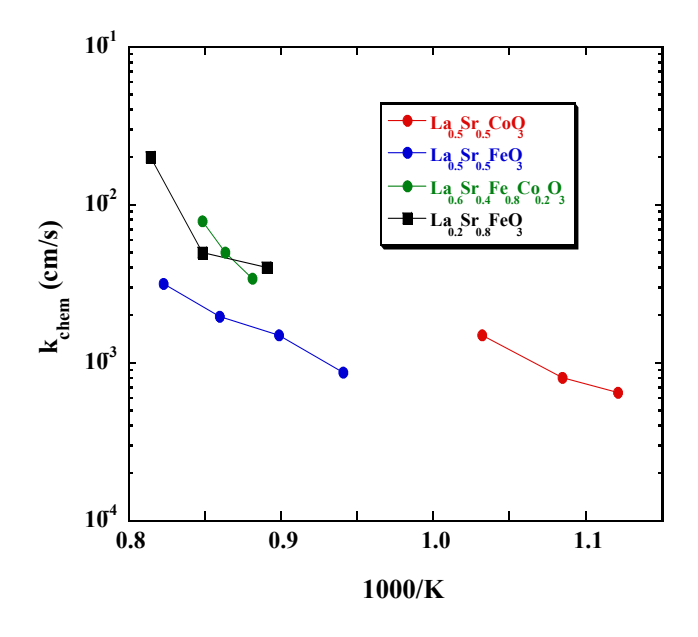


Figure 205 Comparison of  $k_{\text{chem}}$  values measured by electrical conductivity relaxation. In both sets of data, the results for  $La_{0.2}Sr_{0.8}FeO_{3-x}$  are anomalous most likely due to chemical inhomogeneity. The results show that the addition of cobalt increases both D and k relative to iron as anticipated from previous data

# 5.5.3. $La_{0.2}Sr_{0.8}Fe_{0.8}Cr_{0.2}O_{3-x}$ .

# **5.5.3.1 Electrical Conductivity**

The pO<sub>2</sub> dependence of electrical conductivities ( $\sigma$  S cm<sup>-1</sup>) at 752, 802, 854, 902, 942, 985, 1024, and 1055°C measured with increasing oxygen partial pressure after the cell had been initially pumped out are shown in Figure 206.

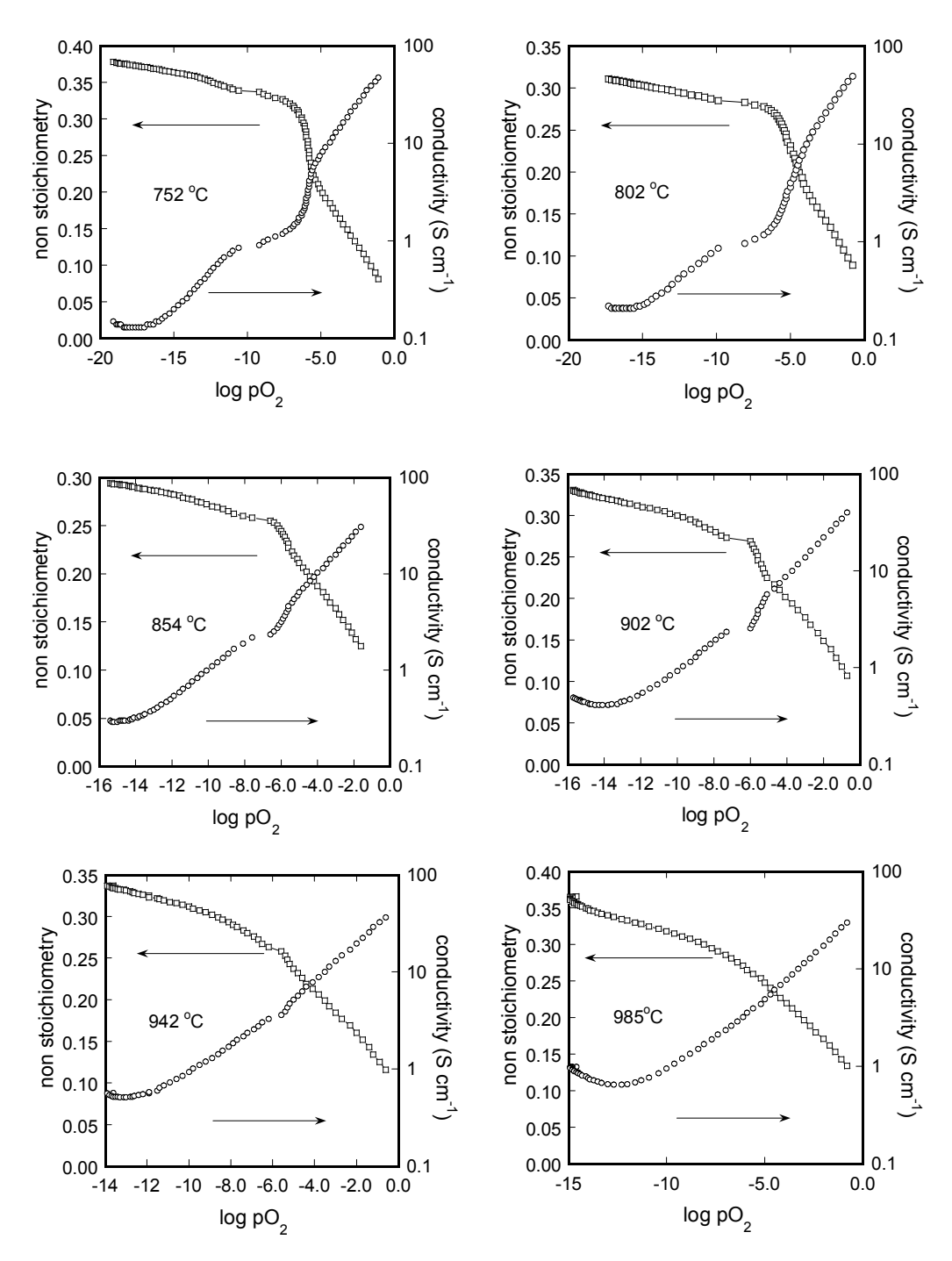


Figure 206. pO<sub>2</sub> dependence of electrical conductivities and oxygen non-stoichiometry at 752, 802, 854, 902, 942, 985, 1024, and 1055°C.

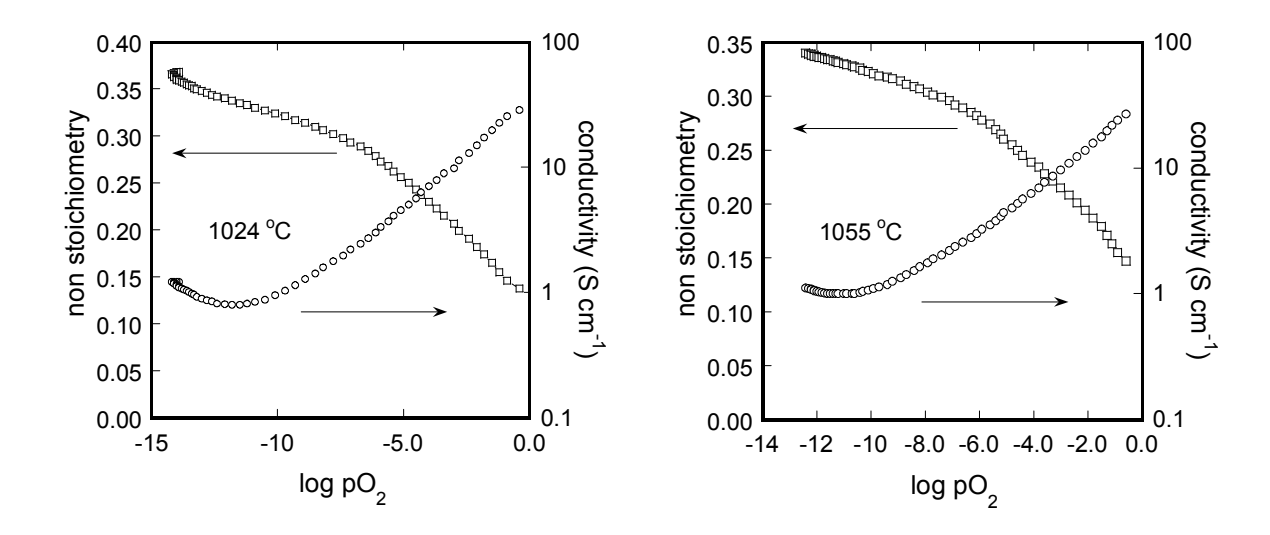


Figure 206 (cont.).  $pO_2$  dependence of electrical conductivities and oxygen non-stoichiometry at 752, 802, 854, 902, 942, 985, 1024, and 1055°C.

The conductivity data show p type behavior at high oxygen partial pressures as expected. The slope of the isotherms is dependent on pO<sub>2</sub>, and is  $\sim 1/5$  almost irrespective of T in the p-type region, pO<sub>2</sub> =  $10^{-5} \sim 10^{-1}$  atm (Fig. 207).

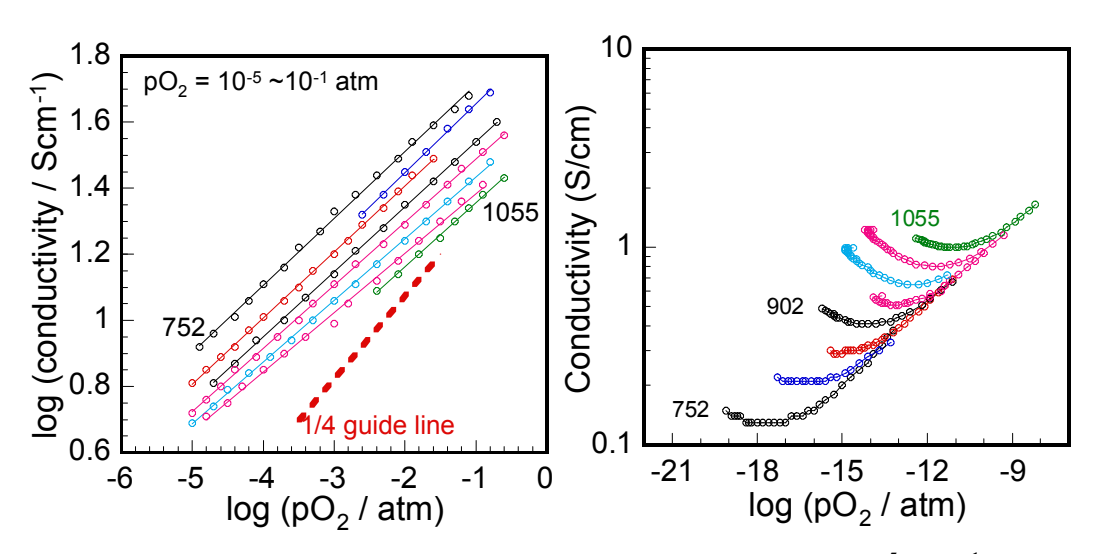


Figure 207. a) pO<sub>2</sub> dependence of electrical conductivities in the pO<sub>2</sub> =  $10^{-5} \sim 10^{-1}$  atm b) The temperature dependence of p-n transition behavior.

In the pO<sub>2</sub> range between the plateau and the minimum value of  $\sigma$  in the isotherms shown in Figure 207b, the electrical conductivity values are nearly independent of temperature, for example, at pO<sub>2</sub> =  $10^{-10}$  atm the conductivity varies from 0.8 to 1.1 S/cm. The total conductivity ( $\sigma_t$ ) is approximately the sum of the electron hole conductivity ( $\sigma_h$ ) and the ionic conductivity

 $(\sigma_i)$  in this region. Since the values of  $\sigma_h$  and  $\sigma_i$  are comparable in this pO<sub>2</sub> range, a  $\sigma \propto (pO_2)^{1/4}$  dependence is not expected. The weak temperature dependence arises because of the opposite temperature dependences of  $\sigma_h$  and  $\sigma_i$ . Thus the decrease in  $\sigma_h$  at higher T is compensated by a higher  $\sigma_i$ .

At low partial pressures a transition to n-type behavior is observed. The pO<sub>2</sub> conductivity isotherms are shown in the vicinity of the p-n transition region in Fig. 207b. The pO<sub>2</sub> at which the minimum occurs increases with increasing temperature as expected. The p-n transitions of LSCrF occur at pO<sub>2</sub> (atm) =  $2.36 \times 10^{-18}$  at  $752^{\circ}$ C,  $3.65 \times 10^{-17}$  at  $802^{\circ}$ C,  $6.99 \times 10^{-16}$  at  $854^{\circ}$ C,  $8.67 \times 10^{-15}$  at  $902^{\circ}$ C,  $7.41 \times 10^{-14}$  at  $942^{\circ}$ C,  $2.20 \times 10^{-13}$  at  $985^{\circ}$ C,  $1.67 \times 10^{-12}$  at  $1024^{\circ}$ C, and  $6.80 \times 10^{-12}$  at  $1055^{\circ}$ C. At the highest temperature the transition from p to n type behavior is smooth but at lower temperatures there is evidence for the formation of an intermediate phase presumably as a consequence of vacancy ordering. If it is assumed that at the minimum in the conductivity data the electronic contributions are negligible and the conductivity is primarily ionic, the temperature dependence of the ionic conductivity can be obtained. The measured conductivity is in the range of 0.1 to 1 S/cm over the temperature range measured with an activation energy of 0.76 eV.

#### 5.5.3.2 Stoichiometry

The relative stoichiometry data measured also from low to high oxygen partial pressure are also shown in Figure 206. Measurements on  $La_{0.2}Sr_{0.8}Fe_{0.8}Cr_{0.2}O_{3-x}$  proved difficult because of the difficulties in attaining equilibrium. The measurements were made on a powdered sample by coulometric titration in a sealed electrochemical cell with a YSZ pump and a YSZ sensor to monitor the internal  $pO_2$  and the approach to equilibrium.

The absence of any change in the stoichiometry in the range of oxygen partial pressures corresponding to the plateau in the conductivity data also indicate non equilibrium behavior. The sharp change in stoichiometry at nearly constant  $pO_2$  indicates two phase behavior.

#### 5.5. 3.3 Phase Transition

The plateau region observed in the  $pO_2$  variation of the conductivity and stoichiometry suggests that a two-phase region exists in the temperature range between 752 and 942 °C (Figure 206.). At

high vacancy concentrations and lower temperatures perovskite oxides often phase separate and form vacancy ordered phases to reduce coulombic repulsion among defects.

The general shape of the data suggests, however, that equilibrium is not achieved in this region. Specifically, if a well-defined two-phase region exists then the conductivity should change discontinuously at the pO<sub>2</sub> value at which the two phases are in equilibrium. The magnitude of the discontinuity will depend on the difference in total conductivity between the two phases. The ionic conductivity is directly affected by the vacancy ordering and the electronic conductivity depends on the consequent changes in the electronic structure. The total effect on the conductivity is not easy to predict but general, we might expect the difference to be small since the two phases have the same composition. We note that the change is reported to be small in SrFeO<sub>3-x</sub>. The observed behavior can be interpreted as follows. At a given temperature, on increasing pO<sub>2</sub>, the conductivity increases from the minimum, through a p-type region, until the plateau is reached. The conductivity then remains constant until a large enough excess oxygen pressure (over-potential) is applied to drive the phase transition. As the phase transition occurs, the conductivity increases until the high-pressure equilibrium line is reached. The kinetics of phase separations between ordered and disordered systems are known to be slow in perovskite oxides as discussed in for SrFe<sub>0.2</sub>Co<sub>0.8</sub>O<sub>3-x</sub>. The size of the plateau region decreases with increasing temperature both because the rate of the phase separation increases and also because the width of the two phase region decreases. By 985 °C, the plateau region is no longer apparent although a change in slope remains.

In Figure 208, we show conductivity data at two temperatures measured in the opposite direction, namely from high to low pO<sub>2</sub>. Measurements made in this direction show no plateau region at intermediate pO<sub>2</sub> values but only a change in slope. The data at both high and low partial pressures agree with the measurements made in the reverse direction (note that in each case the two sets of data are offset for clarity). Apparently the phase separation is faster from the high-pressure side but whether this is an intrinsic phenomenon or related to mass transfer effects is not yet known.

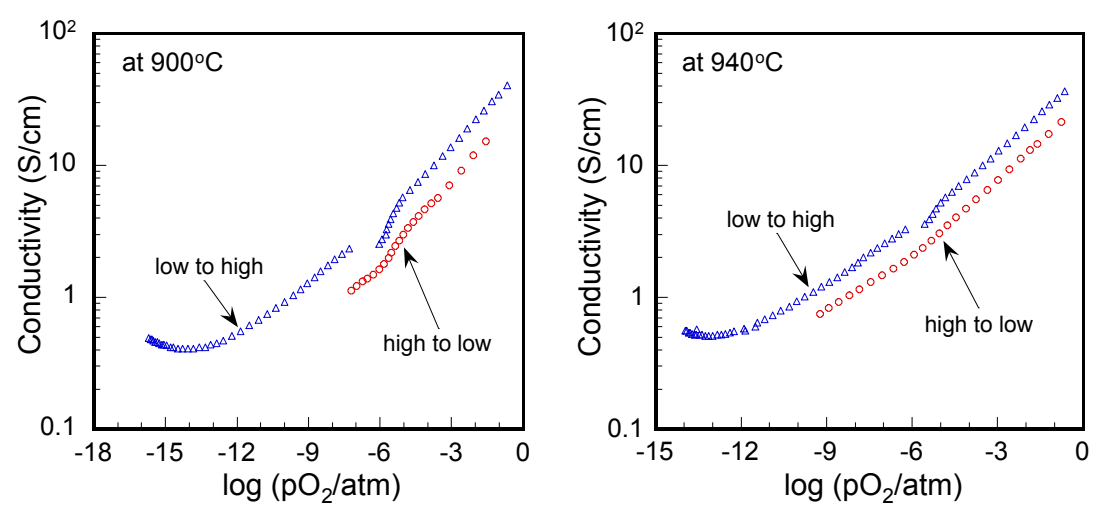


Figure. 208. Comparison of conductivity isotherms according to the direction: "high to low pO<sub>2</sub>" run and "low to high pO<sub>2</sub>" run. For clarity, "high to low pO<sub>2</sub>" runs are offset.

### 5.5.3.4 Thermodynamics

Because of the equilibrium problem, at low pO<sub>2</sub> the uncertainty in the stoichiometry is large and increases with temperature ( $\pm$  0.02 at 1040 °C). The data obtained on increasing and decreasing pO<sub>2</sub>, in the equilibrium range ( $>10^{-8}$  atm), were averaged and fit, in order to extract the temperature dependence of the stoichiometry at different pO<sub>2</sub>s. The interpolated results are shown in Figure 209 as isobars at log(pO<sub>2</sub>) increments of -1 from 0 to -8. The dotted line indicates the position of the phase boundary. The partial molar free energy of oxidation which in turn can be used to extract the partial molar enthalpy and entropy were determined from the pressure dependence of the non stoichiometry and are shown in Figure 210.

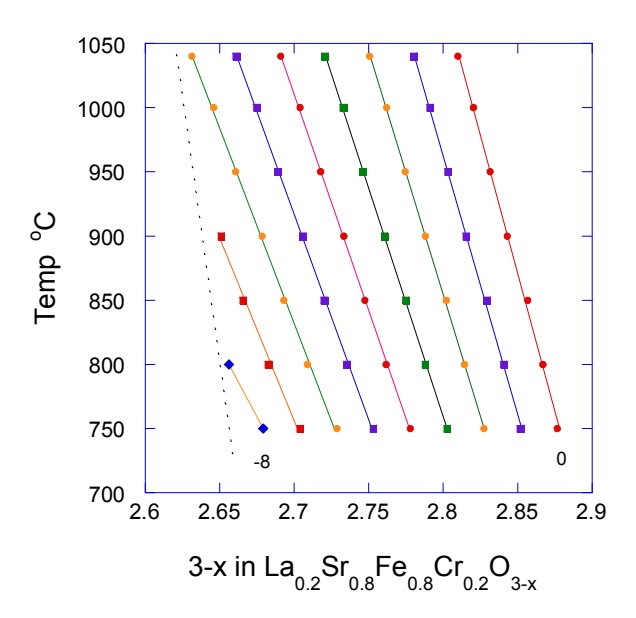


Figure 209. The phase diagram of La<sub>0.2</sub>Sr<sub>0.8</sub>Fe<sub>0.8</sub>Cr<sub>0.2</sub>O<sub>3-x.</sub>

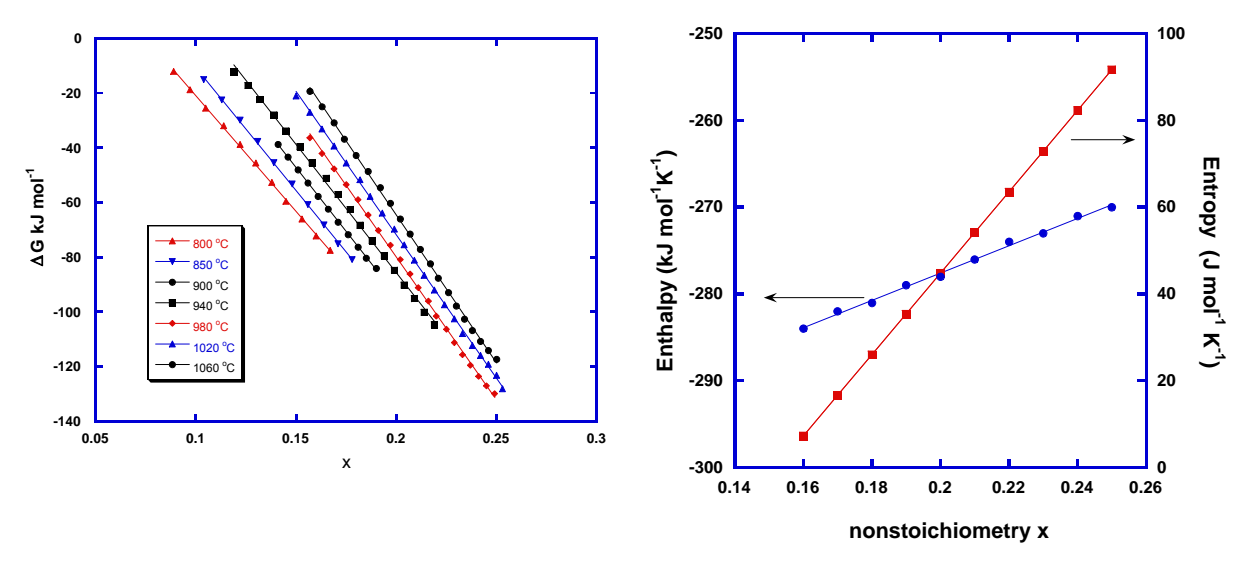


Fig. 210 The partial molar free energy (left) and the partial molar enthalpy and entropy (right).

# 5.5.3.5 Electrical conductivity relaxation

Diffusion and surface exchange in  $La_{0.2}Sr_{0.8}Fe_{0.8}Cr_{0.2}O_{3-x}$  were investigated by electrical conductivity relaxation with pressure switches from 5% to 1%  $O_2$  at 821°C. Initial values of  $D_{chem}$  and  $k_{chem}$  of 4.1 x  $10^{-6}$  cm<sup>2</sup>/s and 6.8 x  $10^{-4}$ cm/s. were obtained. On repeating the experiment

several hours later it was observed that the time constant for the relaxation had decreased. Monitoring the data for several days showed a continuing trend to longer time constants. The data were modeled assuming a constant value of  $D_{chem} = 3.6 \times 10^{-6} \text{ cm}^2/\text{s}$  and values of  $k_{chem}$  determined as a function of time. The measured  $k_{chem}$  was found to increase monotonically with time over a period of 12 d. The results are shown in Figure 211.

During this period the sample was also exposed to pure CO<sub>2</sub> for short periods. As seen in Figure 211, the exposure of CO<sub>2</sub> temporarily accelerates surface kinetics of the sample. However, the sample surface exchange kinetics reverts to the original behavior after a short time. Bulk electrical conductivity was also sampled periodically. The bulk conductivity remained constant as indicated in Figure 211.

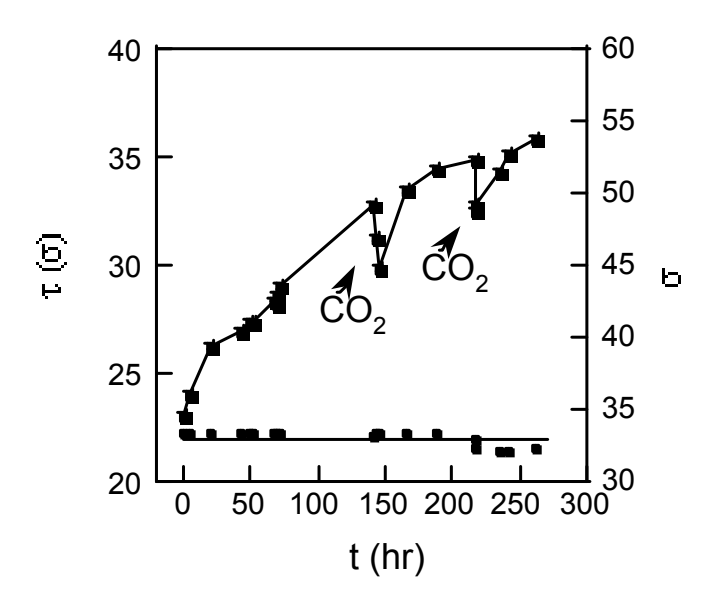


Figure 211. Evolution of the time constant and the effect of CO<sub>2</sub>.

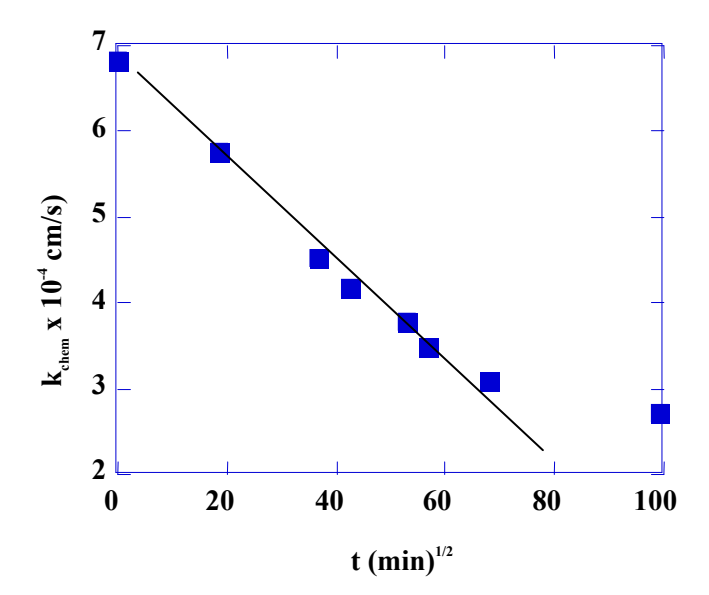


Figure 212. t<sup>1/2</sup> dependence of the time constant at 821°C for La<sub>0.2</sub>Sr<sub>0.8</sub>Cr<sub>0.2</sub>Fe<sub>0.8</sub>O<sub>3</sub>.

The observed behavior suggests a time dependent slow transformation in the sample which affects the surface exchange kinetics adversely but does not affect bulk transport. Furthermore, the variation in the measured time constant is linear with t<sup>1/2</sup> (Figure 212). It is concluded that varying surface concentration of some species is responsible for the observed behavior. XPS investigations have revealed segregation of strontium and chromium on the surfaces of the specimen used in the long-term conductivity relaxation experiment. We suggest that the observed surface strontium segregation is caused by diffusion from strontium rich regions in the interior of samples via high diffusive paths, probably along grain boundaries.

# 5.5.4. La<sub>0.5</sub>Sr<sub>0.5</sub>Fe<sub>0.8</sub>Ga<sub>0.2</sub>O<sub>3-x</sub>

A limited number of experiments were carried out on  $La_{0.5}Sr_{0.5}Fe_{0.8}Ga_{0.2}O_{3-x}$  for comparison with the chromium system.

# 5.5.4.1 Electrical conductivity

The conductivity results for  $La_{0.5}Sr_{0.5}Fe_{0.8}Ga_{0.2}O_{3-x}$  are shown in Figure 213 for five temperatures.

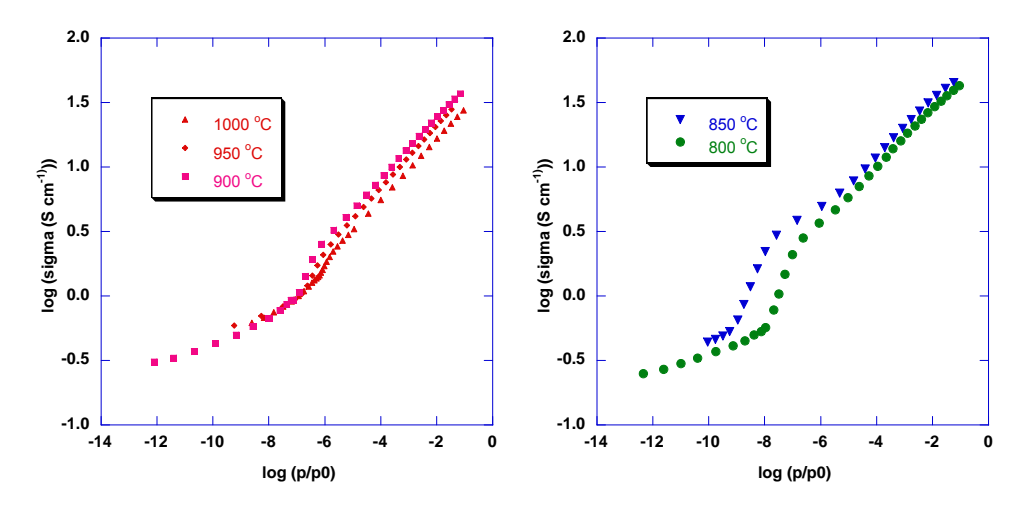


Figure 213. Partial pressure dependence of the electrical conductivity of La<sub>0.5</sub>Sr<sub>0.5</sub>Fe<sub>0.8</sub>Ga<sub>0.2</sub>O<sub>3-x</sub>

The data show p type conductivity at high oxygen partial pressures as expected with slopes that are very close to ¼ as expected for an ideal p type system with doubly ionized oxygen vacancies.

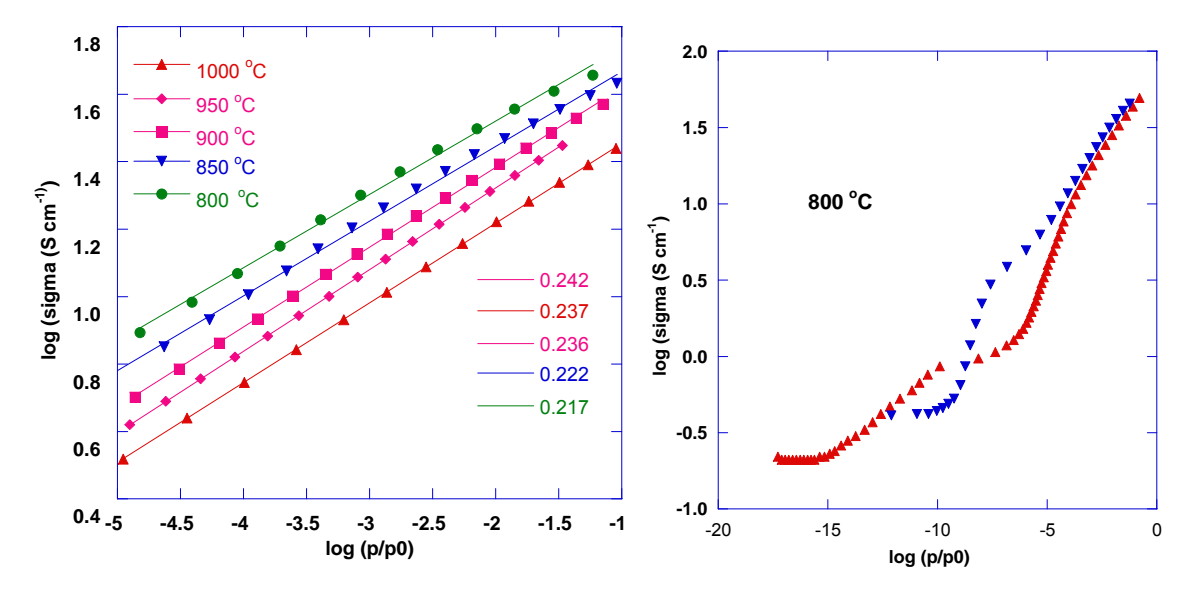


Figure 214. Conductivity data for La<sub>0.5</sub>Sr<sub>0.5</sub>Fe<sub>0.8</sub>Ga<sub>0.2</sub>O<sub>3-x</sub> b) a comparison of Cr (red) and Ga (blue) at 800 °C

At lower temperatures there is clear evidence for the formation of an intermediate phase presumably as a consequence of vacancy ordering. At intermediate oxygen partial pressures approaching the predominantly ionic transition region, the conductivities are almost independent of temperature. In general the results are similar to those of the Cr compound. The onset of the phase transition occurs at lower  $pO_2$  in Ga (Figure 214 b) is due to the lower Sr content.

### $5.5.5 \text{ La}_{0.2}\text{Sr}_{0.8}\text{Fe}_{0.55}\text{Ti}_{0.45}\text{O}_{3-x}$

# **5.5.5.1 Stoichiometry**

The oxygen non-stoichiometry ( $\delta$ ) for La<sub>0.2</sub>Sr<sub>0.8</sub>Fe<sub>0.55</sub>Ti<sub>0.45</sub>O<sub>3- $\delta$ </sub> was measured as a function of oxygen partial pressure at 750  $\leq$  T  $\leq$  1040 °C. Measurements were made in a sealed electrochemical cells at  $10^{-16} \leq pO_2 \leq 0.3$  atm. The measurements were repeated with three different cells. About 0.2~0.5 g of powder was used and measurements made on both decreasing and increasing pO<sub>2</sub>. In the beginning of measurements, the relative  $\delta$ -values as a function of pO<sub>2</sub> were obtained and then the leakage through 8-mol % YSZ leakage corrected over the measured pO<sub>2</sub> ranges. The leakage is more significant at higher temperature and at lower pO<sub>2</sub>. Details of the leakage correction procedures were described previously.

The leakage corrected relative stoichiometry data were normalized as follows. According to Wagner, the minimum value of  $\partial \delta / \partial p O_2$  indicates the stoichiometric composition of the sample at this  $pO_2$ . That is, in  $La_{0.2}{}^{3+}Sr_{0.8}{}^{2+}Fe_{0.55}{}^{3+}Ti_{0.45}{}^{4+}O_{3-\delta}$ , an inflection in the titration data indicates the  $\delta \cong 0.175$ . One example measured at 950 °C is shown in Fig. 215. The solid line in this graph is  $\partial \delta / \partial p O_2$ . The minimum value of  $\partial \delta / \partial p O_2$  at 950 °C was found at  $pO_2 \sim 8.3 \times 10^{-11}$  and  $3.2 \times 10^{-10}$  atm for high to low and low to high  $pO_2$  measurements, respectively.

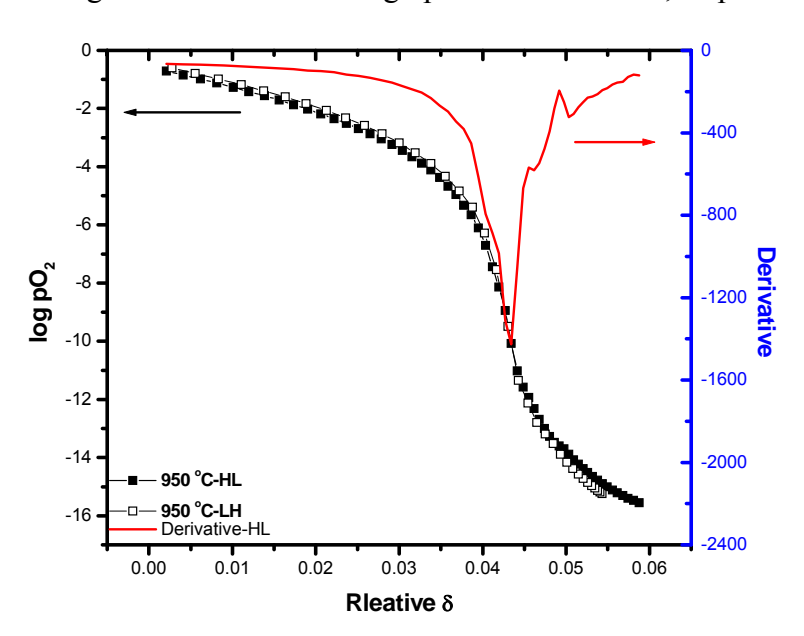


Figure 215 Determination of stoichiometric composition by using the minimum value of  $\partial \delta \partial p O_2$  for La<sub>0.2</sub>Sr<sub>0.8</sub>Fe<sub>0.55</sub>Ti<sub>0.45</sub>O<sub>3- $\delta$ </sub> at 950 °C.

The absolute  $\delta$ -values were obtained with this assumption and the other data points were normalized over the pO<sub>2</sub> range. The entire set of coulometric titration data at different temperatures are shown in Figure 216. The experimental results display good reproducibility irrespective of the pO<sub>2</sub> direction of measurement. They changed very systematically as a function of temperature and the oxygen partial pressure. The  $\delta$ -values increased almost linearly on lowering pO<sub>2</sub> until they approached the ideal stoichiometric composition,  $\delta = 0.175$ . Next, a flat region follows between pO<sub>2</sub>  $\sim 10^{-12}$  and  $10^{-7}$  atm. The pO<sub>2</sub> corresponding to the ideal stoichiometry moved to the high pO<sub>2</sub> side as temperature increased. Then,  $\delta$ -values increased again at further lowering pO<sub>2</sub> regions with a small gap, especially at pO<sub>2</sub>  $\leq 10^{-13}$  atm and at T  $\geq 1000$  °C.

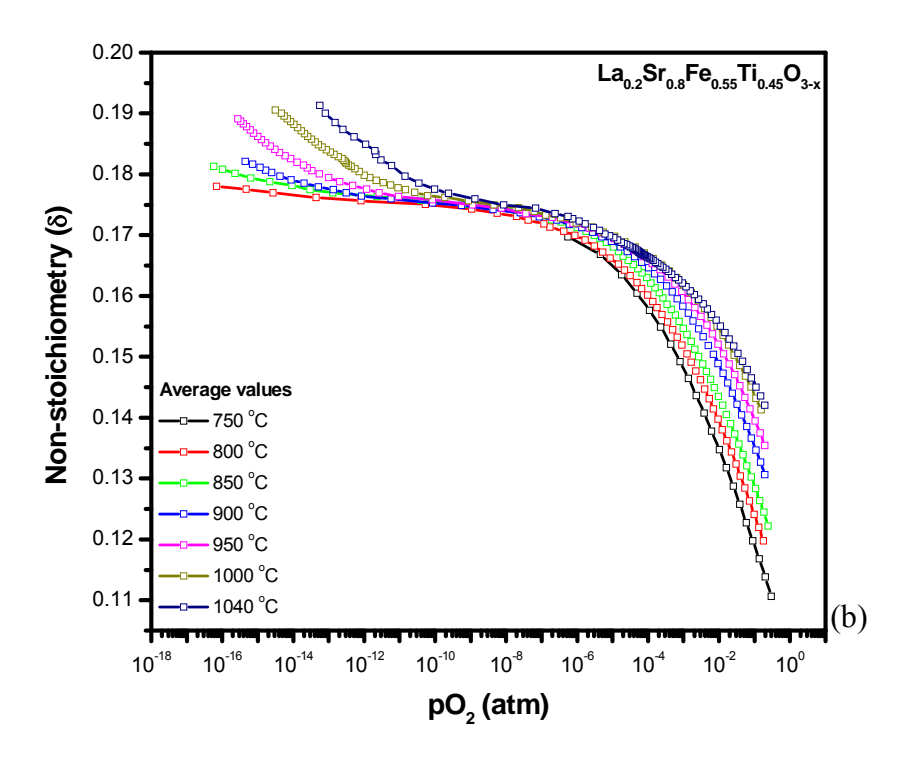


Figure 216. Average stoichiometry data.

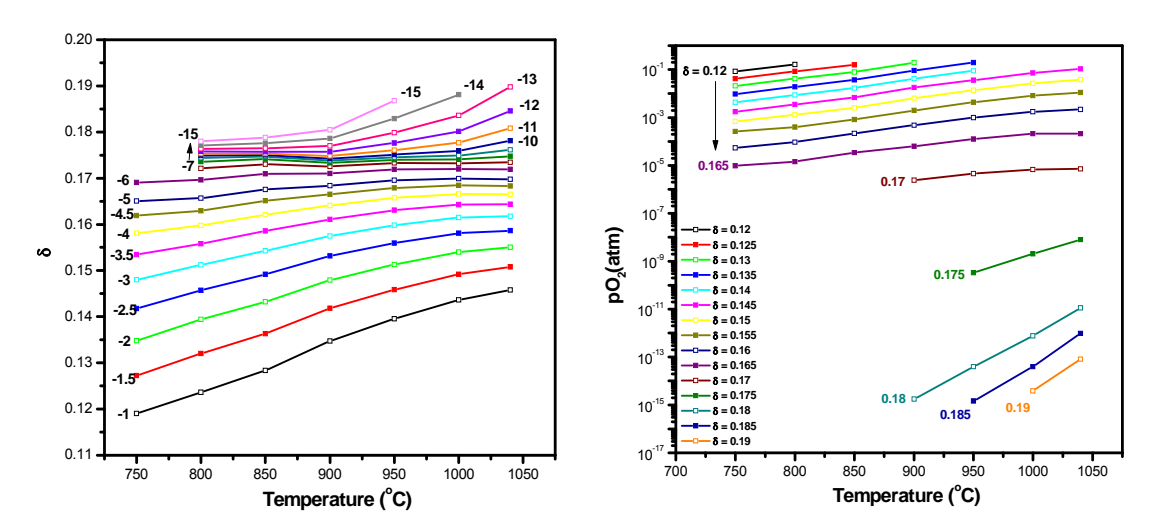


Figure 217. The  $\delta$  dependence on temperature at constant pO<sub>2</sub> (left) and the pO<sub>2</sub> dependence on temperature at constant  $\delta$  (right).

The total changes in  $\delta$  were less than  $\sim 0.1$  at the pO<sub>2</sub> and temperatures measured. All the normalized experimental results were taken as an average of the data with two measurement directions. All measurements covered the whole pO<sub>2</sub> range except for the low pO<sub>2</sub> values at 750 °C where equilibrium times were too long. These reverse S-shape curves are typical of the coulometric titration experiments. The oxygen non-stoichiometric results can be fitted by using polynomial fitting and the results used to investigate the relationships of  $\delta$  vs. T at constant pO<sub>2</sub> and log pO<sub>2</sub> vs. T at constant  $\delta$ .

The  $\delta$  dependence on temperature at constant pO<sub>2</sub> is shown in Figure 217. Equivalent log pO<sub>2</sub> lines are shown for specific values of log pO<sub>2</sub>. The lines gradually closer on going from the lower pO<sub>2</sub> side to log pO<sub>2</sub>  $\sim$  -6 atm and they become very close together between -7 and -15 atm. The pO<sub>2</sub> dependence on temperature at constant  $\delta$  is also shown in Figure 217.

### 5.5.5.2 Conductivity

A rectangular bar with dimensions  $0.67 \times 0.29 \times 0.20$  cm was cut from the sample that was sintered at 1300 °C for conductivity measurements.

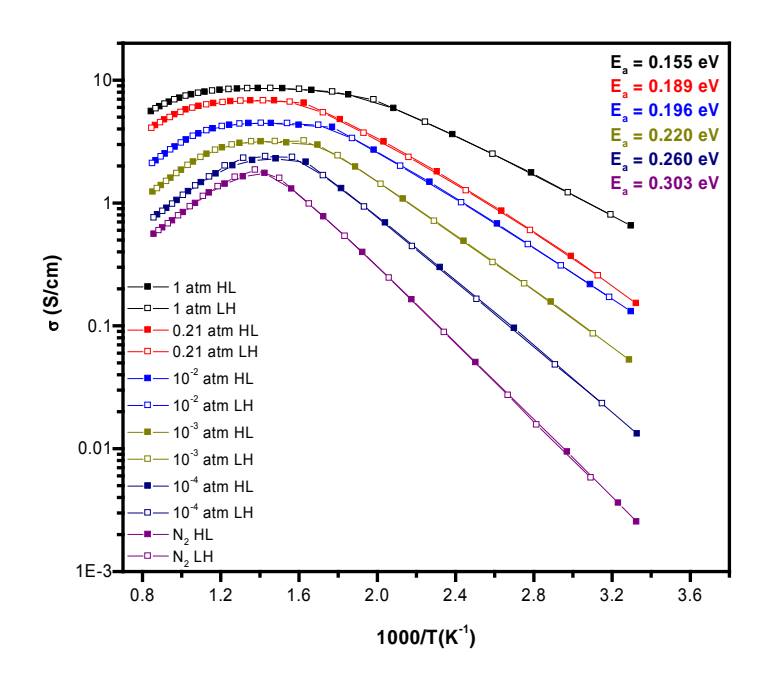


Figure 218. DC conductivity data for La<sub>0.2</sub>Sr<sub>0.8</sub>Fe<sub>0.55</sub>Ti<sub>0.45</sub>O<sub>3-x</sub> in different gas atmospheres as a function of reciprocal temperature.

Conductivity measurements were made as a function of temperature in different gas atmospheres by the four-probe dc method. Gold wires were used as electrodes and measurements were made on both heating and cooling to ensure that equilibrium had been attained. The results are shown in Figure 218. The results are typical for perovskite materials. The conductivity shows Arrhenius behavior at temperatures lower than about 300 °C. The activation energy increases with decreasing oxygen partial pressure as the contribution from ionic conductivity to the total conductivity increases. The maximum conductivity observed in pO<sub>2</sub> = 1 atm is ~10 S cm<sup>-1</sup>. Above 300 °C, the conductivity falls as the oxygen stoichiometry increases because of the relationship  $[Sr'] = [h^{\bullet}] + 2[V^{\bullet \bullet}]$ . At the higher oxygen pressures, a plateau is observed in the conductivity before the steep fall off. The origin of this plateau is not yet known but may be a

consequence of the way in which the stoichiometry depends on temperature or it may be a kinetic effect.

Measurements were made also in a sealed electrochemical cell as a function of oxygen partial pressure at temperatures from 750 °C to 1000 °C down to  $10^{-17}$  atm for the lowest temperature. The measurements were made using and ac technique at a single frequency and the phase angle monitored to confirm the absence of any polarization effects. Measurements were made on both decreasing and increasing pO<sub>2</sub> and the results are shown in Figure 219

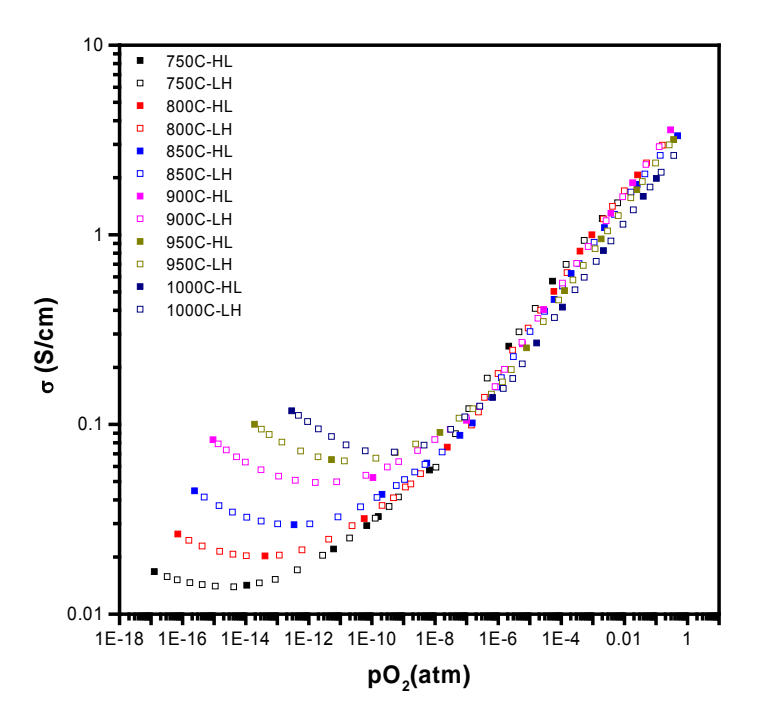


Figure 219. Conductivity measurements for  $La_{0.2}Sr_{0.8}Fe_{0.55}Ti_{0.45}O_{3-x}$  as a function of pO<sub>2</sub> at different temperatures. Open and closed symbols represent data taken on increasing and decreasing temperature.

The conductivity initially p type at high oxygen partial pressure decreases as  $pO_2$  decreases. The slope of the linear region in a log –log plot is  $\sim 1/4$  as expected. Little temperature variation is seen in this region presumably because the decrease in hole conductivity associated with oxygen loss is offset by an increase in the ionic conductivity. As the  $pO_2$  is further decreased, the conductivity goes through a minimum and then becomes n type with a  $pO_2^{-1/4}$  dependence. In general, the system is well behaved with little evidence for problems in attaining equilibrium that

we have found in the other iron systems that we have studied. The p to n transition is well defined at all temperatures.

The pO<sub>2</sub> dependence of the conductivity data for La<sub>0.2</sub>Sr<sub>0.8</sub>Fe<sub>0.55</sub>Ti<sub>0.45</sub>O<sub>3-x</sub> were further analyzed using a simple model that expresses the total conductivity as the sum of the ionic conductivity and the p and n type contributions according to: $\sigma_T = A + B \times pO_2^{-1/4} + C \times pO_2^{-1/4}$ . This simple model fits the data well (see Table 26) though it does not take proper account of the behavior in the p type region where changes in the stoichiometry effect the ionic conductivity (by changing the vacancy concentration) in addition changing the hole contribution. The two off setting effects lead to an apparent near zero activation energy (see Figure 219).

Table 26. Results from the model fit to the pO<sub>2</sub> dependence of the total conductivity data

La <sub>0.2</sub> Sr <sub>0.8</sub> Fe <sub>0.55</sub> Ti <sub>0.45</sub> O <sub>3-x</sub>	A	В	С
750 °C	0.0110	5.844	$3.57 \times 10^{-7}$
800 °C	0.0157	5.090	$9.15 \times 10^{-7}$
850 °C	0.0222	4.591	$2.70 \times 10^{-6}$
900 °C	0.0362	4.428	$8.00 \times 10^{-6}$
950 °C	0.0415	4.183	$2.00 \times 10^{-5}$
1000 °C	0.0423	3.495	$6.00 \times 10^{-5}$

Nevertheless, reasonable values for the ionic conductivity are derived  $\sim 0.03~{\rm Scm}^{-1}$  with an apparent activation energy of 0.66 eV.

#### 5.5.5.3 Polarization Measurements

The oxygen ion conductivities obtained from AC 4-probe conductivity experiments need to be confirmed or compared to those determined by a different experimental technique such as the ion blocking electrode method.

According to E. Bucher *et al.*,[11] the polarization and the depolarization process can be defined as follows:

$$U_{p}(t) = -\frac{jL}{\sigma_{i}} + \frac{jLt_{e}}{\sigma_{i}} \left( \frac{8}{\pi^{2}} \exp\left(-\frac{t}{\tau}\right) \right)$$
 (2)

and

$$U_d(t) = -\frac{jLt_e}{\sigma_i} \left( \frac{8}{\pi^2} \exp\left(-\frac{t}{\tau}\right) \right)$$
 (3)

These equations are based on two assumptions which are that the electronic transport number  $t_e$  of the mixed oxide is close to unity and that the kinetics of the mixed conducting interlayers can be neglected due to their small thickness compared to the relaxation process in the bulk sample.

 $\ln |U(t) - U(t = \infty)|$  vs. t-plots yield linear relations in t for time  $t \ge \tau/2$ 

$$\ln |U(t) - U(t = \infty)| = -\frac{t}{\tau} + \ln \left(\frac{8}{\pi^2} \frac{t_e jL}{\sigma_i}\right)$$
 (4)

The slop k of and the intercept A on the y-axis are given by

$$k = -\frac{1}{\tau} = -\frac{\pi \widetilde{D}}{L^2} \tag{5}$$

$$A = \ln \left( \frac{8}{\pi^2} \frac{t_e jL}{\sigma_i} \right) \tag{6}$$

where j is the total current density, L is the length of the sample, and  $\tau$  is the relaxation time of the sample defined as

$$\tau = \frac{L^2}{\pi^2 \widetilde{D}} \tag{7}$$

The data in Figure 220 show a typical depolarization curve for LSFTO after the sample has reached steady state with an applied current of 0.1 mA at 850 °C after the current is stopped. The voltage decay is monitored as a function of time. In order to analyze the relaxation, the measured voltage at time t minus the final voltage is plotted in log form. The results can then be analyzed using equations 4 and 5. The chemical diffusion coefficient and the ionic conductivity are from the preliminary results  $\widetilde{D}$ :  $1.7 \times 10^{-6}$  cm<sup>2</sup>/s and  $\sigma_i$ :  $4.88 \times 10^{-4}$  S/cm. It became apparent in the preliminary measurements that the long time data needs to be measured more precisely in order to define the slope of the curve. The present results appear to be too low. Further work on this project was not continued because of other priorities.

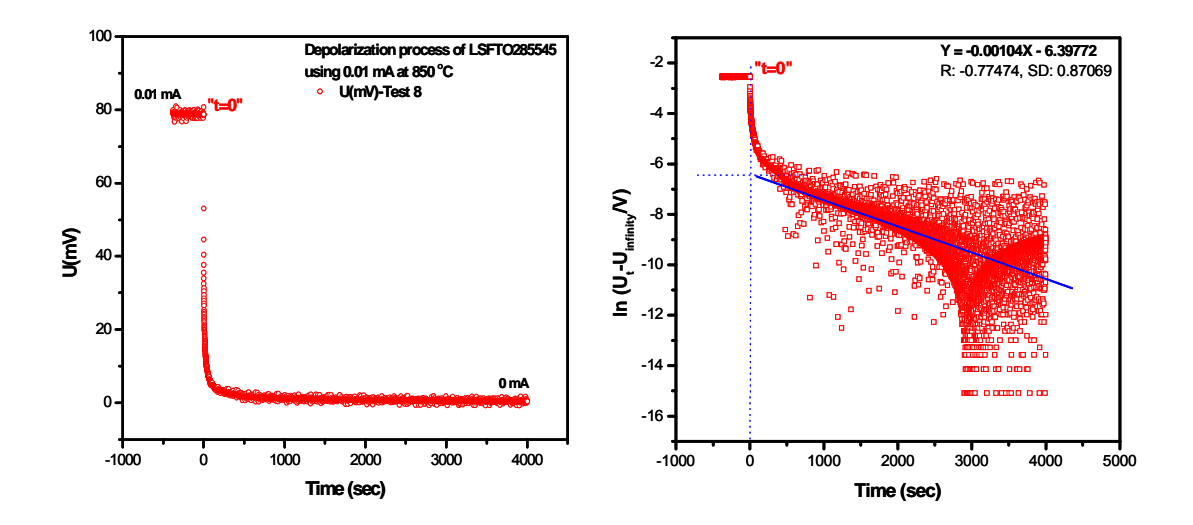


Figure 220. A depolarization curve of La<sub>0.2</sub>Sr<sub>0.8</sub>Fe<sub>0.55</sub>Fe<sub>0.45</sub>O<sub>3-δ</sub> at 850 °C in air (a) Voltage response of cell during the depolarization process (b) logarithmic plot of (a)

### 5.5.5.4 Thermopower measurements

Measurements are being made in the cell described above as a function of temperature and pressure at  $750 \le T \le 1000$  °C and  $\sim 10^{-17} \le pO_2 \le 0.3$  atm, respectively. All data points have been obtained manually in order to maintain a stringent equilibrium criterion. As expected it takes more than 7 h to obtain one data point especially in the middle of  $pO_2$  region due to the extremely slow equilibrium kinetics. The Seebeck Coefficient (Q) was calculated from the observed Seebeck voltage by using the following equations:

$$Q = Q_{sample/Pt} - Q_{Pt}$$
 (8)

$$Q_{sample/Pt} = \frac{E_{sample/Pt}}{T_h - T_c} \tag{9}$$

where  $Q_{Pt}$  is Seebeck coefficient of Pt and  $E_{sample/Pt}$  is the observed Seebeck voltage.  $T_h$  and  $T_c$  are the temperatures of the hot and cold end of the sample, respectively. The values of  $Q_{Pt}$  at each temperature were taken from previous results.[12] The data obtained thus far at 850 °C from high to low pO<sub>2</sub> are shown in Figure 221. The values of Seebeck coefficient increase

slightly as the  $pO_2$  decreases and then they decrease on further decrease of  $pO_2$ . The turning point of  $pO_2$  was  $\sim 2 \times 10^{-5}$  atm with  $Q \sim 40.7 \ \mu\text{V/K}$  at 850 °C. This behavior is frequently found in SrFeO<sub>3- $\delta$ </sub> based perovskites. [10, 13]

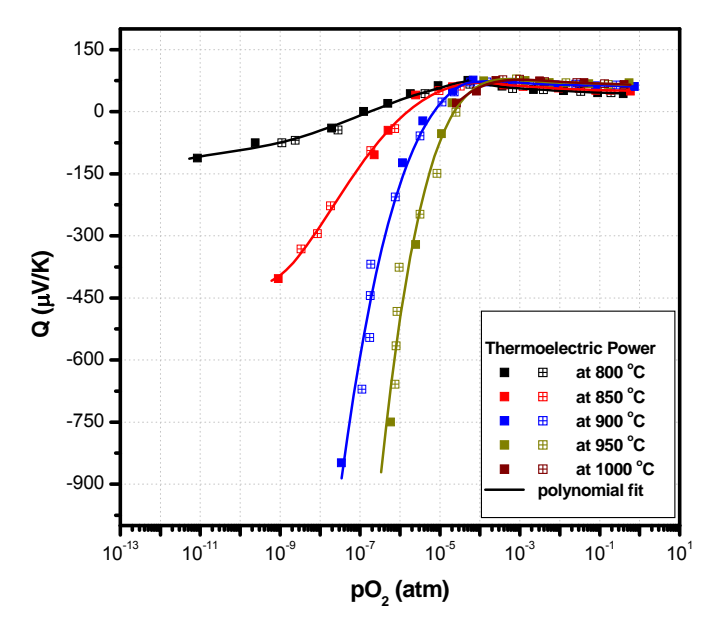


Figure 221. Thermopower results for LSFTO

### 5.5.5.5 Thermal Expansion Data

A rectangular sample bar with dimensions 14.38 mm  $\times$  4.47 mm  $\times$  5.33 mm was sintered at 1450 °C for 10 h for use in dilatometry measurements of La<sub>0.2</sub>Sr<sub>0.8</sub>Fe<sub>0.55</sub>Ti<sub>0.45</sub>O<sub>3-x</sub>. Figure 222a shows the thermal expansion data in air for in the temperature range 25  $\leq$  T  $\leq$  1200 °C. The measurements were made with a heating and cooling rate of 3 °C per minute. The expansion of the sample is essentially constant in the isothermal regions as expected and the expansion contraction behavior is reversible. The sample expansion with increasing temperature as shown in Figure 222b and four dilatometric curves indicate very good reproducibility. The change of slope in the thermal expansion curve at a temperature  $\sim$  320 °C can be attributed to the onset of oxygen loss upon heating. This temperature is in good agreement with the temperature at which the total conductivity is observed to decrease in DC conductivity measurements and the onset of the weight loss in TGA experiments.

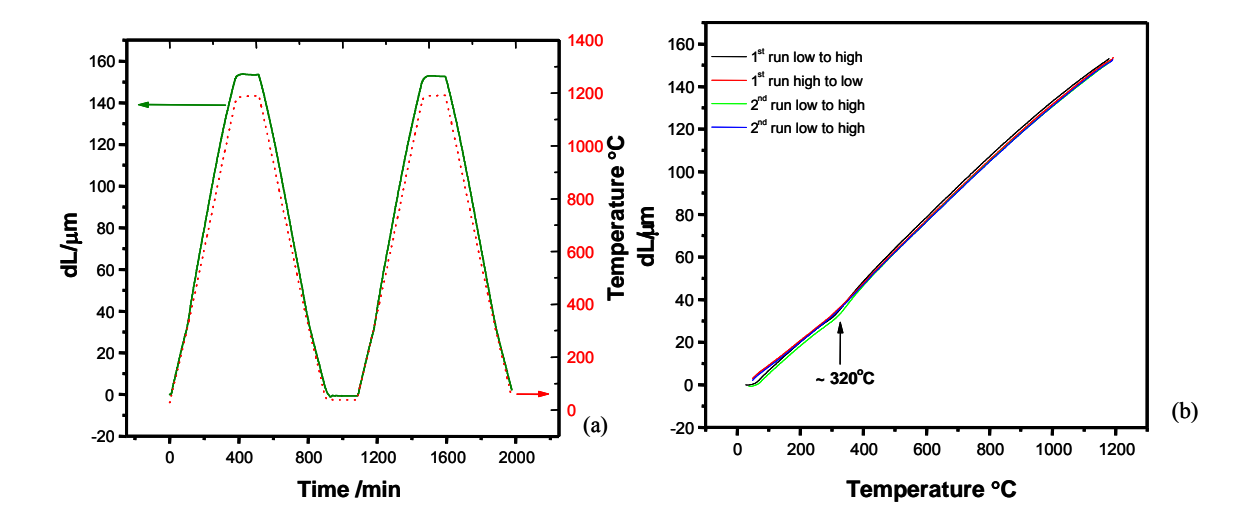


Figure 222. Dilatometry data for  $La_{0.2}Sr_{0.8}Fe_{0.55}Ti_{0.45}O_{3-\delta}$  (a) dL vs. time and (b) dL vs. temperature. The dotted line in a indicates the temperature profile.

Based on these dilatometry results, the average thermal expansion coefficients (TECs) can be calculated as follows:

$$\alpha_i = \underset{T_i \to T_0}{limit} \frac{L_t - L_0}{L(T_t - T_0)} = \frac{1}{L} \frac{dL}{dT}$$

$$\tag{10}$$

where  $\alpha_i$  is the coefficient of linear thermal expansion per degree.  $L_t$  and  $L_0$  are the specimen length at temperature  $T_t$  and  $T_0$  respectively and dL/dT is the slope of the length-temperature curve. The results obtained by taking the derivative of dL/L with respect to temperature are shown in Fig. 223 for the two cycles of heating and cooling (the data has been smoothed to eliminate noise in the derivative). The data are reproducible for the two heating cycles and the two cooling cycles but show some differences below 550 °C presumably due to the differences in the relative rates of oxygen loss or re-oxidation. It is interesting to note that the heating and cooling curves cross over at 320 °C, the temperature at which the kinetic of oxygen insertion or removal become limiting. On heating, the expansion coefficient reaches a maximum value of  $\sim$  12  $\times$  10<sup>-6</sup> K<sup>-1</sup> and then falls to  $\sim$  10  $\times$  10<sup>-6</sup> K<sup>-1</sup> at 550 °C. Above 750 °C, the expansion

coefficient drops smoothly to  $\sim 8 \times 10^{\text{-}6}~\text{K}^{\text{-}1}$  at 1100 °C. The average TEC of  $La_{0.2}Sr_{0.8}Fe_{0.55}Ti_{0.45}O_{3-\delta}$  over the whole temperature range is  $9.3 \pm 1.1 \times 10^{\text{-}6}~\text{K}^{\text{-}1}$ .

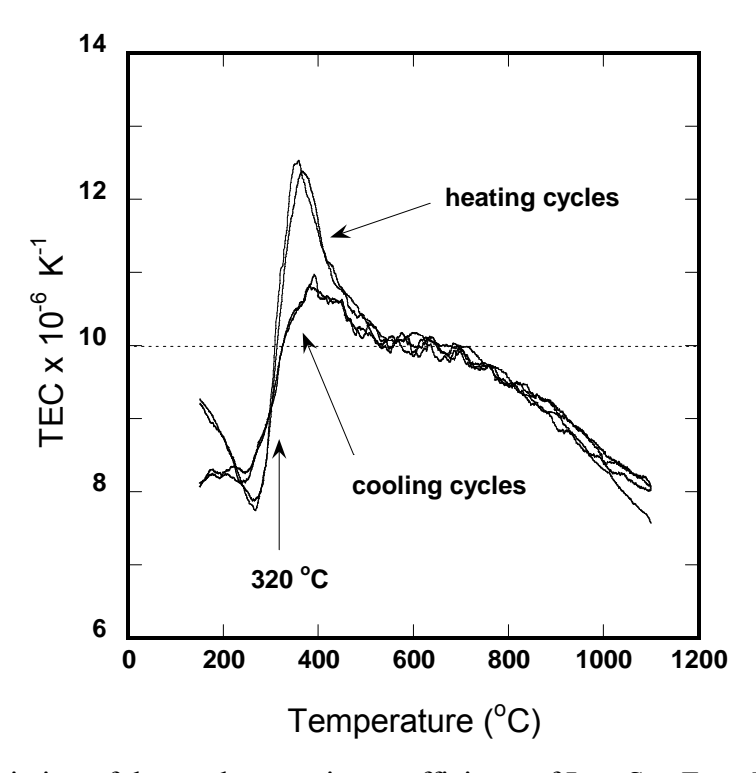


**Figure 223.** The variation of the total expansion coefficients of  $La_{0.2}Sr_{0.8}Fe_{0.55}Ti_{0.45}O_{3-\delta}$  on heating and cooling in air at 3 °C min<sup>-1</sup>.

Chemical expansion data for La<sub>0.2</sub>Sr<sub>0.8</sub>Fe<sub>0.55</sub>Ti<sub>0.45</sub>O<sub>3- $\delta$ </sub> were obtained at 800  $\leq$  T  $\leq$  1000  $^{\circ}$ C and at  $\sim 10^{-4} \leq pO_2 \leq 0.21$  atm in the following way. The sample was first heated to 800  $^{\circ}$ C in air and the total expansion measured. The temperature of the sample was then held at 800  $^{\circ}$ C to reach a constant length. At this point, the gas was switched from air to argon leading to chemical expansion of the sample due to loss of oxygen. The pO<sub>2</sub> was monitored and the conditions maintained until no further change in length occurred. Constant length is obtained after  $\sim 220$  min with a length change of  $\sim 28.43$  µm. After several hours, argon gas is switched back to air in order to determine the degree and the rate of contraction. The amount of contraction agrees well with the expansion but equilibrium is achieved occurs  $\sim 83$  min suggesting that the reaction rate is at least three times faster. The experiment was then repeated at temperatures from to 850 to

1000 °C in 50 °C increments with similar results. Flow rates of 80 ml/min of air and argon (pO<sub>2</sub> =  $2 \times 10^{-4}$  atm) were used in the experiment and the switch time from argon to air is limited by the time it takes to switch out the gas. The present experiment is not designed to extract reliable kinetic data because of the long switch out time. Faster equilibration times and smaller changes in length were observed as the temperature was increased.

The change in the chemical expansion is linear with temperature. The expansion coefficient in air in this temperature range is  $9.6 \times 10^{-6} \, \text{K}^{-1}$  while the value obtained at  $pO_2 = 2 \times 10^{-4} \, \text{atm}$  is smaller at  $7.4 \times 10^{-6} \, \text{K}^{-1}$ . Consequently, the chemical expansion decreases at the temperature increases as shown in Figure 224b.

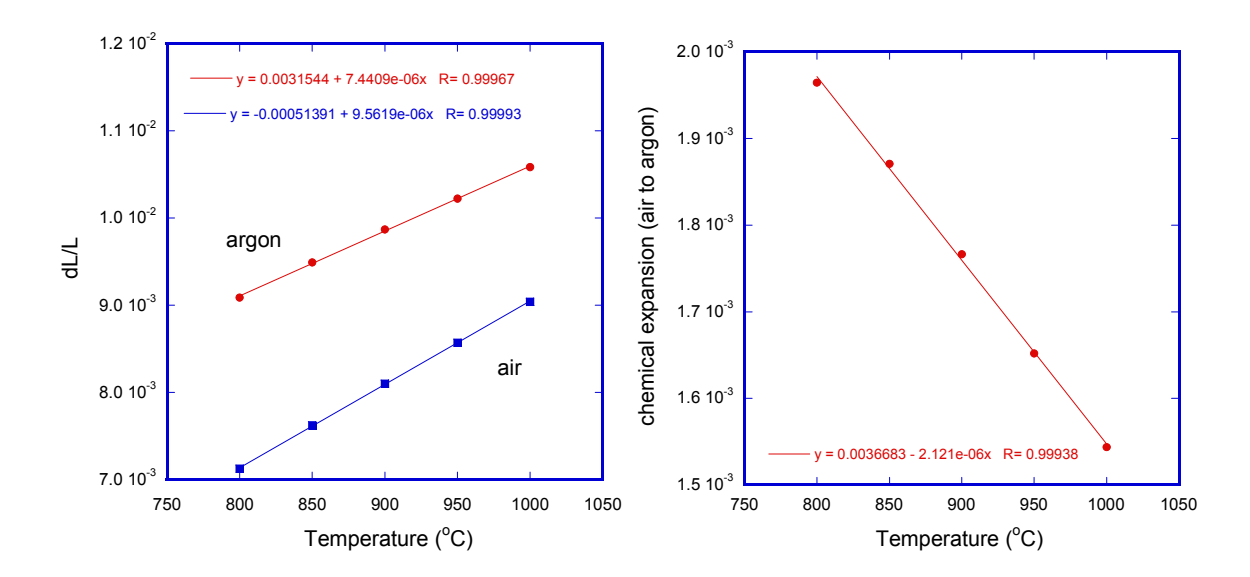


Figure 224 Expansion of La<sub>0.2</sub>Sr<sub>0.8</sub>Fe<sub>0.55</sub>Ti<sub>0.45</sub>O<sub>3- $\delta$ </sub> in air and argon, the difference between the two lines is the chemical expansion on changing from pO<sub>2</sub> = 0.21 atm to 2×10<sup>-4</sup> atm; (b) the change in chemical expansion with temperature.

The chemical expansion as a function of oxygen partial pressure for  $La_{0.2}Sr_{0.8}Fe_{0.55}Ti_{0.45}O_{3-\delta}$  at  $790 \le T \le 956$  °C and at  $\sim 10^{-15} \le pO_2 \le 0.21$  atm are shown in Figure 225. In the high pO<sub>2</sub>

# Chapter 5 - Measurement of Surface Activation ....

region ( $< 10^{-4}$  atm), the results agree well with the data obtained using argon to air switches. The oxygen non-stoichiometries ( $\delta$ ) obtained by solid-state coulometric titration are also shown in shown in Figure 225. Both the expansion and stoichiometry data were normalized with respect to the total change over the same pO<sub>2</sub> interval. The comparison shows several interesting features that were partially visible in the data below pO<sub>2</sub>  $< 10^{-4}$  atm.

The data taken at 790 °C show a close correspondence between the variations of the chemical expansion and stoichiometry with the exception of a small deviation that begins at  $pO_2 \sim 5 \times 10^{-6}$  atm. At  $pO_2 < 10^{-8}$  the correlation between stoichiometry and stoichiometry is again very good. At higher temperatures the deviations become more pronounced and increase with increasing temperature. The chemical expansion initially increases faster and then plateaus at a lower  $pO_2$  than would be predicted by the stoichiometry. The exact appearance of the correlation between stoichiometry and expansion in Figure 225 depends somewhat on the range of  $pO_2$  used in the normalization but the general trend is clear.

The chemical expansion data show pronounced non-equilibrium behavior in the same range of pO<sub>2</sub> as observed previously in conductivity measurements of LSFTO and in similar data for other ferrite compositions.

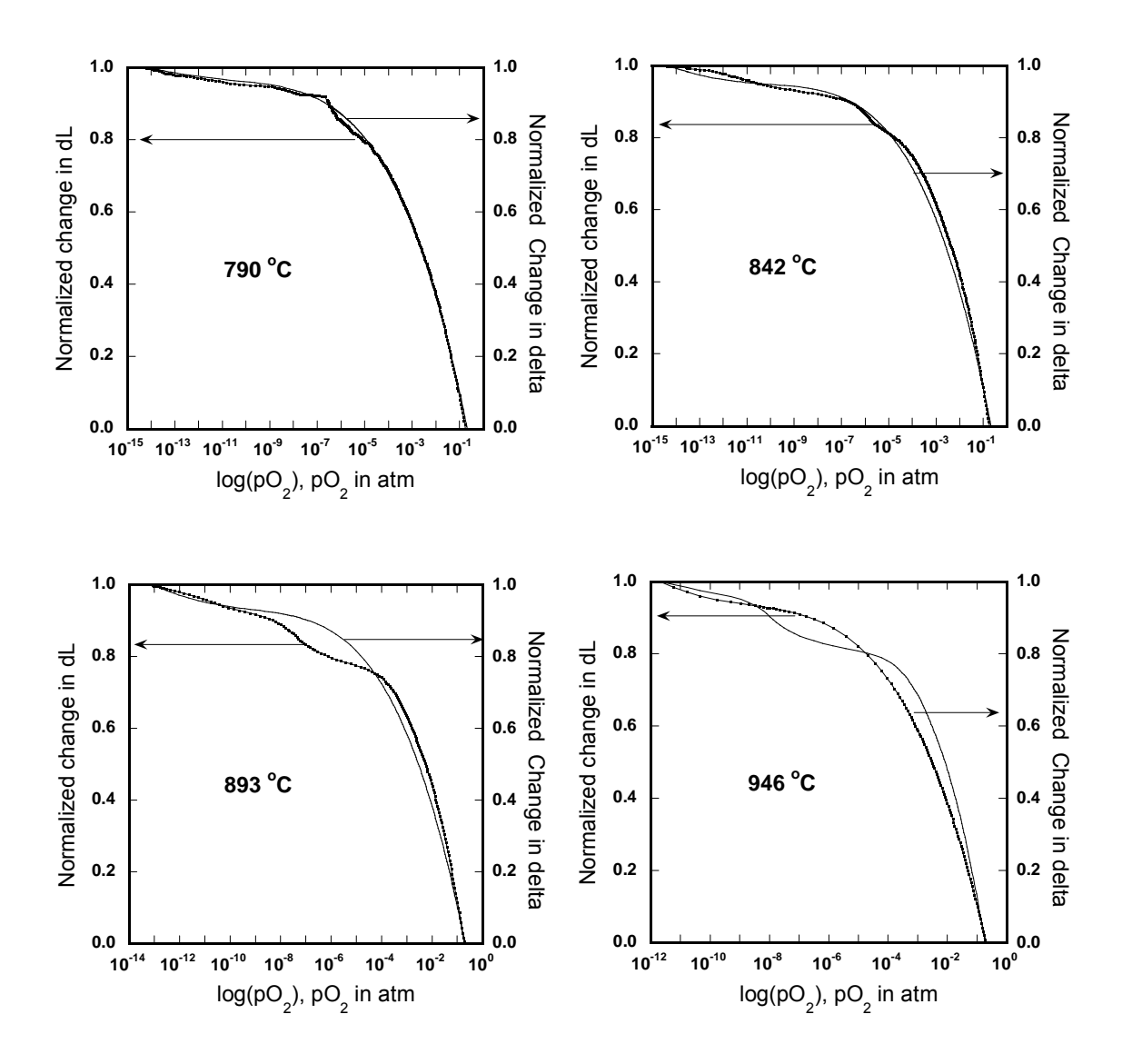


**Figure 225.** The chemical expansion and corresponding stoichiometry variations for  $La_{0.2}Sr_{0.8}Fe_{0.55}Ti_{0.45}O_{3-\delta}$  as a function of  $pO_2$  at four different temperatures. The data are normalized to the total change in each case.

### 5.5.5.6 Neutron Diffraction Measurements

In situ neutron diffraction measurements were made at Argonne National Laboratory in collaboration with Yaping Li, J. Jorgensen, and J. Richardson. Measurements were made at three temperatures and at different oxygen partial pressures. The data were taken as short scans and the fitted using the Reitveld method to obtain the lattice parameter and oxygen occupancy. One set of data taken at 1040 °C is shown in Figure 226. The Figure shows the variation in lattice

parameter (left axis) as a function of time as it responds to changes in oxygen partial pressure (shown on right axis). The lattice parameter increases as the pressure is decreased. At high  $pO_2$  values the response of the sample to changing the  $pO_2$  is fast whereas below  $10^{-4}$  atm the response is very slow. The response rate increase again when the pressure is dropped to  $10^{-14}$  atm. These results mirror the previous stoichiometry and conductivity observations on this material and on other ferrites that all show very slow kinetics in the intermediate pressure range. We understand in part the origin of this effect and more details will be given in the next report. From the fits to the neutron diffraction data, the stoichiometry was determined at each of the  $pO_2$  ranges. The results are shown in Figure 227 where the neutron diffraction values are plotted on top of the stoichiometry data measured by coulometric titration. The neutron diffraction data are in good agreement with the coulometric titration data except in the intermediate pressure region as anticipated from the previous results.

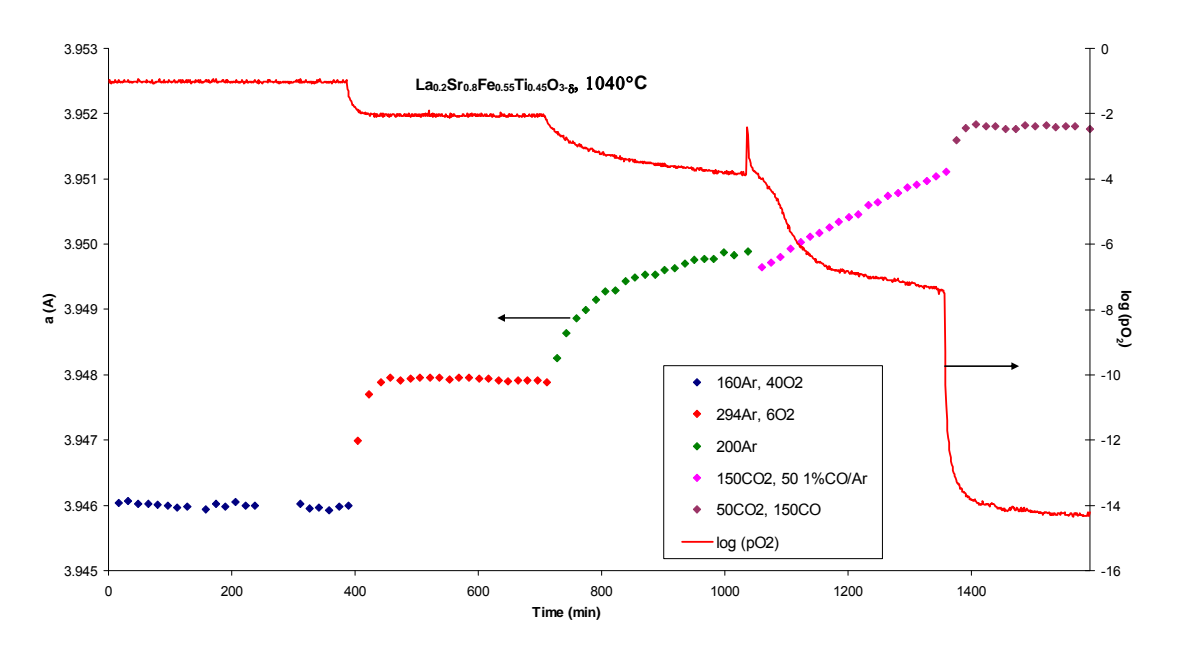


Figure 226. In situ Neutron Diffraction Data for La<sub>0.2</sub>Sr<sub>0.8</sub>Fe<sub>0.55</sub>Ti<sub>0.45</sub>O<sub>3-δ</sub> at 1040 °C

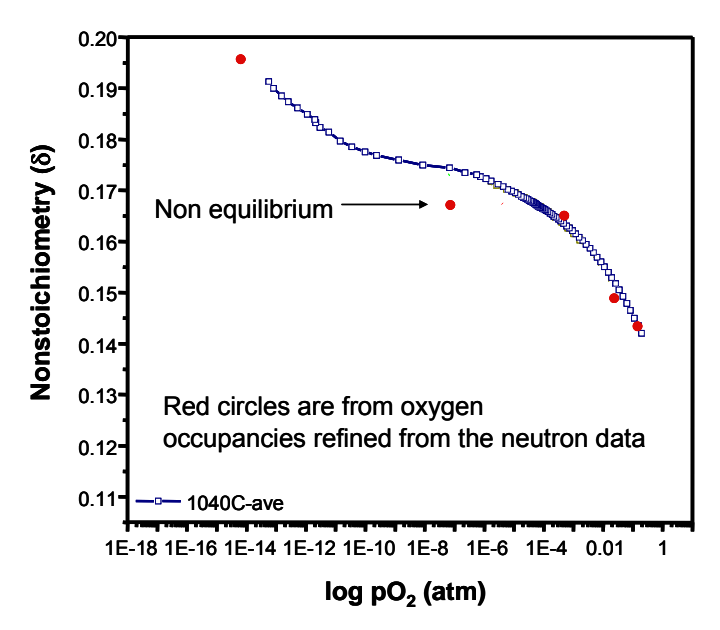


Figure 227. Comparison of the oxygen stoichiometry measure by neutron diffraction and coulometric titration.

# 5.5.5.7 Non-equilibrium behavior

The general observations on non-equilibrium behavior in LSFTO are reviewed in this section.

*Slow kinetics observed in conductivity measurements:* 

The electrical conductivity data  $La_{0.2}Sr_{0.8}Fe_{0.55}Ti_{0.45}O_{3-x}$  at 850 °C is shown in Figure 228 as a typical example. The measurements were made on both decreasing and increasing  $pO_2$  using two different criteria for equilibrium. The conductivity data represented by the open and closed square symbols were obtained when the conductivity change was  $\leq 0.0002~Scm^{-1}min^{-1}$  and when the difference between the values of  $pO_2$  measured by the pump and sensor cells differed by less than a half and order of magnitude at all  $pO_2$  regions. Under these conditions the data taken on increasing and decreasing  $pO_2$  agree suggesting that equilibrium was achieved. These data are compared with the results (open circles) obtained using an equilibrium criterion of  $\leq 0.0005~Scm^{-1}min^{-1}$ . A difference between the measured values of  $pO_2$  by the sensor and pump cells of more than one order of magnitude  $pO_2$  was found under these conditions. The  $pO_2$  differences between sensor and pump are slow to converge due to the slow kinetics and consequently both conductivity and  $pO_2$  difference criteria are needed to ensure that equilibrium is reached.

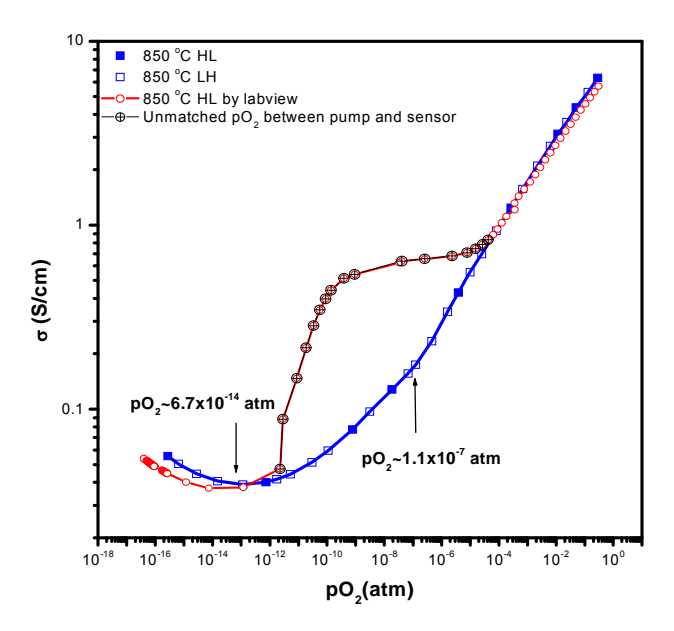


Figure 228. Comparison of two different sets of conductivity data measured for La<sub>0.2</sub>Sr<sub>0.8</sub>Fe<sub>0.55</sub>Ti<sub>0.45</sub>O<sub>3-x</sub> at 850 °C with different criteria for attainment of equilibrium.

The most striking feature of the comparison between the two experiments is the large difference in the conductivity in the range between  $10^{-12} \le pO_2 \le 10^{-5}$  atm indicating that the reduction kinetics are very slow in this region. Similar slow equilibration kinetics have been observed in other ferrite perovskites including SrFeO<sub>3-x</sub> [10], La<sub>1-x</sub>Sr<sub>x</sub>FeO<sub>3-y</sub> [6,14,15,16], La<sub>0.2</sub>Sr<sub>0.8</sub>Fe<sub>0.8</sub>Cr<sub>0.2</sub>O<sub>3-x</sub> [2, 3] LaSr<sub>2</sub>Fe<sub>3-y</sub>Cr<sub>y</sub>O<sub>8+x</sub> [17], and Ti-substituted La<sub>1-x</sub>Sr<sub>x</sub>FeO<sub>3-y</sub> (x = 0.5-0.7) [18].

*Slow kinetics observed in dilatometry measurements:* 

The stoichiometry and thermal expansion data for La<sub>0.2</sub>Sr<sub>0.8</sub>Fe<sub>0.55</sub>Ti<sub>0.45</sub>O<sub>3-δ</sub> are shown in Figure 229. At 790 °C, a linear relation between the chemical expansion and stoichiometry is observed. At higher temperatures deviations become more pronounced and increase with increasing temperature. The chemical expansion initially increases faster and then plateaus at a lower pO<sub>2</sub> than would be predicted by the stoichiometry. The non equilibrium behavior observed in the chemical expansion data parallels that observed in the conductivity and suggests the occurrence of microscopic phase segregation on reduction.

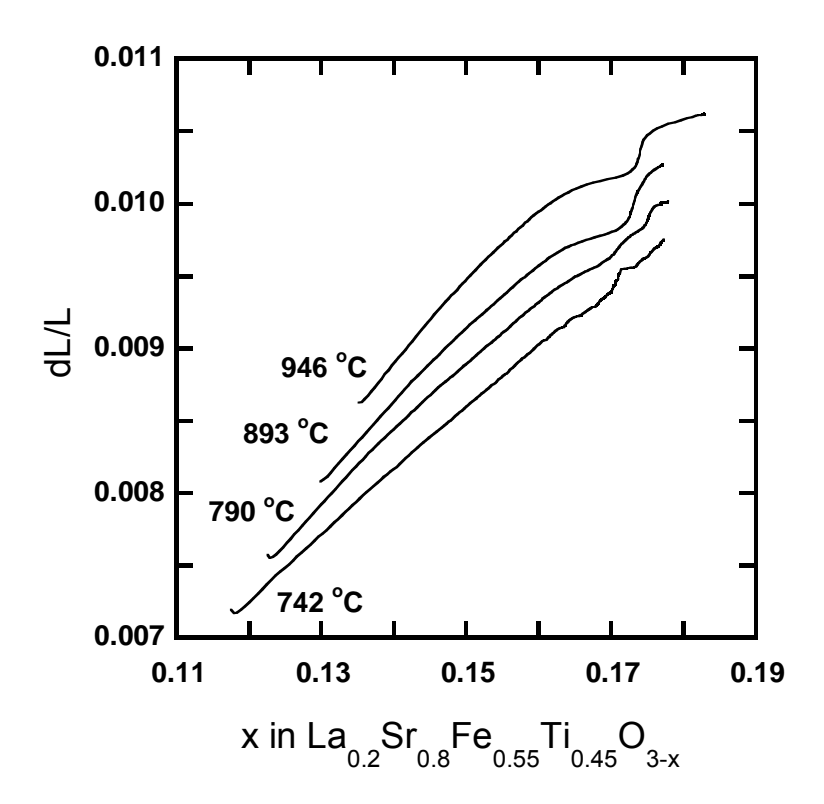


Figure 229. The dependence of the chemical expansion on non - stoichiometry in  $La_{0.2}Sr_{0.8}Fe_{0.55}Ti_{0.45}O_{3-x}$  (from reference 6).

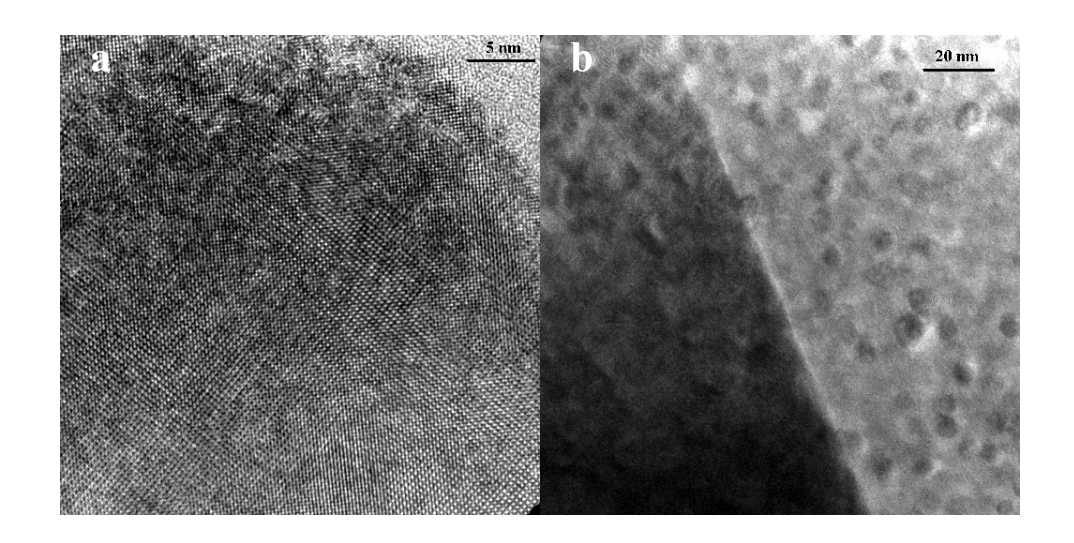
#### Micro-structural Studies:

Samples of  $La_{0.2}Sr_{0.8}Fe_{0.55}Ti_{0.45}O_{3-\delta}$  were quenched in air from 900 °C and different oxygen partial pressures  $pO_2 = \sim 1.3 \times 10^{-4}$ ,  $1.1 \times 10^{-7}$ ,  $1.2 \times 10^{-10}$ ,  $6.7 \times 10^{-14}$  atm. All peaks in the X-ray powder diffraction patterns of the air quenched and non-quenched samples were indexed as corresponding to a cubic perovskite. No evidence is found of a phase transition in the whole region of  $pO_2$  though the lattice parameter increases with the degree of reduction as expected.

Two samples were examined by transmission electron microscopy (#2, #5). For sample #2 TEM observations indicate that there are two kinds of crystal grains existing in the sample. The major phase in the sample has well-crystallized cubic  $La_{0.2}Sr_{0.8}Fe_{0.55}Ti_{0.45}O_{3-\delta}$  grains (about 90 %) (Figure 230a) but a small number of grains (10%) are of the cubic matrix containing pure Fe nanoparticles and a Fe-rich amorphous phase.

The compositions of the amorphous regions were determined by X-ray analysis and the iron nano particles by analysis of the lattice fringes. The iron nanoparticles were ~ 5nm in size The Moiré fringe covered areas in Figure 230 c are Fe nano-particles overlapped with the cubic

LSFTO crystal matrix. TEM observation of sample #5 also showed two distinct microstructures, one corresponding to well-crystallized cubic LSFTO (about 90 % of the whole sample) and the second area (~ 10%) containing an amorphous phase with a higher Fe concentration. No nanoparticles were observed in this sample.



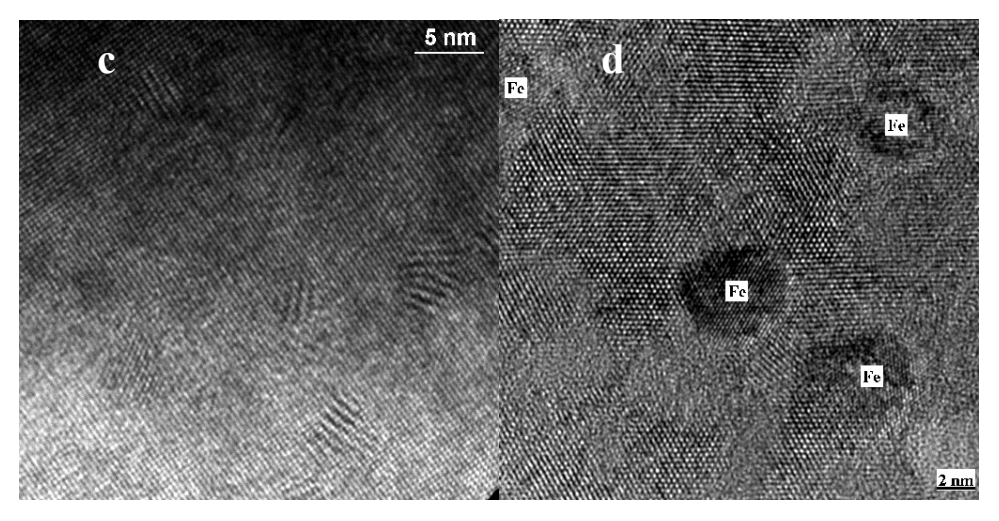


Figure 230. (a) a high resolution image of a defect free LSFTO grain, (b-d) three different magnifications a grain showing the presence of Fe nanoparticles and amorphous iron rich regions.LaSrFeTiO Bulk Sample 0285545#2

# Comparison with LSFO

The reduction behavior of LSFTO is complex because of the number of components and the large number of possible decomposition pathways. The compound La<sub>0.5</sub>Sr<sub>0.5</sub>FeO<sub>3</sub> is simpler but shows the same general behavior in the conductivity on reduction. A preliminary study of the

reduction behavior in hydrogen indicated that the reduction was slow. After 24 h of treatment in flowing 5% H<sub>2</sub> at 950 °C, the X-ray diffraction data indicated partial decomposition to a mixture of the perovskite phase, LaSrFeO<sub>4</sub> and Fe. After a further 24 h under the same conditions, the X-ray data indicate complete decomposition. It is interesting to note that similar results have been obtained in the deposition of perovskite thin films by pulsed laser deposition using a target of composition La<sub>0.5</sub>Sr<sub>0.5</sub>FeO<sub>3</sub> [19]. Under oxidizing conditions the films had the perovskite structure but under reducing conditions were found to contain iron nanowires and LaSrFeO<sub>4</sub>.

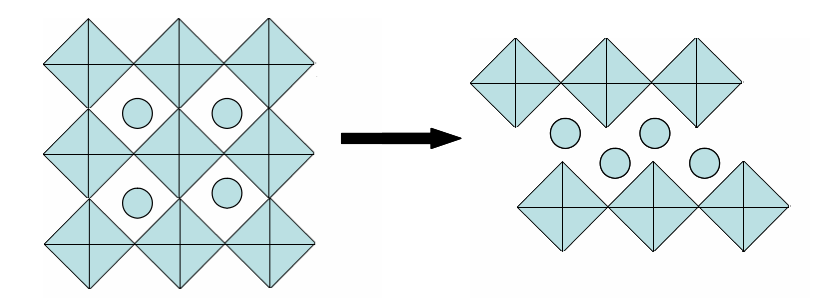
#### General Comments

The reduction behavior for LSFTO and LSFO is complex and proceeds with the introduction secondary phases. Cation rearrangements are responsible for the slow kinetic behavior. What is less clear is whether for a given set of reaction conditions, the behavior represents a slow approach to equilibrium or the formation of a metastable intermediate. In other systems, both kinds of behavior are observed. For example, in the reduction-SrFeO<sub>3-x</sub> at a temperature and pO<sub>2</sub> in the two phase region equilibrium is slow because of the kinetics of nucleation and growth of the brownmillerite structure [20]. The reduction behavior of LaCoO<sub>3</sub> was investigated by reaction with zirconium metal in sealed tubes at 400 °C. Two discrete vacancy ordered phases were observed, with compositions namely LaCoO<sub>2.5</sub> and LaCoO<sub>2.67</sub>; LaCoO<sub>2.5</sub> reoxidizes via LaCoO<sub>2.67</sub> to LaCoO<sub>3</sub>. Both oxygen deficient phases are metastable, and undergo irreversible decomposition to CoO and the Ruddlesden–Popper type phases La<sub>2</sub>CoO<sub>4</sub> and La<sub>3</sub>Co<sub>3</sub>O<sub>10</sub> when heated above 650 °C in an inert atmosphere [21].

Considering all of the experimental data, the preferred kinetic pathway to reduction when the vacancy concentration corresponds to the formation of significant concentrations of  $Fe^{2+}$  is via the formation of a Ruddlesden –Popper phases as indicated below for the reduction of  $La_{0.5}Sr_{0.5}FeO_{2.75}$ .

$$La_{0.5}Sr_{0.5}FeO_{2.75} \, \rightarrow \, La_{0.5}Sr_{0.5}FeO_{2.75-\delta} \, \rightarrow \, (1-\delta/3)La_{0.5}Sr_{0.5}FeO_{2.75-\delta} \, + \, \delta/3LaSrFeO_4 \, + \, \delta/3FeO_{2.75-\delta} \, + \, \delta/3LaSrFeO_4 \, + \, \delta/3FeO_4 \, + \, \delta/3FeO_4$$

Microscopically this may be viewed as beginning with the introduction of a planar defect as shown in the scheme below. Such defects have been observed in partially reduced (La,Sr)FeO<sub>3-x</sub> by high resolution electron microscopy [22].



In the more complex composition, LSFTO, iron or iron rich phases are observed locally but we have found no evidence for the existence of presence of a Ruddlesden – Popper phase.

Finally, we note that both in stoichiometry and conductivity measurements in sealed cells, long equilibration times lead to equilibrium in the sense that measurements on increasing and decreasing  $pO_2$  agree, indicating that at least under these conditions phase separation on reduction is kinetically and not thermodynamically controlled.

### 5.6 CONCLUSIONS

At UH, we investigated the  $pO_2$  and temperature dependence of the conductivity, non-stoichiometry and thermal-expansion behavior of compositions with increasing complexity of substitution on the perovskite A and B sites. The most detailed measurements o the thermodynamics and the ionic and electronic transport were made for La<sub>0.5</sub>Sr<sub>0.5</sub>FeO<sub>3-x</sub>, La<sub>0.2</sub>Sr<sub>0.8</sub>Fe<sub>0.8</sub>Cr<sub>0.2</sub>O<sub>3-x</sub>, and La<sub>0.2</sub>Sr<sub>0.8</sub>Fe<sub>0.55</sub>Ti<sub>0.45</sub>O<sub>3-x</sub>.

These and other recent studies of ferrites with the perovskite structure show anomalous behavior at low oxygen partial pressures (<10<sup>-5</sup> atm). The anomalies are due to non-equilibrium effects and can be avoided by using very strict criteria for the attainment of equilibrium. The slowness of the oxygen equilibration kinetics arises from two different mechanisms. In the first, a two phase region occurs between an oxygen vacancy ordered phase such as brownmillerite SrFeO<sub>2.5</sub> and perovskite SrFeO<sub>3-x</sub>. The slow kinetics are associated with crossing the two phase region. The width of the miscibility gap decreases with increasing temperature and consequently the effect is less pronounced at higher temperature. Both SrFeO<sub>3-x</sub> and La<sub>0.2</sub>Sr<sub>0.8</sub>Fe<sub>0.8</sub>Cr<sub>0.2</sub>O<sub>3-x</sub> show this behavior.

In contrast, in La<sub>0.2</sub>Sr<sub>0.8</sub>Fe<sub>0.55</sub>Ti<sub>0.45</sub>O<sub>3-x</sub> deviations between equilibrium and non-equilibrium behavior become larger with increasing temperature suggesting that cation rearrangements or phase separation must take place. We conclude that the preferred kinetic pathway to reduction of

perovskite ferrites when the vacancy concentration corresponds to the formation of significant concentrations of Fe<sup>2+</sup> is via the formation of a Ruddlesden –Popper (RP) phases as clearly observed in the case of La<sub>0.5</sub>Sr<sub>0.5</sub>FeO<sub>3-x</sub> where LaSrFeO<sub>4</sub> is found together with Fe. In more complex compositions, such as LSFTO, iron or iron rich phases are observed locally with no evidence for the presence of discrete RP phase.

# 5.7 LIST OF ACRONYMS AND ABBREVIATIONS

SrE<sub>2</sub>O

CEO

SFO	SrFeO <sub>3-x</sub>	
LSFO	$La_{0.2}Sr_{0.8}FeO_{3-x}$	
LSFO	$La_{0.5}Sr_{0.5}FeO_{3-x}$	
LSFCO	$La_{0.2}Sr_{0.8}Fe_{0.8}Cr_{0.2}O_{3-x}$	
LSFGO	$La_{0.5}Sr_{0.5}Fe_{0.8}Ga_{0.2}O_{3-x}$	
$LSFCoOLa_{0.6}Sr_{0.4}Fe_{0.8}Co_{0.2}O_{3-x}$		
LSFTO	$La_{0.2}Sr_{0.8}Fe_{0.55}Ti_{0.45}O_{3-x}$	
SHS	Self Propagating High Temperature Synthesis	
YSZ	yttria stabilized zirconia	
XRD	X-ray diffraction	
CIP	cold isostatic pressing	
ECR	electrical conductivity relaxation	
<b>EMPA</b>	electron-probe microanalysis	
BSE	back scattered electron imaging	
TGA	thermogravimetric analysis	
TEC	thermal expansion coefficient	
IEDP	isotope exchange and depth profiling	
SIMS	secondary Ion Mass Spectroscopy	
RP	Ruddlesden –Popper	

# 5.8 PUBLICATIONS (for Chapter 5)

- 1. Kim, S.; Wang, S.; Chen, X.; Yang, Y. L.; Wu, N.; Ignatiev, A.; Jacobson, A.J.; Abeles, B., "Oxygen Surface Exchange in Mixed Electronic Ionic Conductors: Application to La<sub>0.5</sub>Sr<sub>0.5</sub>Fe<sub>0.8</sub>Ga<sub>0.2</sub>O<sub>3</sub>," *J. Electrochem. Soc.*, 2000, 147, 2398-2406.
- 2. Jacobson, A.J., "Guest Viewpoint: Ion Transport Ceramic Membrane Reactors," *Membrane Quarterly*, 1999, *14*, 8-10.
- 3. Chen, X.; Wang, S.; Yang, Y. L.; Smith, L.; Wu, N. J.; Jacobson, A. J.; Ignatiev, I., "A Study of the Oxygen Surface Exchange Coefficient on La<sub>0.5</sub>Sr<sub>0.5</sub>CoO<sub>3-x</sub> Thin Films," *Mat. Res. Soc. Symp. Proc.*, 2000, 606, 275.

- 4. Zhang, K.; Miranova, M.; Yang, Y. L.; Jacobson, A. J.; Salama, K., "Effects of microstructure on the electrical conductivity of SrCo<sub>0.8</sub>Fe<sub>0.2</sub>O<sub>3-x</sub>," *Mater. Res. Symp. Ser.* 2000, *575*, 315-320.
- 5. Yoo, J.; Verma, A.; Jacobson, A.J., "Electrical Conductivity Measurements of La<sub>0.2</sub>Sr<sub>0.8</sub>Cr<sub>0.2</sub>Fe<sub>0.8</sub>O<sub>3-x</sub>", *Proc. Electrochem. Soc.* 2002 *PV2001-28*, 27.
- 6. Wang, S.; van der Heide, P. A. W.; Chavez, C.; Jacobson, A. J.; Adler, S. B. "An Electrical Conductivity Relaxation Study of La<sub>0.6</sub>Sr<sub>0.4</sub>Fe<sub>0.8</sub>Co<sub>0.2</sub>O<sub>3-x</sub>" *Solid State Ionics* 2003 *156* 201-208.
- 7. Yoo, J.; Jacobson, A. J., "A Study of the Oxygen Transport Kinetics in SrFeO<sub>3-x</sub>," *Mat. Res. Soc. Symp. Proc.* 2003 *756* 105-110.
- 8. Yoo, J.; Jacobson, A. J., "Determination of the Oxygen Non-stoichiometry of SrFeO<sub>3-x</sub>," *Proc. Electrochem. Soc.* 2003 *PV2002-26* 354.
- 9. Majkic, G.; Jacobson, A. J.; Salama, K. "Stress-induced diffusion and defect chemistry of La<sub>0.2</sub>Sr<sub>0.8</sub>Fe<sub>0.8</sub>Cr<sub>0.2</sub>O<sub>3-8</sub> Part 3. Defect-chemistry-based modeling," *Solid State Ionics* 2004 *167(3-4)* 255-262.
- 10. Yoo, Jiho; Park, Chan Young; Jacobson, Allan J.. Determination of the equilibrium oxygen non-stoichiometry and the electrical conductivity of La<sub>0.5</sub>Sr<sub>0.5</sub>FeO<sub>3-x</sub>," *Solid State Ionics* 2004 *175*(*1-4*) 55-58.
- 11. Yoo, J.; Verma, A; Wang, S.; Jacobson, A. J. "Oxygen transport kinetics in SrFeO<sub>3-x</sub>, La<sub>0.5</sub>Sr<sub>0.5</sub>FeO<sub>3-x</sub>, and La<sub>0.2</sub>Sr<sub>0.8</sub>Cr<sub>0.2</sub>Fe<sub>0.8</sub>O<sub>3-x</sub> measured by electrical conductivity relaxation," *J. Electrochem. Soc.* 2005 *152(3)* A497-A505.
- 12. Mims, C. A.; Bayani, N.; Jacobson, A. J.; van der Heide, P. A. W., "Modes of surface exchange in La<sub>0.2</sub>Sr<sub>0.8</sub>Cr<sub>0.2</sub>Fe<sub>0.8</sub>O<sub>3-x</sub>," *Solid State Ionics* 2005 *176(3-4)* 319-323.
- 13. La<sub>0.5</sub>Sr<sub>0.5</sub>FeO<sub>3-x</sub>, and La<sub>0.2</sub>Sr<sub>0.8</sub>Cr<sub>0.2</sub>Fe<sub>0.8</sub>O<sub>3-x</sub> measured by electrical conductivity relaxation." J. Electrochem. Soc. 2005 *152* A497-A505.
- 14. Park, C. Y.; Jacobson, A. J. "Electrical Conductivity and Oxygen Non-stoichiometry of La<sub>0.2</sub>Sr<sub>0.8</sub>Fe<sub>0.55</sub>Ti<sub>0.45</sub>O<sub>3-8</sub>," J. Electrochem. Soc. 2005 *152* J65-J73.
- 15. Park, C. Y.; Jacobson, A. J. "Thermal and chemical expansion properties of La<sub>0.2</sub>Sr<sub>0.8</sub>Fe<sub>0.55</sub>Ti<sub>0.45</sub>O<sub>3-x</sub>," Solid State Ionics 2005 *176/35-36* 2671-2676.
- 16. Park, C. Y.; Huang, D. X.; Jacobson, A. J.; Hu, L.; Mims, C. A. "Transport properties and phase stability of mixed conducting oxide membranes" Solid State Ionics 2006 *177* 2227-2233.

#### 5.9 PRESENTATIONS

- 1. "Mixed Conducting Oxide Ceramics" Allan J. Jacobson, 2nd International Conference on Composites, Lake Louise, Canada, Nov 1st 1999. (invited)
- 2. "Oxygen Transport Kinetics in the Mixed Conductor La<sub>0.5</sub>Sr<sub>0.5</sub>Fe<sub>0.8</sub>Ga<sub>0.2</sub>O<sub>3-x</sub>." A. J. Jacobson, S. Wang, J. Yoo, Y. L. Yang, and B. Abeles, American Ceramic Society, May 1, 2000. (invited)
- 3. "Mixed Conducting Oxide Electrode and Membranes." A. J. Jacobson, Gordon Conference on High Temperature Chemistry, July 23, 2000. (invited)
- 4. "Ion Transport Ceramic Membrane Reactors," A. J. Jacobson, SSI2001, July 10<sup>th</sup>, 2001. (plenary)
- 5. "Materials for Energy Conversion and Storage," A. J. Jacobson, NSF Workshop on the Future of Solid State Chemistry, UC Davis, Oct. 10<sup>th</sup>, 2001. (invited)
- 6. "An electrical conductivity relaxation study of La<sub>0.6</sub>Sr<sub>0.4</sub>Fe<sub>0.8</sub>Co<sub>0.2</sub>O<sub>3-δ</sub>," S. Wang, C. Chavez and A. J. Jacobson, SSI2001, July 10<sup>th</sup>, 2001.
- 7. "The Temperature and Oxygen Partial Pressure Dependence of the Electrical Conductivity of La<sub>0.2</sub>Sr<sub>0.8</sub>Cr<sub>0.2</sub>Fe<sub>0.8</sub>O<sub>3-δ</sub>," J. Yoo, A. Verma, and A. J. Jacobson, Electrochem. Soc. Mtg., Sept 2001 (invited).
- 8. "Oxide catalysts and electrocatalysts," A. J. Jacobson, Shell Chemicals, Houston, Oct 24<sup>th</sup> 2001. (invited).
- 9. "Oxygen Ion Transport in Mixed Conducting Oxide Thin Films," A. J. Jacobson, American Ceramic Society Meeting, April 30<sup>th</sup> 2002 (invited).
- "Oxygen Non-Stoichiometry And Transport Properties Of Strontium Iron Oxide," <u>J. Yoo</u>,
   A. J. Jacobson, Mat. Res. Soc. Symp. Dec. 2<sup>nd</sup> 2002.
- 11. "IEDP Studies of Substituted Lanthanum Ferrites in Reducing and Oxidizing Atmospheres," N. Bayani, P. van der Heide, A. J. Jacobson, <u>C. A. Mims</u>, Mat. Res. Soc. Symp. Dec. 4<sup>nd</sup> 2002.
- 12. "Ion Transport Membrane Reactors for Syn Gas Generation" A. J. Jacobson, Gordon Research Conference on Hydrocarbon Resources, Ventura, Jan. 15<sup>th</sup> 2003 (invited).
- 13. "Ion Transport Membrane Reactors for Oxygen Separation and Syn Gas Generation" A. J. Jacobson, University of Washington, Feb 10<sup>th</sup> 2003 (invited).
- 14. "Oxygen Transport Kinetics In Mixed Ionic And Electronic Conducting Membrane Materials," A. J. Jacobson, S. Wang and J. Yoo, American Chemical Society Mtg, New Orleans, Mar 25<sup>th</sup> 2003 (invited).
- 15. "Oxygen Non-stoichiometry, Electrical Conductivity, and Oxygen Transport in La<sub>1</sub>. <sub>x</sub>Sr<sub>x</sub>FeO<sub>3-x</sub> (x=0.5, 1.0)," J.Yoo, C.-Y. Park, and A.J. Jacobson, SSI 14 June 24, 2003, Monterey California.
- 16. "Oxygen Transport Kinetics in Mixed Ionic and Electronic Conducting Membrane Materials," J. Yoo, C.Y. Park, L.J. Hu, N. Bayani, A. J. Jacobson, <u>C. A. Mims</u>, SSI 14 June 24, 2003, Monterey California.

- 17. "Oxygen Non-stoichiometry and Transport Kinetics of La<sub>1-x</sub>Sr<sub>x</sub>FeO<sub>3-x</sub> (x = 0.5, 1.0) Oxides" J. Yoo, C.-Y. Park, A. J. Jacobson, C. A. Mims, ASM International, Pittsburgh, Oct. 15<sup>th</sup>, 2003 (invited).
- 18. "Oxygen Non-stoichiometry and Oxygen Transport Kinetics of ABO<sub>3-x</sub> and A<sub>2</sub>BO<sub>4+x</sub> Mixed Conductors," A. J. Jacobson, C. A. Mims, American Ceramic Society Annual Meeting, Indianapolis, April 20<sup>th</sup>, 2004 (invited).
- 19. "Mixed Electronic Ionic Conductors: Ion transport membrane reactors for oxygen separation and syngas generation," A.J. Jacobson, Barcelona, Spain, July 5 2004 (invited).
- 20. "Transition Metal Oxides Bulk and Surface Chemistry: Ion transport membrane reactors for oxygen separation and syngas generation," A. J. Jacobson and C. A. Mims, Gordon Research Conference on Solid State Chemistry, July 25-29, 2004 (invited).
- 21. "Electrical Conductivity and Oxygen Non-stoichiometry of La<sub>0.2</sub>Sr<sub>0.8</sub>Fe<sub>0.55</sub>Ti<sub>0.45</sub>O<sub>3-8</sub>." C. Y. Park and A. J. Jacobson, Electrochemical Society Meeting, San Antonio, May 9-13 2004 (invited).
- 22. "Applications of Mixed Conducting Oxides in Solid Oxide Fuel Cells and Ion Transport Membranes: Oxygen Non-stoichiometry and Oxygen Transport Kinetics." A. J. Jacobson, Department of Chemical Engineering, University of Houston, March 25, 2005 (invited).
- 23. "Isotope Transient Studies of La<sub>0.2</sub>Sr<sub>0.8</sub>Fe<sub>0.8</sub>Cr<sub>0.2</sub>O<sub>3-x</sub> Oxygen Transport Membranes under High and Low Oxygen GradientsC.A. Mims, L. J. Hu and Allan J. Jacobson Solid State Ionics-15, Baden- Baden Germany, July 20, 2005. "Transport Properties and Phase Stability of Mixed Conducting Oxide." A. J. Jacobson and C. A. Mims Solid State Ionics-15, Baden-Baden Germany, July 20, 2005. (invited).

# 5.10. REFERENCES (for Chapter 5)

- 1 H. J. M. Bouwmeester, A. J. Burggraaf, "The CRC Handbook of Solid State Electrochemistry", Eds. P. J. Gellings and H. J. M. Bouwmeester, CRC Press, Boca Raton, (1997) 481.
- 2 J. Yoo, A. Verma, and A. J. Jacobson, Proc. Electrochem. Soc. PV2001-28 (2002) 27.
- 3 J. Yoo, A. Verma, S. Wang, and A. J. Jacobson, J. Electrochem. Soc. 152 (2005) A497.
- 4 C. Y. Park and A. J. Jacobson, J. Electrochem. Soc. 152 (2005) J65.
- 5 C. Y. Park and A. J. Jacobson, Solid State Ionics 176/35-36 (2005) 2671.
- 6 J. Yoo, C. Y. Park and A. J. Jacobson, Solid State Ionics 175(1-4) (2004) 55.
- 7 J. H. Park and R. N. Blumenthal, J. Electrochem. Soc., 136, (1989) 2867.
- 8 J. Mizusaki, M. Okayasu, S. Yamauchi, K. Fueki, J. Solid State Chem., 99 (1992) 166.
- 9 Y. Takeda, K. Kanno, T. Takada, O. Yamamoto, M. Takano, N. Nakayama, Y.Bando, J. Solid State Chem., 63 (1986) 237.

- 10 V. L. Kozhevnikov, I. A. Leonidov, M. V. Patrakeev, E. B. Mitberg, and K. R. Poeppelmeier, J. Solid State Chem. 158 (2001) 320
- 11 E. Bucher, A. Benisek, W. Sitte, Solid State Ionics, 157 (2003), 39.
- 12 N. Cusak and P. Kendall, Proc. Phys. Soc. (London), 72 (1958) 898.
- 13 J. Mizusaki et al., J. Am. Ceram. Soc. 66, (1983), 247.
- 14 I. A. Leonidov, V. L. Kozhevnikov, M. V. Patrakeev, E. B. Mitberg, and K. R. Poeppelmeier, Solid State Ionics 144 (2001) 361.
- 15 M. V. Patrakeev, J. A. Bahteeva, E. B. Mitberg, I. A. Leonidov, V. L. Kozhevnikov, and K. R. Poeppelmeier, J. Solid State Chem. 172 (2003) 219.
- 16 M. V. Patrakeev, I. A. Leonidov, V. L. Kozhevnikov, K. R. Poeppelmeier, J. Solid State Chem. 178 (2005) 921.
- 17 V. L. Kozhevnikov, I. A. Leonidov, J. A. Bahteeva, M. V. Patrakeev, E. B. Mitberg, and K. R. Poeppelmeier, Chem. Mater. 16 (2004) 5014.
- 18 E. V. Tsipis, M. V. Patrakeev, V. V. Kharton, A. A. Yaremchenko, G. C. Mather, A. L. Shaula, I. A. Leonidov, V. L. Kozhevnikov, and J. R. Frade, Solid State Sciences 7 (2005) 355.
- 19 L. Mohaddes-Ardabili, H. Zheng, S. B. Ogale, B. Hannoyer, W. Tian, J. Wang, S. E. Lofland, S. R. Shinde, T. Zhao, Y. Jia, L. Salamanca-Riba, D. G. Schlom, M. Wuttig, and R. Ramesh, Nature Materials 3 (2004) 533.
- 20 L. M. Liu, T. H. Lee, L.Qiu, Y.L. Yang, and A.J. Jacobson, Mater. Res. Bull., 31 (1996) 29.
- 21 O. H. Hansteen, H. Fjellvåg and B. C. Hauback, J. Mater. Chem. 8 (1998) 2081.
- 22 R. F. Klie and N. D. Browing, Microsc. Microanal. 8 (2002) 475.